NASA SP-459

ANTARCTIC SEA ICE, 1973–1976:
SATELLITE PASSIVE-MICROWAVE OBSERVATIONS

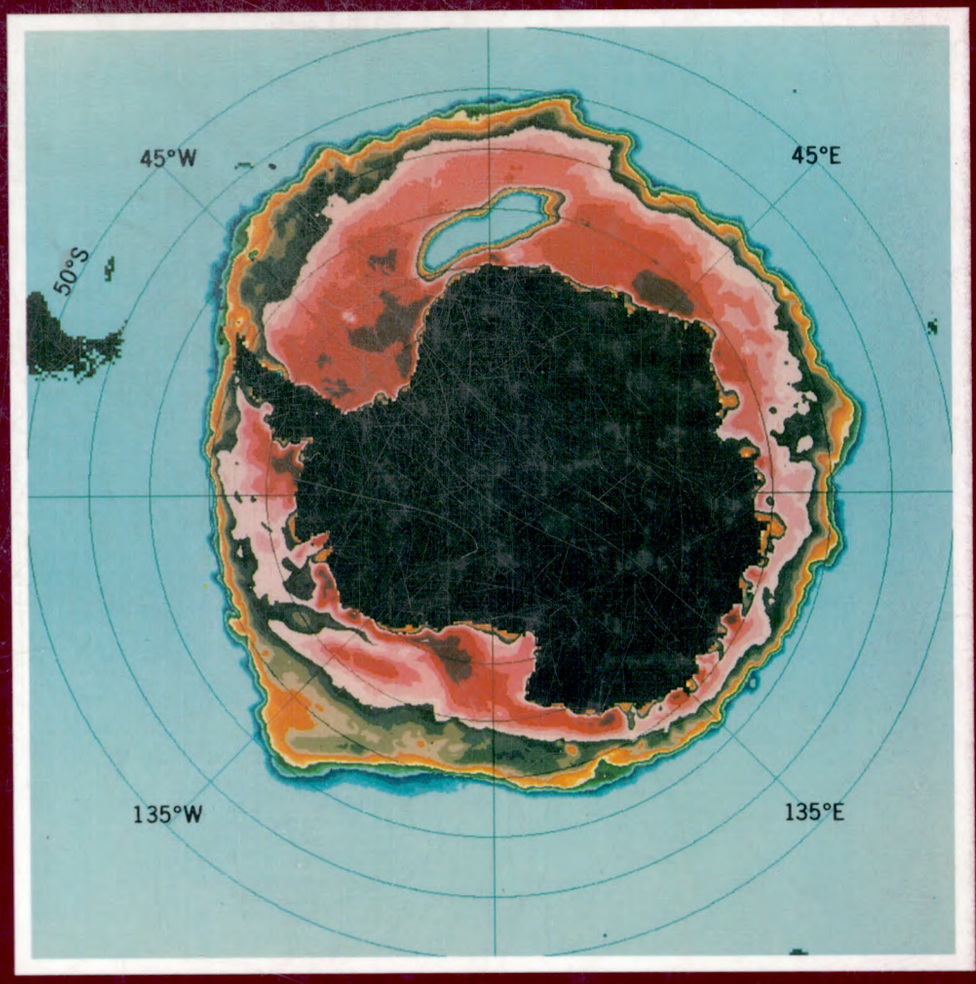

NATIONAL AERONAUTICS AND SPACE ADMINISTRATION

ANTARCTIC SEA ICE, 1973-1976:
SATELLITE PASSIVE-MICROWAVE OBSERVATIONS

Library of Congress Cataloging in Publication Data
Main entry under title:

Antarctic sea ice, 1973–1976 satellite passive microwave observations.

(NASA SP; 459)
Bibliography: p.
Includes index.
Supt. of Docs. no.: NAS 1.21:459
1. Sea ice—Antarctic regions—Remote sensing. I. Zwally, H. Jay. II. Series.
GB2597.A47 1983 551.3'42 83-600167

For sale by the Superintendent of Documents, U.S. Government Printing Office
Washington, D.C. 20402

NASA SP-459

ANTARCTIC SEA ICE, 1973-1976:
SATELLITE PASSIVE-MICROWAVE OBSERVATIONS

H. Jay Zwally, Josefino C. Comiso, and Claire L. Parkinson
Goddard Laboratory for Atmospheric Sciences
Goddard Space Flight Center
Greenbelt, Maryland 20771

William J. Campbell
U.S. Geological Survey and
University of Puget Sound
Takoma, Washington 98416

Frank D. Carsey
Jet Propulsion Laboratory
Pasadena, California 91109

Per Gloersen
Goddard Laboratory for Atmospheric Sciences
Goddard Space Flight Center
Greenbelt, Maryland 20771

NASA Scientific and Technical Information Branch 1983
National Aeronautics and Space Administration
Washington, DC

FOREWORD

Progress in climate research will depend on the availability of a variety of geophysical data sets that describe the boundary conditions and internal and external forcings of the climate system. The importance of such data is underscored in the 5-Year Plan for the U.S. National Climate Program, in which NASA plays a major role.

The polar regions constitute a key component of the climate system, particularly regarding the annual cycle of sea ice advance and recession. The principal interactions involve ice-albedo feedback that affects the Earth's radiative balance, which in turn drives the atmospheric and oceanic circulation system. The presence of sea ice also serves to limit the interface between the polar atmosphere and ocean, thus constraining the transfer of sensible heat.

A principal NASA contribution to the National Climate Program derives from broad applications of space technology. The unique perspective from space provides the opportunity for continuing global synoptic observations well suited for establishing the most critical climate data sets, including sea ice. This publication summarizes the Antarctic sea ice cover observed by the Nimbus 5 research satellite over the period 1973-1976. It is hoped that this information will be a useful reference to climatologists and cryospheric scientists.

Robert A. Schiffer
Manager, Climate Research Program
Office of Space Science and Applications

David Atlas
Chief, Laboratory for Atmospheric Sciences
Goddard Space Flight Center

PREFACE

This volume signals a striking step forward in both the technology of remote sensing of the Earth's environment from satellites and the provision of new and important geophysical data on the Antarctic. Furthermore, it again reminds us of the crucial role that the Antarctic plays as an indicator of climatic changes and as a crucial component of the system that determines our climate. I will briefly explain each of these points.

It has always been the dream of meteorologists and oceanographers to visualize the Earth's restless covering of air, water, and ice in three dimensions, and to follow its changes in time. The first meteorological satellites did indeed give us a global picture of the cloud patterns, using visible and infrared sensors, but we could not look through those clouds to follow what was happening at the surface. Microwaves can penetrate clouds, however, and the opportunities that microwave radiometers could provide were clearly seen and pursued by the late William Nordberg and his colleagues at the Goddard Space Flight Center and elsewhere. The result of many years of development effort culminated with the Electrically Scanning Microwave Radiometer (ESMR—affectionately pronounced "Esmer") that flew on Nimbus 5, launched in December 1972. This instrument could detect the thermal microwave (1.55 cm) emission from an area on the ground or the surface of the ocean about 30 by 30 kilometers in size, and the "spot" could be electrically scanned across the satellite path to create synoptic coverage after several orbits. The data obtained by ESMR during the subsequent 4 years are summarized here in the form of maps.

The sea ice data from ESMR will be of interest to all those concerned with the Antarctic (or sea ice generally), from the navigators of ocean vessels who must penetrate the pack ice to climatologists seeking further clues to the heat balance of the Southern Hemisphere. The data are marvelously presented in the form of color-coded maps of the Antarctic and the southern oceans that show "brightness temperatures" and "concentrations of pack ice," averaged for each month, 4-year monthly averages, month-to-month changes, and so forth. There are also graphs summarizing the results, such as areas of sea ice as a function of time in the various sectors of the southern ocean. The text explains in detail how this marvel of computer-drawn graphics was achieved, although the authors are modest in glossing over the enormous effort required to perfect the computer software.

Some important facts have already emerged from the analysis presented in this volume—facts that raise a host of highly intriguing questions. For example:

- What is the significance of the steady shrinking of the average total area of sea ice during this 4-year period? (See Chapter 5.)
- Why has this general retreat varied so greatly between the different sectors of the southern ocean?

- How does one explain the unexpectedly large and shifting areas of open water (polynyas) within the ice pack, even in winter?
- Why does the ice pack area shrink so rapidly in spring compared to its growth in the fall?
- How does the ice pack interact with the atmosphere and ocean circulations, and how does it influence the processes that form intermediate and bottom water?

Thus, this atlas opens up a number of lines of investigation that can now be pursued further with this treasury of data. But I hasten to add that this volume is much more than a data set—it includes what is, in effect, a treatise or textbook on the subject of polar sea ice and the remote sensing of it with microwaves. The text has been prepared by acknowledged experts in the several fields involved. It explains, at least in a preliminary way, what the data mean in terms of the physics and dynamics of sea ice.

In the process of planning the U.S. National Climate Program and clarifying the role to be played by the various Federal agencies, it became clear that NASA would have to bear the primary responsibility for developing and demonstrating new satellite techniques for studying the factors governing our climate. This volume is good evidence that NASA is continuing to fulfill this part of its mission.

Now that the sea ice team has given birth to this fine compilation—and in the process has presumably solved the many data reduction and presentation problems—we can look forward to further reports on subsequent observations from satellites. There have been other scanning microwave radiometers flown since Nimbus 5. Furthermore, let us not forget the Arctic and its ice pack. We can hope that NASA will not rest on its laurels before giving the world more of this invaluable new information.

William W. Kellogg
Senior Scientist
National Center for Atmospheric Research
Boulder, Colorado

ACKNOWLEDGMENTS

We are indebted to many groups and individuals who have made this volume possible. For most of the computer programming efforts required to produce the images and the analysis, we are especially grateful to Margot Osborne, Jerry Bohse, Doug Love, John Morris, and Ray Pelletier of Computer Sciences Corporation. The technical support provided by Jim Manning and Debbie Johnson of Computer Sciences Technicolor Associates is also greatly appreciated. We thank Joe Barksdale for assistance in data processing and Pete Bracken, Joe Johns, and others, who were responsible for the excellent support from the facilities of GSFC's Atmospheric and Oceanographic Information Processing System used to create the color images. We appreciate the assistance of GSFC's Technical Information and Administrative Division, the fine photographic reproduction by Bara Photographic, Inc., and the editorial services of Eileen Sapcariu, Anne Schmidt, and Larry Mooney of Engineering & Economics Research, Inc. Tracy Pepin did an outstanding job in typing and retyping the manuscript. We thank Tom Wilheit, A. T. C. Chang, and Rene Ramseier for illuminating discussions on interpretation of the data, Jim Mueller for discussions on oceanographic features, and Steve Ackley, Roger Barry, Arnold Gordon, Richard Moore, James L. Rasmussen, and Chester Ropelewski for their thorough reviews of the text. We are particularly grateful for the support and encouragement of GSFC's Applications Directorate and NASA's Environmental Observations Division, which supported this work under NASA's Climate Program.

CONTENTS

SUMMARY

Sea ice is an important, highly variable feature of the Earth's surface, both reflecting and influencing climatic conditions. Sea ice covers approximately 7 percent of the world's oceans, significantly reduces the amount of solar radiation absorbed at the Earth's surface, greatly restricts the transfer of heat from the ocean to the atmosphere in winter, and influences global atmospheric and oceanic circulation. In this document, the sea ice distribution of the Southern Hemisphere is described in detail for the 4-year period 1973 through 1976, a period marked by the advent of satellites with passive microwave imagers that have provided unique data on this remote region of the world's ocean.

The extent and distribution of Antarctic sea ice is determined by using data from the Electrically Scanning Microwave Radiometer (ESMR) on the Nimbus 5 satellite. For 41 months of the 4-year period, microwave brightness temperatures in monthly averages are displayed in color-coded polar maps. The large contrast between the microwave emissivity of open water compared to that of sea ice enables a conversion of the brightness temperatures to sea ice concentration (the percentage of ocean area covered by sea ice). The resulting sea ice concentrations are also displayed in monthly averaged maps, and variables such as the total areal extent of sea ice, the area of ice in various concentration categories, and the area of actual ice coverage are plotted both for the southern ocean as a whole and for each of five sectors: the Weddell Sea (60°W - 20°E), the Indian Ocean (20° - 90°E), the Pacific Ocean (90° - 160°E), the Ross Sea (160°E - 130°W), and the Bellingshausen-Amundsen Seas (130° - 60°W).

The characteristics of the southern ocean, bounded to the south by the Antarctic Continent and unbounded to the north, include a westward flow near the continent and an eastward circumpolar current near the northern reaches of the sea ice cover. The ESMR data reveal many details of the distribution and dynamics of the Antarctic sea ice cover, such as irregularities in the outer boundary that are presumably caused by ocean currents or by variations in atmospheric circulation and surface winds. In general, the extent of ice coverage increases from a minimum of 4×10^6 square kilometers in February to a maximum of 20×10^6 square kilometers in September, with a greater rate of ice decay in spring than rate of growth in fall. Within the sea ice pack, mean ice concentrations range from about 50 percent in summer to about 80 percent in winter, indicating the existence of more open water in leads and polynyas within the ice pack than was previously known. Open water is measured in ice-free polynyas that are larger than the 30-kilometer microwave resolution and in regions of reduced average ice concentrations caused by numerous leads and polynyas smaller than 30 kilometers. Around most of the continent, except in the western Weddell Sea and the Bellingshausen-Amundsen Seas, the ice edge retreats to the coast in summer.

Considerable interannual variability and interregional contrast occurs in the ice cover. Although the total sea ice coverage decreased significantly (by 10 percent in the annual

mean) over this 4-year period, the behavior was not the same in all regions or all seasons. Most of the overall decrease was due to the large 23-percent decrease in the Weddell Sea sector, where the maximum winter ice extent was several hundred kilometers less and a very large open-water area, the Weddell polynya, persisted throughout the winters of the latter 3 years. The Weddell polynya, which drifted westward both within each of the three winter seasons and from one winter to the next, accounted for only part of the overall decrease in ice cover. In the Weddell Sea and Pacific Ocean sectors, the ice extent decreased in all seasons, with the largest single-month percentage decreases occurring in December for the Weddell Sea and in October for the Pacific Ocean. The decreases in these cases were 25 and 30 percent, respectively. In the other sectors, the sea ice extent increased over the 4-year period for some seasons and decreased for others. The high degree of interannual variability of sea ice precludes the determination of long-term trends from such a short record, but the images in this document demonstrate that satellite microwave data provide unique information on large-scale sea ice conditions, information that is needed for determining climatic conditions in polar regions and possible global climatic changes.

1

INTRODUCTION

Antarctic sea ice is a highly variable feature of the Earth's surface. Each year it recedes from its maximum area of approximately 20×10^6 square kilometers in September to its minimum area of approximately 4×10^6 square kilometers in February. As a variable ice feature, the area of seasonal sea ice is exceeded only by the seasonal snow cover on the continents in the Northern Hemisphere. Although the areal extent of winter sea ice in the southern ocean is 50 percent larger than the area of permanent ice cover on the continent, the volume of sea ice is 1000 times less than that of continental ice. These general characteristics of Antarctic sea ice were known decades before the advent of observations from space, but with recent satellite microwave sensors, not only the extent of the ice but also the area of open water in polynyas and leads within the ice pack has been obtained. This document presents a detailed analysis and description of the growth, decay, regional characteristics, and interannual variations of Antarctic sea ice based on passive microwave observations for the period 1973 through 1976.

The variable year-to-year positions of the sea ice edge at its winter maxima and its summer minima have often been used as indicators of changes in global climate. Generally, sea ice extends farther from the poles during colder climatic periods (Lamb, 1972) such as the Little Ice Age in the eighteenth century and the last glaciation of the Pleistocene epoch, which ended approximately 10,000 years ago. For the distant past, information on the location of the ice edge has been deduced from the geologic record in sea-floor sediments. For the past several centuries, this information has been supplemented by historical records for select locations such as Iceland. For recent decades, a more detailed record of sea ice has been obtained from numerous ship, aircraft, and satellite observations.

Sea ice occurs in many physical forms (WMO, 1970; and Armstrong et al., 1973), varying from fine ice particles suspended in water to thick multiyear ice floes. Some small-scale characteristics of sea ice are illustrated in photographs from the Weddell Sea (Figures 1-1 through 1-5). Generally, ice crystals that form in near-surface waters coalesce into several forms and by accretion grow into relatively flat sheets or floes varying in size from about 20 meters to many kilometers across. Thicknesses of ice floes are usually in the range of a few tens of centimeters to several meters. The physical and chemical structure of sea ice is affected by snowfall, brine drainage in the upper layers, and other aging processes. Stresses acting on the ice induce deformation in the form of ridging, overriding or rafting, and fractures that form linear openings in the ice pack called leads and nonlinear openings called polynyas. Figure 1-4 shows various areas of open water, new ice forms, and older ice floes showing signs of past deformations.

The relationship between climate and sea ice is complex. Regional and global changes in ice extent influence oceanic and atmospheric conditions, which in turn influence the distribution of sea ice. The freezing of ocean water to form sea ice, the deformation of sea ice by winds and ocean currents, and the melting of sea ice are all interactive processes. The physical processes involve sensible and latent heat transfer, wind stress, ocean heat flux, solar radiation, cloud cover, ocean currents, ice drift, and other factors. In spring and summer, for example, the presence of the highly reflective sea ice greatly decreases the amount of solar radiation absorbed at the Earth's surface. In winter, the sea ice acts as an insulator between the cold polar atmosphere and the relatively warm ocean surface, greatly restricting exchanges of heat and mass between the ocean and the atmosphere (Allison et al.,

Figure 1-1. Surface view of sea ice floes near the northern sea ice edge in the Weddell Sea, with approximately 1-meter-tall Emperor penquin. Open water in the foreground between the ice floes does not show signs of new ice formation. Snow depth of 10 to 20 cm thickness on the ice floes is a typical feature of this region. Substantial ice ridging is evident in the background. (Courtesy of S. Ackley, Cold Regions Research and Engineering Laboratory (CRREL).)

Figure 1-2. Surface closeup view of ice ridging showing ice blocks about 1 to 1.5 m in height. Snow cover on the ridges indicates ridge formation several days before the photograph was taken. (Courtesy of S. Ackley, CRREL.)

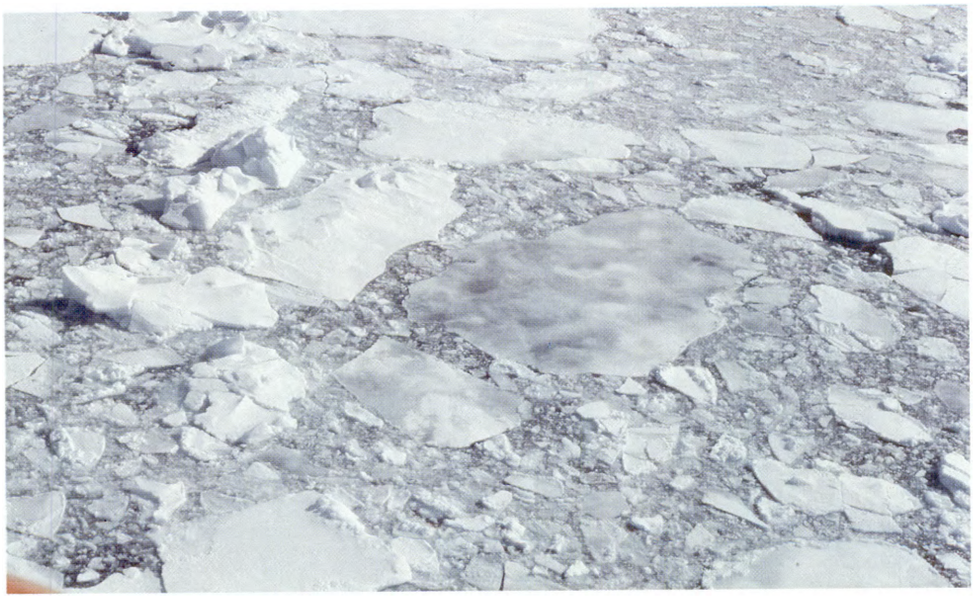

Figure 1-3. Aerial view of ice in the southern Weddell Sea, where the ice is generally younger and thinner than the ice that has drifted northward (Figures 1-1 and 1-2). The large gray or gray-white floes in the center and lower right appear to be remnants of recent ice growth (thinner ice is gray) followed by substantial deformation probably due to both wind and ocean waves within the ice pack. The deformation also created large amounts of highly fractured ice between the larger floes. The presence of some ridged ice, shown here in the upper left, is a typical feature. (Courtesy of S. Ackley, CRREL.)

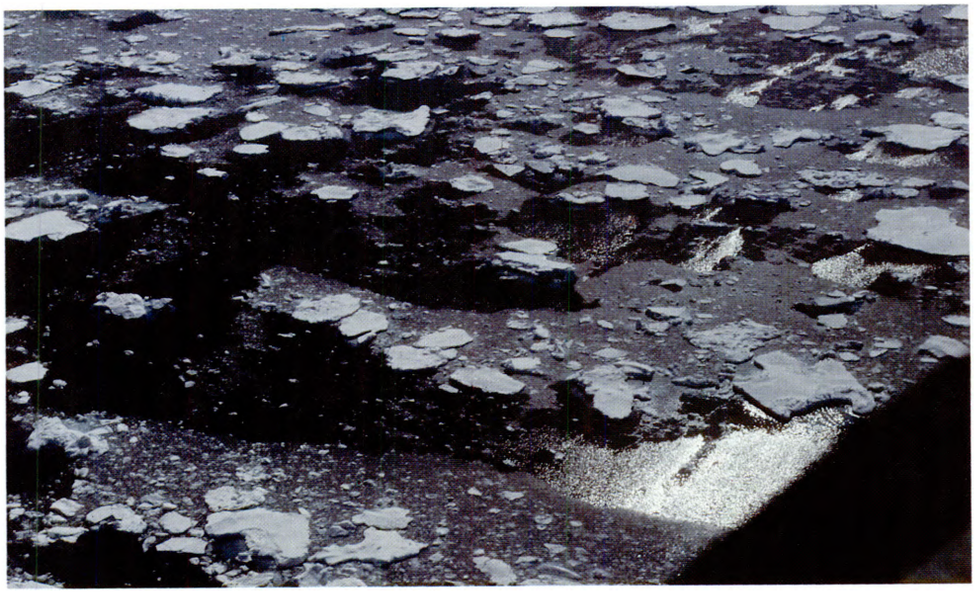

Figure 1-4. Aerial view near the ice edge showing bands of sea ice with ice floes surrounded by thin gray ice, which is approximately 10 cm thick. The bright areas of sunglint on the right indicate ice-free water. Some of the dark areas between the ice bands contain a soupy layer of grease ice, which dampens the small ocean waves and reflects little light. The larger wind drag acting on the ice floes causes separation into bands of ice and open water, a process that accelerates ice melting in spring due to the lower albedo of the ocean between the ice bands. (Courtesy of S. Ackley, CRREL.)

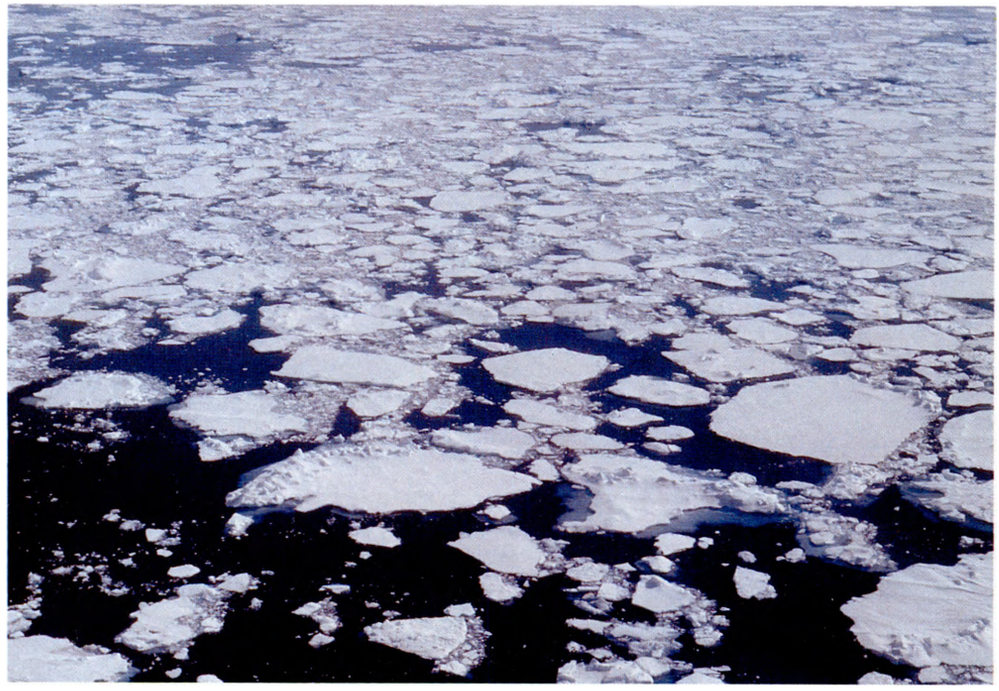

Figure 1-5. Isolated floes of snow-covered ice with no signs of new thin ice. In this intermediate stage of deterioration, most of the thinner ice has melted. The thicker floes have been melted along the edges by the warmer ocean water, as shown by the portions of the larger floes that are below sea level and therefore appear light blue in color. At this point, melting could proceed rapidly because the decreased compaction enhances the solar radiation absorption in the open water and the possibility of wave action on the floe edges. (Courtesy of S. Ackley, CRREL.)

1982; Maykut, 1978; and Untersteiner, 1961). The open water created within the ice pack by the differential motion and cracking of the ice is particularly important because the release of heat to the atmosphere from the open water is up to 100 times greater than the heat conducted through the ice. In spring, the amount of open water within the ice pack is also significant because the solar radiation heats the water, which in turn heats the ice indirectly much faster than the direct solar radiation. The ejection of salt during ice growth and the input of relatively fresh water to the ocean mixed layer during ice melt both influence the circulation of ocean waters. In particular, salt ejection tends to deepen the mixed layer and, in regions with weak or unstable density structures, to induce bottom-water formation. In addition, the movement of the ice northward produces a negative heat transport and a positive freshwater transport. These are examples of some of the dominant interactions involving sea ice.

The causes and the effects of observed variations in the ice cover are not well understood. Better understanding of the climatic significance of observed changes, in particular, requires improved knowledge of the physical processes, as well as an accurate long-term record of ice conditions. The purpose of this document is to present a compilation and analysis of satellite data on sea ice for the 4 years 1973 through 1976, which should be the beginning of a long-term detailed climatic record of global sea ice conditions. Even with only a 4-year period, the analysis provides new insights to the nature of the sea ice cover and its variations. The sea ice distributions obtained may be used for additional studies of climate, atmospheric processes, and oceanic processes. As the microwave observations show, the ice cover often decreases in one region while increasing in another for reasons that are not fully understood. Regional differences during 1973 through 1976 are marked, with ice extents decreasing significantly in the Weddell and

Ross Seas but increasing somewhat over the 4 years in the Bellingshausen-Amundsen Seas. The overall maximum extent of sea ice decreased by 1.2 million square kilometers, or 6 percent of the total ice area. The record of sea ice distributions should also be useful for studies of marine resources in sea ice regions and for the planning of operational activities in the Antarctic.

The source of the data is the Electrically Scanning Microwave Radiometer (ESMR), a passive microwave instrument on the Nimbus 5 spacecraft launched in December 1972. The ESMR instrument has provided the first all-weather, day-or-night capability for observing sea ice that exists in geographical areas that are dark and/or cloud-covered much of the year and where surface investigations are extraordinarily difficult. Data obtained by satellite microwave imagery are unique for: (1) their comprehensive temporal and spatial coverage, and (2) their information regarding the amount of open water within the ice pack. The comprehensive temporal and spatial coverage derives from the ability of the satellite radiometer to detect microwave radiation from the Earth's surface on repeated orbital passes along a broad swath in the presence of clouds and in the absence of light. The open-water information derives from the large contrast between the microwave emission from sea ice and the much lower emission from sea water.

Before the ESMR was launched on Nimbus 5, a prototype of the instrument was flown in the Arctic in 1967, 1970, 1971, and 1972 on the NASA "Galileo-I" Convair 990 Remote Sensing Laboratory. The first two expeditions led to the discovery of the strong contrast in microwave signatures of open ocean and sea ice (Wilheit et al., 1972). The last two expeditions included surface measurements from manned drifting ice stations in the Beaufort Sea (Campbell, 1973). Within 2 weeks of the launch of Nimbus 5, the ESMR provided the first all-season and all-weather synoptic views of the entire Arctic and Antarctic sea ice covers (Campbell et al., 1974; and Gloersen et al., 1974). Quantitative interpretation of the satellite ESMR images has been based on results of a series of combined satellite, aircraft, and *in-situ* observations during three major international experiments in the 1970's, namely:

1. AIDJEX (Arctic Ice Dynamics Joint Experiment), spring 1971, 1972, and spring 1975 through spring 1976
2. BESEX (Joint U.S./U.S.S.R. Bering Sea Experiment), spring 1973
3. Skylab Snow and Ice Experiment, winter and spring 1973 and 1974

The simultaneous surface, aircraft, and satellite observations confirmed several applications of the remote sensing of sea ice that are of fundamental importance. These include the ability to clearly distinguish sea ice from open water (Wilheit et al., 1972; and Gloersen et al., 1975a), to distinguish multiyear sea ice from first-year and younger ice types (Gloersen et al., 1973), to map sea ice concentration (Gloersen et al., 1974), and to delineate the seasonal variation of ice types (Campbell et al., 1978). An essential feature of the passive microwave techniques is the ability to determine the relative areas covered by open water and sea ice even though the separate small areas of open water and ice floes are not resolved by the microwave imagers.

Using the satellite ESMR data, a complete map of southern ocean brightness temperatures—providing a clear delineation of sea ice distribution—has been produced for most 3-day intervals during 1973 through 1976, with occasional gaps because of invalid or lost data. The spatial resolution of the data is approximately 30 kilometers. The brightness temperatures have been averaged over monthly time periods, and for each 30- by 30-kilometer map element, monthly sea ice concentrations (percent of area covered by sea ice versus open water) have been derived from the brightness temperatures to an estimated absolute accuracy of ±15 percent (e.g., 30 ± 15 percent). Relative accuracy from one map element to another is much better.

The following chapters describe the general physical characteristics of the southern ocean (Chapter 2), the theoretical basis for the microwave interpretations and estimates of accuracy (Chapter 3), the average annual cycle of sea ice concentrations (Chapter 4), and the full sequence of monthly average ice concentrations for 1973 through 1976 (Chapter 5). Maps of monthly averaged brightness temperatures for each of the 4 years are included in Chapter 3, whereas maps of monthly averaged ice concentrations (derived from the brightness temperatures) are included in Chapter 5. Maps of

4-year monthly averages of sea ice concentration are included in Chapter 4. Chapters 4 and 5 also include an extensive set of graphs showing various aspects of the sea ice cover for the southern ocean as a whole and for each of five sectors into which the southern ocean has been divided. The text is supplemented by three appendixes, the first of which discusses the processing, compilation, and mapping of the data. (Data are available on magnetic tape through the World Data Center A for Rockets and Satellites/National Space Science Data Center, Greenbelt, Maryland 20771, and the World Data Center A for Glaciology, Boulder, Colorado 80309, and are described in Zwally et al., (1981)). Appendix B presents gray-scale images and contour versions of the ice concentration maps of Chapters 4 and 5, and Appendix C presents sample distributions of the area of sea ice as a function of sea ice concentration. Overall, the data and the analysis presented provide a detailed description of the spatial and temporal variations of the sea ice and the open water within the southern ocean ice pack.

2

SOUTHERN OCEAN

2.1 INTRODUCTION

The southern ocean comprises the water surrounding the Antarctic Continent, including the southernmost parts of the Pacific, the Atlantic, and the Indian Oceans. Adjacent to the continent are the Weddell, Bellingshausen, Amundsen, and Ross Seas (Figure 2-1). The southern ocean is unique among the world's oceans because the configuration of land and water in the Southern Hemisphere permits a circumpolar oceanic flow (Figure 2-2). The only major physical boundaries that constrict zonal flow are in the Drake Passage/Scotia Sea region between South America and the Antarctic Peninsula. In addition, deep passages provide bottom water flow equatorward to the adjacent ocean basins (Heezen et al., 1972). The Antarctic Continent provides the southern boundary of the southern ocean, whereas the northern boundary may be considered to be 50°S, which is the approximate position of the Antarctic polar-front zone. The polar-front zone is characterized by relatively large meridional gradients of temperature, salinity, and density associated with the Antarctic circumpolar current and several mid-ocean ridge systems. The important distinction between this frontal boundary and a landmass barrier is its permeability. In fact, the fluxes of heat, salt, and nutrients across this interface are significant factors in global oceanic budgets. More detailed descriptions of the southern ocean appear in Deacon (1937, 1979), Taljaard et al. (1969), Gordon and Goldberg (1970), Heezen et al. (1972), and Gordon and Molinelli (1982).

To examine regional behavior of the sea ice cover, the southern ocean is divided into five sectors, each characterized by various regional oceanographic and meteorological features (Figure 2-3). The Weddell Sea sector (60°W to 20°E) contains relatively cold ocean waters influenced by a large-scale cyclonic gyre and the topographic barrier of the Antarctic Peninsula (Gordon, 1981). The large area of compact sea ice remaining each summer and the occasional occurrence of the Weddell polynya in winter are partial consequences of these features. In the Indian Ocean sector (20°W to 90°E) and the Pacific sector (90°E to 160°E), the continent extends farther from the poles, and in summer the sea ice edge retreats completely to the coast in many locations. The Ross Sea sector (160°E to 130°W), like the Weddell sector, contains relatively cold water and a cyclonic circulation. Although weaker than the gyre in the Weddell Sea, the Ross Sea gyre significantly influences the formation of open water near the Ross Ice Shelf front. The Bellingshausen-Amundsen Seas sector (130°W to 60°W) is characterized by strong stratification in the upper ocean water that contributes to the retention of a large summer ice cover.

2.2 TEMPERATURE AND WATER-MASS STRUCTURE OF THE SOUTHERN OCEAN

Figure 2-4 is a schematic meridional cross section of water-mass characteristics. Typically, temperatures decrease with increasing latitude. The two major exceptions to approximate radial symmetry occur in the Drake Passage/Scotia Sea region and in the western Weddell Sea. In the Weddell, poleward-flowing water is turned equatorward by a deep gyre, wind-stress vorticity, and the continental barrier (Deacon, 1979). The most abundant water type, the circumpolar deep water extending from a depth of a few hundred meters to a depth of near 4 kilometers, has temperatures above 0.5°C and salinities above 34.65 parts per thousand (Deacon, 1933, 1937; and Gordon and Molinelli, 1982). The circumpolar deep water can be identified in vertical profiles by its characteristic temperature maximum,

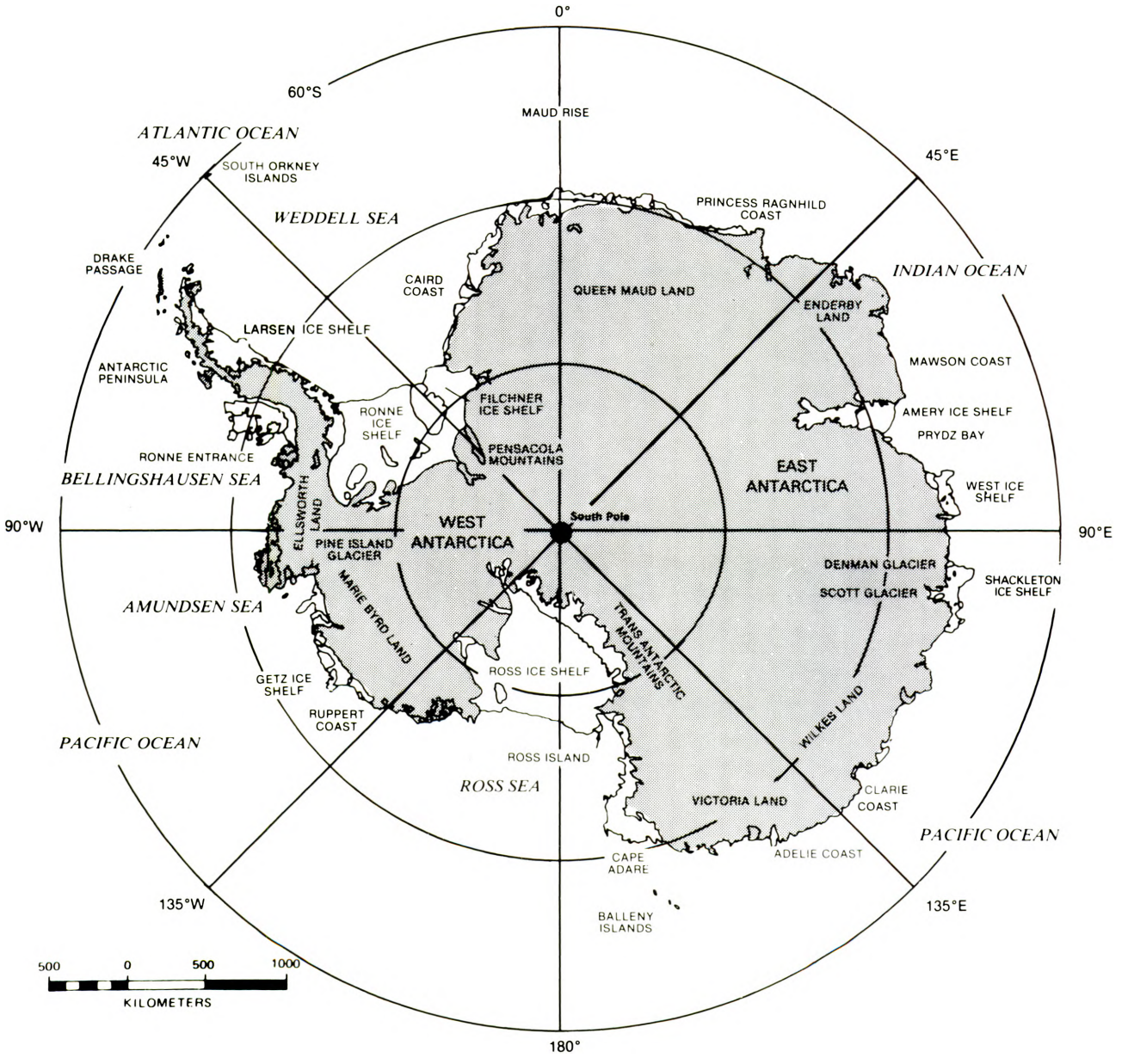

Figure 2-1. Location map for Antarctica and the southern ocean.

which occurs at depths near 1000 meters at the Antarctic polar front and rises to 200 meters off the Antarctic continental shelf, and by a characteristic salinity maximum some 300 to 400 meters deeper than the temperature maximum.

The Antarctic bottom water of the southern ocean extends from the lower limit of the deep water down to the sea floor and is, at most, 1000 meters thick. Temperatures near 0°C and salinities somewhat lower than those of the deep water characterize bottom water (Carmack, 1977). Mixing of cold shelf water and warm deep water in varying ratios to form waters of various temperatures and salinities can be the source of bottom water according to Foster and Carmack (1976), Carmack and Killworth (1978), and Foster and Middleton (1979). The coldest bottom water occurs in the Weddell Basin, where the potential temperature is approximately -1°C (Heezen et al., 1972; and Gordon and Molinelli, 1982, plate 214). According to Foster and Carmack (1976), this bottom water forms primarily from a combination

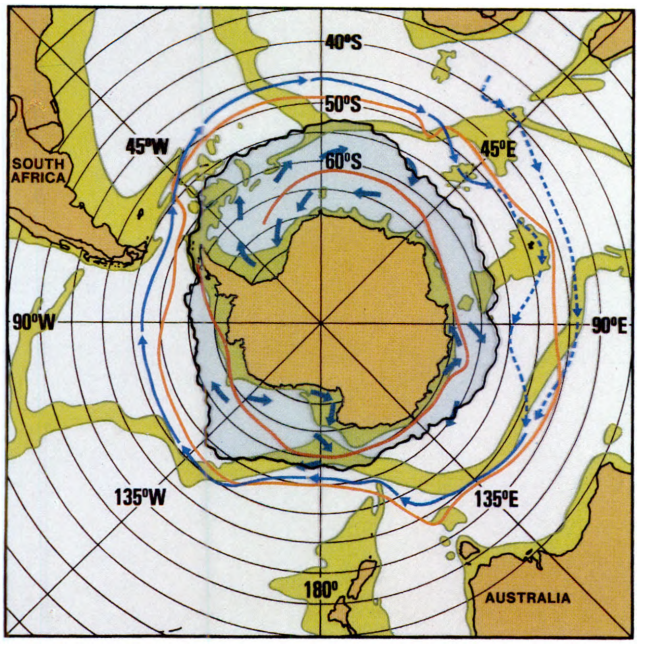

Figure 2-2. Large-scale oceanographic features in the southern ocean. The green areas in the oceans represent bottom topography more shallow than 3000 meters. The axis of the Antarctic circumpolar current is shown by the long blue arrows. The orange line near 50°S indicates the nominal location of the oceanic polar front, called the Antarctic convergence. The red line near the Antarctic Continent indicates the nominal location of the Antarctic divergence. The short blue arrows indicate selected major features of nearshore currents, such as the cyclonic Weddell gyre and the current at the edge of the Ross Ice Shelf. Light-blue shading depicts the region typically covered by sea ice in midwinter.

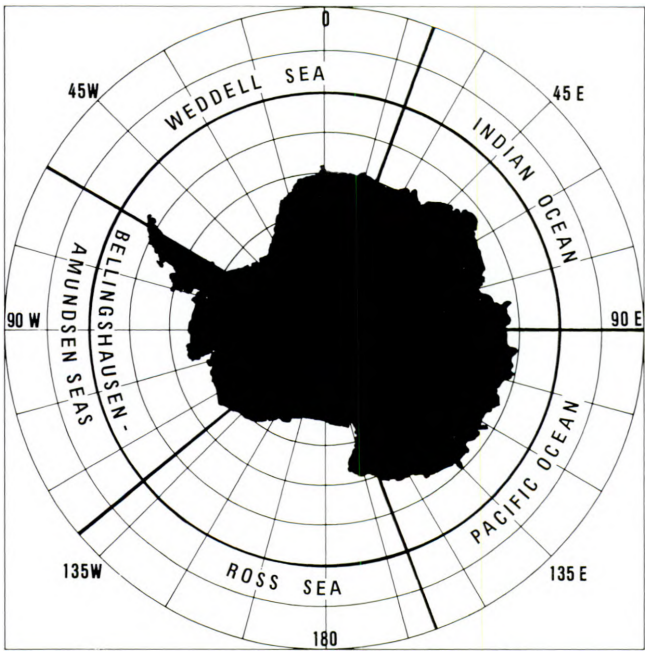

Figure 2-3. Sectors of the southern ocean used for analysis of observed sea ice cover.

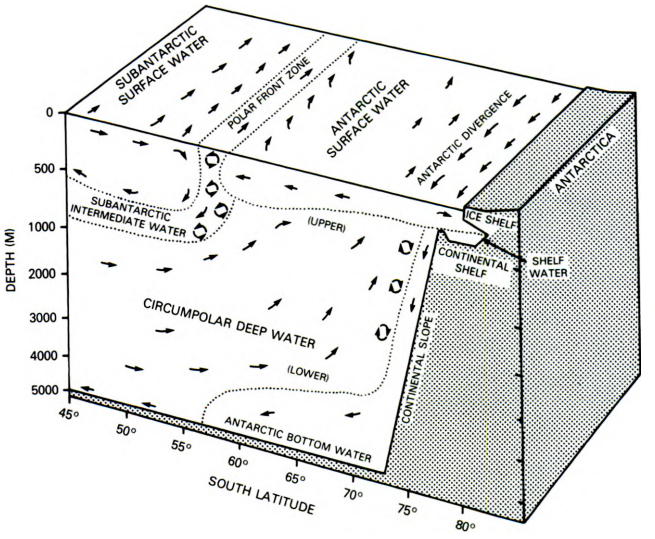

Figure 2-4. Schematic representation of water-mass types and motions (from Gordon and Goldberg, 1970).

of very cold saline shelf water and modified deep water in the Weddell Sea, the bottom water arising through a complicated mixing process at the shelf front. In the plume model of Killworth (1979), this newly formed water sinks along the edge of the shelf to the bottom of the basin. Gordon (1978) and Killworth (1979) offer an additional mechanism for forming bottom water away from continental margins, which involves convective "chimneys," as well as large-scale convection. The possibility of this mechanism occurring in the Weddell polynya is discussed by Carsey (1980) and Martinson et al. (1981).

Throughout the southern ocean, a summertime temperature-minimum layer is found at a depth of 100 to 200 meters. The temperature minimum decreases from about 1.5°C immediately south of the Antarctic polar front to less than 0°C near the continent (Gordon and Molinelli, 1982, plates 196-198). In addition, Toole (1981) has shown that spatial variations in the characteristics of the temperature minimum are strongly correlated with

maximum ice-margin location. The surface waters also show large meridional variations in temperature and salinity. Near the polar front, temperatures approach 6°C in summer and 4°C in winter (Gordon and Molinelli, 1982, plates 7-10), and salinities are approximately 33.8 to 34.2 parts per thousand (Gordon and Molinelli, 1982, plates 13 and 24-26). At the sea ice edge, temperatures are near local freezing, and salinities are approximately 34.0 to 34.3 parts per thousand. Figure 2-4 shows the general form of meridional ocean characteristics and its relationship to zonal characteristics. This pattern of water-mass meridional flux may derive from the eddy field rather than from mean meridional circulation (Bryden, 1979).

2.3 SOUTHERN OCEAN CIRCULATION

The circulation in the southern ocean is dominated by the Antarctic circumpolar current (Sverdrup, 1933; Gordon et al., 1978; and Georgi and Toole, 1981). Figure 2-2 shows this current schematically, as calculated from density slopes at the Antarctic polar front. The location of the current is correlated with the maximum eastward wind stress (Zillman, 1972). Gordon et al. (1978) present the geostrophic ocean circulation at three levels—0 to 1000, 1000 to 2000, and 2000 to 4000 decibars—obtained from hydrographic data; and Lutjeharms and Baker (1979) present data on vertically integrated baroclinic transports. These results indicate a strong eastward-flowing current that appears to be significantly influenced by ocean-floor topography, especially in regions in which major submarine ridge systems cross latitude circles (see Figure 2-2). Using current meter data obtained from long-term moorings in the Drake Passage, Fandry and Pillsbury (1979) estimated the total flow of the Antarctic circumpolar current as $127 \pm 24 \times 10^6$ m^3 s^{-1}.

The circumpolar current appears to influence the position of the ice margin on several spatial scales throughout the year. Suggestions of this influence appear in Figure 2-2, which shows a typical winter ice extent along with the location of the fastest part of the Antarctic circumpolar current, the Antarctic divergence, and selected surface currents. The Antarctic divergence and associated oceanic upwelling is driven primarily by the prevailing easterly winds near the continent and the prevailing westerlies farther north.

2.4 ATMOSPHERIC FIELDS FOR THE ANTARCTIC/SOUTHERN OCEAN REGION

Monthly climatological fields of atmospheric sea-level pressures, geostrophic winds, and surface temperatures for the region poleward of 50°S from the data of Jenne et al. (1974) are presented in Figures 2-5 through 2-7. The sea-level pressure maps (Figure 2-5) are characterized by a polar high-pressure cell centered on East Antarctica and a ring of cyclones located at about 60°S in January and a few hundred kilometers equatorward during the winter months. The cyclone wave number varies from 2 to 5, which is consistent with upper tropospheric data collected by balloon tracking (Webster, 1975). The mean surface geostrophic wind fields derived from the pressure fields show clockwise circulations in the Weddell and Ross Seas, strong westerlies in the midlatitudes, and weaker easterlies near the Antarctic coast (Figure 2-6). These easterlies are strengthened by katabatic flow from the continent (Weller, 1969).

The position and strength of these pressure systems and associated winds are important to sea ice growth and decay. For example, the persistent low over the Weddell Sea results in an equatorward flow of air from the continent over the western portion of the sea. This cold air limits the melting of ice in this region and may in fact maintain ice growth at the edge of the Ronne-Filchner Ice Shelf throughout the year. Orographic flow in the boundary layer, described by Schwerdtfeger (1975), also brings cold continental air over the western Weddell Sea. The characteristics of the summer ice in the Weddell region have been discussed by Ackley (1979).

Another region under the influence of persistent cold-air flow from the continent is the Amundsen Sea, which is also an area of persistent ice cover. By contrast, areas under the influence of warm-air advection from lower latitudes, such as the west coast of the Antarctic Peninsula, often experience rapid melting of ice and smaller ice extents. The recurrent opening and closing of numerous coastal polynyas around the continent are influenced by katabatic flow.

Figure 2-7 shows the monthly climatological air temperatures of Jenne et al. (1974). Over most of the southern ocean, the surface temperature gradients are predominantly meridional, although notable zonal gradients occur in the Ross Sea, the

Antarctic Peninsula, and the Amery Ice Shelf (75°E) areas. Throughout most of the southern ocean, the monthly average temperature does not vary more than 5 K over the 6-month period from May to October. The two major ocean zones of coldest air temperatures are in the western Weddell and Ross Seas.

For an approximate comparison of the ice-edge position with the atmospheric temperatures, Figure 2-8 presents, for six selected months, the position of the ice edge averaged over 1973-1976 plus the 271.2 K freezing isotherm from the climatological surface-air temperatures. During the winter months, the location of the freezing line remains fairly constant, with a maximum shift of no more than 150 kilometers. This isotherm occurs near 55°S in the Weddell sector and, at its most poleward position, extends to 62°S in the Bellingshausen Sea. During these months, the 271.2 K isotherm, at least as indicated by the climatological average, is everywhere north of the 1973-1976 ice edge (Figure 2-8), suggesting that any melt at the winter ice margin is caused principally by oceanic heating and solar radiation or by departures of the atmospheric temperature from the mean values. During times of maximum sea ice growth and decay, the expansion or contraction in the 271.2 K isotherm leads the sea ice edge (Figure 2-8).

As an example of atmospheric influences on the ice, Figure 2-9 displays the mean sea-level pressure field for the 27-day period from April 28 to May 24, 1974, along with the location of the ice edge at the beginning, middle, and end of the period. The region of most rapid ice advance is in the Weddell Sea to the west of the most intense low-pressure center. Thus, the region with the most rapid ice advance coincides with the strongest wind-driven equatorward advection and with an expected decrease in air temperature through cold-air advection. A region with a similar ice advance is in the Indian Ocean sector, also located directly west of a low-pressure system. Over the same period, the ice edge moves poleward in the Amundsen Sea and equatorward in the Bellingshausen Sea, perhaps because of the eastward transport driven by the zonal wind flow. More extensive examinations of the relationship between large-scale atmospheric flow and variations in sea ice extent can be found in Ackley (1981), Cavalieri and Parkinson (1981), and Parkinson and Cavalieri (1982).

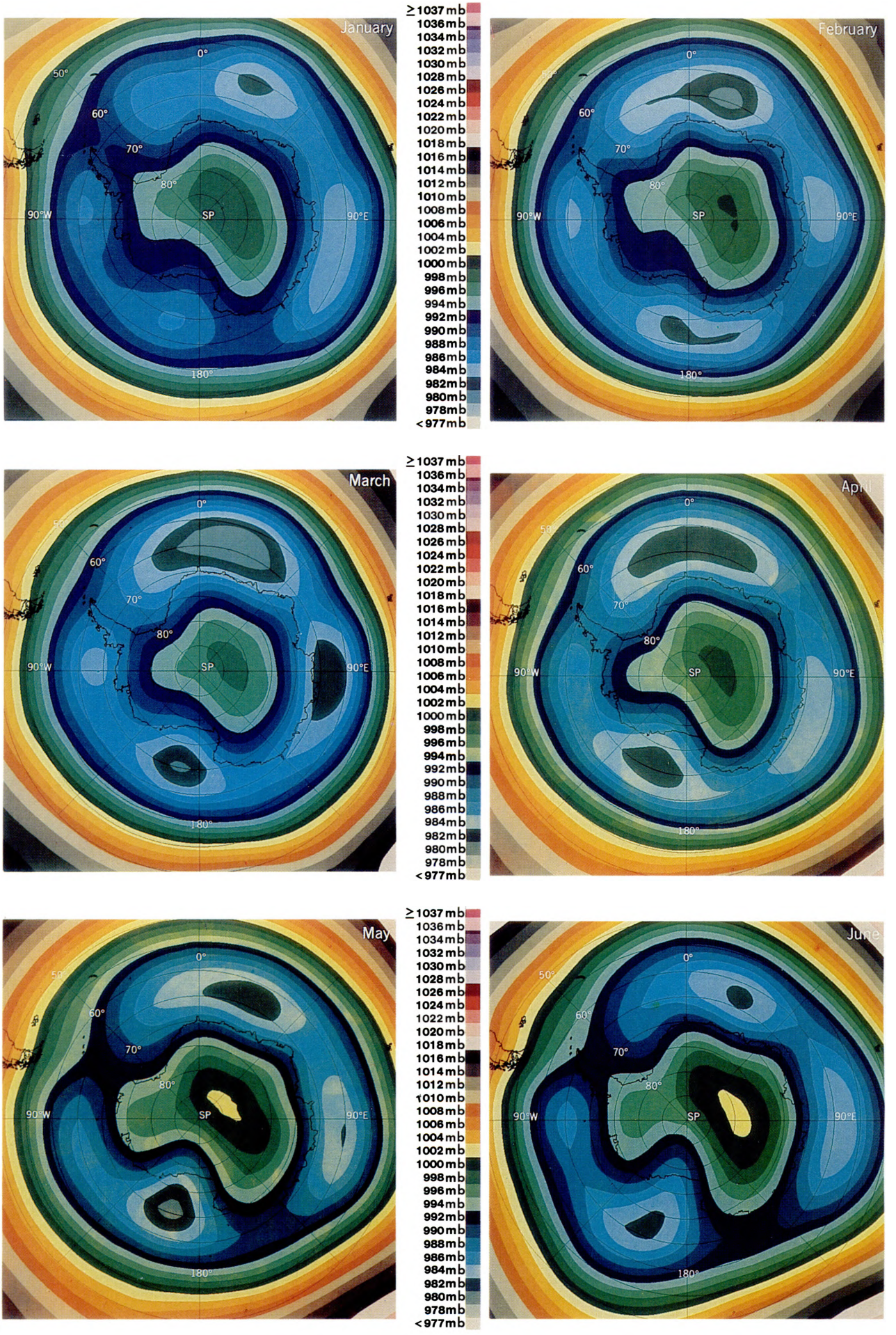

Figure 2-5a. Mean monthly climatological sea-level pressures, January through June. The data for these images were obtained in digitized form from Jenne et al. (1974).

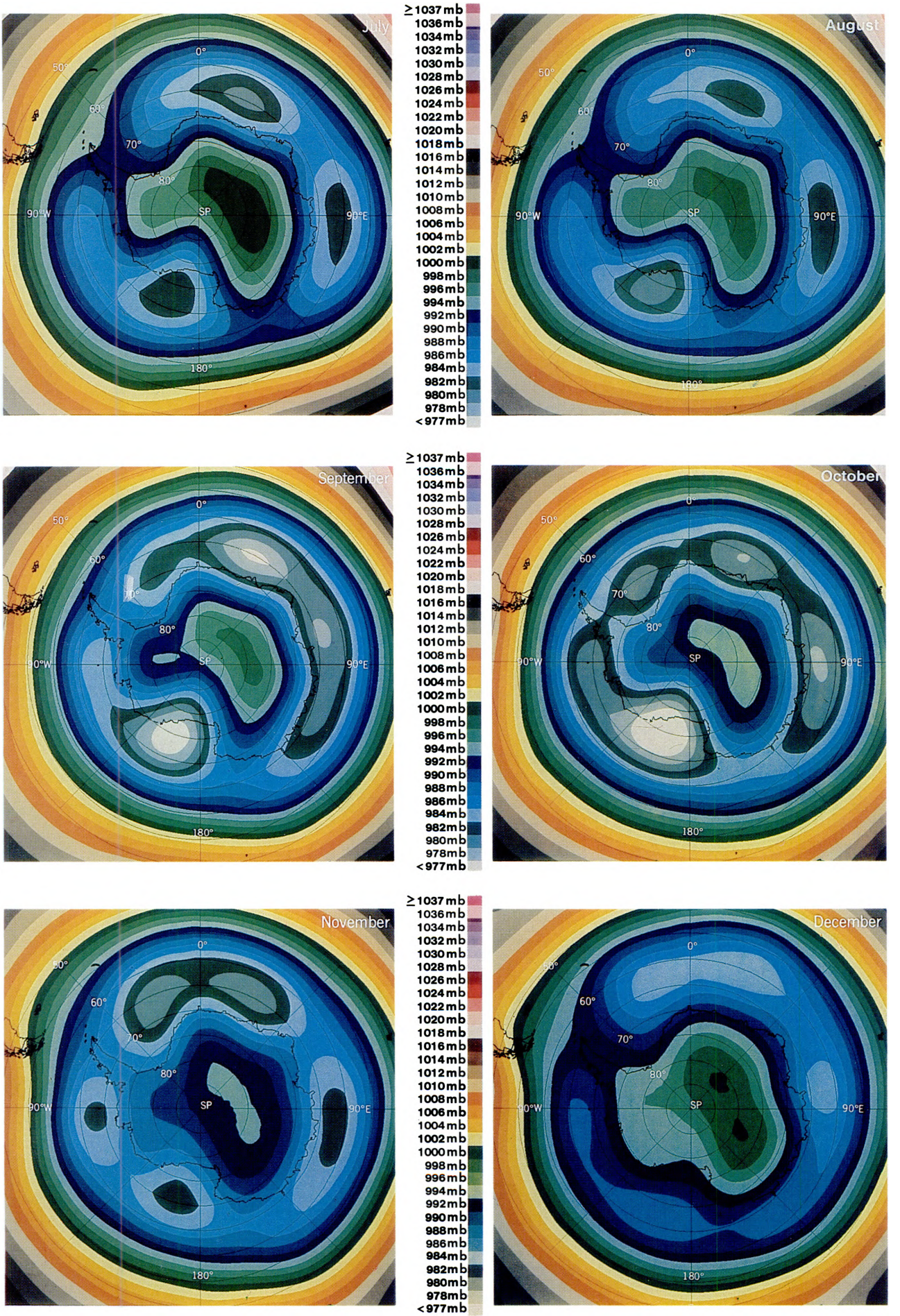

Figure 2-5b. Mean monthly climatological sea-level pressures, July through December. The data for these images were obtained in digitized form from Jenne et al. (1974).

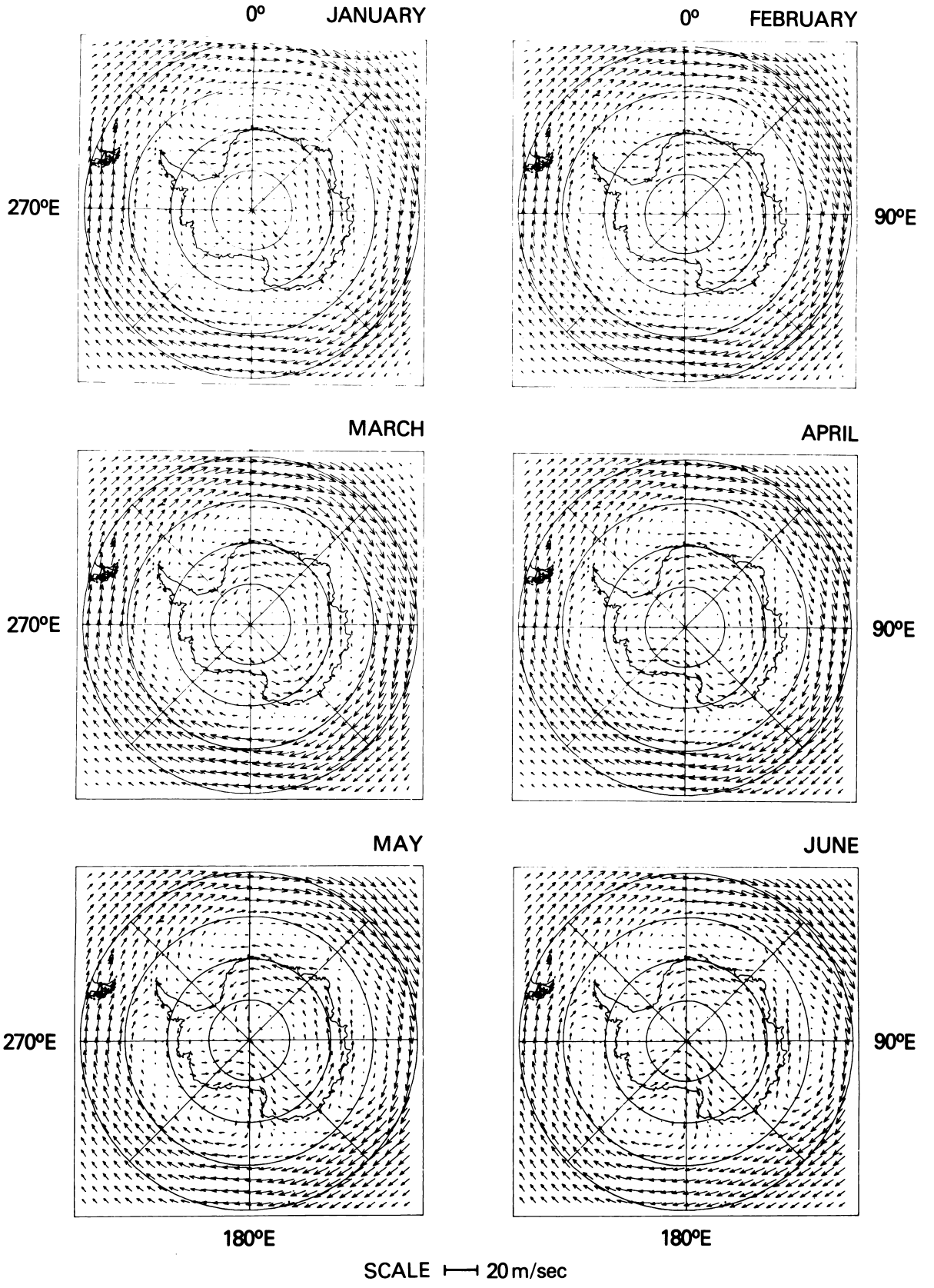

Figure 2-6a. Mean monthly climatological geostrophic winds, January through June. Arrows indicate the direction and relative magnitudes of the wind vectors. The data for these images were obtained in digitized form from Jenne et al. (1974).

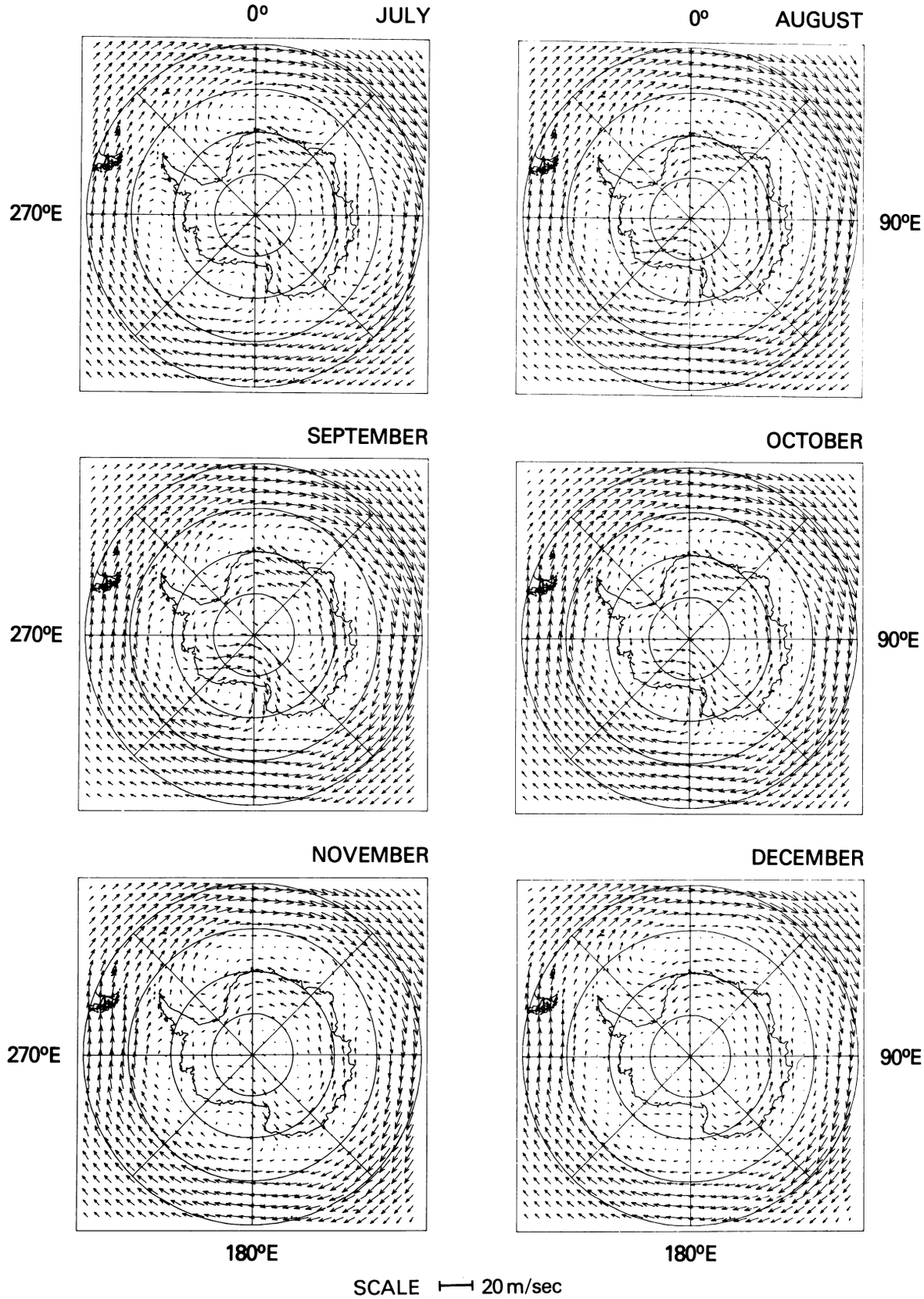

Figure 2-6b. Mean monthly climatological geostrophic winds, July through December. Arrows indicate the direction and relative magnitudes of the wind vectors. The data for these images were obtained in digitized form from Jenne et al. (1974).

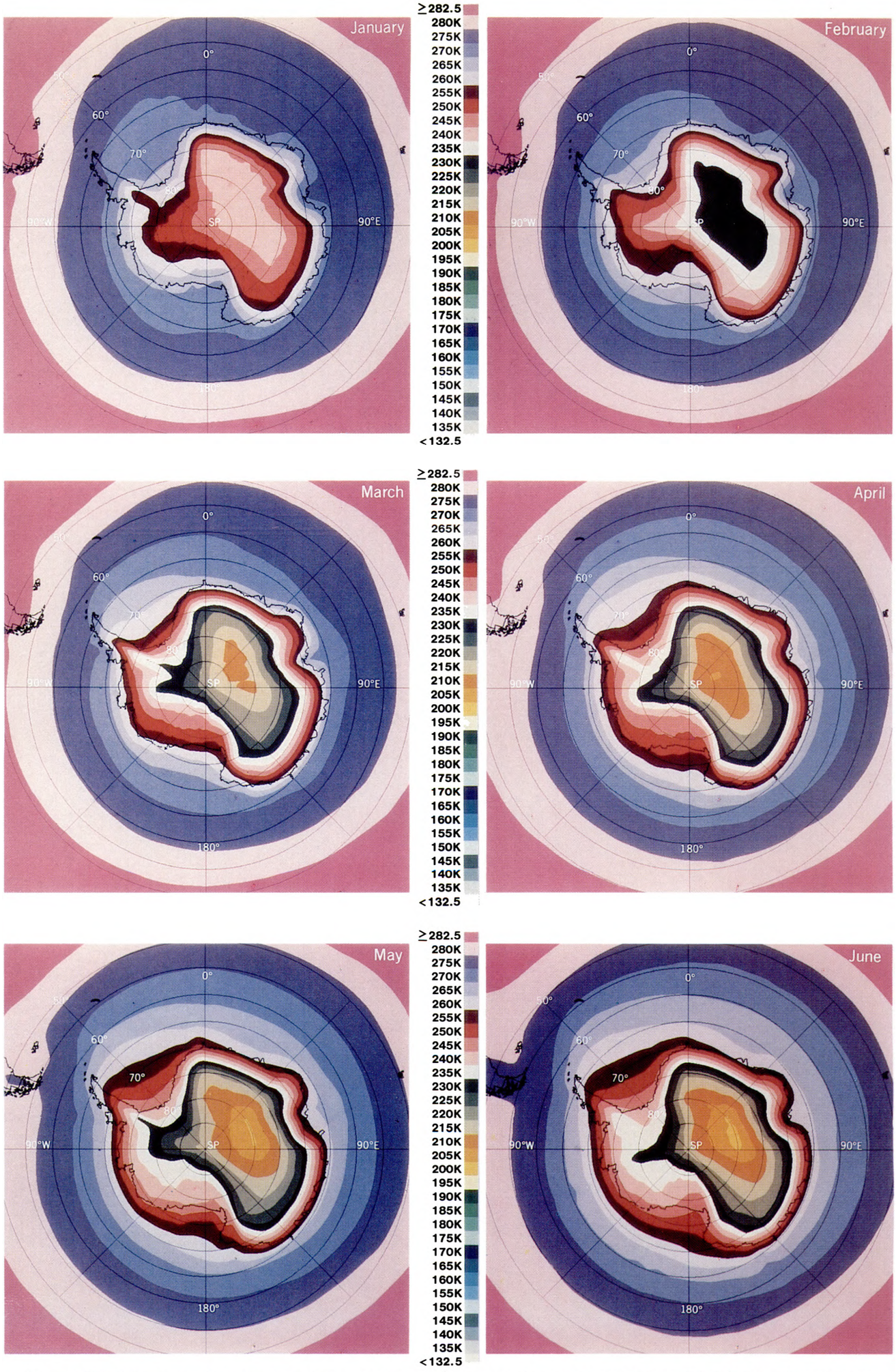

Figure 2-7a. Mean monthly climatological surface air temperatures, January through June. The data for these images were obtained in digitized form from Jenne et al. (1974).

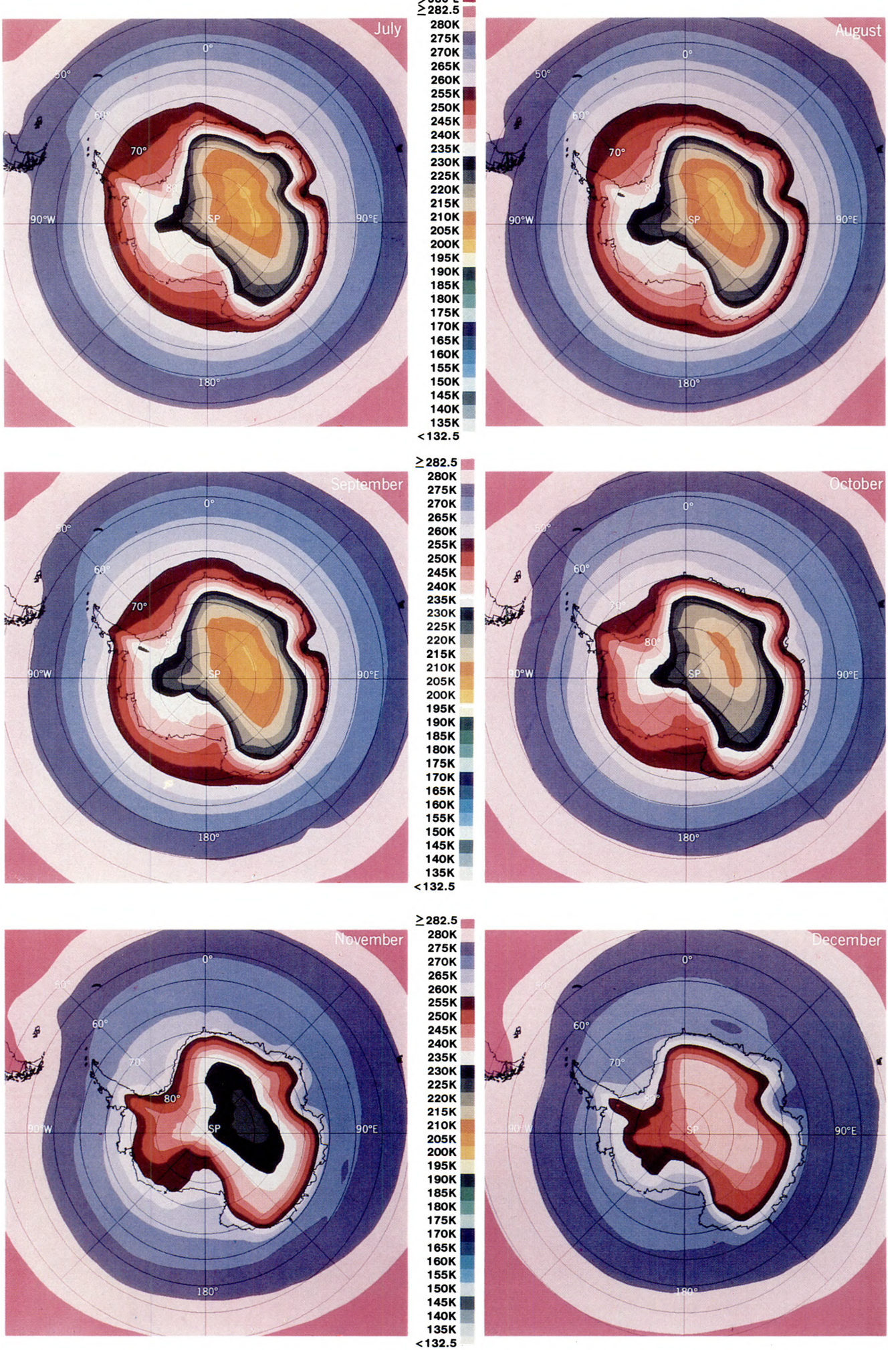

Figure 2-7b. Mean monthly climatological surface air temperatures, July through December. The data for these images were obtained in digitized form from Jenne et al. (1974).

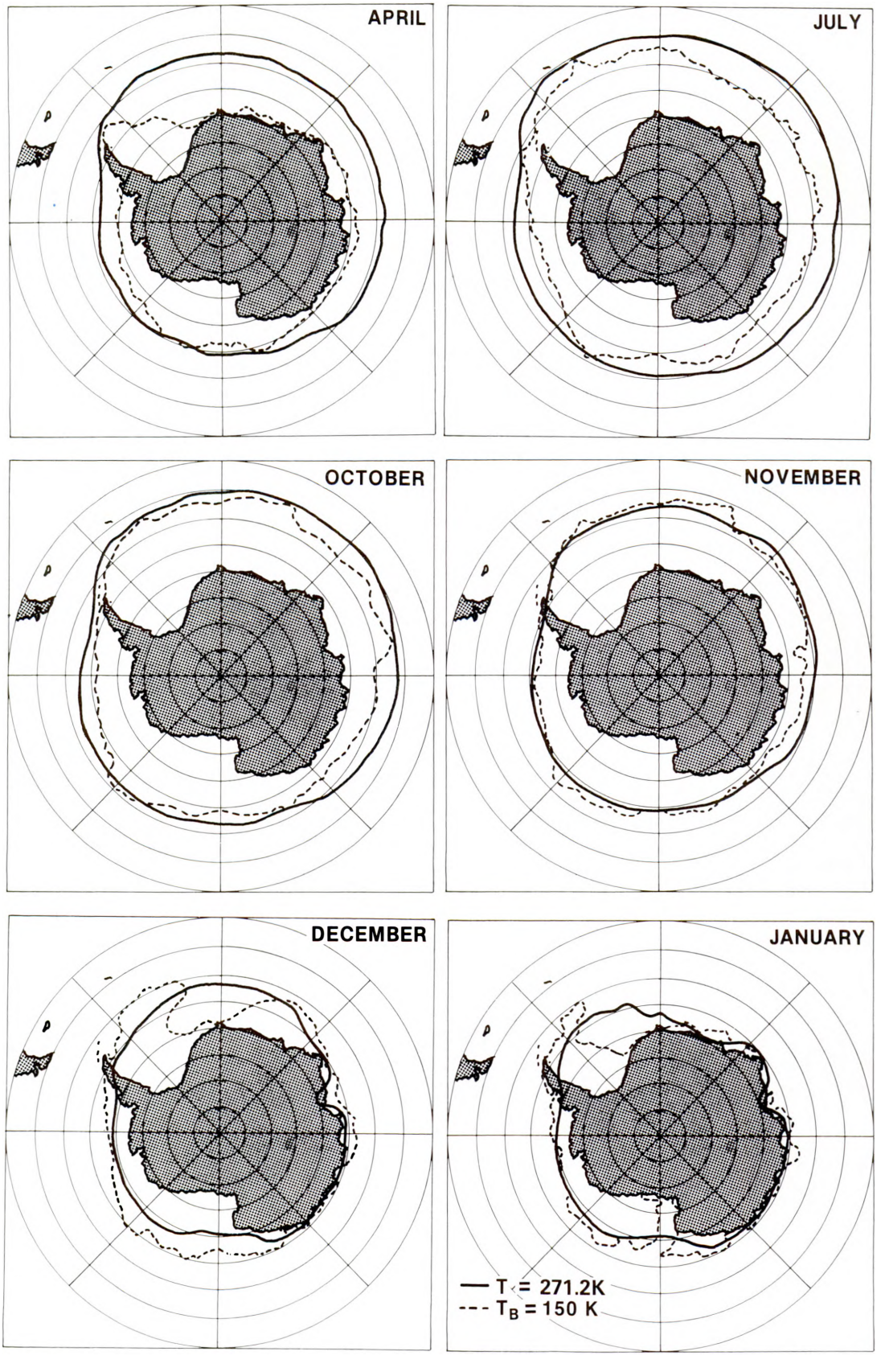

Figure 2-8. Comparison, for six selected months during the growth and decay seasons, of the 271.2 K freezing isotherm from climatological surface air temperatures with the position of the ice edge (T_B = 150 K) averaged for 1973-1976 (Chapter 3).

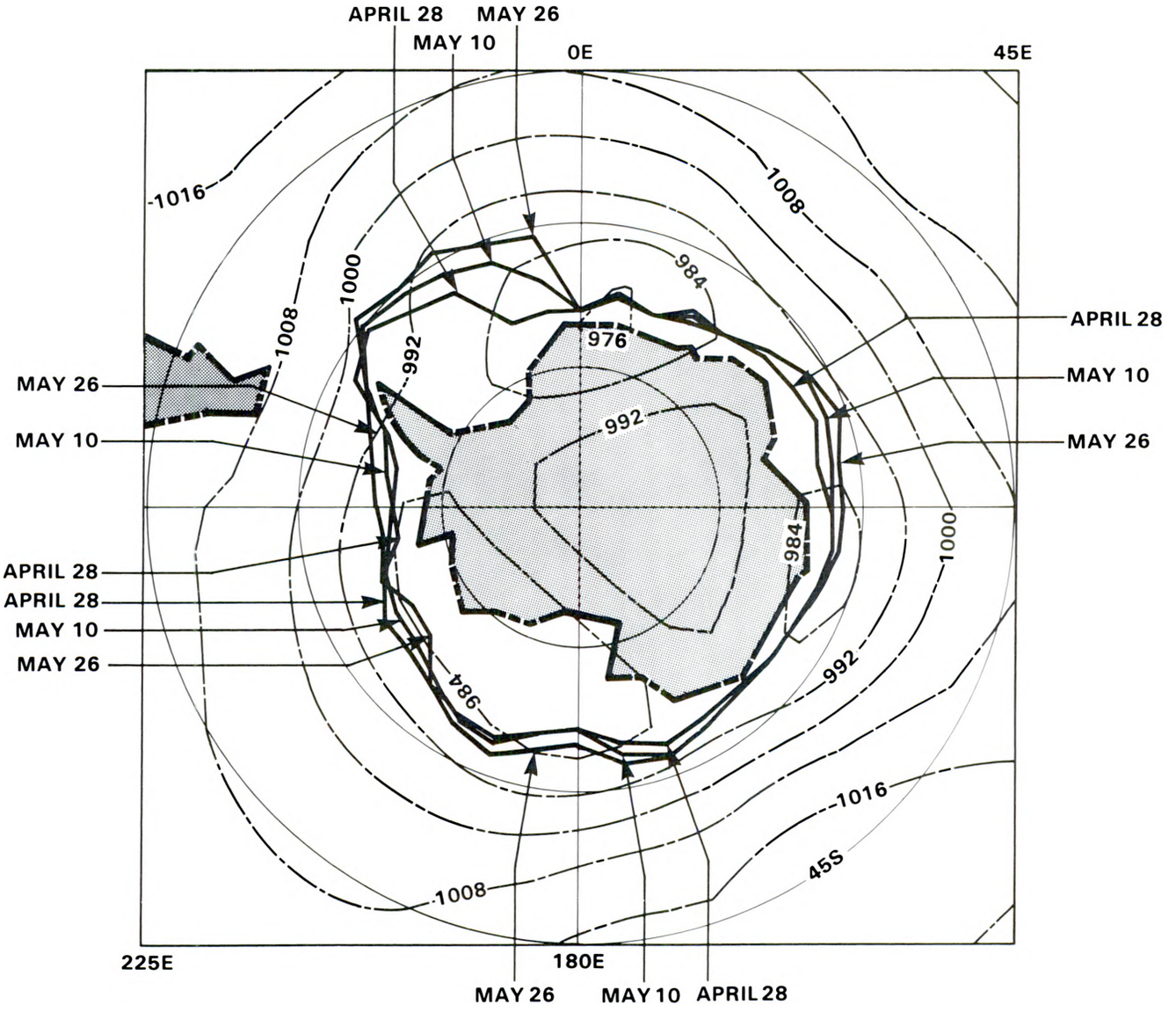

Figure 2-9. Advance/retreat of the sea ice edge from April 28 through May 26, 1974, and the average sea-level pressure field for the 29-day period (Cavalieri and Parkinson, 1981).

3

THEORY AND OBSERVATIONS OF MICROWAVE EMISSIONS AND DERIVED SEA ICE CHARACTERISTICS

3.1 INTRODUCTION

Remote sensing measurements usually consist of the detection of either emitted or reflected electromagnetic radiation at some distance from the source. The passive microwave images in this chapter are principally photographically produced displays of the intensity of naturally emitted radiation from the Earth's surface. In most situations, the microwave images have only minor radiative contributions from the atmosphere and extraterrestrial sources. In this respect, microwave sensing differs greatly from visible and infrared sensing, which are complicated by the large visible reflection and infrared emission from clouds in the atmosphere.

The information contained in the electromagnetic signal detected by the Nimbus 5 ESMR is processed and stored in many forms, including digitally formatted recordings on magnetic tape. The color-coded images shown in this document are representations of digital data maps. For sea ice studies, microwave radiance is converted into quantitative determinations of sea ice concentration. To do this, other physical quantities, such as the microwave emissivity of sea ice and estimates of the ice physical temperature, are combined with the microwave radiance. The procedures used to produce sea ice concentration maps from the microwave data are systematic and objective. Subjective photointerpretative analysis, often applied to remote sensing data, is used only to assist in the evaluation of the data and algorithms. This chapter contains the physical basis and the mathematical formulas used to obtain quantitative sea ice concentrations, along with an analysis of errors.

3.2 MICROWAVE EMISSIVITY AND BRIGHTNESS TEMPERATURE

The intensity of microwave radiation thermally emitted by an object is usually expressed as brightness temperature, T_B. Units of temperature are appropriate because, for radiation wavelengths in the microwave range (1 millimeter to 1 meter), the radiation emitted from a perfect emitter is proportional to its physical temperature, T. The proportionality to temperature is a consequence of the Rayleigh-Jeans approximation to Planck's law of thermal radiative emission. However, most real objects emit only a fraction of the radiation that a perfect emitter would emit at the same physical temperature. This fraction defines the emissivity, ϵ, of the object,

$$\epsilon = T_B/T. \tag{3-1}$$

The usefulness of microwave radiometry as a remote sensing tool derives from the fact that the emissivity of an object depends very much on its composition and physical structure. Thus, measurements of brightness temperature provide information on the emissivity and therefore on the physical properties and conditions of the emitting medium. However, remote sensing of physical properties requires *a priori* knowledge of the emissivity of the various media. A good estimate of first-year sea ice emissivity, for example, can be inferred from Fresnel's law of reflection (Jackson, 1962):

$$r = \left|\frac{1 - n}{1 + n}\right|^2, \tag{3-2}$$

where r is the reflectance of the surface, and n is the index of refraction. The Fresnel equation is applicable to first-year sea ice because the observed radiation comes mainly from a thin saline layer at the snow/ice interface. Using a refractive index of 1.8 (Vant et al., 1974) for sea ice, the emissivity, which is related to the reflectance by $\epsilon = 1 - r$, is 0.918 calculated with this procedure. This value is also consistent with emissivities inferred from the ESMR data in regions of consolidated first-year ice using the climatological air temperatures to estimate the physical temperature, T. Although the emissivity is, in general, a function of the wavelength of the radiation, the wavelength independent equation 3-2 is applicable if the thickness of the layer from which the radiation emanates is small compared to the wavelength. Equation 3-2 cannot be used for multiyear ice because of the effect of internal scattering in the freeboard above the principal emitting ice layer, as will be discussed later. Aircraft measurements (e.g., Wilheit et al., 1972), however, indicated a value of about 0.84 for Arctic multiyear ice at 1.55-centimeter wavelength, nadir angle, and horizontal polarization.

For many other solids or liquids, microwave radiation emanates from only a thin surface layer. Since this layer is nearly isothermal, the emissivity in such a case is well defined. Also, if the material's dielectric properties are known, its emissivity can be readily calculated by considering only the electromagnetic reflection at the surface of the material according to equation 3-2. For example, water has a low emissivity because of the large reflection and small transmission at its surface. However, the situation is more complicated if the radiation emanates from a thicker layer that is not necessarily isothermal and is further complicated if this thicker layer has internal inhomogeneities that cause internal reflections or scattering of the radiation.

To understand the features of the microwave images, it is important to know the approximate depths from which the radiation emanates. For most emitters, the contribution to the external emission tends to decrease approximately exponentially with depth of the radiation source. The optical depth (based on radiative power attenuation by a factor of 1/e) is the thickness of the top layer from which approximately 63 percent of the radiation emanates. At the 1.55-centimeter wavelength, the optical depth is on the order of millimeters for water, soils, and first-year sea ice, on the order of 10 centimeters for the low salinity part of multiyear sea ice, and on the order of meters for dry snow.

In the general case of emission from the bulk of a medium that is not isothermal, the equation, $\epsilon = T_B/T$, is not appropriate because the physical temperature varies within the emitting medium. A general definition of emissivity for bulk emitting media and its specific application to polar firn is given by Zwally (1977). Briefly, a consideration of the radiative transfer through the medium must include the emission, absorption, and scattering by each element of the medium. A radiative transfer function, which describes the transfer of radiation from a given point within the medium to the surface, is used as a weighting function to obtain an effective physical temperature, $\langle T \rangle$. This quantity, $\langle T \rangle$, is a weighted average of the physical temperature over depth within the medium. The weighting represents how well the medium transfers emitted radiation from each depth to the surface. The emissivity in this case equals $T_B/\langle T \rangle$, which is analogous to the isothermal case. Properly defined, emissivity varies between 0 and 1.

Since the emissivity usually varies with the wavelength and polarization of the radiation, it is sometimes possible to deduce the physical temperature or more than one physical property of a medium from radiometric measurements of brightness temperature at more than one microwave wavelength and/or polarization. This potential provides the rationale for multifrequency (and dual polarization) brightness temperature measurements and for the development of inversion techniques (Gloersen and Barath, 1977), which determine the desired physical parameters from a set of brightness temperature values measured at multiple wavelengths (and polarizations). In the case of single-wavelength, single-polarization measurements, an independent estimate or measurement of physical temperature is required.

3.3 SEA ICE EMISSIVITY

The microwave emissivity of sea ice has been the subject of several experimental and theoretical investigations in recent years (Wilheit et al., 1972; Gloersen et al., 1978; Vant et al., 1974; Gloersen and Larabee, 1981; and Troy et al., 1981). Three principal ice types have been identified on the basis

of their radiometric signature: (1) new ice, (2) first-year ice, and (3) multiyear ice. The new ice category includes the standard (WMO, 1970; and Armstrong et al., 1973) newly formed ice types (frazil, grease, slush, and shuga) as well as nilas. The first-year ice category includes the standard first-year ice (30 centimeters to 2 meters in thickness) as well as young ice (10 to 30 centimeters), which is in the transition between nilas and first-year ice. The multiyear category includes all ice that has survived at least one summer melt (i.e., second-year old ice and multiyear old ice). A fourth category is referred to as summer ice, which includes melt ponds and a mixture of standard ice types. Approximate values of the emissivities of sea water at 1.55 centimeters for the different ice types are as follows:

Ice Type	ϵ (nadir view, 1.55 cm)
Open water	0.44
New ice (<10 cm)	0.45 to 0.92
First-year ice (>10 cm)	0.92
Multiyear ice	0.84
Summer ice	0.45 to 0.95

A schematic illustration of the basic differences between the various ice types is shown in Figure 3-1. The differences in emissivity between these ice types are caused mainly by variations in the dielectric properties of sea ice. It has been established experimentally that the dielectric properties, and

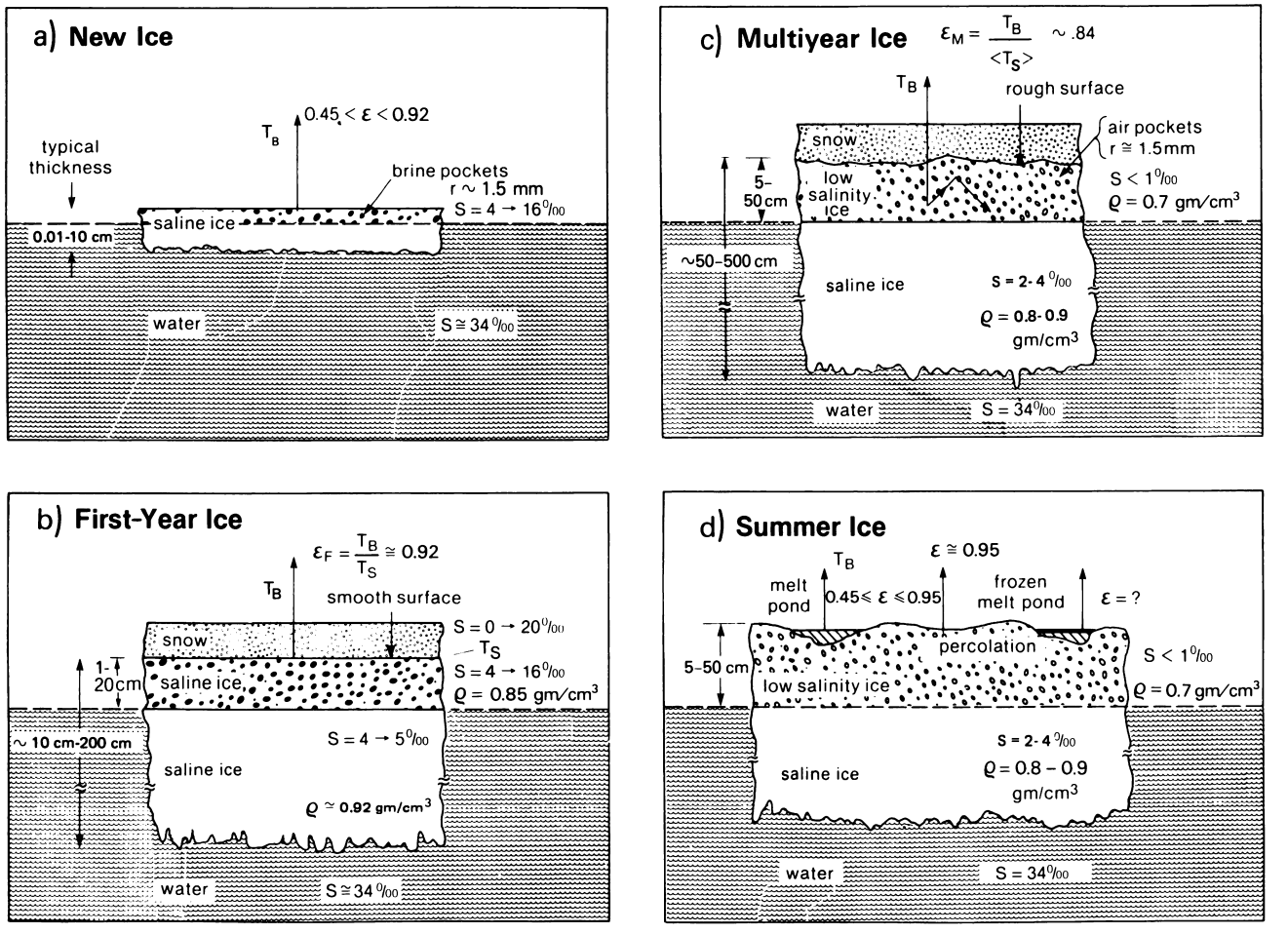

Figure 3-1. Schematic of radiometric and physical properties of the principal types of sea ice.

thus emissivity, depend mainly on salinity and temperature (Ramseier et al., 1974; and Vant et al., 1974, 1978). However, the effects on the measured radiance of thickness, surface properties, density, and structure, although normally less important than the others, can be significant, as discussed below.

The most important physical property that distinguishes new ice and first-year ice from multiyear ice is salinity in the freeboard portion of the ice or part of the ice above sea level. During freezing, concentrated brine pockets are entrapped between lamellae (very fine layers) of tiny ice plates. The amount of brine trapped depends on the temperature during formation and the age of the ice. Thus, sea ice formed at 263 K has a salinity from 4 to 6 parts per thousand, whereas the salinity of ice formed at 233 K ranges from 10 to 15 parts per thousand. The brine is a complex solution of metal salts, mainly NaCl, $MgCl_2$, and NA_2S0_4, which have freezing temperatures as low as 230 K. The amount of brine held in the freeboard portion of the ice gradually decreases as freezing continues through winter and as melt begins in spring and summer (Ramseier, private communication). The brine drainage could be caused by expulsion, which is a thermal process, and flushing, which occurs when surface meltwater percolates through the ice (Untersteiner, 1968). It could also be caused by movement of the heavier brine due to gravitation (Lake and Lewis, 1970). Such drainage processes create characteristic variations of salinity with depth. Generally, new ice has higher salinity near the surface than first-year ice, and multiyear ice has the lowest salinity in the freeboard (Cox and Weeks, 1975; and Campbell et al., 1976).

Salinity is an important microwave property because it determines the dielectric constant and, hence, optical depth or opacity of the ice (Gloersen and Larabee, 1981). The optical depth for typical saline ice is estimated to be less than one wavelength below the upper ice surface, irrespective of whether snow cover exists. A nonsaline and dry snow cover has a large optical depth and, therefore, has little effect on the transmission of radiation from the underlying sea ice. Thus, for first-year ice, the microwave radiation emitted emanates from near the ice surface. Because this layer is approximately an isothermal layer, equation 3-1 can be used to calculate the emissivity. For multiyear ice, with its much lower salinity content in the freeboard, the radiation originates mainly from the ice near sea level (Gloersen and Larabee, 1981) and is modified by scattering in the freeboard layer. The brine pockets become air pockets that scatter the upwelling radiation and thereby reduce the bulk emissivity of the media.

The density profile of the various ice types has been measured by Campbell et al. (1978). Mainly because of brine drainage, the density of multiyear ice is about 5 to 20 percent lower than that of first-year ice in the freeboard layer. The effect is to enhance the difference in optical depth between the first-year and multiyear ice because a decrease in density causes an increase in optical depth. However, if the radiation already originates from the entire freeboard layer and the ice immediately underneath, as in multiyear ice, any further reduction in the density would not affect the emissivity of the ice because the ice underneath the freeboard layer is again saline.

Two radiometrically distinct multiyear sea ice types have been observed in the Antarctic after the summer melt season. One type is radiometrically similar to the multiyear ice found in the Arctic, which undergoes surface melting and freeboard drainage of the brine cells during the melt season. A similar process may occur in the Antarctic in the Bellingshausen-Amundsen Seas, where brightness temperature of the multiyear ice is about 20 K lower than that of the surrounding first-year sea ice (Zwally and Gloersen, 1977). However, no salinity data exist for this radiometrically cold ice in the Bellingshausen-Amundsen Seas. The second type of multiyear ice, which is located in the western Weddell Sea, is radiometrically similar to first-year ice and has not undergone extensive freeboard drainage of the brine cells according to Gow et al. (1982).

Young ice and nilas thicker than a few centimeters might be expected to have the same emissivity as thicker first-year ice. However, some investigators (Gloersen et al., 1975b; Tooma et al., 1975; Ramseier et al., 1975; and Ketchum and Lohanick, 1980) have observed emissivities for young ice that differ from first-year ice. One explanation attributes this observed difference to the existence of a film of moisture on the surface of the young ice that lowers the emissivity compared to first-year ice (Ramseier et al., 1975; and Vant et al., 1974, 1978). A possible secondary effect that might cause the emissivity of young ice to be higher than that of first-year ice is the

slightly higher salinity of young ice. The higher surface temperature caused by greater heat conduction from the ocean would also result in higher T_B for young ice (Vant et al., 1974). For extremely thin ice (on the order of one optical depth), contributions from the water underneath the ice would also affect the emissivity. Gloersen and Larabee (1981) parameterized the contribution of layers of water and ice to the microwave radiation using a mixing model, and results agree with the only available measurement.

Another factor that distinguishes new ice and young ice from first-year ice is the presence of more snow on the latter. The insulating characteristics of the snow layer allow the sea ice to be thermodynamically warm compared to the air above it. The modeled and measured temperature profile of snow-covered ice discussed by Maykut and Untersteiner (1971) indicates that, in winter at about 243 K air temperature, the mean snow-surface temperature is about 14 K lower than the snow/ice interface temperature. The effect of snow cover on microwave emission was reported in Campbell et al. (1978), where removal of snow cover led to a drop in brightness temperature of 7 K at 0.8-centimeter wavelength and 12 K at 2.2 centimeters.

Summer ice is not as easy to define as the other ice types because of several complications illustrated in Figure 3-1(d). Because of large zonal and meridional variation in physical temperature, the surface phenomena associated with seasonal warming and melt occur at different times in various places. In addition, different types of surfaces respond to the same heating in different ways. It is therefore difficult to assign a single average value for the emissivity of summer ice.

As the physical temperature of the snow approaches 273 K, some of the ice particles change into liquid water. Because liquid water has a high refractive index (~8.5 below 20 GHz) compared to that of dry snow (~1.4), the dielectric properties of the snow mixture are strongly influenced by the amount of liquid water it contains. Furthermore, the existence of the highly conductive water particles in the snow volume makes the media inhomogeneous and thus affects the emission and scattering properties. Stiles and Ulaby (1980) measured the passive microwave response to wet and dry snow at 10.7 and 37 GHz. When measured at a snow depth of about 26 centimeters with frozen soil underneath, they found almost no difference between wet and dry snow at 10.7 GHz, but at 37 GHz, the brightness temperature of wet snow was greater than that of dry snow by about 100 K. Assuming a model consisting of a central core of ice and a surrounding shell of water with a thickness of one tenth of the radius of the ice particle, Chang and Gloersen (1975) used a numerical solution to the radiative transfer equation to calculate the brightness temperature of wet and dry snow. At a snow depth of 26 centimeters, their results show a difference of 25 K at 19 GHz. Although this value cannot be compared directly with those of Stiles and Ulaby, because it was measured at a different wavelength, it could qualitatively explain the substantial difference at 37 GHz.

As the snow melts, a layer of water (often referred to as a melt pond) forms on top. Because the emissivity of water is low compared to that of ice, the net emissivity of the ice begins to decrease as the depth of the melt ponds increases. For deep melt ponds (~15 centimeters), the emissivity can be as low as that of open water. However, there are periods when physical temperatures are below freezing even during summer. The surface of the water could freeze and, depending on the thickness, cause the emissivity to increase again. Melt ponds have been observed extensively in the Northern Hemisphere, but have not been seen by investigators (Andreas and Ackley, 1982) in the south polar region.

3.4 BRIGHTNESS TEMPERATURE OBSERVATIONS

The brightness temperature data from single satellite orbits have been converted to polar stereographic maps with a 293 by 293 grid, using a procedure discussed in Appendix A. The maps are linearly interpolated to 879- by 879-grid maps before photographic color-coded images are created. The color-coded images show brightness temperatures at 5 K intervals from 135 to 280 K. This range is sufficient to cover both ocean and ice at the 19-GHz frequency. Also, even though the relative calibration of the microwave sensor is better than 5 K, the interval is fine enough to show most of the salient features in the maps.

To provide complete spatial coverage in the polar regions, orbital brightness temperature data are accumulated and averaged over periods of 3 days (see Appendix A). The 3-day maps allow for

analysis of ice cover based on data averaged over a relatively short time period. Some examples of 3-day average maps of brightness temperature are shown in Figures 3-2 and 3-3. In these images, the orientation of the maps is the same as in Figure 2-1, and the outline of the continental boundaries is superimposed on the microwave data. The strong contrast in the emissivities of ice and water is clearly evident in these images, with the ocean areas having an average brightness temperature of about 135 K, whereas consolidated ice areas have brightness temperatures as high as 250 K. Thus, the ice edge and large open-water areas (polynyas) within the ice pack can be easily identified. The 3-day average maps are not corrected for the occasional anomalous shifts in the brightness temperature of several degrees (Appendix A, paragraph A.2.4).

Figure 3-2 shows images during midwinter for 1973, 1974, 1975, and 1976. In the Weddell Sea region, the appearance of a large polynya is conspicuous in 1974, 1975, and 1976 in contrast to 1973, the first year of ESMR data. The existence of this large polynya was discovered with the ESMR data in 1974 (Zwally et al., 1976), and a more detailed description is given in Carsey (1980).

Similar images during the spring breakup of the ice pack are shown in Figure 3-3. A comparison of the four images clearly shows substantial year-to-year differences, especially in the Weddell Sea, where the polynya is in various stages of opening to the surrounding seas. In the Ross Sea, a springtime polynya located immediately off the Ross Ice Shelf is also observed, with varying sizes and shapes for the different years. Around the continent, smaller coastal polynyas are evident in all years, many of these recurring in the same location.

Monthly average maps are generated by combining all available 3-day maps, properly weighted to cover 3-day periods for which useable ESMR data do not exist. Figures 3-4 through 3-15 show monthly images from January 1973 through December 1976 corrected for anomalous shifts of the brightness temperature (Appendix A, paragraph A.2.4). Monthly images averaged over the different years are also shown in Figures 3-16 through 3-21, and yearly averages are displayed in Figure 3-22. The monthly average maps are the basis of the monthly sea ice concentration maps in Chapters 4 and 5.

A comparison of the 3-day average and monthly average images reveals some noteworthy differences. For example, in the 3-day images, brightness temperatures greater than 175 K can be observed over the open ocean. These high ocean brightness temperatures are caused mainly by atmospheric effects such as precipitation, high water-vapor content, and surface roughness caused by the presence of high near-surface winds. These atmospheric effects are strongly suppressed in the monthly maps because, over any given area, these occurrences tend to be brief. Also, some patterns associated with the orbital track of the satellite are noticeable in the 3-day maps, indicating instrumental noise or imperfection in the relative calibration of the sensor. These patterns are also suppressed in the monthly maps by the data averaging.

A relatively narrow zone of rapidly increasing brightness temperature is generally observed, proceeding from the ice edge into the pack, especially in the 3-day images and during winter. During spring, when rapid ice breakup occurs, and during fall, when ice is advancing, the gradient at the edges is not as strong because of the effect of time averaging over a variable position of the ice edge. Thus, the 3-day maps normally have higher gradients in brightness temperature near the sea ice edge than those of the monthly maps. However, near the ice edge, several effects like flooding, roughness, varying thickness, and some other surface properties may alter the emissivity of the ice and, therefore, the net brightness temperatures, causing the spatial gradient of brightness temperature to be broader than the gradient in ice concentration.

For a particular ice type, sea ice radiance is proportional to physical temperature according to equation 3-1. The physical temperature of the ice is influenced by combined meteorological and oceanographic factors, but as a first approximation, it can be obtained from the mean surface air temperature. Except during summer, the surface air temperature exhibits a strong latitudinal variation that provides a tendency for sea ice brightness temperatures to decrease toward the continent due to the decrease in physical temperature. Because ice concentration tends to increase toward the continent in the direction of decreasing physical temperature, the maximum brightness temperatures normally occur near the center of the pack.

In the April 1974 image of the Amundsen Sea, for example, a low brightness temperature area forms a pattern similar to the distribution of ice

remaining at the end of the melt season in February 1974. In particular, these low brightness temperature regions surround an area of higher brightness temperatures in which first-year ice has formed in the summer polynya west of Thwaites Iceberg Tongue. The low brightness temperature region is evidently occupied by ice that is radiometrically similar to the multiyear ice found in the Arctic, which is discussed in Sections 3.2 and 3.3. The emissivity of most of the remaining ice, including the ice throughout the Weddell Sea, appears to be similar to that of Arctic first-year ice after the melt season.

Additional consideration must be given to the effects of surface melt on emissivity when interpreting these images during periods of melting. The increase in brightness temperature associated with the generation of free water in the surface snow has been discussed previously. An interesting example of the dramatic increase in brightness temperature due to surface melting is shown in the image for December 1974 in the vicinity of the Larsen Ice Shelf on the Antarctic Peninsula (Figure 3-15a). This effect can be clearly seen on both the ice shelf and the adjacent sea ice, but the increase is larger on the shelf ice because the usual brightness temperature of the dry firn on the ice shelf is much lower than the brightness temperature of sea ice.

The microwave properties of the firn on the continental ice sheets and ice shelves are quite different from the microwave properties of sea ice. The continental areas show very little correlation between the brightness temperature and physical temperature because the emissivity variations are even larger than the spatial variations of surface physical temperature. Chang et al. (1976) used a numerical solution to the radiative transfer equation to show that, for a uniform snow medium, volume scattering from the snow grains is the principal factor affecting the microwave emission and that the source of radiation can emanate from several meters within the medium. Subsequently, taking into account variations of snow properties with depth, Zwally (1977) used an analytic approximation to solve for the microwave emissivity of polar firn. The results show that the emissivity can be modeled by taking into account the spatial variations of snow-grain size with depth, with larger grains causing more scattering and lower emissivities. However, the approximation overestimated the effect of radiative scattering in the medium because contributions due to multiple scattering were neglected. Comiso et al. (1982) used a method similar to Chang et al. (1976), but accounted for variations of snow properties with depth and multiple scattering. Their results show a qualitative agreement with Zwally (1977) and substantial improvement in the estimation of scattering effects. In addition, the model was successfully used to simulate the spatial variation of the seasonal distribution of microwave emission in the ice sheet. Thus, qualitatively, the microwave variations are mainly attributed to spatial variations in grain size that determine the bulk emissivity and brightness temperature. The grain size in the firn is determined in part by the accumulation rate (larger grains for low-accumulation rate) so that the observed variations in brightness temperature are related to variations in the accumulation rate over the ice sheet (Zwally, 1977). For example, the lowest brightness temperatures are observed in the low-accumulation region over much of the East Antarctic ice sheet, and the highest are observed in the high-accumulation Ellsworth Land.

Around the Antarctic coast, there are numerous examples in the maps of reduced brightness temperatures extending up to about 500 kilometers inland from major outlet glaciers. The converging ice flow and associated topography may be producing wind-induced accumulation and temperature variations that cause the observed brightness temperature patterns. The reduced sea ice concentration and summer polynyas offshore from many of these features provide evidence of strong winds. A specific example of this phenomenon on the ice sheet is the lower brightness temperature along the 75°S latitude circle at approximately 95°W that extends inland from the Pine Island Glacier (75°S, 101°W) (Figure 3-22). Other examples occur inland from the Ninnis Glacier (68°S, 147°E), Mertz Glacier (67°S, 144°E), Frost Glacier (67°S, 129°E), Dalton Iceberg Tongue (66°S, 122°E), Totten Glacier (67°S, 116°E), Vanderford Glacier (67°S, 111°E), Denman Glacier (67°S, 99°E), Scott Glacier (66°S, 100°E), and Davis Bay and the Dibble Glacier (66°S, 134°E) (Figure 3-22). Near the Mawson coast, the summer images reveal a polynya (67°S, 67°E), and the winter images reveal reduced sea ice concentrations in the same area, just offshore from reduced brightness temperatures that extend inland. Winter visible and IR images have been examined by Knapp (1969) to

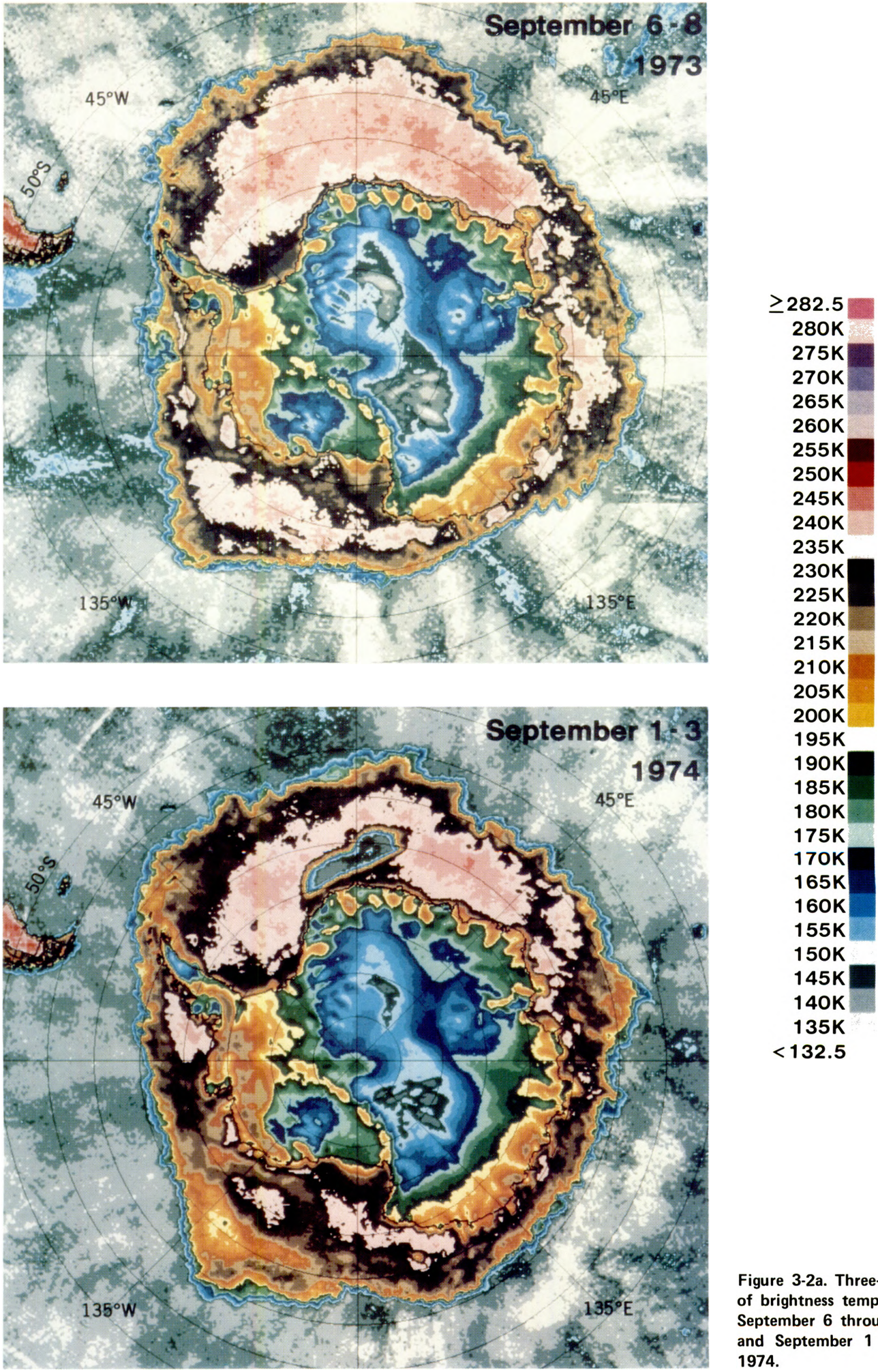

Figure 3-2a. Three-day average of brightness temperatures for September 6 through 8, 1973, and September 1 through 3, 1974.

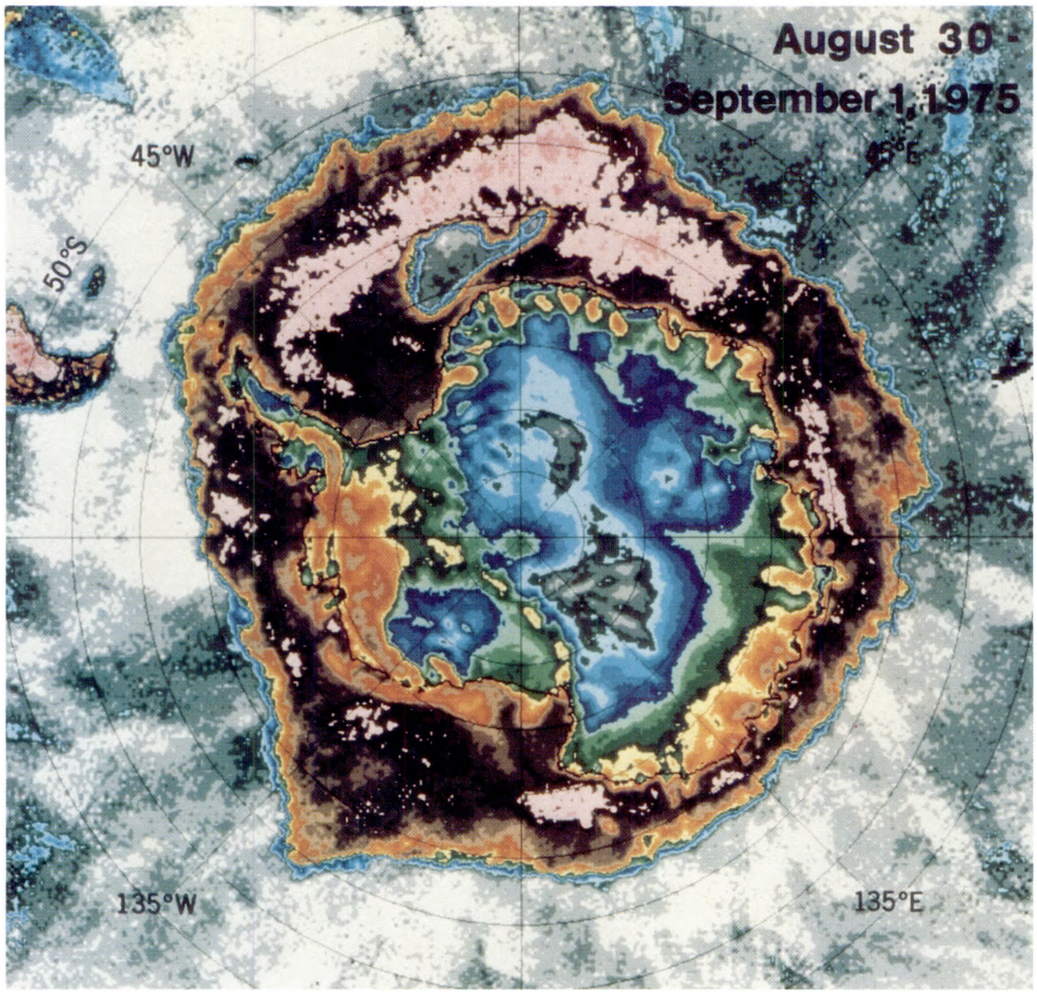

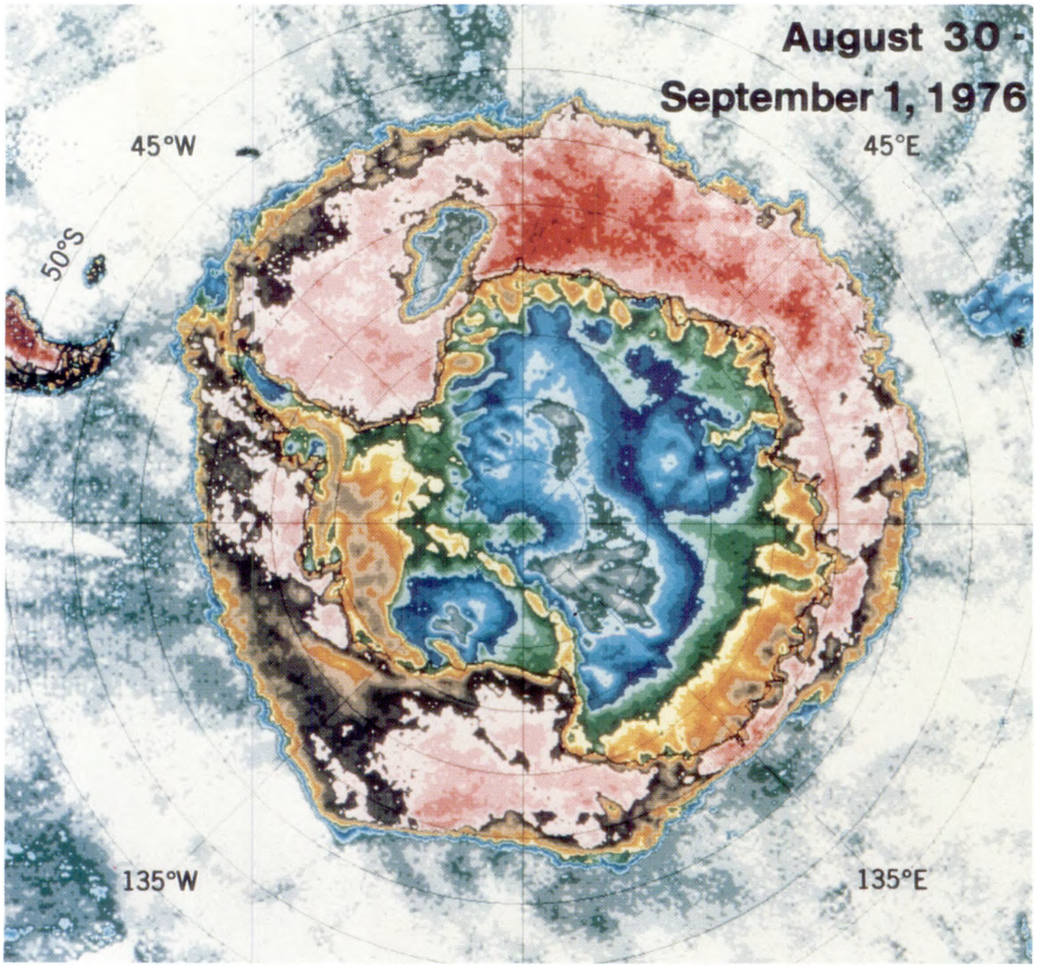

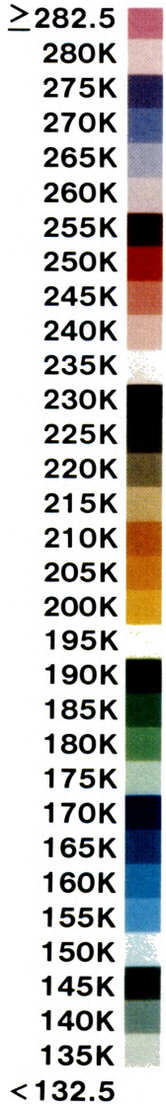

Figure 3-2b. Three-day average of brightness temperatures for August 30 through September 1, 1975, and August 30 through September 1, 1976.

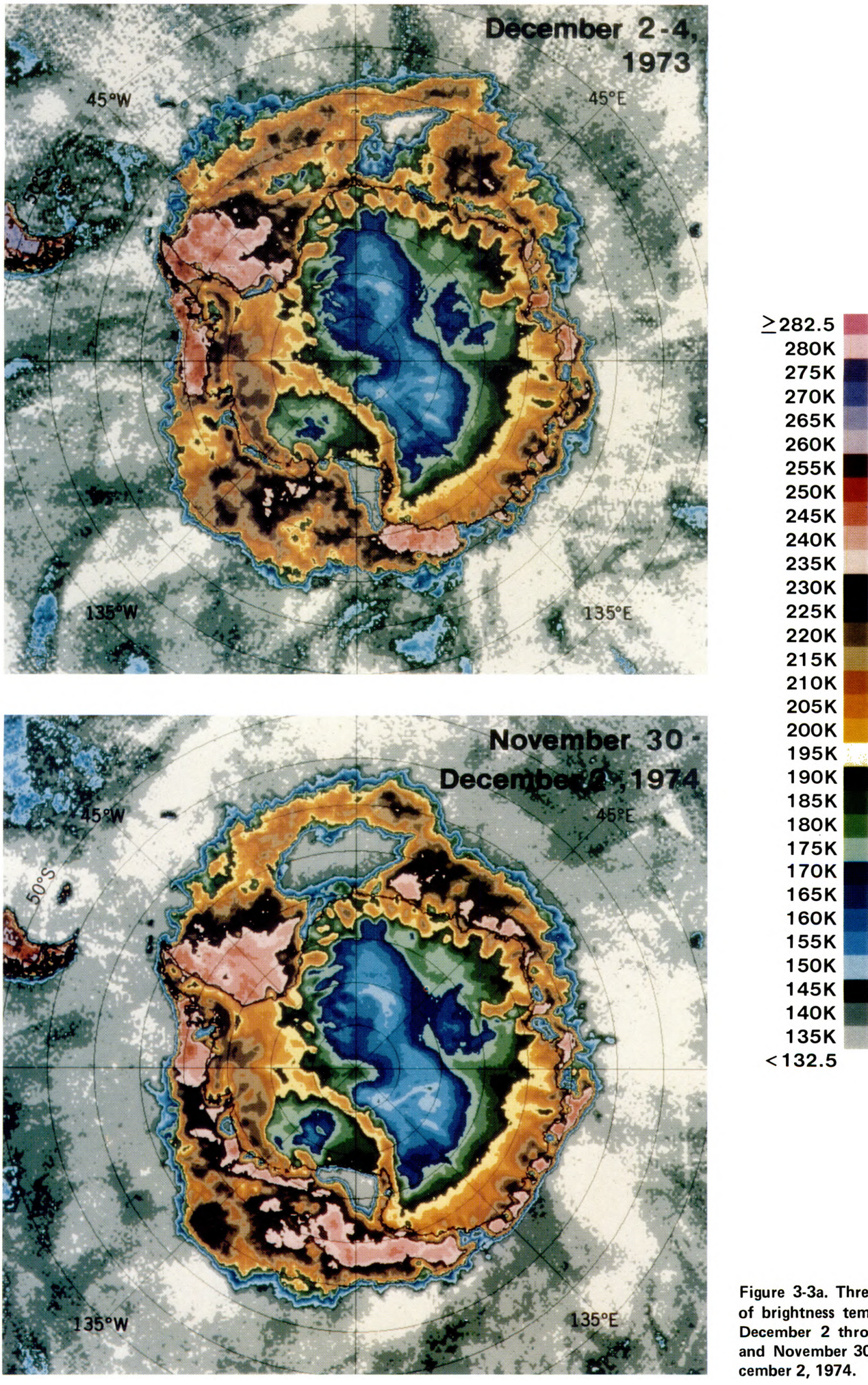

Figure 3-3a. Three-day average of brightness temperatures for December 2 through 4, 1973, and November 30 through December 2, 1974.

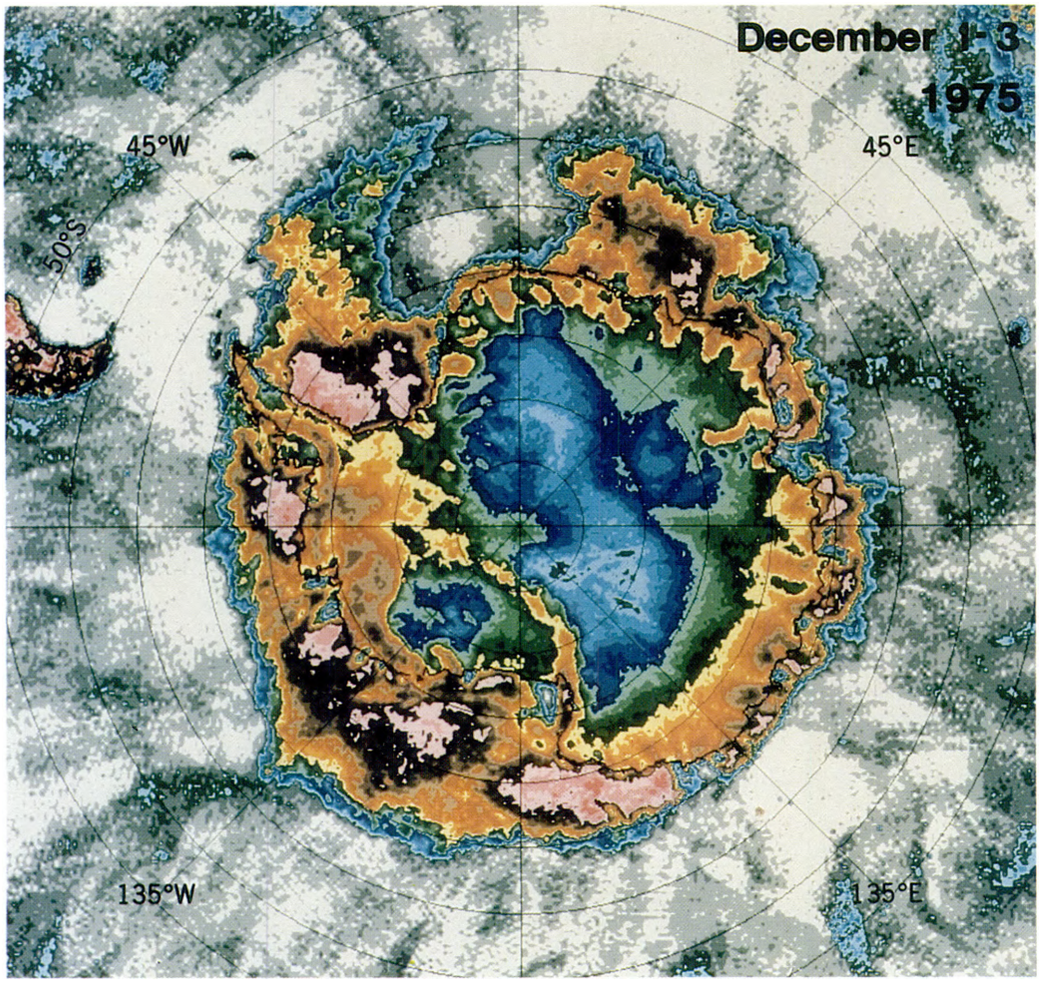

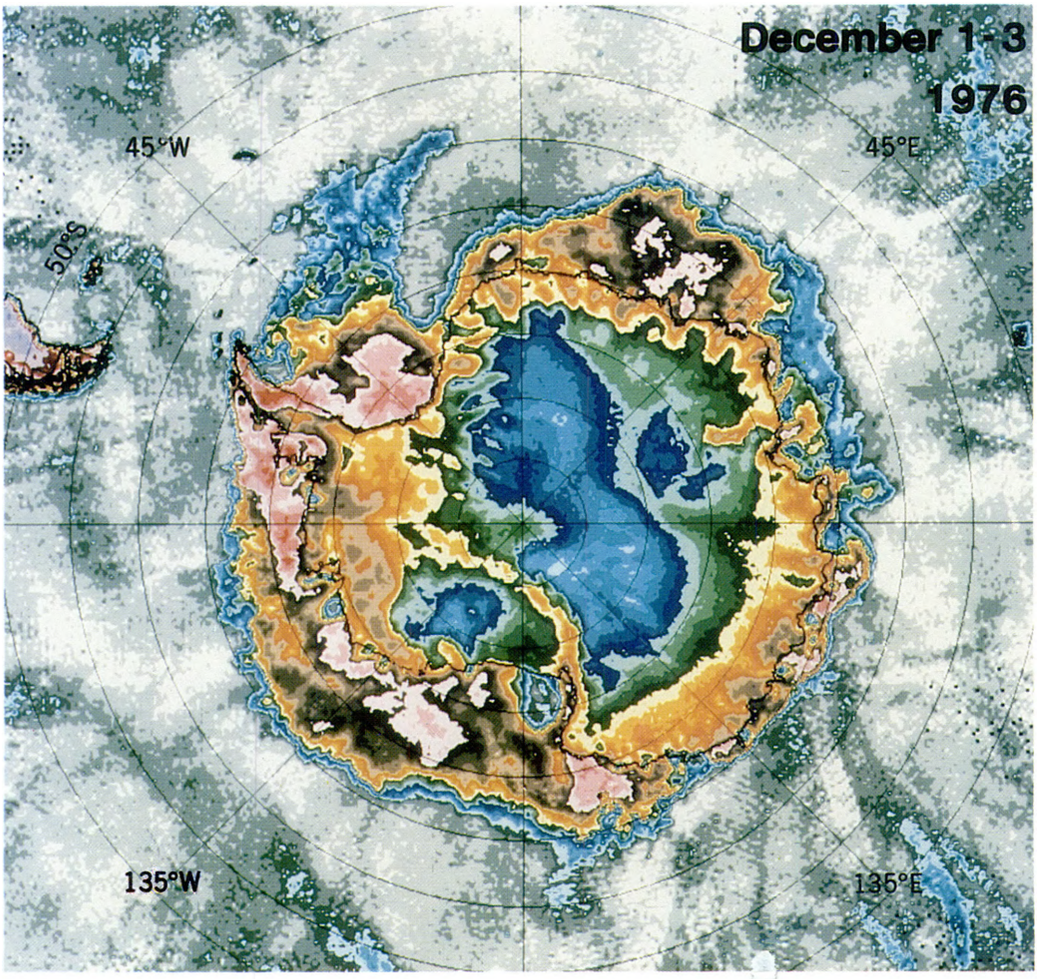

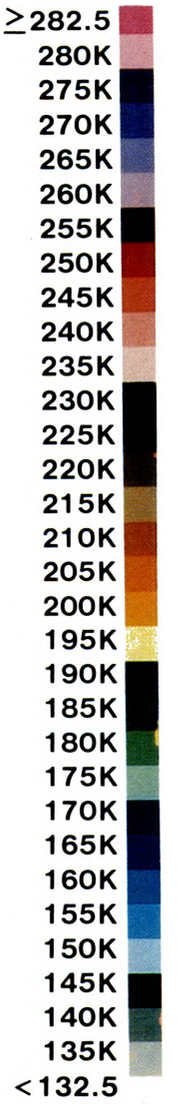

Figure 3-3b. Three-day average of brightness temperatures for December 1 through 3, 1975, and December 1 through 3, 1976.

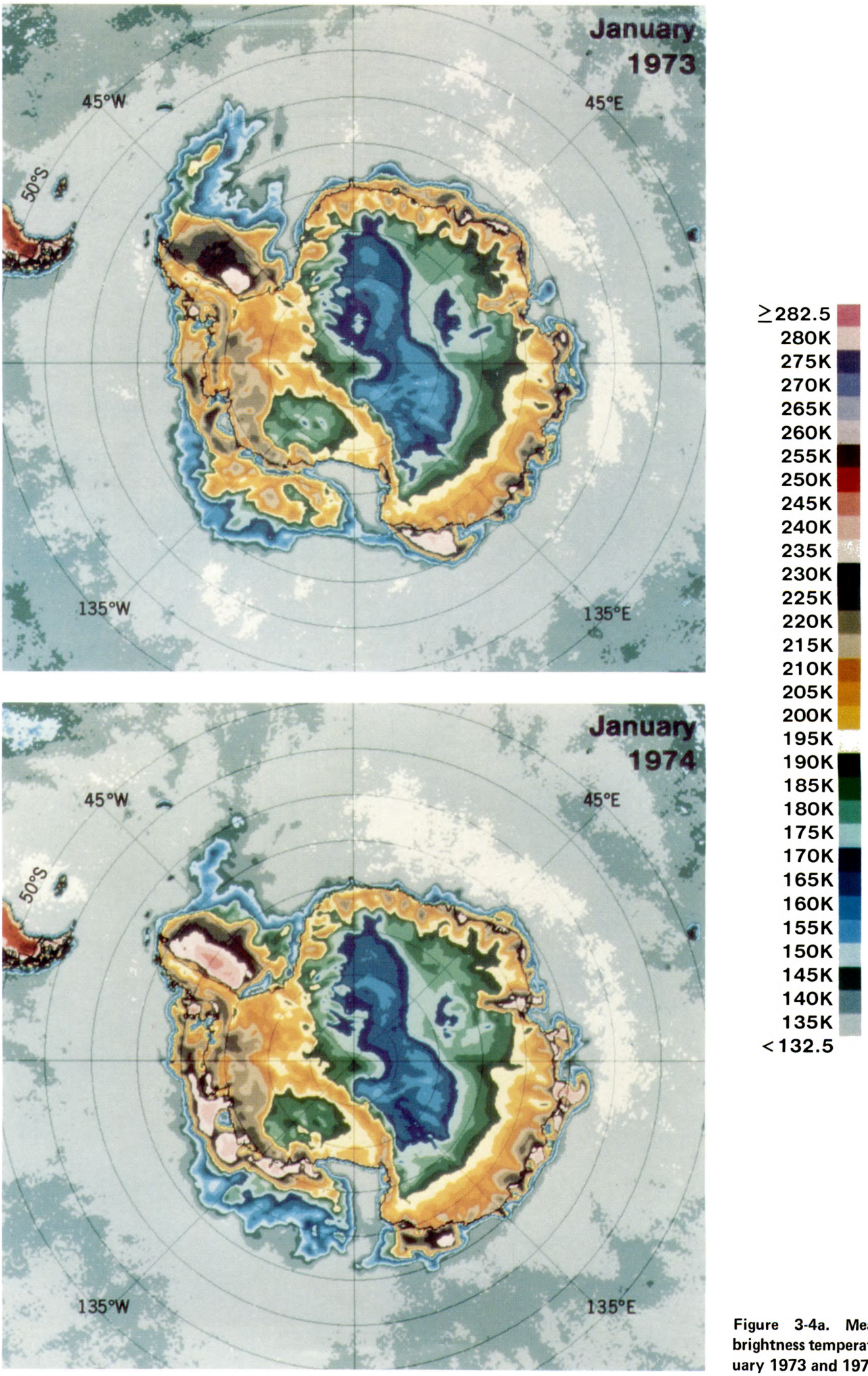

Figure 3-4a. Mean monthly brightness temperatures for January 1973 and 1974.

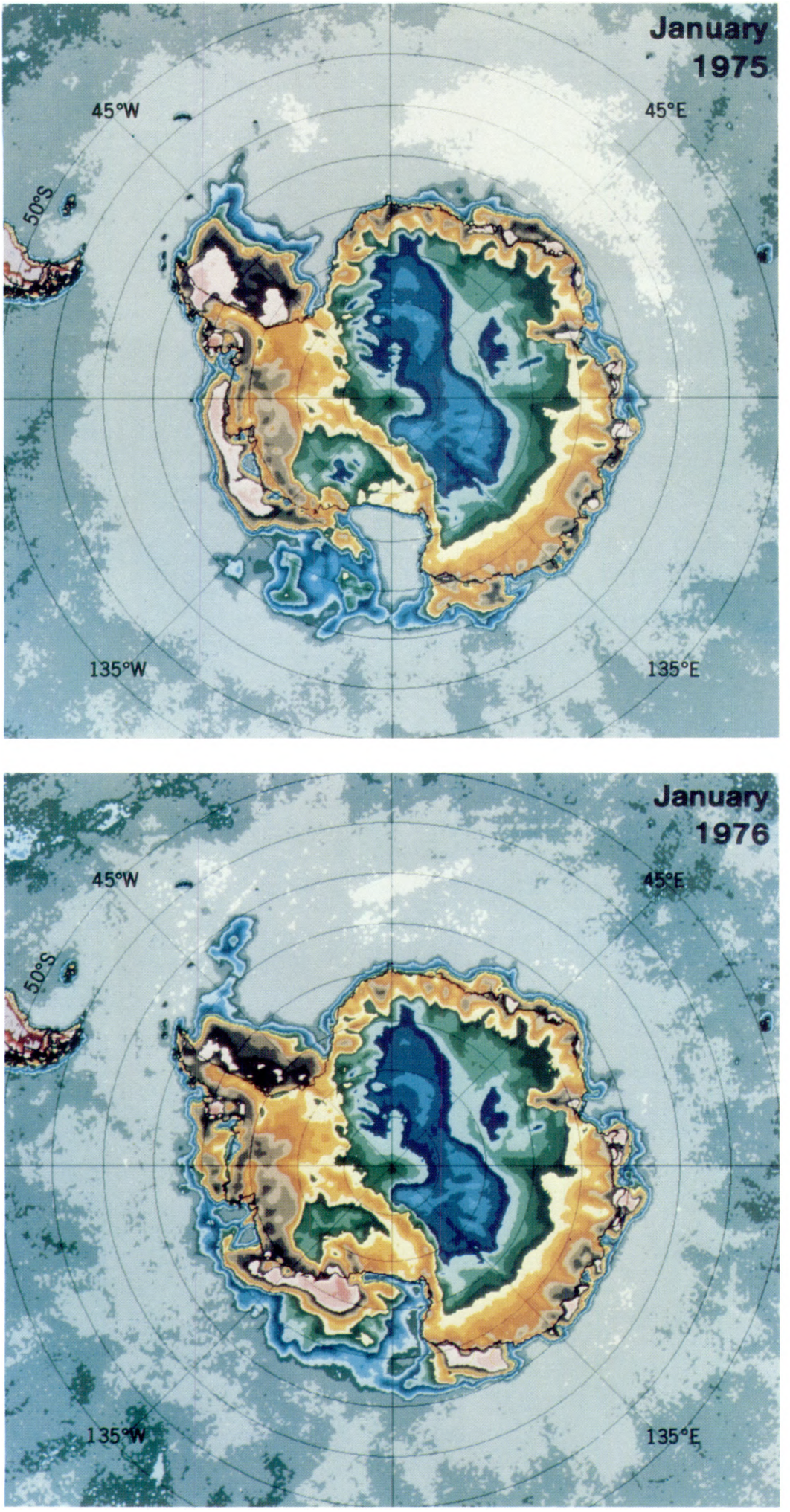

Figure 3-4b. Mean monthly brightness temperatures for January 1975 and 1976.

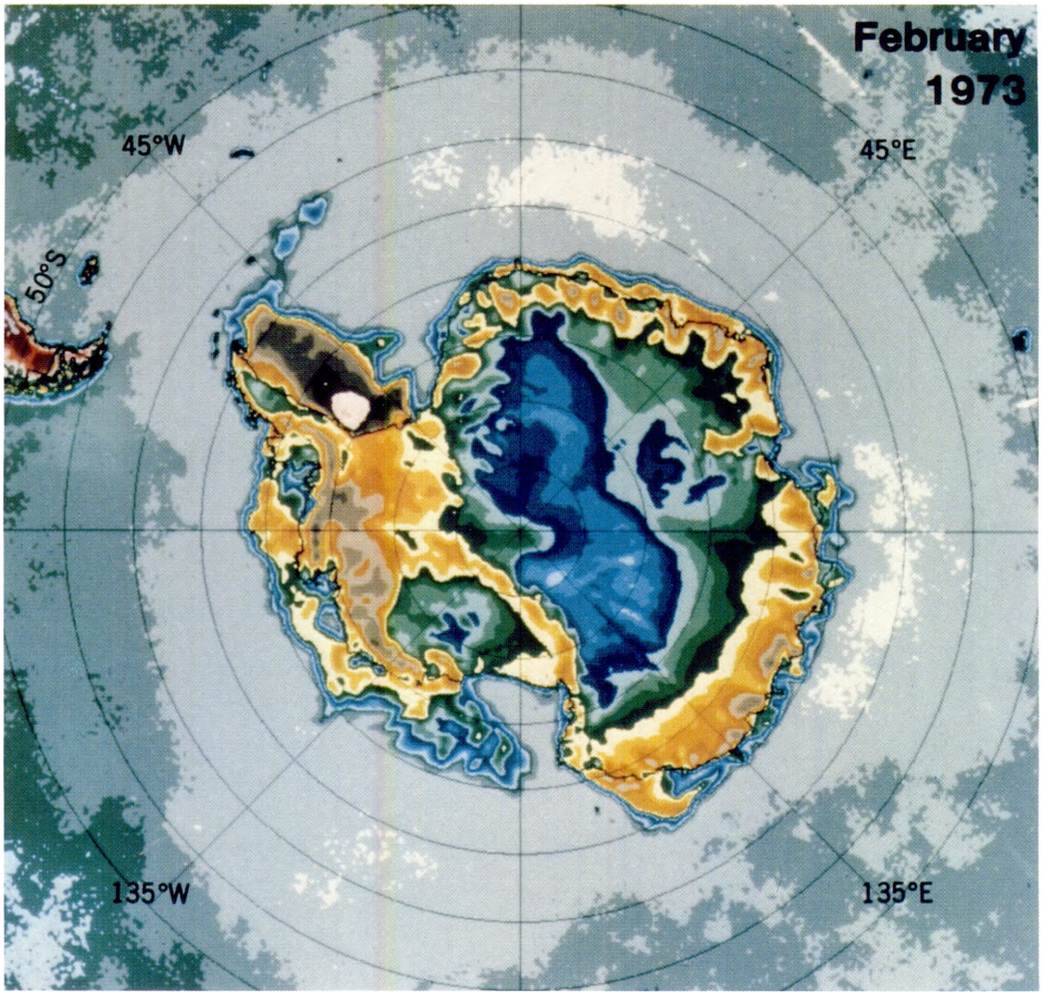

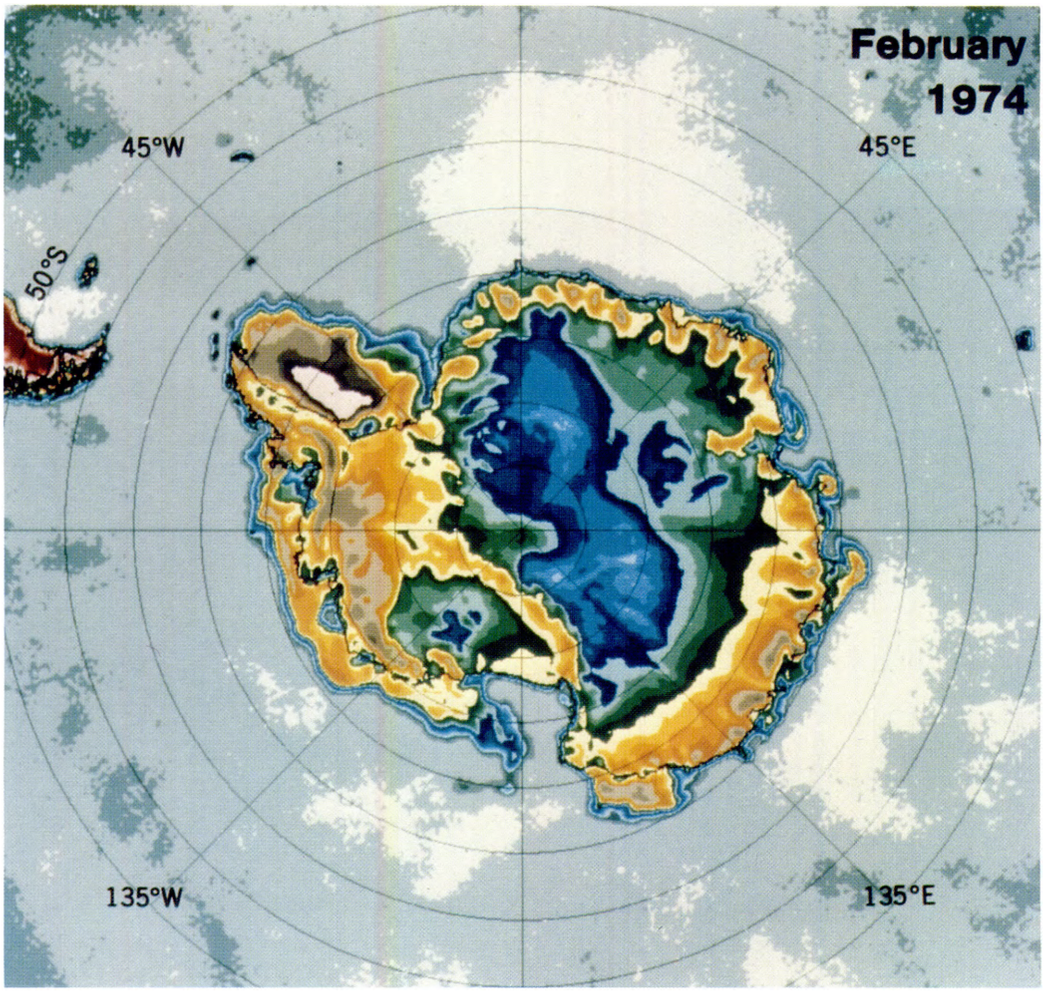

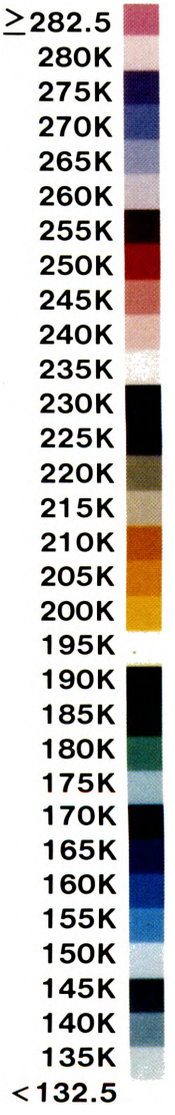

Figure 3-5a. Mean monthly brightness temperatures for February 1973 and 1974.

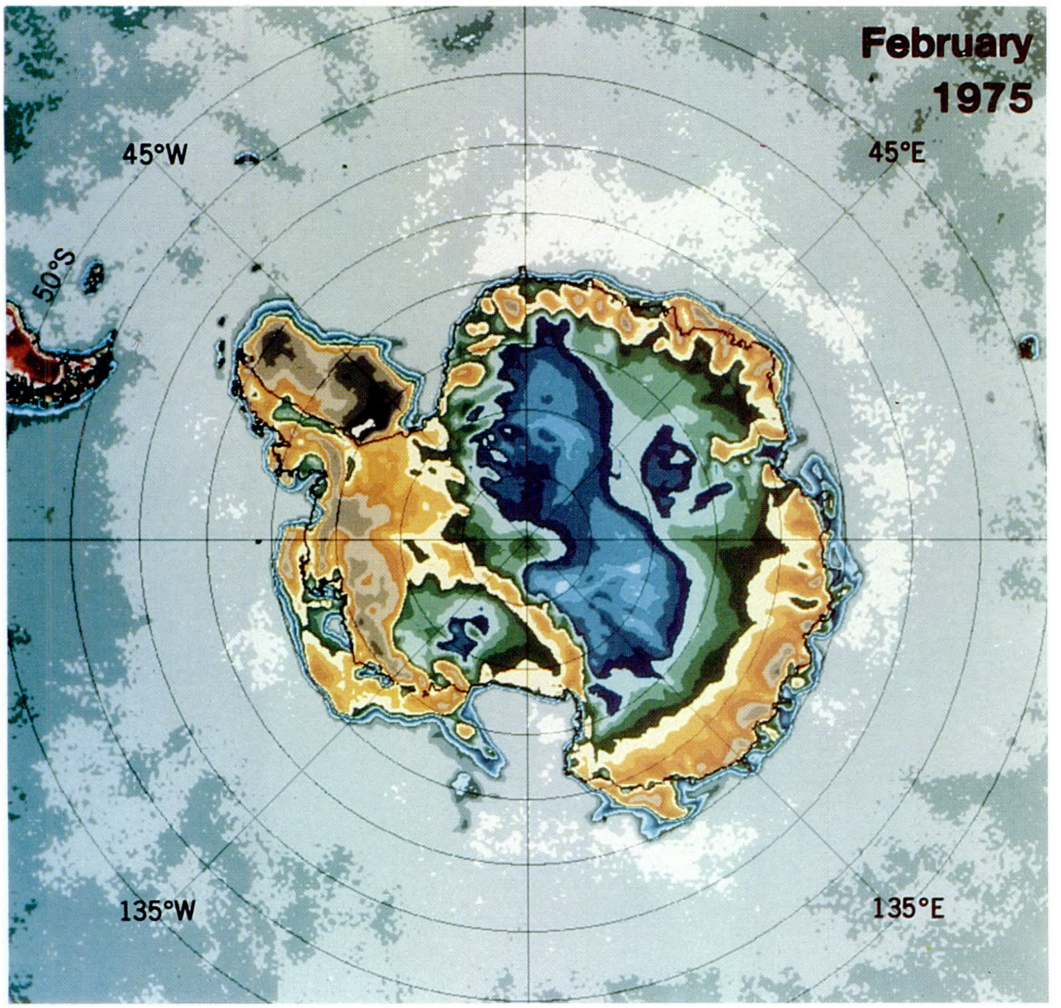

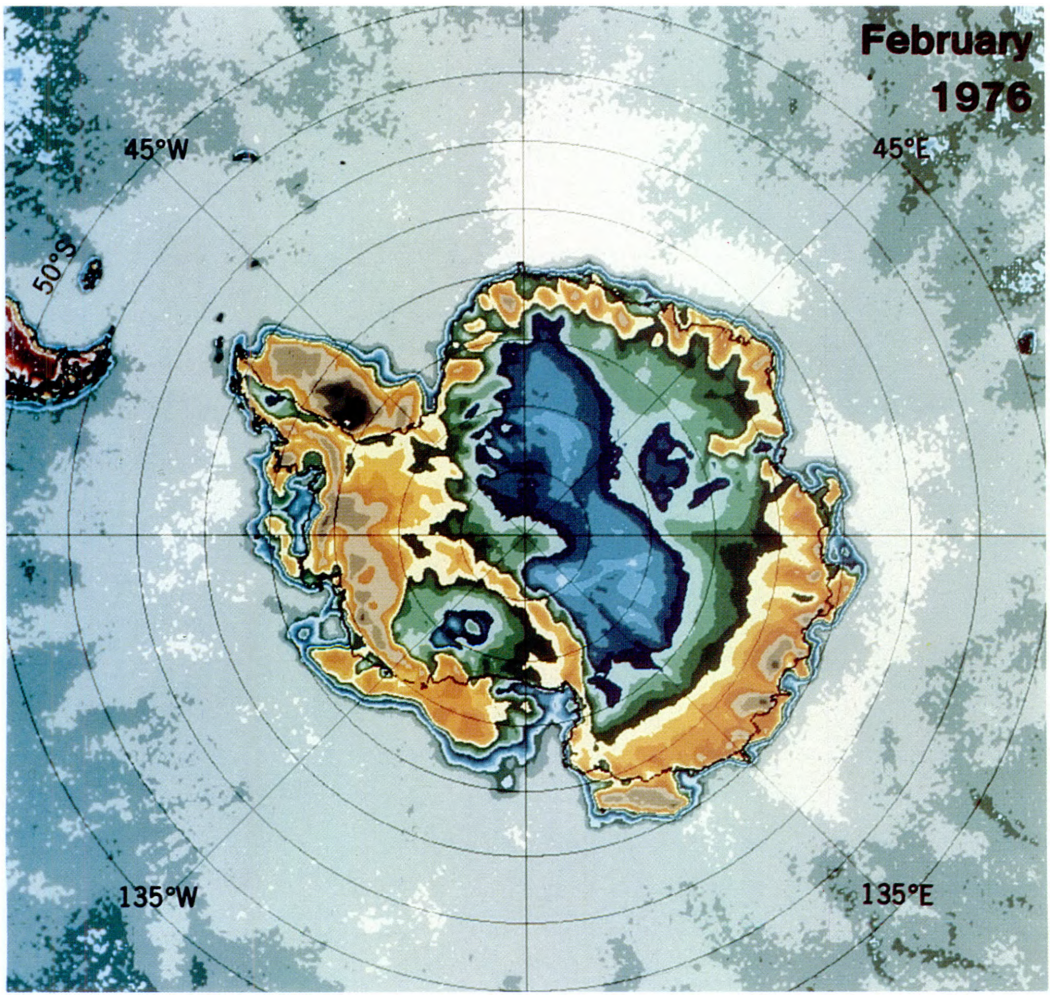

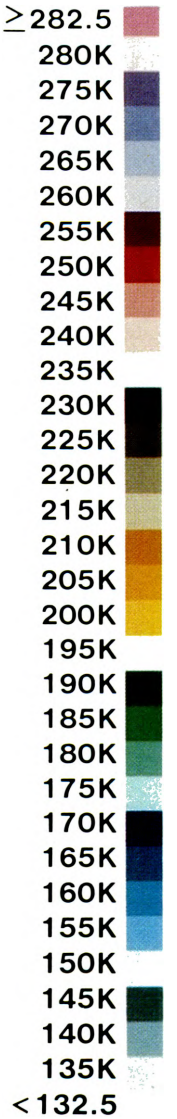

Figure 3-5b. Mean monthly brightness temperatures for February 1975 and 1976.

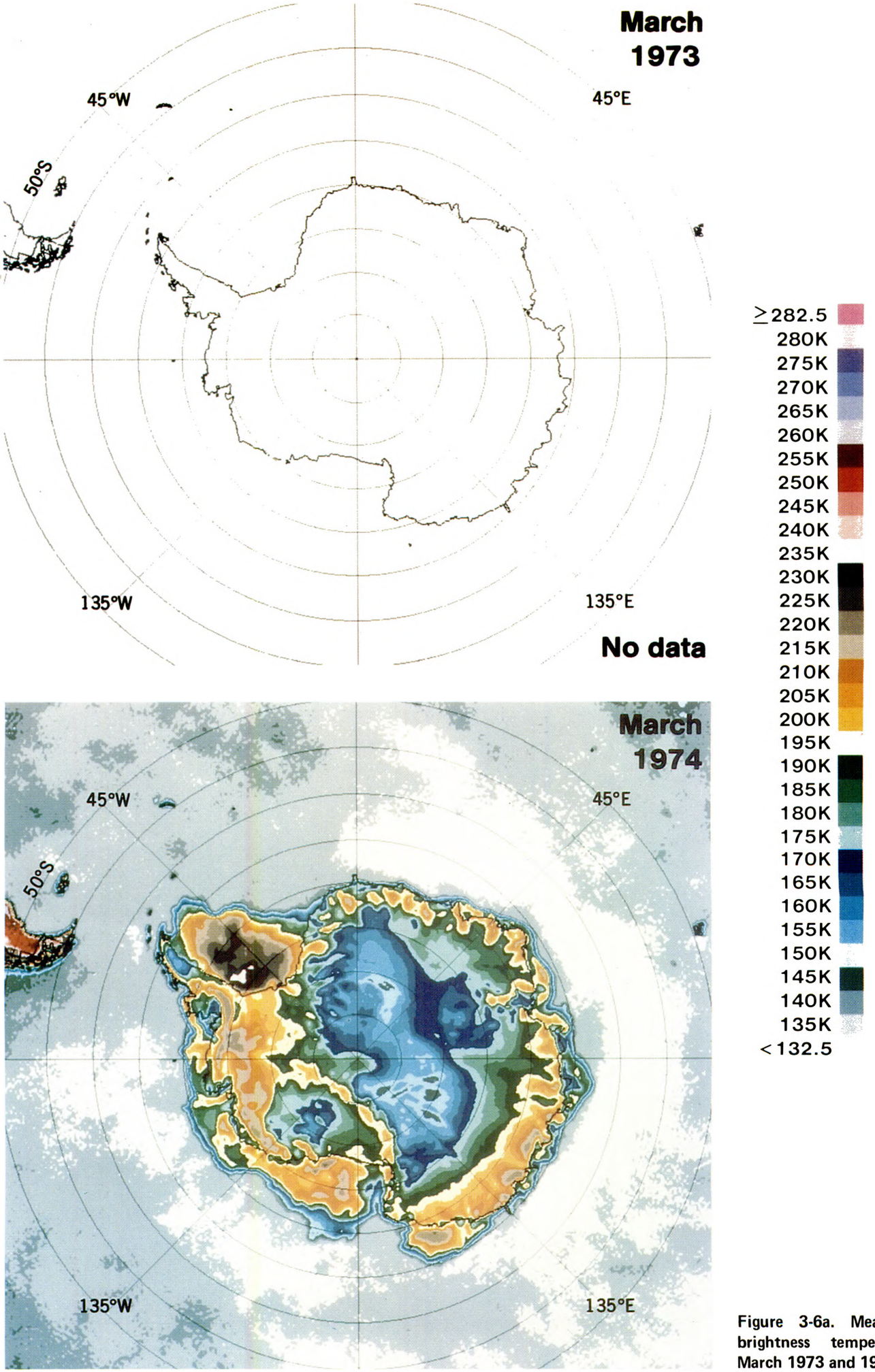

Figure 3-6a. Mean monthly brightness temperatures for March 1973 and 1974.

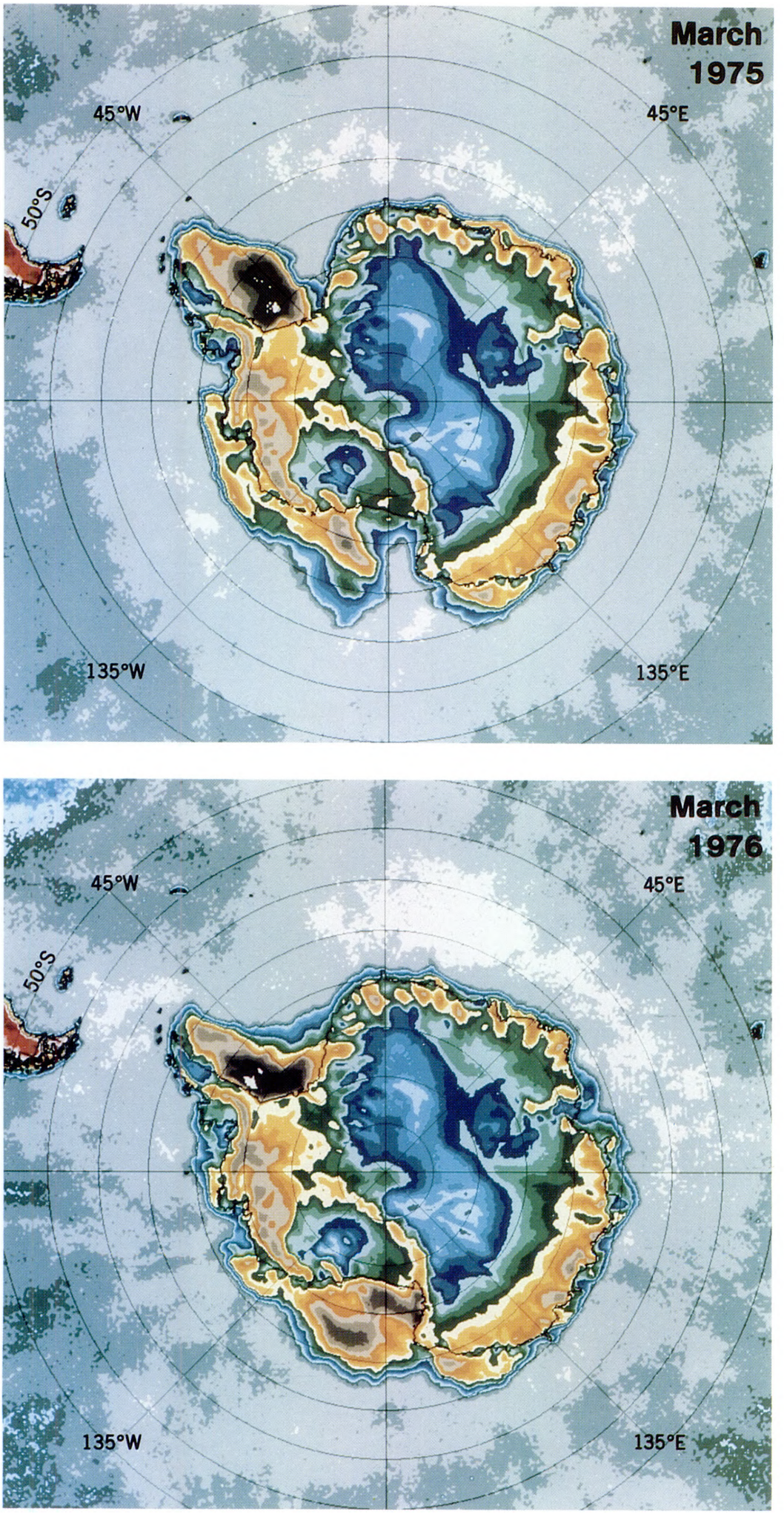

Figure 3-6b. Mean monthly brightness temperatures for March 1975 and 1976.

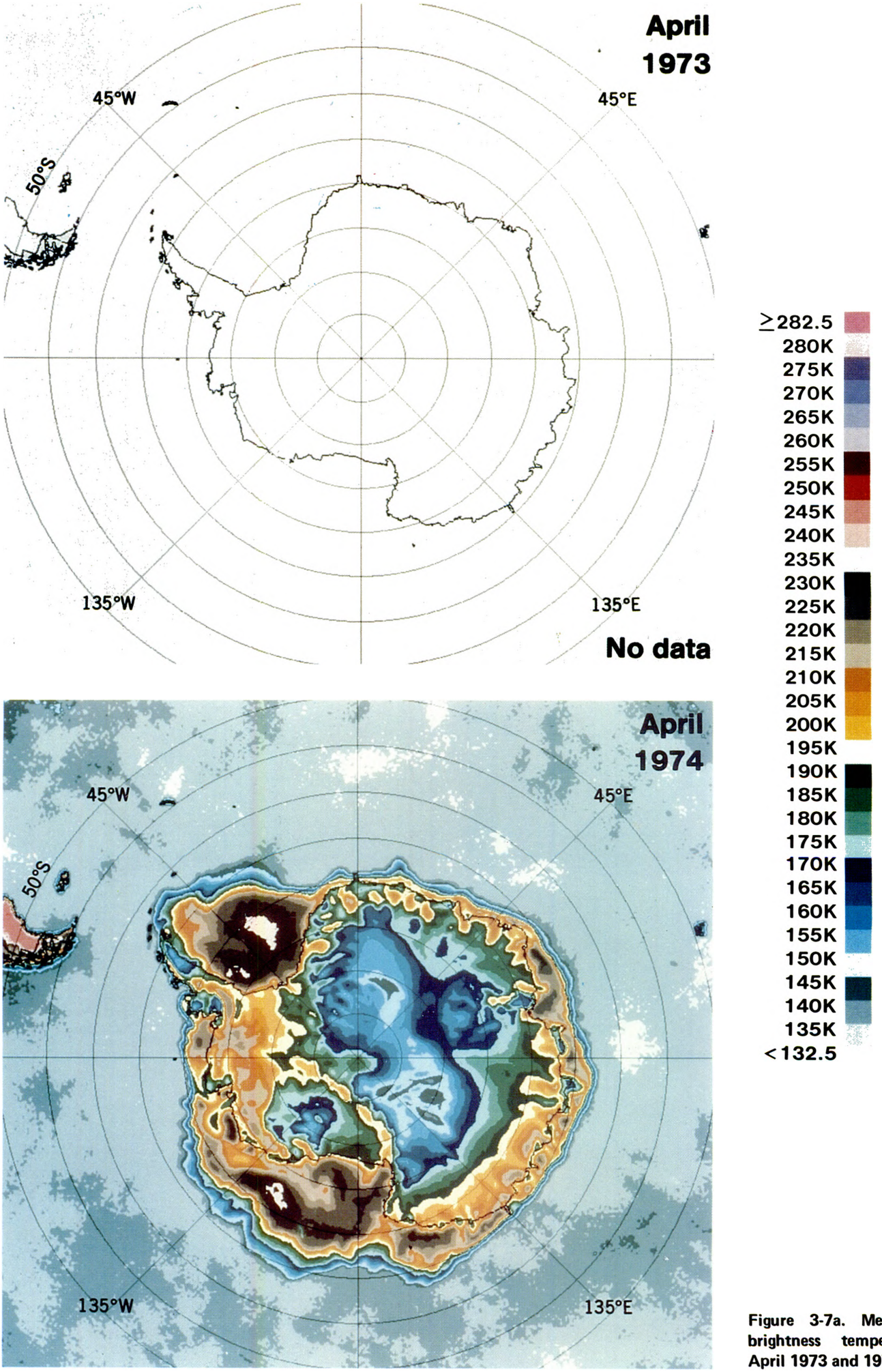

Figure 3-7a. Mean monthly brightness temperatures for April 1973 and 1974.

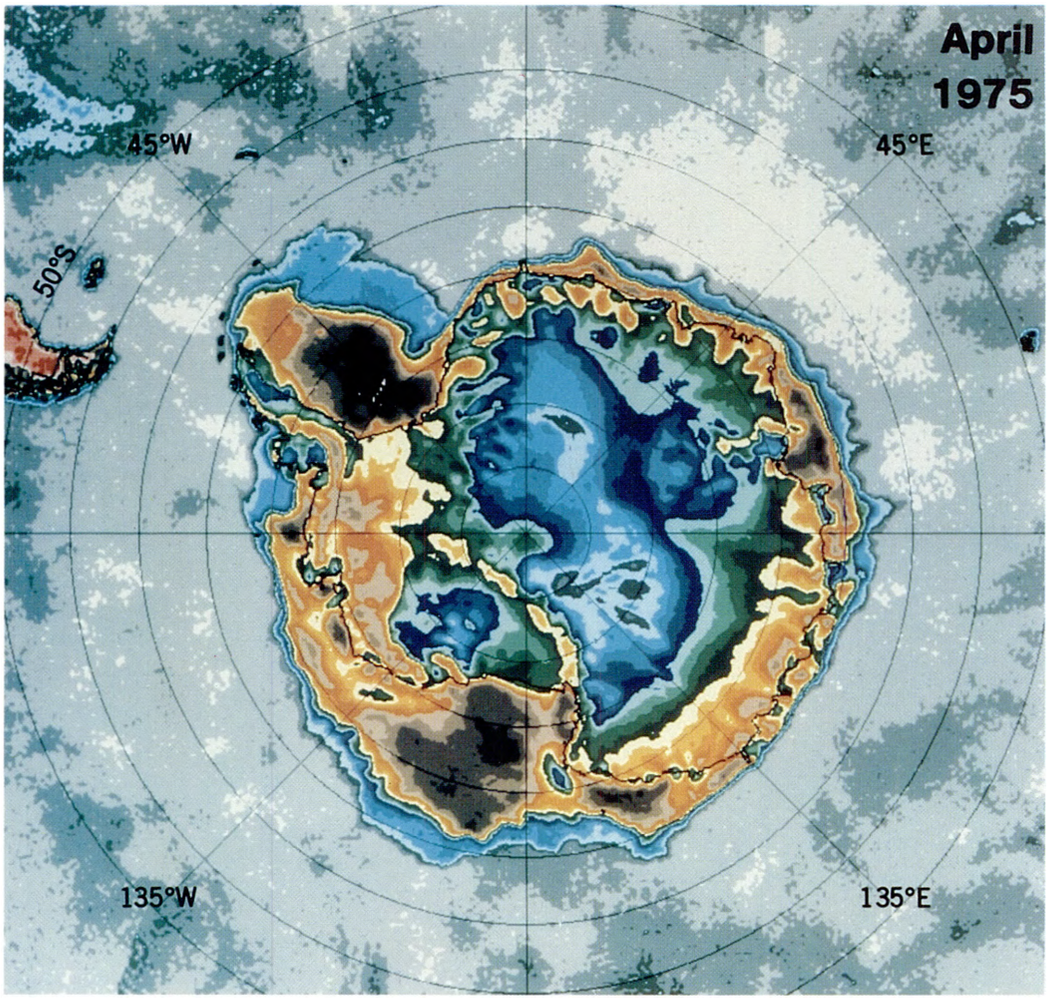

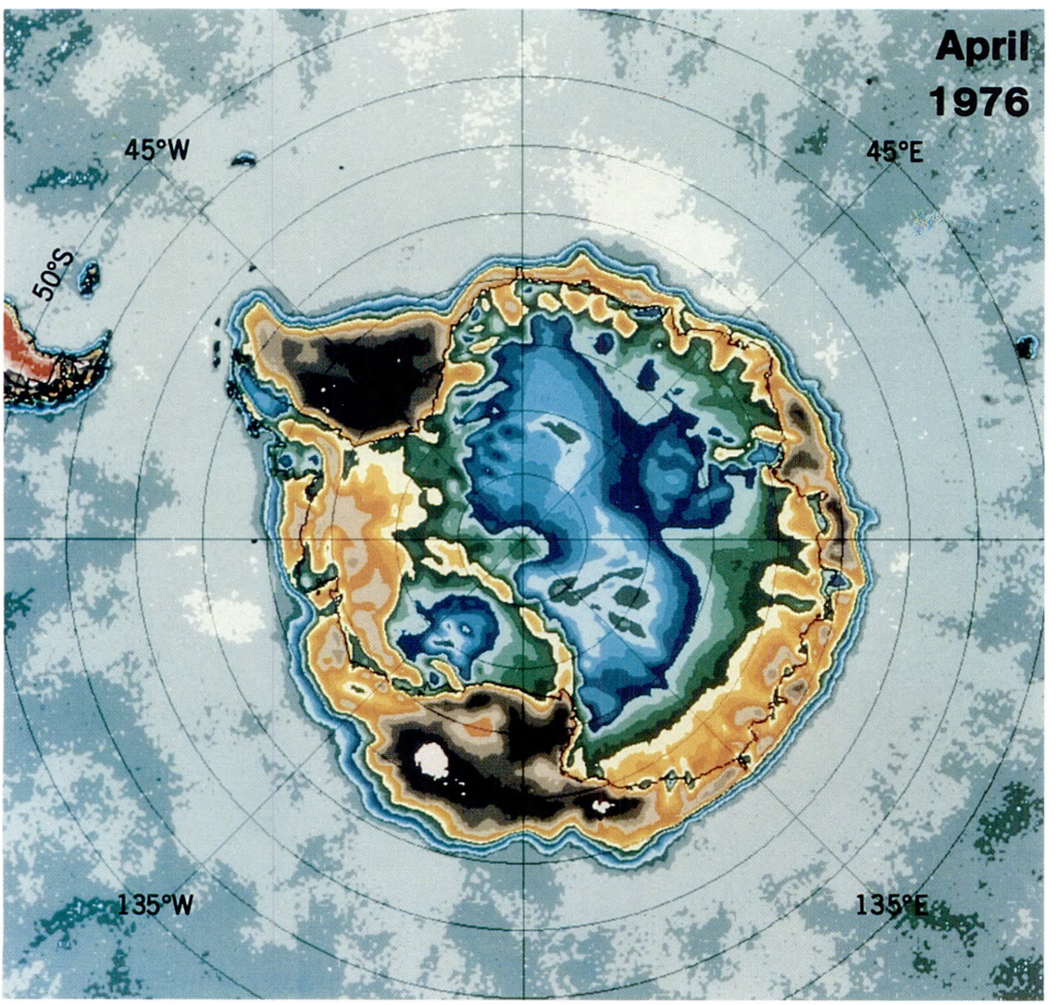

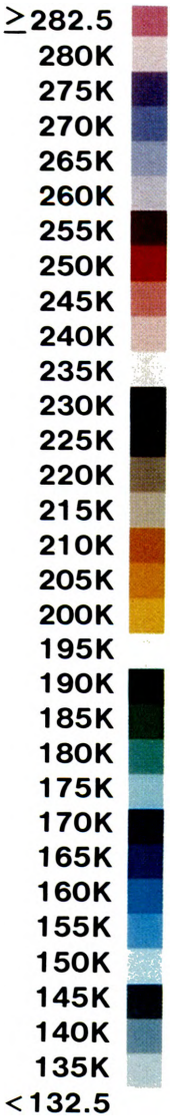

Figure 3-7b. Mean monthly brightness temperatures for April 1975 and 1976.

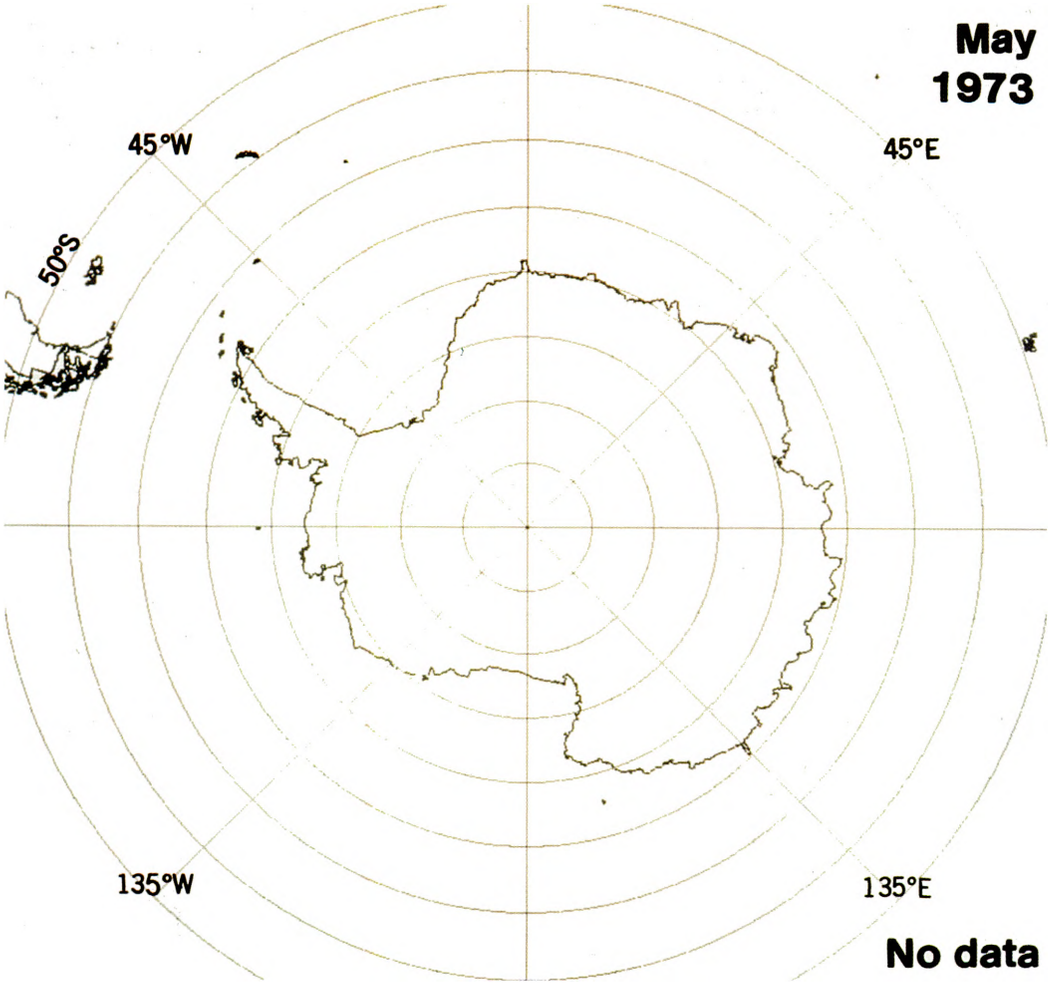

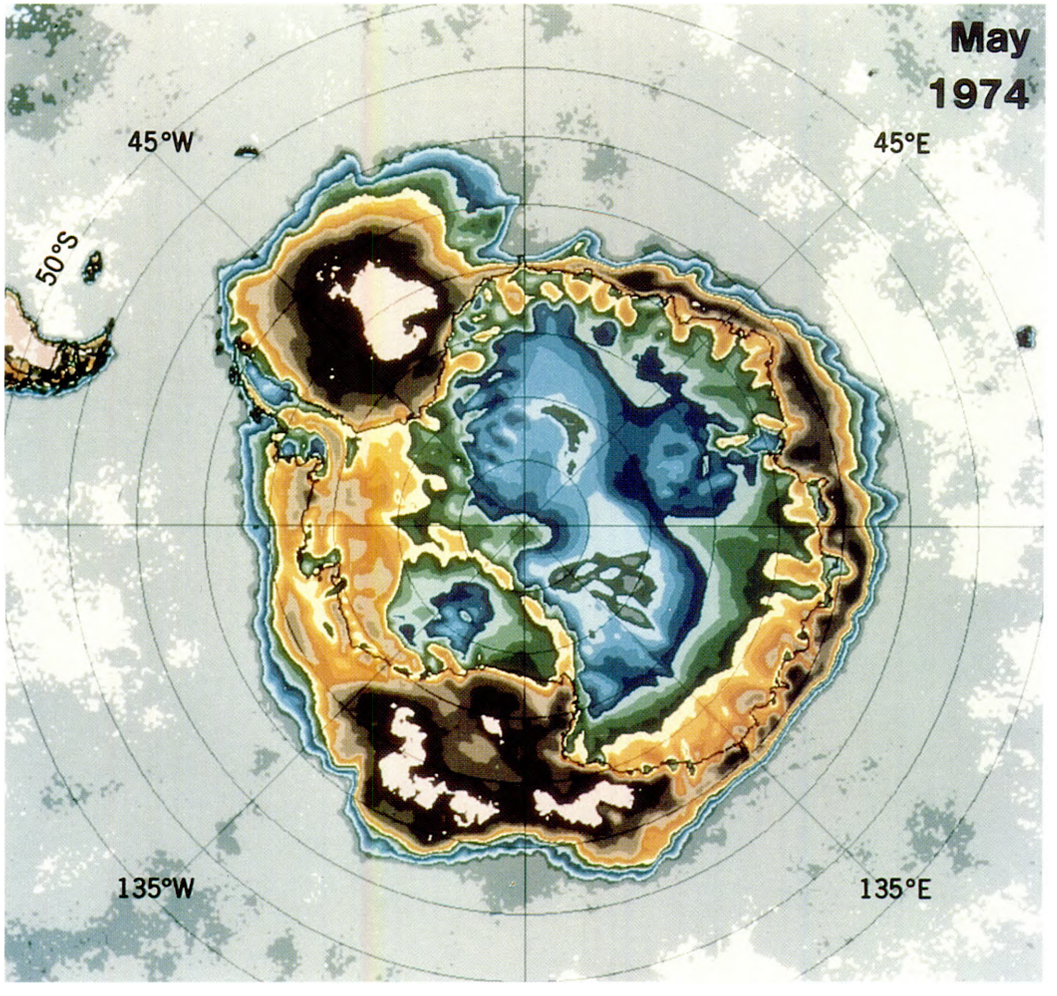

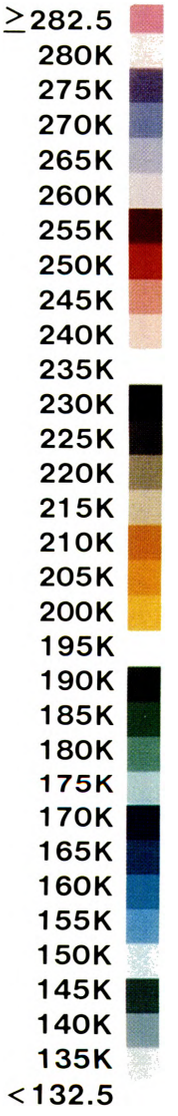

Figure 3-8a. Mean monthly brightness temperatures for May 1973 and 1974.

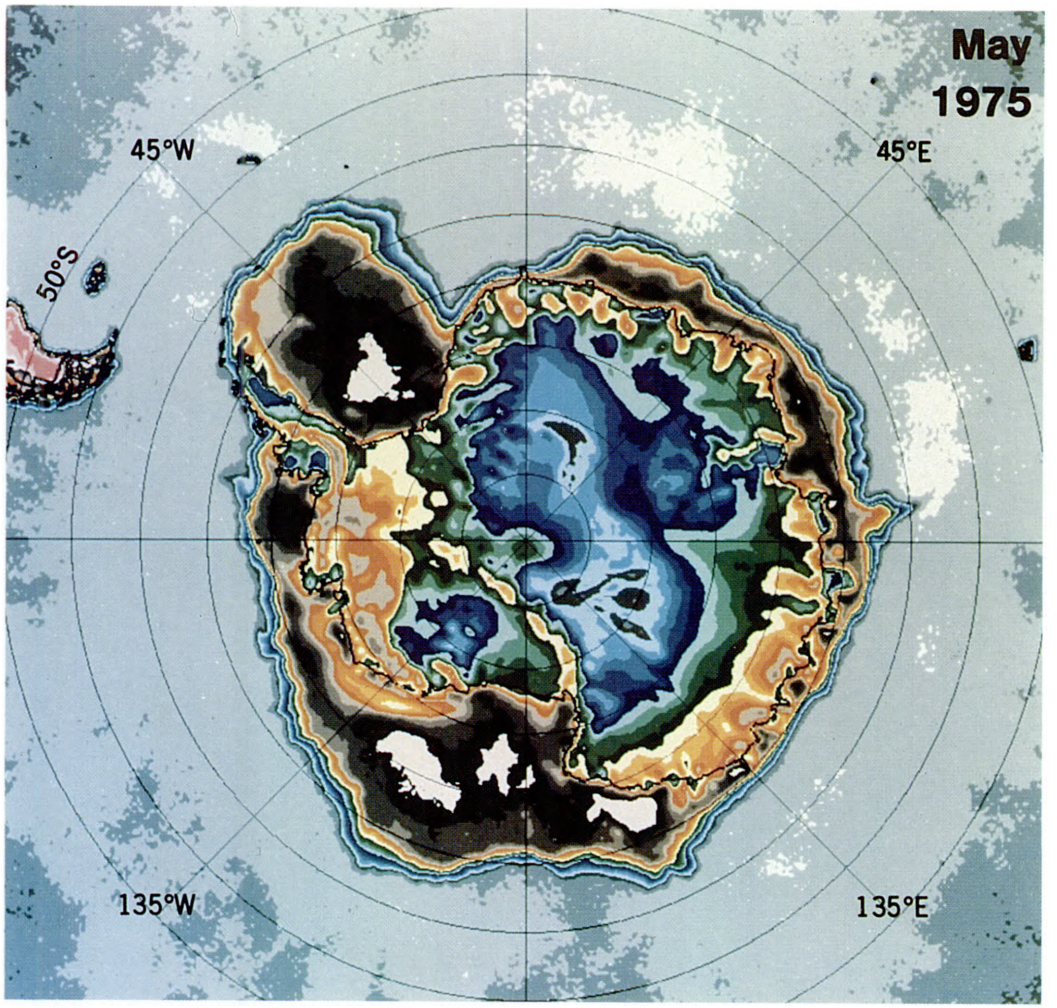

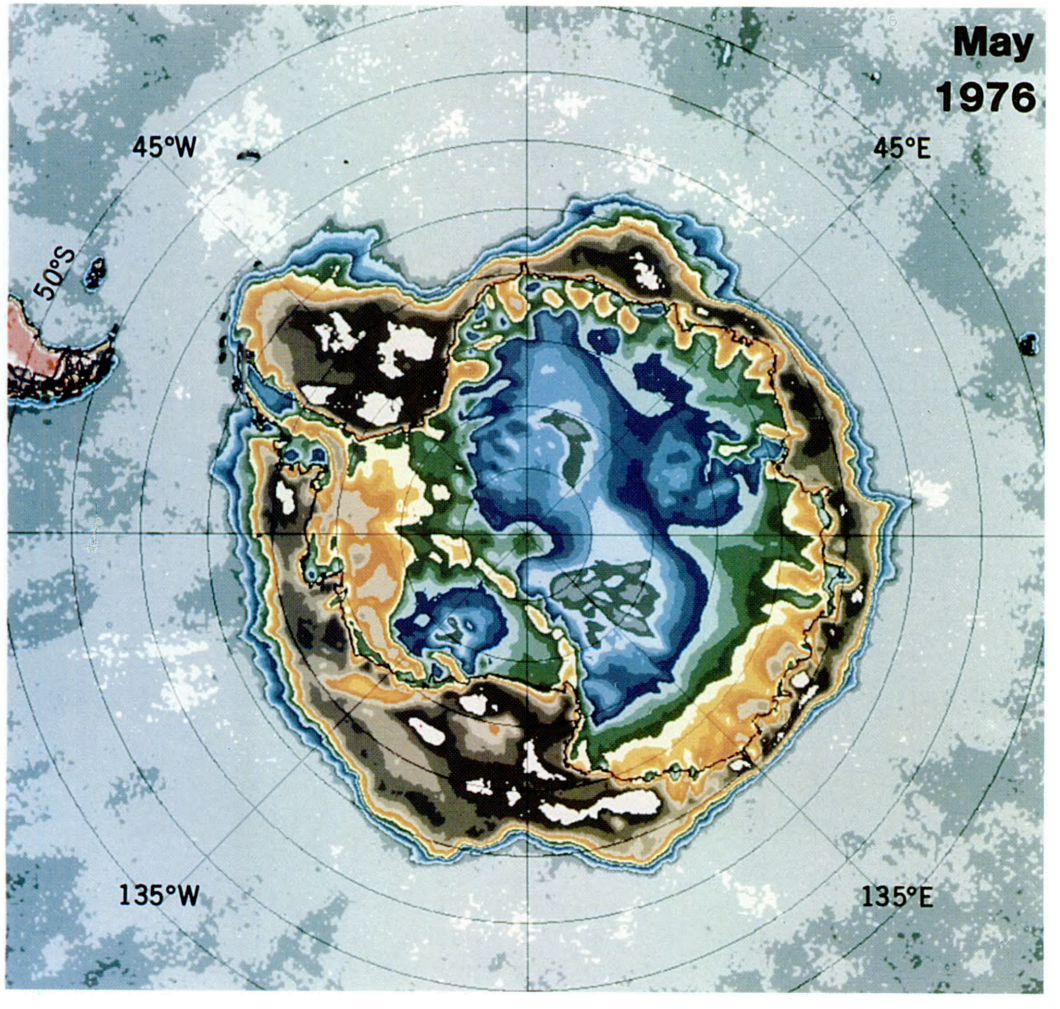

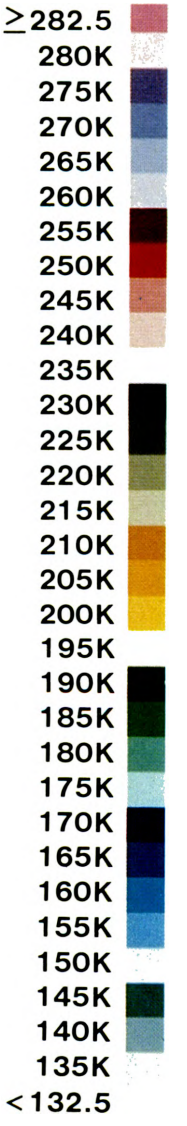

Figure 3-8b. Mean monthly brightness temperatures for May 1975 and 1976.

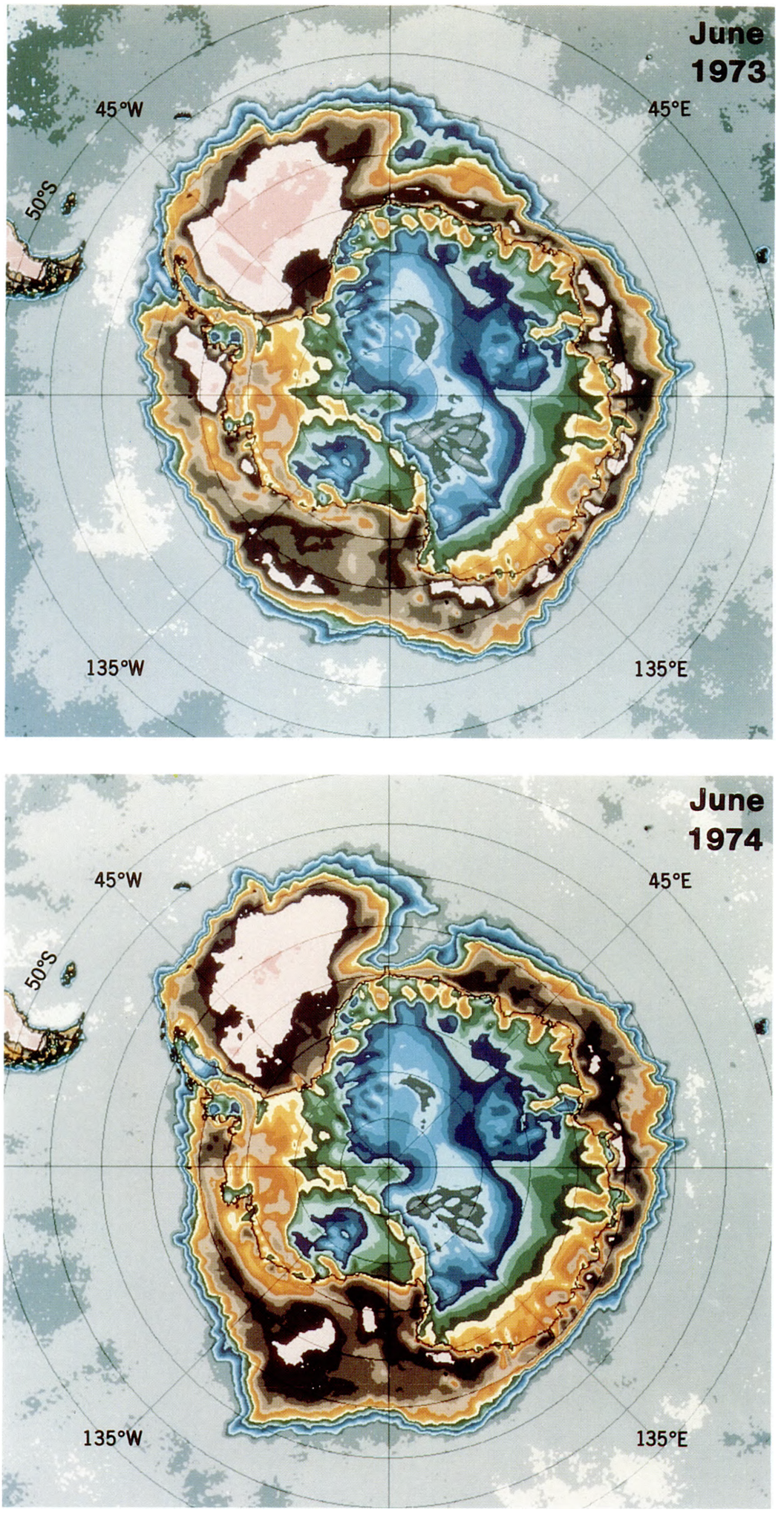

Figure 3-9a. Mean monthly brightness temperatures for June 1973 and 1974.

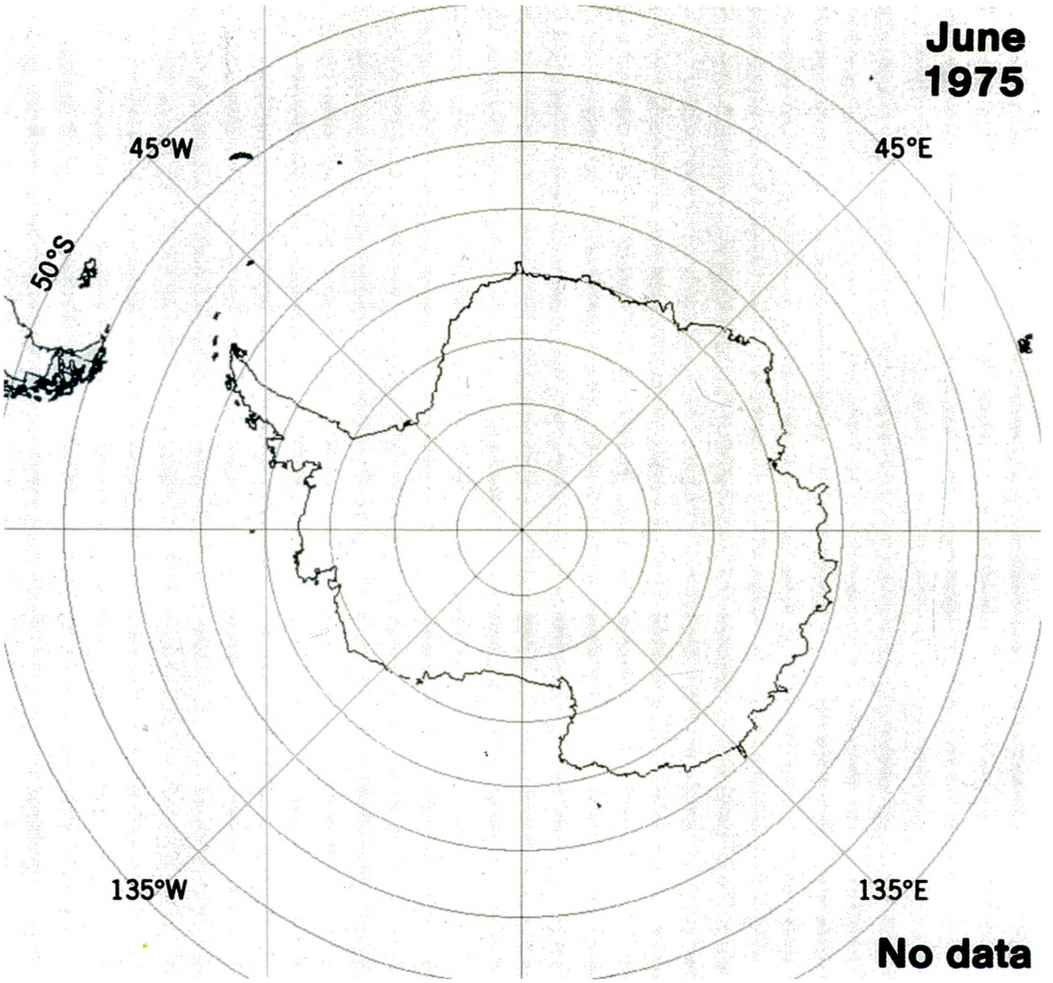

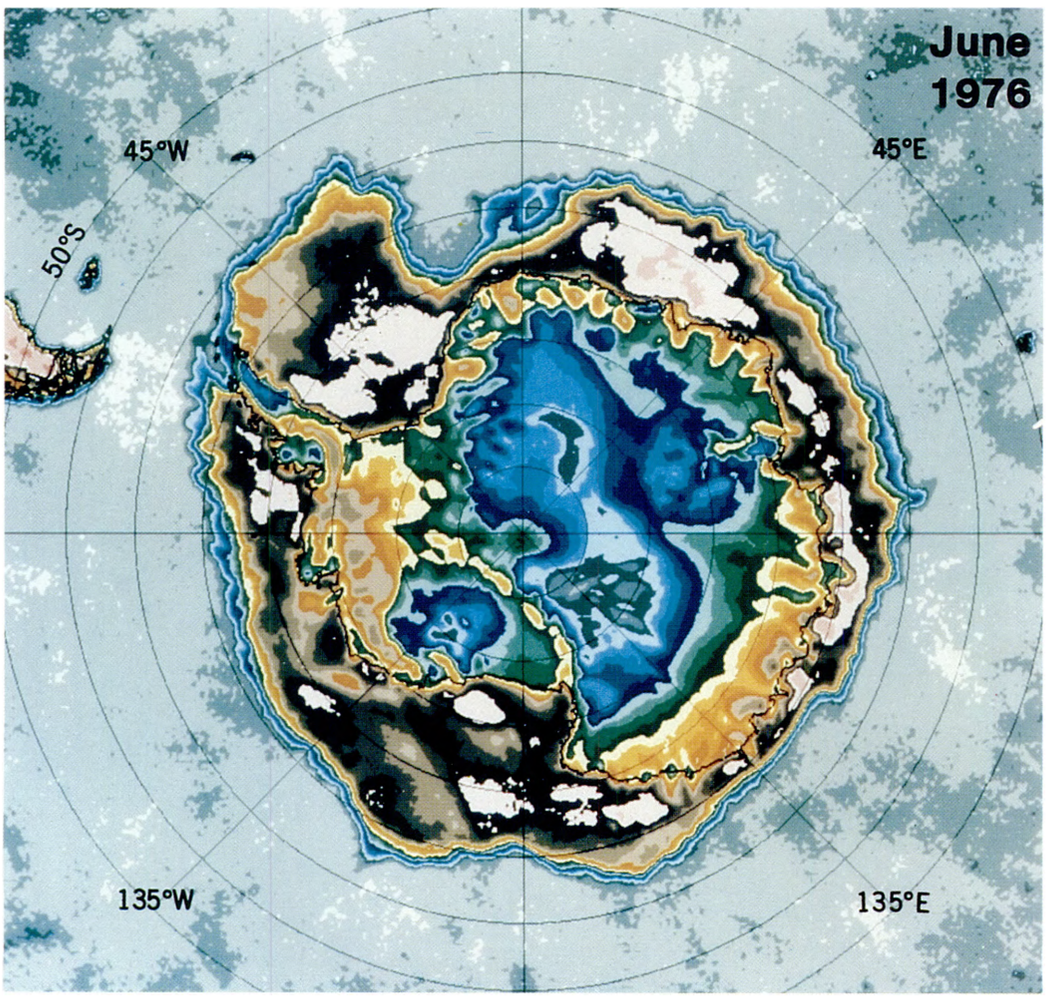

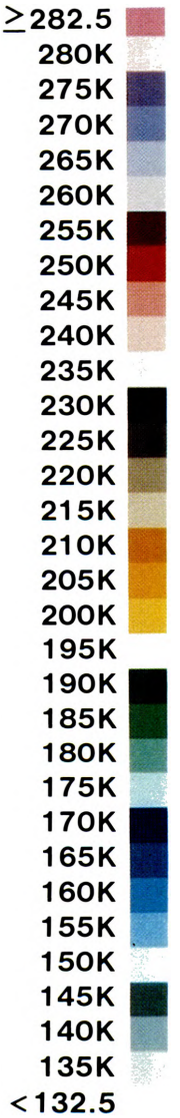

Figure 3-9b. Mean monthly brightness temperatures for June 1975 and 1976.

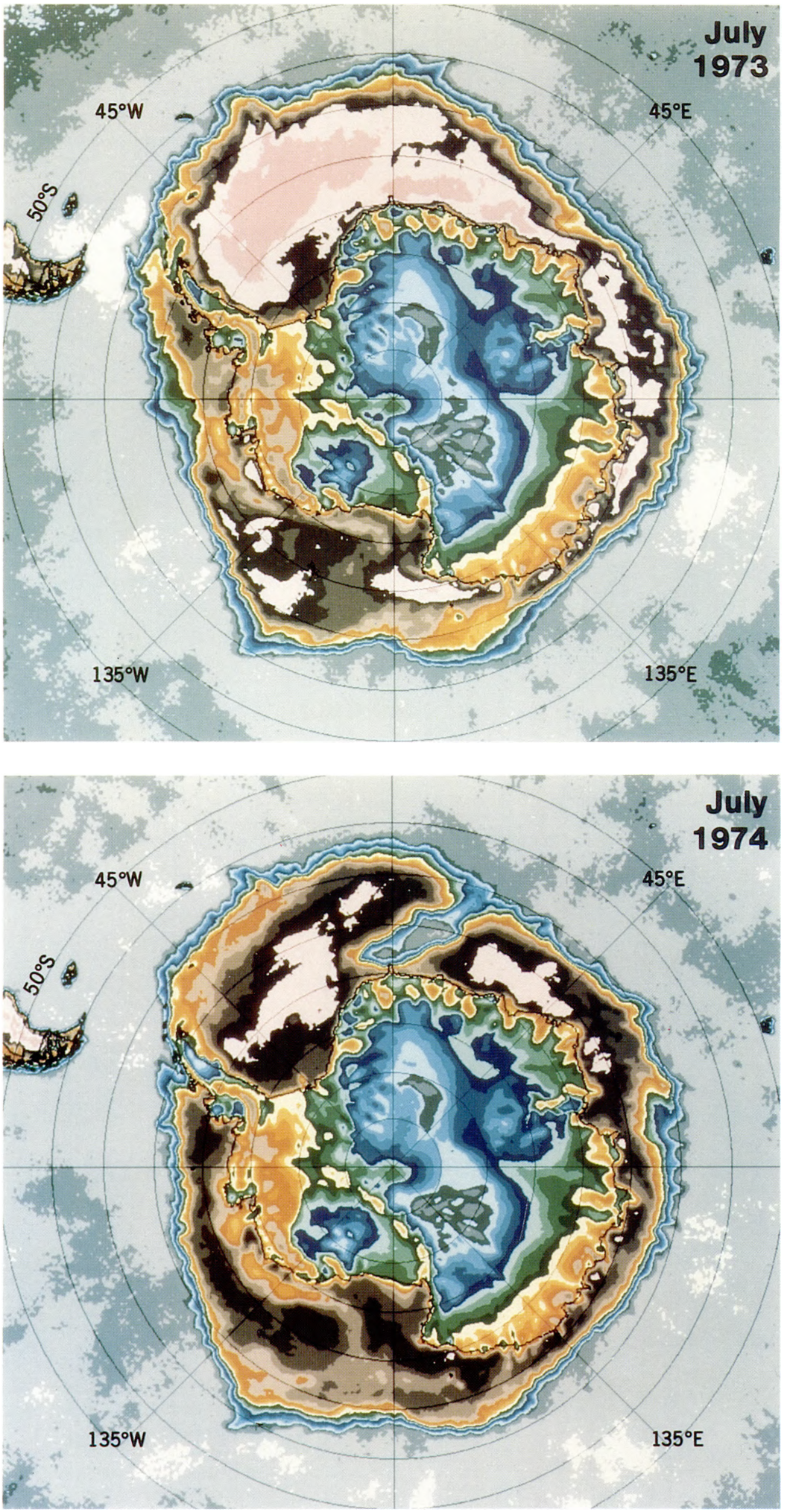

Figure 3-10a. Mean monthly brightness temperatures for July 1973 and 1974.

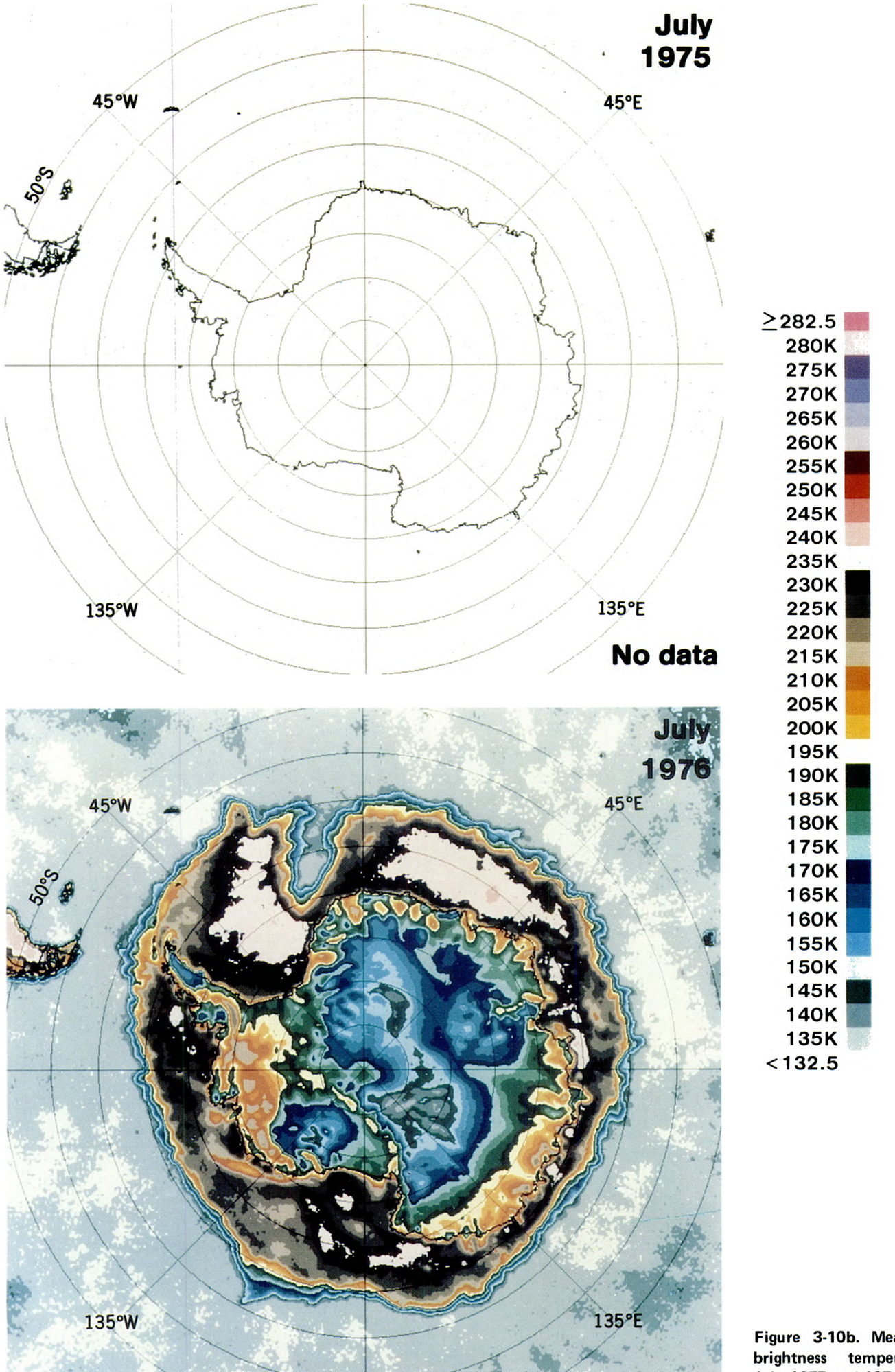

Figure 3-10b. Mean monthly brightness temperatures for July 1975 and 1976.

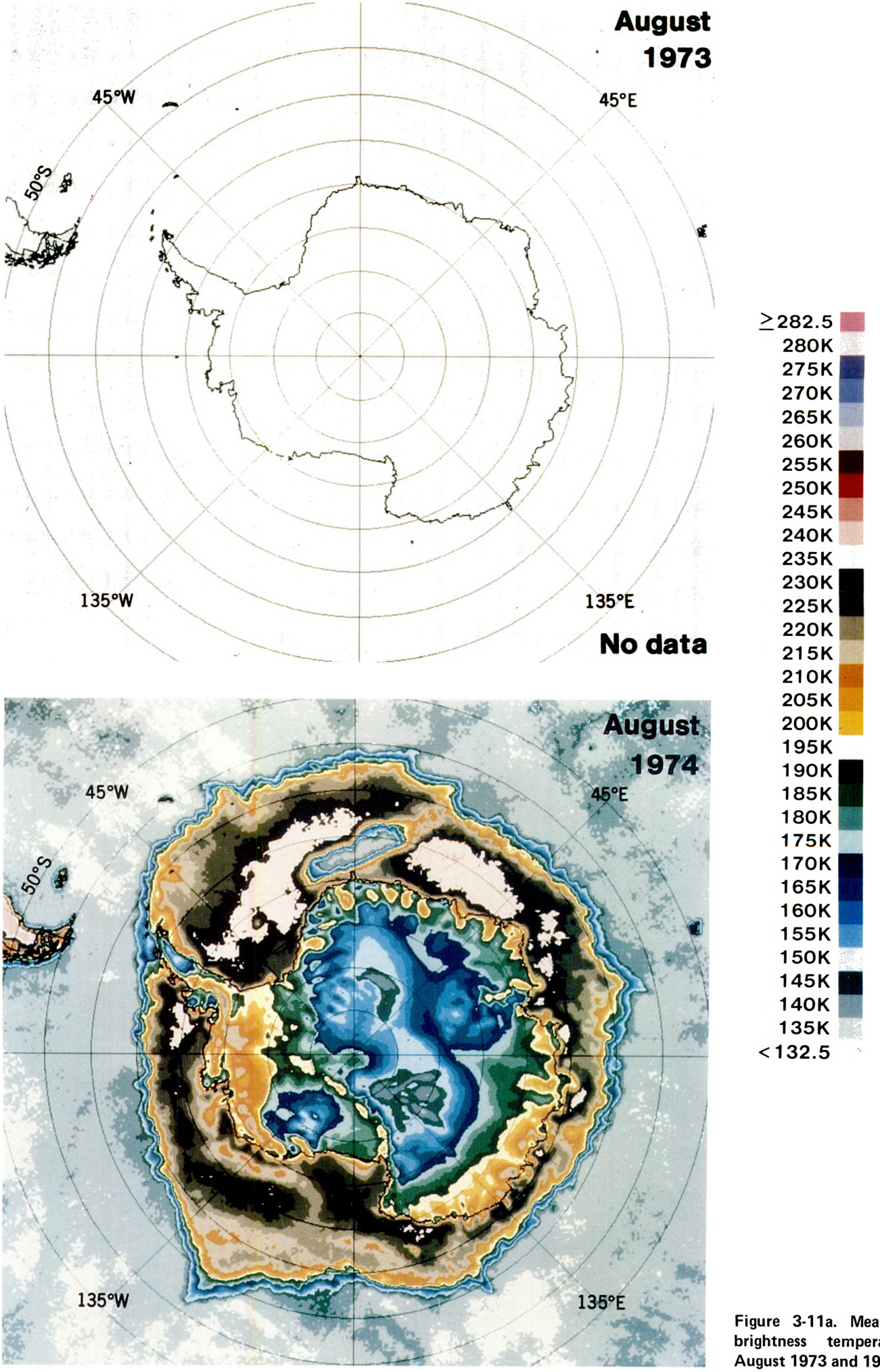

Figure 3-11a. Mean monthly brightness temperatures for August 1973 and 1974.

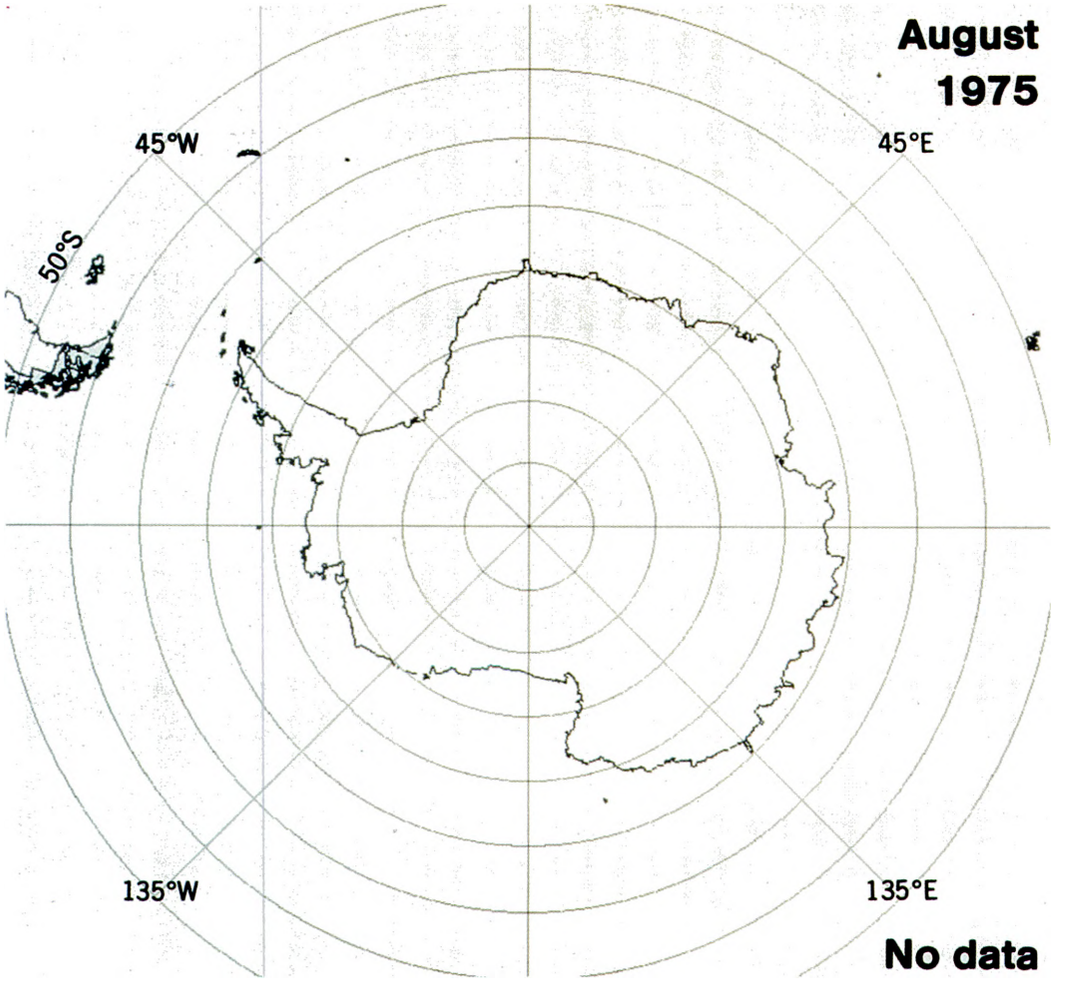

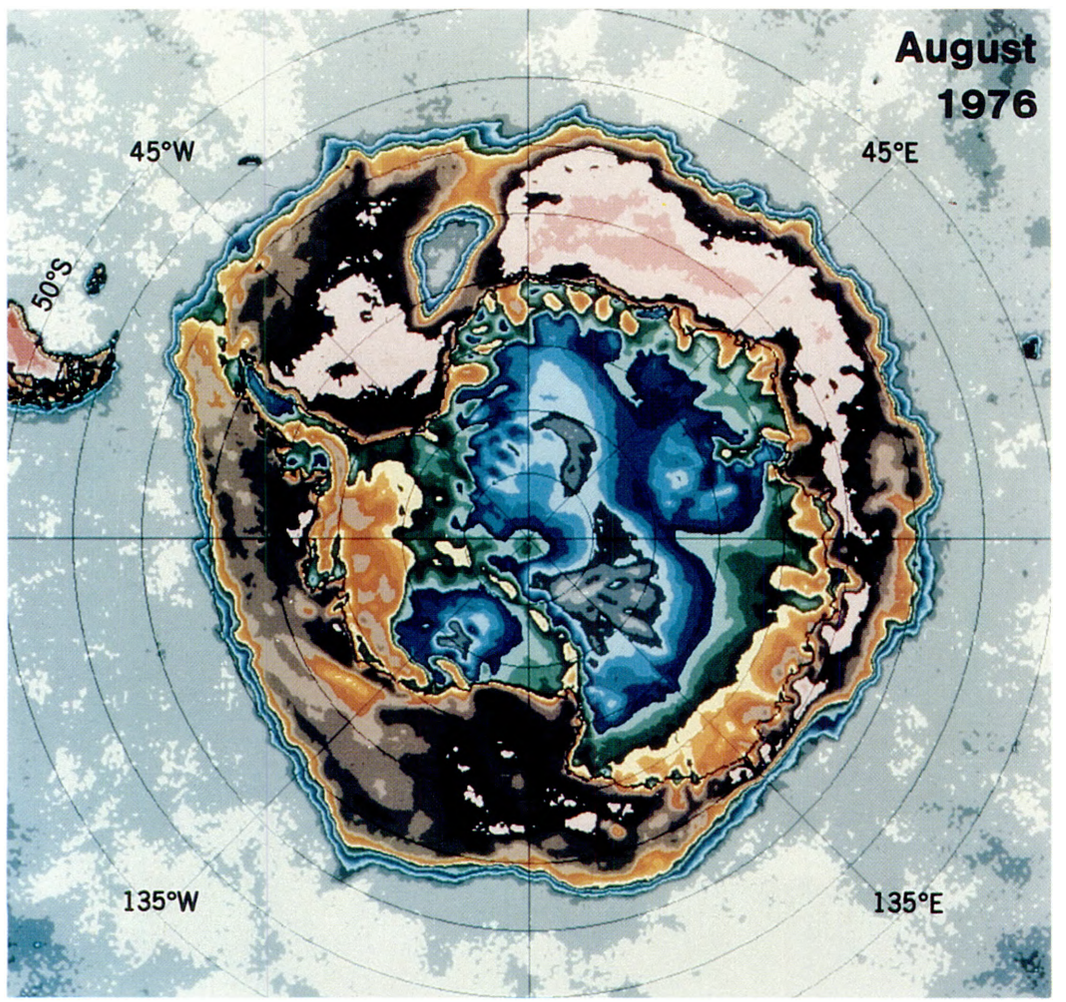

Figure 3-11b. Mean monthly brightness temperatures for August 1975 and 1976.

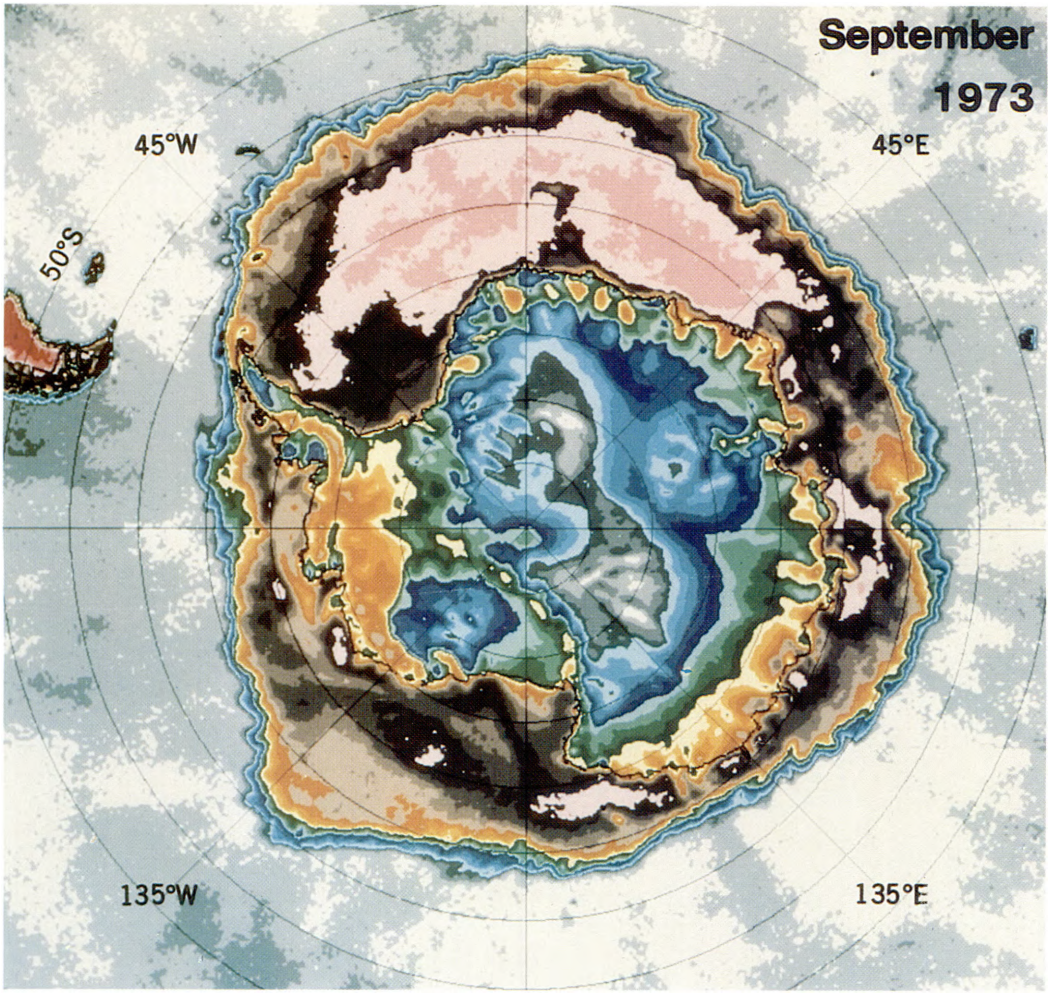

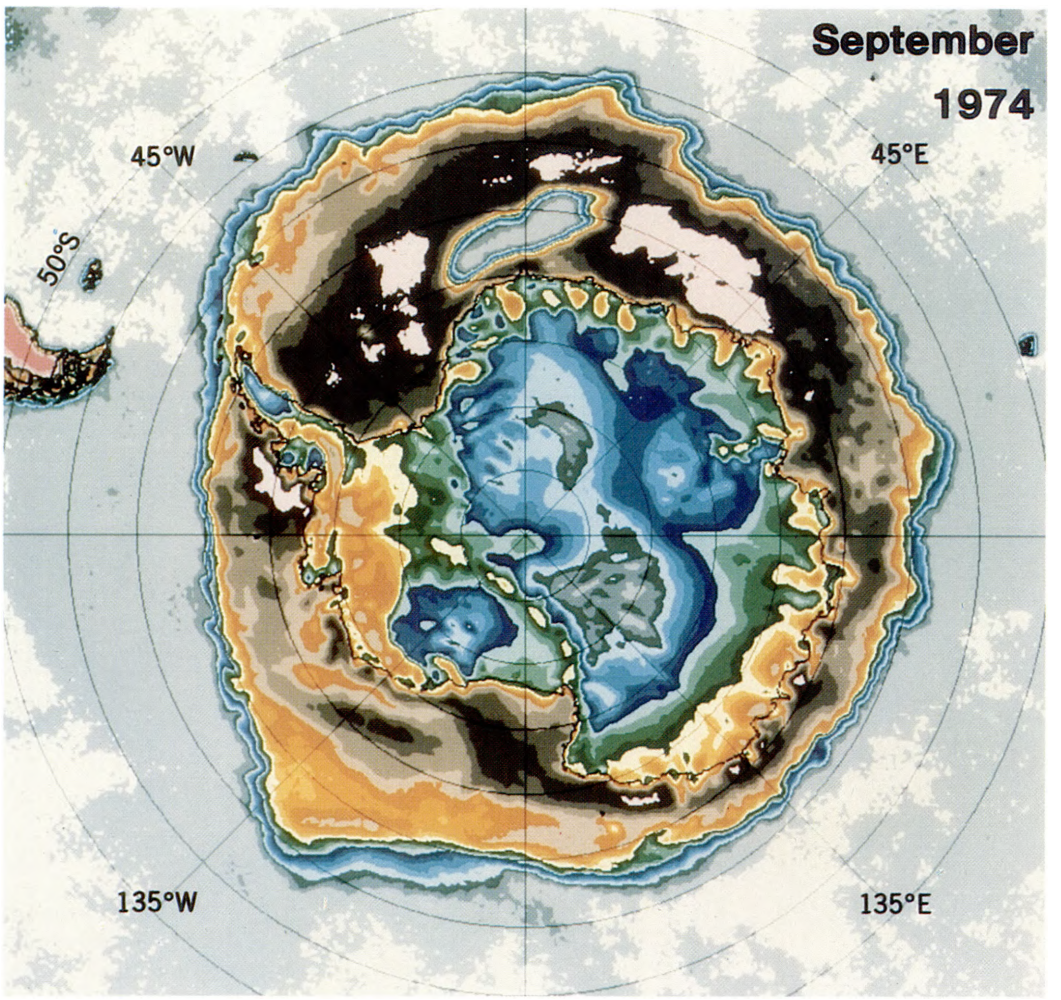

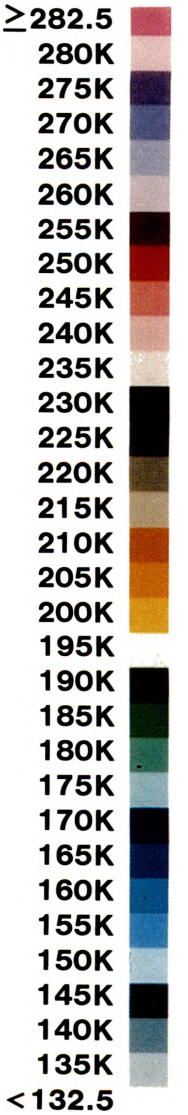

Figure 3-12a. Mean monthly brightness temperatures for September 1973 and 1974.

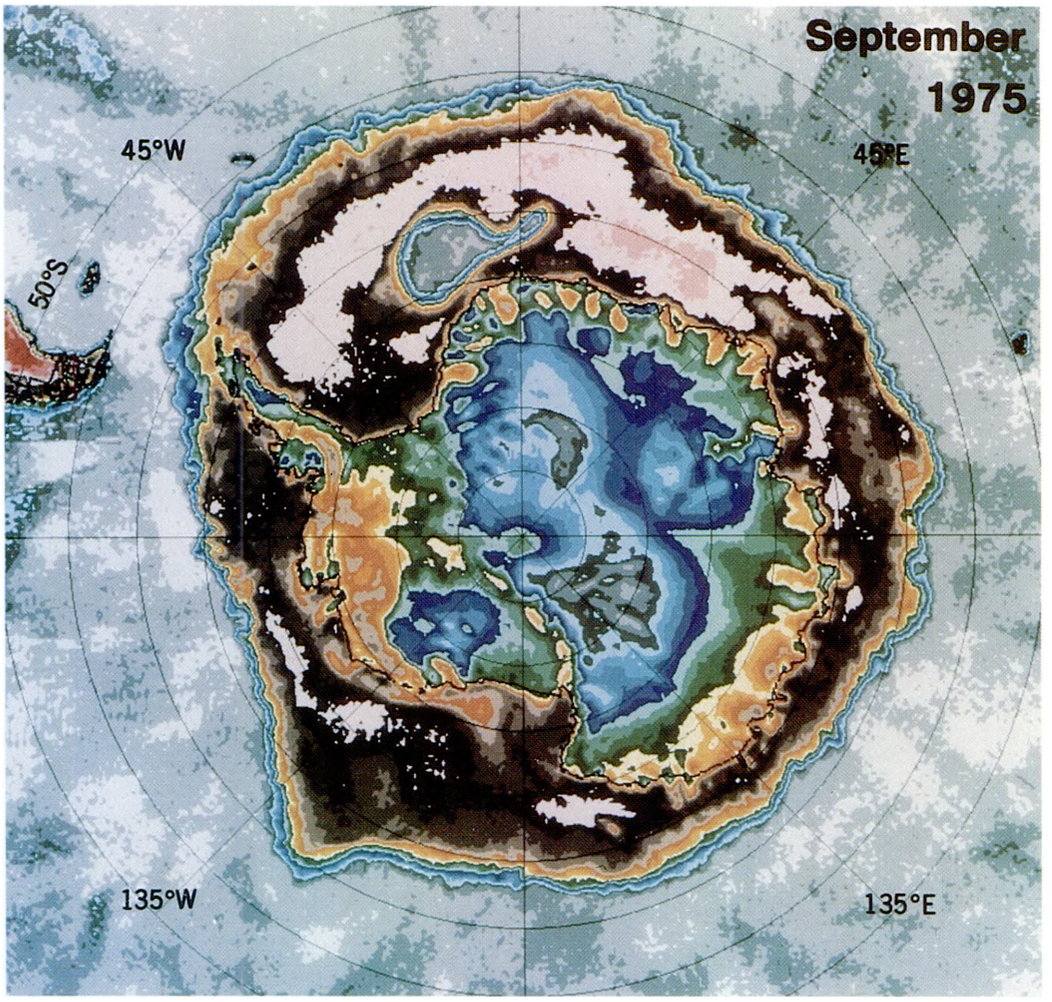

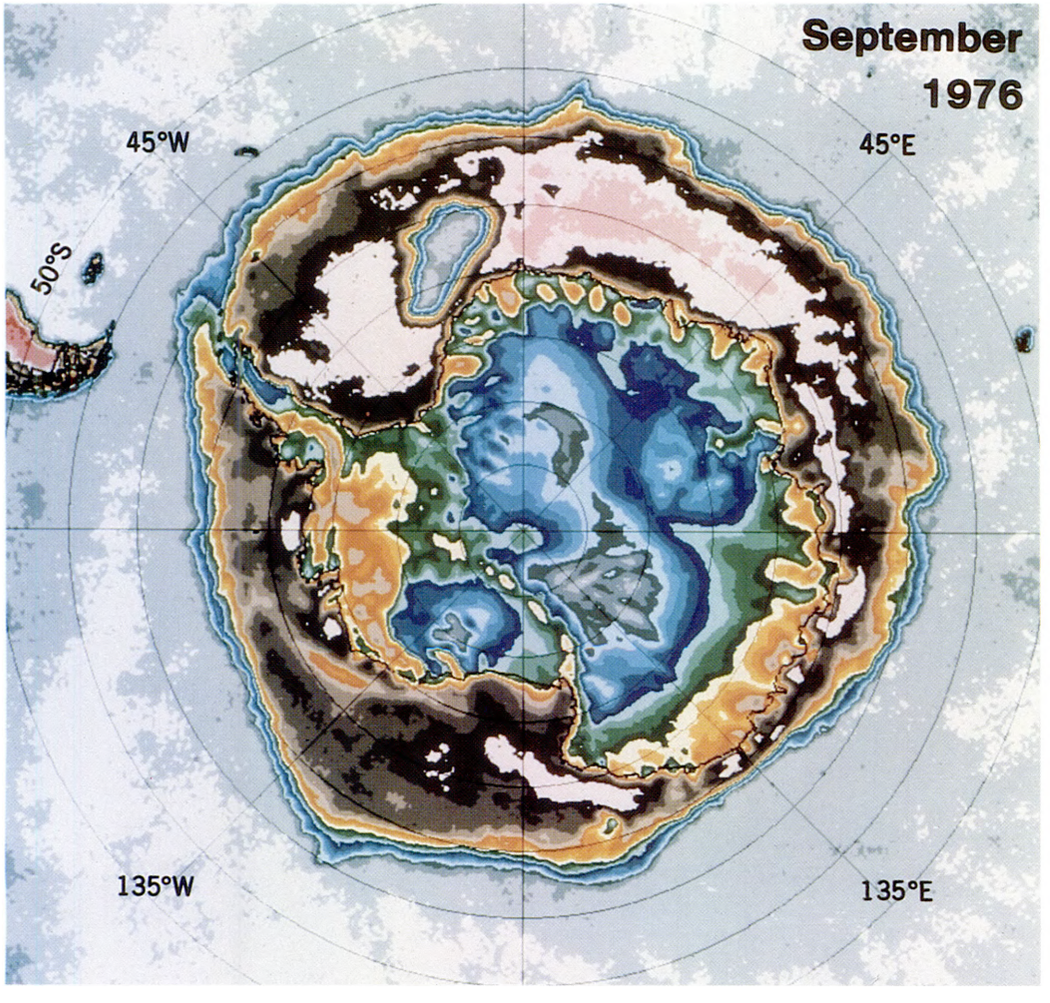

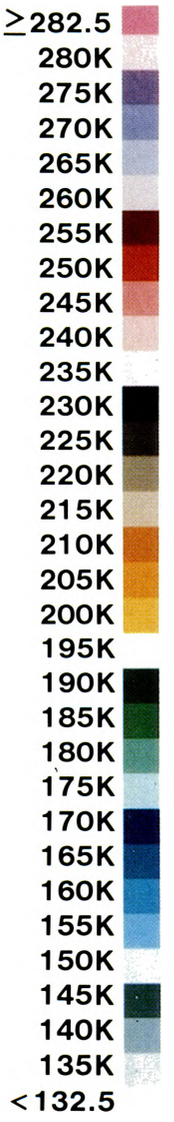

Figure 3-12b. Mean monthly brightness temperatures for September 1975 and 1976.

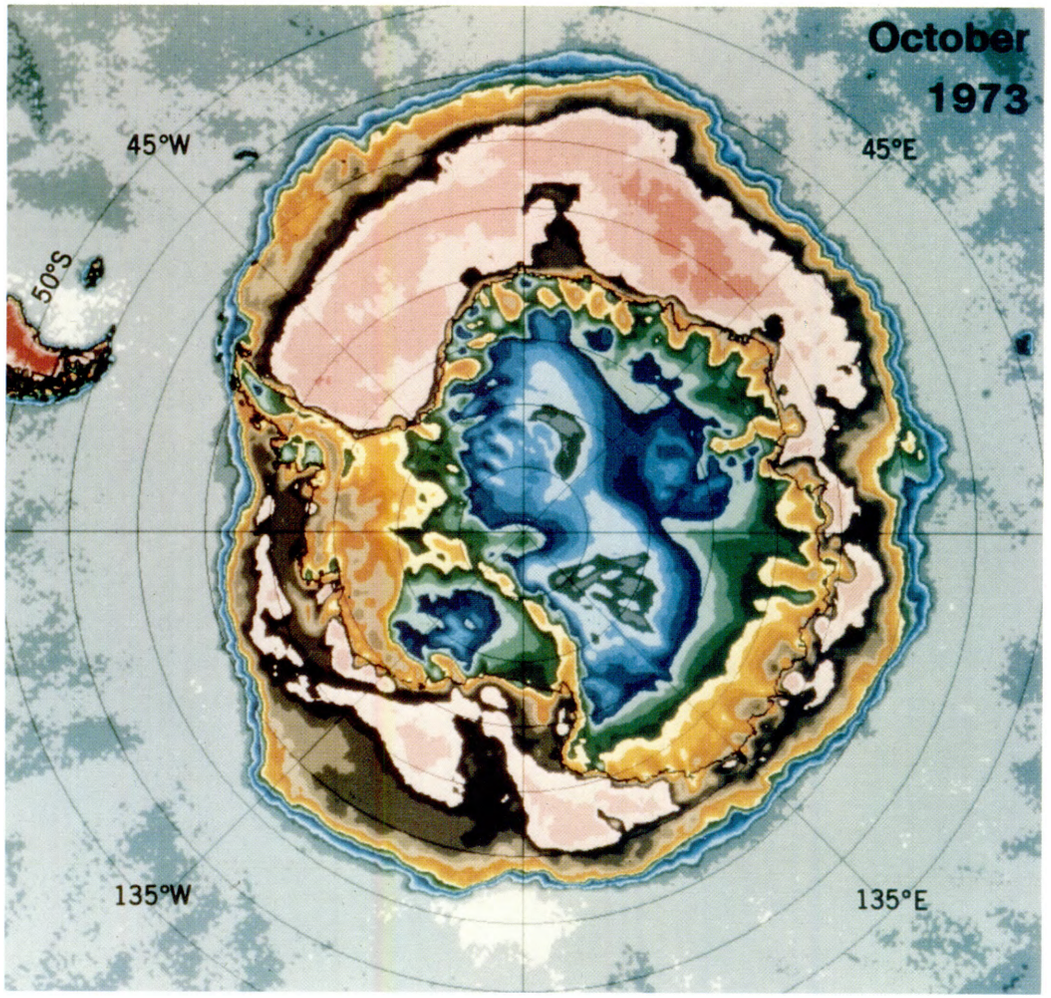

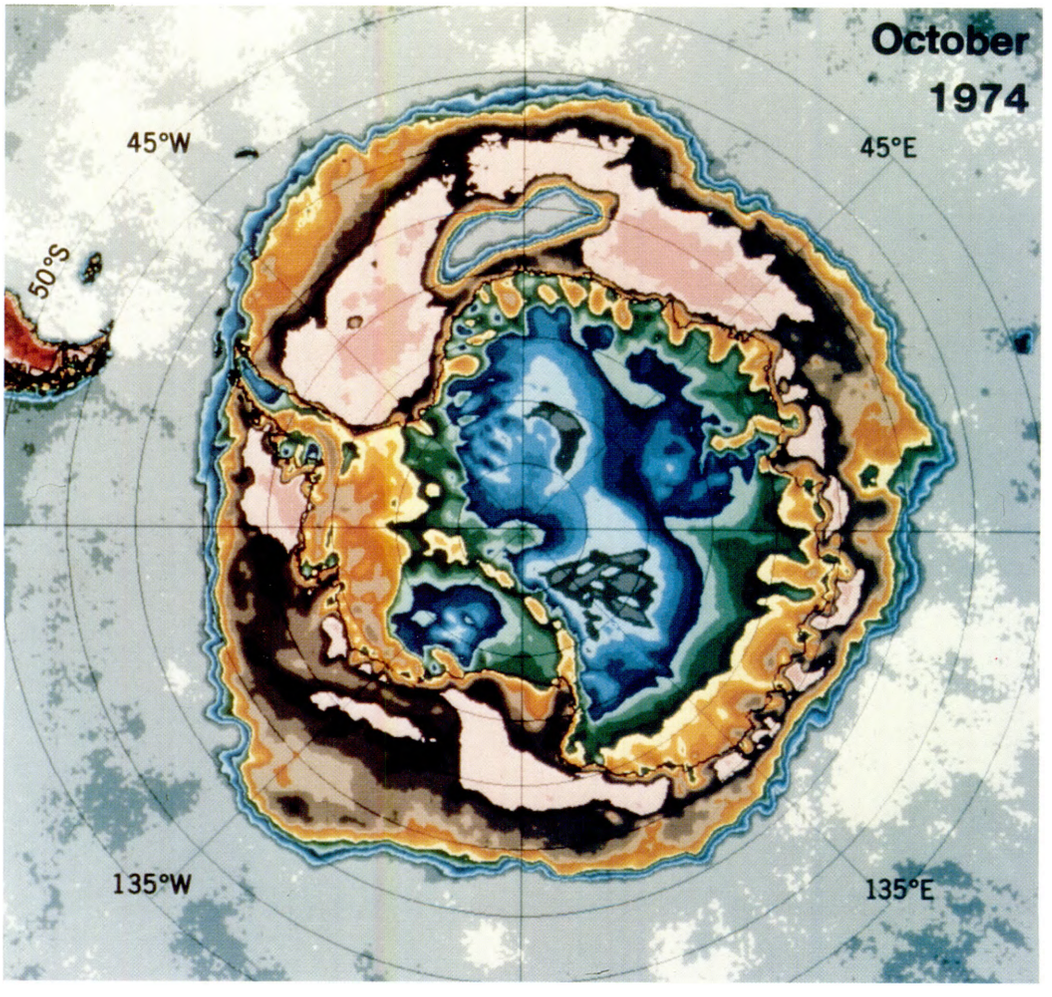

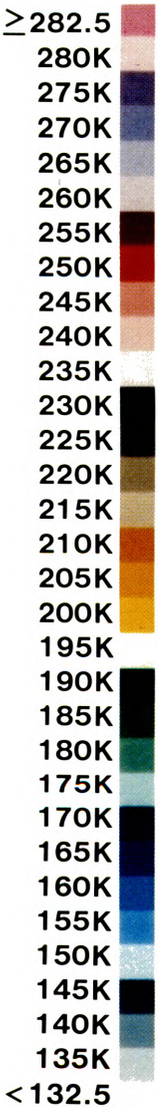

Figure 3-13a. Mean monthly brightness temperatures for October 1973 and 1974.

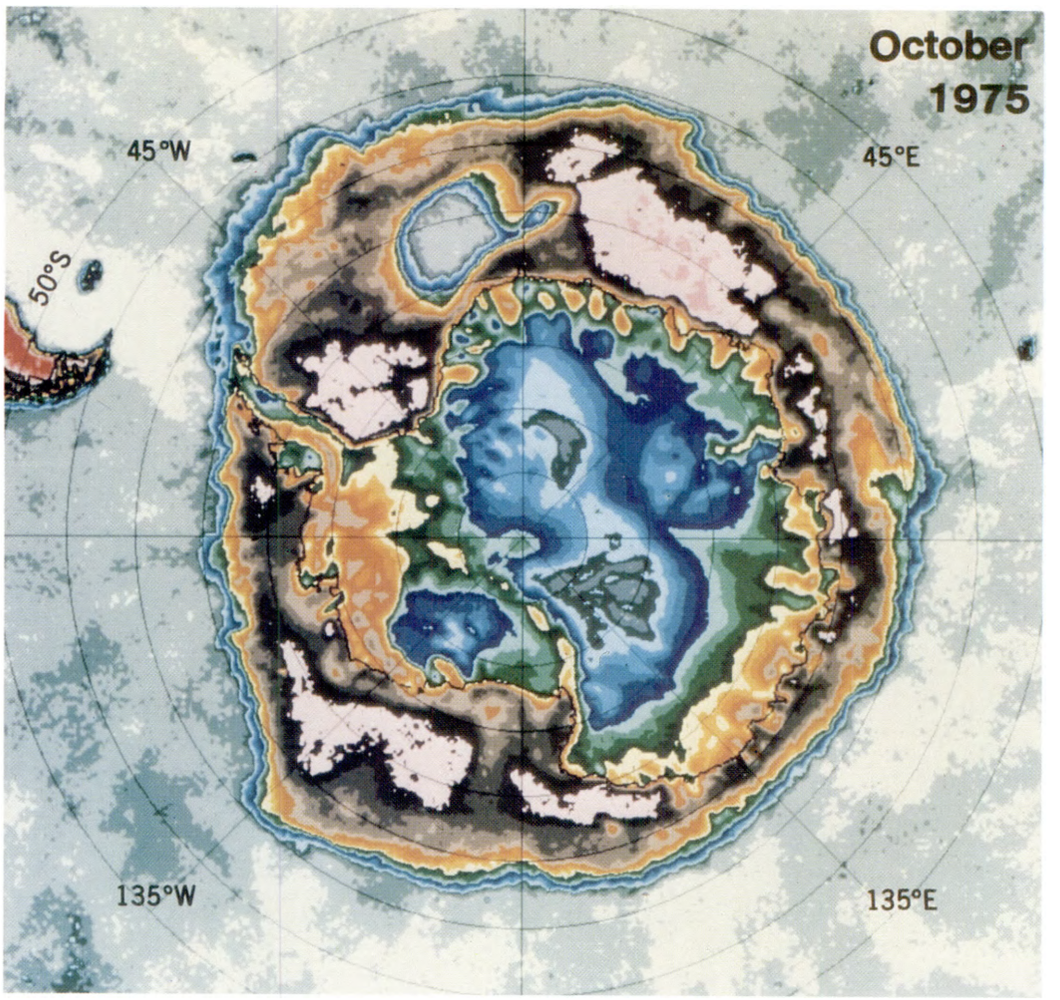

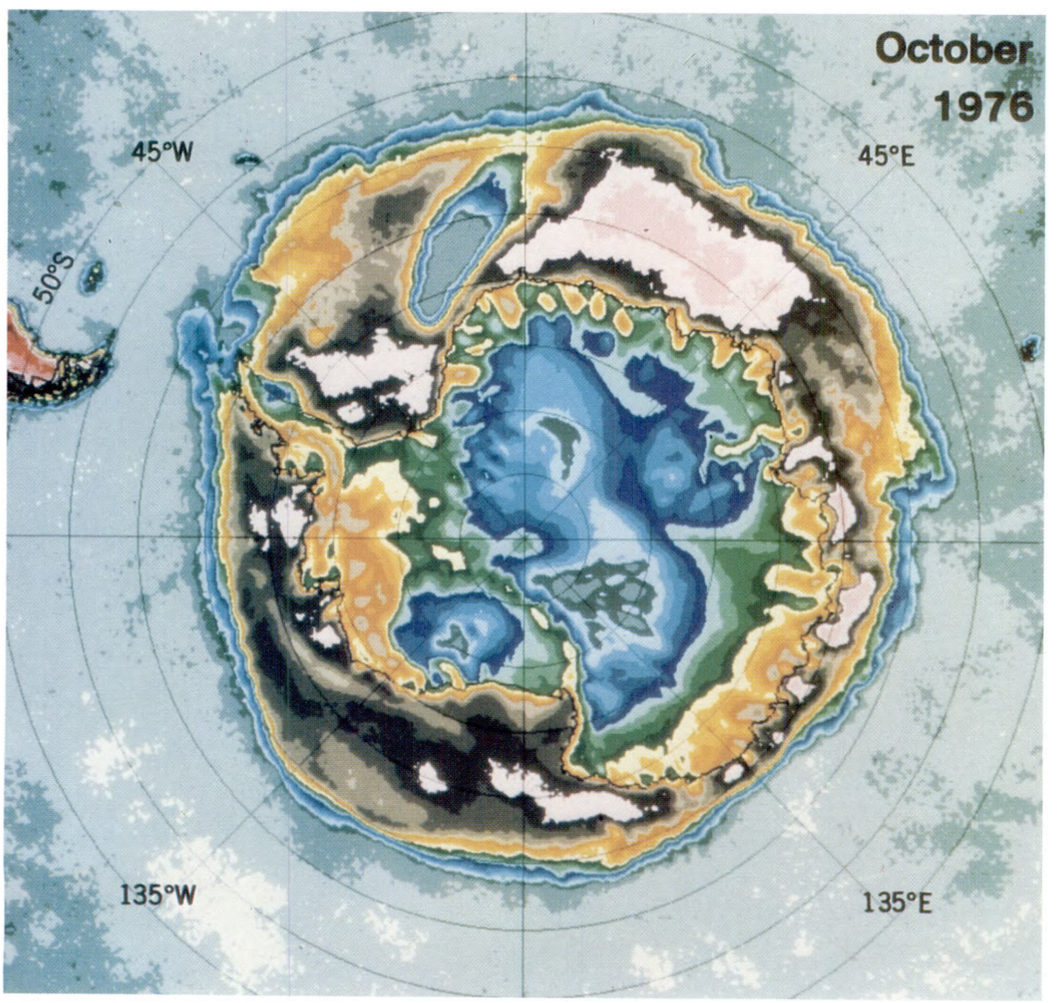

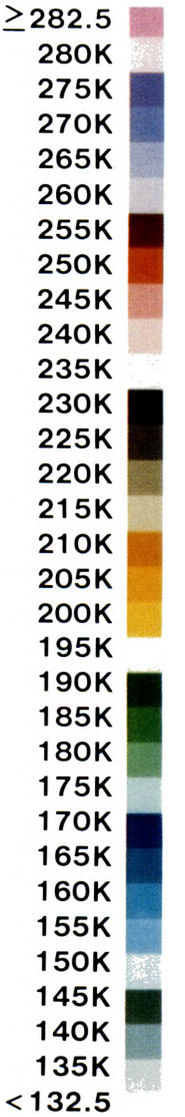

Figure 3-13b. Mean monthly brightness temperatures for October 1975 and 1976.

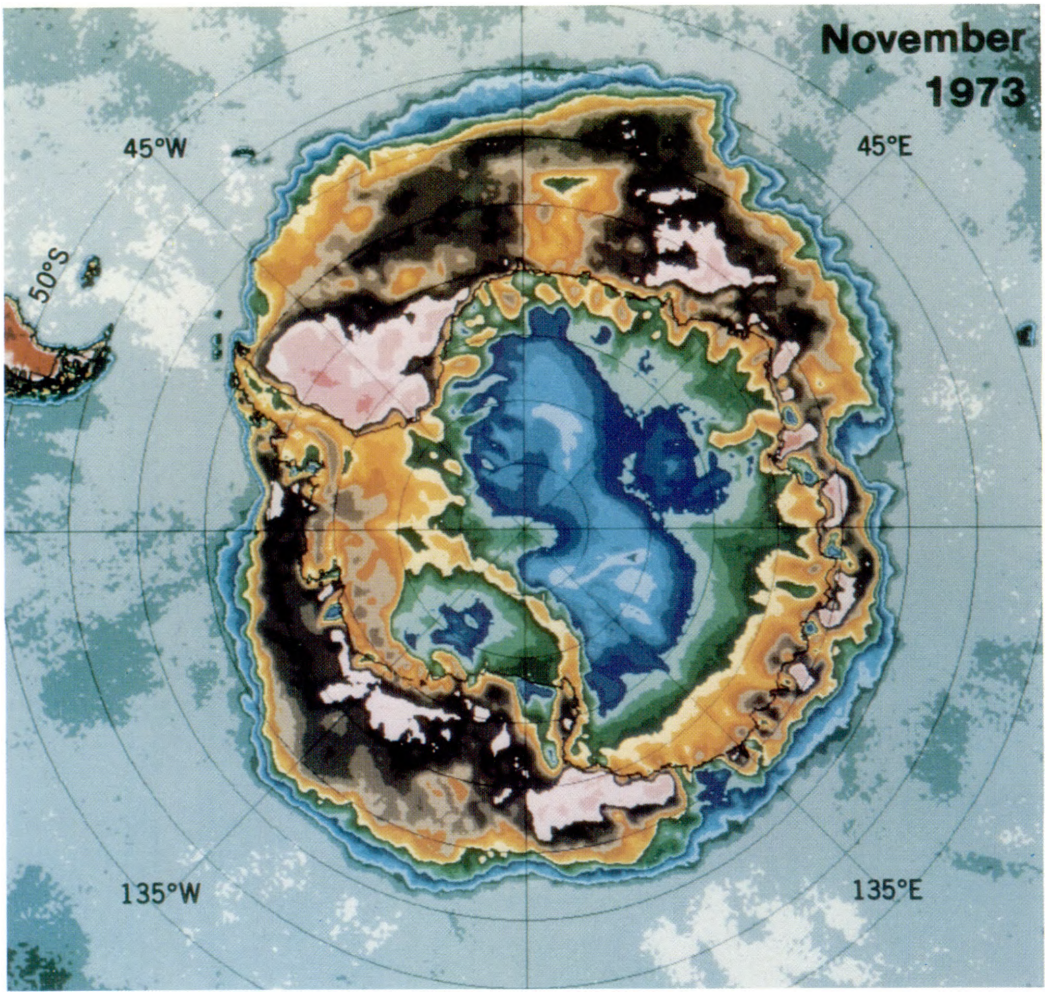

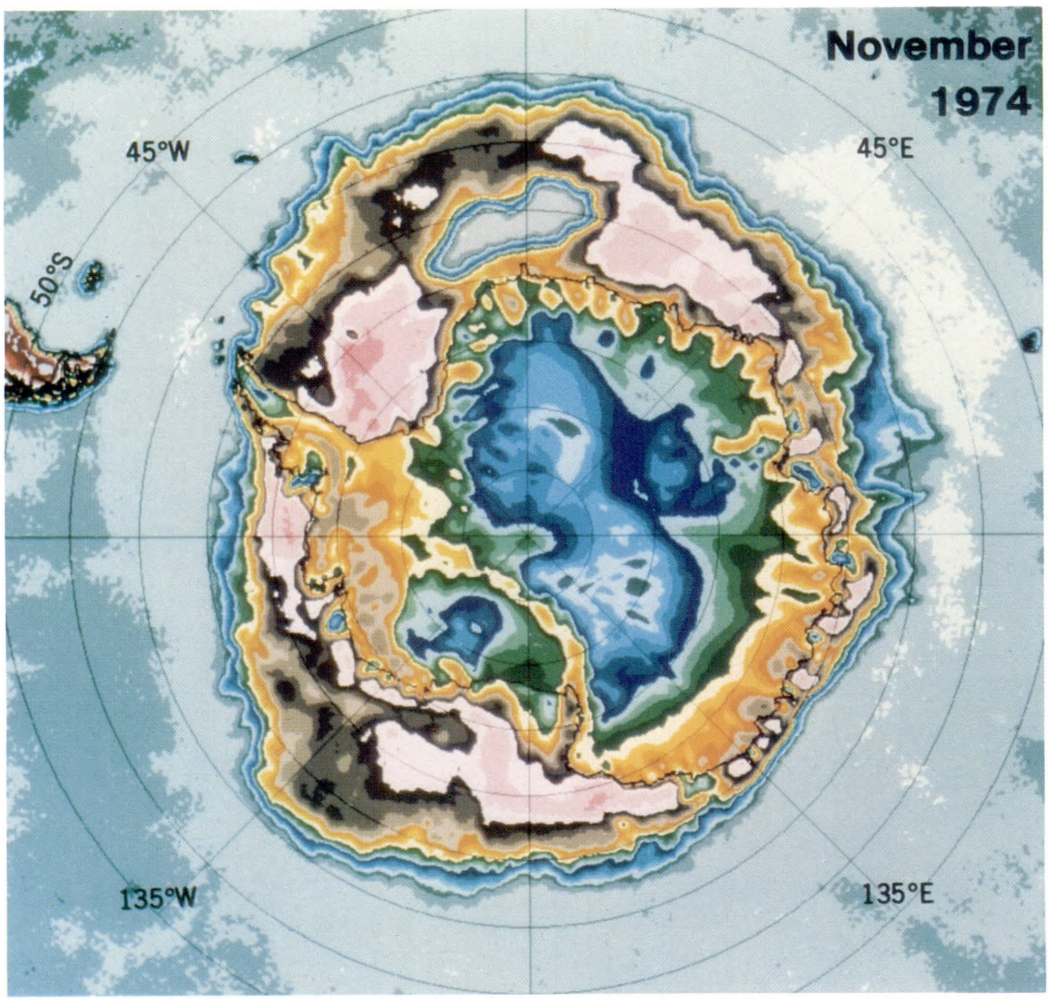

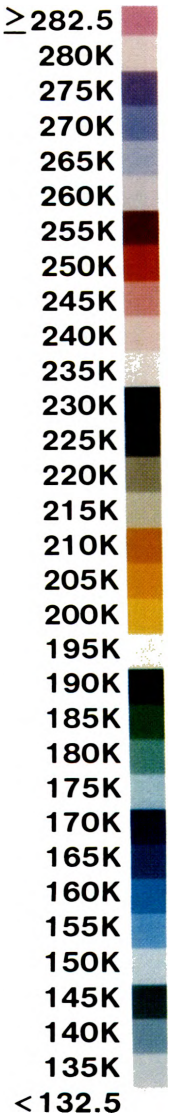

Figure 3-14a. Mean monthly brightness temperatures for November 1973 and 1974.

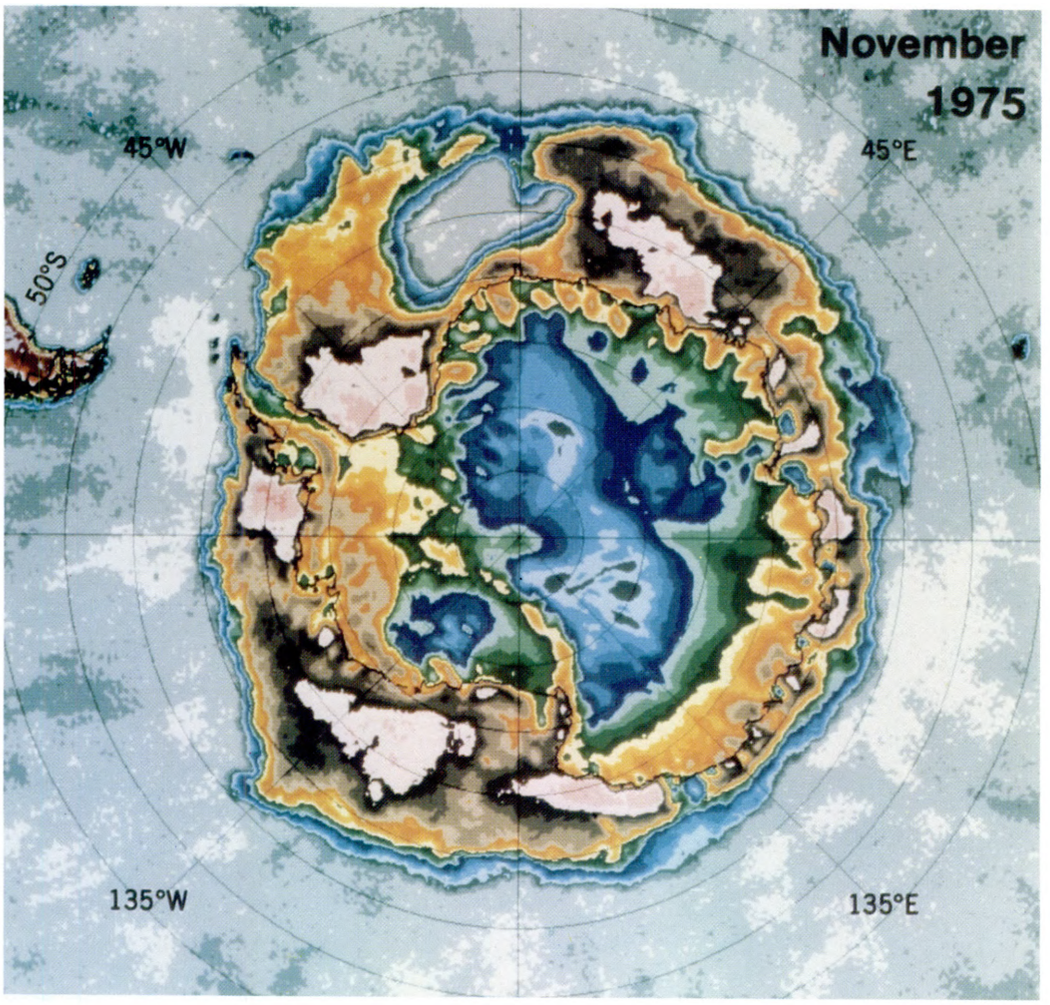

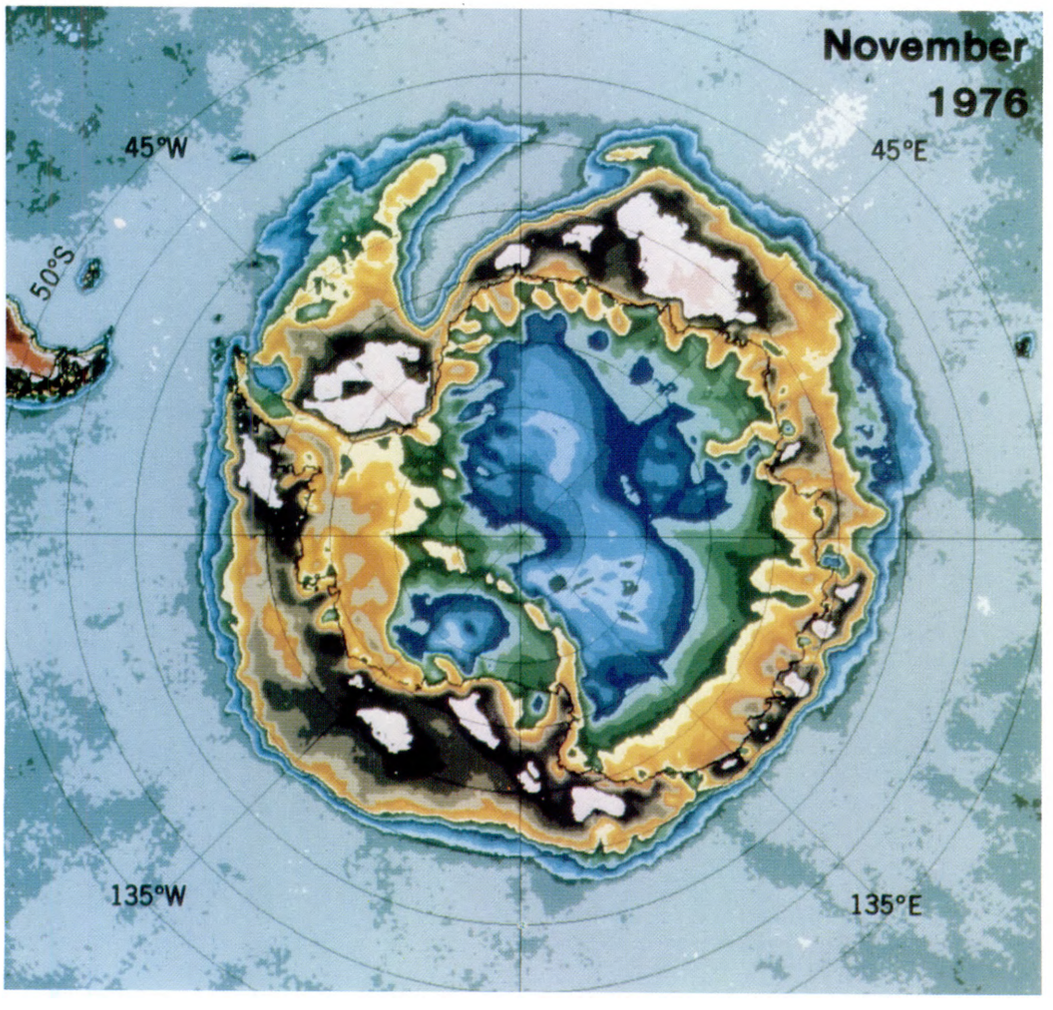

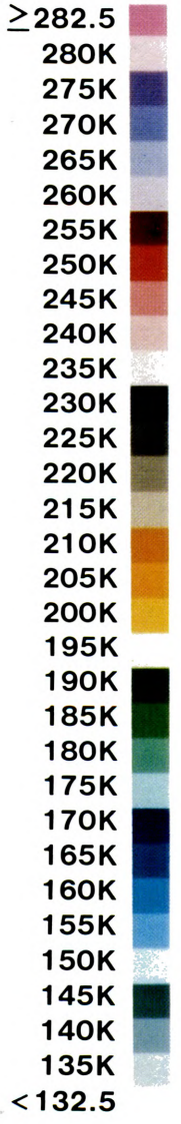

Figure 3-14b. Mean monthly brightness temperatures for November 1975 and 1976.

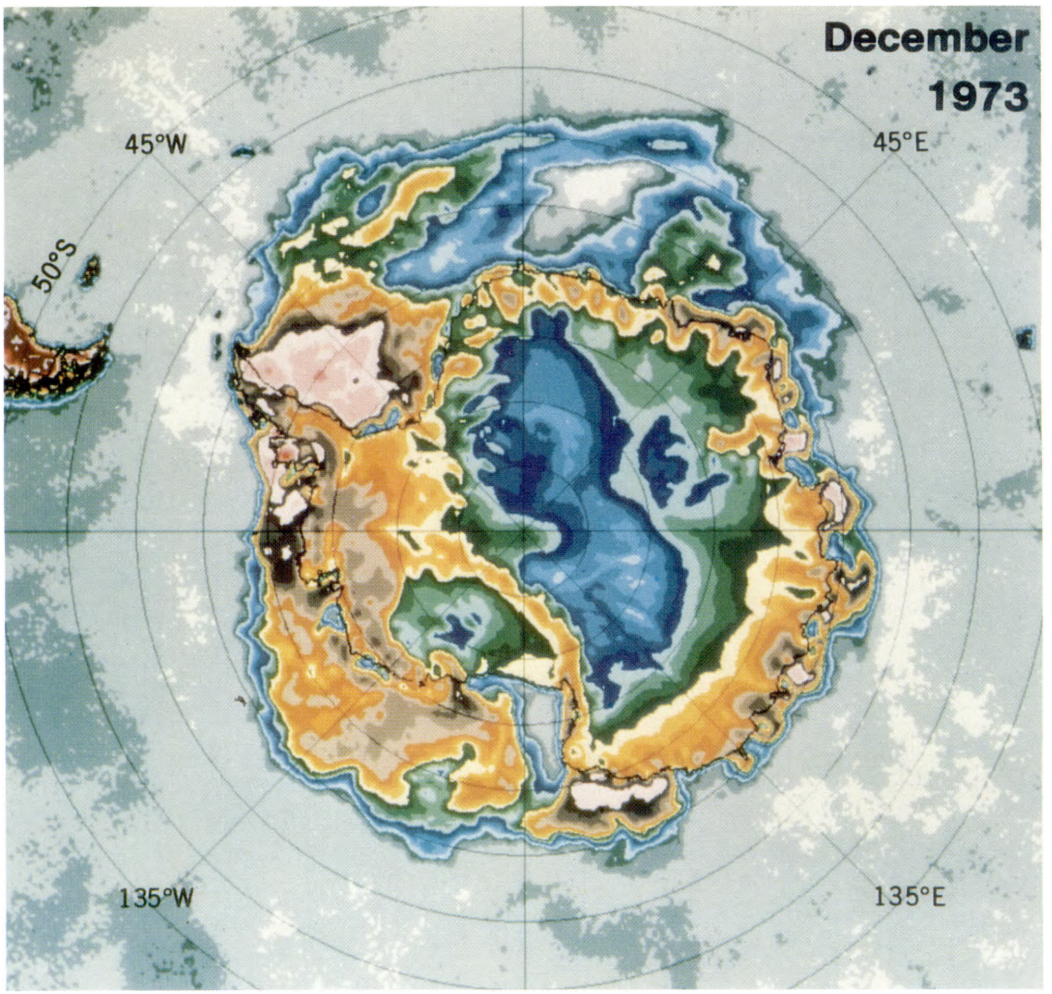

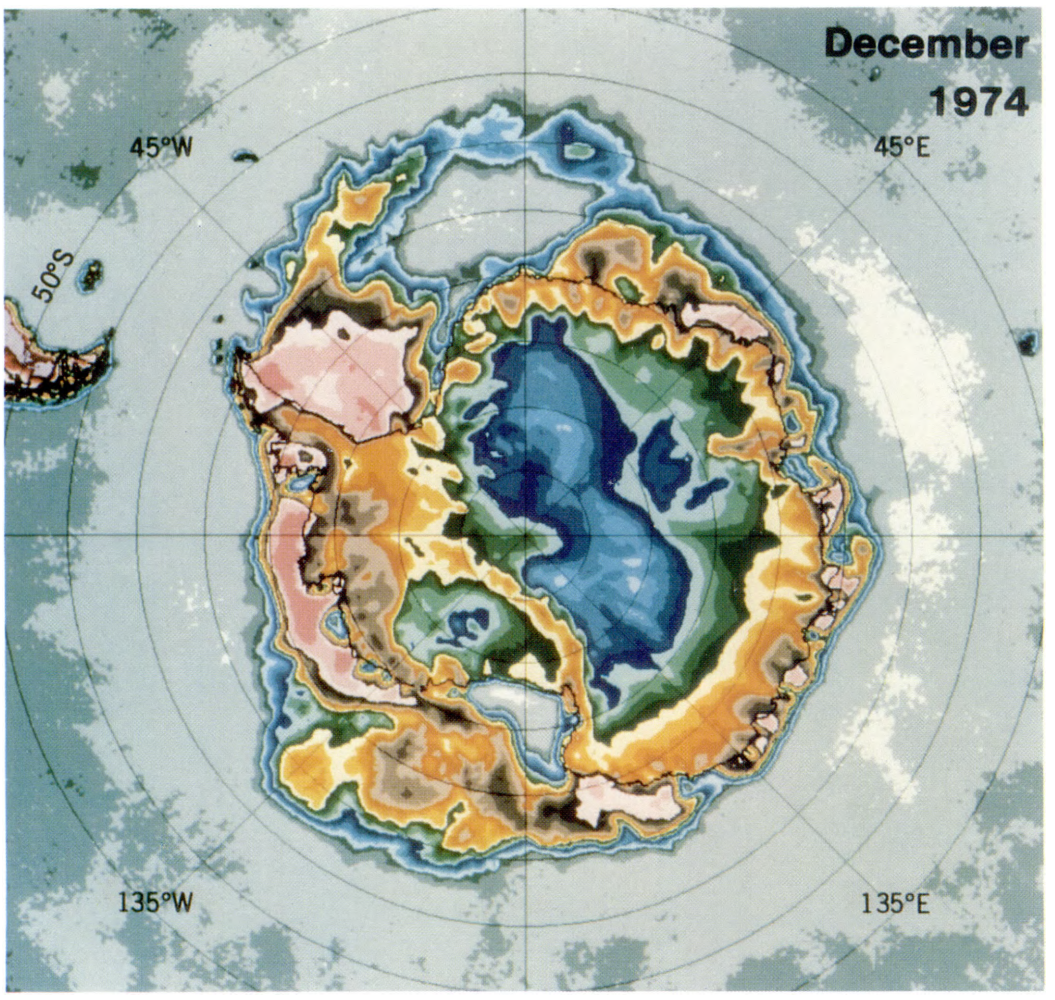

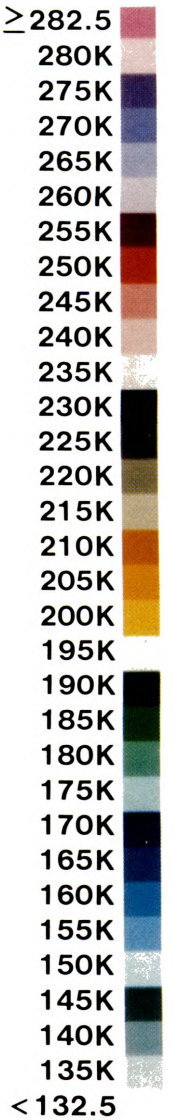

Figure 3-15a. Mean monthly brightness temperatures for December 1973 and 1974.

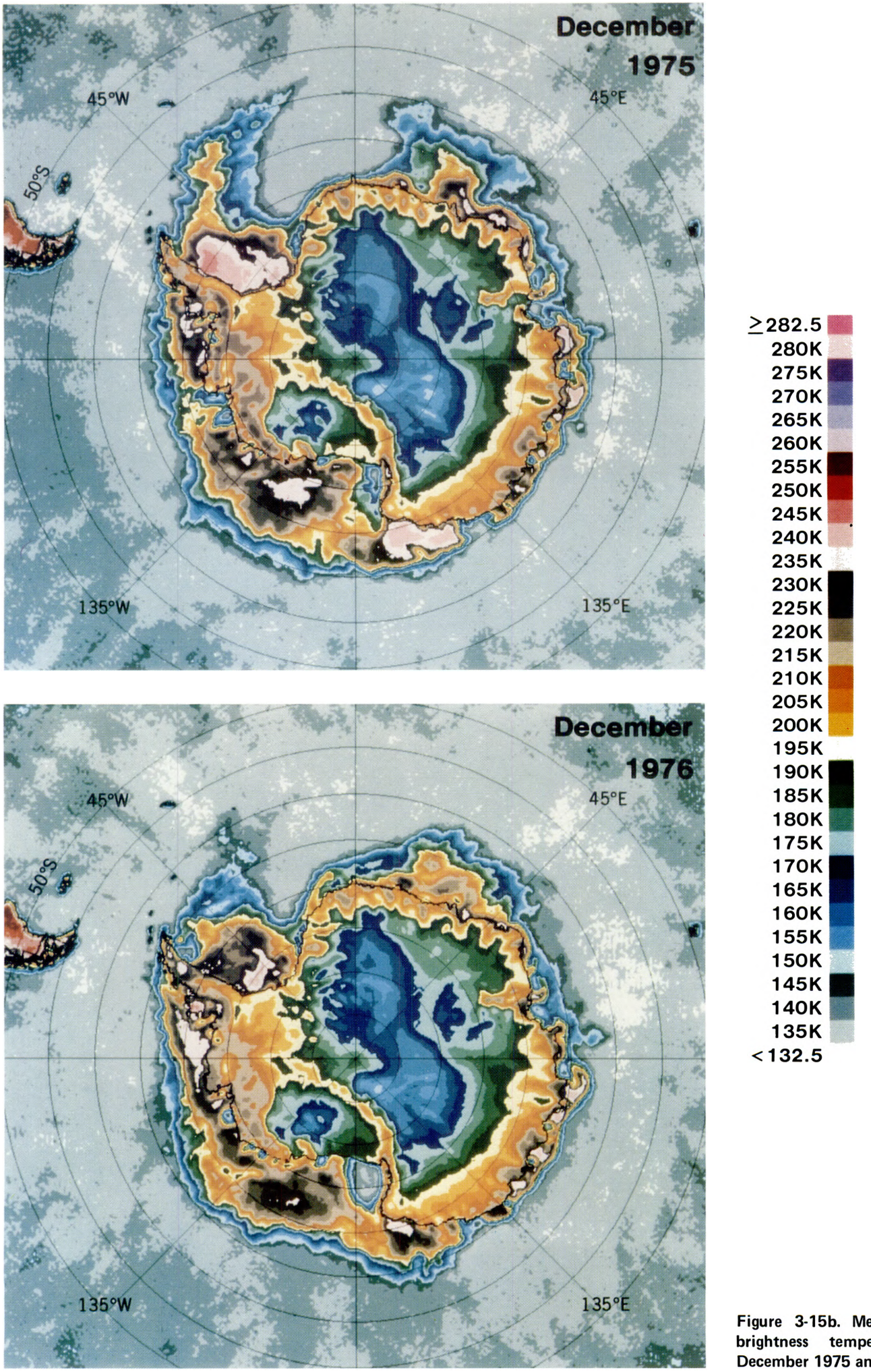

Figure 3-15b. Mean monthly brightness temperatures for December 1975 and 1976.

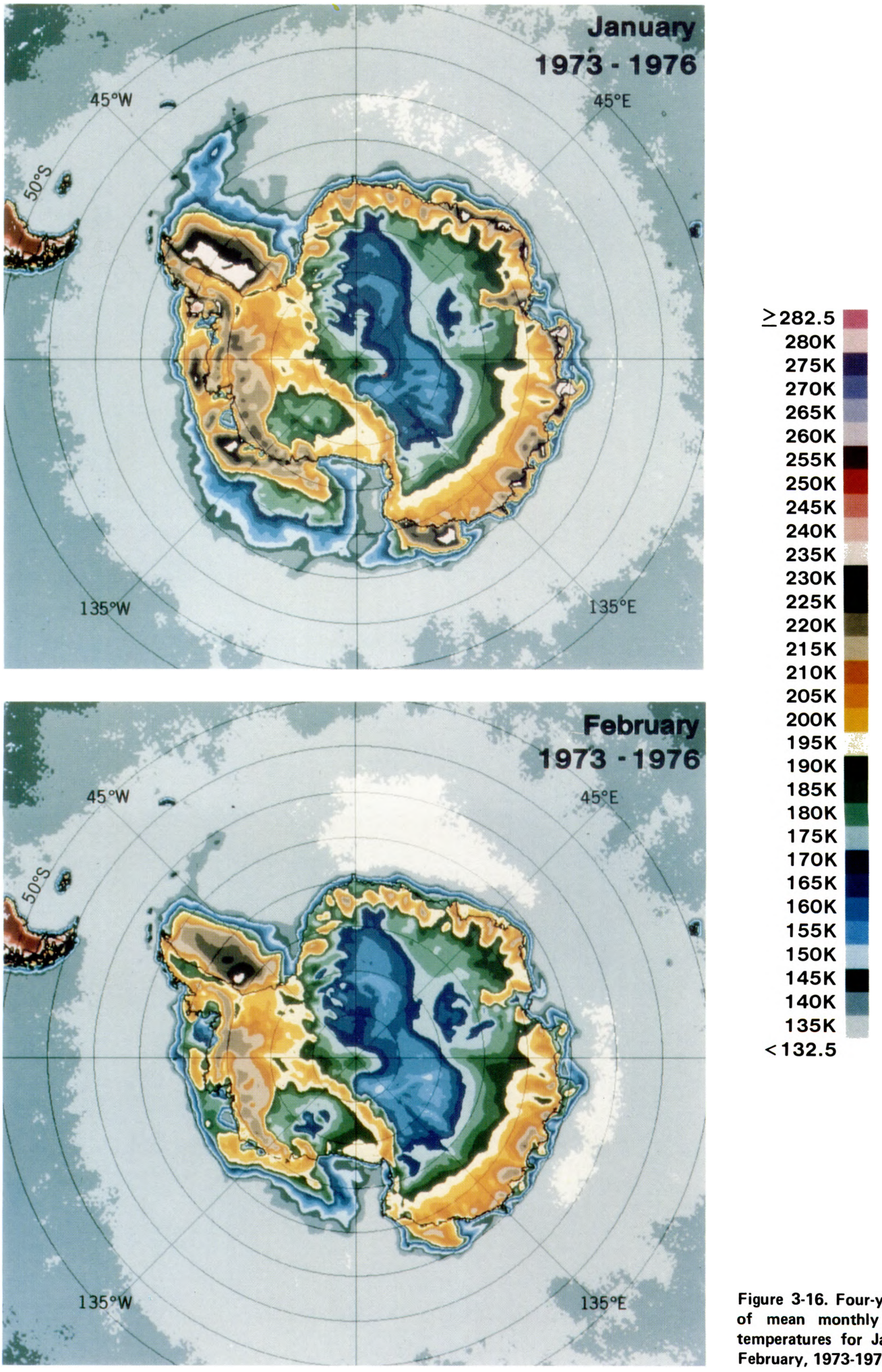

Figure 3-16. Four-year average of mean monthly brightness temperatures for January and February, 1973-1976.

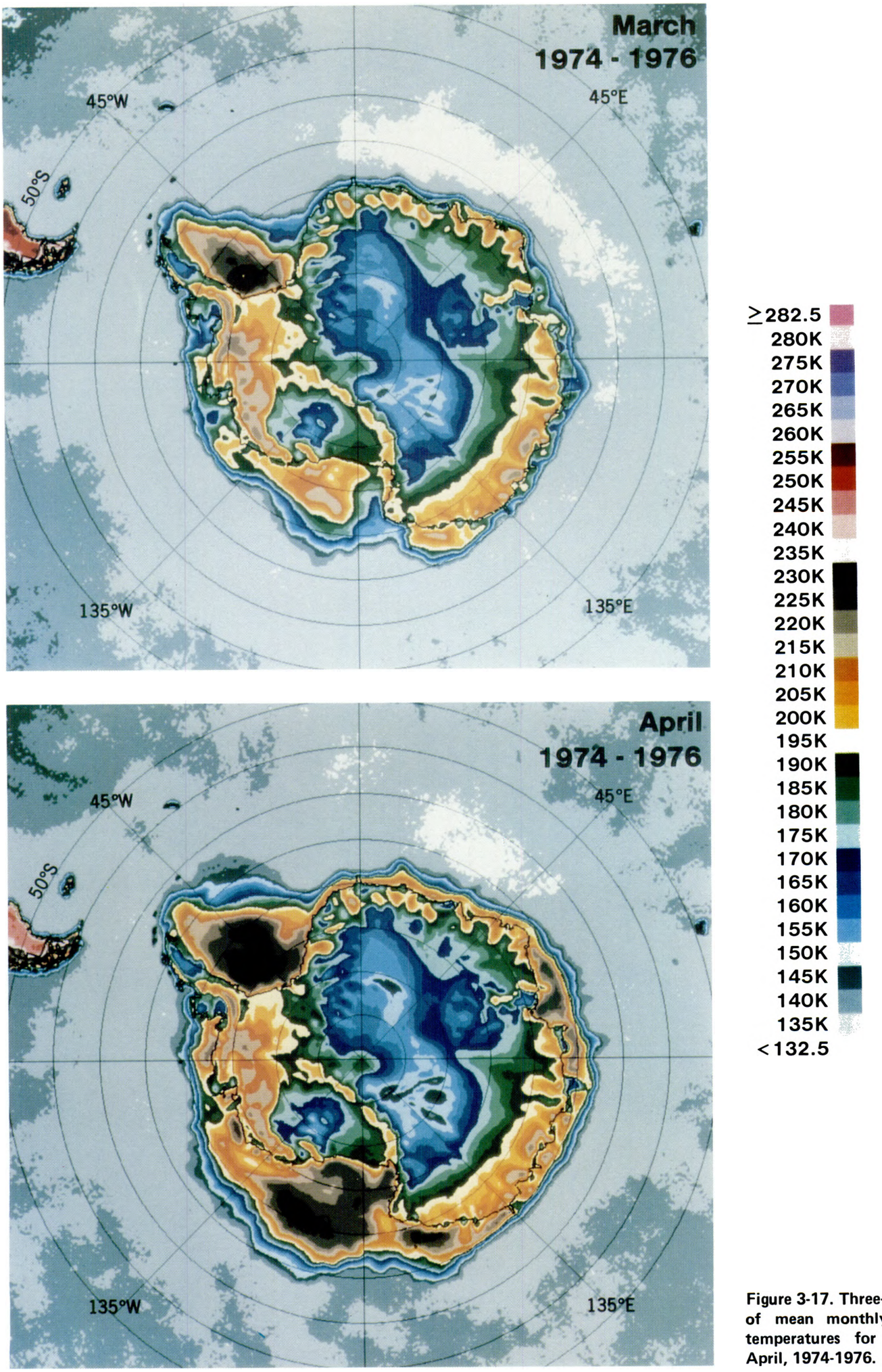

Figure 3-17. Three-year average of mean monthly brightness temperatures for March and April, 1974-1976.

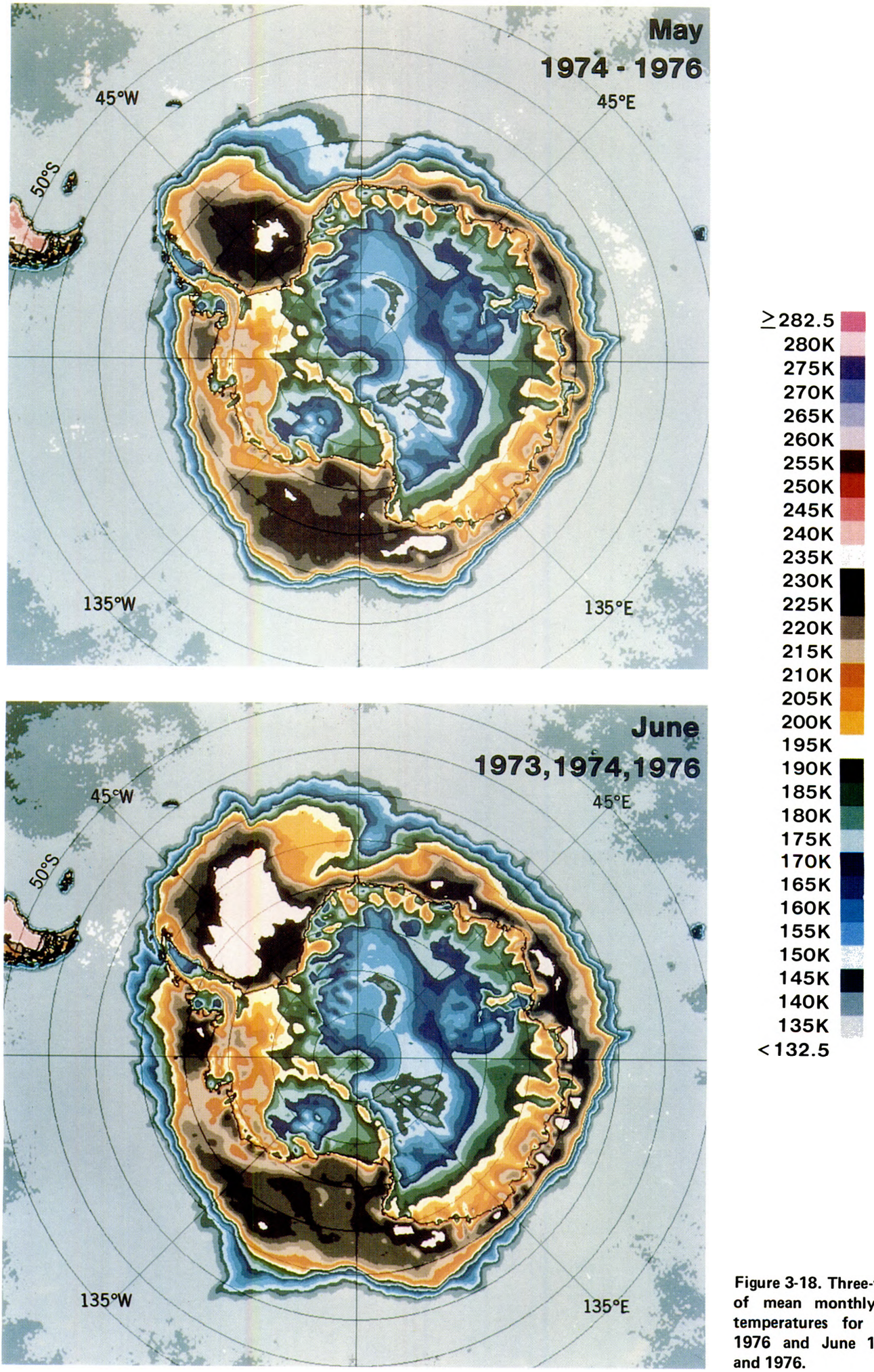

Figure 3-18. Three-year average of mean monthly brightness temperatures for May 1974-1976 and June 1973, 1974, and 1976.

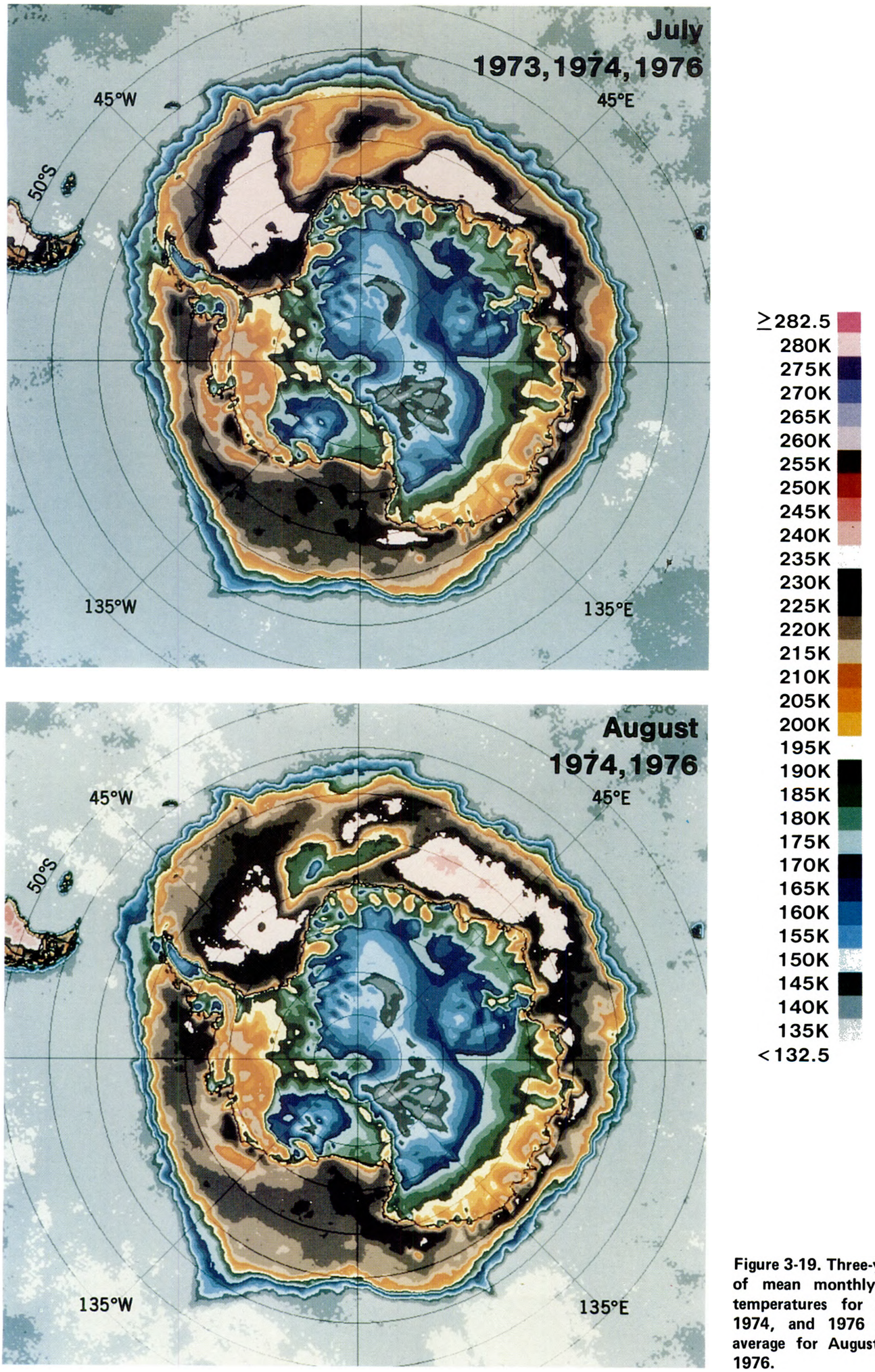

Figure 3-19. Three-year average of mean monthly brightness temperatures for July 1973, 1974, and 1976 and 2-year average for August 1974 and 1976.

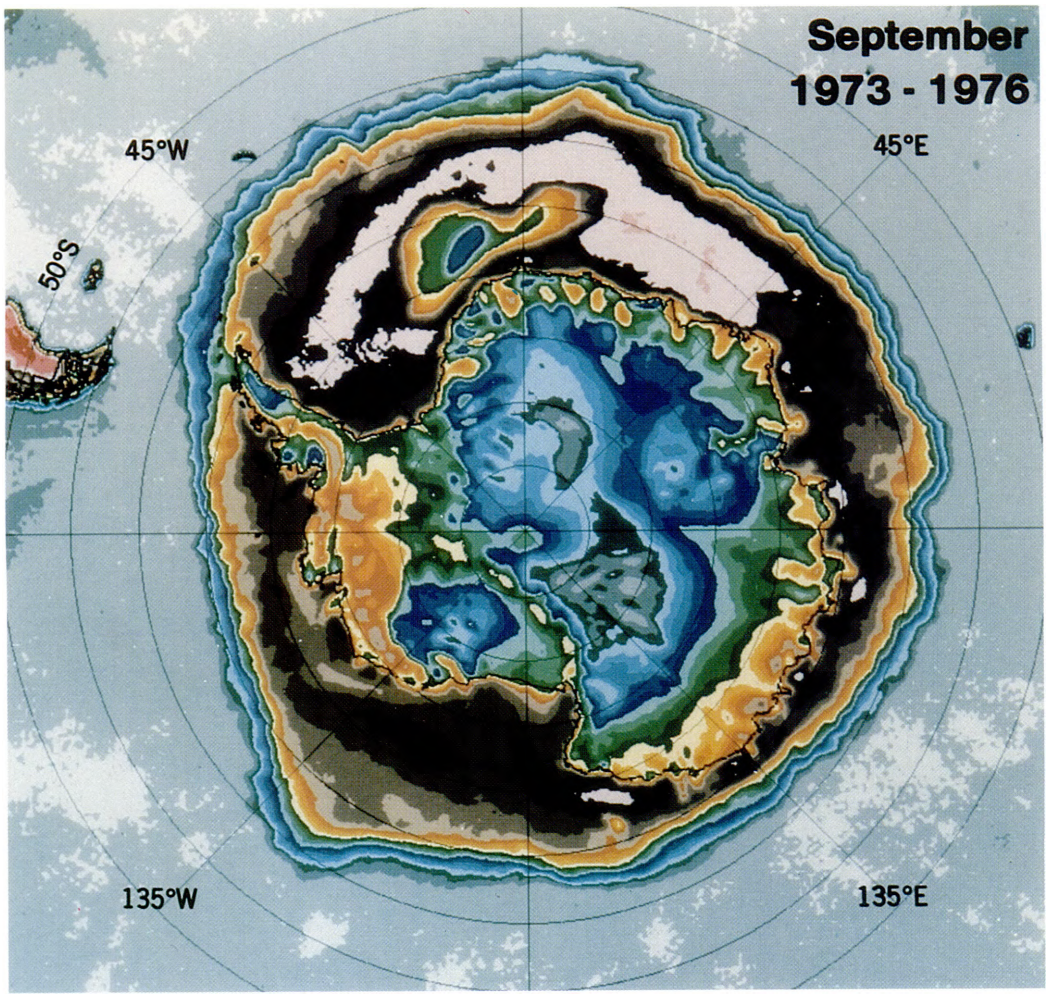

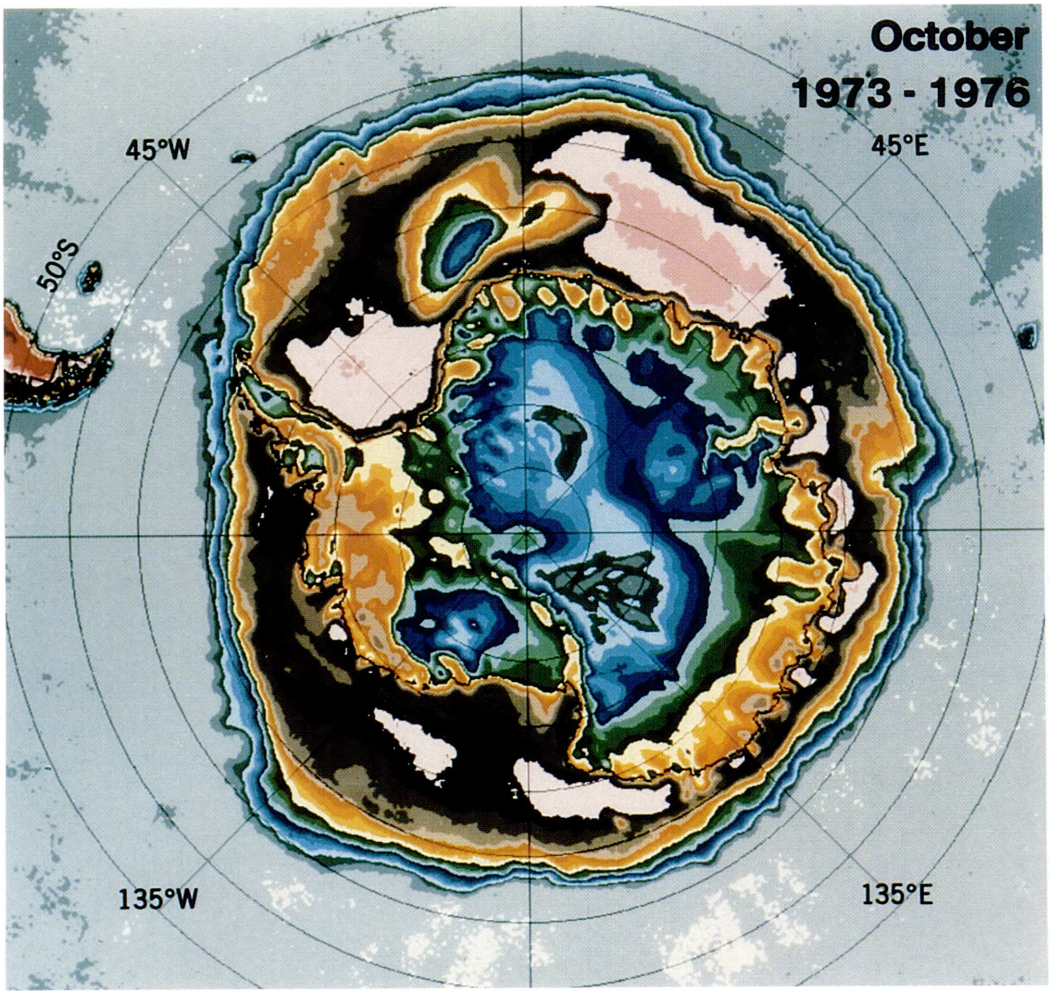

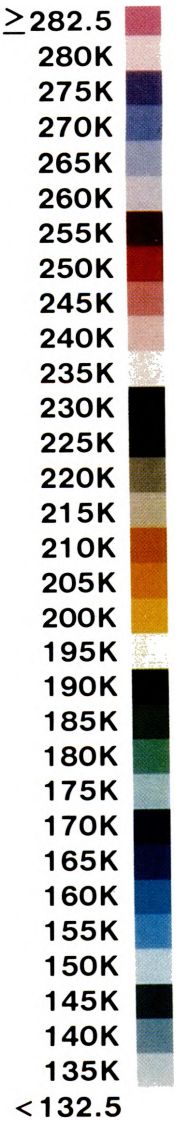

Figure 3-20. Four-year average of mean monthly brightness temperatures for September and October, 1973-1976.

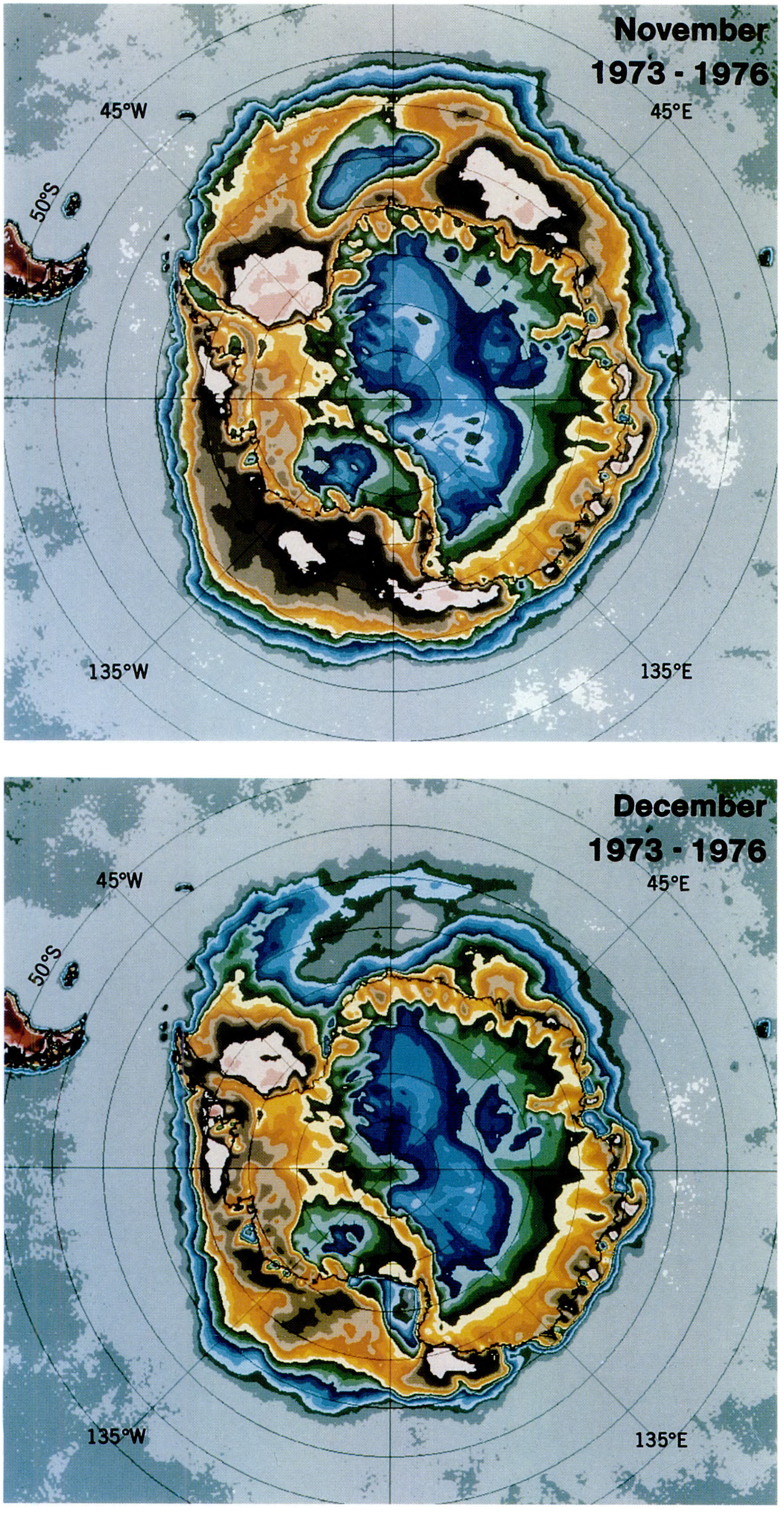

Figure 3-21. Four-year average of mean monthly brightness temperatures for November and December, 1973-1976.

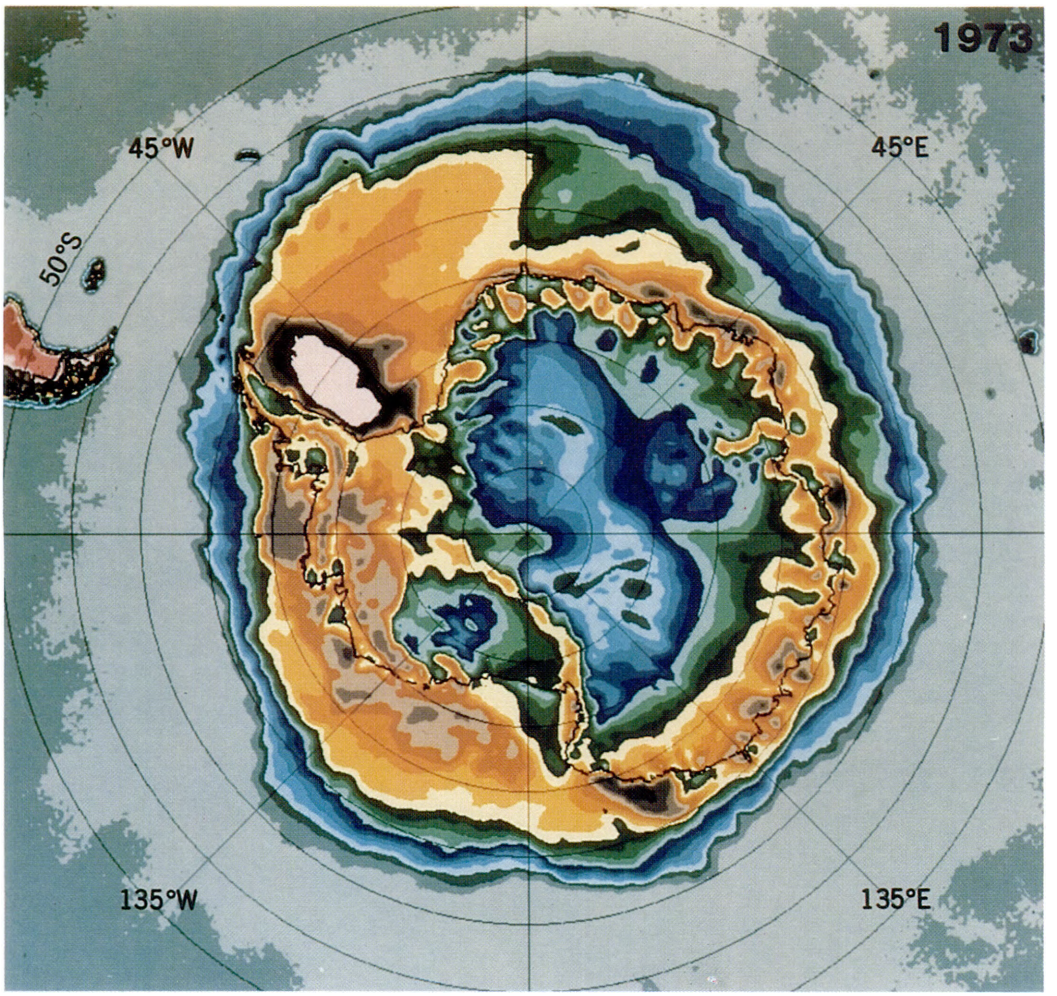

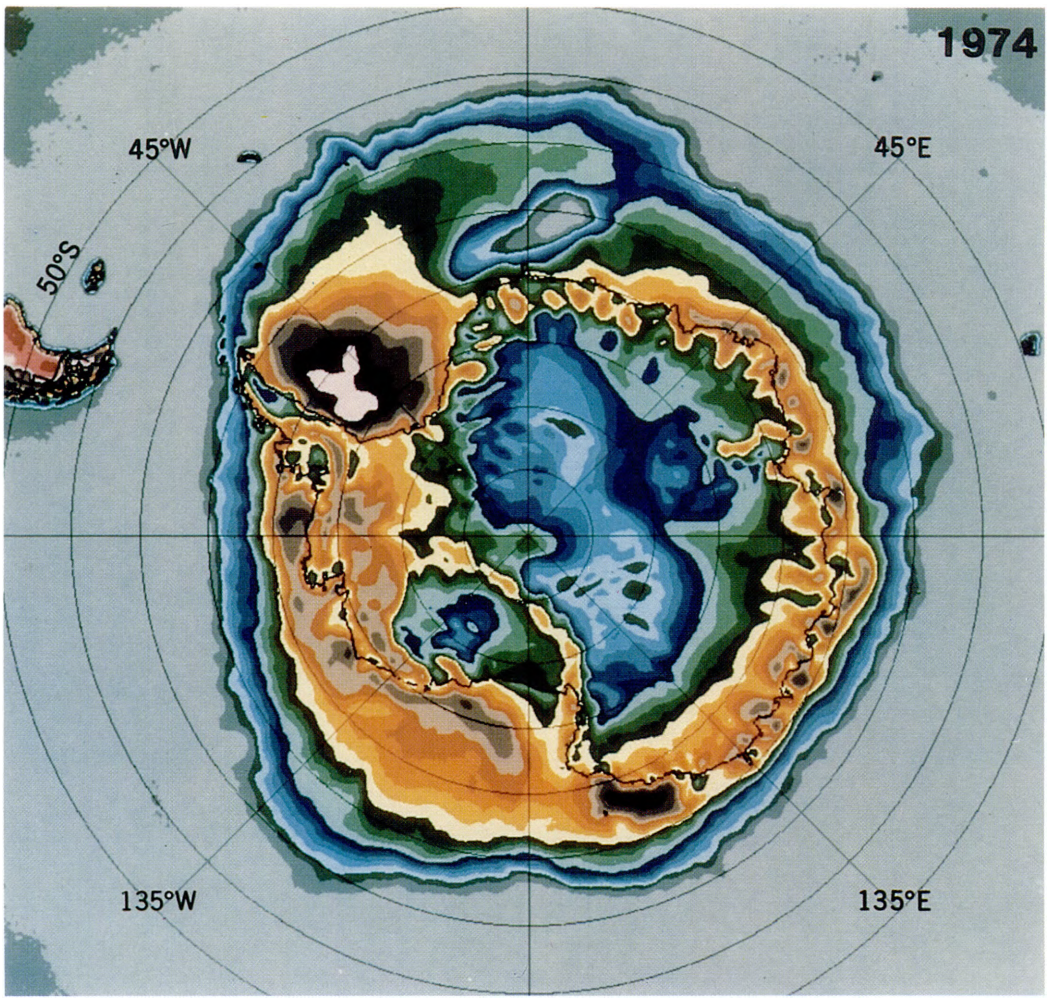

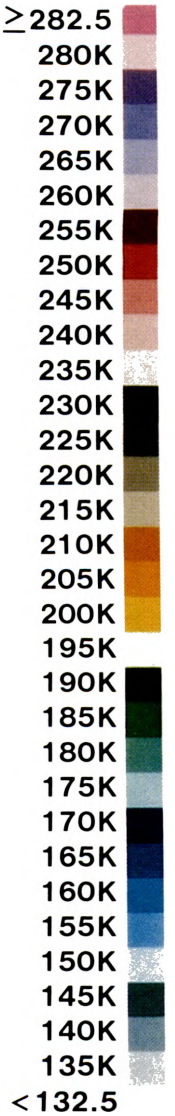

Figure 3-22a. Annual mean brightness temperatures for 1973 and 1974. Months without data were accounted for by interpolation.

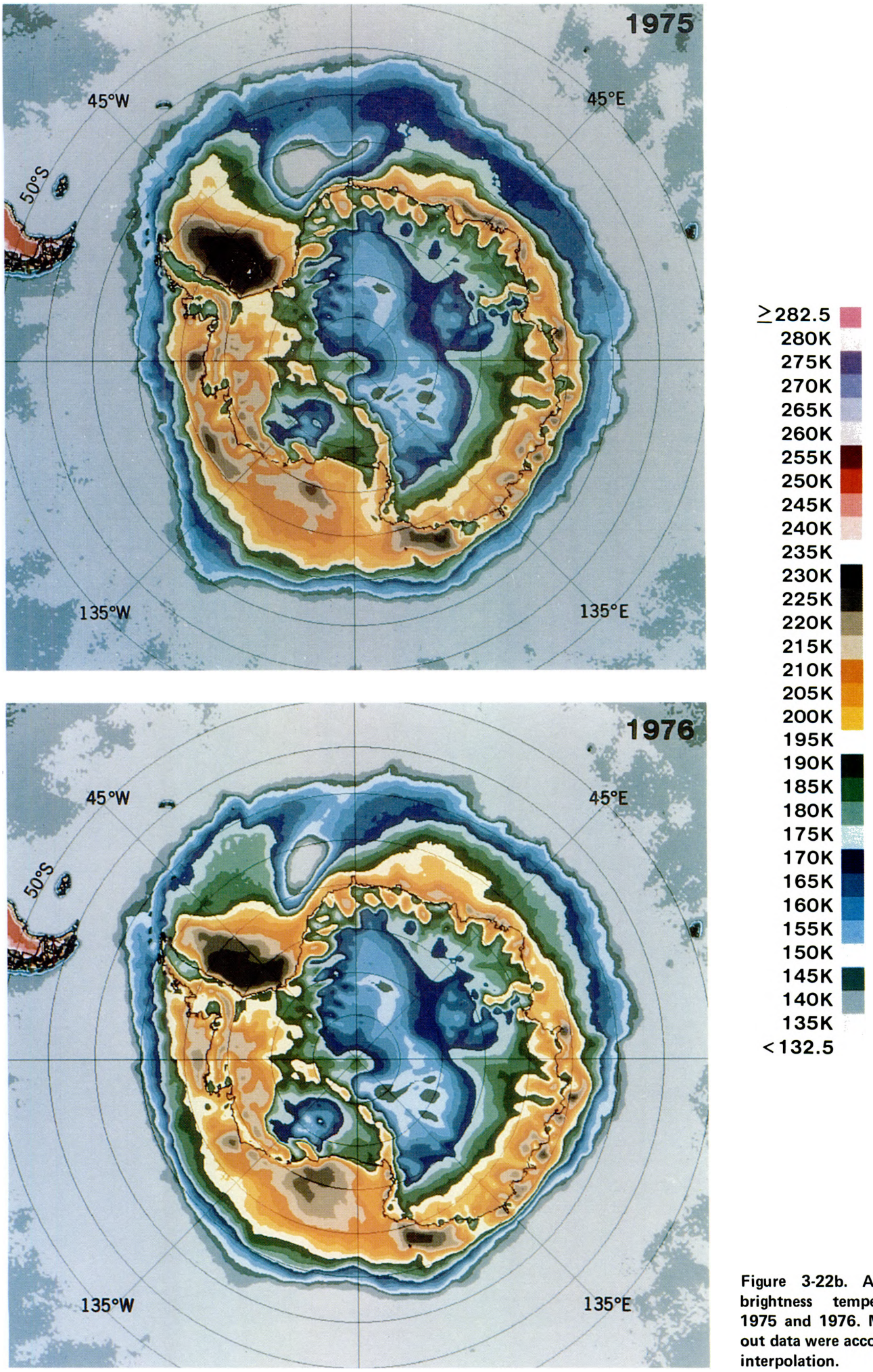

Figure 3-22b. Annual mean brightness temperatures for 1975 and 1976. Months without data were accounted for by interpolation.

determine polynya modification by atmospheric depressions in this region. During the course of the winter, the brightness temperature patterns vary much more offshore than inland, a result of the microwave sensitivity to the short-term effects of winds on the sea ice concentration versus the long-term effects on the ice-sheet surface.

A more detailed interpretation of the areas covered by sea ice and their temporal and spatial variability are presented in the following chapters, using ice concentration maps derived from the brightness temperature maps by methods described in the next section. Interpretation of the ice concentration maps is more straightforward, in contrast to the brightness temperature maps, because the effect of the seasonal and geographical variation in the physical temperature at each map element has been taken into account. The brightness temperature maps, however, are also useful because they show the basic data and contain information on the open oceans and continental ice sheets.

3.5 DETERMINATION OF ICE CONCENTRATION

Because of the strong contrast between the emissivity of sea water and that of ice, the ice concentration can be derived with reasonable accuracy from each of the data elements in the brightness temperature maps. The radiative transfer equation applicable to passive microwave observations at a given wavelength is given by:

$$T_B = \epsilon T_s e^{-\tau} + \int_0^{\tau} T(z)\,\zeta(z)\,e^{-\tau+\tau'(z)}d\tau'(z) \qquad (3\text{-}3)$$

$$+ (1-\epsilon)k\,e^{-\tau}\int_0^{\tau} T(z)\,\zeta(z)\,e^{-\tau'(z)}d\tau'(z),$$

where T_B is the observed brightness temperature, ϵ is the emissivity of the surface, T_s is the physical temperature of the surface, $\tau'(z)$ and τ are the atmospheric opacities from the surface to a height z and from the surface to the satellite height, respectively, k is an estimate of the diffusiveness of the surface reflection, and $\zeta(z)$ is the emittance at z. The reflected contribution of free-space radiance, which is a very small additive constant, is neglected. The emissivity depends on wavelength, as well as on various surface variables. In equation 3-3, the first term on the right-hand side represents the contribution to the observed brightness temperature of the surface as seen through the atmosphere, the second is the upwelling radiation from the atmosphere (directed towards the satellite sensor), and the third is the downwelling atmospheric radiation (directed towards the Earth) as observed after reflection at the surface and transmission back through the atmosphere. Using typical atmospheric conditions over the subpolar oceans, radiative transfer studies have shown that the contribution of the second term is typically 8 K, whereas that of the third is about 5 K. Over Antarctic sea ice, these contributions are expected to be substantially less than these values because of the lower water-vapor content of the atmosphere.

A typical sensor field-of-view in sea ice areas normally contains several types of surfaces, including water, new ice, first-year ice, and multiyear ice. The brightness temperature measured by the satellite instrument is the sum of the contributions from the various surfaces, each of which is characterized by its own emissivity and temperature. Assuming that, in each ESMR field-of-view, the only surface types are water and first-year ice, the radiative transfer formulation can be simplified as:

$$T_B = (C_W \epsilon_W T_W + C_I \epsilon_I T_I)e^{-\tau} + \qquad (3\text{-}4)$$

$$(C_W T_{AW} + C_I T_{AI}),$$

where ϵ_W, ϵ_I, C_W, C_I, T_W, T_I, T_{AW}, and T_{AI} are emissivities, concentrations defined as areal fractions, physical temperatures, and atmospheric contributions for water and ice, respectively.

Because C_W equals 1 - C_I, equation 3-4 can be solved for ice concentration:

$$C_I = \frac{T_B - T_o}{\epsilon_I T_{eff} - T_o}, \qquad (3\text{-}5)$$

where

$$T_{eff} \equiv T_I e^{-\tau} + T_{AI}/\epsilon_I,$$

and

$$T_o \equiv \epsilon_W T_W e^{-\tau} + T_{AW}.$$

The T_o is the brightness temperature over 100-percent open ocean, ϵ_I T_{eff} is the brightness temperature over 100-percent sea ice, and T_B is the brightness temperature over mixtures of ice and open water. This linear relationship between the brightness temperatures and sea ice concentration was also discussed in Gloersen et al. (1974), Zwally and Gloersen (1977), Carsey (1980), and Comiso and Zwally (1982), and is illustrated in Figure 3-23 for two values of ϵ_I and several values of T_{eff}.

The appropriate average value of T_o = 135 K is determined as a unit by investigating ESMR brightness temperature distributions of water near the edge of the ice pack (see Appendix C) and is used throughout the remaining calculations. The value of T_o is approximately independent of ocean temperature, T_W, because of an inverse dependence of ϵ_W on T_W at 1.55 cm wavelength (Wilheit, 1972); and effects such as surface roughness contribute mainly to variations about the average value of T_o. The emissivity of first-year ice has been determined both empirically from ESMR data and with theoretical Fresnel relations (equation 3-2) to be about 0.92. Because real-time data for T_I are not available, interpolated monthly climatological air temperature data (Jenne et al., 1974) are used. The ice temperature, which is normally higher than air temperature but lower than the water temperature underneath the ice, is estimated from the following empirical formula:

$$T_I = T_{air} + f(T_W - T_{air}), \qquad (3\text{-}6)$$

where T_{air} is the mean monthly climatological air temperature, T_W is water temperature (271.16 K), and f is a parameter empirically determined from the observed T_B data. The value of f is determined from July 1974 data by adjusting it until the maximum values of C_I from equation 3-5 are consistently about 100 percent during winter (see Appendix C). The resulting value of 0.25 for f agrees with the overall average of surface measurements at Pond Inlet (Ramseier, private communication). A comparison of the Pond Inlet average values with those used here is shown in Figure 3-24.

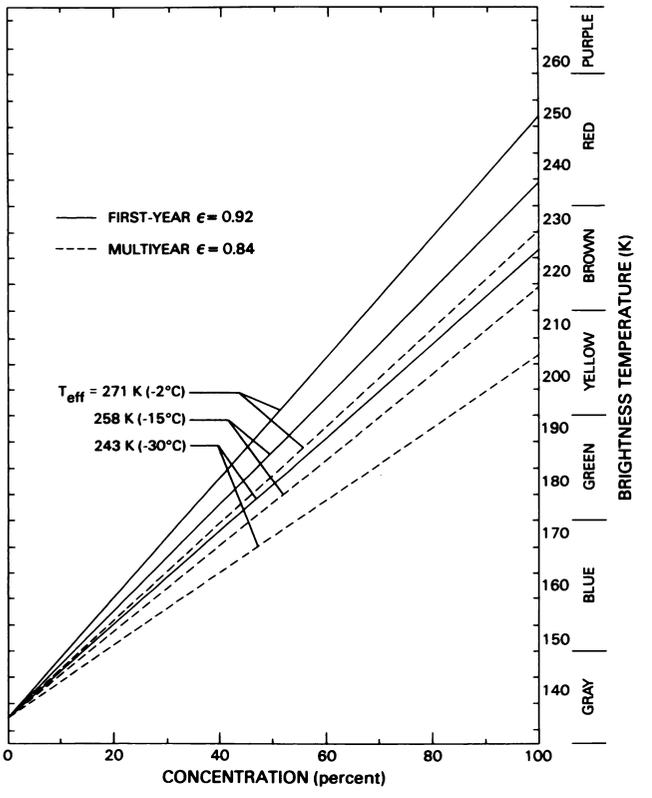

Figure 3-23. Linear relationship between sea ice concentration and microwave brightness temperature (see equation 3-5) for two values of emissivity and several values of the effective physical temperature of the ice radiating layer.

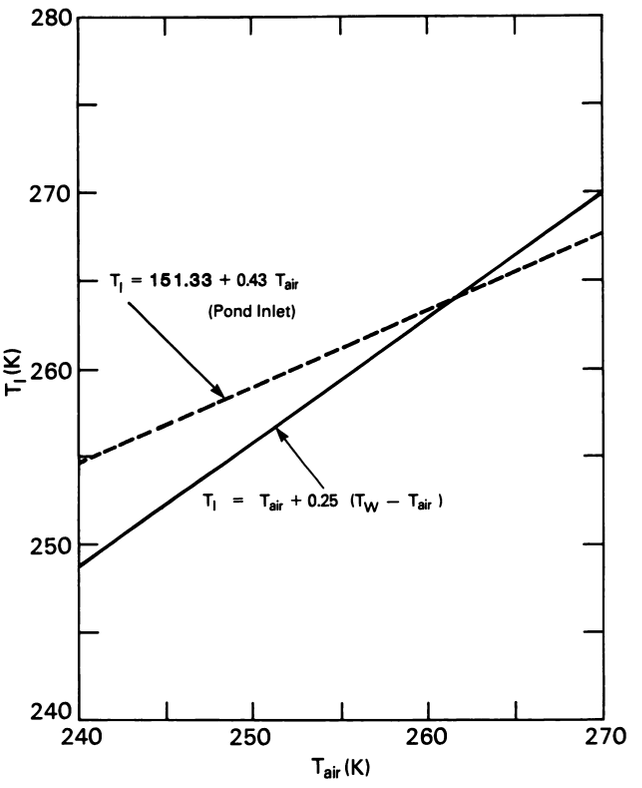

Figure 3-24. Estimated snow/ice interface temperature used to derive sea ice concentration compared with a curve fitted to Pond Inlet temperature data (Ramseier, private communication).

Over the interval 240 to 270 K, the maximum deviation is 6 K. Since the parameterization to determine f uses the observed microwave data, the atmospheric effects are automatically taken into account. T_{eff} is also taken to be equal to T_I determined by equation 3-6.

A quantitative comparison was made by Comiso and Zwally (1982) of ice concentrations derived with the foregoing procedure and those obtained from Landsat 1 and Landsat 2 Multispectral Scanner near-infrared-band images. The set of images compared included regions near the ice edge and near the continental boundary, an example of which is shown in Figure 3-25. Using an overlay procedure, a total of 86 ESMR pixels and the corresponding near-simultaneous Landsat images were analyzed. The results suggest that, although the Landsat data have much better resolution than the ESMR data, the presence of narrow leads, small ice floes, thin ice, and clouds often cause considerable uncertainty in the ice concentrations that can be inferred from the visible sensors. A classification procedure for Landsat, which is often used for ice-cover estimates and is based on a threshold radiance level, overestimated the ice concentration because this method tends to classify mixtures of water and unresolved ice floes as fully ice-covered ocean. When a proportional classification based on observed reflectance was utilized instead, the Landsat data agreed substantially better with ESMR

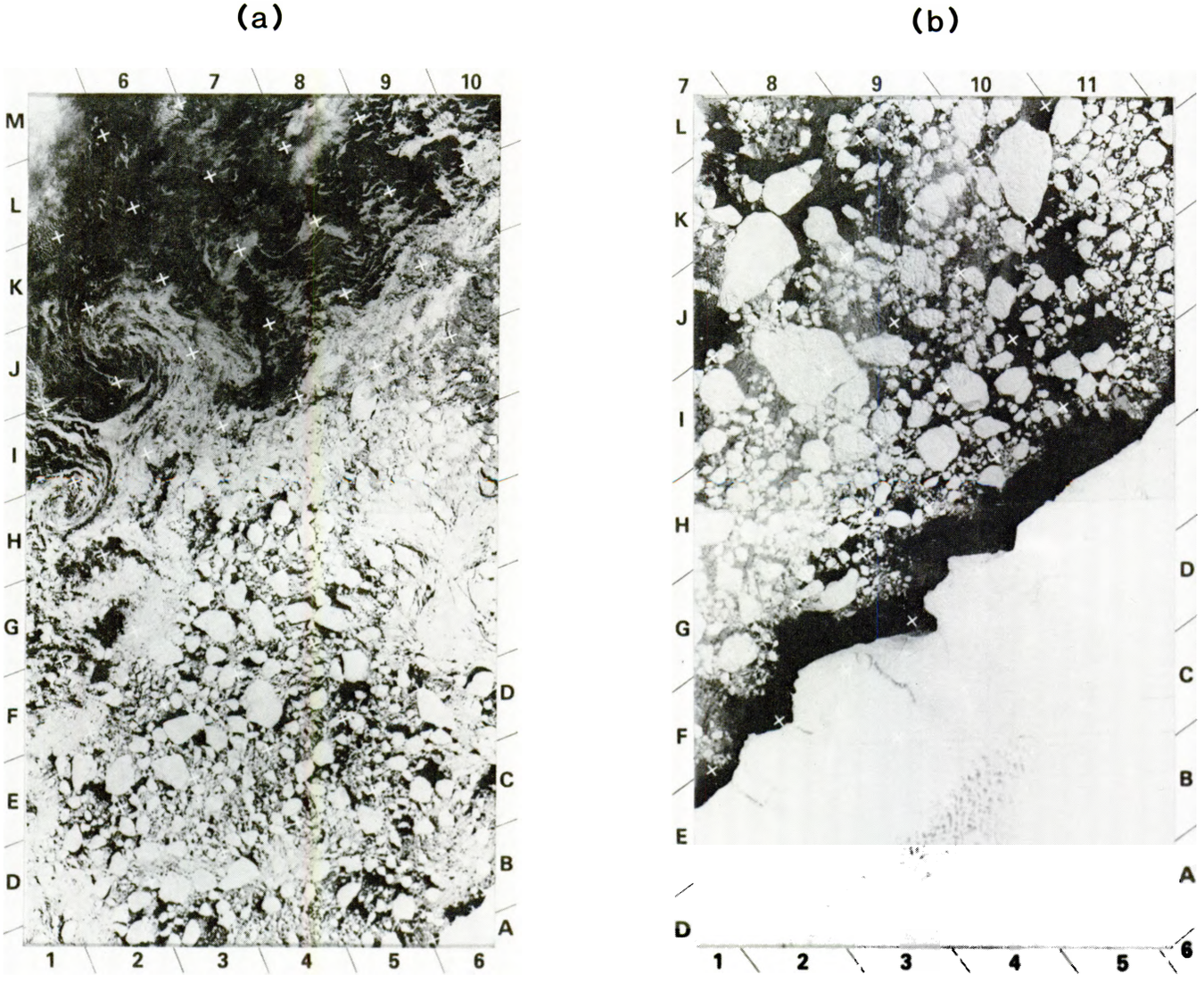

Figure 3-25. Landsat multispectral scanner images at near-infrared (1.1 microns) wavelengths: (a) image for November 23, 1975, centered at 68°1′S, 4°49′W and (b) image for November 13, 1973, centered at 69°2′S, 9°16′E.

values. A plot comparing results from the two sensors using the latter classification procedure is shown in Figure 3-26. The 12-percent standard deviation in the comparison is consistent with the estimated uncertainty of the ESMR ice concentration determination discussed below.

3.6 ERROR ANALYSIS

The uncertainties in the derived ice concentration values are difficult to quantify because of the lack of more accurate observations with which the derived ice concentrations can be compared. Nevertheless, an evaluation of the uncertainties involved in the calculation is made on the basis of principal sources of error in the ice algorithm, which are the uncertainties in brightness temperature, the emissivity, and the physical temperature.

A good estimate for the instrumental uncertainty of brightness temperature can be inferred from temperature distributions over the ocean. For example, Figure 3-27 illustrates the distribution of T_B in the Weddell Sea area of both ice and ocean between 55°S and 65°S. A narrow ocean distribution is seen at about 135 K, indicating that the fluctuation of brightness temperature in the monthly averaged data is very small (<±3 K). The actual uncertainty in brightness temperature should be smaller because atmospheric and ocean-roughness effects are included in the distribution.

An apparent time-dependent shift of the ocean brightness temperature was observed in some of the data as discussed in Appendix A (see also Comiso and Zwally, 1980). Although a correction to the affected data was applied, some uncertainties on the order of a few degrees remained. Spatial and time interpolations applied to the 3-day average data sets to fill empty map elements also affect the brightness temperature accuracy. Furthermore, some 3-day average maps were not obtained because of a lack of useable data, thereby requiring a weighting procedure on available data to create the monthly averages. Nevertheless, for about 90 percent of the data, the error in brightness temperature on the monthly maps is estimated to be about 2 to 3 K. For the remainder, an error estimate of about 5 K is not unreasonable.

The emissivity of first-year ice used in the algorithm (0.92) appears to be a reasonable average value. This quantity, however, is known to undergo spatial and seasonal variations over the Arctic ice pack, as discussed in Gloersen et al. (1978) and Carsey (1982). Similar variation is also expected in the Antarctic ice region. During the melt season, the emissivity could increase by as much as 4 percent (Chang and Gloersen, 1975). Also, salinity of the snow and ice, another parameter that affects the microwave radiative properties, is likely to vary

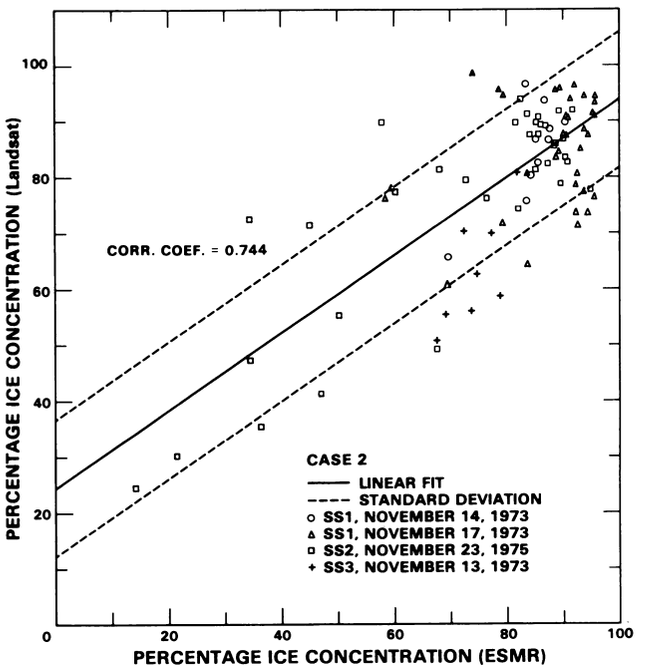

Figure 3-26. Comparison of sea ice concentrations derived from ESMR data with those from Landsat data (from Comiso and Zwally, 1982).

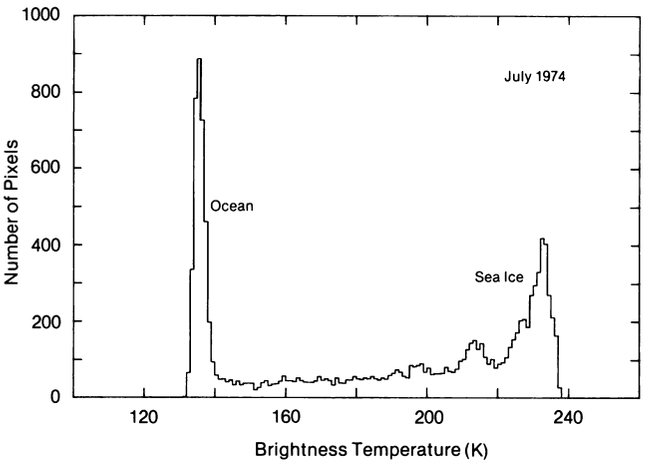

Figure 3-27. Distribution of brightness temperature derived from ESMR data in the Weddell Sea sector (60°W to 20°E) during July 1974.

seasonally and from one area to another. Furthermore, the thickness of the snow on top of the ice, which controls both physical temperature and brightness temperature, could vary both seasonally and spatially. The variability of snow depth on Arctic floes is examined in Hansen (1980).

The presence of ice types other than first-year ice can also introduce error. As indicated earlier, some areas have the microwave signature of multiyear ice. Fortunately, these areas are very limited in coverage, the bulk of this type of ice occurring in the Bellingshausen-Amundsen Seas sector. To study the effect of multiyear ice on the area distributions, 3-day maps during the summer minimum are analyzed to evaluate the amount of ice that survived in this sector each year. The actual area, A_a, covered by ice is calculated by equation A-11 using the emissivity of first-year ice (0.92), and recalculated using the emissivity of multiyear ice (0.84). The difference of the results is taken, and the values for each year appear in Table 3-1.

The effects of this discrepancy in the Bellingshausen-Amundsen Seas on the determination of monthly sea ice area for the total southern ocean and for the Bellingshausen-Amundsen Seas sector are tabulated in Table 3-2. For the total southern ocean, the percentage differences are consistently close to 1 percent, except during the summer when the difference can be as large as 7 percent. However, the emissivities of multiyear ice and first-year ice during the summer melt are about the same because surface effects are dominant. Thus, the summer differences (Table 3-2) should be ignored, and the error in the calculation of effective area in summer is probably small. For the Bellingshausen-Amundsen Seas sector alone, the calculated differences, exclusive of summer months, are close to 10 percent. These differences, however, are upper limits since it is not known whether all the ice that survives summer in the area has desalinated enough to have the emissivity of multiyear ice. Similar analysis was done on the ice extent ($\geqslant$15-percent ice concentration), and the results show no significant difference in areal coverage.

Another uncertainty arises because of the limited knowledge of the emissivity of very thin ice that exists mainly as frazil, grease ice, slush, and dark nilas (<5-cm thickness). The emissivity of consolidated ice forms, such as nilas and first-year ice, depends mainly on thickness. Since the microwave optical depth of sea ice is on the order of 1 centimeter, it is expected that nilas greater than 5 centimeters in thickness has an emissivity close to that of first-year ice and that the emissivity of dark nilas has smaller values than first-year ice. The emissivity of dark nilas increases with thickness. On the other hand, the emissivity of frazil ice, grease ice, and slush is probably closer to the emissivity of open water than to the emissivity of first-year ice. Further scientific investigation is necessary to quantify the areal coverage of very thin ice types, which may be particularly important in the marginal ice zone near the ice edge and in regions of new ice formation near the coast.

Various factors affect the uncertainty of the physical temperature of the ice used in the algorithm. These include: (1) year-to-year variation from the climatological monthly averages, (2) accuracy of the spatial interpolation, (3) reliability of the empirical formula for deriving ice temperatures from air temperatures, and (4) accuracy of the climatological averages themselves.

The climatological data set (Jenne et al., 1974), compiled on a 5-degree-latitude by 5-degree-longitude grid, is interpolated to the 30- by 30-kilometer grid of the ESMR brightness temperature data. Some of the interpolated data (February and

Table 3-1
Areal Ice Coverage During Summer Minimum in the Bellingshausen-Amundsen Seas Calculated for $\epsilon_I = 0.84$ and $\epsilon_I = 0.92$

Date	A_a ($\epsilon_I = 0.84$)	A_a ($\epsilon_I = 0.92$)	ΔA_a
1973, Feb. 11-13	0.926×10^6 km^2	0.739×10^6 km^2	0.187×10^6 km^2
1974, Feb. 24-26	0.751	0.599	0.152
1975, Feb. 28-March 1	0.658	0.525	0.133
1976, Feb. 11-13	0.709	0.563	0.145

Table 3-2
Error in Actual Sea Ice Area due to Classifying Multiyear Ice in the Bellingshausen-Amundsen Seas as First-Year Ice

Date	ΔA_M (km^2)	A_a (km^2)		$\Delta A_M / A_a$	
		All Sectors	B-A Seas	All Sectors	B-A Sector
January 1973*	0.187×10^6	3.861×10^6	0.785×10^6	0.048	0.238
February 1973*	0.187×10^6	2.712	0.693	0.069	0.270
June 1973	0.187×10^6	11.911	1.892	0.016	0.102
July 1973	0.187×10^6	14.590	1.690	0.013	0.111
September 1973	0.187×10^6	15.872	1.707	0.012	0.110
October 1973	0.187×10^6	16.226	1.671	0.012	0.112
November 1973	0.187×10^6	12.691	1.426	0.015	0.131
December 1973	0.187×10^6	6.685	1.108	0.028	0.169
January 1974*	0.187×10^6	3.670	0.845	0.051	0.221
February 1974*	0.152×10^6	2.146	0.527	0.071	0.288
March 1974*	0.152×10^6	2.874	0.480	0.053	0.317
April 1974	0.152×10^6	6.037	0.792	0.025	0.192
May 1974	0.152×10^6	8.681	0.853	0.018	0.178
June 1974	0.152×10^6	11.359	1.146	0.013	0.133
July 1974	0.152×10^6	13.193	1.602	0.012	0.095
August 1974	0.152×10^6	15.002	1.968	0.010	0.077
September 1974	0.152×10^6	14.679	1.977	0.010	0.077
October 1974	0.152×10^6	14.799	2.057	0.010	0.074
November 1974	0.152×10^6	12.078	1.660	0.013	0.092
December 1974	0.152×10^6	6.862	1.073	0.022	0.142
January 1975*	0.152×10^6	3.606	0.794	0.042	0.191
February 1975*	0.133×10^6	2.201	0.527	0.060	0.252
March 1975*	0.133×10^6	3.012	0.525	0.044	0.253
April 1975	0.133×10^6	5.475	0.711	0.024	0.187
May 1975	0.133×10^6	8.251	1.072	0.016	0.124
September 1975	0.133×10^6	15.561	1.966	0.009	0.068
October 1975	0.133×10^6	14.080	1.758	0.009	0.076
November 1975	0.133×10^6	11.066	1.639	0.012	0.081
December 1975	0.133×10^6	6.304	1.146	0.021	0.116
January 1976*	0.133×10^6	3.937	0.749	0.034	0.183
February 1976*	0.145×10^6	2.272	0.447	0.064	0.324
March 1976*	0.145×10^6	3.422	0.493	0.042	0.294
April 1976	0.145×10^6	5.629	0.598	0.026	0.242
May 1976	0.145×10^6	8.405	1.276	0.017	0.114
June 1976	0.145×10^6	11.138	1.708	0.013	0.085
July 1976	0.145×10^6	13.236	2.028	0.011	0.071
August 1976	0.145×10^6	14.704	2.076	0.010	0.070
September 1976	0.145×10^6	14.851	2.033	0.010	0.071
October 1976	0.145×10^6	13.333	1.761	0.011	0.082
November 1976	0.145×10^6	9.894	1.536	0.014	0.094
December 1976	0.145×10^6	5.673	1.178	0.026	0.123

*Summer months, see text.

August) were compared with the interpolated Australian data set for 1974, and most of the deviations were less than 3 K. Deviations as large as 15 K occurred in winter near the continent at the Weddell Sea, but it is also known from comparison of data buoy measurements that the Australian analysis had many discrepancies greater than 10 K (Hibler and Ackley, 1982). As mentioned earlier, the empirical formula for extracting ice temperature from air temperature was compared with ground measurements at Pond Inlet in the Arctic region (Figure 3-24), indicating deviations less than 6 K.

A sensitivity study is made to establish the effect of errors in the various parameters on the derived ice concentrations. The uncertainty in ice concentration, $\Delta C/C$, can be calculated from equation 3-5 as follows:

$$\frac{\Delta C}{C} = \sqrt{\left(\frac{\Delta T_B}{T_B - T_o}\right)^2 + \left(\frac{\Delta(\epsilon_I T_{eff})}{\epsilon_I T_{eff} - T_o}\right)^2}, \quad (3\text{-}7)$$

where ΔT_B and $\Delta(\epsilon_I T_{eff})$ are the uncertainties in brightness temperature and $\epsilon_I T_{eff}$ ($\equiv T_I'$), respectively, and T_o = 135 K. Typical values of brightness temperature and the corresponding effective temperature representing ice concentration values from minimum to maximum are selected from various locations in the southern ocean. Using equation 3-7 and some reasonable values of ΔT_B (2.0 and 3.0 K) and $\Delta T_I'$ (2.5, 5.0, and 10.0 K), the uncertainties of ice concentration for these selected areas are calculated and plotted in Figure 3-28. The plot shows an approximately exponential decrease in percentage uncertainty ($\Delta C/C$), depending on the values of ΔT_B and $\Delta T_I'$, from a range of about 12 to 20 percent near the ice edge (~15 percent) to a range of about 3 to 8 percent near the consolidated ice regions. The uncertainty is quite sensitive to ΔT_B in the low-concentration regions, mainly because T_B - 135 K is small in these areas. The effect of a higher $\Delta T_I'$ becomes very important in the higher ice concentration regions. The upper curve for ΔT_B = 3 K and $\Delta T_I'$ = 10 K is probably a good upper limit of the overall error in the data set, considering also uncertainties that cannot be adequately evaluated. The weighted average of the ice concentration error from this upper curve is about

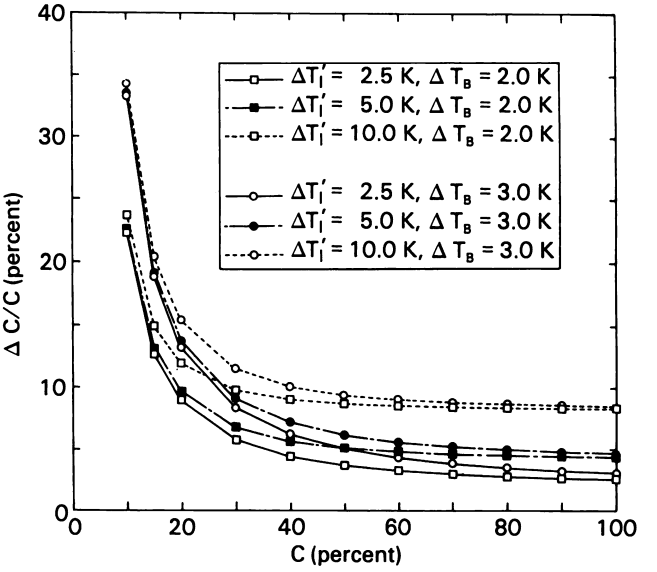

Figure 3-28. Uncertainty in ice concentration derived from ESMR data as a function of ice concentration, presented for several errors in brightness temperature (ΔT_B = 2.0 and 3.0 K) and for several errors in estimated snow/ice interface temperature ($\Delta T_I'$ = 2.5, 5.0, and 10 K).

12 percent for $\Delta C/C$, whereas ΔC ranges from 3 percent at low values of C to 9 percent at C equal to 100 percent.

Another consideration is how the uncertainties in brightness temperature and T_I' affect the calculation of area covered by ice, as discussed in the next chapter. To investigate the sensitivity of this calculation, the areas are calculated for T_B + 2.5 K and T_I' + 2.5 K and also for T_B - 2.5 K and T_I' - 2.5 K from the 4-year monthly maps. Note that, although the uncertainty in T_I' for individual pixels is probably higher, an uncertainty of 2.5 K for a large-scale area is statistically quite substantial. Over a large area, overestimates at some locations are compensated by underestimates at other locations. This area sensitivity study is done for various percent areal coverages and for various sectors, with the results appearing in Figure 3-29. The calculated area is least sensitive to errors for the ≥15-percent concentration areas and is most sensitive for the ≥85-percent areas in all cases because, for example, the integral area of the band from 15 - 2.5 percent to 15 + 2.5 percent ice cover is substantially smaller than that between 85 - 2.5 percent and 85 + 2.5 percent, especially during winter (e.g., Figure C-1). Other error bands can be

interpreted in a similar manner. Variations from one sector to another can also be understood by investigating the areal distributions of ice concentration, some examples of which are shown in Figures C-4 to C-6.

To summarize, the error (ΔC) in each of the ice concentration map elements is estimated to range from 5 to 15 percent. The relative accuracy from one map element to adjacent map elements is probably better than the estimated ΔC. The accuracy of the sea ice areal extent (i.e., $\geqslant$15-percent concentration) determination is very good (less than 5-percent error), since the ice-free ocean is consistently used as a reference point.

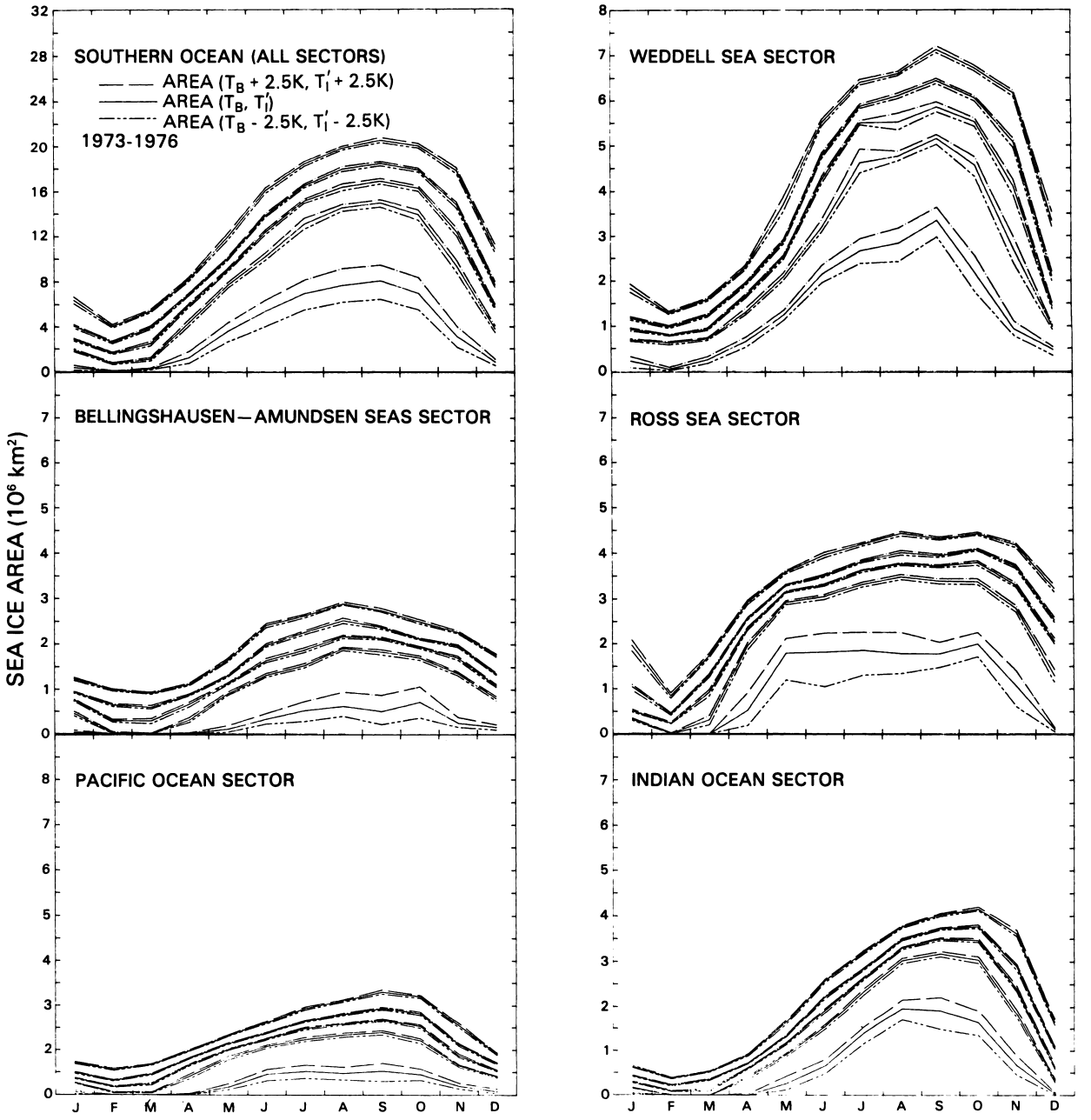

Figure 3-29. Sensitivity of the ocean area covered by sea ice with concentration $\geqslant$15 (top curves), $\geqslant$35, $\geqslant$50, $\geqslant$65, and $\geqslant$85 percent (bottom curves) to a 2.5 K error in both the brightness temperature, T_B, and the estimated snow/ice interface temperature, T_I (see Figure 4-8).

4

SEA ICE SEASONAL GROWTH/DECAY CYCLE

4.1 INTRODUCTION

The seasonal advance and recession of sea ice around the Antarctic Continent is driven both indirectly and directly by the annual variation of solar radiation. The sea ice cycle differs significantly from the solar cycle, indicating that the indirect processes involving the ocean and atmosphere affect the sea ice cycle more than direct radiative heating of the ice. The seasonal sea ice cycle also varies from one part of the southern ocean to another and from year to year. The characteristics of the growth/decay cycle (Figure 4-1) and its relationship to other atmospheric and oceanic variables provide information on interactive physical processes such as the relative influence on ice extent of ocean heat fluxes, ocean currents, direct solar radiation, winds, and air temperatures.

An interesting characteristic of the southern ocean shown by the microwave data is the faster spring/summer melt compared to the fall/winter growth, a phenomenon that contrasts markedly with the Arctic sea ice cycle (Walsh and Johnson, 1979). Noting this phenomenon, Gordon (1980) showed that the atmosphere-to-ocean heat flux is not sufficient to account for the rapid mid-November to mid-January melting and that upwelling of relatively warm deep water is a probable source of the additional heating.

Numerical models of the sea ice cover attempt to account for the various thermodynamic and dynamic processes and to simulate the seasonal growth and decay cycle (Parkinson and Washington, 1979; Hibler, 1979; and Hibler and Ackley, 1982). In turn, discrepancies between observed sea ice distributions and the modeled ice fields provide information on the nature of the atmospheric and oceanic processes that determine the ice distribution.

This chapter describes the general characteristics of the growth/decay cycle and regional differences as reflected in data averages over the 4 years 1973 to 1976. Chapter 5 emphasizes the observed seasonal growth/decay cycle for individual years and interannual variations of the ice cover. The sea ice concentrations are derived from the microwave brightness temperatures. (See Chapter 3.) The monthly average sea ice concentrations for the individual years 1973 to 1976 are combined (equation A-9) to produce 4-year monthly averages. (See Figures 4-2 through 4-7.) For months when useable data were not obtained for all 4 years, the maps depict either 2- or 3-year averages.

To quantify the spatial distribution of the ice cover and its seasonal cycle, the data represented in the ice concentration maps are spatially integrated to determine the area of ice cover as a function of time, producing the graphs shown in Figures 4-8 and 4-9. The areas of coverage are determined in this manner for the total ice extent, various concentration categories, the actual ice area, and open water within the ice pack over the entire southern ocean and over each of the five sectors described in Chapter 2. For each month, the area of ice-covered ocean (i.e., the total ice extent) is calculated by summing the areas of all map elements having at least 15-percent ice coverage (equation A-10). Similarly, the areas of ocean covered by ice of at least 35-, 50-, 65-, and 85-percent concentration are determined by summing the areas of all map elements having at least 35-, 50-, 65-, and 85-percent coverage, respectively. The yearly sequences of the values obtained for each ocean sector (as shown in Figure 2-3) and for the total southern ocean are plotted in Figure 4-8. These plots also include the actual ice areas obtained by summing the products of ice concentration and geographic area of each map element (equation A-11). To show more clearly the areal

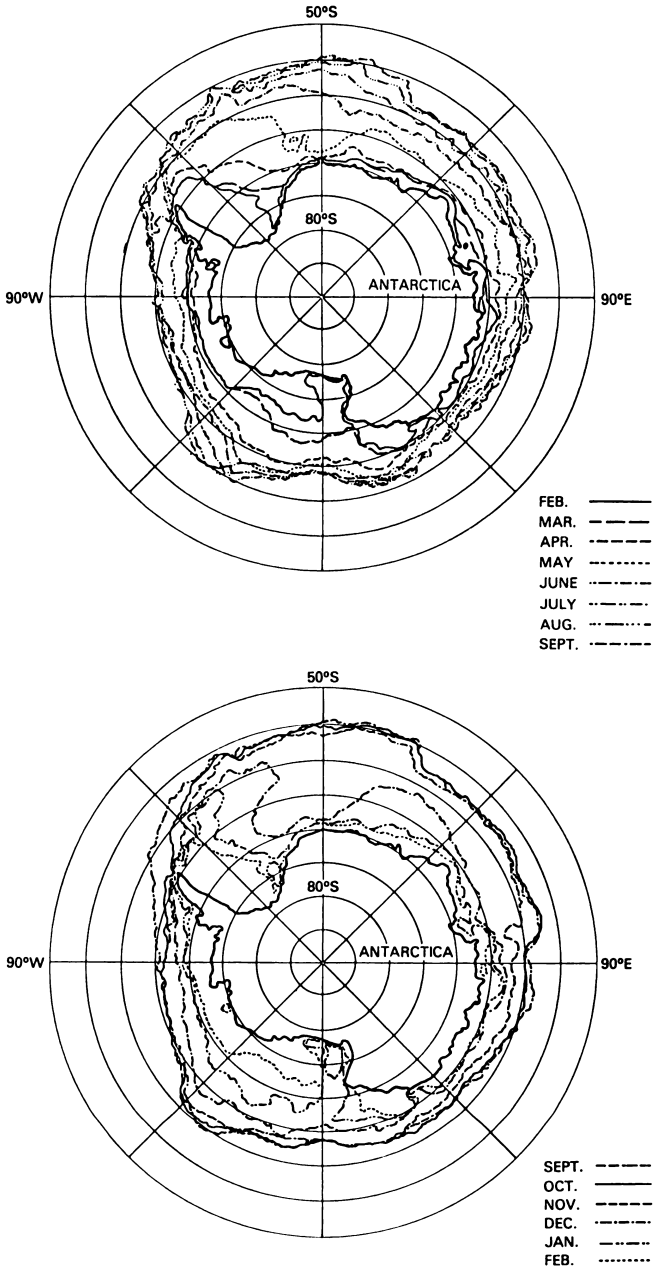

Figure 4-1. Monthly sea ice extents (≥15-percent concentration) averaged for 1973-1976 during the growth and decay seasons (obtained from ice concentration maps in Figures 4-2 through 4-7).

coverage by the various concentration intervals, the data are plotted in Figure 4-9 for the intervals 15 to 35, 35 to 50, 50 to 65, 65 to 85, and 85 to 100 percent.

Quantitative displays similar to Figures 4-8 and 4-9 are given for the individual years in Chapter 5. Because of characteristics of the time averaging and spatial summation procedures, the areas derived from the 4-year averages (Chapter 4 data) differ slightly from average areas obtained by averaging the respective areas for the individual years (Chapter 5 data), as explained further in Appendix A. For example, in winter, the 4-year average ice extent is about 4 percent more than the average of the 4 individual years, and in summer, it is about 5.5 percent more. For the actual ice area, the difference is smaller and in the other direction, with the 4-year average being about 0.6 percent less in winter and about 2.5 percent less in summer. These differences are caused by reversing the order of the time averaging and spatial summations and are about the same magnitude as the interannual variations. Consequently, the best absolute values are given by the individual year data in Chapter 5. Nevertheless, the 4-year averages show the typical ice distributions and seasonal cycles. These graphic presentations are used along with the 4-year monthly average images of sea ice concentration to describe the seasonal cycle in detail. The ice concentration change maps in Figure 4-12 display the growth and decay from one month to the next throughout the annual cycle.

4.2 ANNUAL CYCLE AND REGIONAL CHARACTERISTICS

Southern ocean sea ice extent undergoes a strong seasonal growth/decay cycle, expanding fivefold in area from summer to winter. The extent reaches a minimum of 4×10^6 square kilometers during February and then expands equatorward at a maximum rate of 4.2×10^6 square kilometers per month from May to June and an average rate of 2.4×10^6 square kilometers per month as shown in Figures 4-8 and 4-10. The maximum extent of 20×10^6 square kilometers is reached during September. The ice edge retreats slightly from September to October, after which a rapid retreat of 4.6×10^6 square kilometers per month occurs from October to December. The maximum retreat rate of 6.9×10^6 square kilometers per month occurs from November to December, and the average retreat rate is 3.3×10^6 square kilometers per month between September and February. The area of the Antarctic Continent is 14×10^6 square kilometers, so that the total area of snow and ice cover in the Antarctic is approximately 34×10^6 square kilometers at the winter maximum.

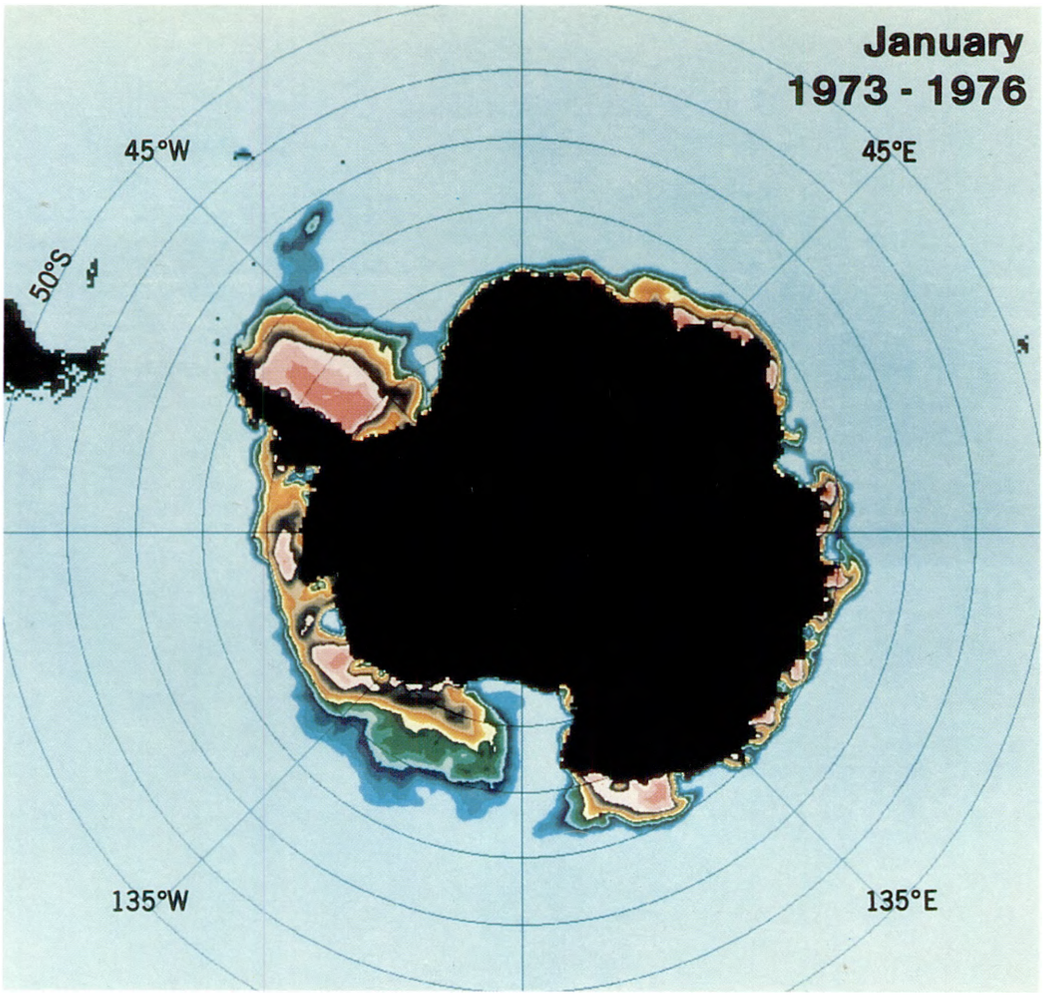

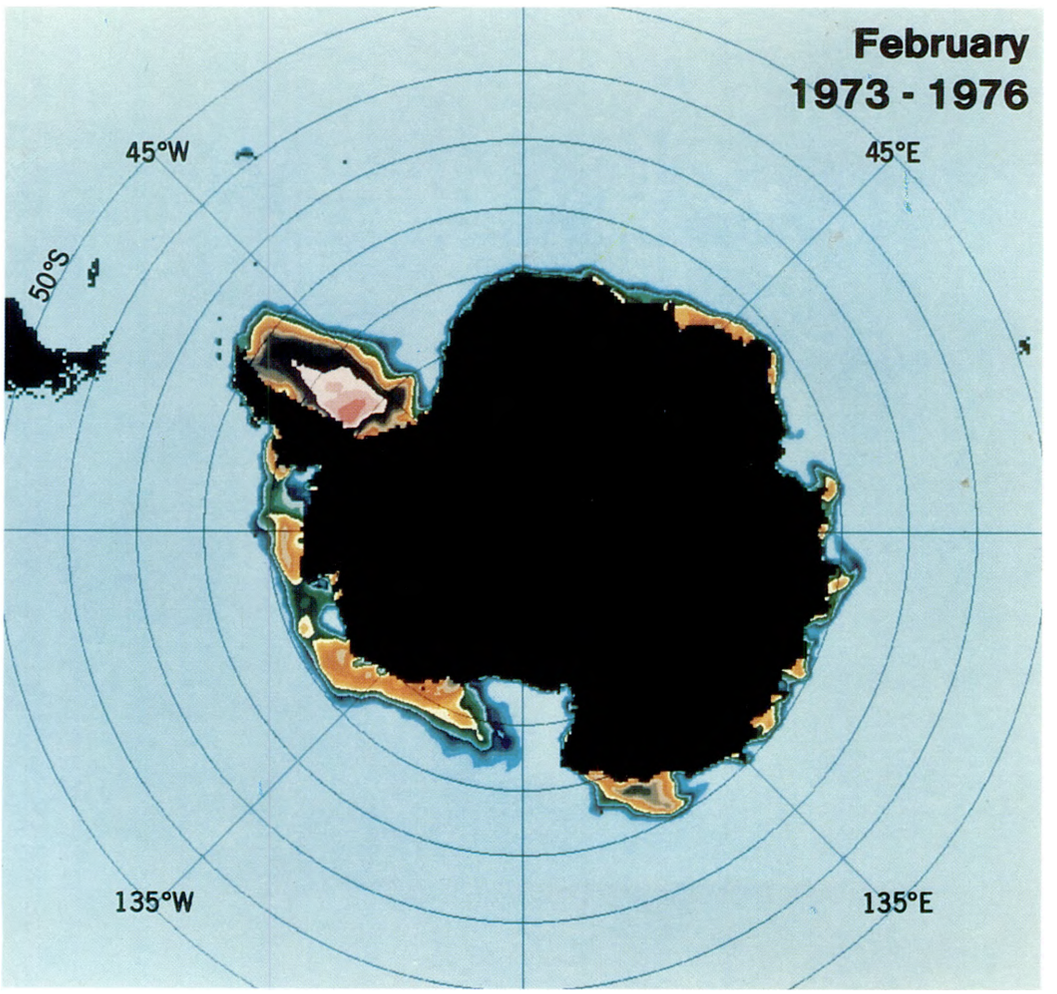

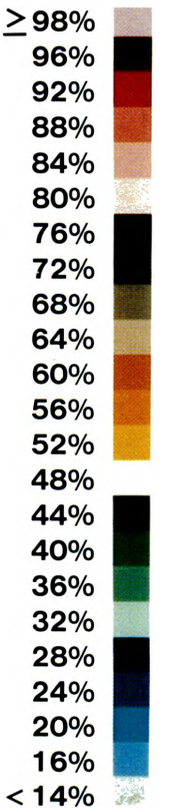

Figure 4-2. Four-year average of mean monthly sea ice concentrations for January and February, 1973-1976.

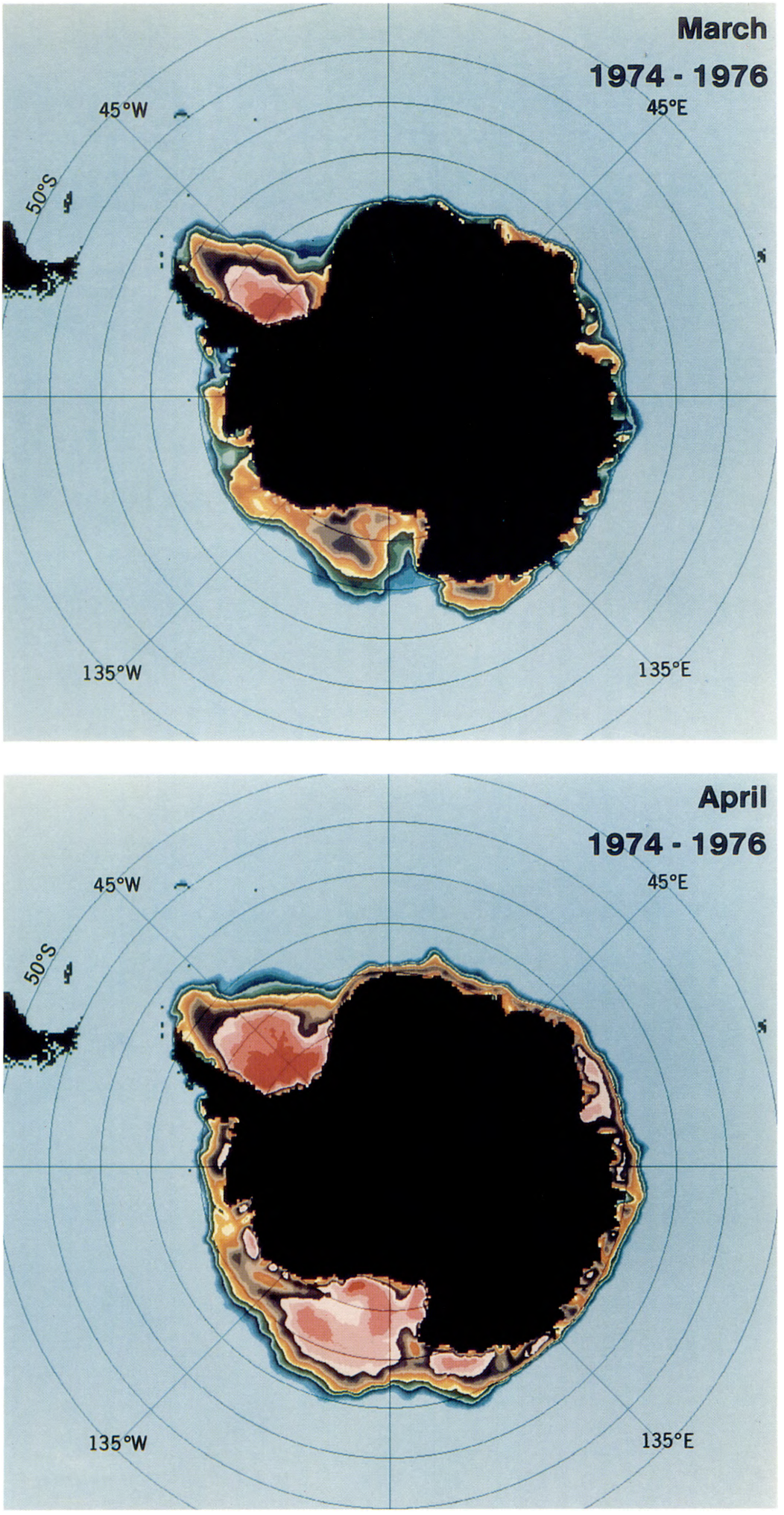

Figure 4-3. Three-year average of mean monthly sea ice concentrations for March and April, 1974-1976.

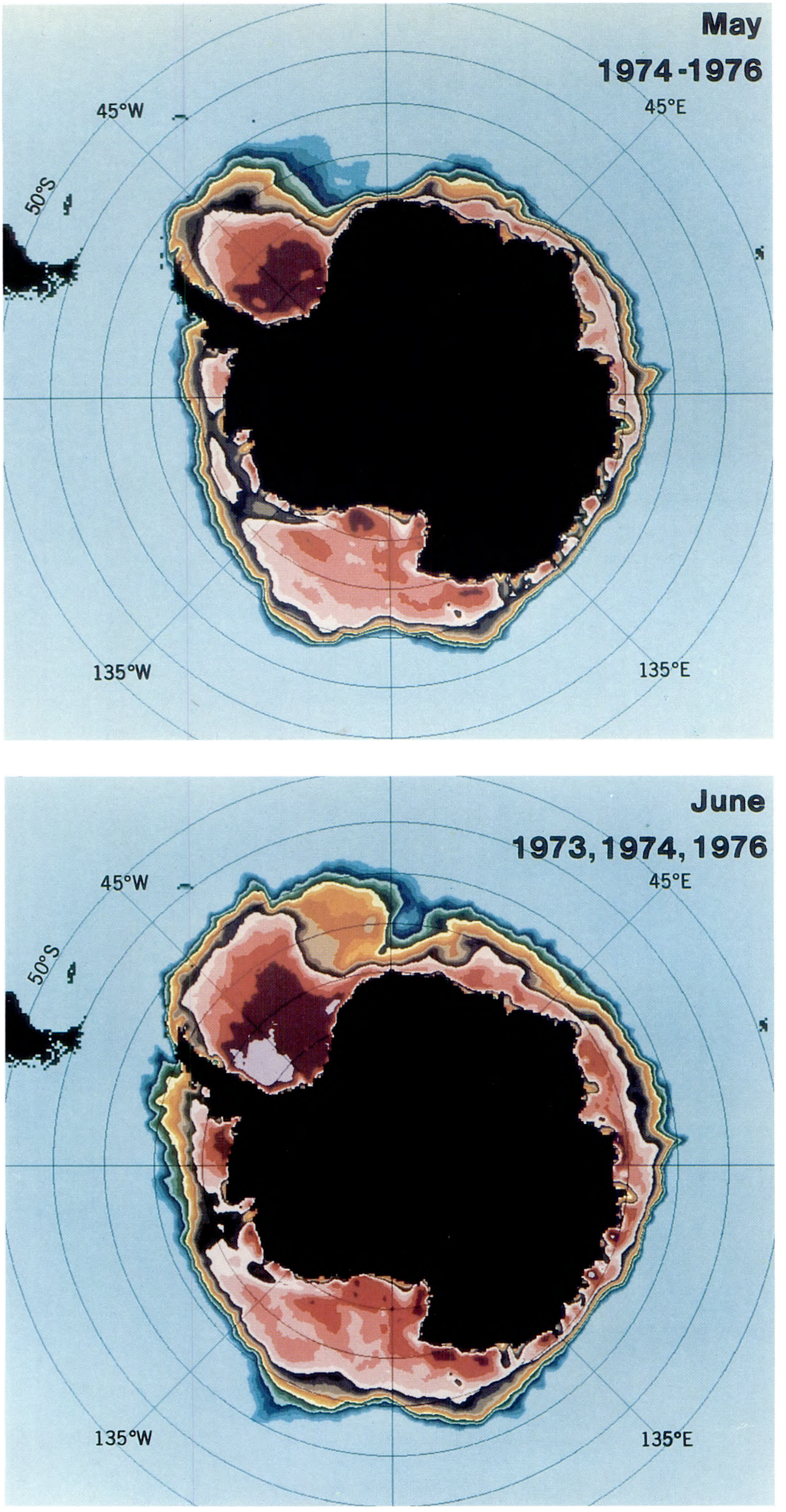

Figure 4-4. Three-year average of mean monthly sea ice concentrations for May 1974-1976 and June 1973, 1974, and 1976.

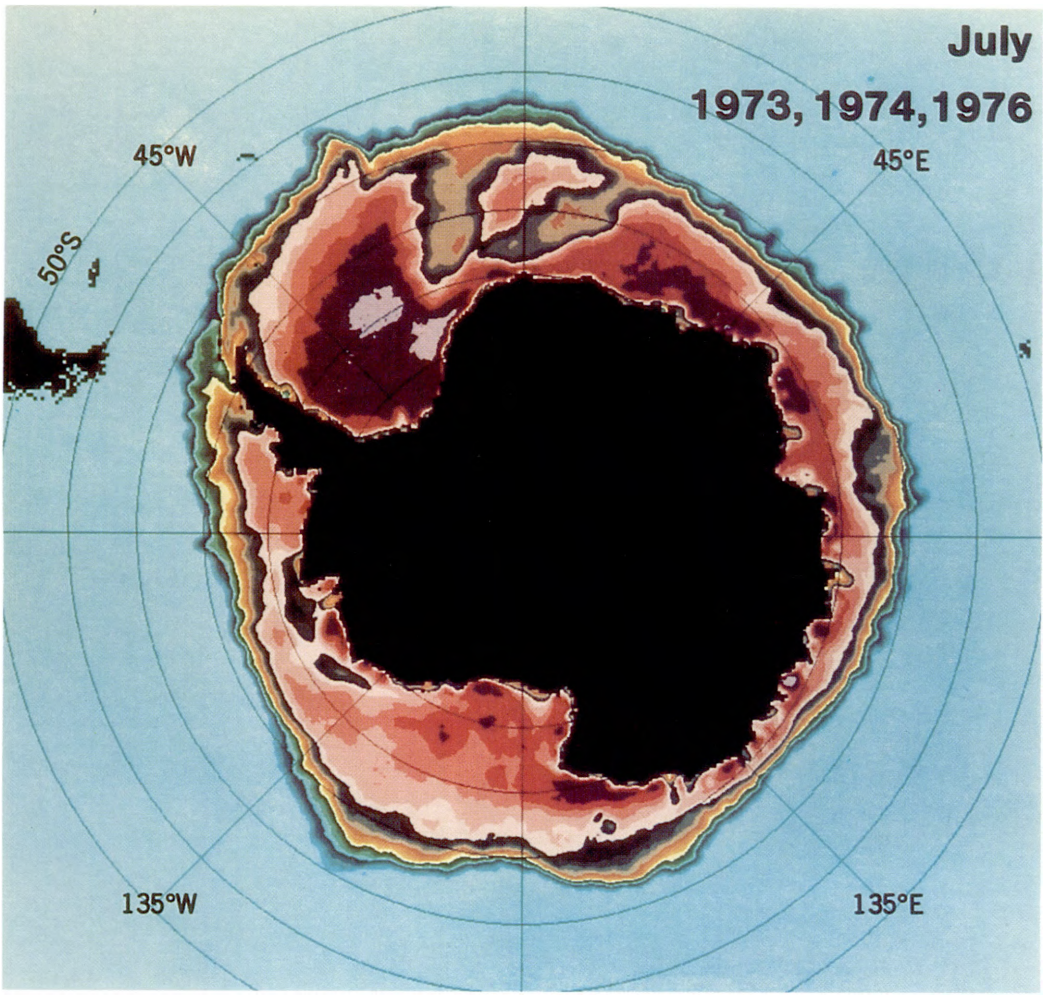

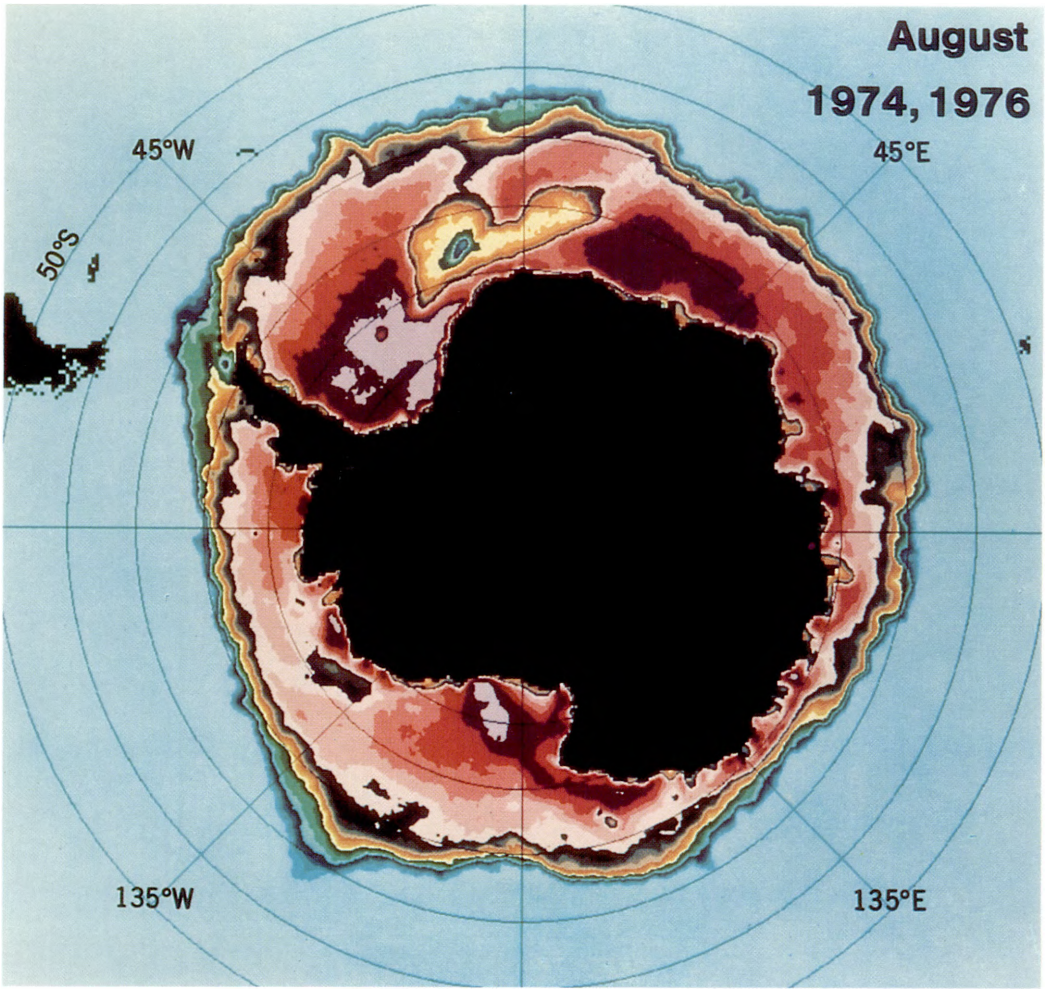

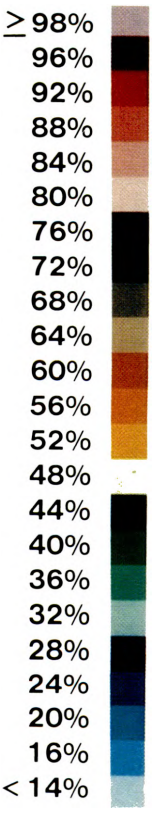

Figure 4-5. Three-year average of mean monthly sea ice concentrations for July 1973, 1974, and 1976 and 2-year average of August 1974 and 1976.

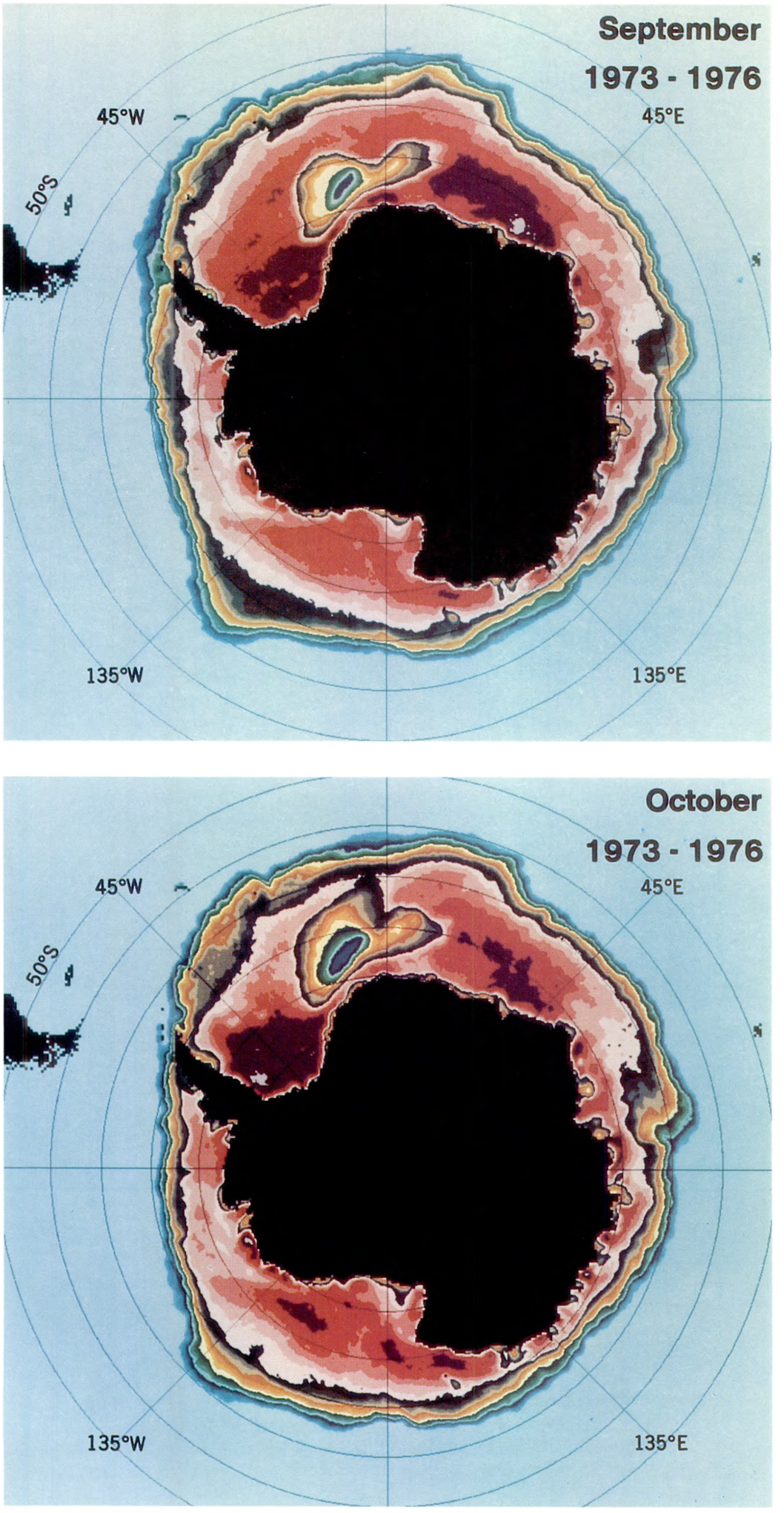

Figure 4-6. Four-year average of mean monthly sea ice concentrations for September and October, 1973-1976.

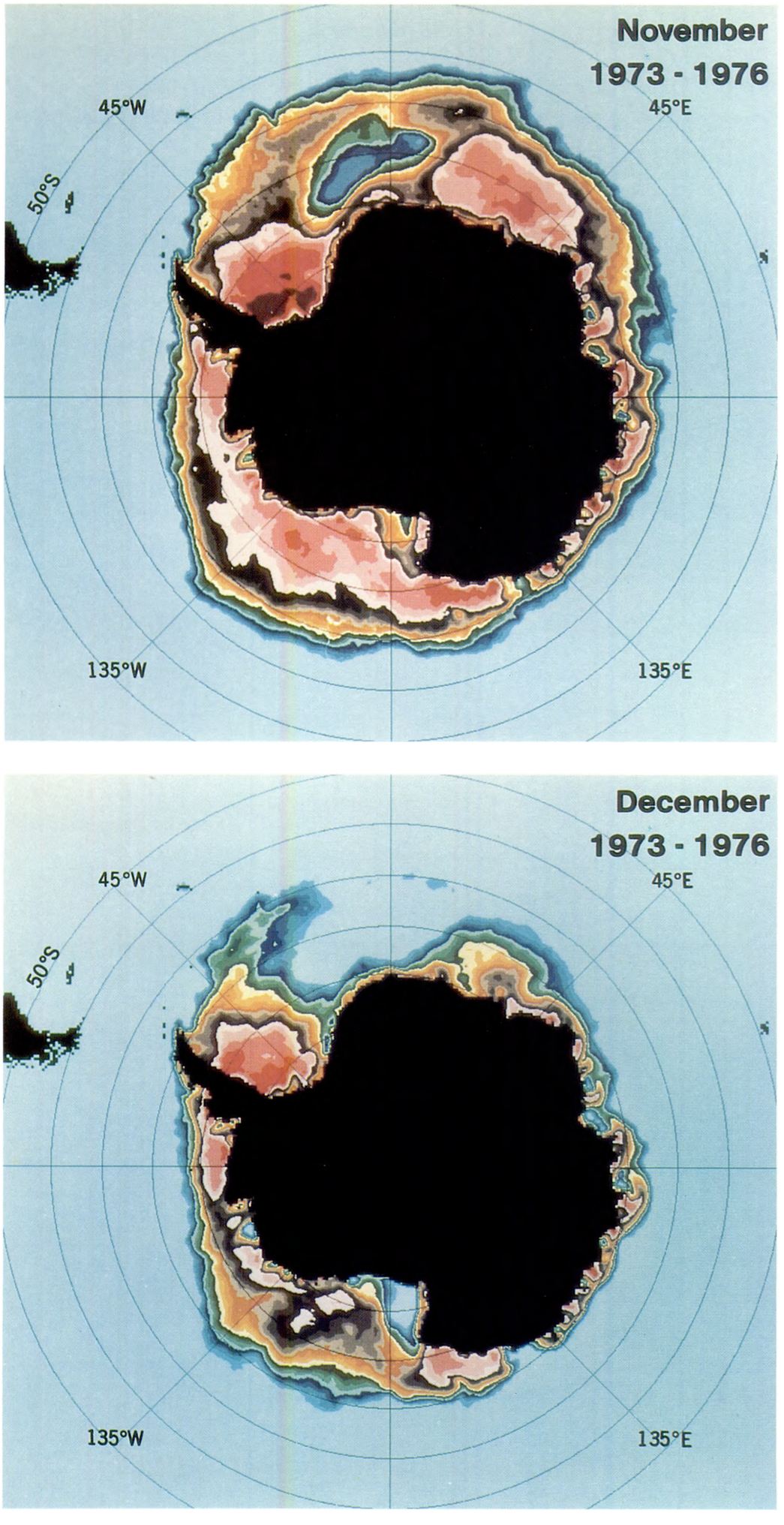

Figure 4-7. Four-year average of mean monthly sea ice concentrations for November and December, 1973-1976.

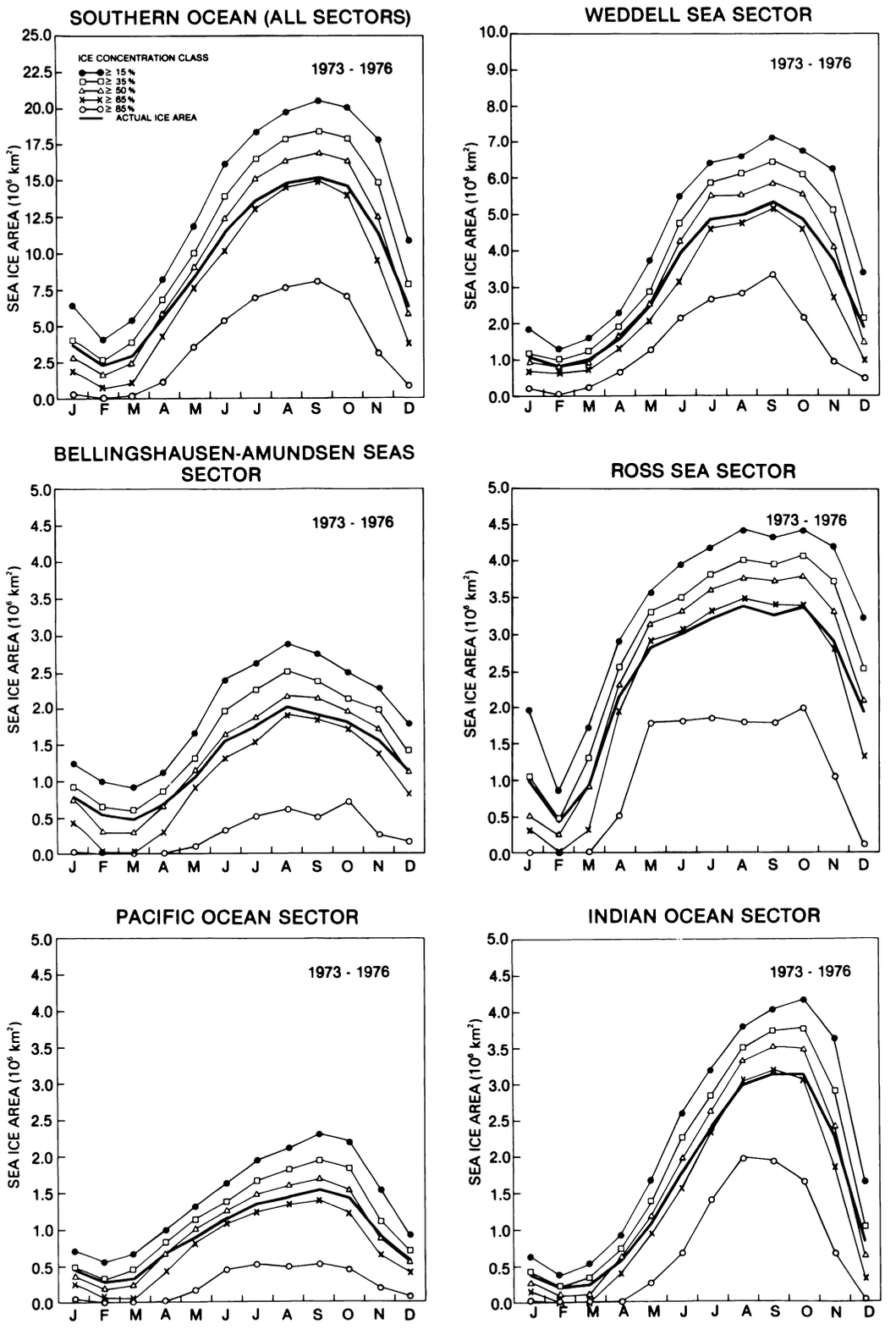

Figure 4-8. Yearly cycle of the ocean area covered by sea ice with concentration ⩾15 (ice extent), ⩾35, ⩾50, ⩾65, and ⩾85 percent and yearly cycle of the actual ice area, for the total southern ocean and for each sector. The actual ice area is the total ocean surface covered by sea ice, excluding all open leads and polynyas within the ice pack.

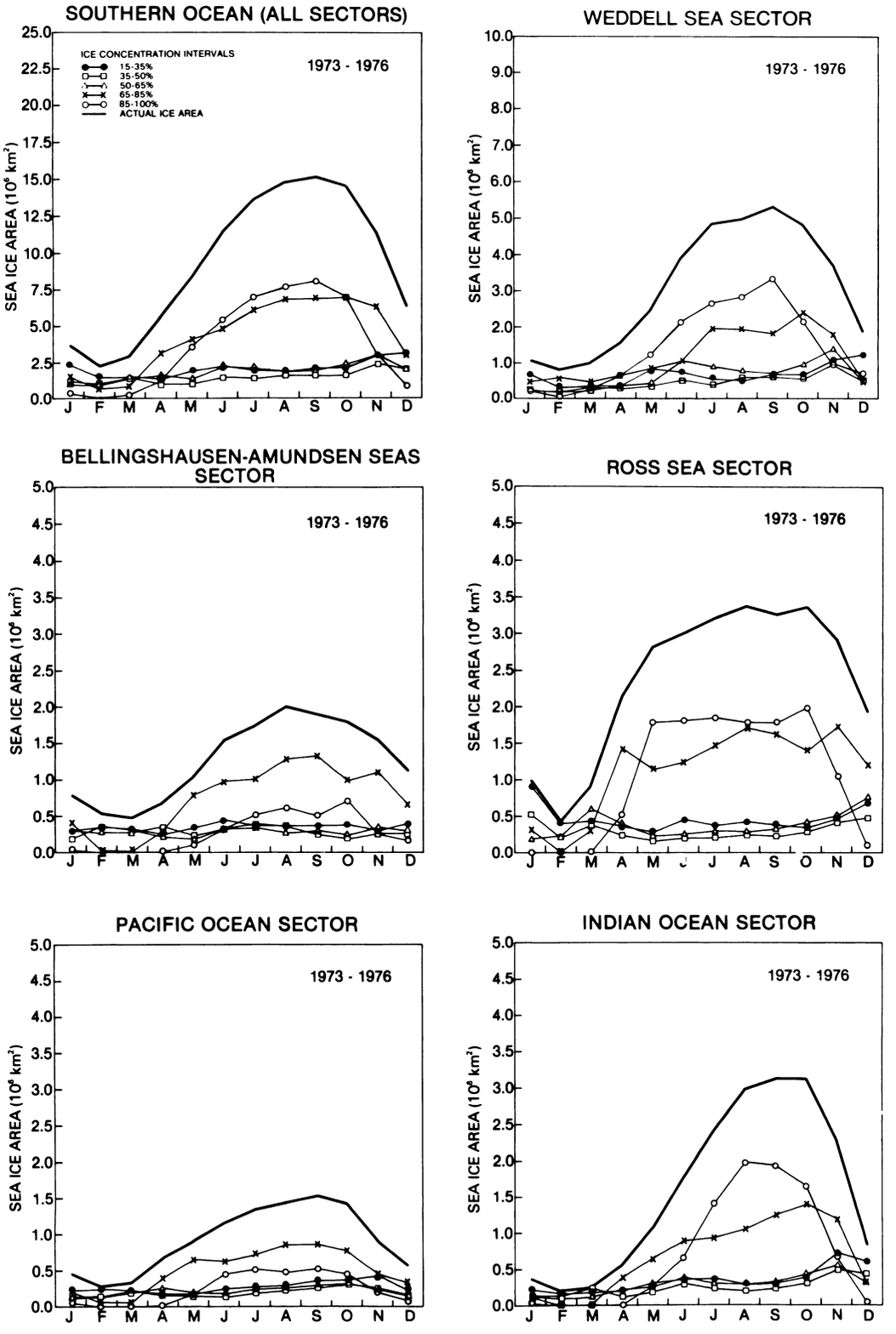

Figure 4-9. Yearly cycle of the ocean area covered by sea ice within ice concentration intervals 15 to 35, 35 to 50, 50 to 65, 65 to 85, and 85 to 100 percent and yearly cycle of the actual ice area, for the total southern ocean and for each sector.

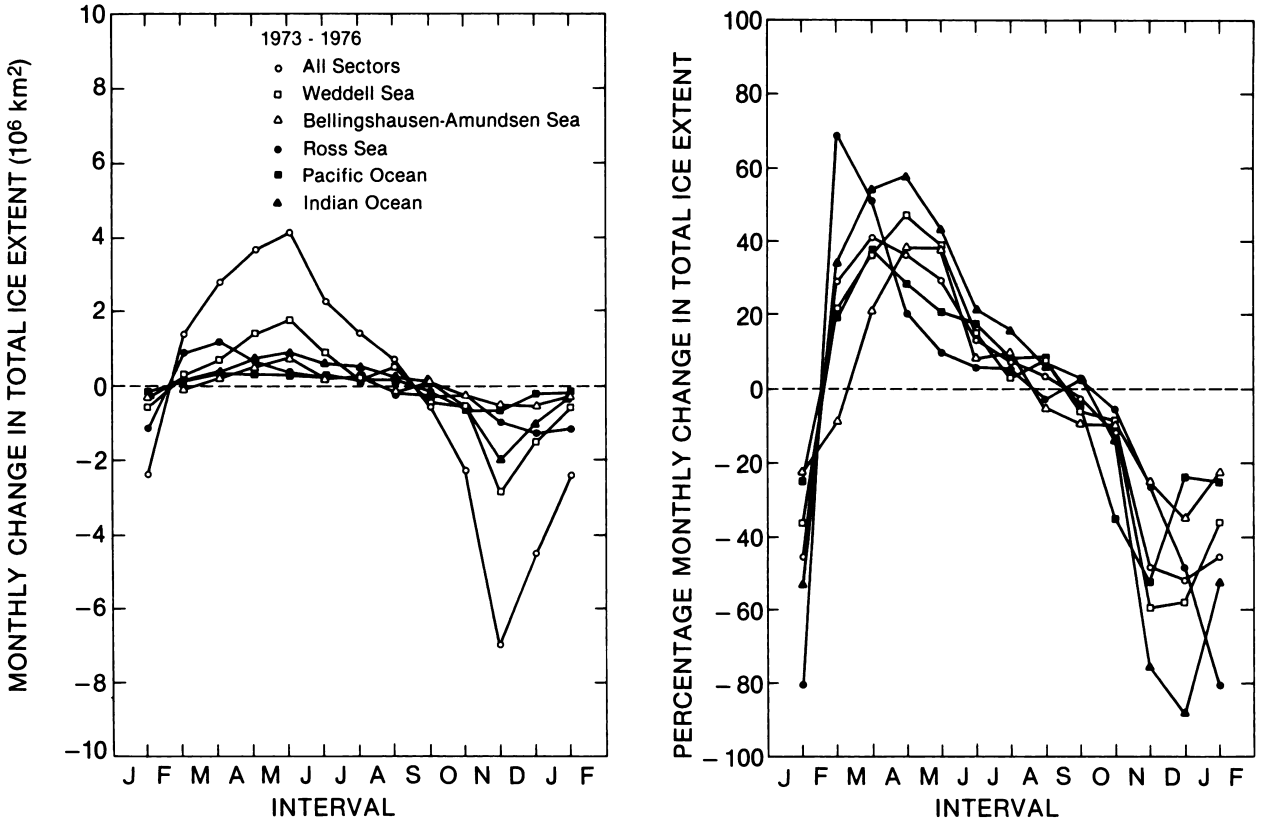

Figure 4-10. Growth/decay rates of total ice extent (≥15-percent concentration) shown as: (a) monthly change in area, and (b) percentage monthly change in area, calculated with respect to the average area in the 2 months.

During the period of minimum ice extent in February (Figure 4-2), scattered regions along the entire coast of East Antarctica retain a small amount of ice coverage. Essentially no ice remains immediately to the north of the Ross Ice Shelf. A substantial amount of ice remains within a 5-degree-latitude band of the coast to the east of the Ross Ice Shelf and in the Bellingshausen and Amundsen Seas, and a large area of ice remains in the western portion of the Weddell Sea. Also visible on the map (Figure 4-2) are the large coastal polynyas in the Ronne Entrance at the southwest corner of the Antarctic Peninsula and in the Amundsen Sea off the Getz Ice Shelf. As Figures 4-8 and 4-9 illustrate, over one third of the 2.6×10^6 square kilometers of actual ice area remaining in the February average is located in the Weddell Sea, and only a small area has a concentration greater than 85 percent.

In visual interpretation of these map images, the effects of time averaging on the ice edge must be considered. One effect results from averaging over 1 month. For instance, the February image (Figure 4-2) provides a good indication of minimum ice coverage and, consequently, the amount of multi-year ice the following winter. However, because the absolute minimum ice extent is less than the monthly average, the monthly average shows slightly greater ice extent than the true minimum. In addition, the indicated low ice concentrations in the region of the ice boundary should not be interpreted as typical; in fact, at any time the transition from open water to highly concentrated ice is much sharper than shown. Because the ice edge moves over the span of 1 month and the measured location of the edge in any given month varies over the 4 years, the averaging process combines times of zero ice cover with times of positive ice cover beyond the typical ice boundary, reducing the sharpness of the calculated edge. Finally, because of 4-year arithmetic averaging, the position of the ice edge on the maps will be biased toward the position of the year that had the greatest ice extent.

From February to March (Figures 4-2 and 4-3), the ice advances rapidly in the Ross Sea sector and

slowly in the Pacific Ocean, Indian Ocean, and Weddell Sea sectors and recedes slightly in the Bellingshausen and Amundsen Seas. Over the next 4 months, from March to July (Figures 4-3 through 4-5), the ice cover undergoes steady rapid growth, which slows for the southern ocean as a whole from July to September (Figures 4-5 and 4-6).

In September (Figure 4-6), the month of overall maximum ice extent, when approximately 20×10^6 square kilometers of the southern ocean are partially covered with ice, the actual area of ice is 15×10^6 square kilometers (Figure 4-8). The difference of 4 to 5×10^6 square kilometers is the area of open water within the total ice extent. Of the total actual ice area, 5.3×10^6 square kilometers lie in the Weddell Sea sector and about 3.2×10^6 square kilometers lie in each of the Ross Sea and Indian Ocean sectors.

The latitude of the winter ice margin ranges from 65°S at 105°W to 55°S at 10°E. The overall shape of the ice boundary is nearly circular—similar to the temperature and pressure-field maps (Figures 2-5 and 2-7). Some of the asymmetries in the ice extent can be related to oceanographic and meteorologic influences. For example, the prominent corner in the ice edge at 144°W to 150°W reflects the deflections of the circumpolar ocean current by the submarine topography, and the persistent extension at 25°W lies over the South Sandwich Trench (Zwally et al., 1976; see also discussion in Chapter 2). An example of other deviations more related to atmospheric circulation are discussed later in relation to the change in ice field from September to October (Section 4.3).

The major wintertime anomaly clearly visible in the September map (Figure 4-6) is the large area of reduced ice concentrations in the eastern Weddell Sea. These reduced ice concentrations result from averaging a compact ice cover in the region during 1973 with large areas of open water in the Weddell polynya, which occurs in the other three Septembers (discussed in Chapter 5). Similarly, the regions of reduced concentrations off the coast are locations of small temporary coastal polynyas caused by drainage winds from the continental ice sheet. However, the size of the coastal polynyas in winter is generally less than the 30-kilometer resolution of the ESMR, and the frequency of their openings and closings is much less than 1 month. Therefore, even on the monthly averages in Chapter 5, coastal polynyas appear only as reduced ice concentrations rather than open water.

From September to October (Figure 4-6), the ice edge retreats slightly in the Bellingshausen, Amundsen, and Weddell Seas, although it advances slightly in part of the Ross Sea and off Wilkes Land. The Weddell polynya and several of the coastal polynyas enlarge over this period, further signifying the entry into the decay season. The decay is more widespread from October to November (Figures 4-6 and 4-7), with noticeably further enlargement of polynyas and with edge retreat particularly apparent in the vicinity of 90°E and in the Bellingshausen Sea. This is followed by a very strong acceleration of the decay, with close to 40 percent of the November ice cover being eliminated in the November to December interval (Figure 4-7). The rapidity of this decay is far greater than the growth rate in any one month during fall and winter. Antarctic ice decay proceeds more slowly from December to January and then at a much reduced rate from January to February (Figures 4-2 and 4-7).

Some generalizations can be made from the 4-year average maps. In the western Weddell Sea, the ice edge advances toward the northeast during the growth season and retreats predominantly westward during the decay season. In the other sectors, the ice cover typically decays from north to south, as also noted by Ackley (1979). The corner of the Ross Sea ice edge at roughly 150°W undergoes an eastward progression during the ice growth from May to September. During the decay season, when the retreat is more uniformly poleward, no corresponding westward progression occurs in the Ross Sea. In the Weddell sector, the Weddell polynya is prominent in the midwinter months, whereas the Ross Sea polynya is principally a characteristic of the spring melt season. The Ross Sea polynya is fully visible as a large open-water feature on the December map (Figure 4-7), whereas the reduced concentrations on the October and November maps (Figures 4-6 and 4-7) indicate the formation of open water in smaller leads and polynyas. The Ross Sea polynya may result from the mean large-scale winds off the Ross Ice Shelf, which are described in Chapter 2. Numerous other coastal polynyas are also visible in the melt season (Figure 4-7), some of which were examined by Knapp (1969).

In the Ross Sea sector, the maximum growth rate occurs from March to April, and the maximum decay rate occurs from December to January (Figure 4-10a). This maximum growth rate in the

Ross Sea occurs 2 months earlier and the maximum decay rate occurs 1 month later than the respective rates in the Weddell Sea sector, the Indian Ocean sector, and the total southern ocean. The retreat of the outer Weddell and Indian Ocean ice is minimal from September through November and is rapid from November to December. Most of the growth in the Bellingshausen Sea occurs during May, and most of the decay in both the Bellingshausen and Amundsen Seas occurs in December. Overall, the Pacific Ocean sector shows the least amount of ice growth, and the Weddell Sea sector shows the most. Expressed in terms of percentage change in the ice extent (Figure 4-10b), the magnitudes of the growth and decay rates are similar for all sectors and the entire southern ocean, although the times of their maximum rates differ by 1 to 2 months. In addition, the maximum percentage change in area is about 1 month earlier and the maximum percentage decay rate is about 1 month later than the respective absolute changes. The growth and decay rates of the actual ice area (Figure 4-11) have similar characteristics to the rates of change in total ice extent.

4.3 MONTH-TO-MONTH CHANGES

To display changes in the ice cover from month to month, ice concentration change maps (Figure 4-12) are created by subtracting the ice concentration for consecutive months element by element, using the data of Figures 4-2 through 4-7. Since blues, greens, and grays denote increases in computed concentrations and reds, purples, and oranges denote decreases, the regions experiencing positive or negative concentration changes are immediately distinguishable. Physically, increases in ice concentration are caused either by ice production or by convergence of the ice field, and decreases are caused either by melt or by divergence. Although the increases dominate in winter and the decreases dominate in summer, significant departures from this predominant cycle occur. The

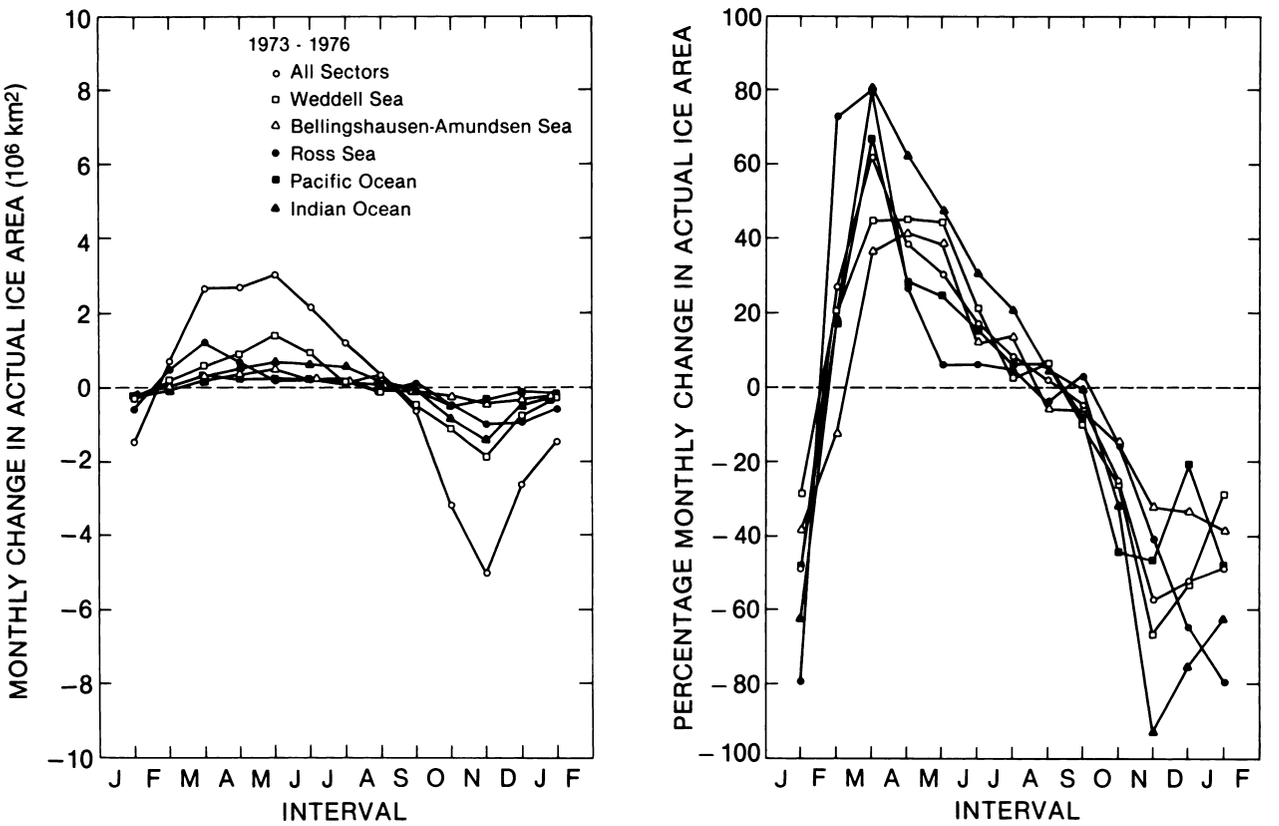

Figure 4-11. Growth/decay rates of actual ice area shown as: (a) monthly change in area, and (b) percentage monthly change in area, calculated with respect to the average area in the 2 months.

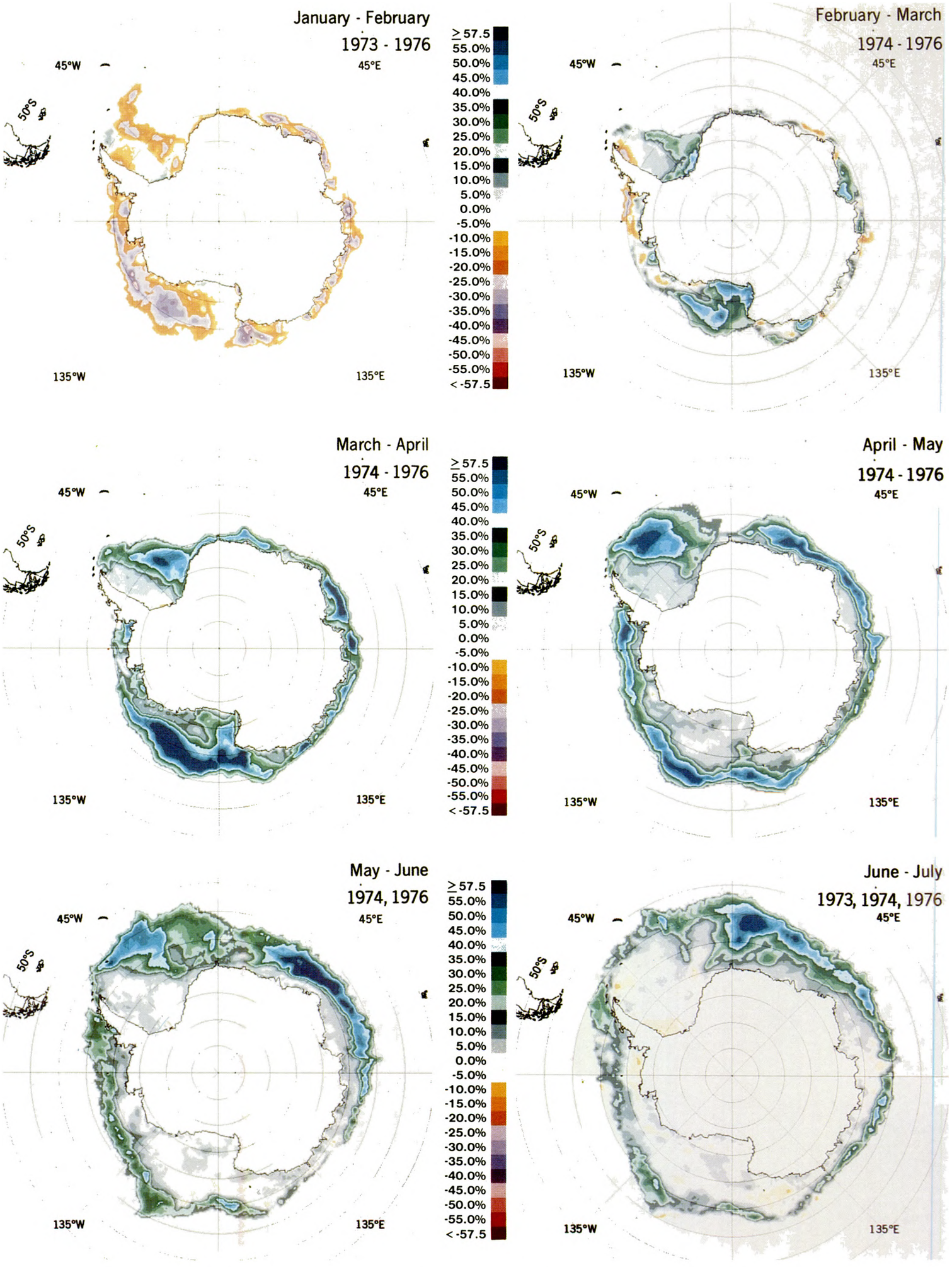

Figure 4-12a. Sea ice concentration monthly change maps for January-February through June-July. Years without data in either month of a pair are excluded in the averages.

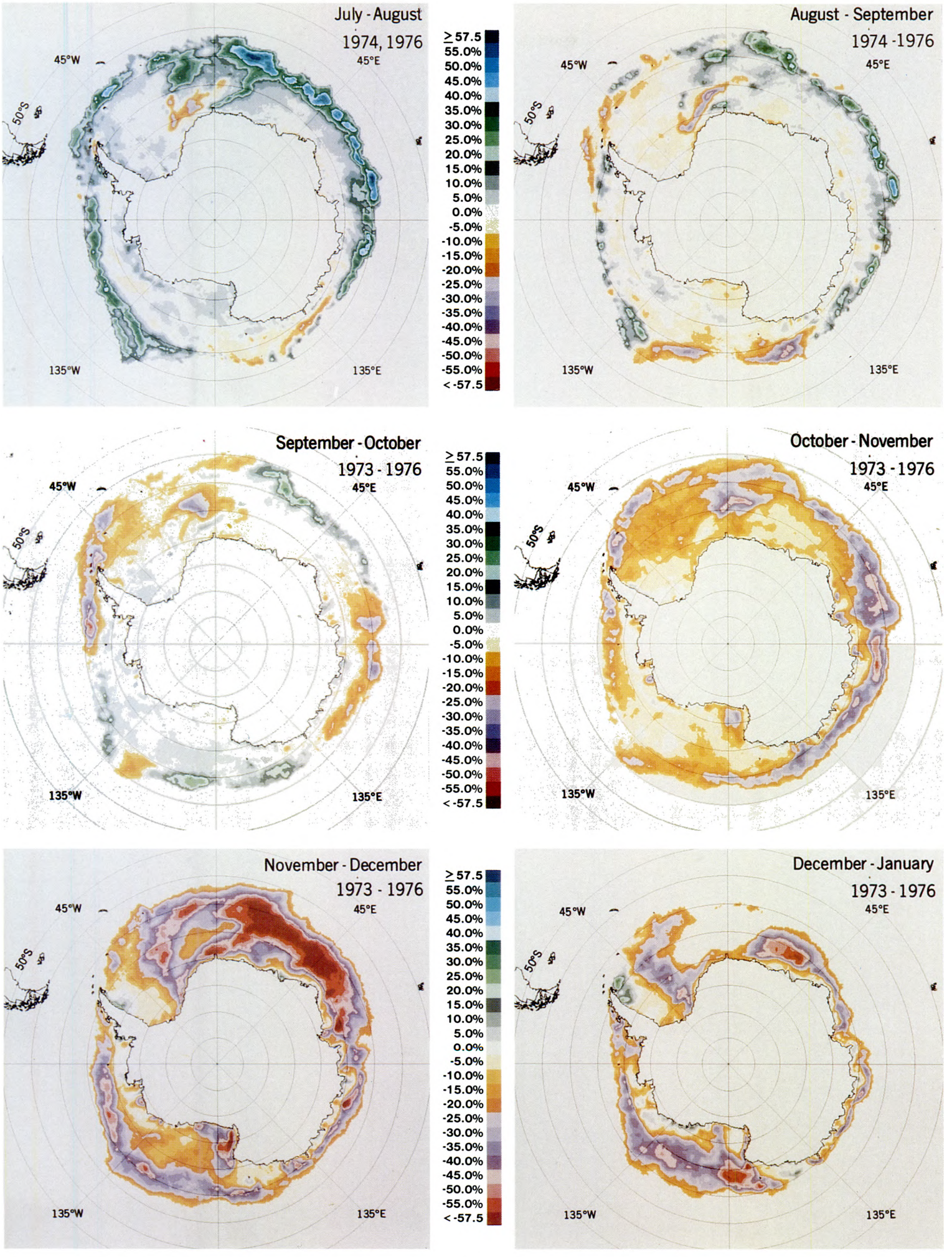

Figure 4-12b. Sea ice concentration monthly change maps for July-August through December-January. Years without data in either month of a pair are excluded in the averages.

following paragraphs discuss observations related to this cycle.

In the January to February map (Figure 4-12), the largest decreases in ice concentrations are associated with the continued retreat of the ice edge in late summer. In some limited regions, ice concentration increases are observed. For instance, in the Weddell Sea, advance of the sea ice cover near the tip of the Antarctic Peninsula is caused by edge advection, and near the Ronne Ice Shelf, open water is covered by new ice growth.

The growth season begins in late February in many regions, particularly the Ross Sea, south-central Weddell Sea, and near the Amery Ice Shelf. The monthly difference map from February to March reflects the growth in these regions, as well as the continued summer decay in the remaining one third of the ice-covered ocean. By mid-March, the growth season has begun throughout, with substantial concentration increases within the pack and generally larger increases where the ice edge is expanding.

During the entire period from March to May, only a few small areas indicate any decrease. From May to June, the ice edge in the Ross Sea sector is expanding less rapidly in contrast to the expansion occurring around most of the rest of the ice border. This limited expansion in the Ross Sea reflects the confining influence of the ocean topography and currents. From June to July, the ice cover grows along the entire perimeter, but only small changes occur within the pack. However, this average growth pattern is not typical of each year; in some years, the data show substantial regions of significant ice concentration decreases within the pack at this time, as discussed in Chapter 5.

From July to August, when the overall ice cover is still growing, the area of the southern ocean affected by decreases in concentration is even greater than that in the May to June and the June to July transitions. Two regions that experience large decreases lie in the eastern Weddell Sea sector and off the east Antarctic coast from 125°E to 175°E. In the case of the Weddell Sea, these decreases result from the westward movement of the Weddell polynya.

In the Drake Passage and Ross Sea regions, marked retreat of the ice edge occurs between August and September. For the Ross Sea region, this retreat is only temporary; the edge shifts outward again between September and October. However, in the Drake Passage region, the retreat from August to September precedes a stronger retreat in the following months.

From September to October, widespread decay of the ice cover dominates in the Weddell and Bellingshausen Seas and in the Pacific and Indian Ocean sectors around 90°E. A spatial coherence in concentration changes near the ice edge occurs over distances on the order of 3000 kilometers. Three pairs of adjacent growth/decay segments evident around the ice edge (mode 3) are consistent with the mode 3 to 5 expected behavior in the atmospheric circulation (Cavalieri and Parkinson, 1981). As already mentioned, the ice edge in the Ross Sea sector expands from September to October, following its earlier retreat, whereas other areas show the more expected reversal from ice growth to decay.

From October to November and from November to December, extensive ice decay can be seen throughout the ice-pack region. The sea ice cover decreases by more than 25-percent concentration over large areas during 1-month periods—more than 25 percent from October to November and more than 50 percent from November to December. The regions of maximum decrease in ice concentration are associated with the retreat of the ice edge or the opening of polynyas. At a few places along the coast, small ice concentration increases that appear in the image may not be real increases. During the melt season, the indicated changes in concentration may be in error up to 20 percent at places because of increases in emissivity caused by melting of the snow surface (discussed in Chapter 3). Therefore, the concentration increases that are smaller than 15 percent during the melt season may not reflect actual concentration increases.

In the December to January map, however, ice concentration increases in a region along the northeast coast of the Peninsula are of sufficient magnitude (greater than 20 percent) to be interpreted as actual ice concentration increases. In addition, an equatorward advance of the ice edge is evident near the tip of the Peninsula in the individual monthly ice concentration maps (see Chapter 5).

These pictorial displays of the changes in ice cover presented in the difference maps utilize the unique capability of the microwave observations to determine the changes in the actual ice cover, as well as the ice edge. The concentration interval curves (Figure 4-9) provide additional insight into the nature of the growth and decay of sea ice

cover. The areas of less compact ice (15 to 35, 35 to 50, and 50 to 65 percent) are nearly constant throughout most of the year. As might be expected, an increase in the area of less compact ice cover is observed during November and December, while the areas of compact ice are decaying rapidly. Clearly, the seasonal cycle consists of the growth and decay of the more compact ice cover areas (65 to 85 and 85 to 100 percent), as well as the migration of the ice edge, where less compact ice is located. Generally, the cycle of more compact ice resembles the cycles of actual ice area and the total ice extent. The rapid increase of compact ice in the Ross Sea during the growth season and its near constancy for 6 winter months differentiates it from the slower increases in other sectors. In most sectors, decay of the most compact ice areas (85 to 100 percent) precedes or occurs more rapidly than decay of the areas with 65- to 85-percent ice cover. Chapter 5 describes the increase in the amount of open water within the ice pack from February through November, the characteristics of individual years, and the interannual variations of sea ice cover.

5

MONTHLY SEA ICE CONCENTRATIONS AND INTERANNUAL VARIATIONS

5.1 INTRODUCTION

The observed southern ocean ice cover for individual years deviates significantly from the multiyear averages described in Chapter 4. Aspects of the distribution of Antarctic sea ice, the annual cycle, and interannual variability are also described in Rayner and Howarth (1979), Lemke et al. (1980), and Zwally et al. (1979), for example. In this chapter, the regional and seasonal characteristics of the interannual variations in the ice cover are examined for the years 1973 through 1976. For any given month, substantial interannual differences occur in the amount and distribution of ice. Overall, the largest interannual change, an 18-percent decrease in ice extent from 1973 to 1976, occurred during the spring melt months of November and December. The smallest interannual changes occurred in the late summer and fall months, and the annual mean decreased by 12 percent. Regional ice extents show far more relative variability than the ice extent for the southern ocean as a whole. Most of the 1973 to 1976 decrease in ice extent was in the Weddell Sea, whereas smaller decreases or, in some cases, increases occurred in the other sectors.

Individual monthly ice concentration maps for the 41 months of available data from 1973 to 1976 illustrate interannual variations of the regional and total ice extents (Figures 5-1 to 5-12). The monthly average sea ice concentration maps are derived from the microwave brightness temperature maps (see Chapter 3). Because useable data were not obtained for some months, the set of maps is incomplete. Section 5.2 describes the regional characteristics and interannual differences, which are evident in the monthly ice concentration maps, and gives the annual cycle of sea ice cover in various concentration intervals. Similar to the maps of monthly change in sea ice concentration in Chapter 4, monthly change maps for the individual years (Section 5.3) highlight the regional characteristics of the growth/decay cycle, as well as the interannual variations.

Section 5.4 provides a quantitative description of the interannual variations in ice extent, in actual ice area, and in open water within the ice pack for each region and for each month. The monthly ice concentrations have been further averaged for each year, resulting in annual mean ice concentration maps (Figure 5-39). The average of these four annual mean maps (Figure 5-41) is the average of all microwave data used in this volume. The figures in Section 5.4 describe pictorially the 4-year trend in the annual mean sea ice extent. The final maps in Figure 5-42 display the deviation of each annual mean from the 4-year average distribution of sea ice concentration.

5.2 YEAR-TO-YEAR COMPARISON OF MONTHLY CONCENTRATIONS AND ANNUAL CYCLES

In all four January maps, very little ice remains around East Antarctica after the spring melt, whereas much more ice remains in the Weddell, Bellingshausen, Amundsen, and eastern Ross Seas (Figure 5-1); in the western Ross Sea, a prominent open-water area extends north of the Ross Ice Shelf. The region with the largest area of compact ice, with 80-percent or greater concentration, lies in the western portion of the Weddell Sea, where the ice extends in the north-south direction along the Antarctic Peninsula. By contrast, the eastern portion of the Weddell Sea is almost entirely ice-free, with open water extending to the Filchner Ice Shelf (78°S) well south of the highly concentrated ice along the Peninsula. This contrast is caused, at

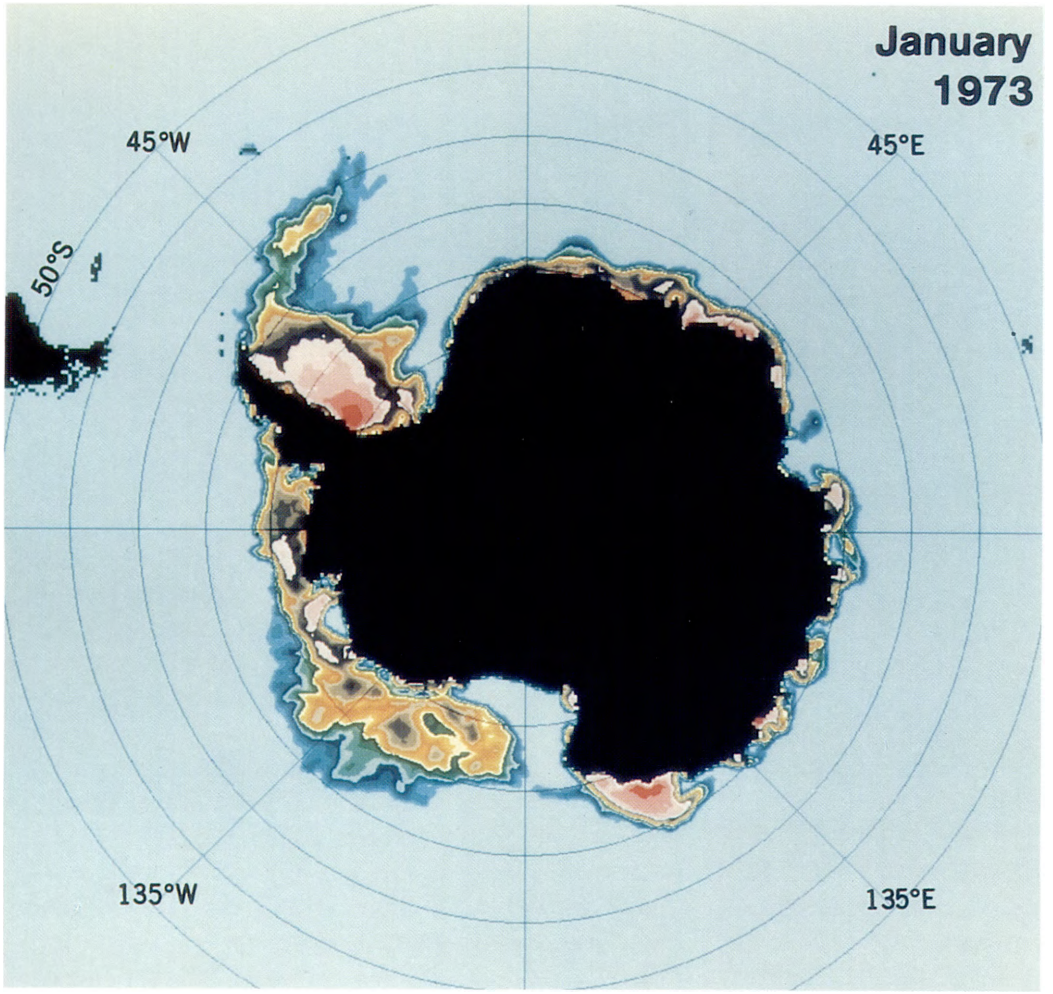

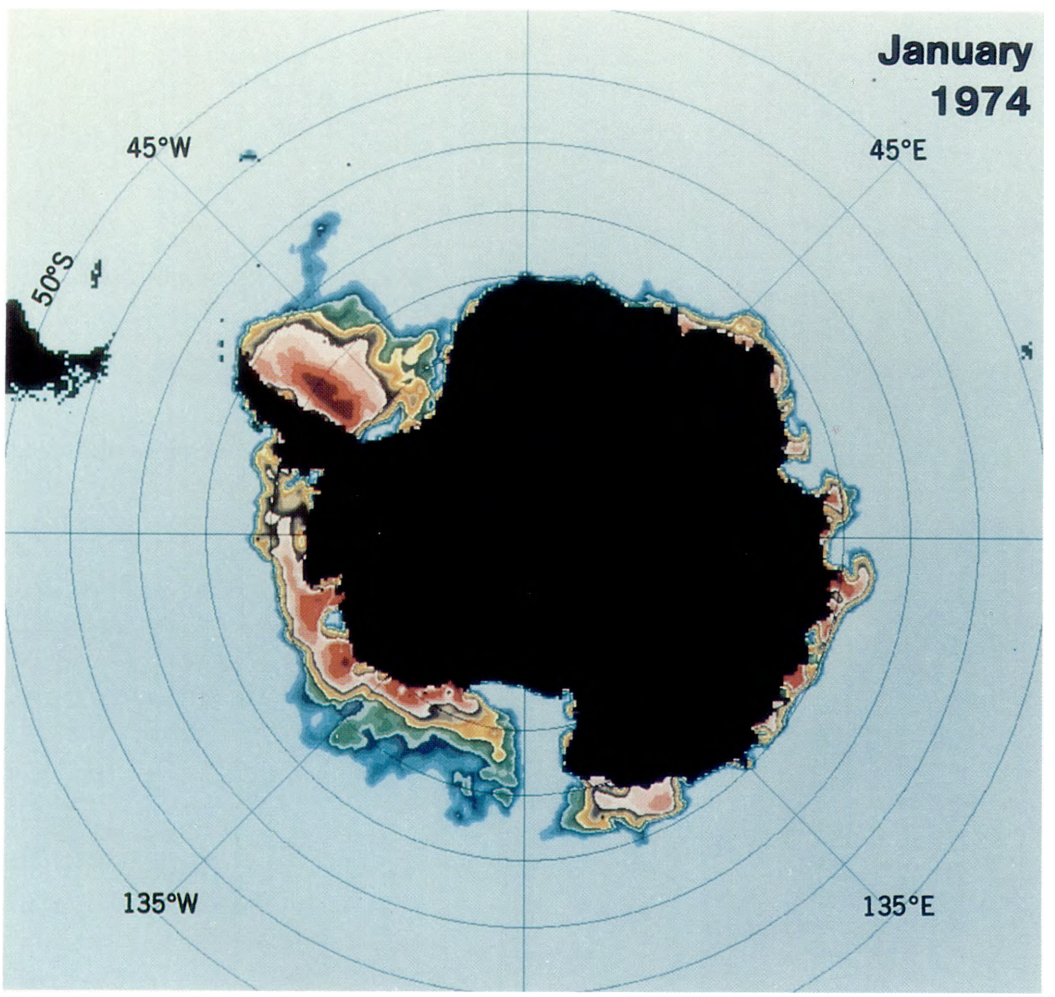

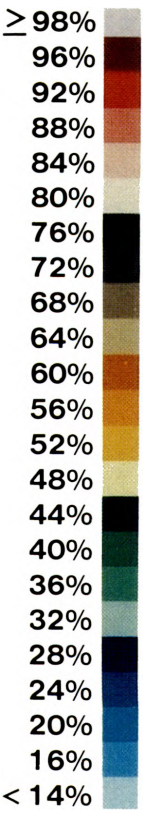

Figure 5-1a. Mean monthly sea ice concentrations for January 1973 and 1974.

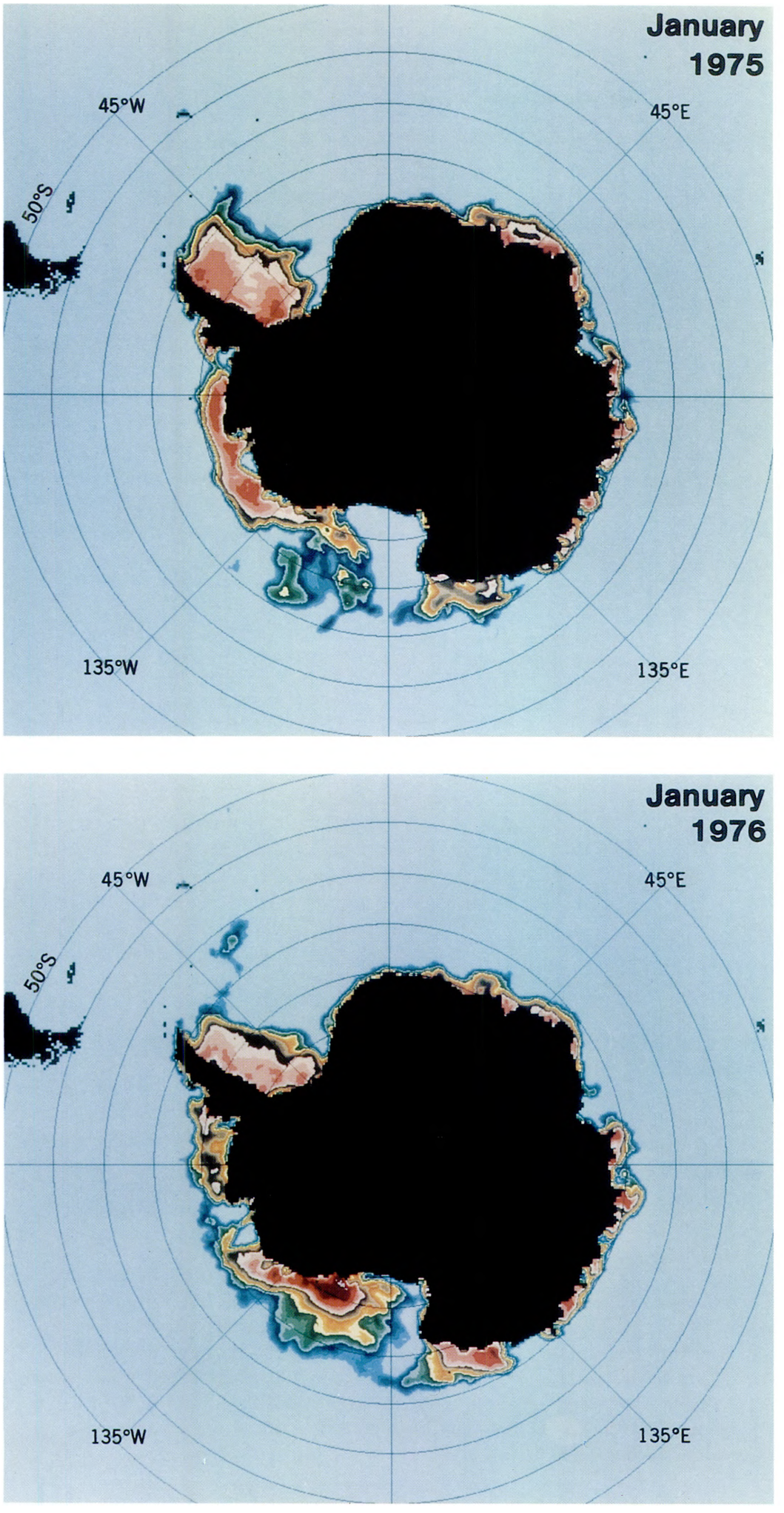

Figure 5-1b. Mean monthly sea ice concentrations for January 1975 and 1976.

least in part, by the cyclonic gyre in the surface water circulation and the confining effect of the Antarctic Peninsula.

Comparison of the individual years shows that the smallest extent of ice in the Weddell Sea occurs in 1976, whereas the largest ice extent occurs in 1973, with a prominent extension at 62°S from 45°W to 30°W. This 4-year trend is discussed in more detail later. (See Figure 5-14.) Farther west, the Bellingshausen Sea has markedly less ice extent in 1975 than in the other 3 years, and the Amundsen Sea has less in 1976. In the eastern Ross Sea, more ice exists in 1973 and 1976 than in the 2 intervening years. Closer to 180 degrees longitude, the open-water area north of the Ross Ice Shelf appears much less expansive in 1976, providing an interesting contrast to the Weddell Sea region, where the greatest amount of open water exists in 1976. The occurrence and positioning of other open-water areas also vary from year to year. For instance, a prominent polynya lies at the base of the Peninsula in 1974, whereas reduced concentrations occur in the same region in both 1973 and 1976. During all 4 years, some coastal polynyas occur in the Bellingshausen and Amundsen Seas, with the polynya off the Getz Ice Shelf (76°S, 125°W) being the most prominent. In contrast to the variability in the Western Hemisphere, the ice conditions around East Antarctica are similar in all 4 years; in particular, the open water tends to reach the continent in the same locations each year.

In February, the monthly average ice extent reaches its annual minimum in all sectors in each of the 4 years (Figure 5-2). As in January, the western Weddell Sea retains the largest area of concentrated ice, while the eastern Weddell (east of the Caird Coast) retains almost no ice in any of the 4 years except 1973. Farther west, the Bellingshausen Sea has less ice in 1975 and 1976 than in the 2 preceding years, and the Ronne Entrance has open water in all 4 years. In the Amundsen Sea, the least amount of ice occurs in 1976, the same year that the greatest amount of ice occurs in the Ross Sea. Around 180 degrees longitude, the sea north of the Ross Ice Shelf has a broad opening in all years except 1976, when only reduced ice concentrations appear. Thus, substantial year-to-year regional differences are evident in the ice cover throughout the Western Hemisphere during the month of minimum ice extent. As in January, minimal variations in ice extent occur along the east Antarctic coast.

In March, April, and May, useable data were not obtained for 1973; therefore, results are presented for 1974, 1975, and 1976 only. In March of 1974 and 1976, sea ice covers the region of the southeastern Weddell Sea off the Caird Coast (Figure 5-3). In March of 1975, the ice has not progressed to the same extent; during 1975, however, the ice adjacent to the Peninsula reaches farther equatorward than in the other 2 years, nearing 62°S. The images for all 3 years indicate reduced ice concentrations off the Larsen Ice Shelf at 60°W. Farther west, the Bellingshausen Sea continues to show the largest amount of open water in 1975, and the Amundsen Sea continues to show the largest amount of open water in 1976. A sizable amount of open water remains north of the Ross Ice Shelf in 1975, a lesser embayment occurs in the area in 1974, and in 1976, the ice has covered the entire region with at least 50-percent concentration. Coastal ice has expanded slightly since February all along the east Antarctic coast in 1975 and 1976, whereas in 1974, little if any ice has formed along much of the coast from 0°E to 35°E.

In April, the ice cover continues to expand equatorward (Figure 5-4). For the 3 years of available data, the Weddell Sea contains the greatest amount of ice in 1974, while a considerable area of very low ice concentration (less than or equal to 26 percent) is indicated in 1975 because of the rapid eastward advance of the ice at the end of the month and the effects of monthly averaging. The low concentrations off the Larsen Ice Shelf remain from the previous month in all 3 years. Farther west in the Bellingshausen Sea, the smallest area of ice continues to occur in 1975, while ice covers the Ronne Entrance in all years. Similarly, the coastal polynyas have frozen over along the Bellingshausen and Amundsen coasts. In the Ross Sea, the 1975 map shows a small polynya seaward of Cape Adare. Adjacent to Wilkes Land, less ice exists in 1975 than in either 1974 or 1976, while along the rest of the east Antarctic coast, ice extents are comparable for the 3 years. In each of the 3 years, the largest east Antarctic coastal polynya is off the Shackleton Ice Shelf (100°E).

In May, the ice concentration continues to increase along the coast, although it varies from year to year. A clear interannual contrast occurs for the ice extents of the Weddell Sea; considerably more ice exists in 1974 than in either 1975 or 1976, especially in the eastward extent (Figure 5-5). In

all 3 years, most of the Weddell ice cover has concentrations above 80 percent; lower concentrations remain along the northeast coast of the Peninsula. Farther west, the ice cover in both the Bellingshausen and Amundsen Seas has expanded farthest equatorward in 1976 and shows the least expanse of ice in 1974. In the Ross Sea, the ice has expanded to nearly its maximum extent. Along the east Antarctic coast adjacent to Wilkes Land, the least ice occurs in 1975, whereas off Princess Ragnhild Coast, the least ice occurs in 1974—the same year that exhibits the most ice directly to the west in the Weddell Sea.

In June and July, useable data were not obtained for 1975; therefore, results are presented only for 1973, 1974, and 1976. In the Weddell Sea in June, there is a clear trend toward reduced ice extent from 1973 to 1976 (Figure 5-6). No such consistent interannual trend exists in the Bellingshausen and Amundsen Seas, where the least extent occurs in 1974, or in the Ross Sea where, by contrast, the greatest extent occurs in 1974. This latter fact is illustrated by the prominence of ice in the northern Ross Sea in the vicinity of 150 degrees west longitude, which extends 4 degrees of latitude farther equatorward than in either 1973 or 1976. The slight embayment at 180°E occurs in each of the 3 years. North of the Adelie Coast, the greatest extent of ice occurs in 1973, although off most of the Wilkes Coast, comparable extents occur in each of the 3 years. At roughly 85°E, there is consistently a prominent point in the ice edge, extending equatorward of 60°S. To the west of that point in the Indian Ocean sector, the most ice occurs in 1974 and the least in 1973. In the region 0° to 45°E, significant interannual differences occur in the ice configuration related to the formation of the Weddell polynya evident in July.

In July, there is a noticeably greater equatorward extent of ice in the Weddell Sea in 1973 than there is in 1974 and 1976 (Figure 5-7). Although some less concentrated ice exists along the Peninsula in each of the 3 years, the amount is less than it was in June. In the Bellingshausen Sea, the ice extents are comparable in 1973 and 1976 but are noticeably less in 1974. (See Ackley and Keliher, 1976.) By contrast, the Amundsen Sea ice extent is greatest in 1974. In both these seas, the amount of less concentrated ice (less than or equal to 78 percent) is largest in 1973. The ice edge in the Ross Sea now has a prominent corner at about 150°W in all years, with a somewhat lesser equatorward extent in 1976. Off the Clarie Coast, a slight trend toward greater ice extents occurs from 1973 to 1976, although farther to the west (80°E to 120°E), the trend is in the opposite direction; still farther west (45°E), the trend shifts back to its direction off the Clarie Coast. In 1974 in the eastern Weddell Sea, the ice is closing to form the Weddell polynya to the east of the Greenwich meridian, whereas no polynya exists in 1973. In 1976, the polynya is located farther to the west and does not form until August.

In August, the Weddell polynya stands out in both 1974 and 1976, while no data are available for 1973 or 1975. Off the northern tip of the Peninsula, considerably more ice is evident in 1976 than in 1974 (Figure 5-8). In the northern Ross Sea, the sharp corner seen in the ice extent in July and still prominent in August of 1974 is less apparent in August of 1976. Overall, the extent of ice in the Ross Sea region is greater in 1974 than in 1976.

In September, the ice reaches its maximum areal coverage. The September images reveal a sizable polynya in the eastern Weddell Sea region in 1974, 1975, and 1976 (Figure 5-9), with a 3-year westward drift in position. In the Drake Passage, the later 2 years contain considerably more ice than the earlier years. In the Bellingshausen and Amundsen Seas, the ice extent is slightly less in 1973 than in the other 3 years; in 1975, however, the reduced extent in the Amundsen Sea roughly balances the greater extent in the Bellingshausen Sea. The pointed extension of ice in the northern Ross Sea is visible in each of the years, and the equatorward extent is largest in 1974. Off the Clarie Coast, the extent is least in 1976. Farther to the west (100°E), the ice extents are most in 1973 and are comparable for the 3 later years.

In October, the region of the Weddell polynya continues to have the most prominent interannual contrast (Figure 5-10). In 1973, highly concentrated ice covers much of the Weddell Sea, although a small region of reduced concentration exists at 5°E, 64°S, northeast of Maud Rise. In 1974, the area of the polynya is almost equally divided in the Eastern and Western Hemispheres, but in 1975 and 1976, the polynya is located progressively farther west. Also, in 1975, the Weddell polynya is more nearly circular than the elongated polynyas in 1974 and 1976. Another sharp interannual contrast during October is the far lesser extent of ice in the eastern Ross Sea region in 1976 than in the

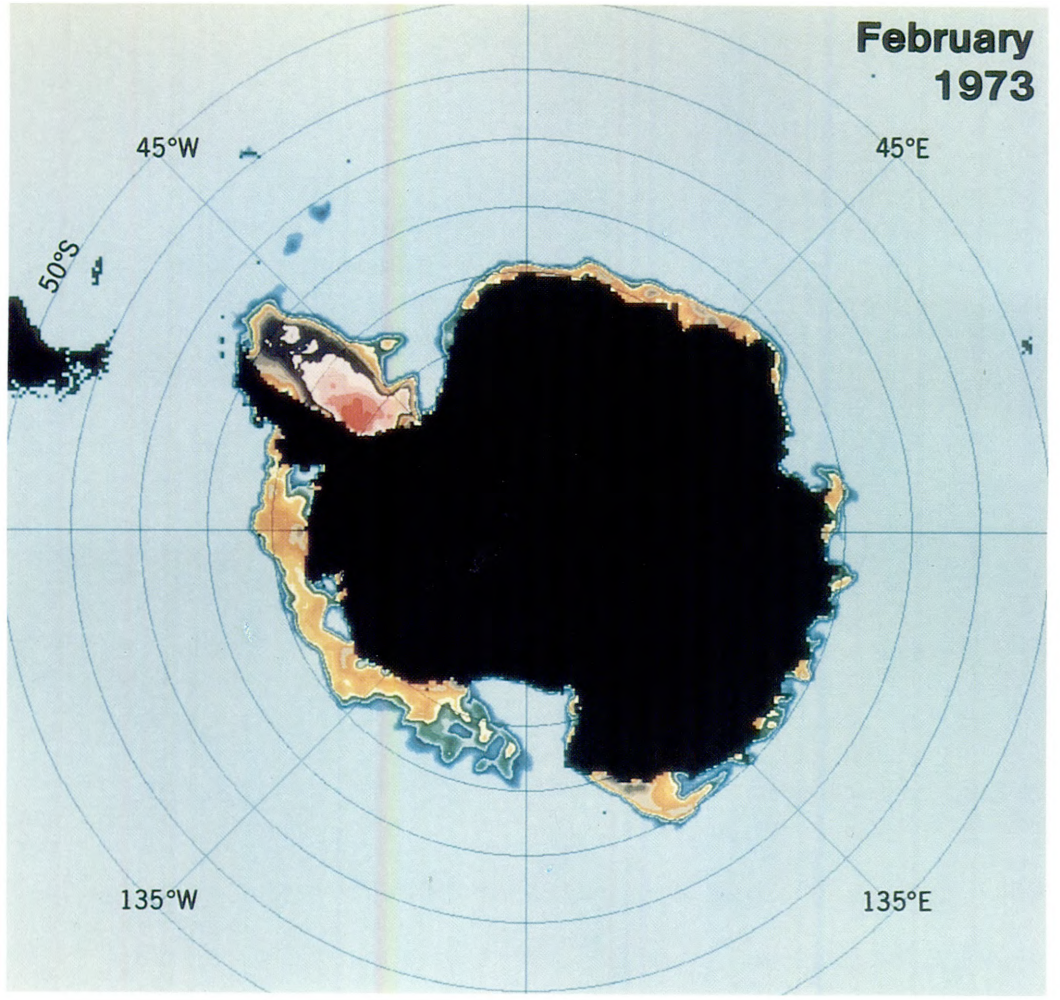

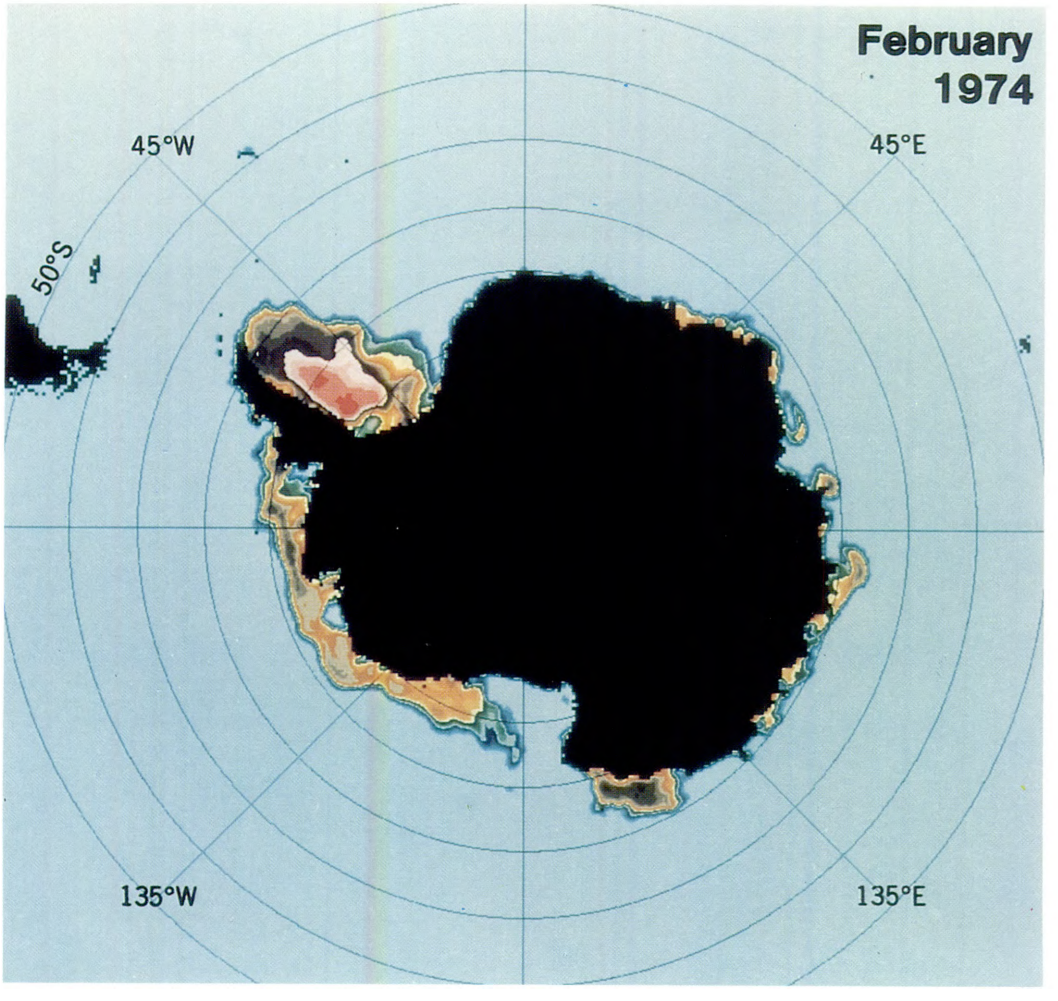

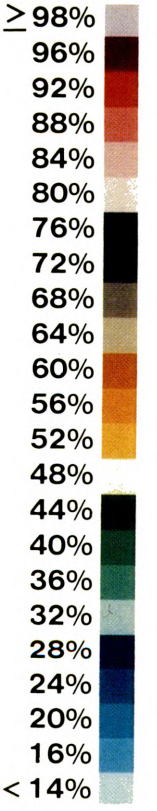

Figure 5-2a. Mean monthly sea ice concentrations for February 1973 and 1974.

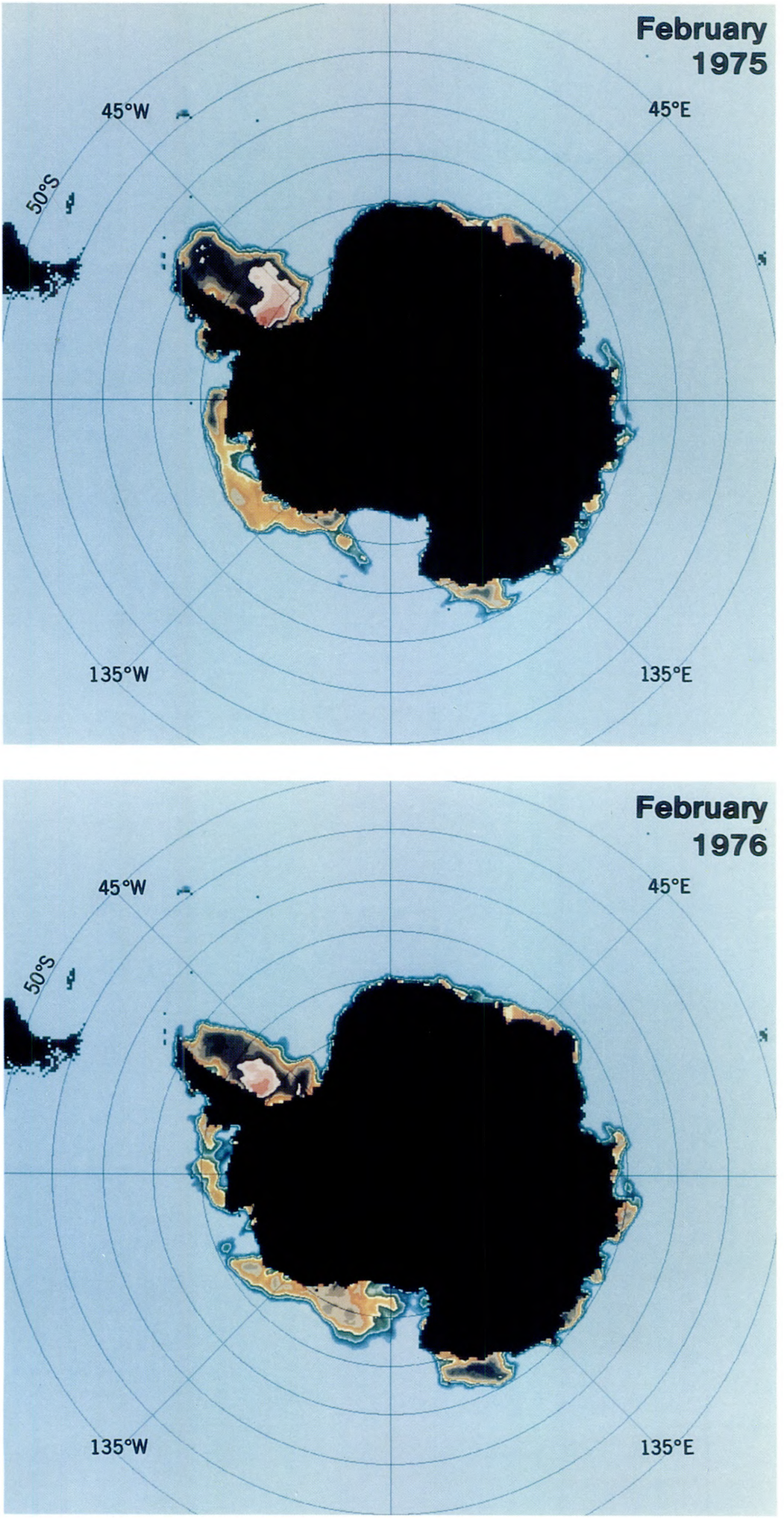

Figure 5-2b. Mean monthly sea ice concentrations for February 1975 and 1976.

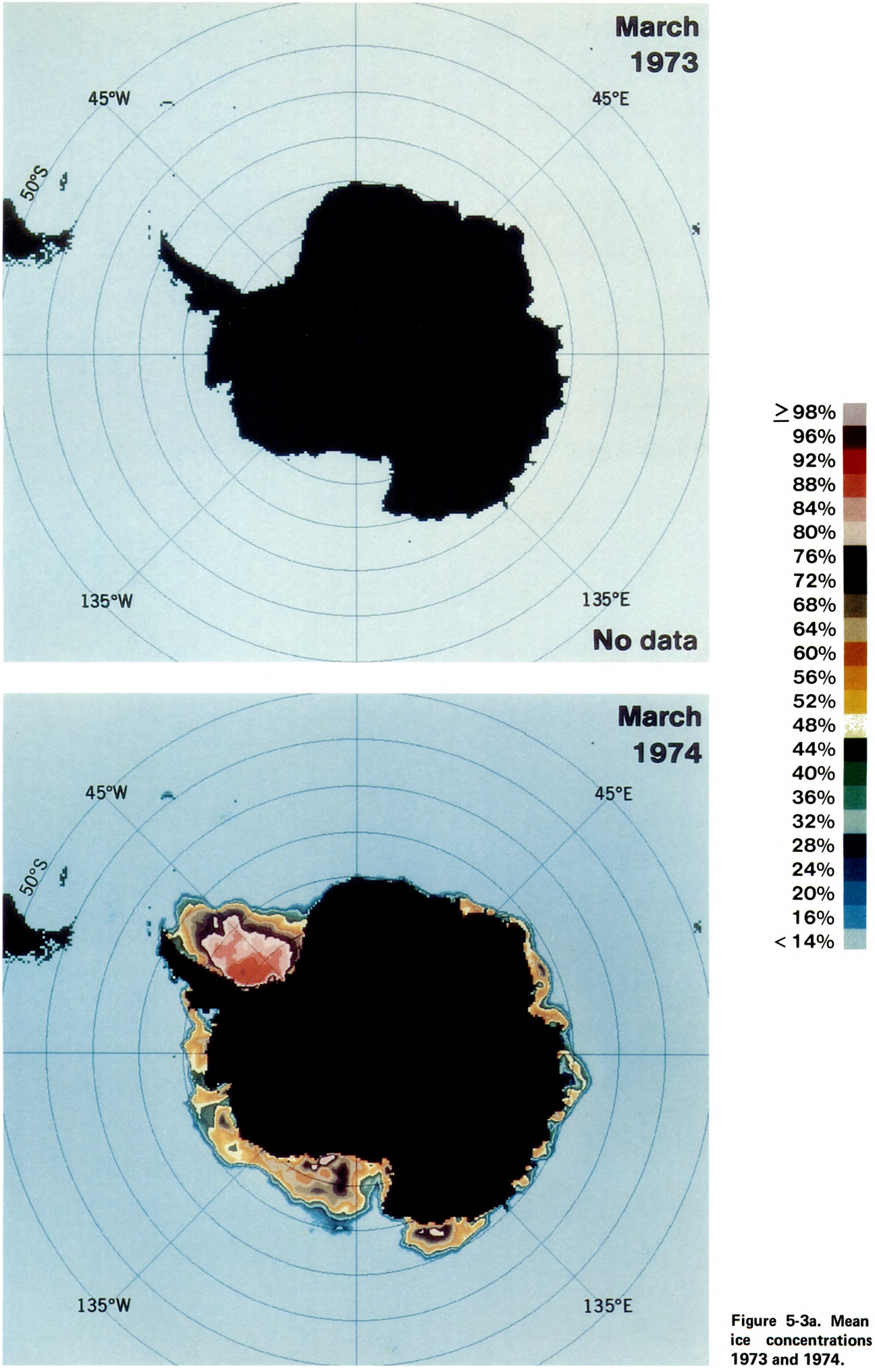

Figure 5-3a. Mean monthly sea ice concentrations for March 1973 and 1974.

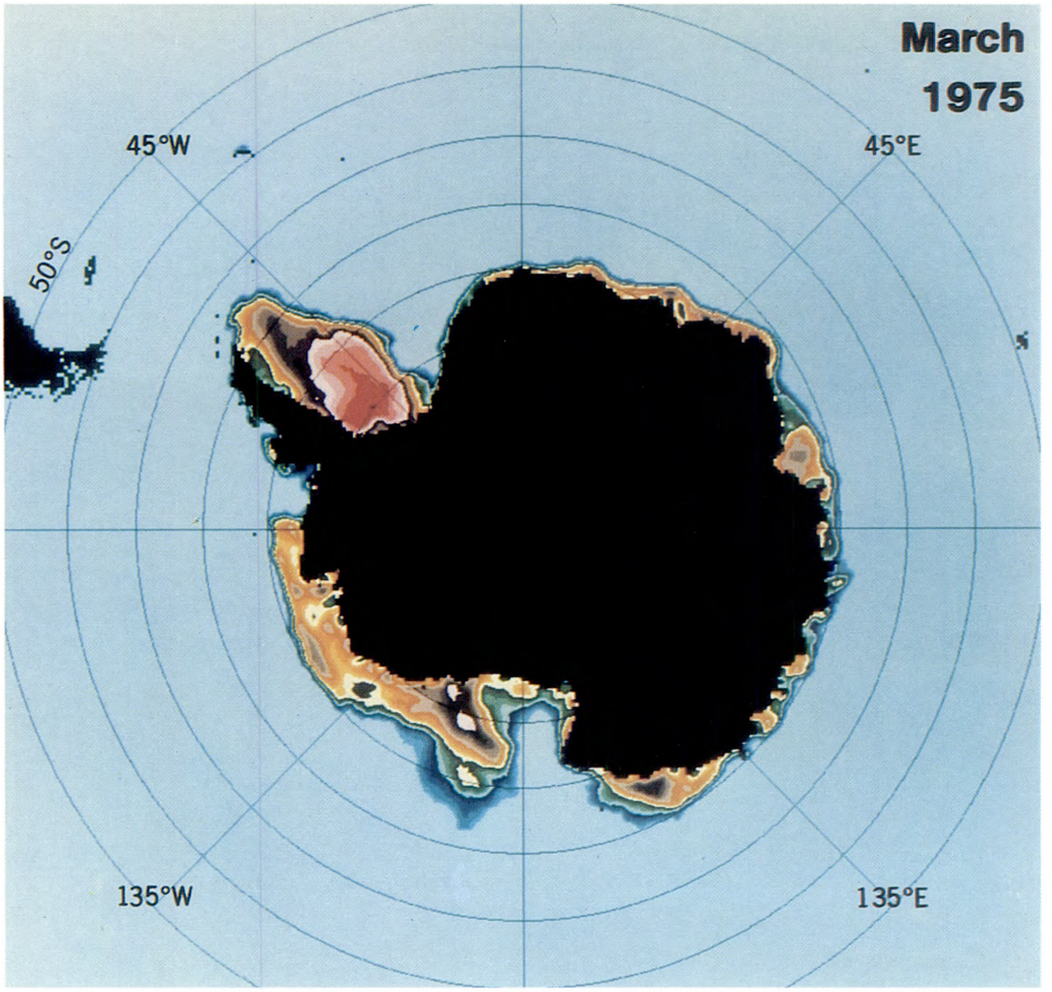

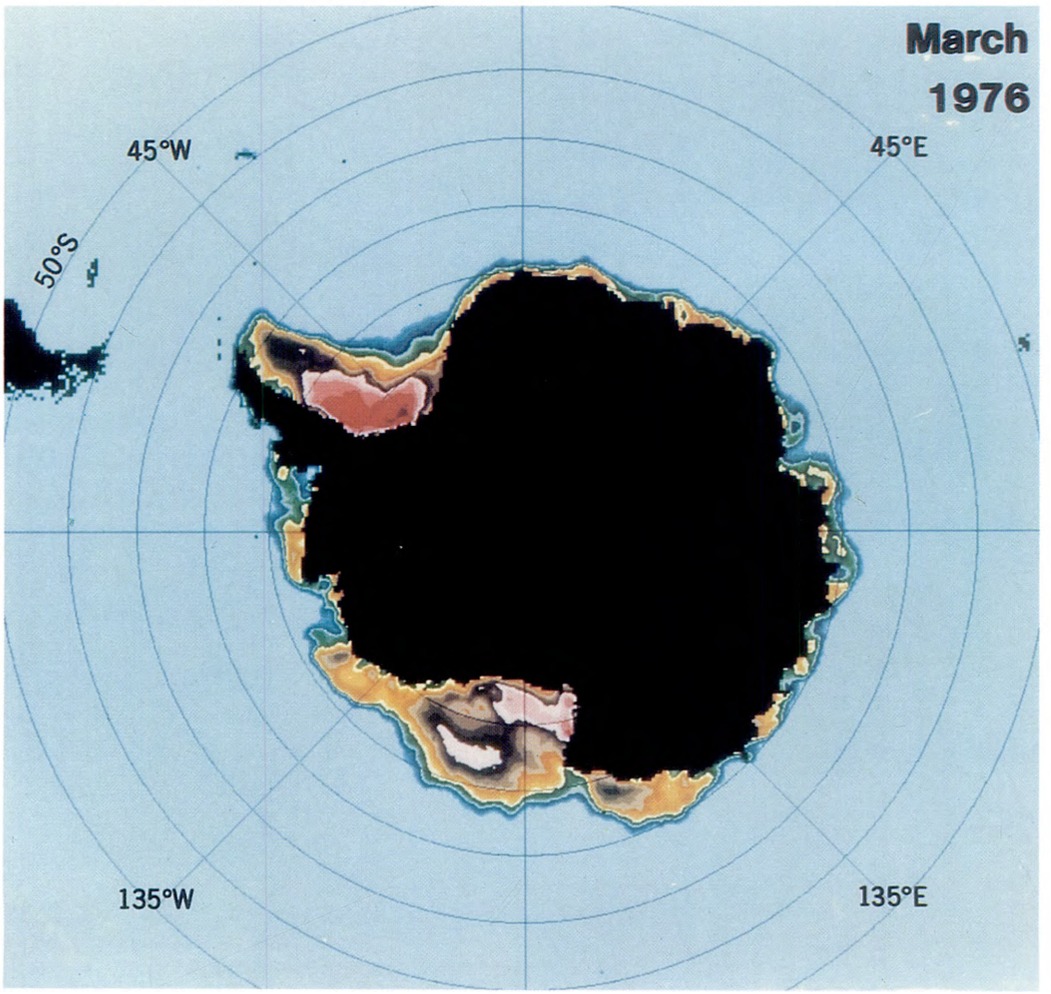

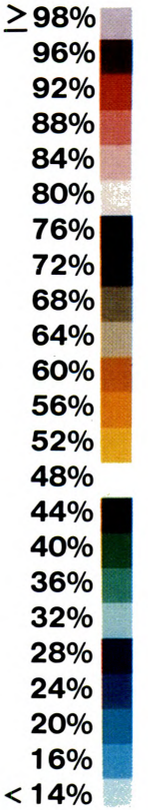

Figure 5-3b. Mean monthly sea ice concentrations for March 1975 and 1976.

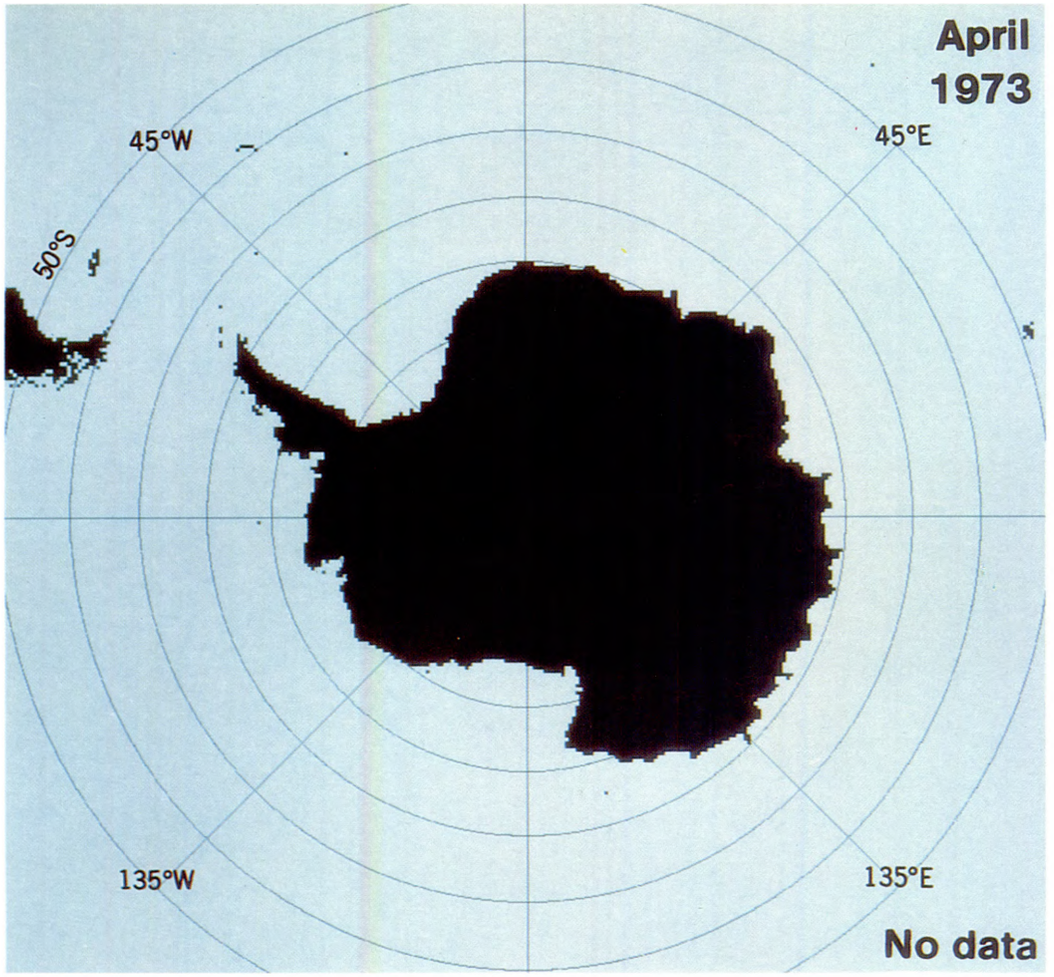

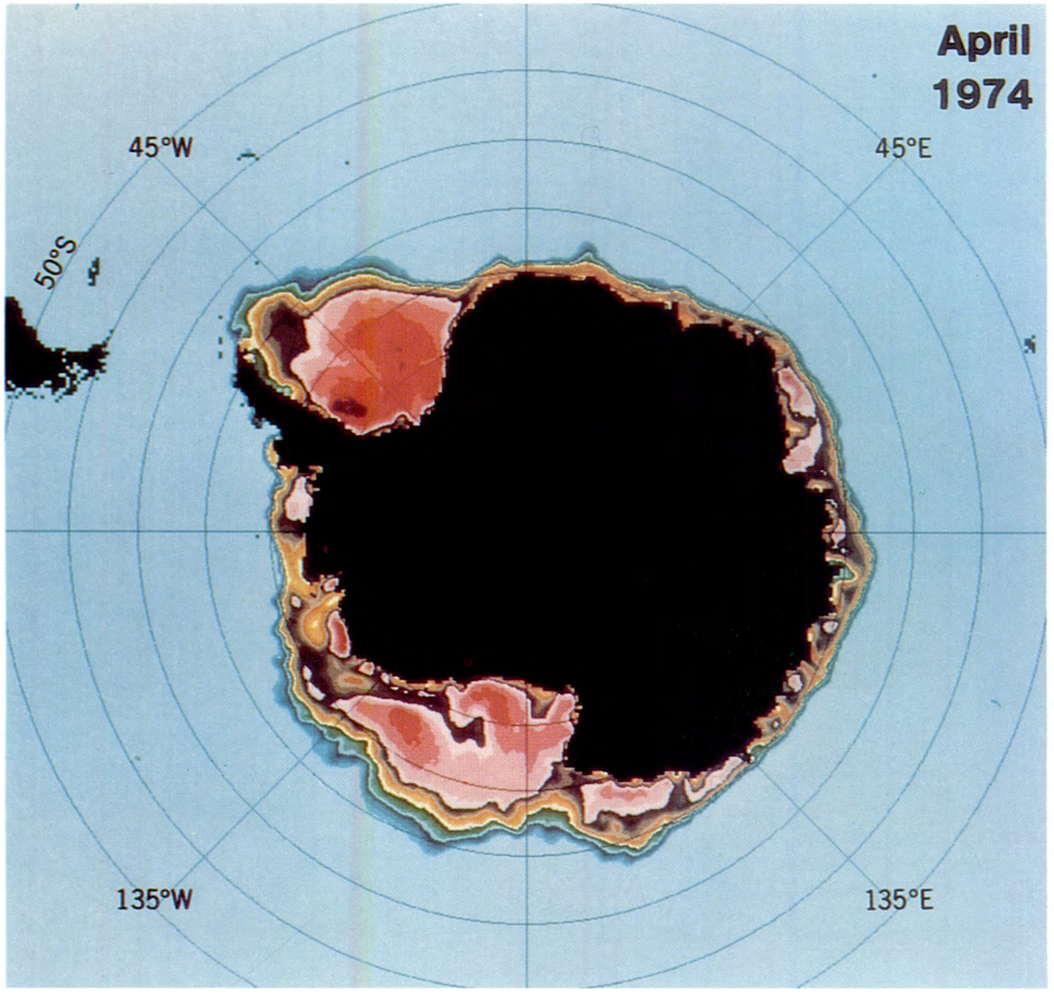

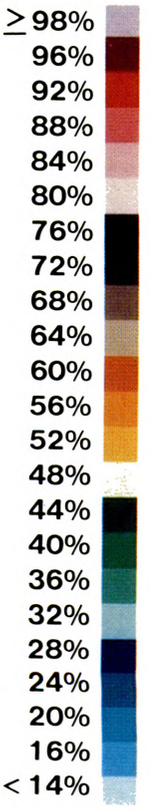

Figure 5-4a. Mean monthly sea ice concentrations for April 1973 and 1974.

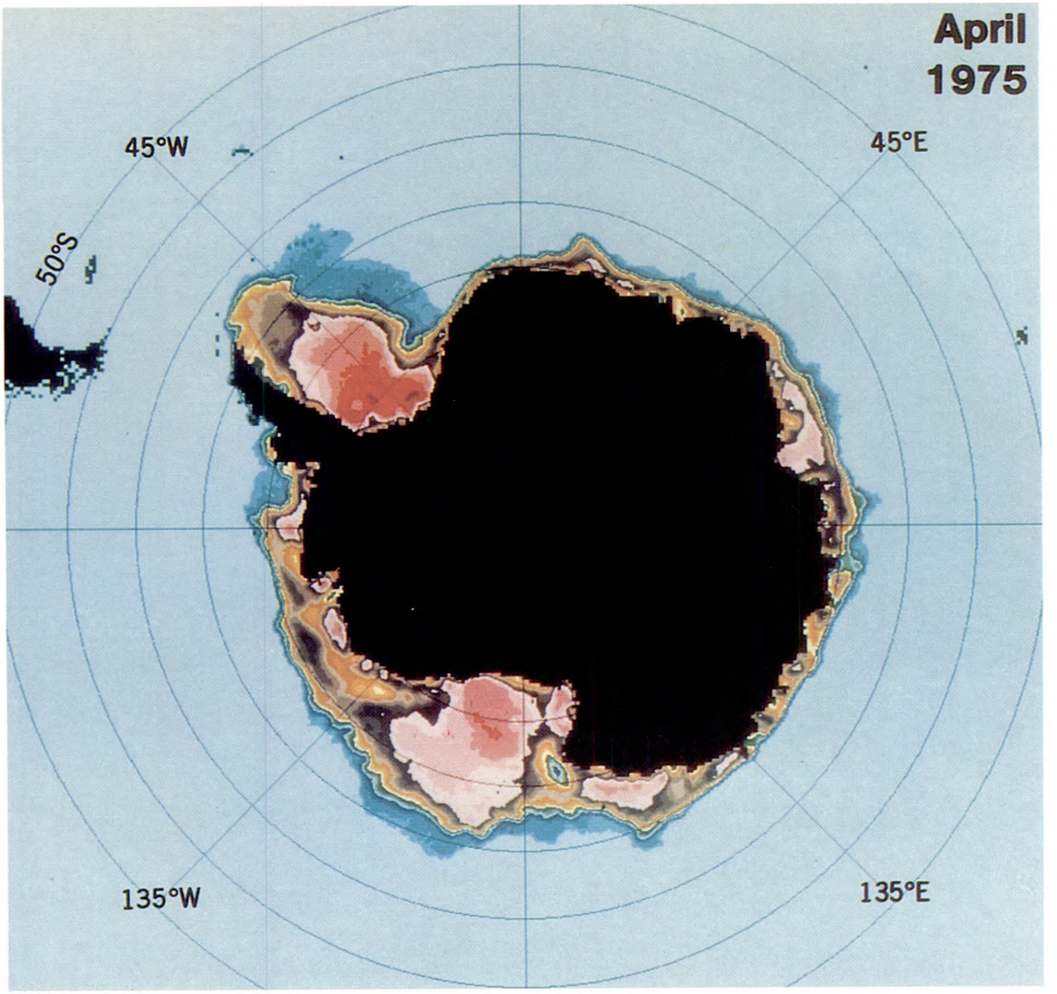

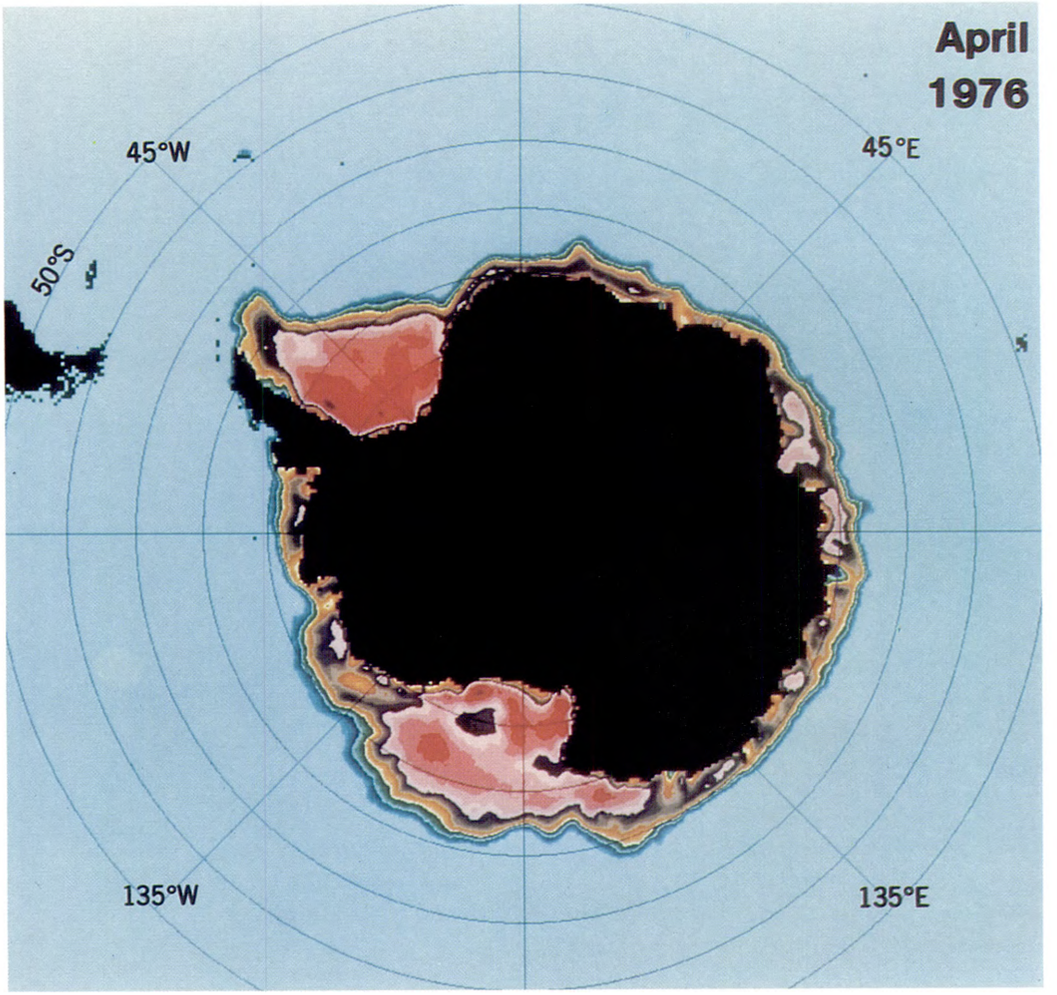

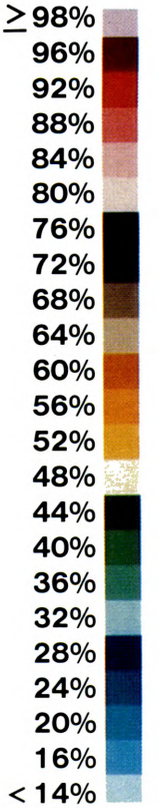

Figure 5-4b. Mean monthly sea ice concentrations for April 1975 and 1976.

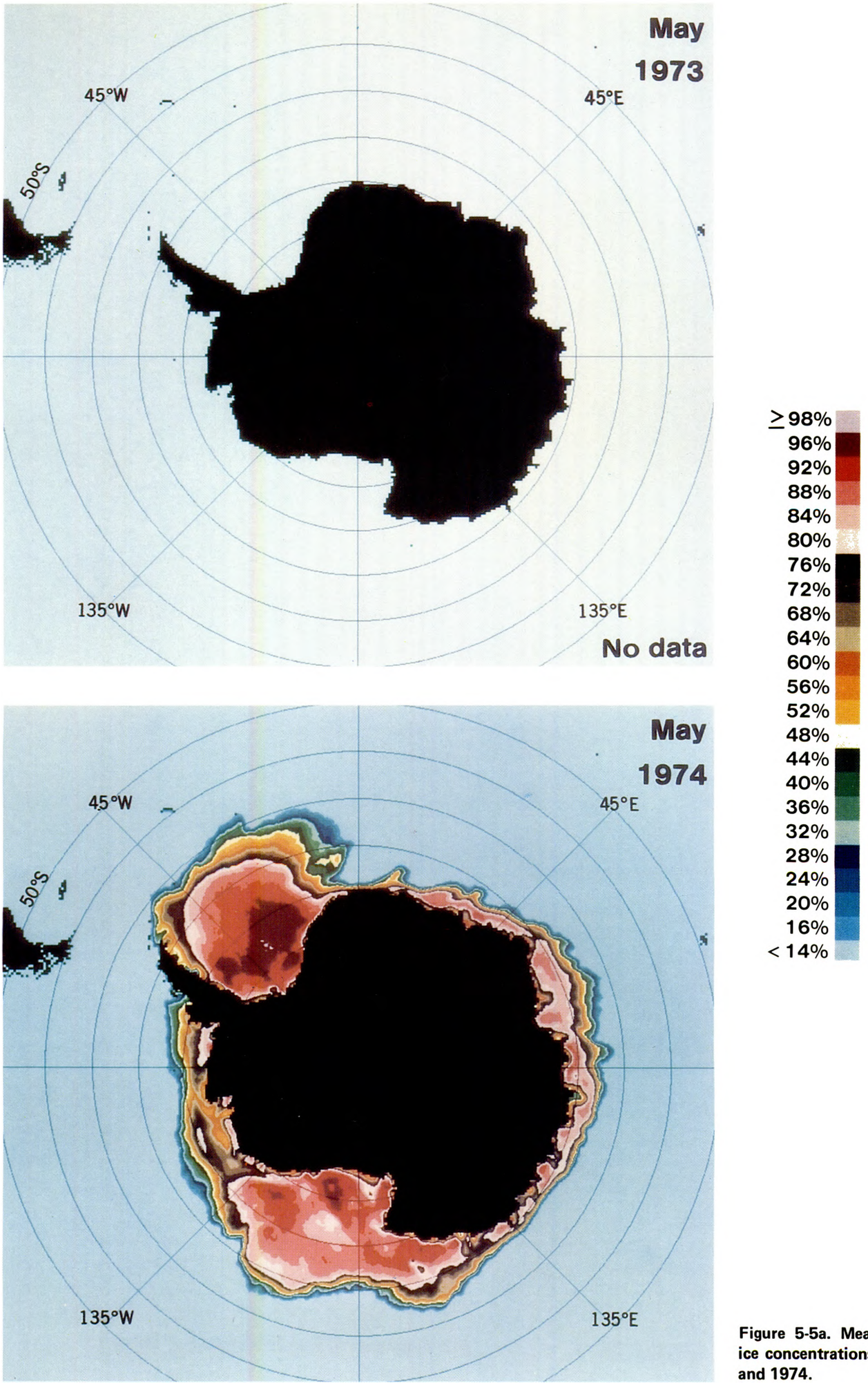

Figure 5-5a. Mean monthly sea ice concentrations for May 1973 and 1974.

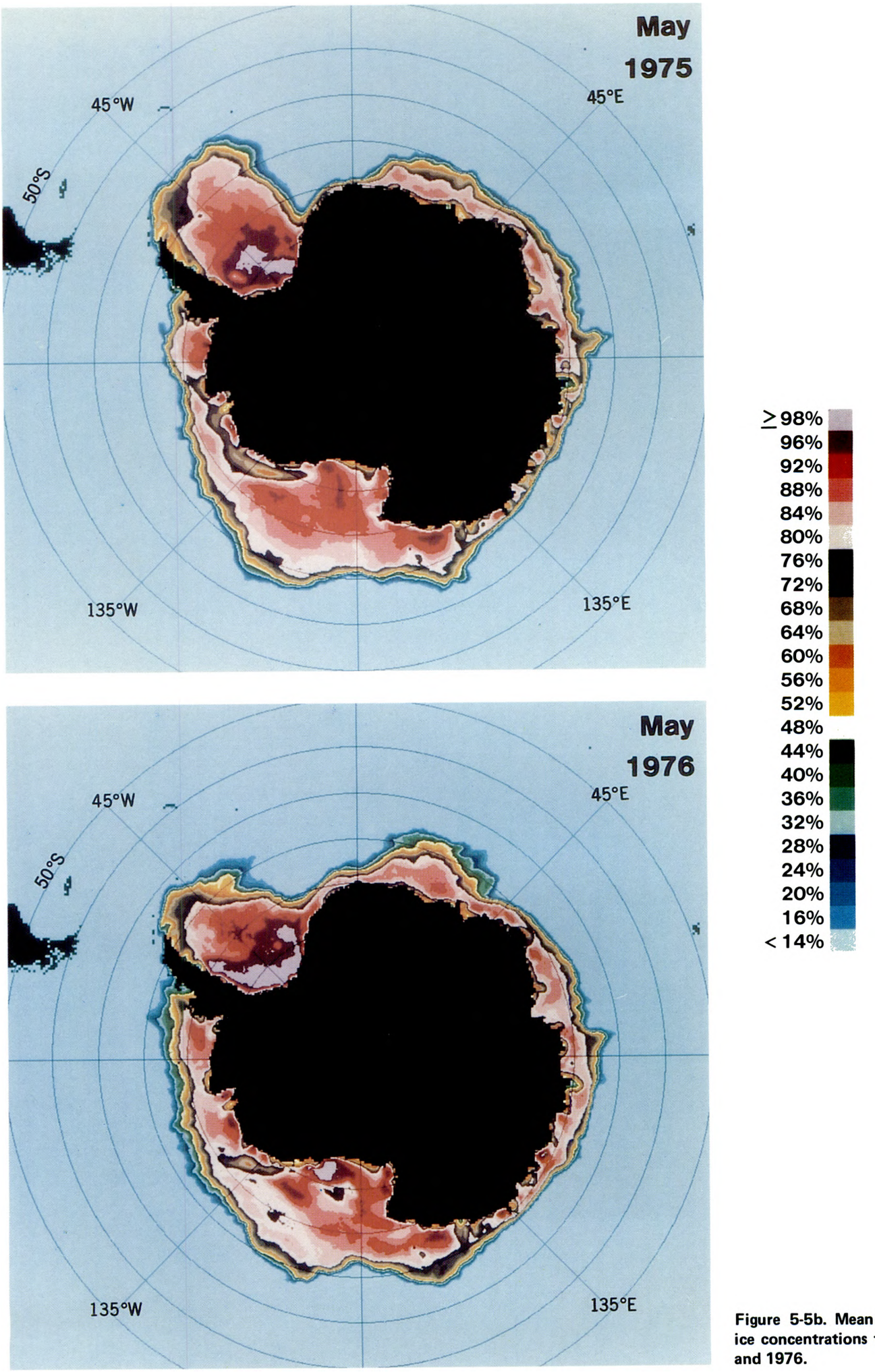

Figure 5-5b. Mean monthly sea ice concentrations for May 1975 and 1976.

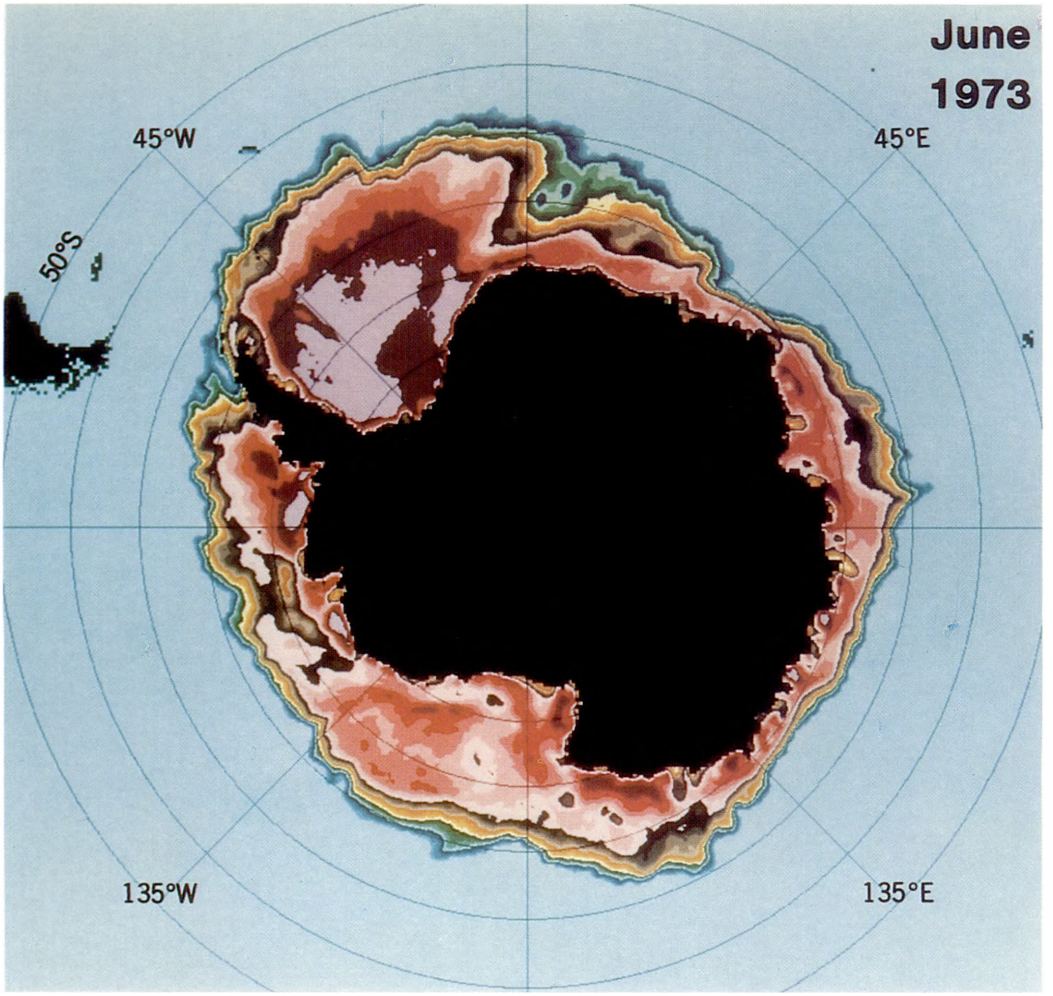

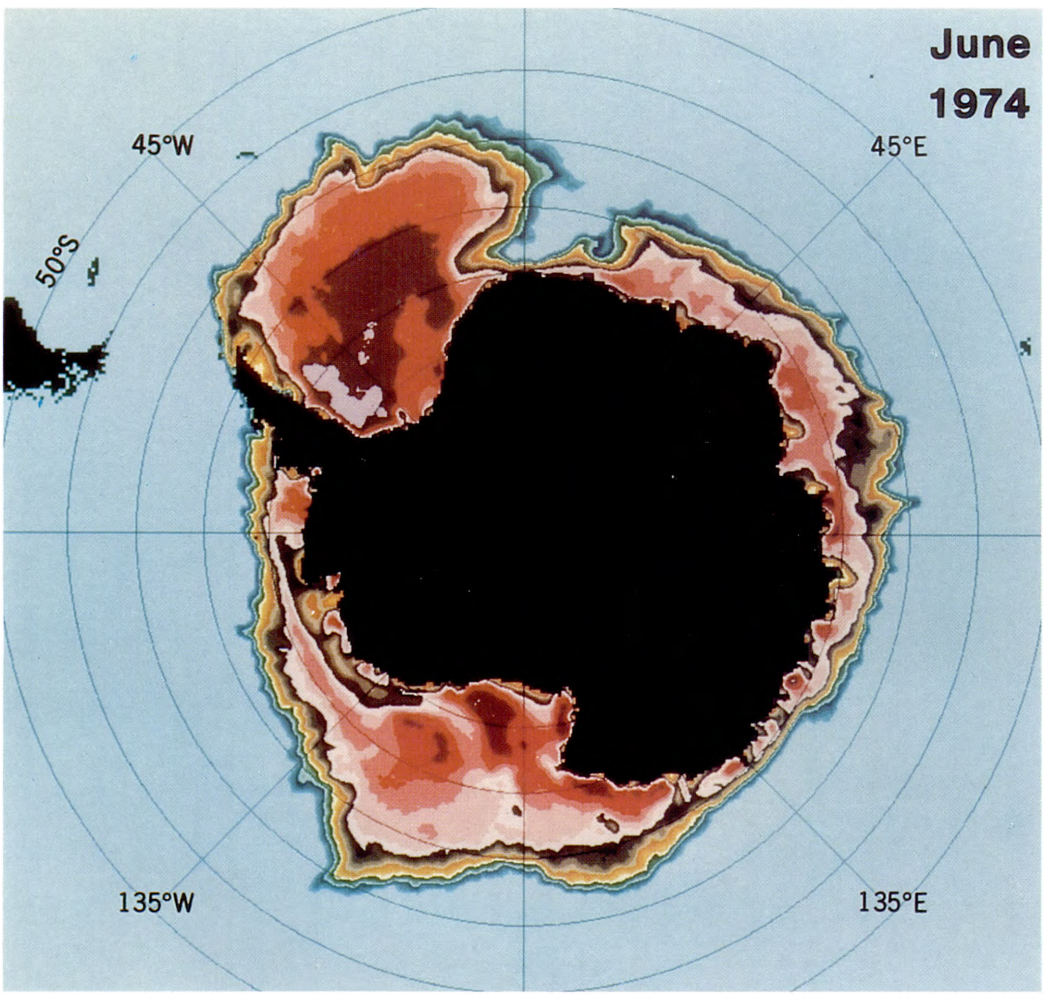

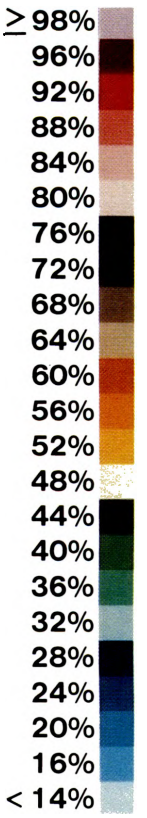

Figure 5-6a. Mean monthly sea ice concentrations for June 1973 and 1974.

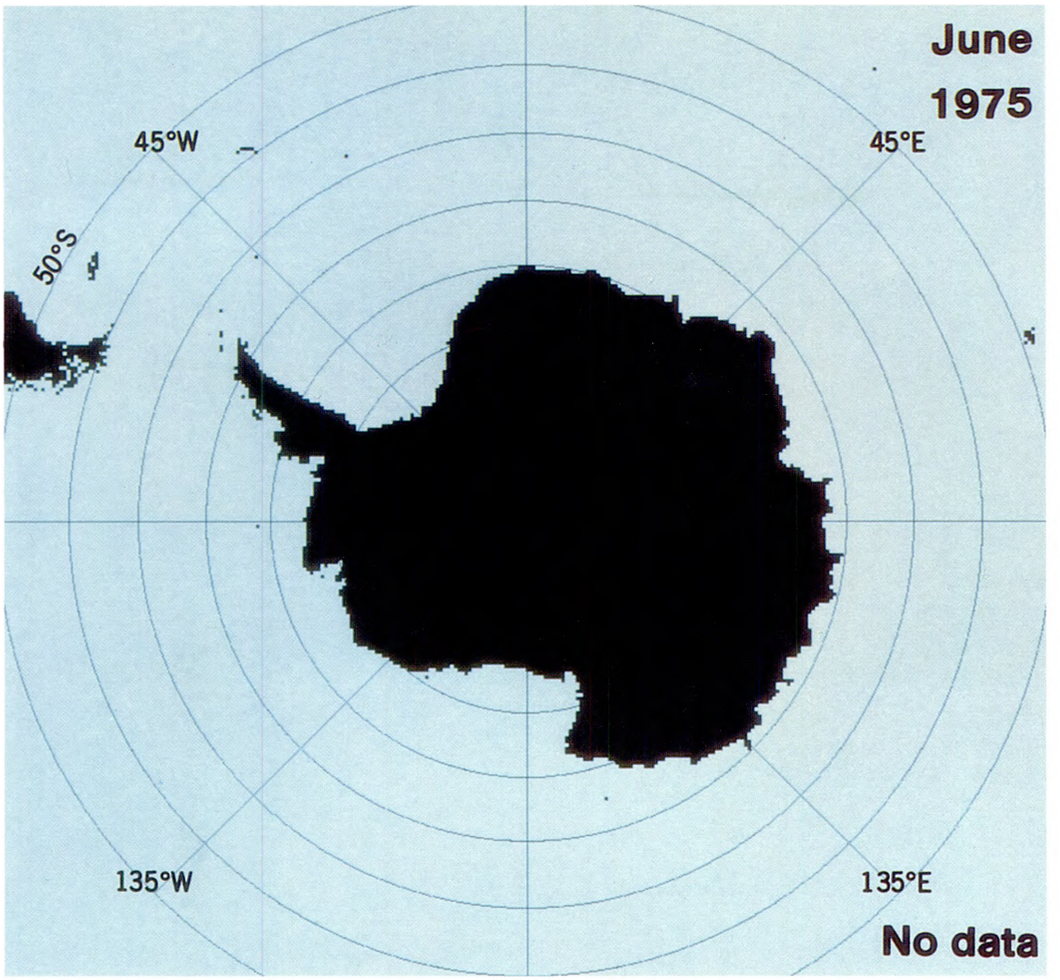

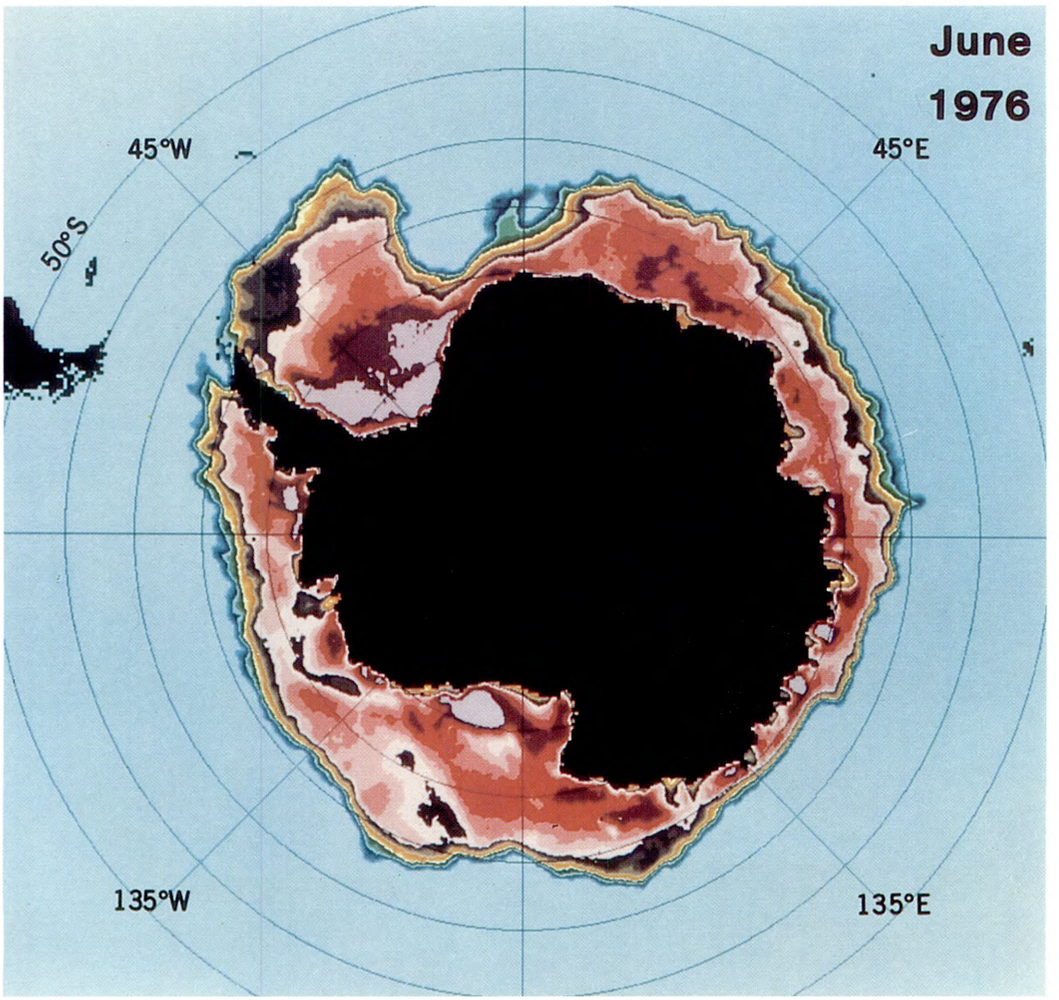

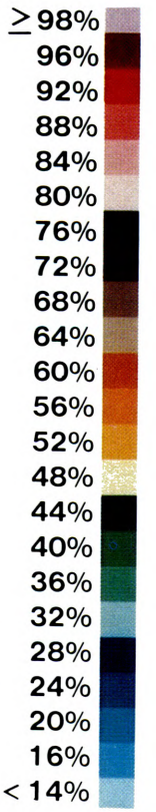

Figure 5-6b. Mean monthly sea ice concentrations for June 1975 and 1976.

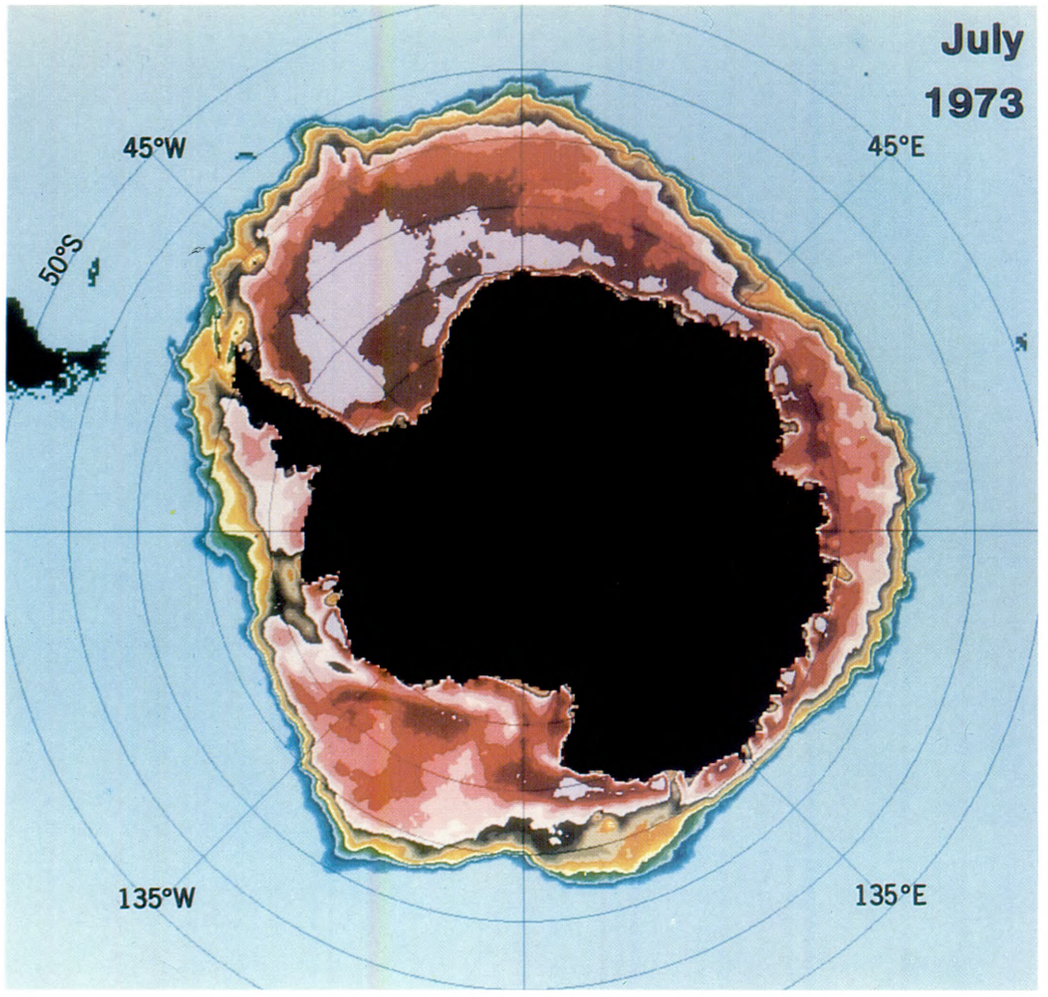

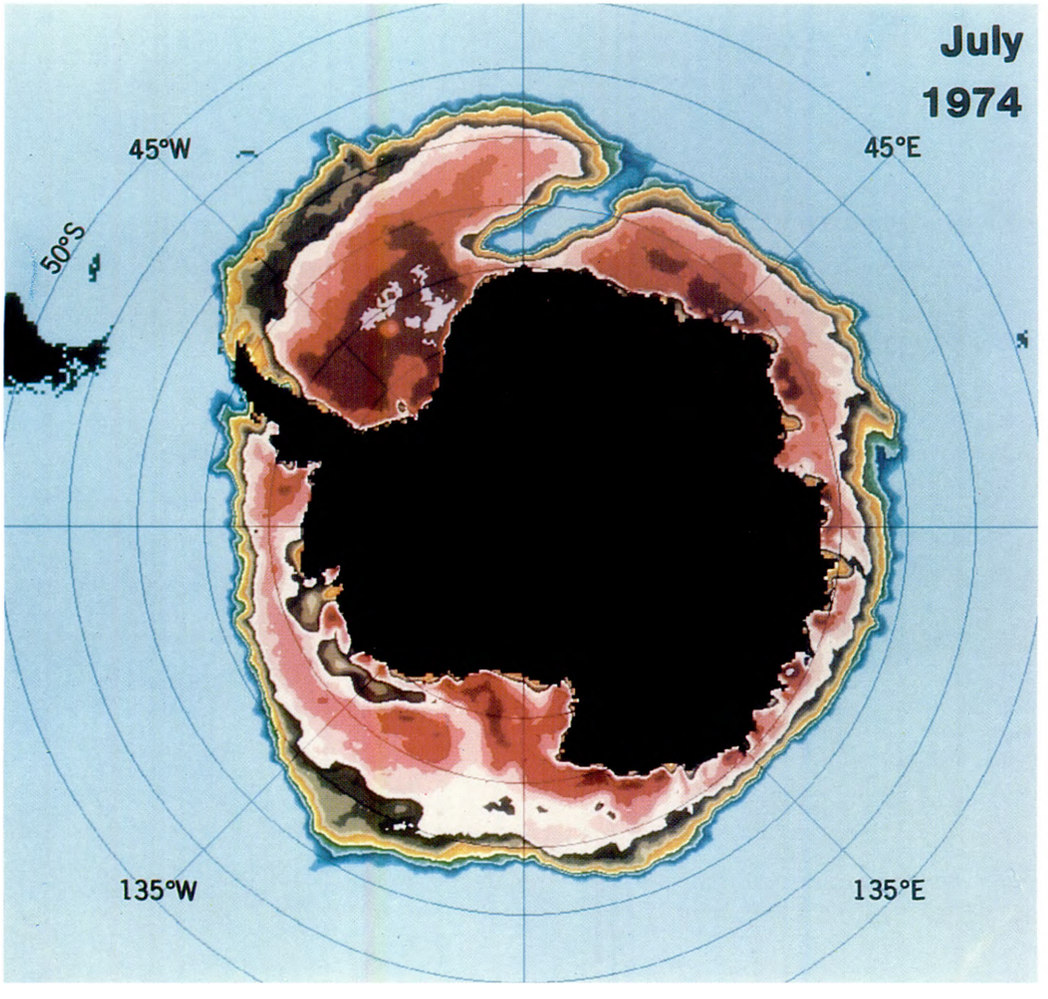

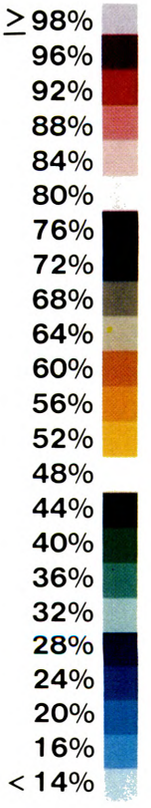

Figure 5-7a. Mean monthly sea ice concentrations for July 1973 and 1974.

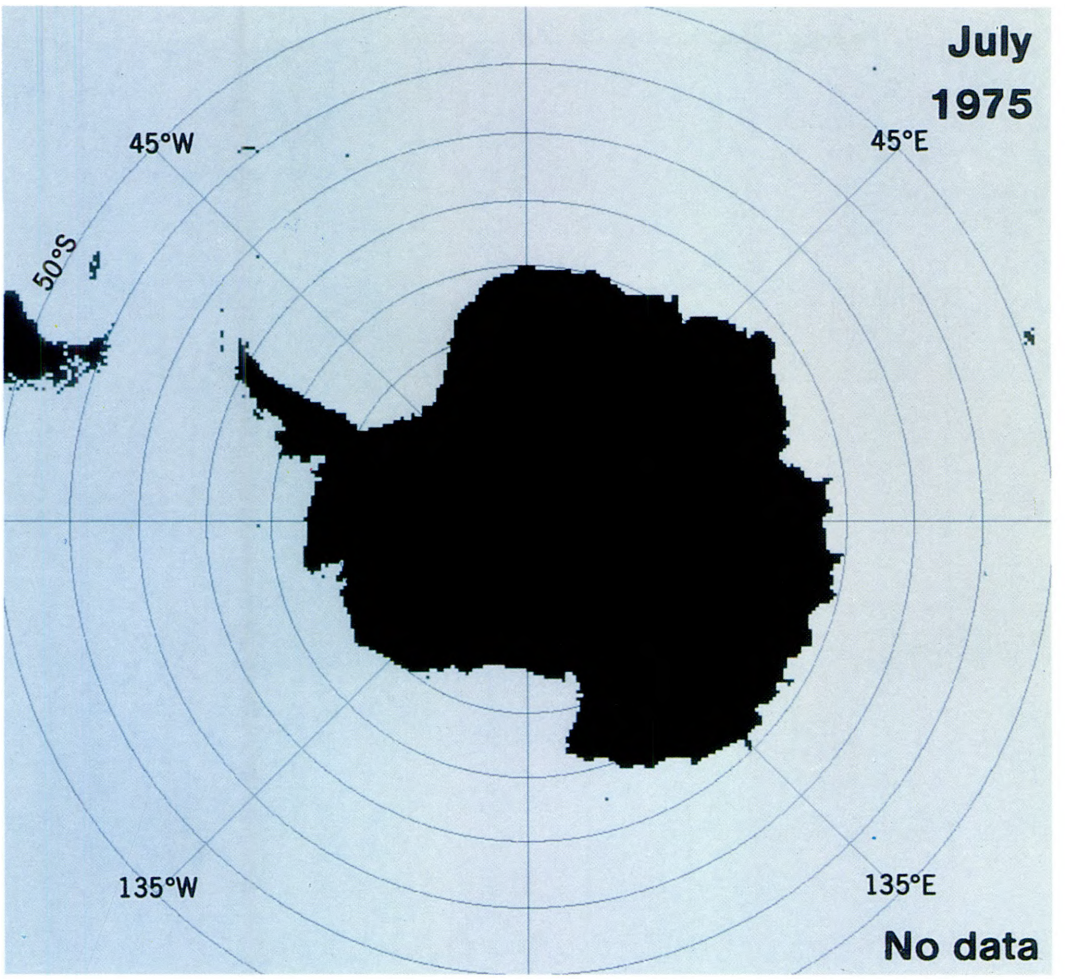

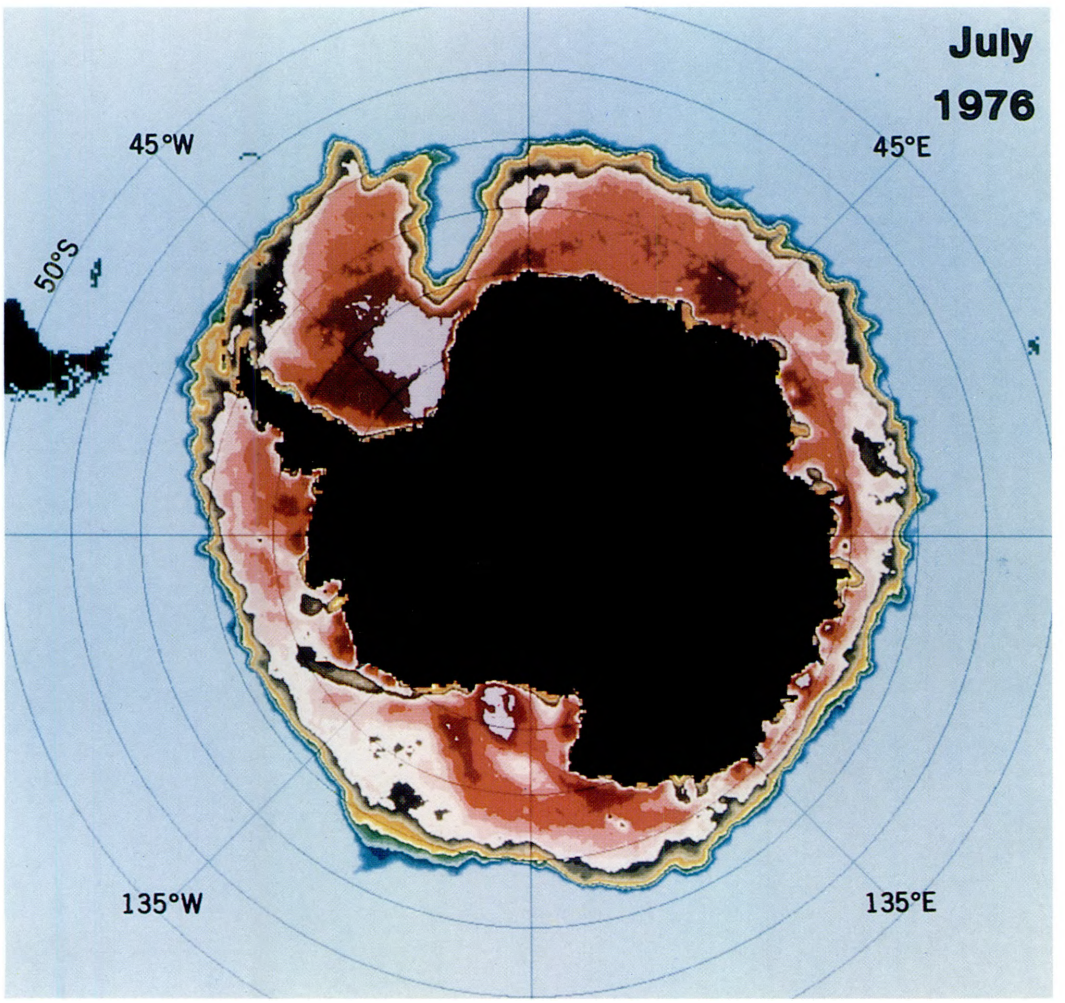

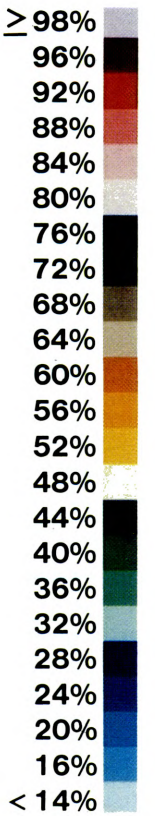

Figure 5-7b. Mean monthly sea ice concentrations for July 1975 and 1976.

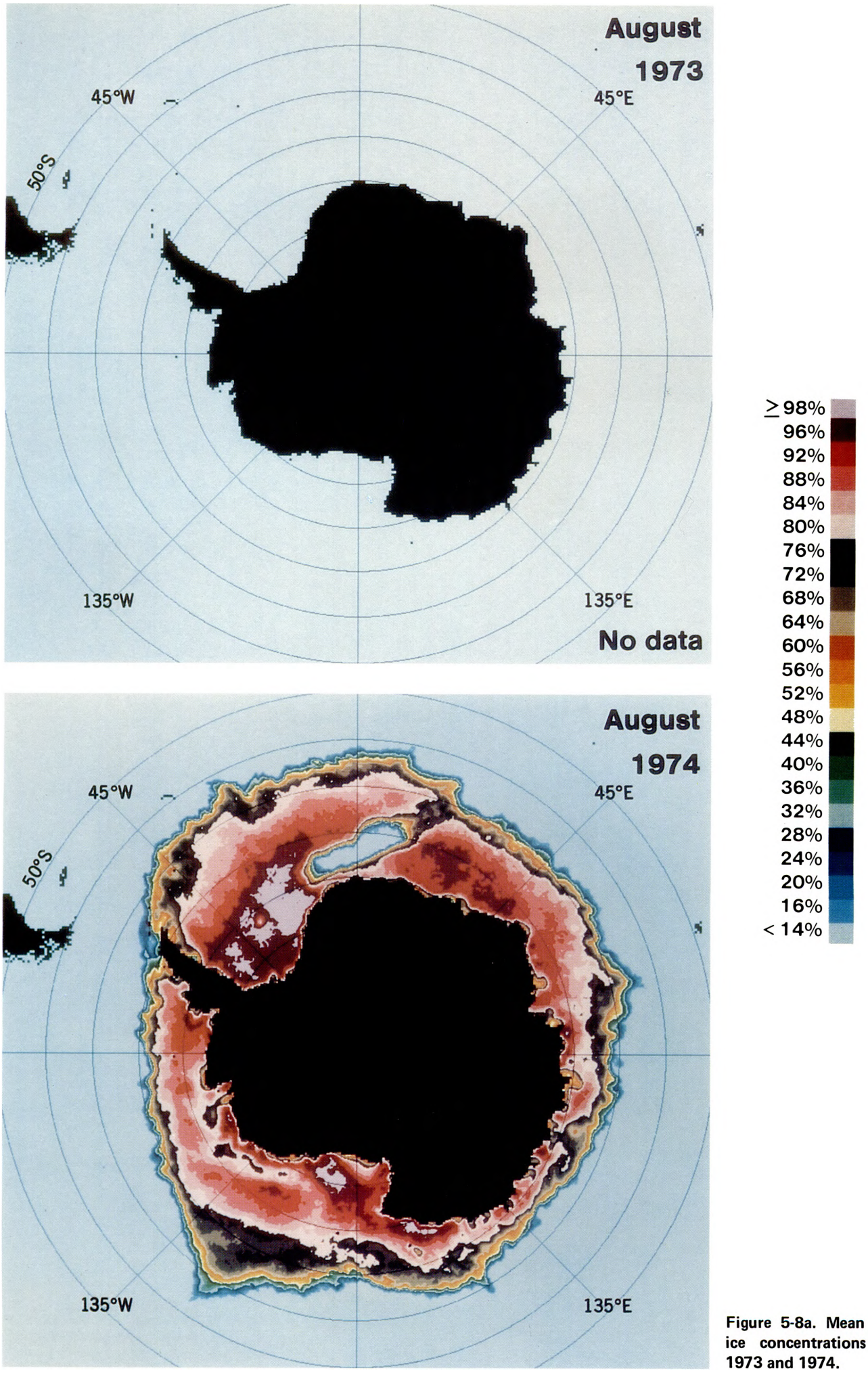

Figure 5-8a. Mean monthly sea ice concentrations for August 1973 and 1974.

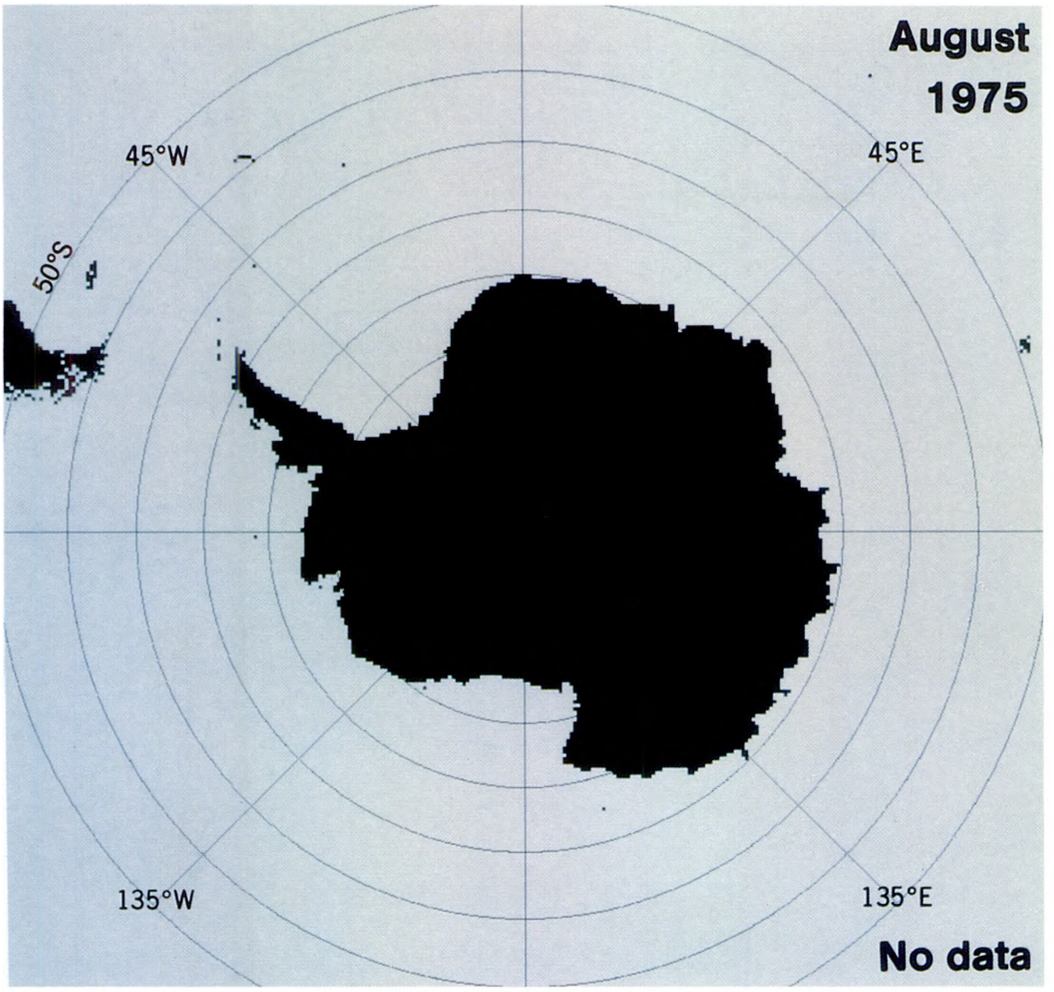

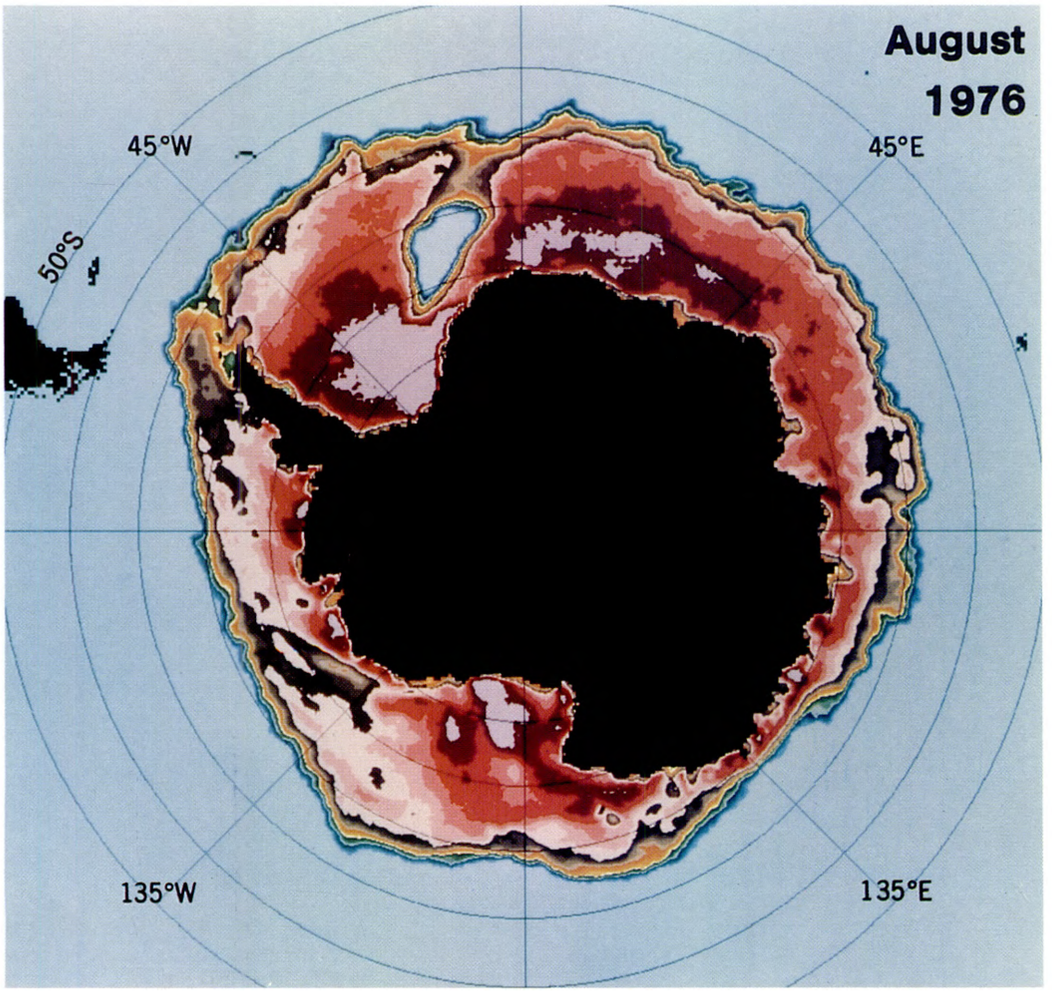

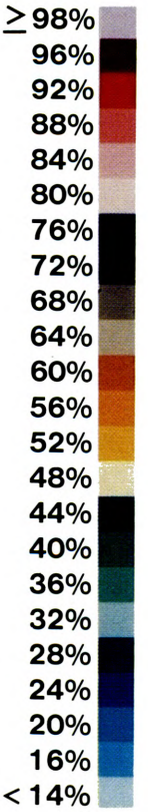

Figure 5-8b. Mean monthly sea ice concentrations for August 1975 and 1976.

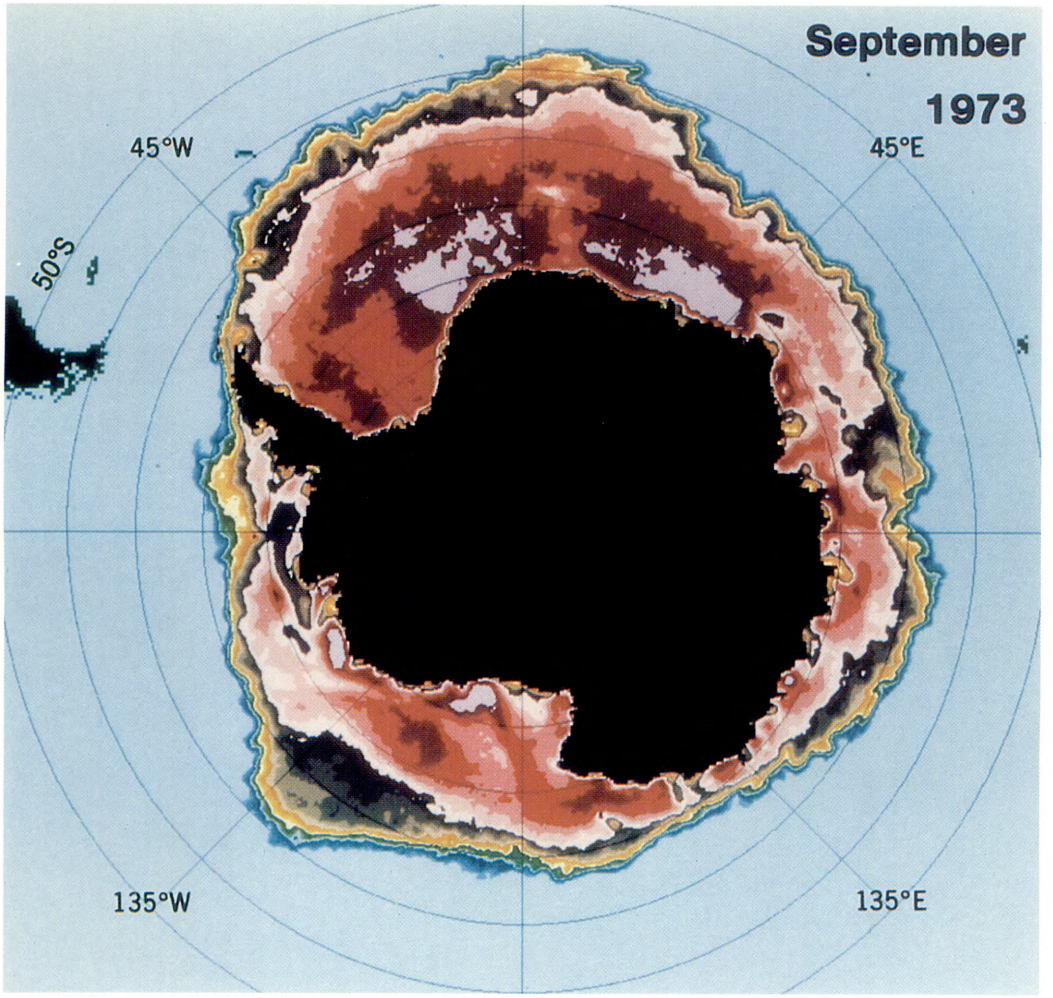

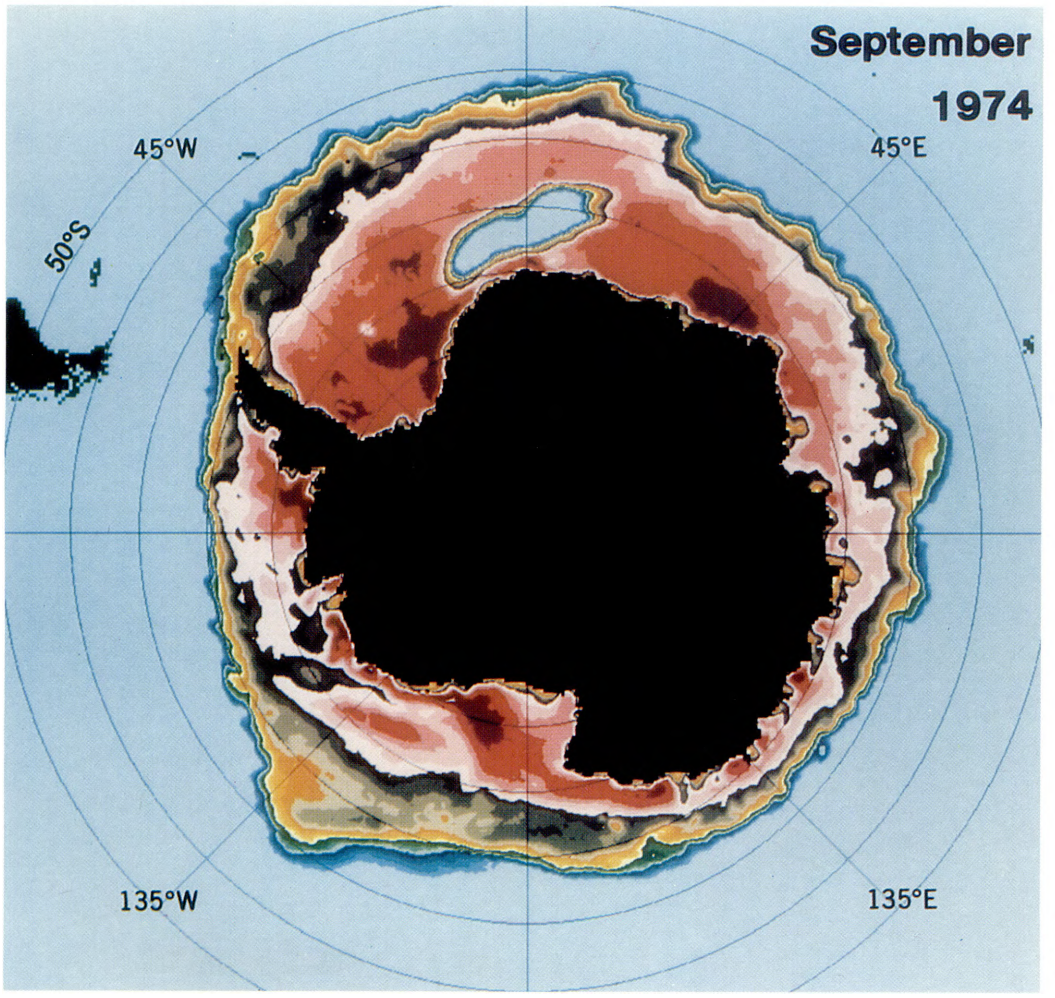

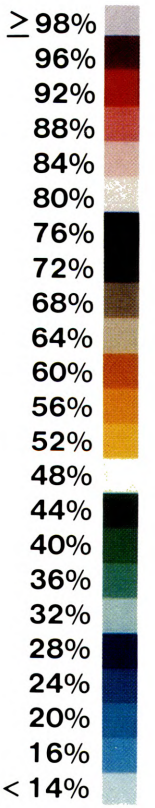

Figure 5-9a. Mean monthly sea ice concentrations for September 1973 and 1974.

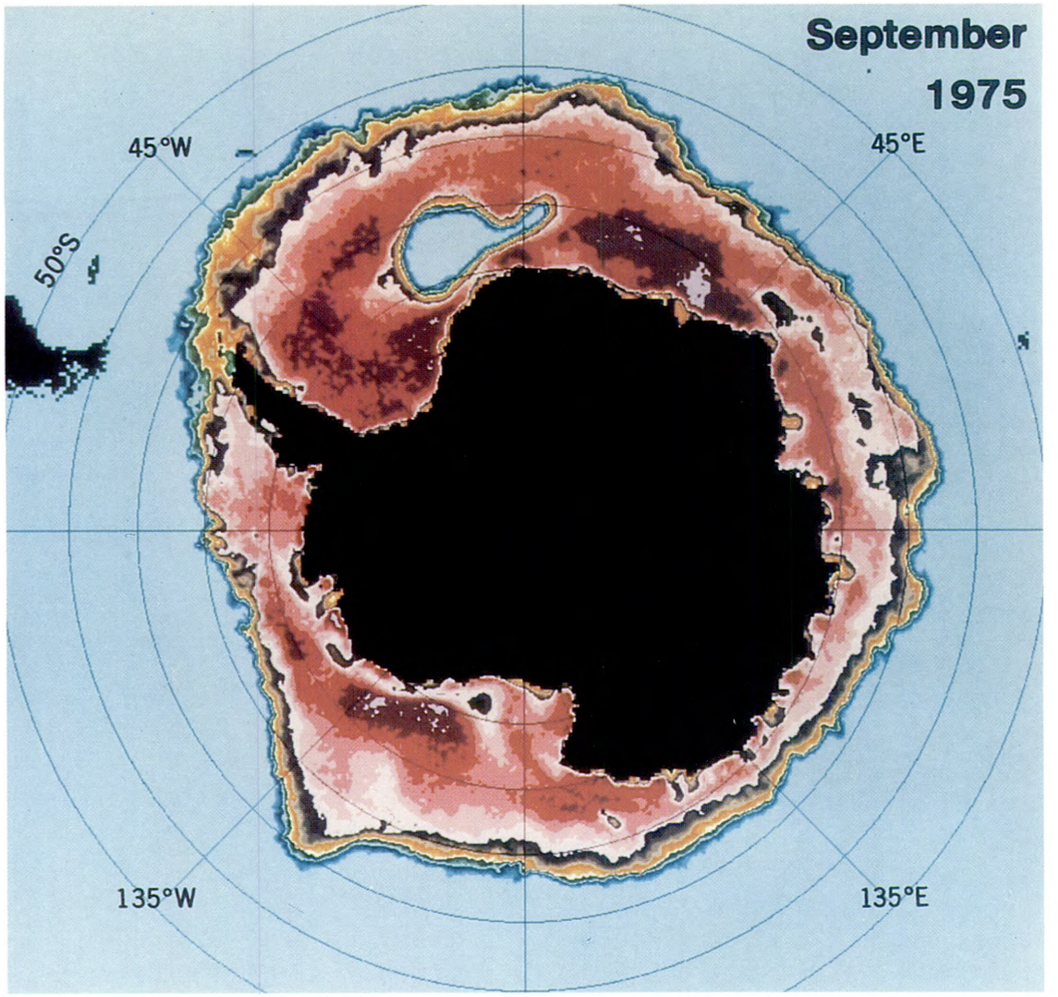

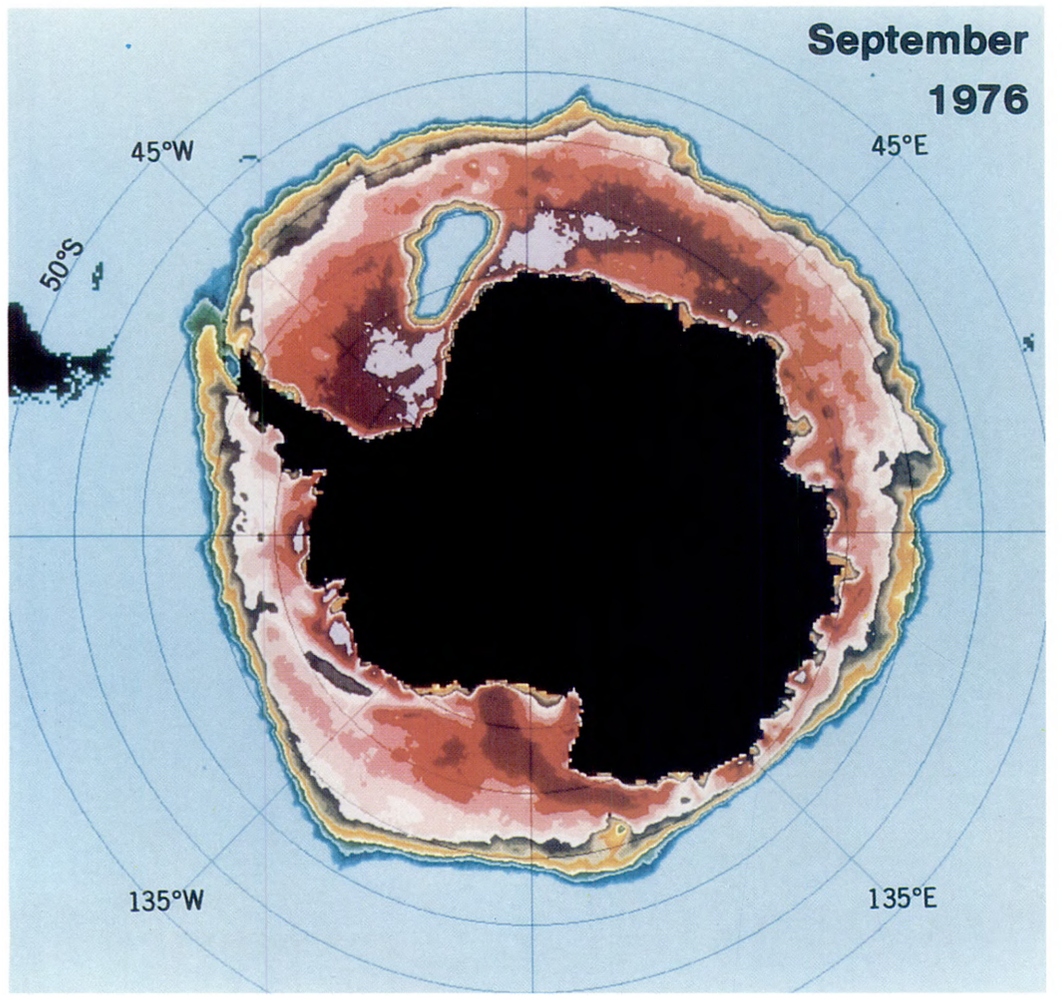

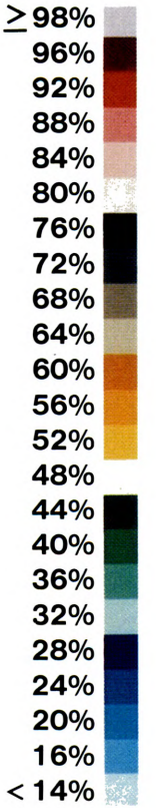

Figure 5-9b. Mean monthly sea ice concentrations for September 1975 and 1976.

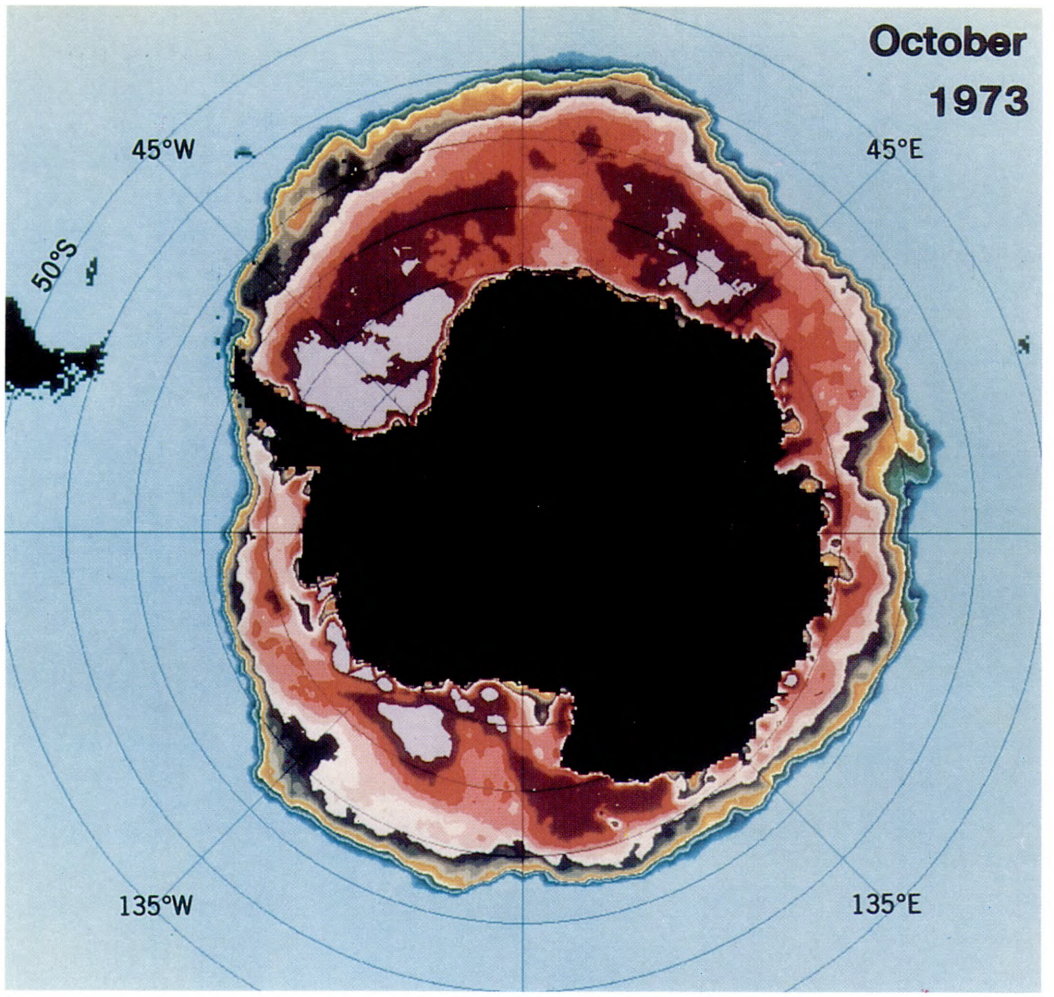

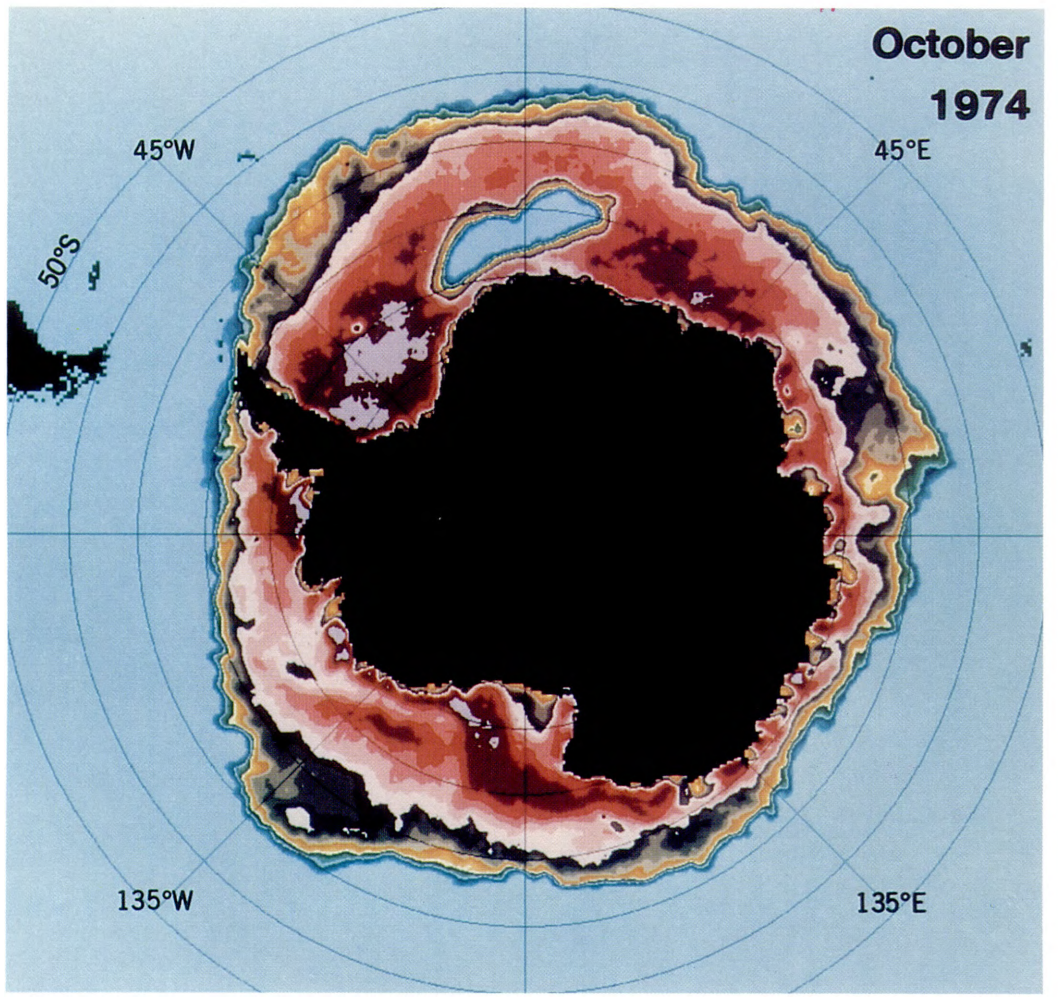

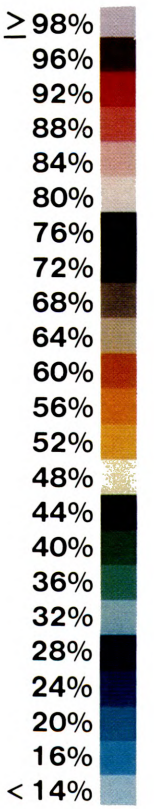

Figure 5-10a. Mean monthly sea ice concentrations for October 1973 and 1974.

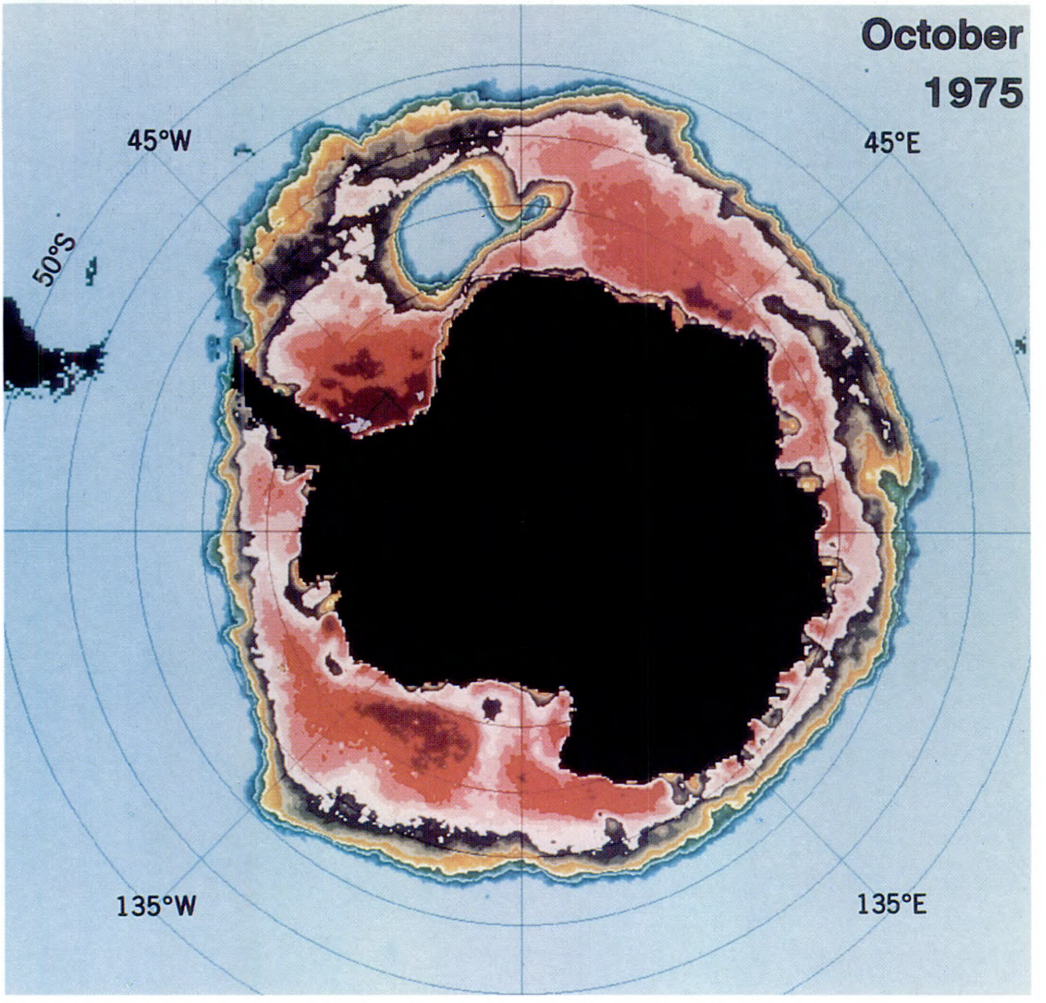

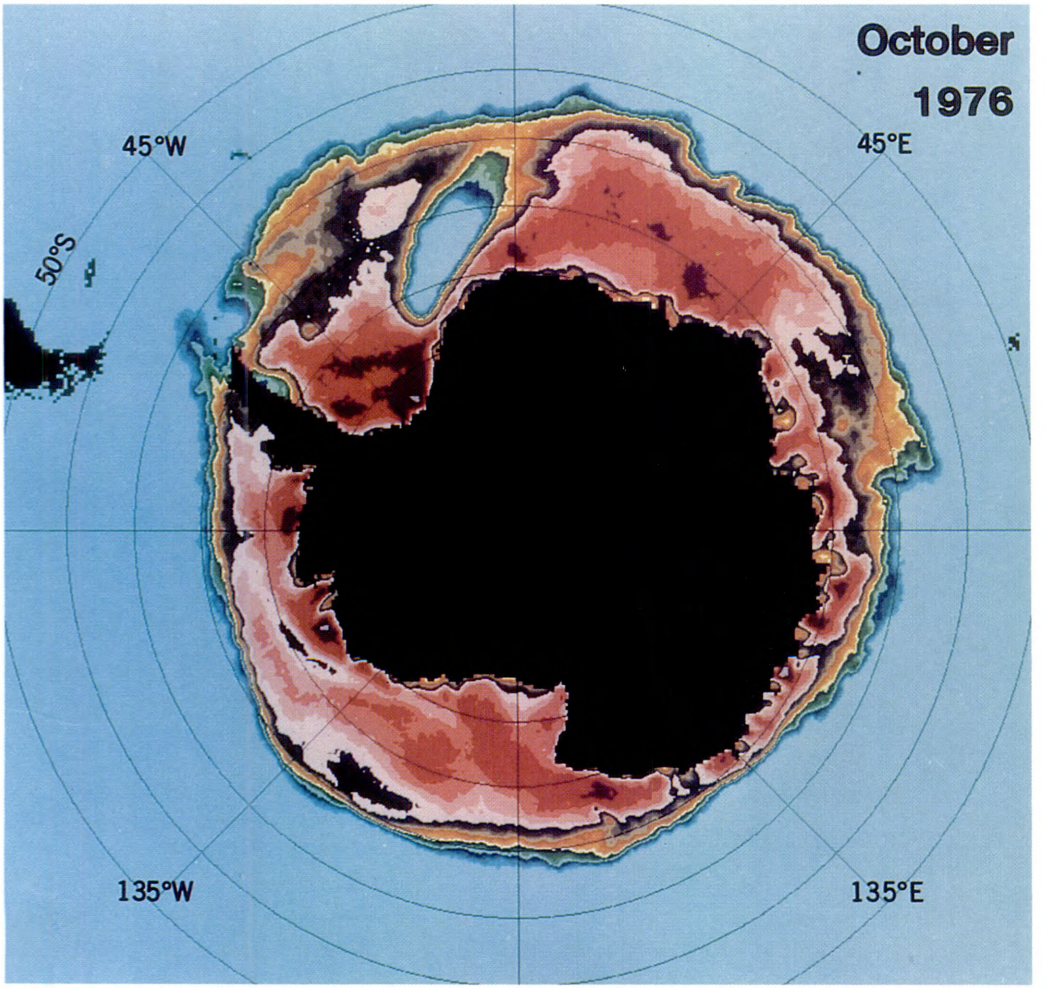

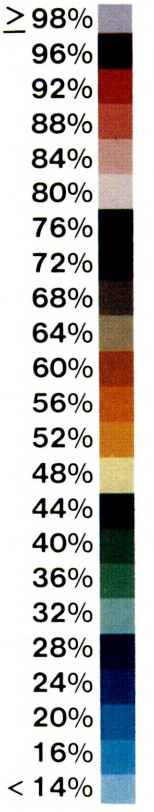

Figure 5-10b. Mean monthly sea ice concentrations for October 1975 and 1976.

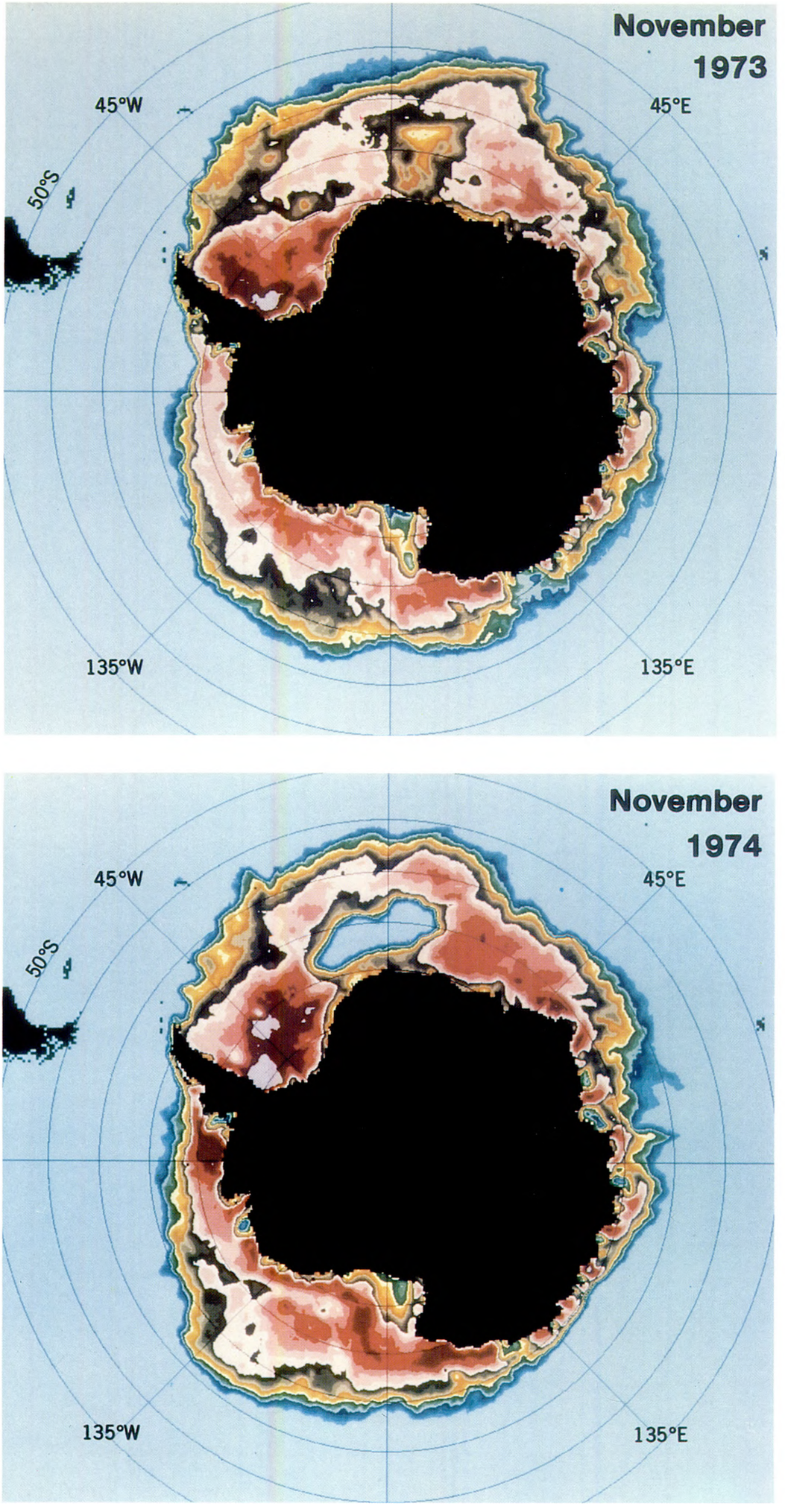

Figure 5-11a. Mean monthly sea ice concentrations for November 1973 and 1974.

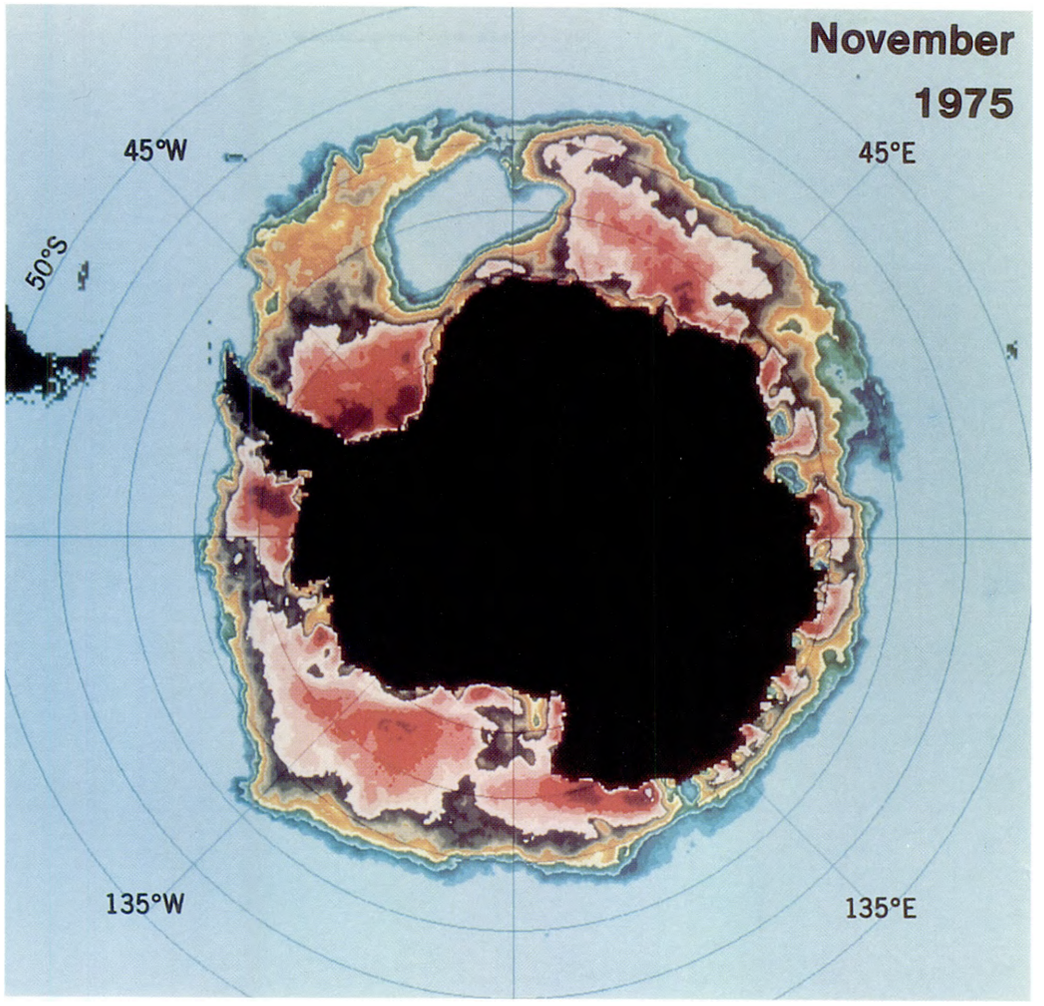

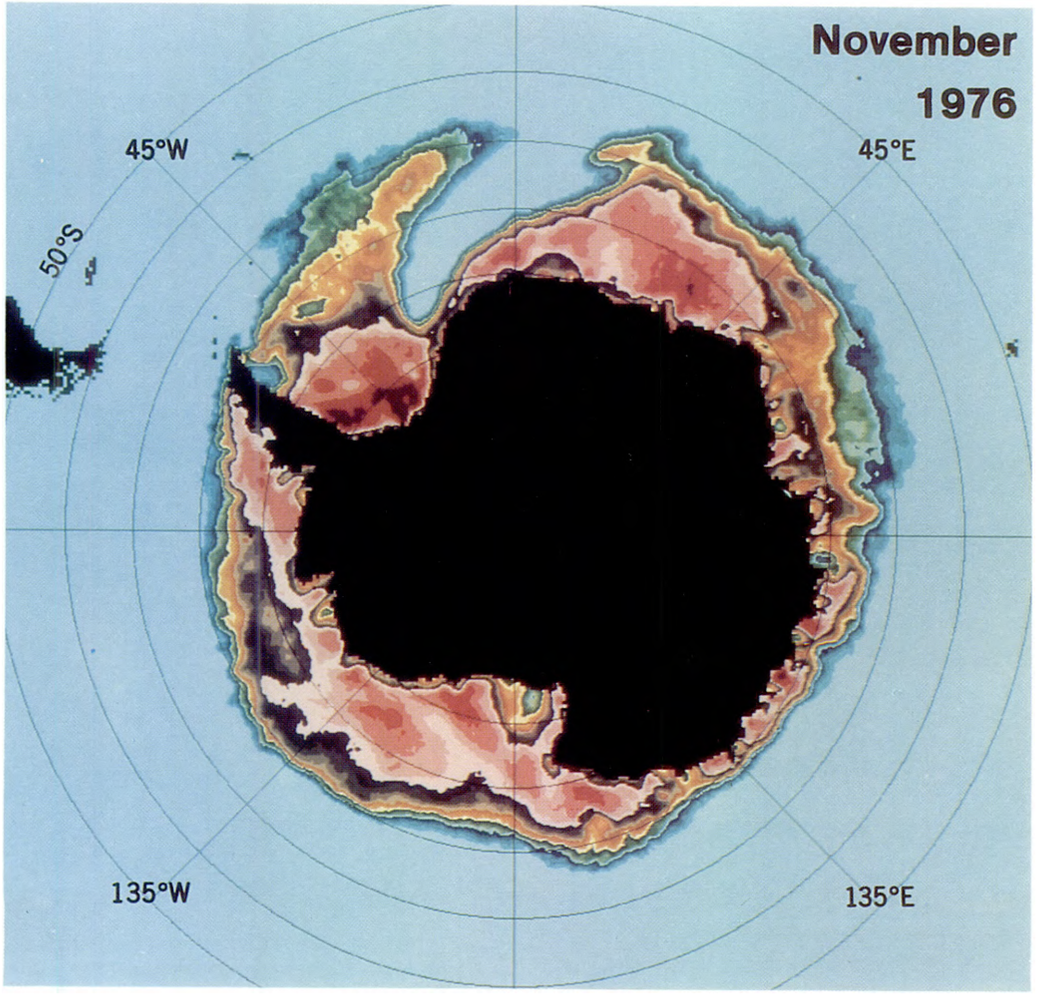

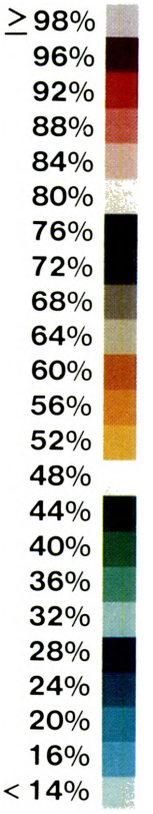

Figure 5-11b. Mean monthly sea ice concentrations for November 1975 and 1976.

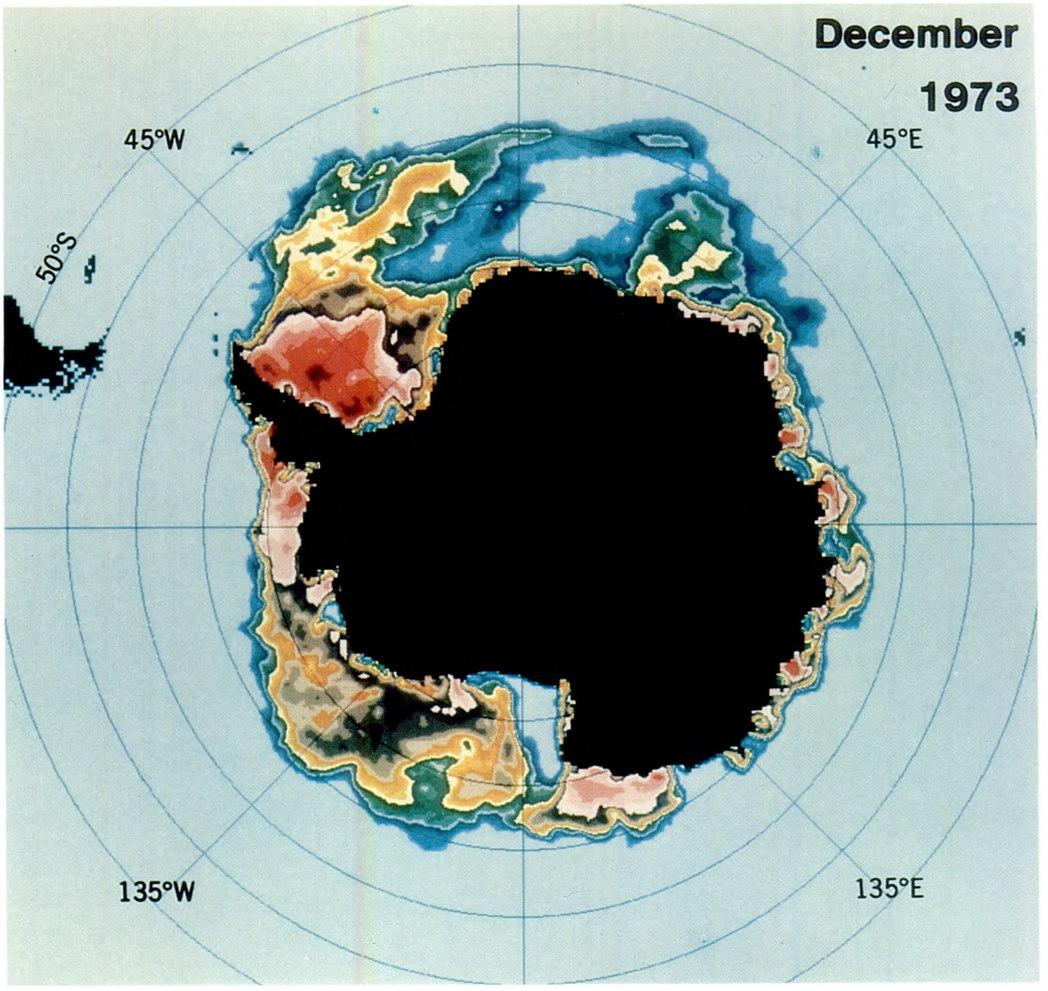

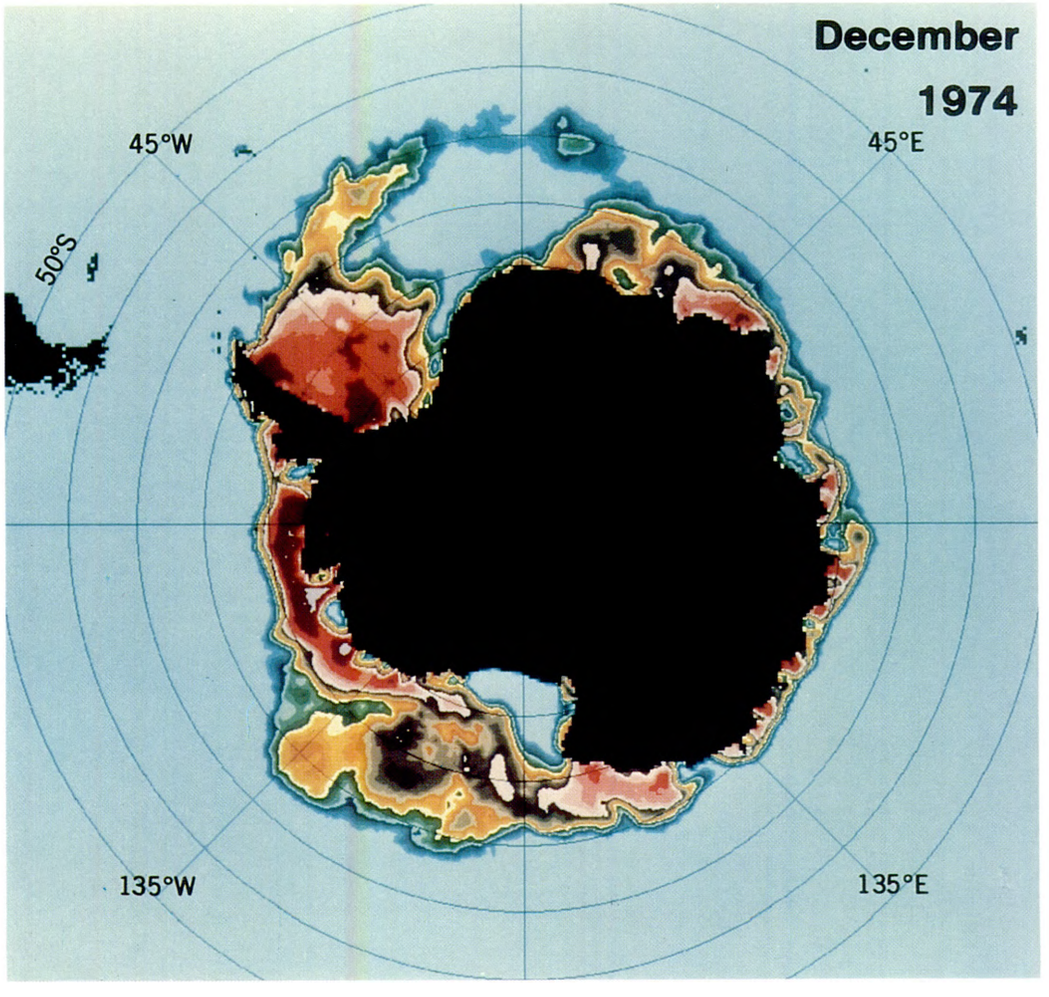

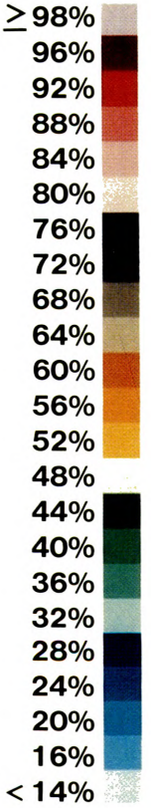

Figure 5-12a. Mean monthly sea ice concentrations for December 1973 and 1974.

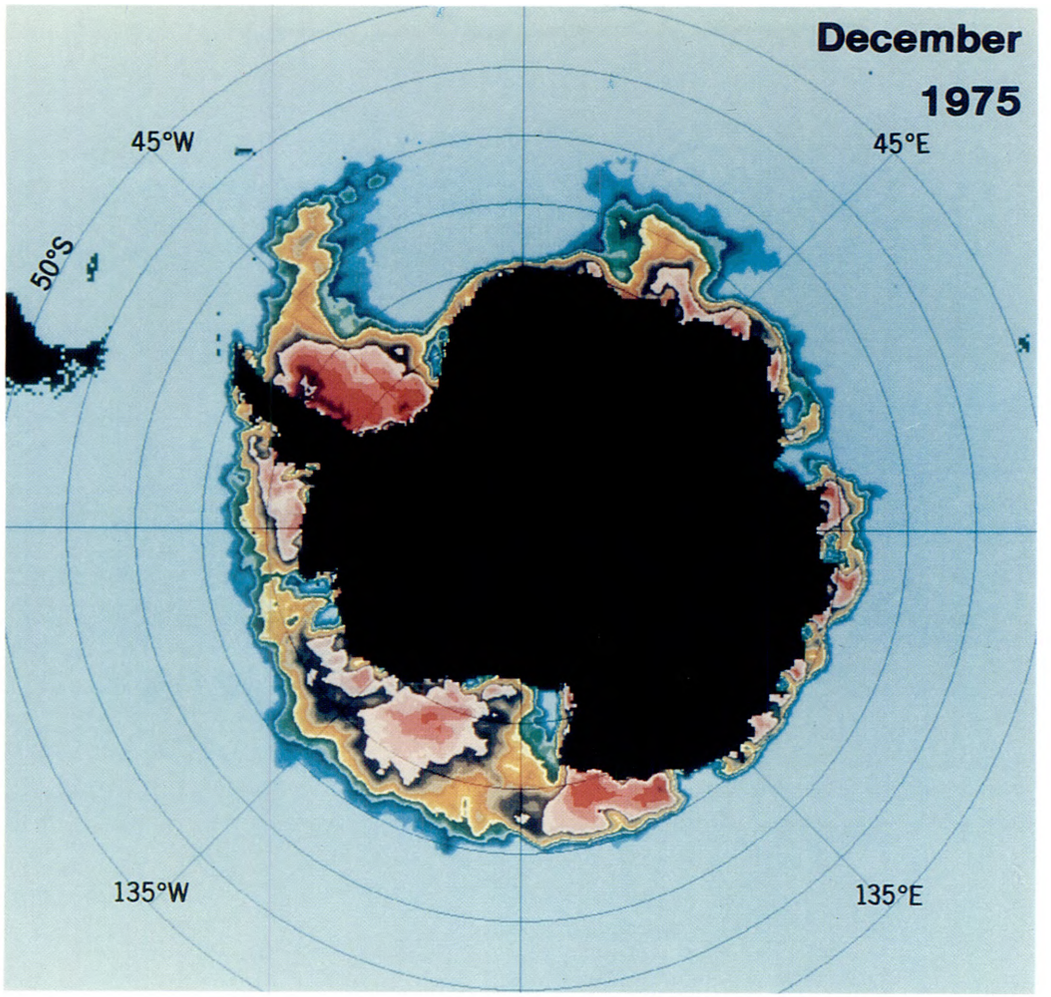

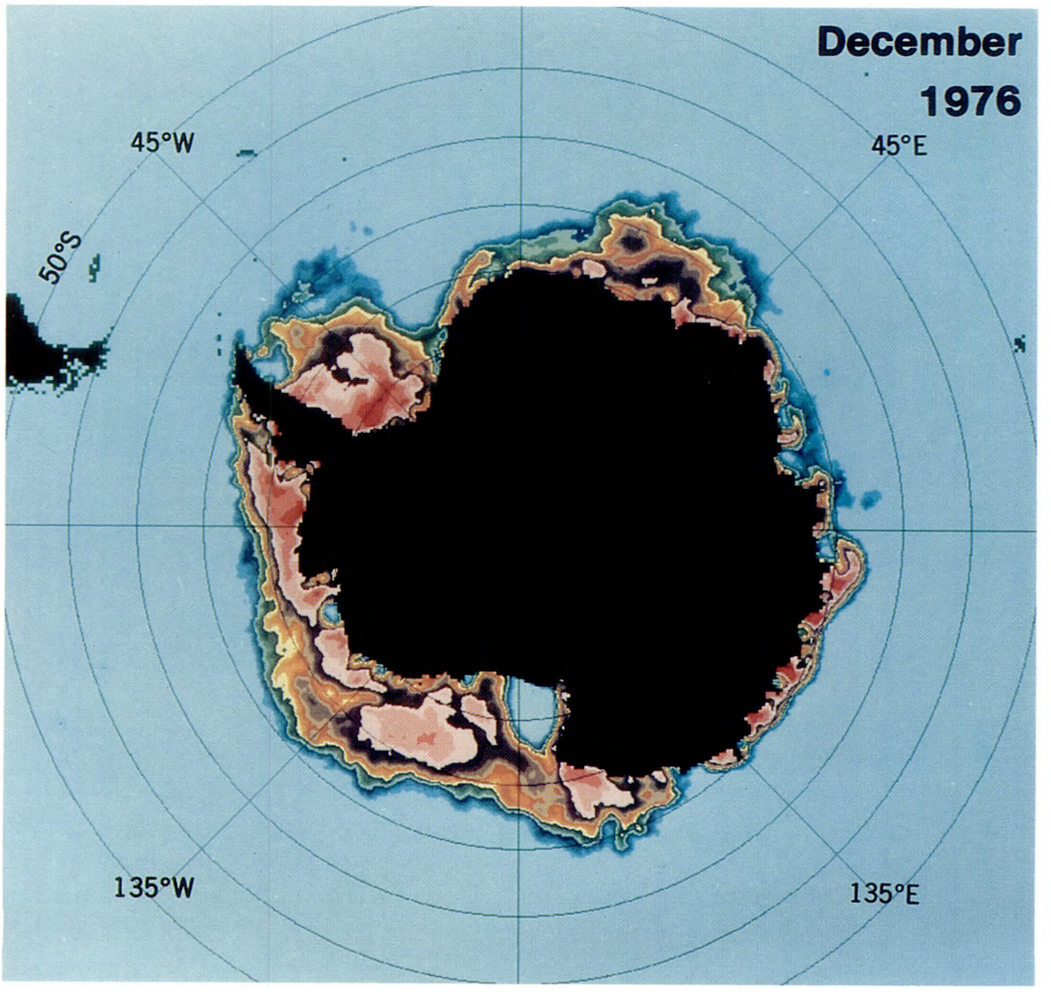

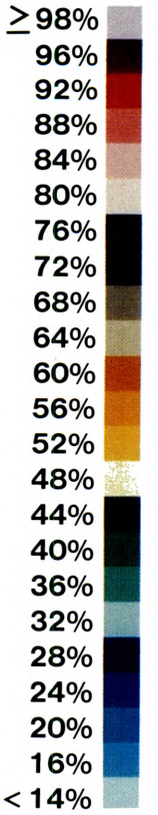

Figure 5-12b. Mean monthly sea ice concentrations for December 1975 and 1976.

other 3 years. Off the Clarie Coast (135°E) as well, the minimum ice cover again occurs in 1976. Off the remainder of East Antarctica, west of the Clarie Coast, the ice extents are comparable during the 4 years.

By November, marked retreat from the October ice margin has taken place in all 4 years, with the greatest retreat occurring in 1976 (Figure 5-11). This is particularly true in the Weddell area, where the 1976 ice concentrations also show considerable decreases and where the former polynya has become an embayment. By contrast, in the Bellingshausen Sea, retreat of the ice margin from October to November is strongest in 1973. In the Amundsen Sea, the extents are similar in all 4 years. In the Ross Sea region, the extent is least in 1976, when the margin lies near 65°S throughout and shows the least zonal variation. In the other 3 years, the ice extends northward to about 61°S in parts of this region. Immediately off the western Ross Ice Shelf, the ice concentrations are lower than in the surrounding ice pack in all 4 years, with the greatest area of such lessened concentrations occurring in 1973. Figure 5-11 shows coastal polynyas around East Antarctica, with similar patterns appearing in all 4 years, except for the absence of a polynya in 1976 in Prydz Bay near the Amery Ice Shelf. Ice extents are comparable around most of East Antarctica, although in the eastern Weddell Sea (in the vicinity of 10°E), the 4-year trend is clearly toward lesser extents.

In December, the 4-year trend toward lesser ice extents has become apparent in the western as well as the eastern Weddell Sea regions (Figure 5-12). A major coastal polynya off the Ronne Ice Shelf can be observed on the 1973 map but not on the maps for the other years. In general, during December, coastal polynyas develop in many regions around the continent. In the Amundsen Sea, polynyas are most extensive in 1975, while the ice extent is least in 1974. In the Ross Sea, the extents are least in 1976, and the polynya off the Ice Shelf is largest in 1973 and 1974. Around East Antarctica, the open-water region reaching to the coast is broader in 1973 and 1975 than in 1974 or 1976. Prydz Bay has the most open water in 1975. In the 0°E to 60°E region, the greatest extent of the ice boundary occurs in 1973, although the concentrations within the ice pack in that year are less than in the 3 later years.

For the entire southern ocean and for each of the five sectors, the area of ice cover in various concentration categories is displayed as a function of time (Figures 5-13 to 5-22). Figures 5-13 to 5-18 compare 4 years for the total southern ocean and for each sector, showing the overall seasonal progression of the sea ice cover for concentrations greater than 15-, 35-, 50-, 65-, and 85-percent concentration, and for the actual ice area (see Chapter 4). Figures 5-19 to 5-22 compare the total southern ocean and all the sectors in each year, showing the area of ice cover in concentration intervals of 15 to 35, 35 to 50, 50 to 65, 65 to 85, and 85 to 100 percent, as well as the actual ice area.

The maximum Antarctic ice extent occurs in late September or early October in 1973, but 2 to 4 weeks earlier in 1974 through 1976. The largest rate of decrease in the area of highly concentrated ice (85 to 100 percent) occurs with a dramatic 1-month decay of 7×10^6 square kilometers from October to November of 1973. Slower 2-month decreases of slightly less total magnitude occur from October to December of 1974 and from September to November of 1975 and 1976. These decreases in highly concentrated ice area precede by about 1 month the largest rates of decrease in total ice extent. The curves for ice cover of at least 35-, 50-, and 65-percent concentration consistently follow the ice-extent curve (15 to 100 percent) more closely than they follow the curve for highly concentrated (85 to 100 percent) ice. The sharp reduction of highly concentrated ice from September to November in 1975 and 1976 (Figure 5-13) could be due to an increase in ice divergence, melting, or, more likely, to a decrease in ice production in newly formed leads. Similarly, the September dip in the amount of highly concentrated ice in 1973 is probably the result of a divergent field of motion that mainly relocated the existent ice. In 1974, however, the fact that both the actual ice area and the high concentration ice area decreased from August to September suggests that in that year the actual amount of ice did decrease between those 2 months. Most of this September dip occurred in the Ross Sea (Figure 5-16). An examination of the individual 3-day maps, as well as the monthly concentration maps (Figures 5-8 and 5-9), reveals that the ice-cover decrease was predominantly in the northeast portion of the Ross Sea (58°S to 65°S, 150°W), where a prominent bulge in ice extent usually peaks in early September and then retreats.

Of the five sectors, the Weddell Sea contains the largest areal extent of sea ice. Roughly one third of

the southern ocean sea ice area is within this region, and not surprisingly, Weddell Sea ice cover also reaches a peak in September and descends to a minimum in February. The September maximum ice cover in the Weddell Sea is greatest in 1973 and least in 1976, although the 1975 peak is slightly above that of 1974. In the eastern portion of the Weddell Sea, the Weddell polynya exists from July through November in 1974, 1975, and 1976. Over the 3-year period 1974 through 1976, its position shifts noticeably westward. Although the polynya is approximately 300 by 1000 kilometers, it accounts for less than one half the decrease in ice cover, the remainder being accounted for by a lesser equatorward extent of the outer ice edge. In 1973, the ice extended to 54°S at the Greenwich meridian, whereas in the succeeding 3 years, the extent was to 55.5°S, 55.5°S, and 58°S, successively.

Although the Weddell polynya was not known as a persistent winter feature until its appearance on the ESMR images in the winter of 1974, the

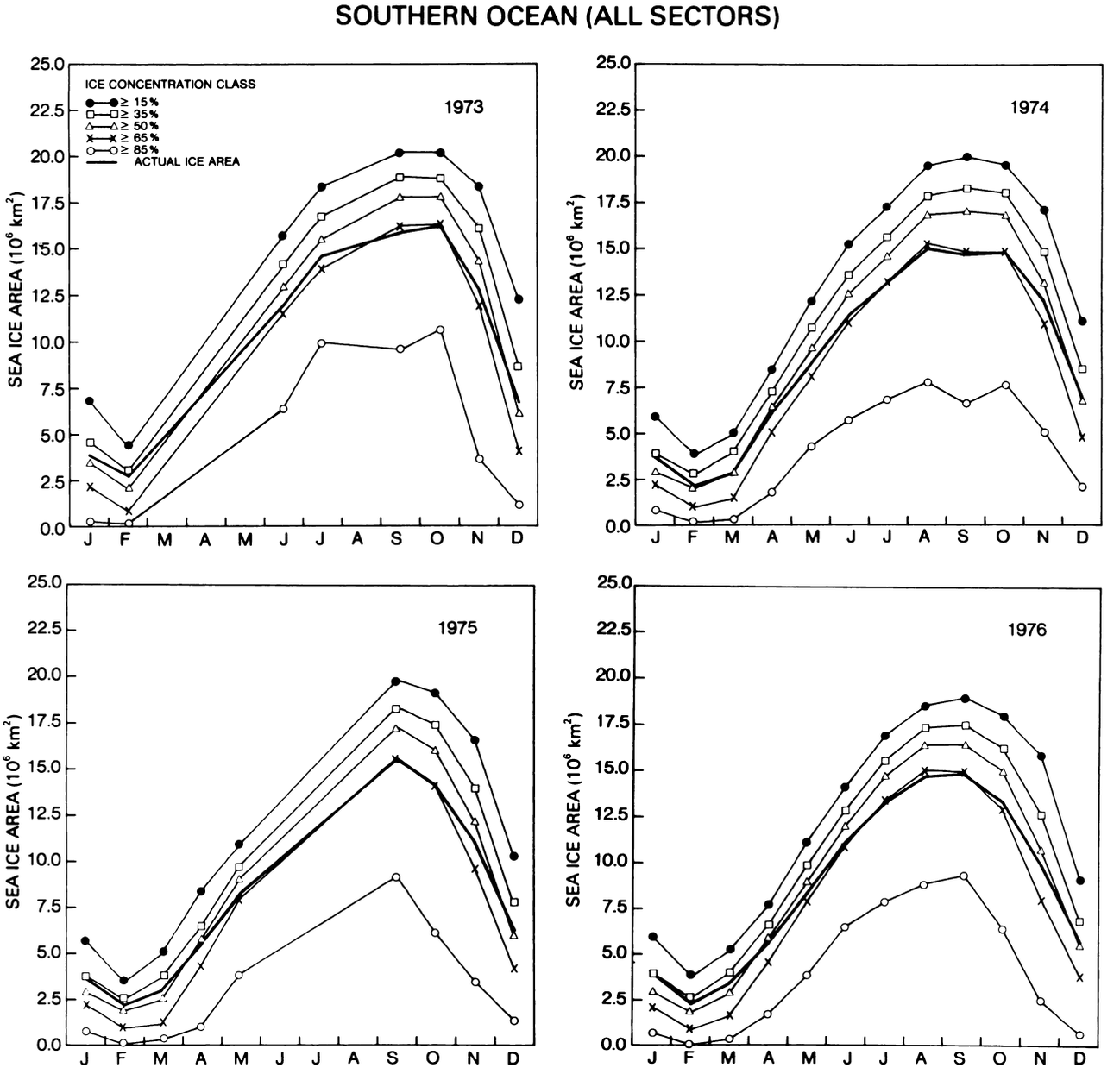

Figure 5-13. Yearly cycle of the ocean area covered by sea ice with concentration ≥15 (ice extent), ≥35, ≥50, ≥65, and ≥85 percent and yearly cycle of the actual ice area, for the total southern ocean in 1973, 1974, 1975, and 1976. The actual ice area is the total ocean surface covered by sea ice, excluding all open leads and polynyas within the ice pack.

closely connected phenomenon of an arm of ice sweeping meridionally from the northwestern Weddell to the northeastern Weddell had been well documented earlier, notably in the Soviet *Atlas of the Antarctic* (Tolstikov, 1966). The occurrence and growth of this huge arm of ice is quite noticeable in the 1974 monthly sequence. The ice front advances almost 700 kilometers from April to May and then continues sweeping eastward over the latitude band 57°S to 65°S until, by July and August, it has closed off the open-water region to the south, thereby forming the polynya. Similarly, an early spring opening in the region of the polynya was also known to occur (Streten, 1973). In 1973, when the Weddell polynya did not occur, reduced ice concentration is observed in the region of 5°E and 64°S throughout much of the winter, suggesting that, although the large-scale persistent polynya did not occur in 1973, there may have been a number of small short-duration polynyas in the region.

Although no explanation of the polynya is generally accepted, Zwally et al. (1976) noted that the

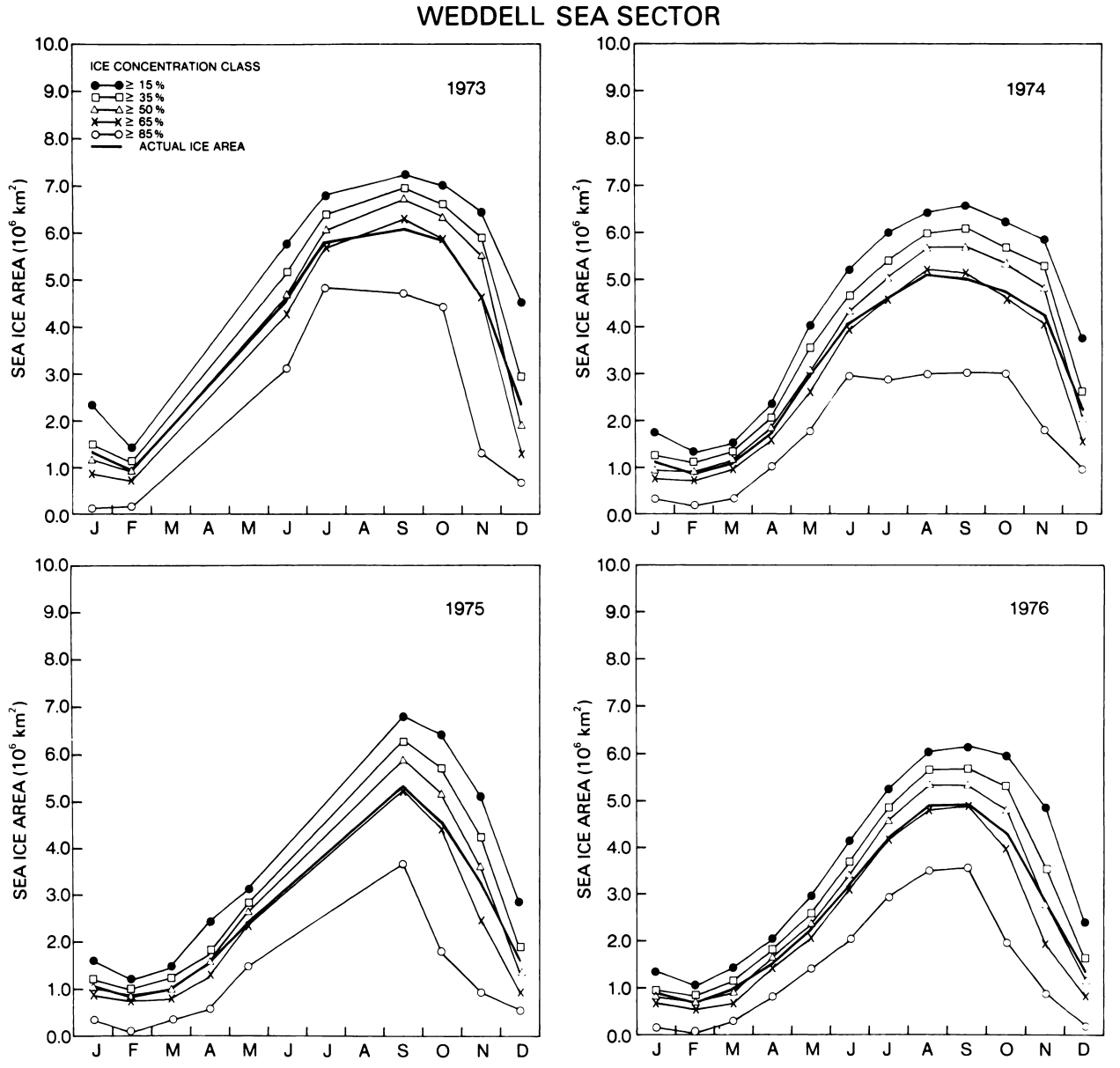

Figure 5-14. Yearly cycle of the ocean area covered by sea ice with concentration ≥15 (ice extent), ≥35, ≥50, ≥65, and ≥85 percent and yearly cycle of the actual ice area, for the Weddell Sea sector in 1973, 1974, 1975, and 1976. The actual ice area is the total ocean surface covered by sea ice, excluding all open leads and polynyas within the ice pack.

polynya lies in the region of the Antarctic divergence (Figures 2-2 and 2-4) and the circumpolar pressure trough (Figure 2-5) and suggested that intensified oceanic upwelling supplies the heat to maintain the open polynya. Martinson et al. (1981), considering various oceanographic mechanisms for polynya formation, suggested that a shallow pycnocline, regionally preconditioned in some manner, allows convective overturning driven by surface cooling and salt ejection during freezing to bring warm salty water to the surface to inhibit ice formation. Recent sea ice modeling experiments show that the wind fields in the vicinity of the persistent low at 0°E (Figure 2-5) may play a crucial role in polynya formation (Parkinson, 1983).

As with the Ross Sea to the west, the Bellingshausen-Amundsen Seas show a highly variable cycle of sea ice over the 4 years (Figures 5-15 and

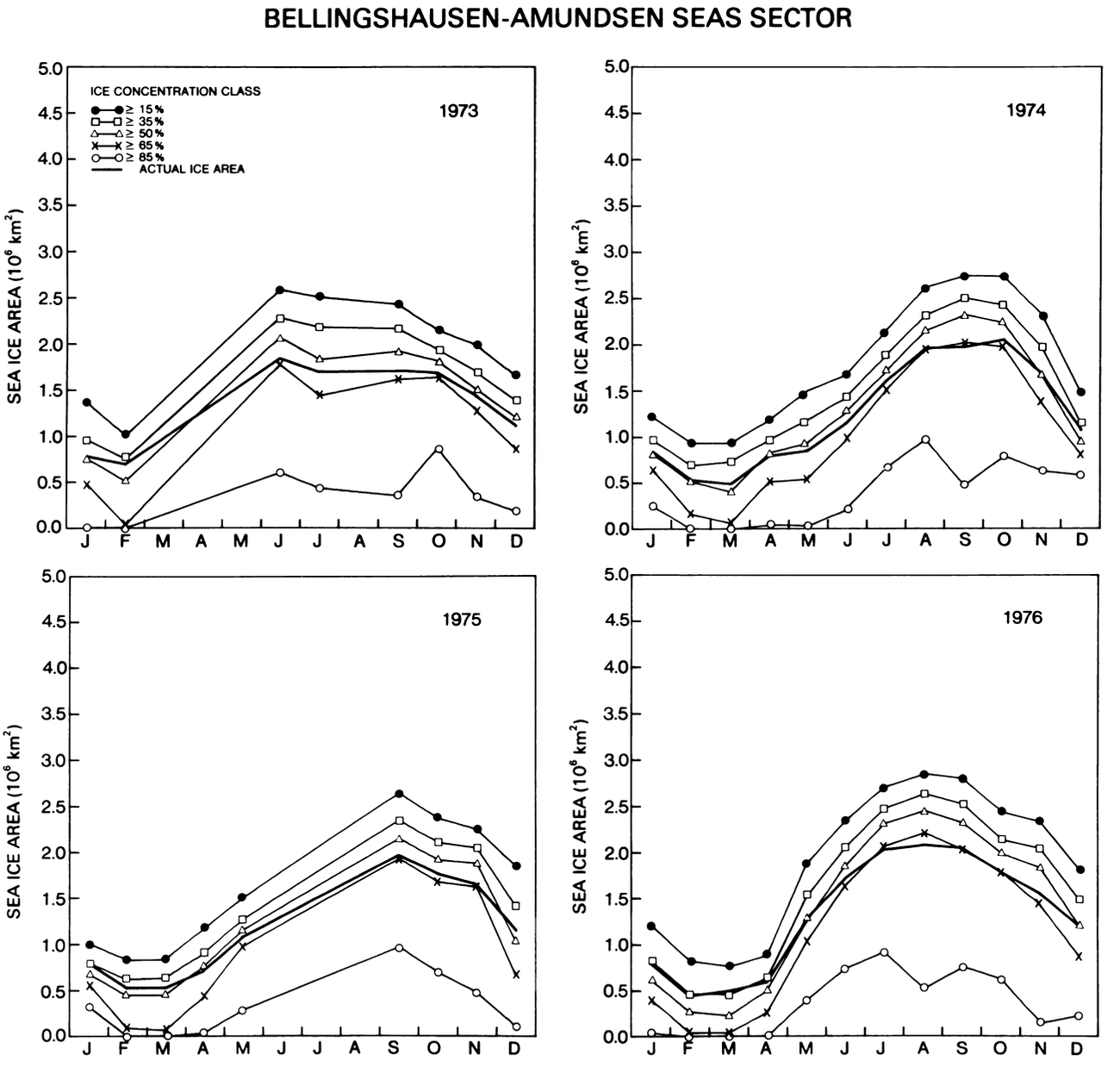

Figure 5-15. Yearly cycle of the ocean area covered by sea ice with concentration ≥15 (ice extent), ≥35, ≥50, ≥65, and ≥85 percent and yearly cycle of the actual ice area, for the Bellingshausen-Amundsen Seas sector in 1973, 1974, 1975, and 1976. The actual ice area is the total ocean surface covered by sea ice, excluding all open leads and polynyas within the ice pack.

5-16) with changes that may be interrelated. In the years 1973 and 1976, when the ice in the Bellingshausen-Amundsen Seas sector grows to near maximum coverage early in the season, the growth in the Ross Sea is slower, and conversely, in the years 1974 and 1975, when the early season growth is slower in the Bellingshausen-Amundsen Seas, it is more rapid in the Ross Sea. Both differences in ice transport and differences in freezing rates caused by interannual changes in the wind fields may play a role in the variations in these yearly cycles. Interannual variations in the yearly cycle are described further in Section 5.4.

5.3 MONTH-TO-MONTH CHANGES

Certain aspects of the annual cycles are brought into sharper focus by the maps of monthly differences (Figures 5-23 through 5-26). These show the growth (gray, green, and blue regions) and

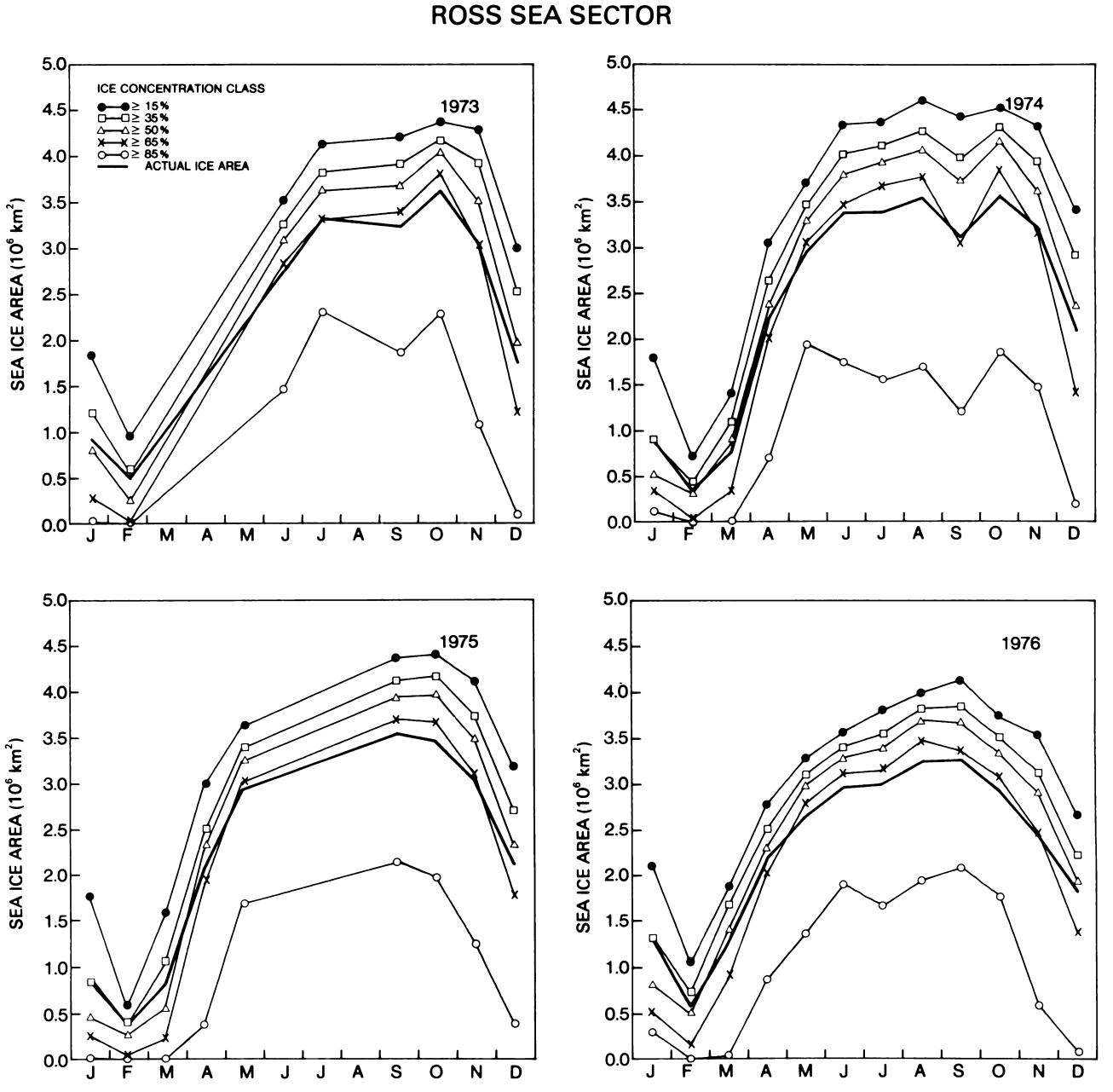

Figure 5-16. Yearly cycle of the ocean area covered by sea ice with concentration ≥15 (ice extent), ≥35, ≥50, ≥65, and ≥85 percent and yearly cycle of the actual ice area, for the Ross Sea sector in 1973, 1974, 1975, and 1976. The actual ice area is the total ocean surface covered by sea ice, excluding all open leads and polynyas within the ice pack.

decay (yellow, purple, and red regions) of the ice pack from one month to the next. Although these maps are simply differences of the monthly images already discussed (Figures 5-1 through 5-12), they present information on the growth/decay cycle that is not obvious in the other images. The discussion here highlights a few specifics to illustrate the usefulness of the difference maps.

From January to February (Figures 5-23a, 5-24a, 5-25a, and 5-26a) of each of the 4 years, the ice decay is significant. Although each year has substantial overall ice decay at this time, the largest region of decay exceeding 50-percent concentration decrease is located in the eastern Ross Sea in 1973. Each year does have a few scattered regions with ice concentration increases, generally

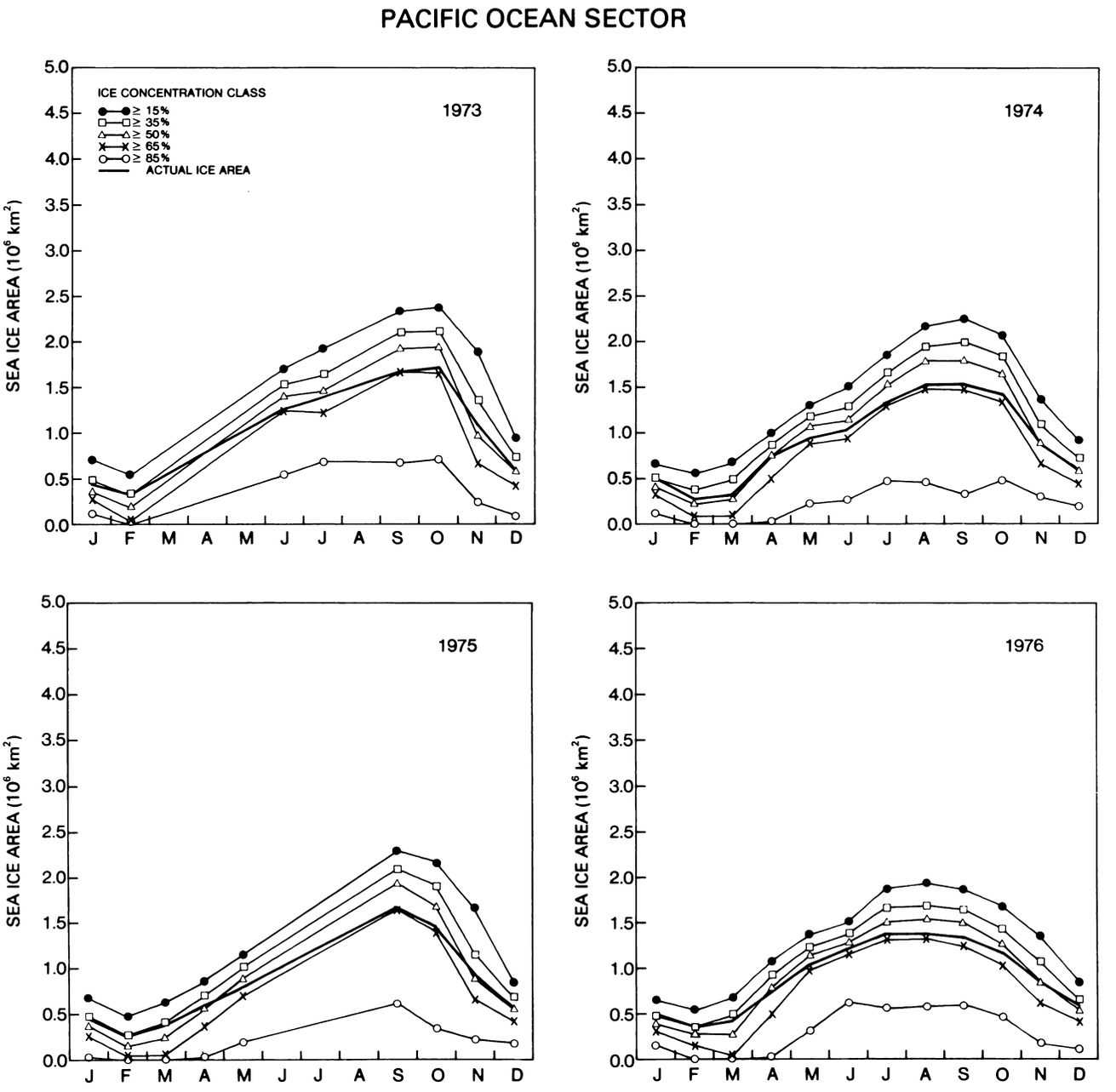

Figure 5-17. Yearly cycle of the ocean area covered by sea ice with concentration ≥15 (ice extent), ≥35, ≥50, ≥65, and ≥85 percent and yearly cycle of the actual ice area, for the Pacific Ocean sector in 1973, 1974, 1975, and 1976. The actual ice area is the total ocean surface covered by sea ice, excluding all open leads and polynyas within the ice pack.

along the coast. From February to March (Figures 5-24a, 5-25a, and 5-26a), some regions show continued ice decay, although the growth season has begun in most areas. Because late February tends to be the time of minimum Antarctic ice cover, the finding of some regions with growth and some regions with decay between February and March is not unexpected. The region with the heaviest ice-cover change is the Ross Sea in 1976, with much of the central Ross Sea experiencing greater than 50-percent increase in ice concentration (Figure 5-26a).

From March to April (Figures 5-24a, 5-25a, and 5-26a), almost the entire sea ice region is undergoing ice concentration increases. Some of the decreases apparent in a few small areas may be due to ice divergence and advection into adjacent areas.

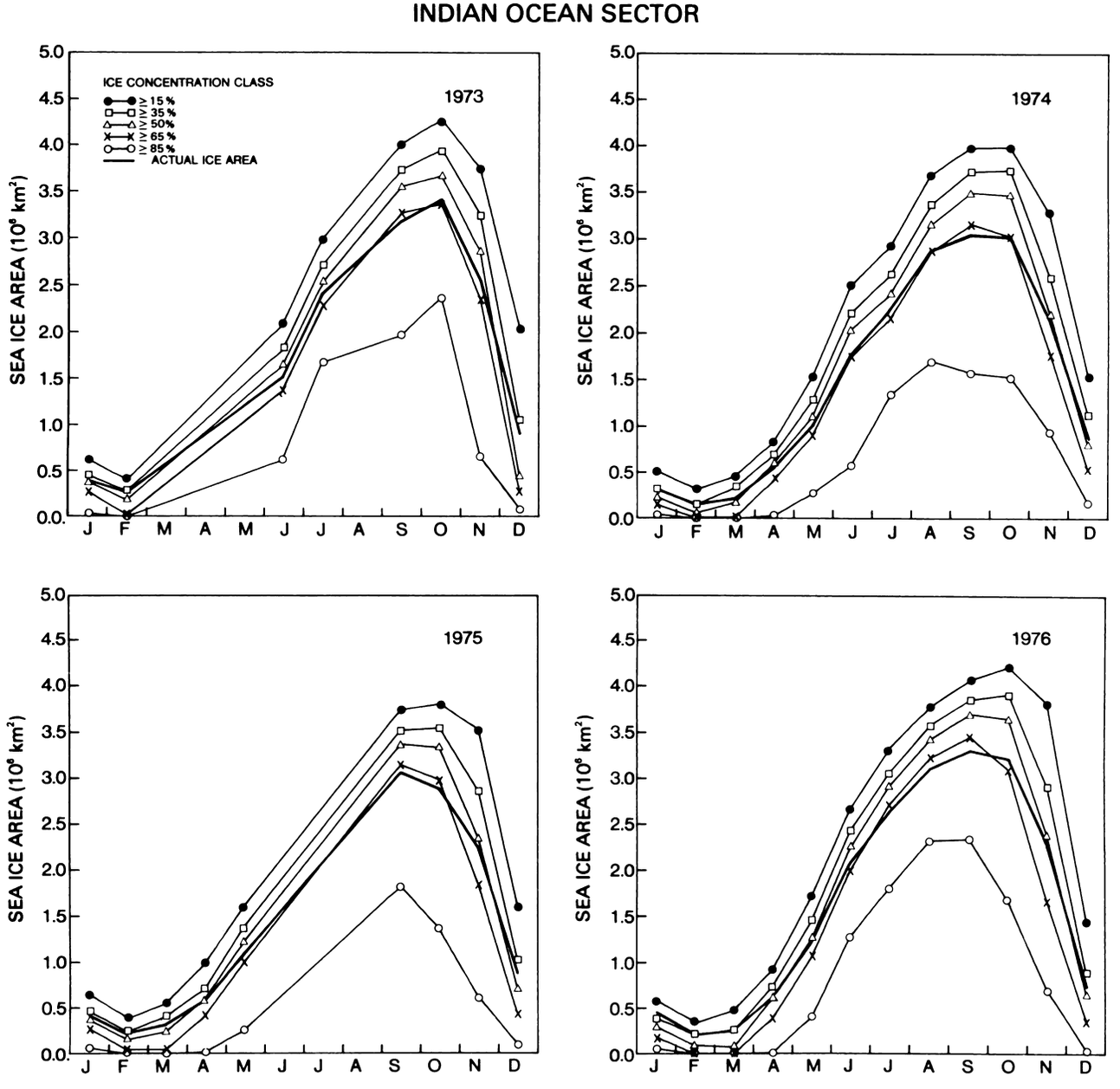

Figure 5-18. Yearly cycle of the ocean area covered by sea ice with concentration ≥15 (ice extent), ≥35, ≥50, ≥65, and ≥85 percent and yearly cycle of the actual ice area, for the Indian Ocean sector in 1973, 1974, 1975, and 1976. The actual ice area is the total ocean surface covered by sea ice, excluding all open leads and polynyas within the ice pack.

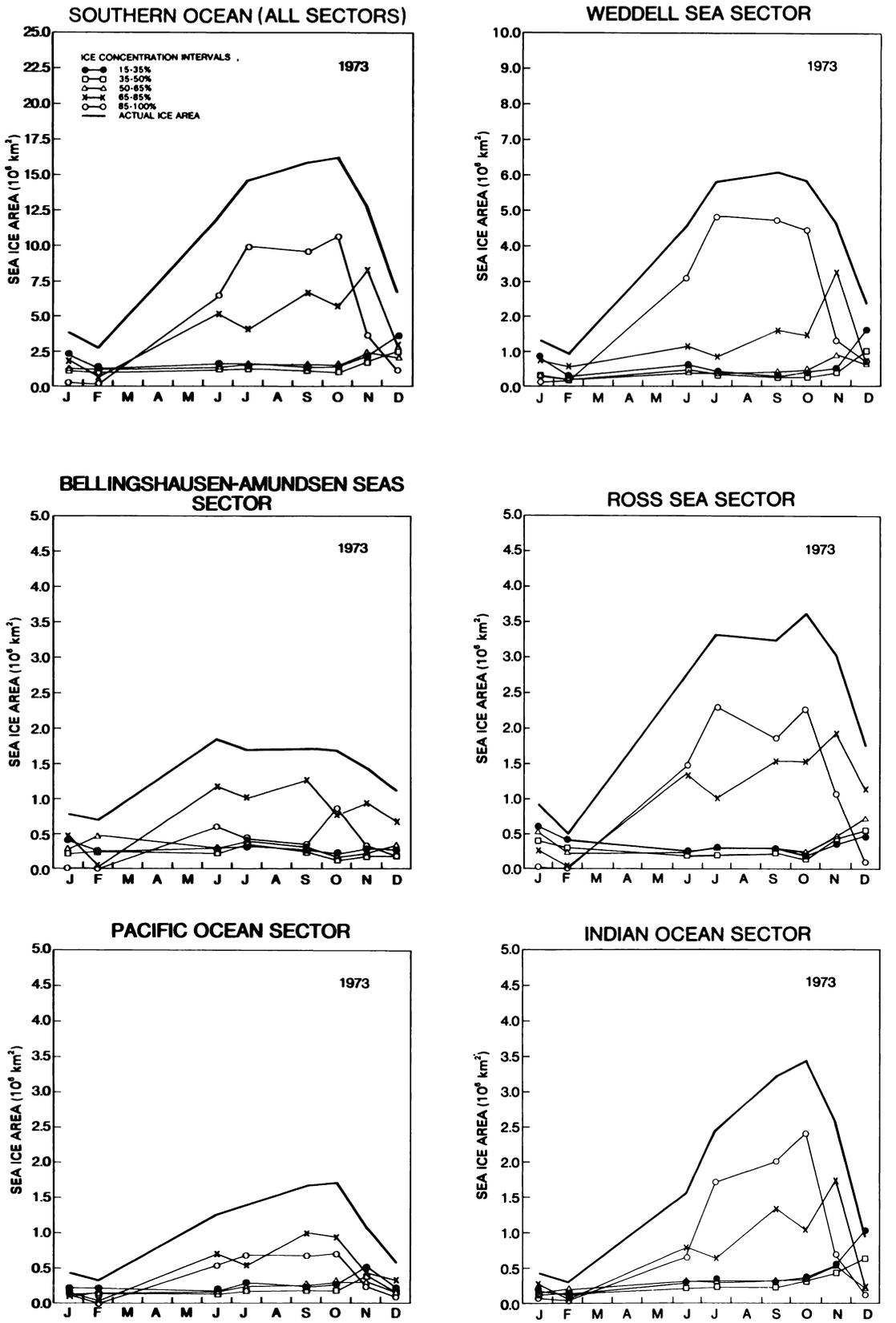

Figure 5-19. Yearly cycle (for 1973) of the ocean area covered by sea ice within ice concentration intervals 15 to 35, 35 to 50, 50 to 65, 65 to 85, 85 to 100 percent and yearly cycle of the actual ice area, for the total southern ocean and for each sector.

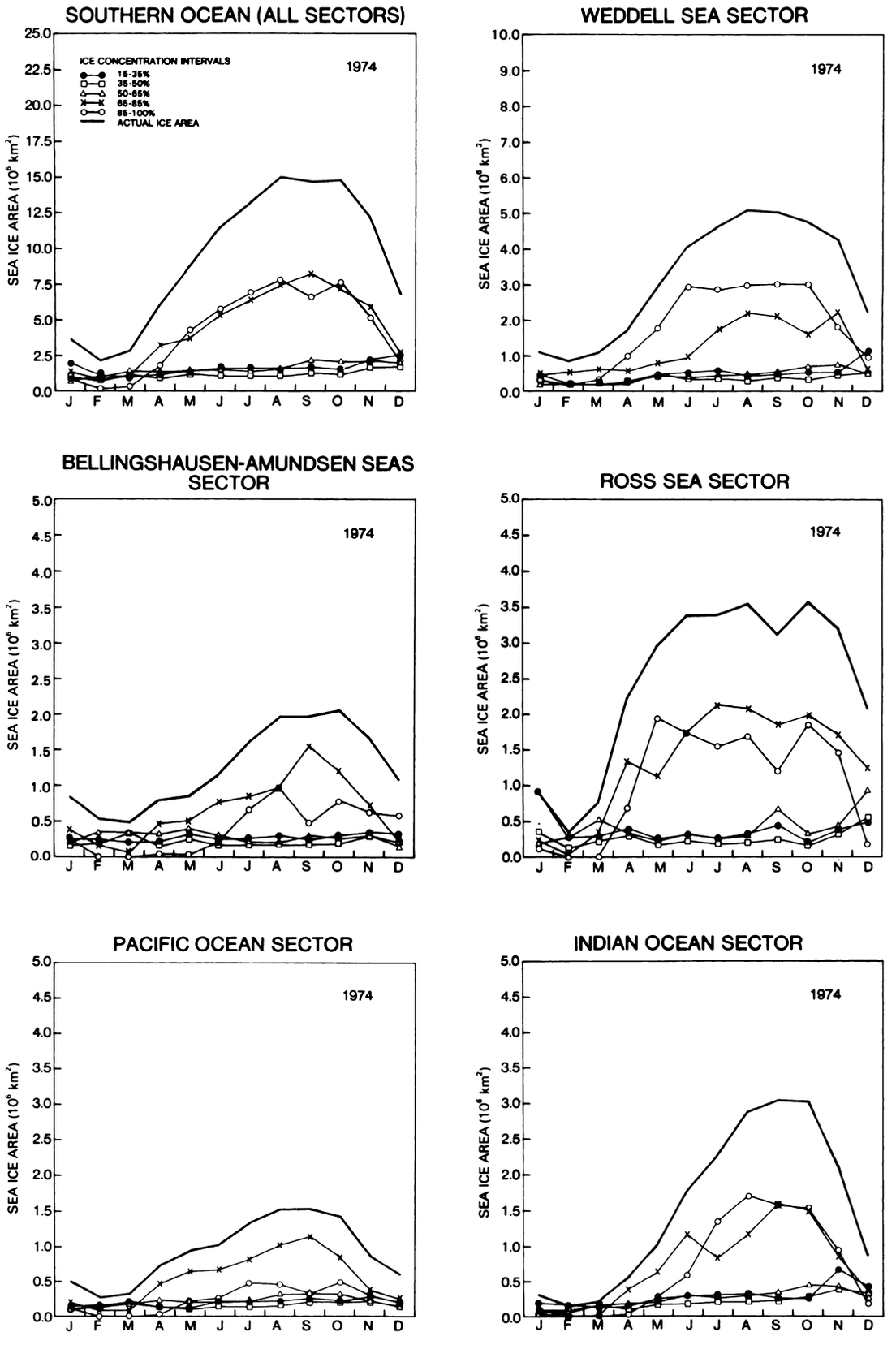

Figure 5-20. Yearly cycle (for 1974) of the ocean area covered by sea ice within ice concentration intervals 15 to 35, 35 to 50, 50 to 65, 65 to 85, 85 to 100 percent and yearly cycle of the actual ice area, for the total southern ocean and for each sector.

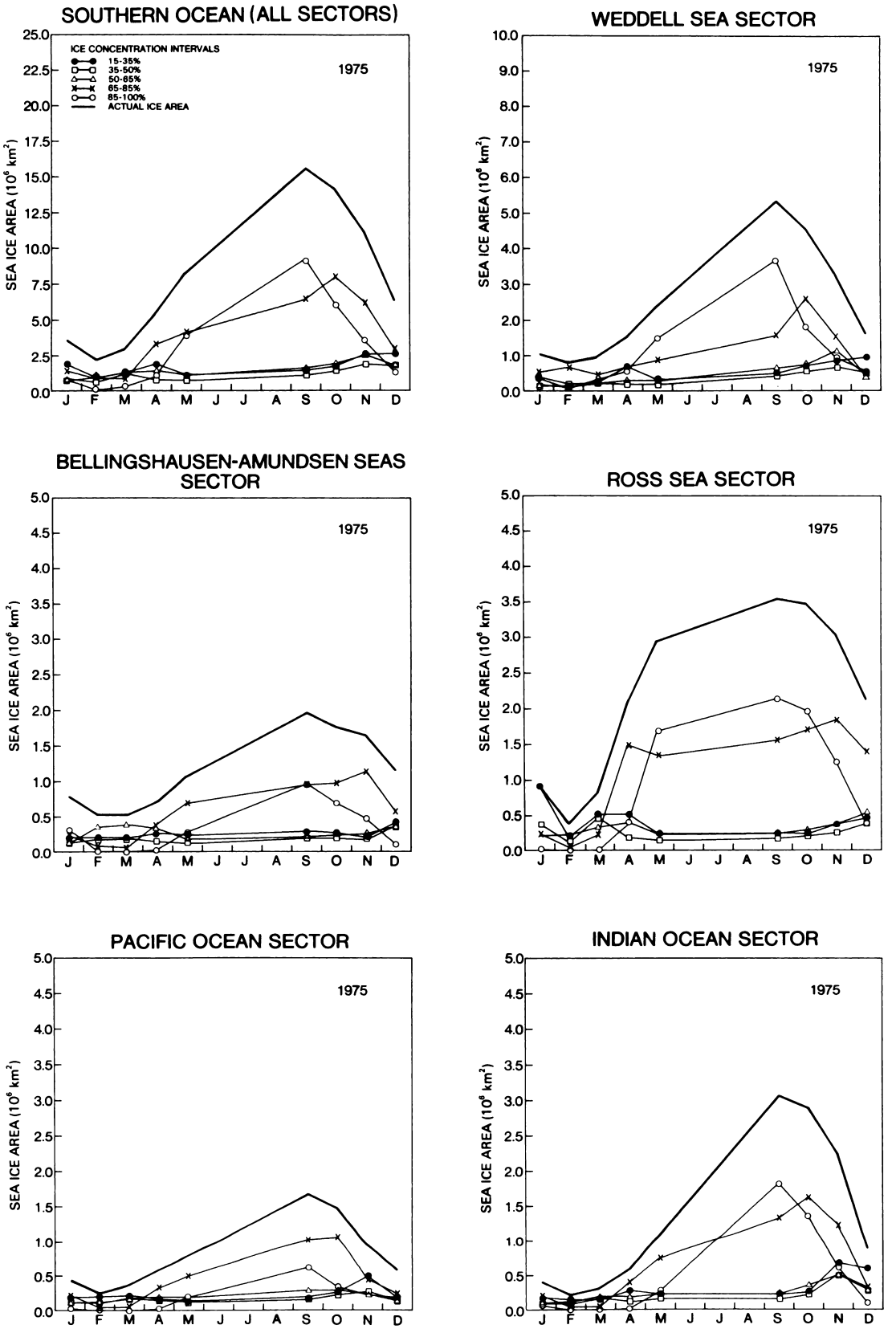

Figure 5-21. Yearly cycle (for 1975) of the ocean area covered by sea ice within ice concentration intervals 15 to 35, 35 to 50, 50 to 65, 65 to 85, 85 to 100 percent and yearly cycle of the actual ice area, for the total southern ocean and for each sector.

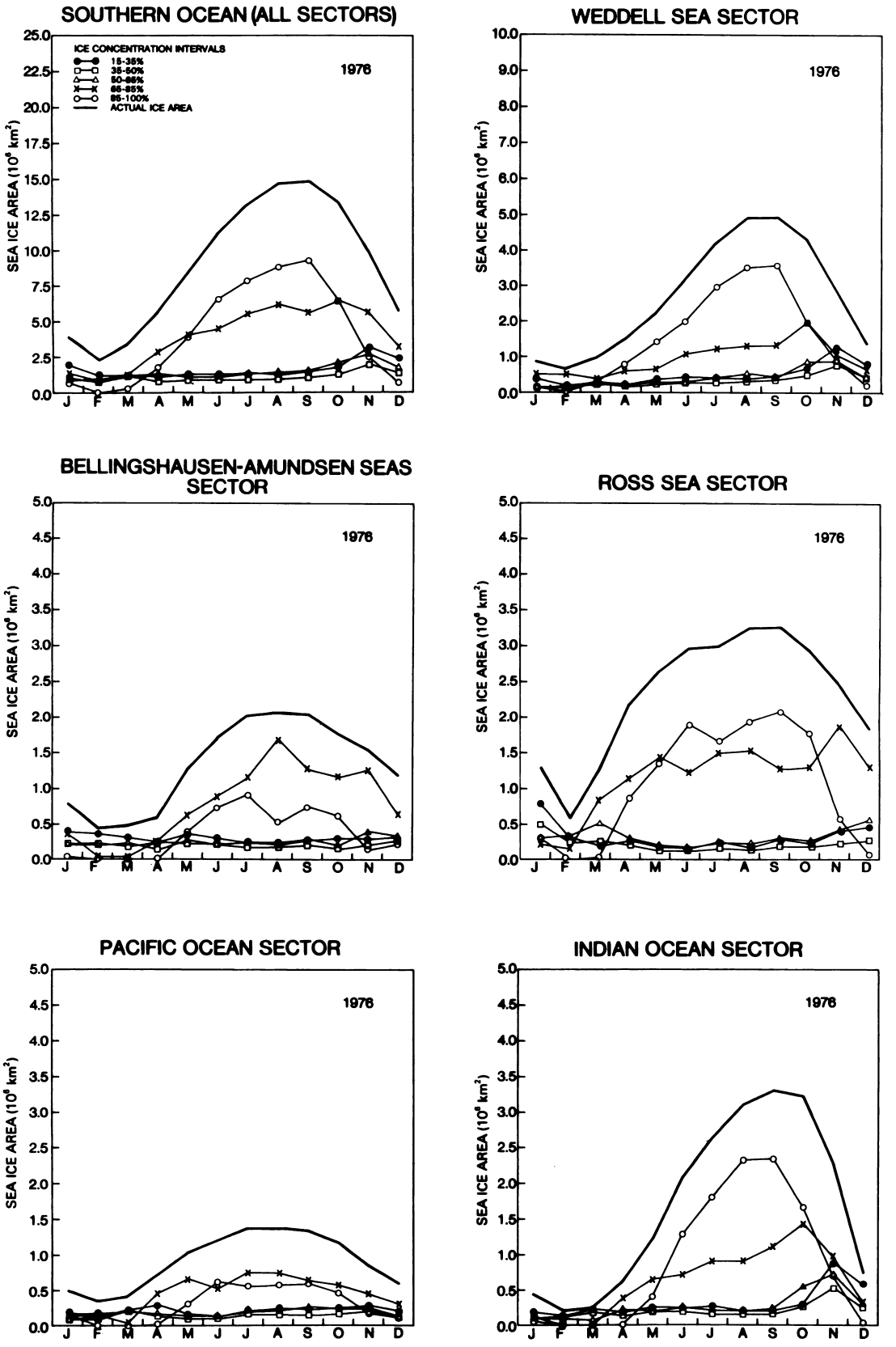

Figure 5-22. Yearly cycle (for 1976) of the ocean area covered by sea ice within ice concentration intervals 15 to 35, 35 to 50, 50 to 65, 65 to 85, 85 to 100 percent and yearly cycle of the actual ice area, for the total southern ocean and for each sector.

The same general pattern of ice growth predominates from April to May, although in the Amundsen Sea in 1974 the growth is slower and there is also a region of ice concentration decrease.

From May to June, the 2 years with available data (1974 and 1976) have continued ice growth throughout most of the Antarctic region (Figures 5-24a and 5-26a), particularly in the Weddell Sea and Indian Ocean sectors. Although there are some sizable areas of ice decay, most ice concentration decreases at this time are less than 20 percent.

From June to July (Figures 5-23a, 5-24a, and 5-26a), the regions of ice decay are much larger and more intense, although the bulk of the southern ocean continues to have increasing ice concentrations. This interesting and unexpected phenomenon of very large regions of ice concentration decreases in the midst of the growth season is one of the prime features readily visible in these monthly change maps. Among the largest such regions of ice concentration decreases are those in the Bellingshausen Sea and off the George V Coast (150°E) during 1973 and those in the northeastern Ross Sea and northwestern Weddell Sea in 1974.

Growth continues from July to August (Figures 5-24b and 5-26b), especially at the ice edge, although there is also a small amount of ice decay both in the inner pack and at the edge. In the inner pack, the most intense decay occurs because of the westward movement of the Weddell polynya in both 1974 and 1976. At the ice edge, the largest expanse of ice concentration decrease is in the western Ross Sea during 1974 and 40 degrees westward off the Adelie and Clarie Coasts during 1976.

The August to September interval (Figures 5-24b and 5-26b) includes the time of maximum ice extent. Hence, in this transition, as in the transition from February to March, large areas of decay occur coincident with large areas of growth. In 1974, the remaining ice growth is predominantly at the ice edge, with substantial decay along the ice edge in the Ross Sea and the westward edge of the westward-moving Weddell polynya. A southwestward movement of the polynya is apparent in 1976, as are the alternating regions of concentration increases and decreases along the ice edge.

The September to October transition (Figures 5-23b, 5-24b, 5-25b, and 5-26b) also shows large regions of growth and large regions of decay. A very interesting contrast during these months is that the continuing growth is significantly greater in the 2 earlier years, whereas the decay season has much more completely taken over in both 1975 and 1976.

By October to November (Figures 5-23b, 5-24b, 5-25b, and 5-26b), wide-scale decay predominates with only minor regions of ice concentration increases. Similarly, from November to December (Figures 5-23b, 5-24b, 5-25b, and 5-26b), ice-cover decay predominates, whereas from December to January (Figures 5-23b, 5-24b, and 5-25b), some regions of ice increase appear along the coast, and from December 1974 to January 1975 in particular, ice growth appears off the northeast promontory of the Antarctic Peninsula.

5.4 INTERANNUAL VARIATIONS IN ICE COVER, OPEN WATER, AND MEAN ICE CONCENTRATION

The interannual variations in ice extent, actual ice area, and open water within the pack are displayed in Figures 5-27 through 5-32. The open-water area is the difference between the ice extent (ocean area with at least 15-percent sea ice cover) and the actual ice area (spatially integrated ice concentration). Open water within the regions covered by less than 15-percent ice is not included. The mean ice concentration in Figure 5-33 is the actual ice area divided by the total ice extent. Any two of these four parameters are sufficient to describe the area of ice coverage and its compactness.

The annual cycle of open water clearly differs from the annual cycles of ice extent and actual ice area. Typically, the area of open water increases linearly for about 9 months from February to November and then decreases sharply, although there is considerable monthly variation about the mean behavior. The effects of the open water on the ocean-atmosphere heat flux and the south polar energy balance have been considered by Allison et al. (1982), Gordon (1981), and Weller (1980). The open water in winter is particularly important because of the much larger ocean-atmosphere heat and moisture fluxes over open water compared to sea ice. During the growth season, the total open-water area within the ice pack naturally increases as the increase in total ice extent expands the region in which open water can occur. The amount of open water is also related to the mean ice concentration, which reflects the rates of

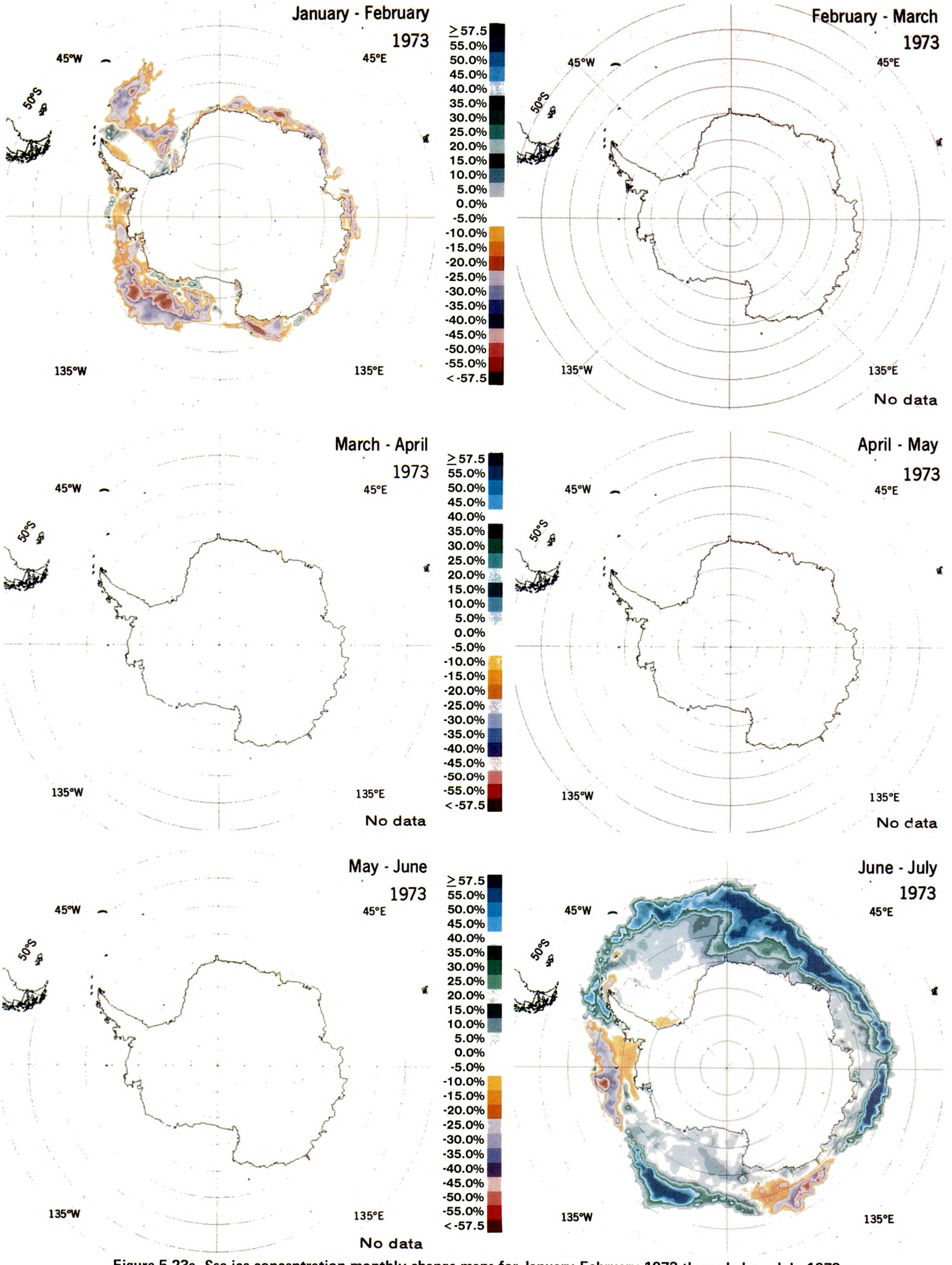

Figure 5-23a. Sea ice concentration monthly change maps for January-February 1973 through June-July 1973.

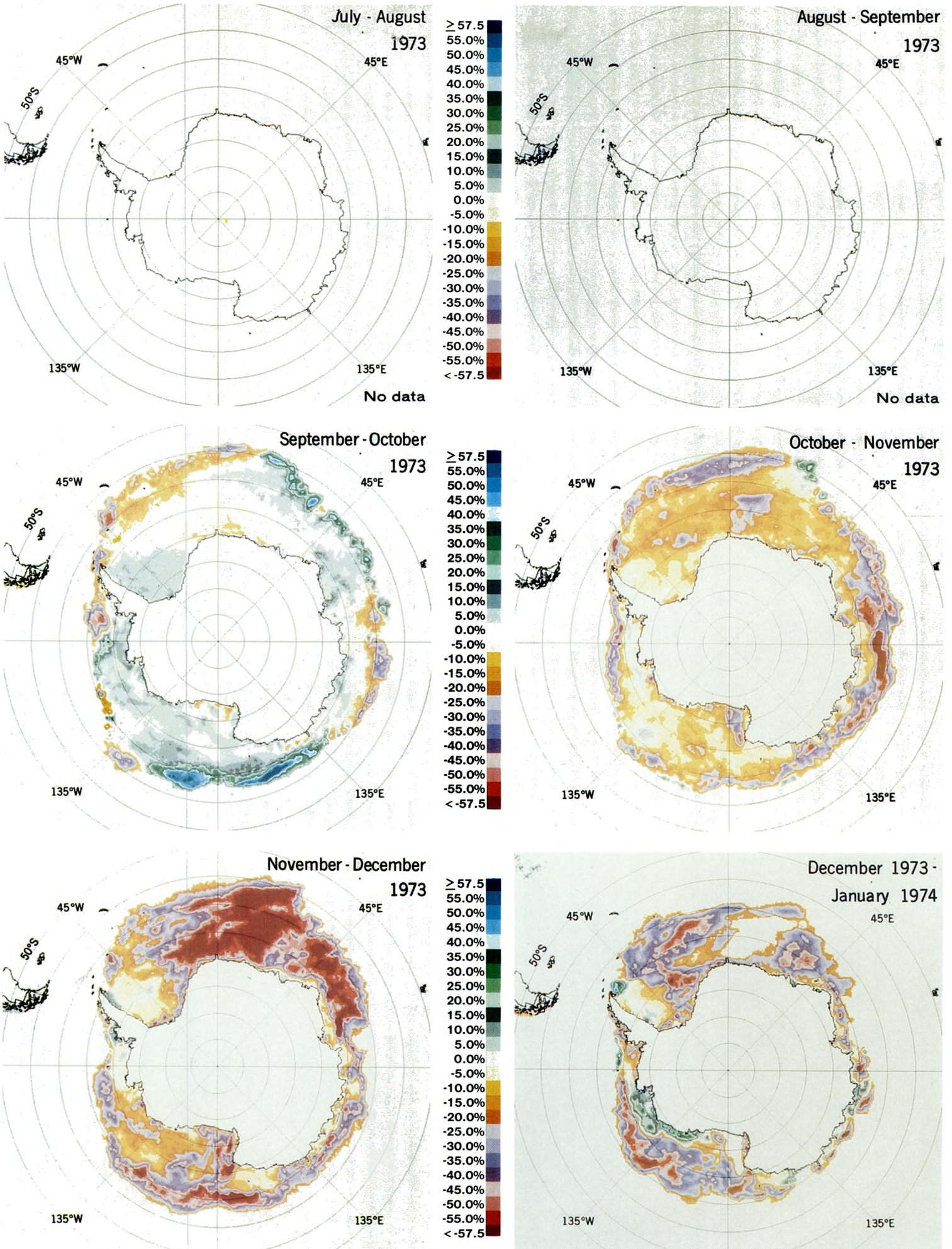

Figure 5-23b. Sea ice concentration monthly change maps for July-August 1973 through December 1973-January 1974.

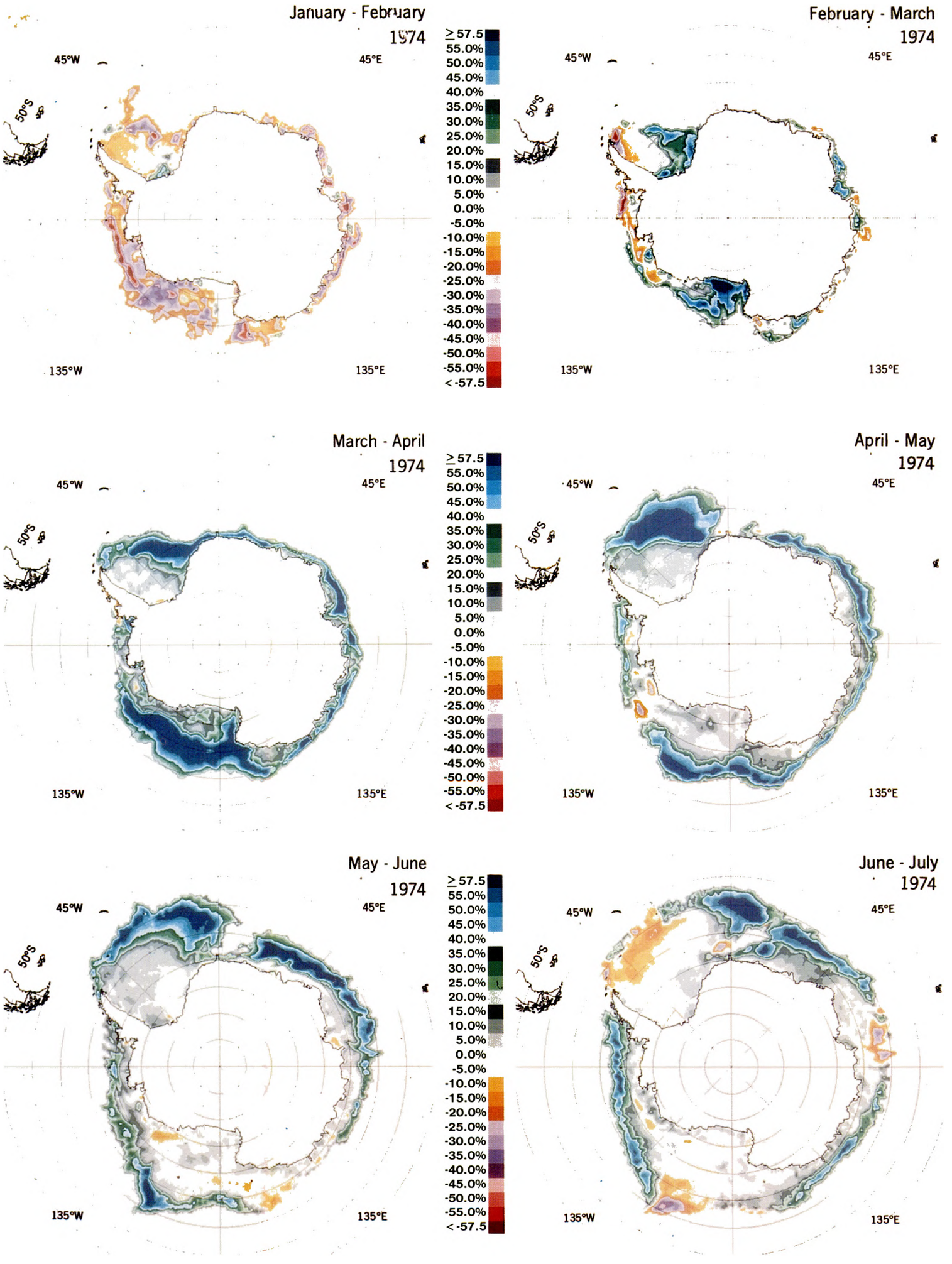

Figure 5-24a. Sea ice concentration monthly change maps for January-February 1974 through June-July 1974.

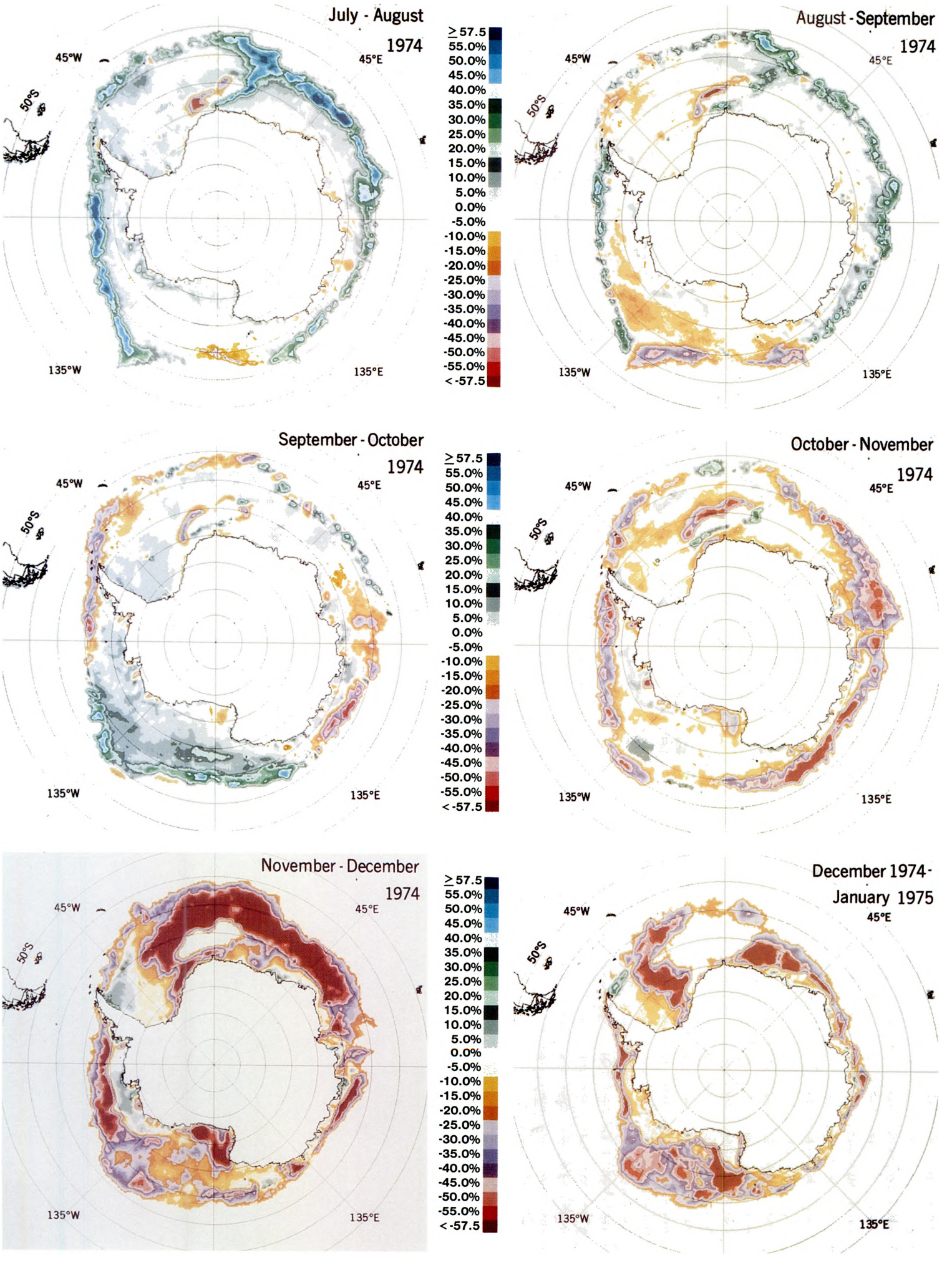

Figure 5-24b. Sea ice concentration monthly change maps for July-August 1974 through December 1974-January 1975.

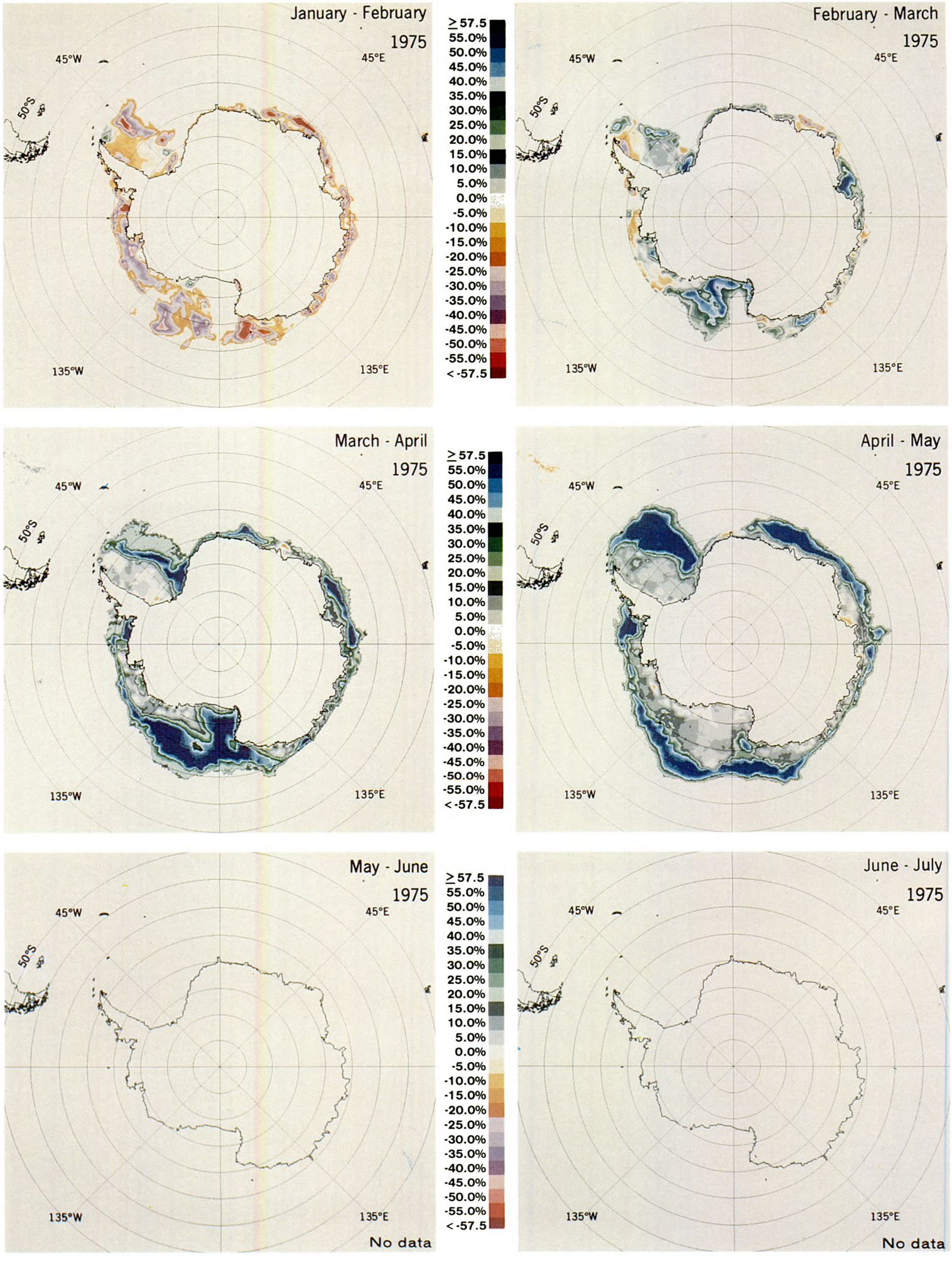

Figure 5-25a. Sea ice concentration monthly change maps for January-February 1975 through June-July 1975.

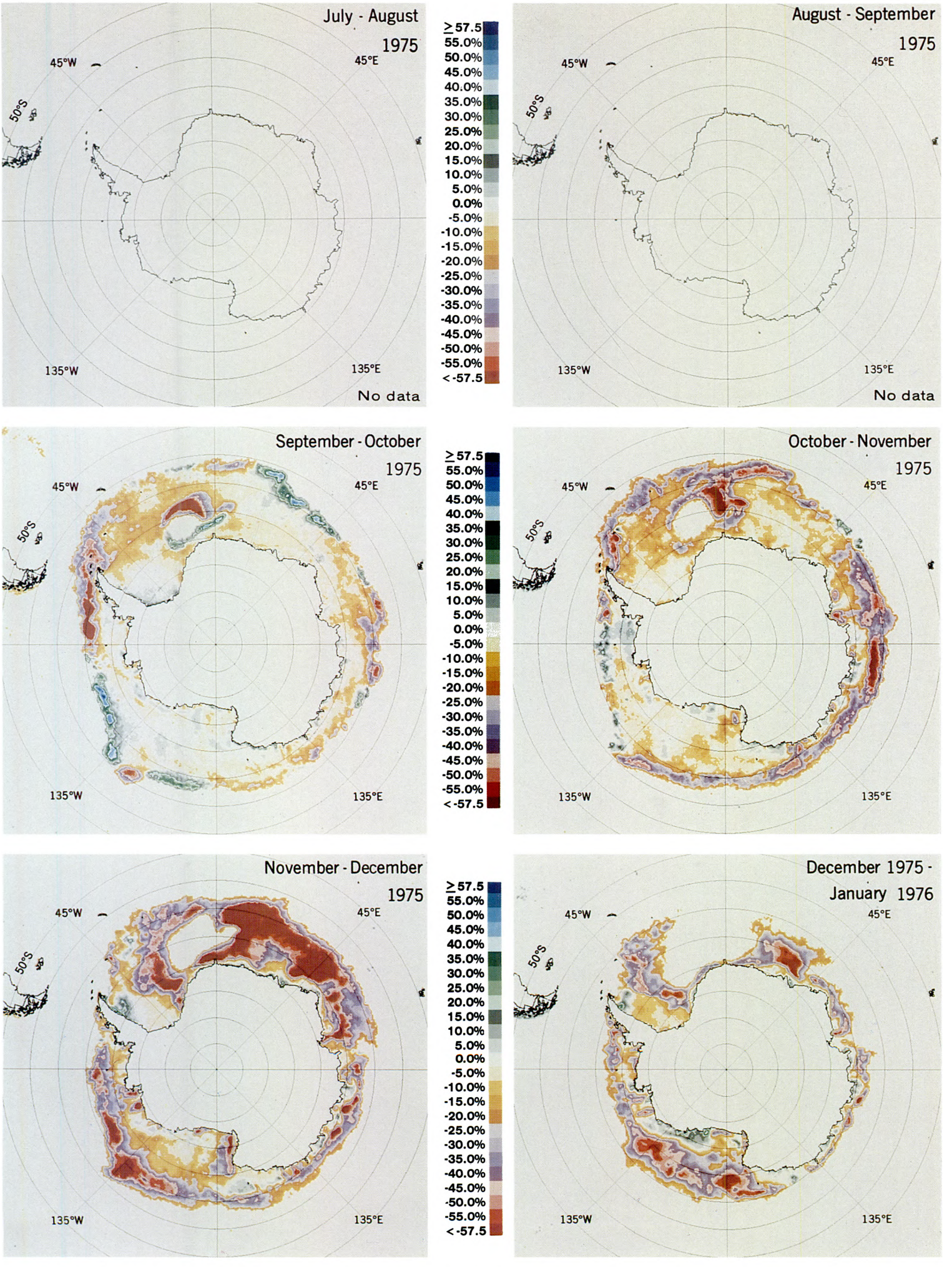

Figure 5-25b. Sea ice concentration monthly change maps for July-August 1975 through December 1975-January 1976.

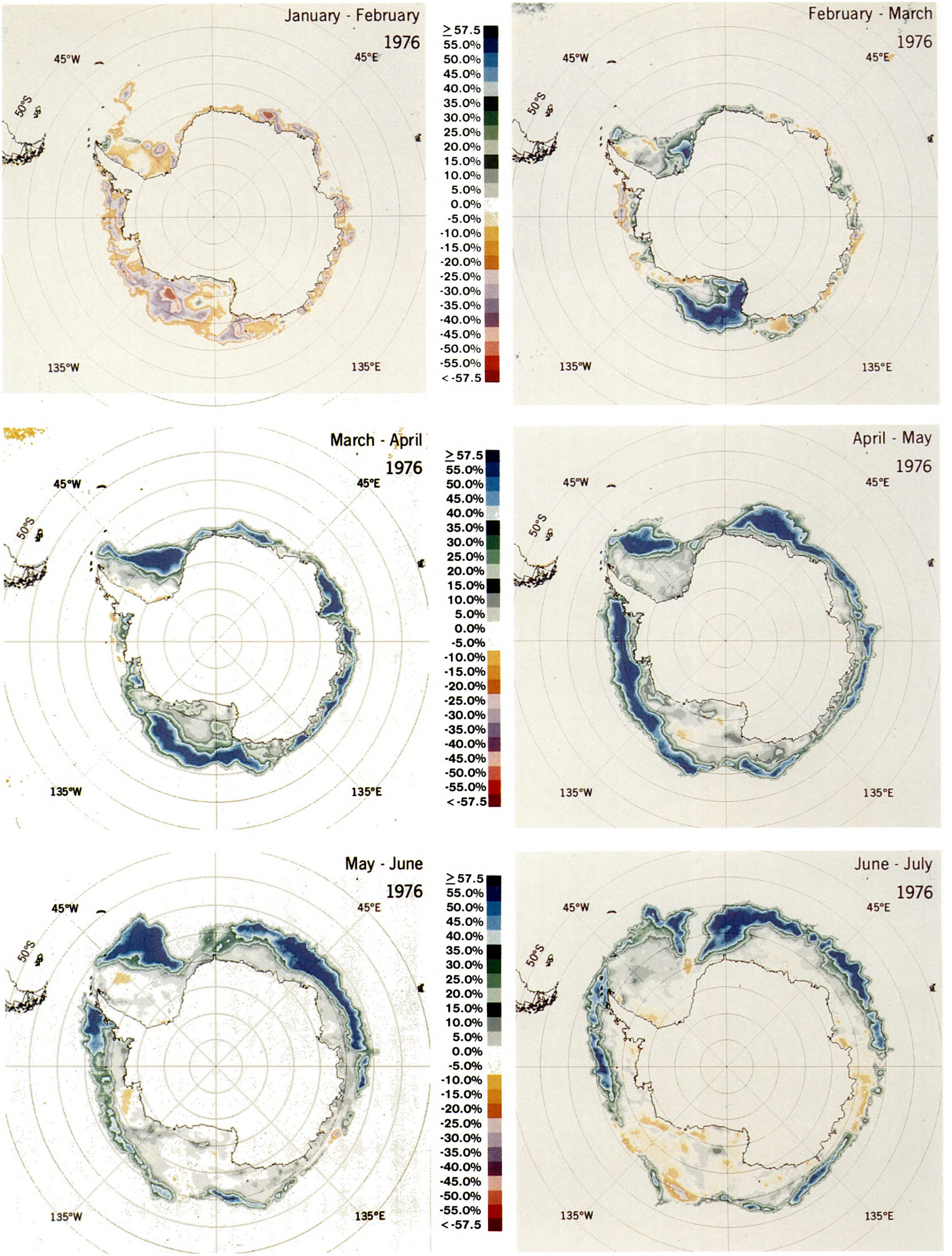

Figure 5-26a. Sea ice concentration monthly change maps for January-February 1976 through June-July 1976.

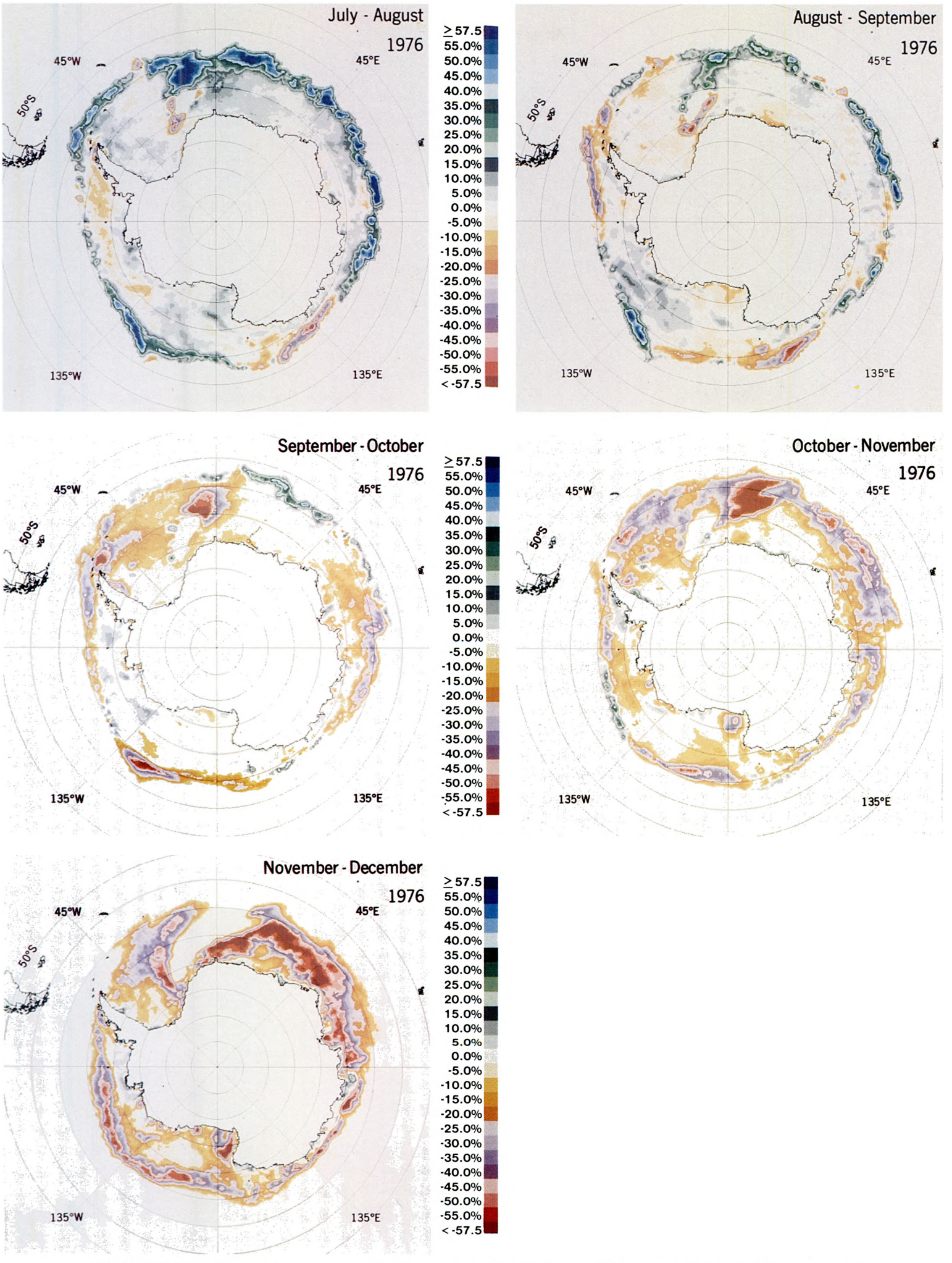

Figure 5-26b. Sea ice concentration monthly change maps for July-August 1976 through November-December 1976.

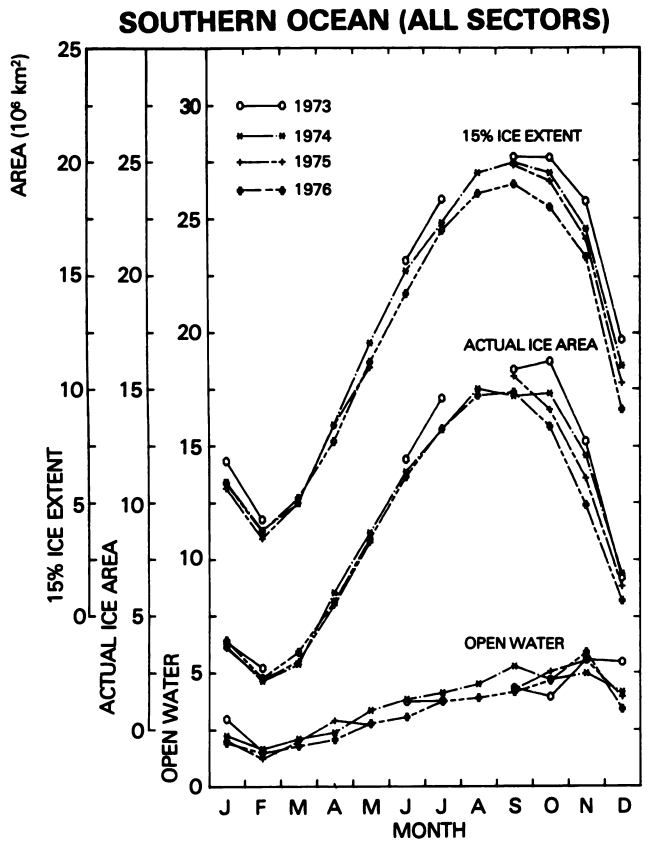

Figure 5-27. Internannual variation of the yearly cycle of the 15-percent extent, the actual ice area, and the open water within the ice pack for the total southern ocean.

ice divergence and refreezing within the ice pack and the resulting areas of open leads and polynyas. The area of open water continues to increase for 1 to 2 months after the time of maximum ice extent, which is also shown by the faster decrease in the actual ice area than in the ice extent just after their maxima. This continued increase of open water during the early part of the decay season is consistent with the rapid early decrease in areas of highly concentrated ice (Figure 5-13) and the corresponding decrease in mean concentration (Figure 5-33).

The mean ice concentration on the southern ocean ranges from approximately 55 to 80 percent throughout the year (Figure 5-33). The annual cycle of mean concentration resembles somewhat the cycle of ice extent. The mean concentration is lowest near the time of ice minimum, increases during the growth season, and reaches its maximum around the time of maximum ice extent. Typically, the maximum mean concentration is about 80 percent in the Weddell Sea, Ross Sea, and Indian Ocean sectors and is about 75 percent in the Pacific Ocean sector. In the Bellingshausen-Amundsen Seas sector, the calculated mean concentration values are probably lower than the actual, due to the error resulting from the multiyear ice emissivity in that sector (see Chapter 3). The mean concentration in the Ross Sea sector approaches its maximum early in the growth season, similar to the rapid growth in the ice extent in the Ross Sea, whereas the Weddell sector has a near linear increase from January through August.

The wintertime values of mean concentration for the southern ocean are between 75 and 80 percent, which are somewhat higher than previous estimates from the ESMR data that used a higher emissivity (ϵ = 0.95) and used less accurate estimates of the effective ice physical temperature. However, the ESMR indication of 20- to 25-percent open water during winter is still much larger than is shown on the Navy-National Oceanic and

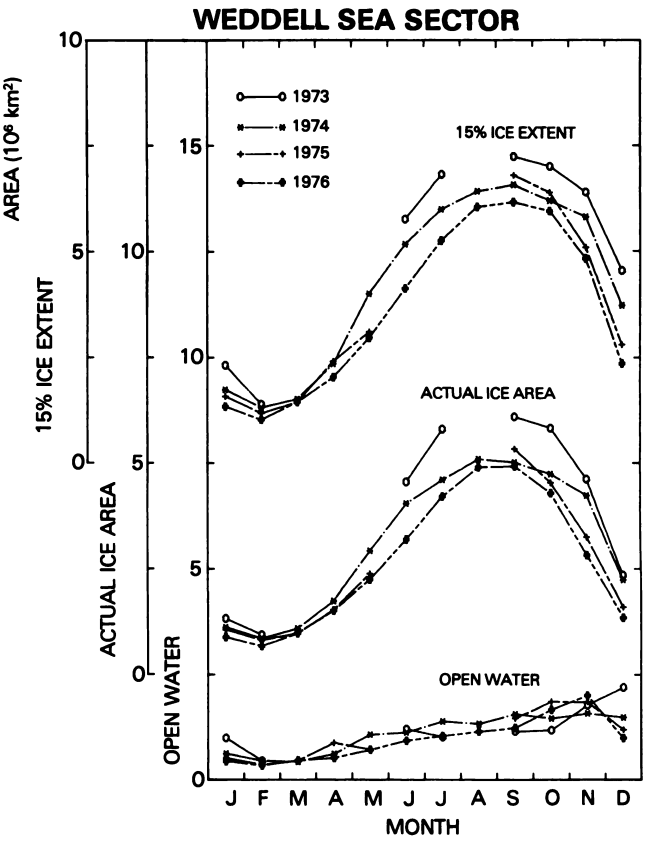

Figure 5-28. Interannual variation of the yearly cycle of the 15-percent extent, the actual ice area, and the open water within the ice pack for the Weddell Sea sector.

Atmospheric Administration (NOAA) sea ice maps (Godin and Barnett, 1979) and reported, for example, by Kukla and Gavin (1981), who indicate less than 5-percent open water during winter. The low wintertime values on the Navy-NOAA maps reflect the inadequacy of their techniques for determining the total amount of open water, particularly in winter. In principle, their photointerpretation of the ESMR gray-scale images, which represent relative brightness temperatures, could give approximately the same ice concentration values as the digital analysis of the ESMR data in this volume, except that the variations in ice physical temperature would not be taken into account in the photointerpretation. However, accurate photointerpretation of relative brightness temperatures is very difficult, as may be judged by examination of the gray-scale images of sea ice concentration in Appendix B. The visible and infrared satellite images, which are also used for the Navy-

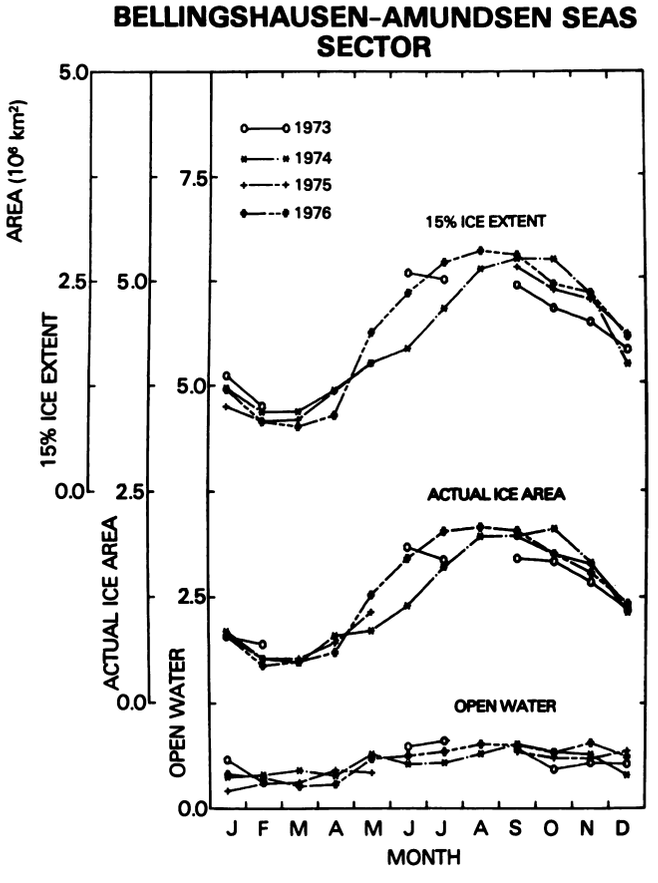

Figure 5-29. Interannual variation of the yearly cycle of the 15-percent extent, the actual ice area, and the open water within the ice pack for the Bellingshausen-Amundsen Seas sector.

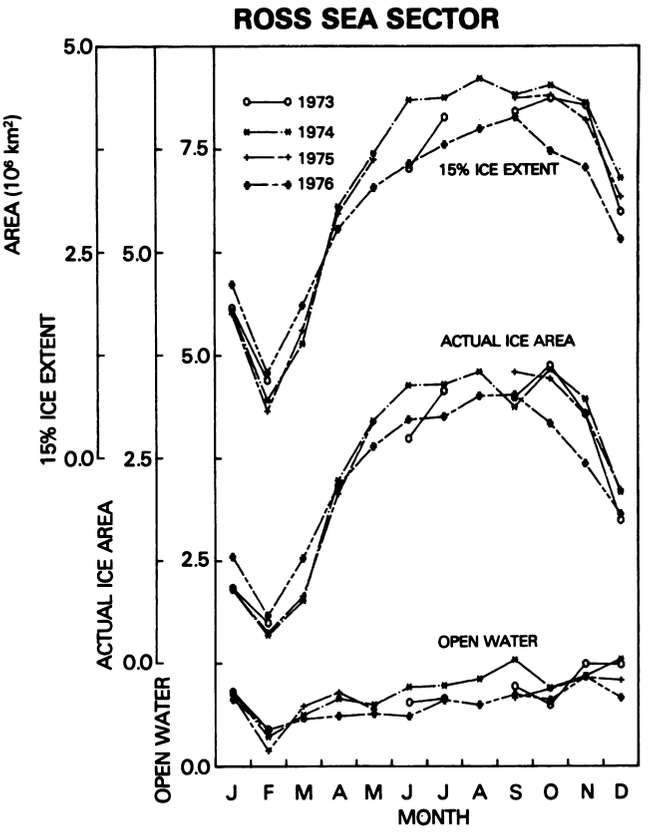

Figure 5-30. Interannual variation of the yearly cycle of the 15-percent extent, the actual ice area, and the open water within the ice pack for the Ross Sea sector.

NOAA maps, have a limitation in principle because unresolved open water in leads and polynyas smaller than the approximately 1-kilometer image resolution simply cannot be included accurately in estimates of ice concentration. Unless special techniques are used to account for unresolved open water, estimates of the area of open water from visible and infrared sensing are too low (Comiso and Zwally, 1982). On the other hand, as noted in Chapter 3, there is some uncertainty as to the microwave emissivity of very thin ice under about 5 centimeters (new ice and dark nilas). Nevertheless, while unconsolidated frazil ice, grease ice, and other new ice forms probably have microwave emissivities more like open water than first-year ice, thin ice of more than about 5 centimeters thickness (light nilas, gray ice, and gray-white ice) has an emissivity close to that of first-year ice. Therefore, some fraction of the areas of very thin ice under about 5 centimeters, including, in particular, areas of unconsolidated frazil ice and grease ice, may be included in the ESMR-derived values

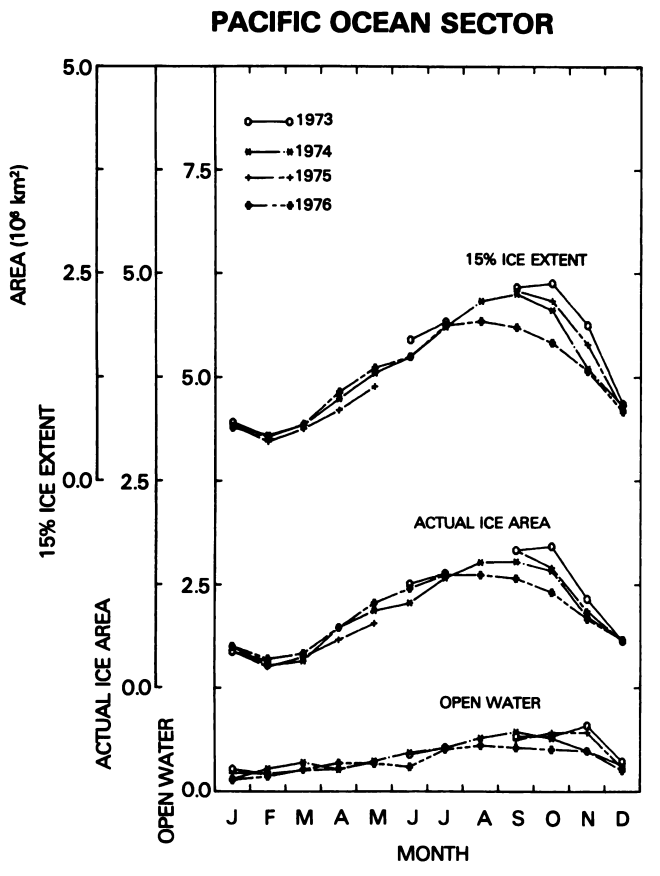

Figure 5-31. Interannual variation of the yearly cycle of the 15-percent extent, the actual ice area, and the open water within the ice pack for the Pacific Ocean sector.

of open water. Consequently, the area of totally ice-free water may be slightly less than the total area of open water indicated by the ESMR. Although the difference is usually small, it should be taken into account whenever it is important to distinguish between totally ice-free water and areas with some very thin ice.

In the summertime (December, January, and February), the Navy-NOAA estimates of mean ice concentration range between 60 and 80 percent (Kukla and Gavin, 1981). Although somewhat higher than the ESMR-derived values in Figure 5-33, these mean concentrations in summer are much closer to the ESMR values than are the Navy-NOAA concentrations in wintertime. From February to March, the Navy-NOAA mean concentration estimates increase abruptly from 70 percent to approximately 95 percent and in April to 99 percent—values that would be typical of the highly constrained wintertime ice in the central Arctic Ocean. The ESMR-derived values show a much smoother increase in mean concentration throughout the growth season as the ice cover expands equatorward.

Examination of Figures 5-1 through 5-12 shows that much of the open water observed by ESMR is actually in the regions near the ice edge. In the southern ocean, the unconstrained ice, particularly near the ice edge, is much more divergent than in the Arctic Ocean, producing large areas of reduced ice concentration. Within the center of the ice pack, much of the ice cover has concentrations within the range of 88 to 100 percent, or 12- to 0-percent open water.

The year-to-year changes in ice cover differ both regionally and seasonally. Many aspects of these changes, particularly variations in the regional distributions, have been discussed in Sections 5.2 and 5.3. Overall, the ice extent decreased significantly from 1973 to 1976, with the most pronounced year-to-year decrease during the winter and spring

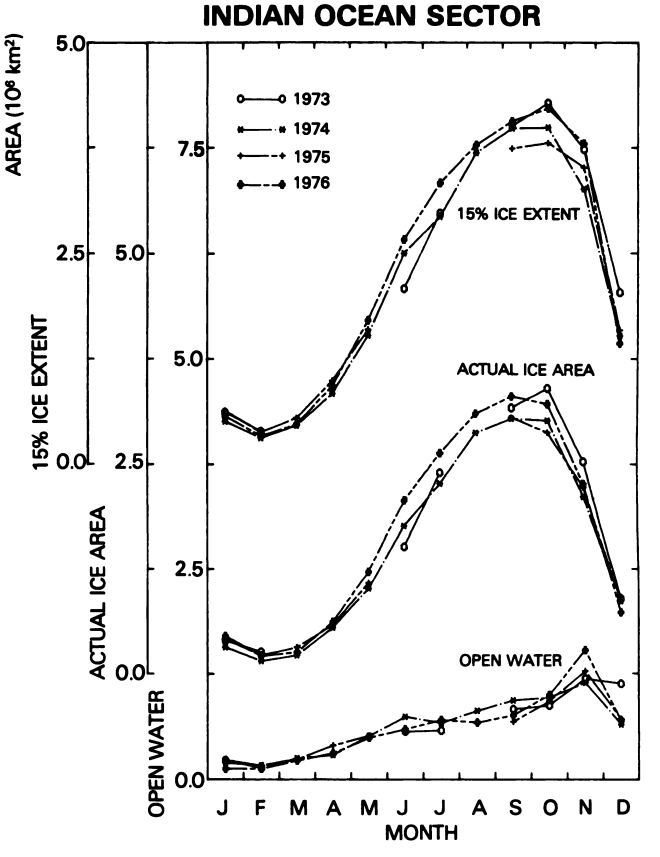

Figure 5-32. Interannual variation of the yearly cycle of the 15-percent extent, the actual ice area, and the open water within the ice pack for the Indian Ocean sector.

months as shown in Figures 5-27 through 5-32. The Weddell Sea and Pacific Ocean sectors had significantly less ice in 1976 than in 1973 during most seasons and in the annual mean (Figure 5-34). For the years 1973 and 1975, the months without ESMR maps are included in the annual means in Figure 5-34 by using ice extents from the Navy-NOAA maps, a procedure that produced values very close to those obtained exclusively from the ESMR data by linear interpolation in time, with the largest difference between the two procedures being for March, April, and May 1973 in the Ross Sea sector. The Bellingshausen-Amundsen Seas, the Ross Sea, and the Indian Ocean sectors had

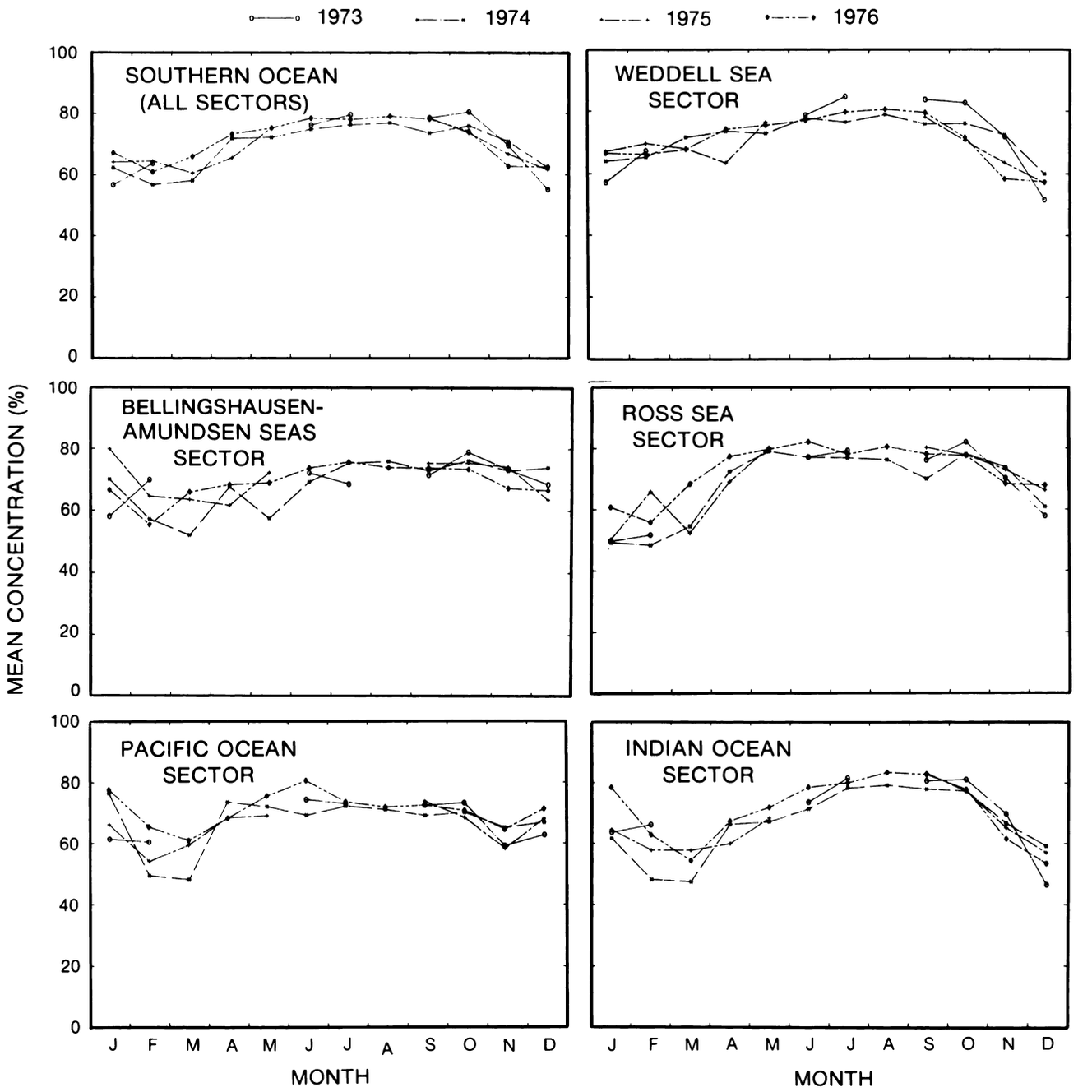

Figure 5-33. Mean sea ice concentrations showing yearly cycle and interannual variations in the total southern ocean and each sector.

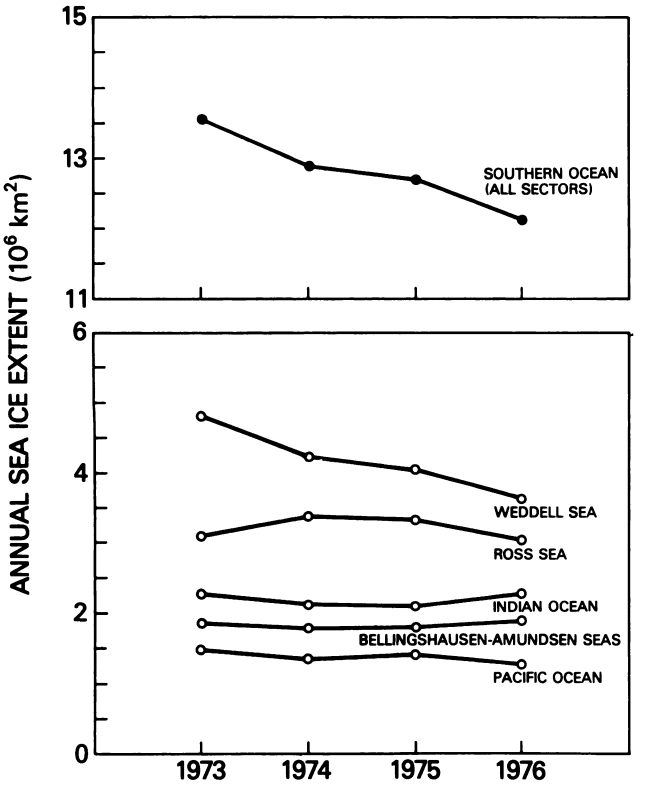

Figure 5-34. Year-to-year changes in annual mean sea ice extent, for the total southern ocean and each sector. (Navy-NOAA maps (Godin and Barnett, 1979) were used for the months in 1973 and 1975 for which no ESMR maps were available. See Table 5-1.)

almost the same annual mean ice extent in 1976 as in 1973; however, in the intervening years, the ice extent was greater in the Ross Sea sector and smaller in the Bellingshausen-Amundsen Seas and Indian Ocean sectors. Clearly, the large decrease of 22.7 percent in the Weddell Sea sector is mainly responsible for the overall decrease of 9.7 percent in the annual mean southern ocean sea ice extent from 1973 to 1976. In the Ross Sea, an increase from 1973 to 1974 partially compensated for the large decrease in the Weddell Sea sector, although 1973 to 1974 was still the period of largest overall decrease for the southern ocean as a whole. Although changes in one sector are sometimes compensated by opposite changes in another sector, in a manner that may reflect possible changes in atmospheric conditions, a consistent pattern of compensating changes does not appear throughout the 4 years.

The interannual changes in ice extent for each month and sector are shown more clearly in Figure 5-35, with corresponding graphs for the interannual changes in actual ice area, the interannual changes in open water, and the interannual changes in mean concentration appearing in Figures 5-36 through 5-38. Most of the following discussion of interannual variations is based on variations in ice extent, rather than the other three parameters, for the following reasons: (1) the trends in actual ice area appear to be generally the same as the trends in ice extent, (2) ice extent is the most accurately determined parameter, and (3) ice extent can be most readily compared with longer term records.

Some differences in the trends of ice extent and actual ice area, which are also reflected in the open-water and mean concentration parameters, are notable and may be caused by differences in the convergence/divergence and melt/freeze conditions of the sea ice. Most of the differences in the trends of these two parameters appear to be of short duration and probably result from differences in synoptic weather patterns. Nevertheless, there is the possibility of longer term trends in the differences between ice extent and actual ice area due, for example, to a more or less vigorous atmospheric circulation or storm frequency. Therefore, longer term observation and analysis of both actual ice area and ice extent are needed to describe and understand fully the changes in the sea ice cover.

An example of the differences in the interannual variations of ice extent and actual ice area is given by the winter ice covers in 1973 and 1974, for which the year-to-year decrease in actual ice area was greater than the decrease in ice extent (Figure 5-27). During July, September, and October, the year 1973 had less open water within the ice pack in the total southern ocean, in the Weddell Sea sector, in the Ross Sea sector, and in the Indian Ocean sector than in 1974 (Figures 5-27 through 5-32 or Figure 5-37). The fact that both a greater ice extent and a lesser amount of open water existed in 1973 than in 1974 suggests that the ice pack was also generally less divergent during the winter of 1973 even though the ice extent was greater. (See also the mean concentration in Figure 5-38.) However, a more detailed analysis of such interannual differences in the amount of open water requires careful examination of the measurement errors for the area of open water. Even the 1973-1974 difference just discussed is only about twice the estimated error. The histograms of ice concentration in Figure C-3 show that the maximum ice concentration for July and October 1973 may be

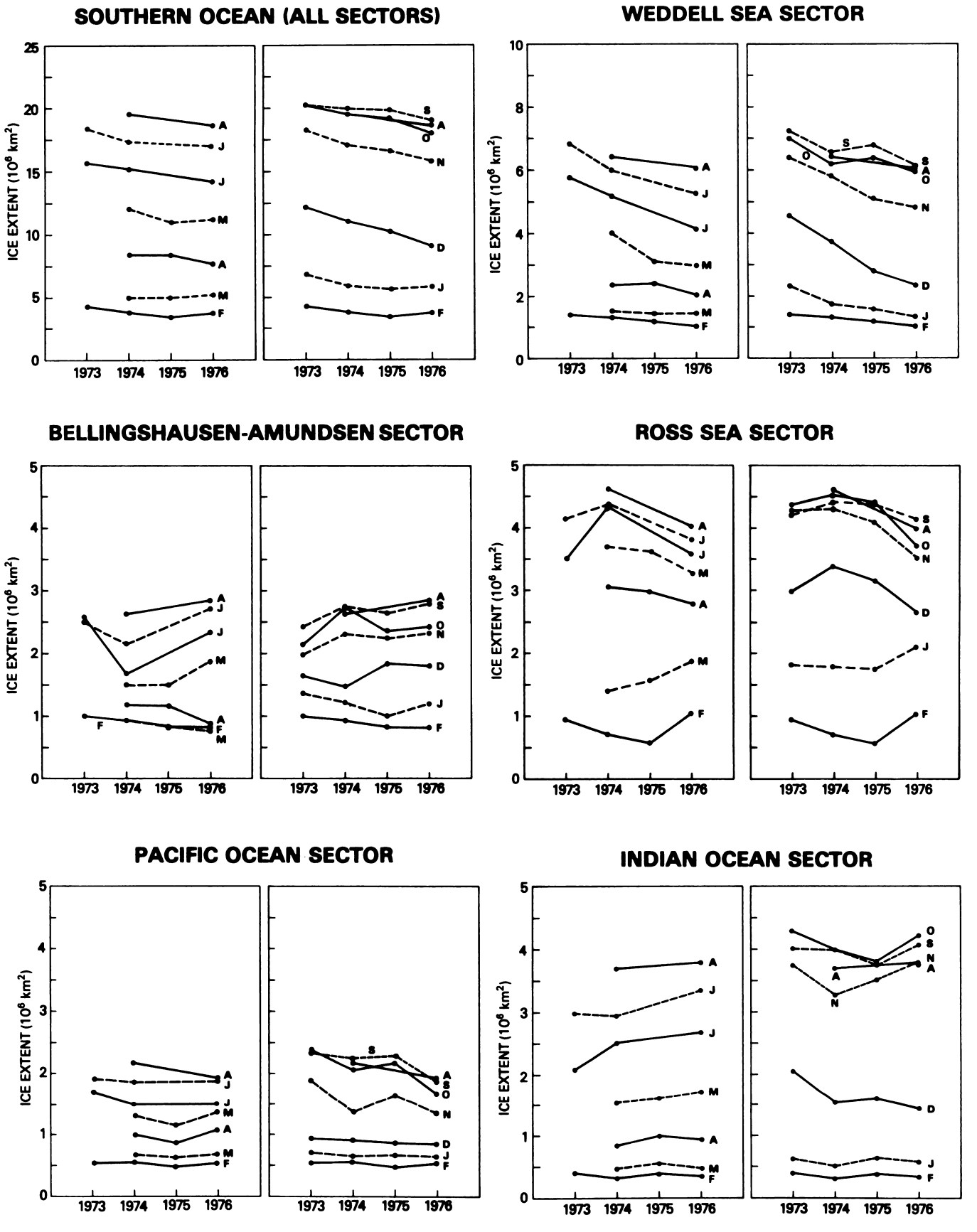

Figure 5-35. Year-to-year changes in sea ice extent for each month, for the total southern ocean and each sector.

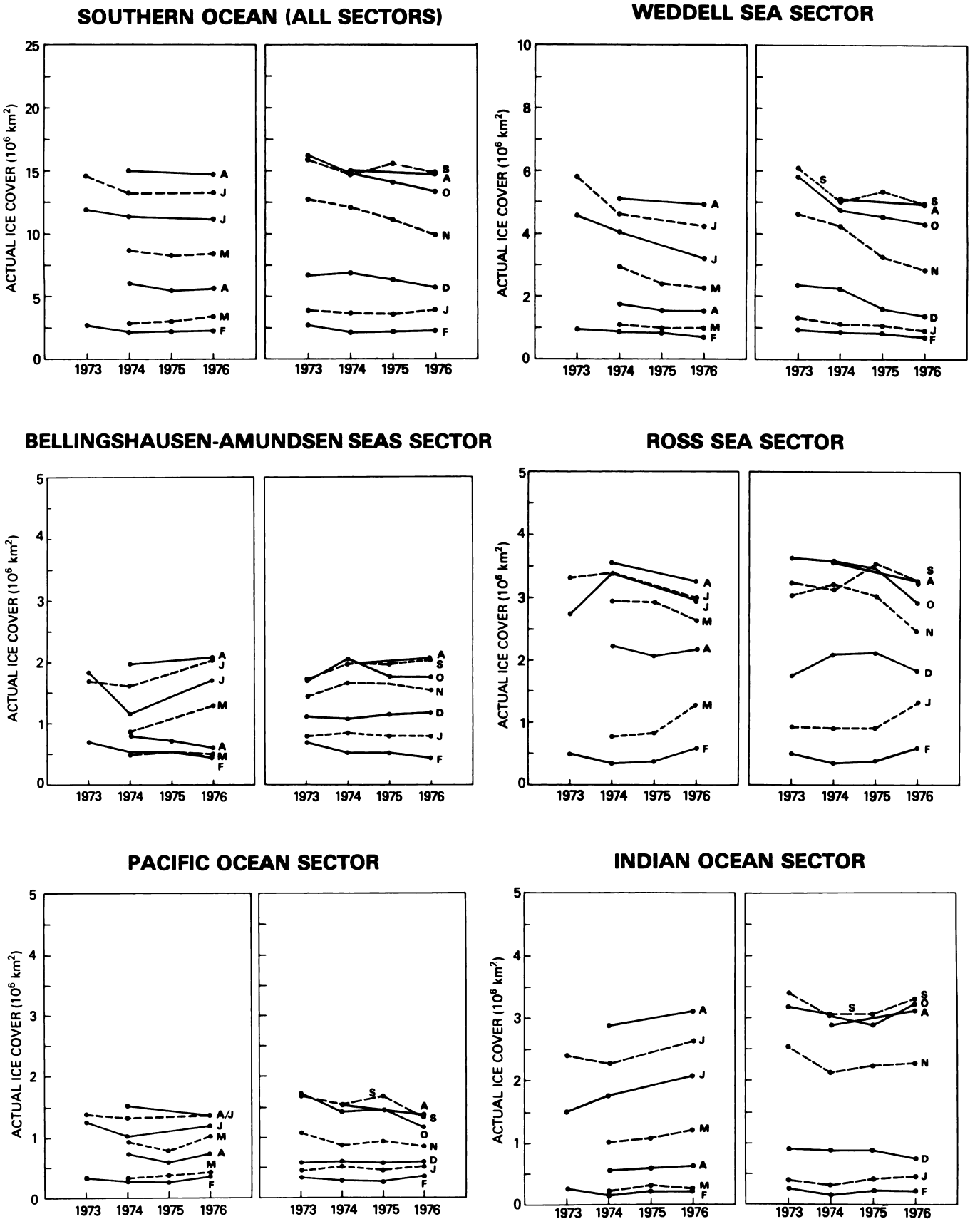

Figure 5-36. Year-to-year changes in actual ice area for each month, for the total southern ocean and each sector.

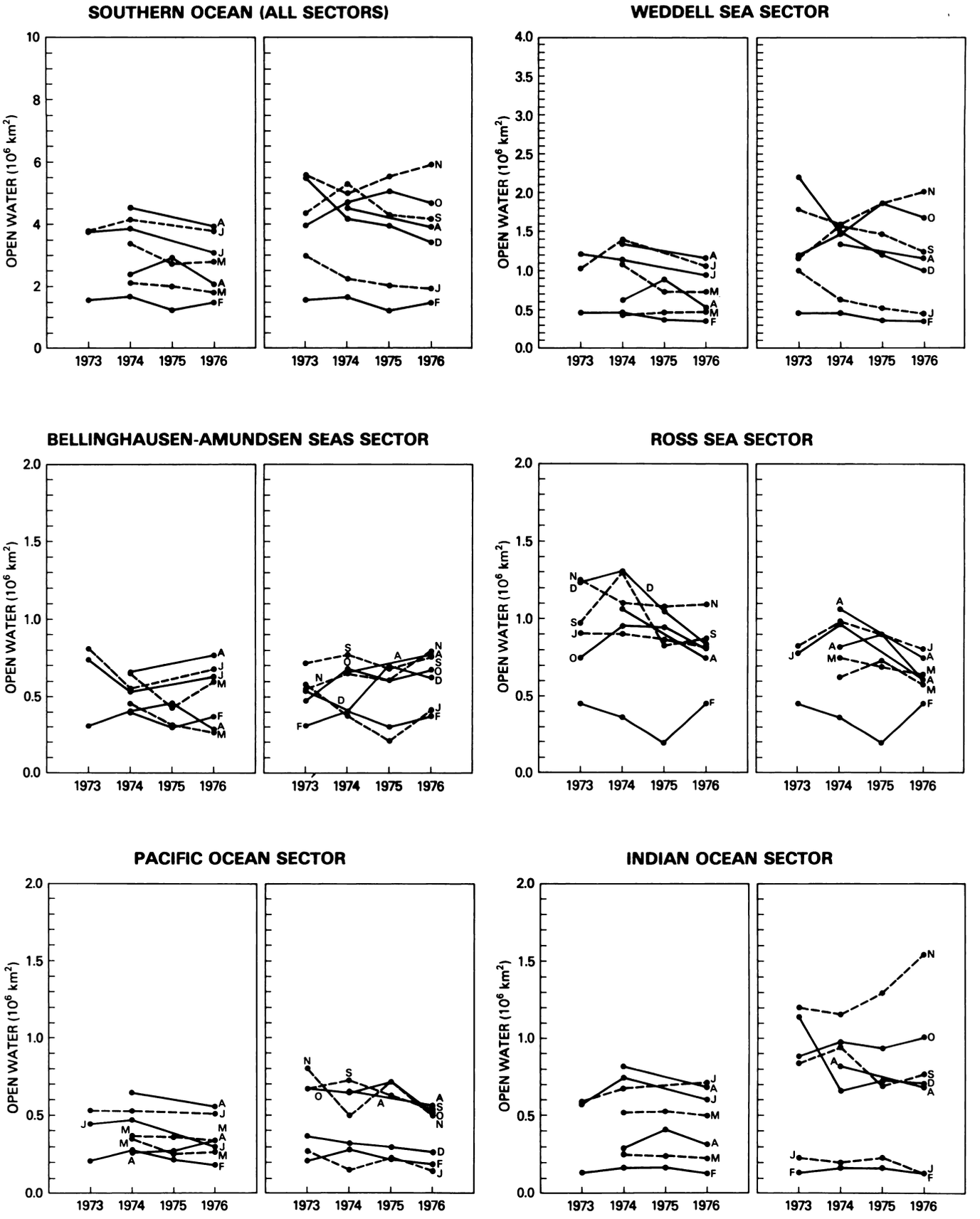

Figure 5-37. Year-to-year changes in open water within the ice pack, for the total southern ocean and each sector.

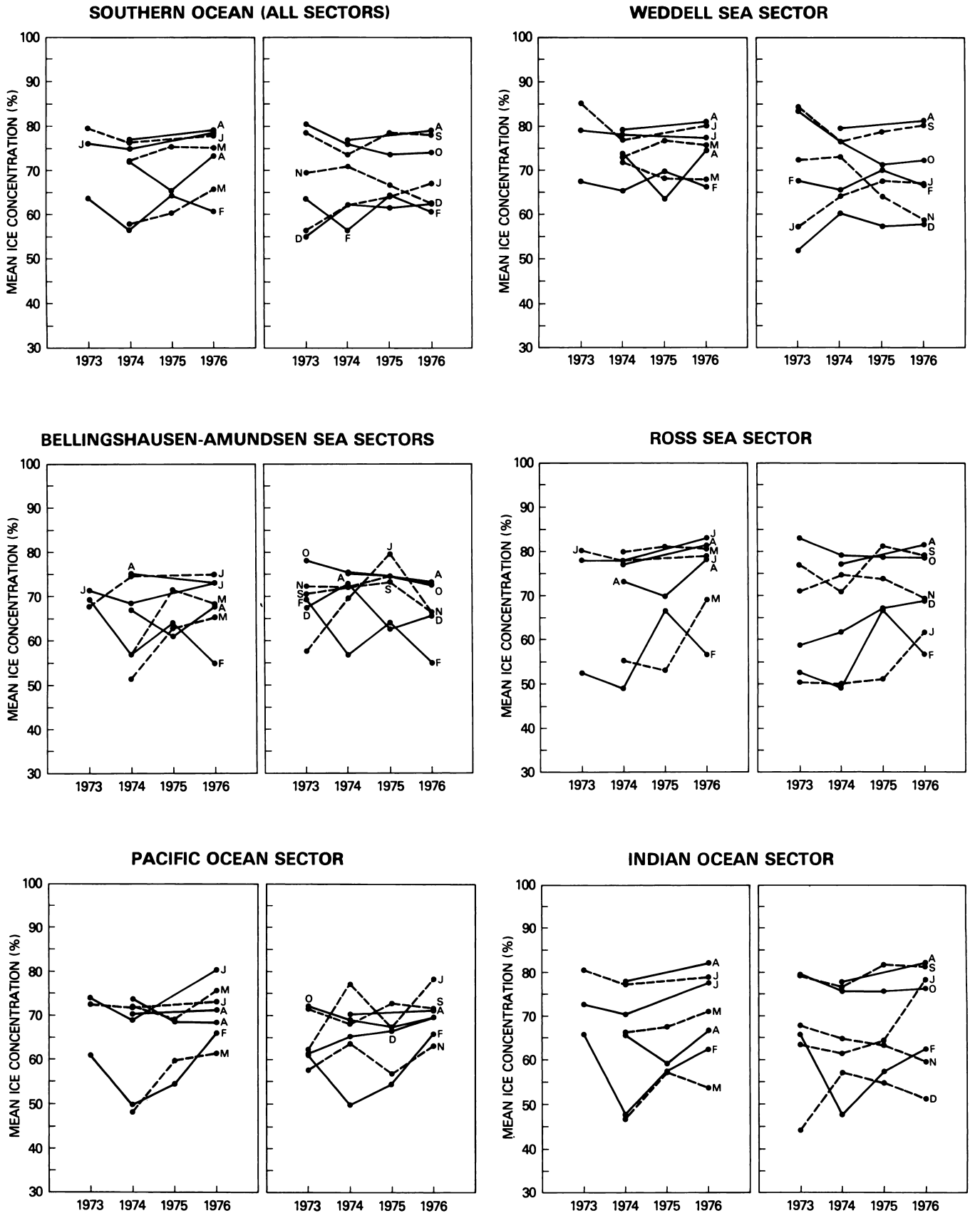

Figure 5-38. Year-to-year changes in mean sea ice concentration, for the total southern ocean and each sector.

about 3 percent too high relative to 1974, causing a relative error in the open-water area of as much as 0.04×10^6 square kilometers for the total southern ocean compared to the 1973-1974 difference of about 0.08×10^6 square kilometers of open water, exclusive of the Weddell polynya. Examination of the histograms also shows, however, that the distributions in 1973 are more peaked toward higher concentrations than in 1974, supporting the result of less open water in 1973.

Over the 4 years from 1973 to 1976, Figure 5-37 shows a slight trend (except for October and November) toward less open water within the ice pack, which is consistent with the trend of lesser ice extent if the open water and ice extent change proportionately. Although there is no apparent overall trend in the mean ice concentration for all seasons (Figure 5-38), it is interesting that 1973 has both the highest single-month mean concentration (80 percent in October) for the total southern ocean and the lowest single-month mean concentration (55 percent in December). In the Weddell Sea sector, the highest mean concentration is 85 percent in July 1973 and the lowest is 52 percent in December 1973, and in the Ross Sea sector, the highest is 83 percent in October 1973 and the lowest is 49 percent in February 1974. Thus, a winter with high mean ice concentration and large ice extent is followed by a spring and summer melt season with low mean concentration.

The large variability of Antarctic sea ice extent is particularly evident in Figure 5-35. Changes in ice cover in certain seasons could be related to changes in other seasons by various physical processes. For example, an anomalously early decay of the sea ice by only several weeks in spring would significantly increase the heat absorbed by the ocean during the period when the solar insolation is approaching its annual maximum (Fletcher, 1972). Increased heat in the upper layers of the ocean could affect the ice cover in subsequent seasons. However, the large differences in the observed changes among seasons and regions illustrate the lack of a consistent overall behavior, but may provide insight to the interactive processes involved in the changes. For the southern ocean, the largest decreases from 1973 to 1976 occur in the months of November and December, with decreases of 13.5 and 25.3 percent, respectively, compared to a 9.7-percent decrease in the annual mean, a 6.0-percent decrease at the September maximum, and a 12.3-percent decrease at the February minimum (Table 5-1). The 4-year trends in the Weddell Sea sector are similar to the total southern ocean, with a 24.5-percent decrease in November and a 48.3-percent decrease in December, compared to a 22.7-percent decrease in the annual mean, a 14.9-percent decrease at the September maximum, and a 26.5-percent decrease at the February minimum. The Pacific Ocean sector also shows a decrease in most months, but the maximum decrease is earlier in the fall, being 30.0 percent in October compared to 29.4 percent in November, 9.8 percent in December, 14.6 percent in the annual mean, 20.6 percent at the September maximum, and 0.5 percent at the February minimum. The Bellingshausen-Amundsen Seas, Ross Sea, and Indian Ocean sectors have clear decreasing trends in some months and increasing trends in other months, resulting in the small changes (less than 3 percent) in their annual means.

In certain sectors, there appears to be a tendency for a smaller summer-minimum ice extent in years having a larger winter-maximum ice extent. For example, compare 1973 and 1976 in the Ross Sea with the other 2 years, and compare 1976 in the Bellingshausen-Amundsen Seas with previous years in Figure 5-35.

The annual mean sea ice distribution for each year, the year-to-year changes in the annual mean, the 4-year average annual mean, and the deviations of each annual mean from the 4-year average annual mean are displayed in the images in Figures 5-39 through 5-42. These concluding figures and, in particular, the 4-year average of the annual mean concentrations (Figure 5-41), incorporate all the microwave data presented and discussed in this document. A linear interpolation in time for each map element is used to account for months with no microwave data. The 4-year average of annual mean sea ice concentration (Figure 5-41) is a useful base for comparing the individual years; it represents the time-averaged probability of finding sea ice at a given location or the typical yearly averaged sea ice concentration.

The annual mean sea ice concentrations in Figure 5-39 are useful for comparing persistent and nonpersistent features of the sea ice cover. For example, the extension of sea ice over the South Sandwich trench at 25°W appears in all images. The decrease in ice cover in the Weddell Sea is evident, as is the progressive decrease in the extent of the reduced sea ice concentration near the Ross Ice Shelf. The year-to-year change in the annual

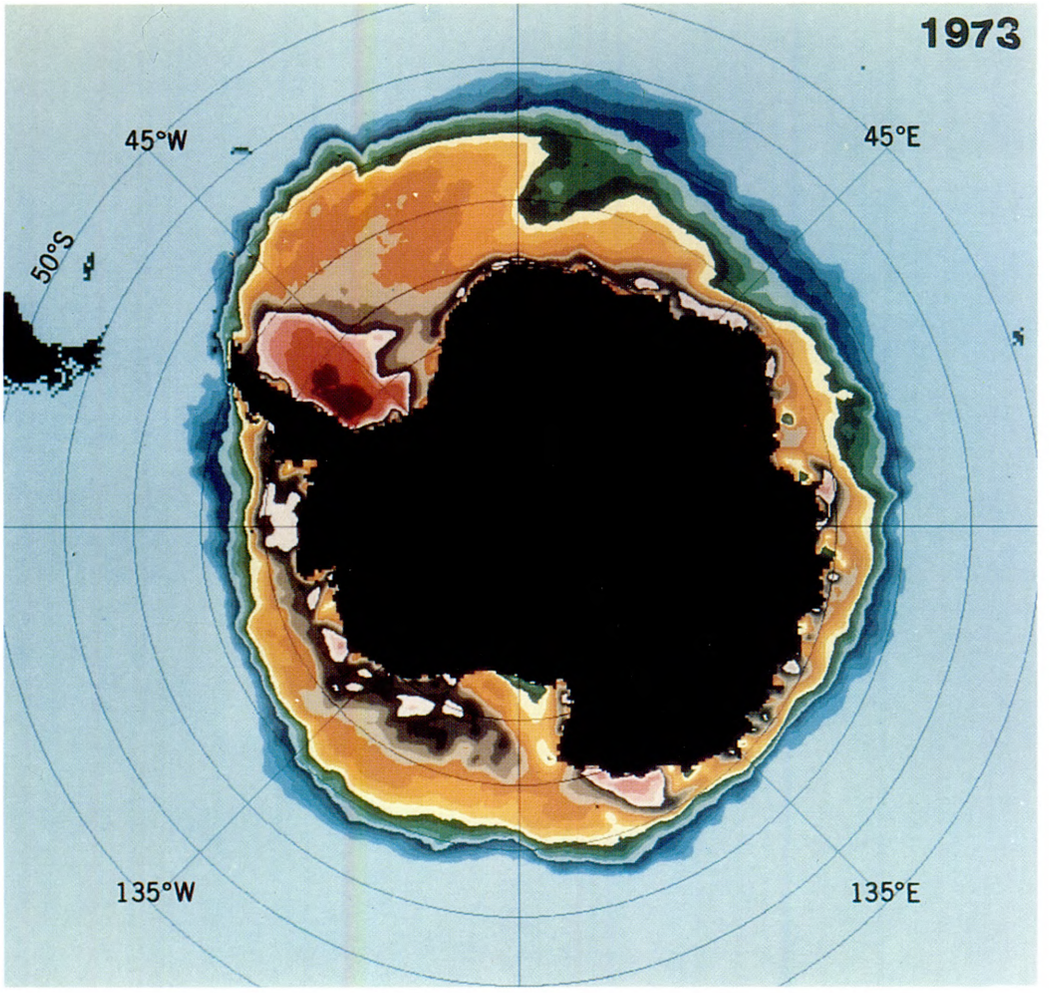

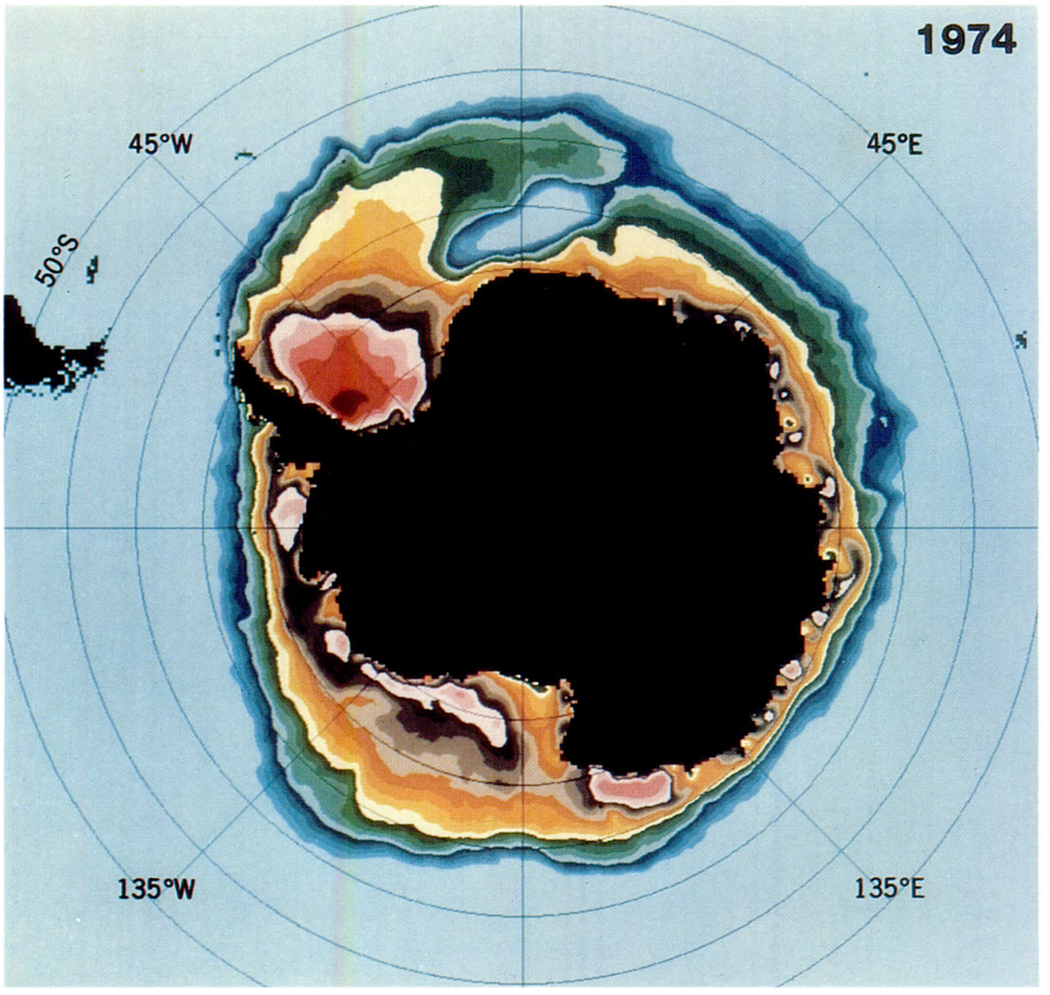

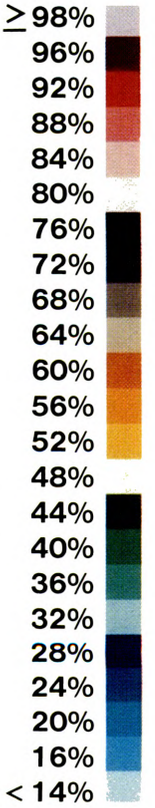

Figure 5-39a. Annual mean sea ice concentrations for 1973 and 1974. Months without data are accounted for by interpolation.

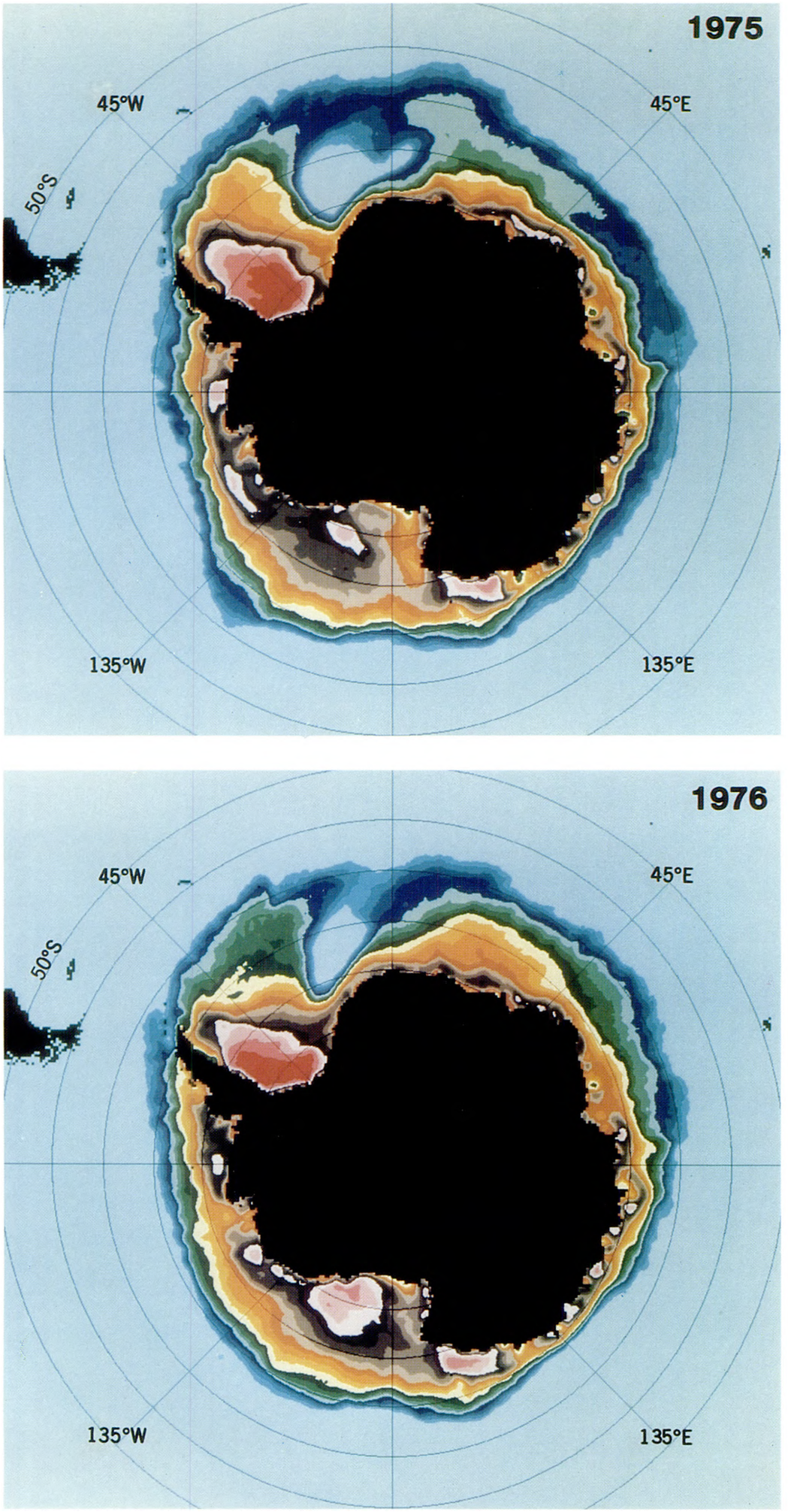

Figure 5-39b. Annual mean sea ice concentrations for 1975 and 1976. Months without data are accounted for by interpolation.

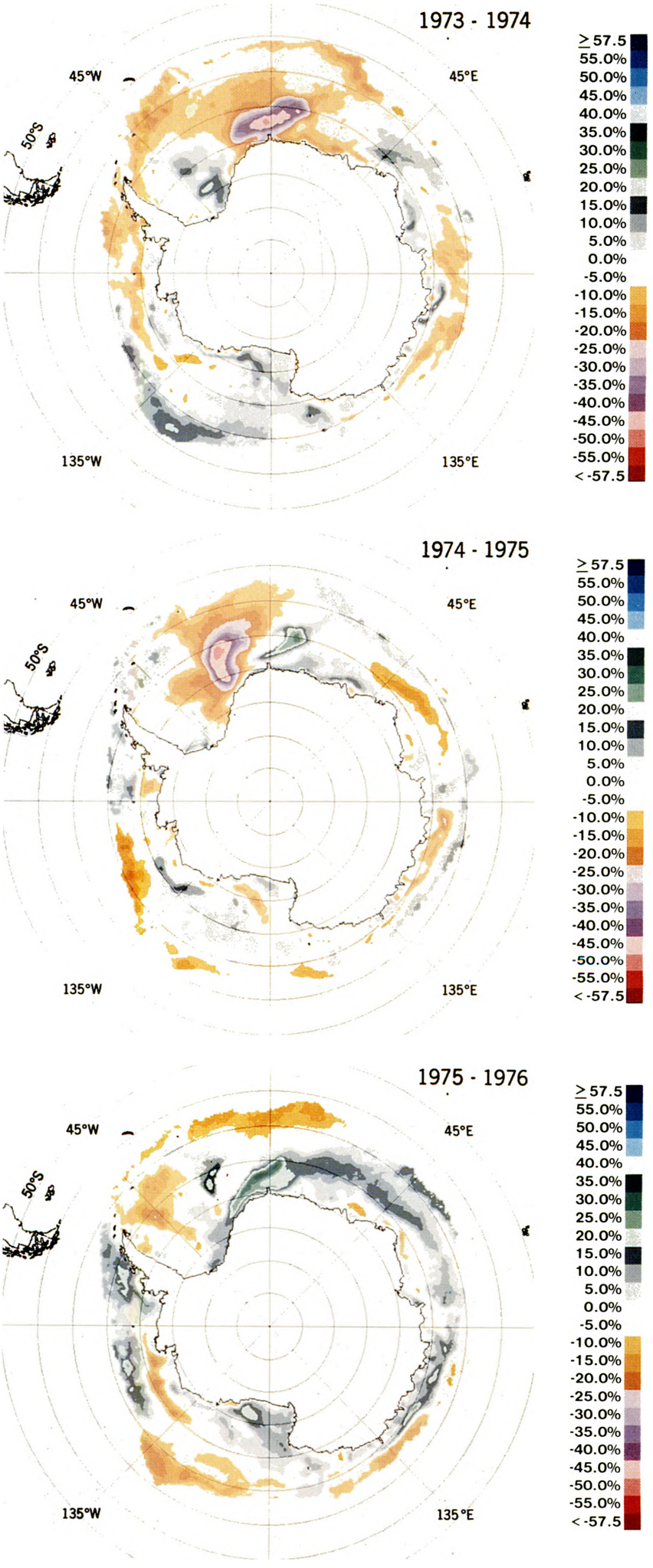

Figure 5-40. Change in annual mean sea ice concentrations from 1973 to 1974, from 1974 to 1975, and from 1975 to 1976.

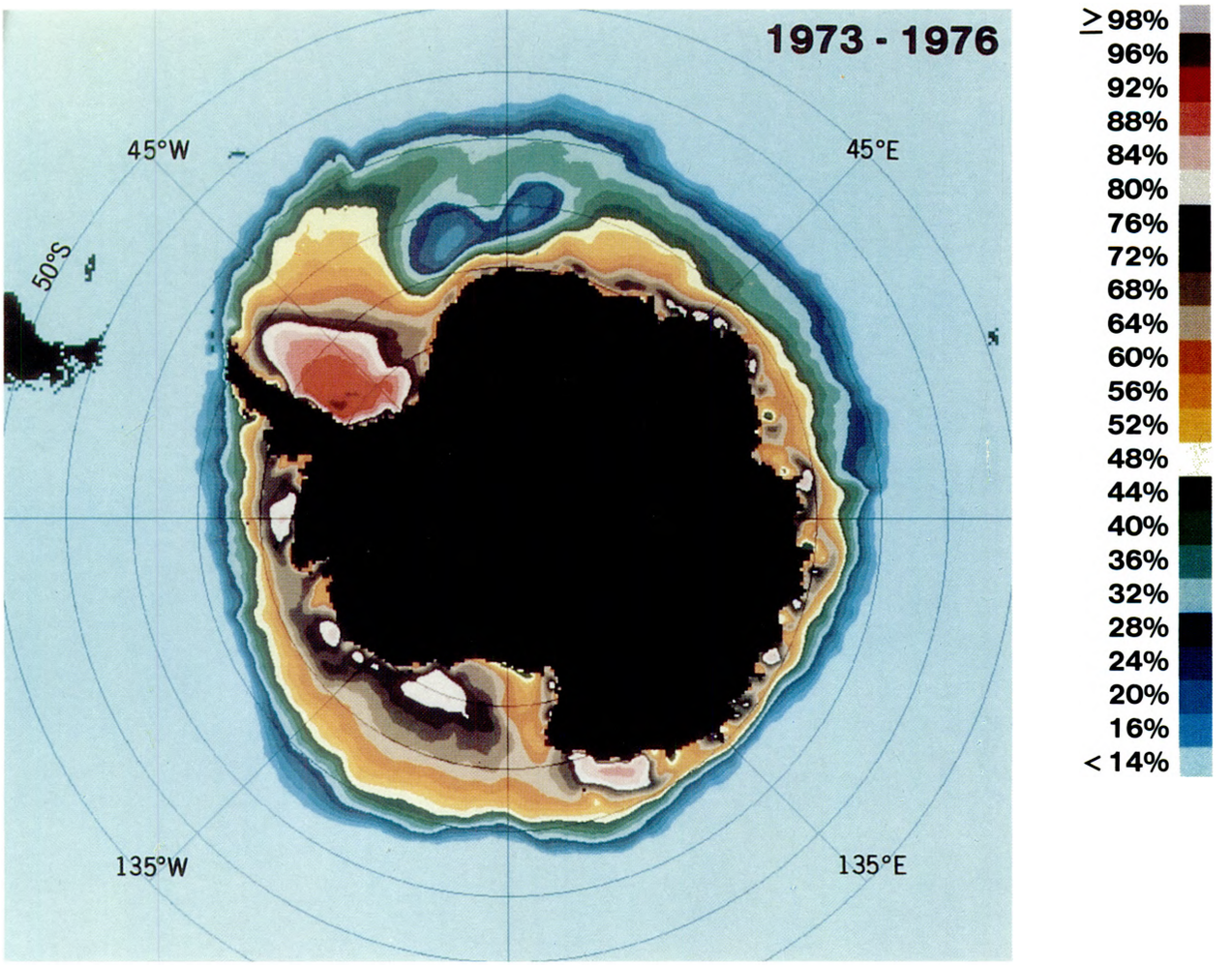

Figure 5-41. Four-year average of annual mean sea ice concentrations.

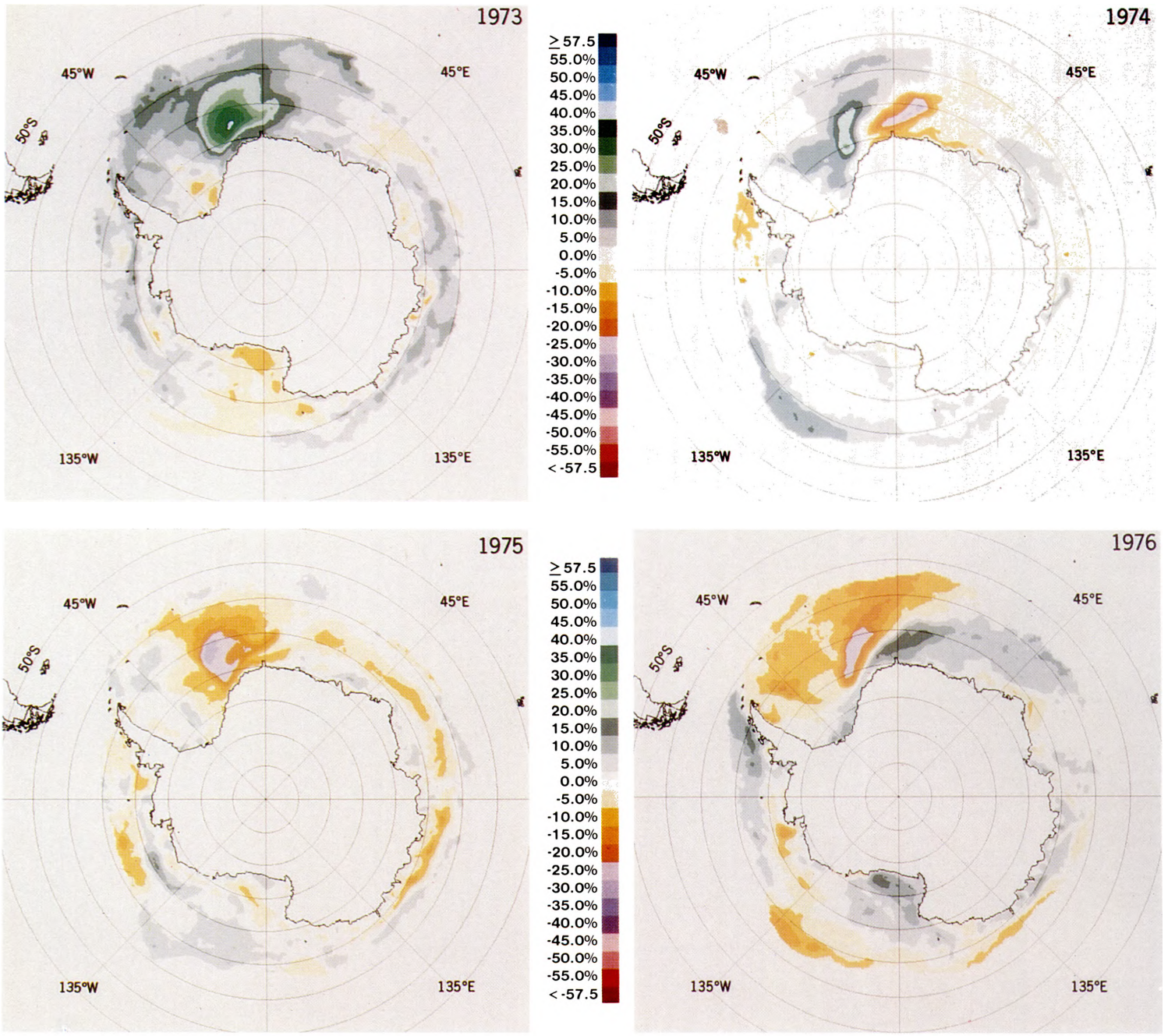

Figure 5-42. Deviations of annual mean sea ice concentrations from 4-year average of annual means.

Table 5-1
Percent Change in Sea Ice Extent from 1973 to 1976

Month	Southern Ocean	Weddell Sea	Bellingshausen-Amundsen Seas	Ross Sea	Pacific Ocean	Indian Ocean
Annual Mean*	-9.7 (-9.8)	-22.7 (-24.7)	2.1 (-2.8)	-2.6 (1.9)	-14.6 (-13.1)	0.9 (3.2)
January	-14.2	-42.5	-11.8	15.8	-8.7	-7.8
February	-12.3	-26.5	-18.4	9.5	-0.5	-14.6
March*	-14.8 (0.4)	-10.3 (-19.3)	-31.5 (-37.6)	10.0 (86.1)	-21.9 (2.3)	-43.6 (-10.0)
April*	-13.4 (-4.7)	-17.2 (-29.5)	-39.9 (-49.0)	15.5 (69.4)	-14.2 (9.1)	-28.7 (11.1)
May*	-2.1 (-5.8)	-14.2 (-31.4)	-4.3 (-18.0)	6.7 (27.2)	-7.0 (0.0)	15.8 (28.4)
June	-9.2	-28.4	-9.4	1.7	-11.9	27.9
July	-7.5	-22.9	8.4	-8.1	-2.1	12.0
August*	1.7 (-5.3)	-15.6 (-16.3)	38.0 (14.0)	1.7 (-5.3)	3.1 (-9.5)	16.0 (5.9)
September	-6.0	-14.9	15.2	-1.6	-20.6	1.5
October	-10.0	-15.0	13.5	-14.7	-30.0	-1.5
November	-13.5	-24.5	17.5	-17.6	-29.4	1.8
December	-25.3	-48.3	9.4	-11.1	-9.8	-29.6

*Values for months in 1973 with no ESMR map are obtained by two methods: upper value is from Navy-NOAA maps (Godin and Barnett, 1979) and lower value (in parentheses) is from interpolation of ESMR data using spline fit to annual cycle.

mean sea ice concentration (Figure 5-40) illustrates, for example, the appearance and yearly migration of the Weddell polynya. Also apparent are the spatial distributions of the progressive decreases in ice cover in the Weddell Sea sector, the increase followed by a decrease in the Ross Sea sector, and the opposite pattern of a decrease followed by an increase in the Indian Ocean and Bellingshausen-Amundsen Seas sectors. Similarly, changes in the yearly distributions are presented with respect to the 4-year average of the annual mean sea ice concentration in Figure 5-42.

In this document, the Antarctic sea ice cover is described with a multiplicity of image formats and graphical displays. The use of alternative displays of the ice cover and its changes are intended to increase our insight into the unique characteristics of the Antarctic sea ice cover. Fortunately, the years 1973 through 1976, in which global microwave observation of sea ice was initiated, coincided with a period of significant changes in the sea ice cover. Certainly, the appearance of the Weddell polynya in 1974, 1975, and 1976 and its non-appearance the preceding year is a very interesting geophysical phenomenon. Similarly, the large decrease of the sea ice cover from 1973 to 1976 was probably unusual (see Zwally et al., 1983) and, if continued, would have resulted in a 30-percent reduction in the annual mean sea ice cover by 1981. Clearly, an extended record of sea ice cover is needed to understand the changes in the ice cover and detect any secular trends. Hopefully, the publication of this document will assist in clarifying the need for continued passive microwave satellite observations and the need for the selective and systematic processing of the microwave data acquired since 1976.

REFERENCES

Ackley, S. F., Mass balance aspects of Weddell Sea pack ice, *J. Glaciol.*, **24**, 391-406, 1979.

Ackley, S. F., A review of sea-ice weather relationships in the Southern Hemisphere, in *Sea Level, Ice and Climatic Change*, I. Allison, ed., International Association of Hydrological Sciences, Guildford, Great Britain, 127-159, 1981.

Ackley, S. F., and T. E. Keliher, Antarctic sea ice dynamics and its possible climatic effects, *Aidjex Bull.*, **33**, 53-76, 1976.

Allison, I., C. M. Tivendale, G. J. Akerman, J. M. Tann, and R. H. Wills, Seasonal variations in the surface energy exchanges over Antarctic sea ice and coastal waters, *Ann. Glaciol.*, **3**, 12-16, 1982.

Andreas, E. L., and S. F. Ackley, On the differences in ablation seasons of Arctic and Antarctic sea ice, *J. Atmos. Sci.*, **39**, 440-447, 1982.

Armstrong, T., B. Roberts, C. Swithinbank, *Illustrated Glossary of Snow and Ice*, Scott Polar Research Institute, Cambridge, Great Britain, 60 pp., 1973.

Bryden, H. L., Poleward heat flux and conversion of available potential energy in Drake Passage, *J. Mar. Res.*, **37**, 1-22, 1979.

Campbell, W. J., Analysis of Arctic ice features, in *Earth Resources Technology Satellite-1 Symposium Proceedings, September 29, 1972*, W. A. Finch Jr., comp., NASA TM X-66193, Greenbelt, Maryland, 129-130, 1973.

Campbell, W. J., P. Gloersen, W. Nordberg, and T. T. Wilheit, Dynamics and morphology of Beaufort Sea ice determined from satellites, aircraft, and drifting stations, in *Proceedings of the Symposium on Approaches to Earth Survey Problems Through Use of Space Techniques (COSPAR)*, P. Bock, F. W. G. Baker, and S. Ruttenberg, ed., Akademie Verlag, Berlin, 311-327, 1974.

Campbell, W. J., P. Gloersen, W. J. Webster, T. T. Wilheit, and R. O. Ramseier, Beaufort Sea ice zones as delineated by microwave imagery, *J. Geophys. Res.*, **81**, 1103-1110, 1976.

Campbell, W. J., J. Wayenberg, J. B. Ramseyer, R. O. Ramseier, M. R. Vant, R. Weaver, A. Redmond, L. Arsenault, P. Gloersen, H. J. Zwally, T. T. Wilheit, T. C. Chang, D. Hall, L. Gray, D. C. Meeks, M. L. Bryan, F. T. Barath, C. Elachi, R. Leberl, and T. Farr, Microwave remote sensing of sea ice in the AIDJEX main experiment, *Boundary Layer Meteorol.*, **13**, 309-337, 1978.

Carmack, E. C., Water characteristics of the southern ocean south of the polar front, in *A Voyage of Discovery, George Deacon 7th Anniversary Volume*, M. Angel, ed., Pergamon Press, Oxford, 15-41, 1977.

Carmack, E. C., and P. D. Killworth, Formation of interleaving of abyssal water masses off Wilkes Land, Antarctica, *Deep Sea Res.*, **25**, 357-369, 1978.

Carsey, F. D., Microwave observation of the Weddell Polynya, *Mon. Weather Rev.*, **108**, 2032-2044, 1980.

Carsey, F. D., Arctic sea ice distribution at end of summer 1973-1976 from satellite microwave data, *J. Geophys. Res.*, **87**, 5809-5835, 1982.

Cavalieri, D., and C. L. Parkinson, Large-scale variation in observed Antarctic sea ice extent and associated atmospheric circulation, *Mon. Weather Rev.*, **109**, 2323-2336, 1981.

Chang, T. C., and P. Gloersen, Microwave emission from dry and wet snow, in *Operational Applications of Satellite Snow Cover Observations*, A. Rango, ed., NASA SP-391, 399-407, 1975.

Chang, T. C., P. Gloersen, T. Schmugge, T. T. Wilheit, and H. J. Zwally, Microwave emission from snow and glacier ice, *J. Glaciol.*, **16**, 23-39, 1976.

Comiso, J. C., and H. J. Zwally, Corrections for anomalous time dependent shifts in the brightness temperature from Nimbus 5 ESMR, NASA TM-82055, Greenbelt, Maryland, 18 pp., 1980.

Comiso, J. C., and H. J. Zwally, Antarctic sea ice concentrations inferred from Nimbus 5 ESMR and Landsat imagery, *J. Geophys. Res.*, **87**, 5836-5844, 1982.

Comiso, J. C., H. J. Zwally, and J. L. Saba, Radiative transfer modeling of microwave emission and dependence on firn properties, *Ann. Glaciol.*, **3**, 54-58, 1982.

Cox, G. F. N., and W. F. Weeks, Salinity variations in sea ice, *J. Glaciol.*, **13**, 109-120, 1974.

Deacon, G. E. R., A general account of the hydrology of the southern ocean, *Discovery Rep.*, **7**, 171-238, 1933.

Deacon, G. E. R., The hydrology of the southern ocean, *Discovery Rep.*, **15**, 1-124, 1937.

Deacon, G. E. R., The Weddell gyre, *Deep Sea Res.*, **26**, 981-995, 1979.

Fandry, C. J., and R. D. Pillsbury, On the estimation of absolute geostropic volume transport applied to the Antarctic circumpolar current, *J. Phys. Oceanogr.*, **9**, 449-455, 1979.

Fletcher, J. O., Ice on the ocean and world climate, in *Beneficial Modifications of the Marine Environment*, National Academy of Sciences, Washington, D.C., 4-49, 1972.

Foster, T. D., and E. C. Carmack, Temperature and salinity structure in the Weddell Sea, *J. Phys. Oceanogr.*, **6**, 36-44, 1976.

Foster, T. D., and J. H. Middleton, Variability in the bottom water of the Weddell Sea, *Deep Sea Res.*, **26**, 743-762, 1979.

Georgi, D. P., and J. M. Toole, The Antarctic circumpolar current and the oceanic heat and freshwater budgets, *J. Mar. Res.*, **40**, 183-197, 1982.

Gloersen, P., and F. Barath, A scanning multichannel microwave radiometer for Nimbus G and Seasat, *IEEE Oceanic Engr.*, **OE-2**, 172-178, 1977.

Gloersen, P., and Larabee, An optical model for the microwave properties of sea ice, NASA TM-83865, Greenbelt, Maryland, 25 pp., 1981.

Gloersen, P., W. Nordberg, T. J. Schmugge, and T. T. Wilheit, Microwave signatures of first-year and multiyear sea ice, *J. Geophys. Res.*, **78**, 3564-3572, 1973.

Gloersen, P., R. Ramseier, W. J. Campbell, T. C. Chang, and T. T. Wilheit, Variation of ice morphology of selected mesoscale test areas during the Bering Sea Experiment, in *Proceedings of the Final Symposium on the Results of the Joint Soviet-American Expedition, Leningrad, May 12-17, 1974*, K. Ya. Kondratyev, Yu. I. Rabinovich, and W. Nordberg, ed., Gidrometeoizdat, Leningrad, 196-218, 1975a.

Gloersen, P., R. O. Ramseier, W. J. Campbell, P. M. Kuhn, and W. J. Webster, Jr., Ice thickness distribution as inferred from infrared and microwave remote sensing during the Bering Sea Experiment, in *Proceedings of the Final Symposium on the Results of the Joint Soviet-American Expedition, Leningrad, May 12-17, 1974*, K. Ya. Kondratyev, Yu. I. Rabinovich, and W. Nordberg, ed., Gidrometeoizdat, Leningrad, 282-293, 1975b.

Gloersen, P., T. T. Wilheit, T. C. Chang, and W. Nordberg, Microwave maps of the polar ice of the Earth, *Bull. Amer. Meteorol. Soc.*, **55**, 1442-1448, 1974.

Gloersen, P., H. J. Zwally, A. T. C. Chang, D. K. Hall, W. J. Campbell, and R. O. Ramseier, Time dependence of sea ice concentration and multiyear ice fraction in the Arctic Basin, *Boundary Layer Meteorol.*, **13**, 339-359, 1978.

Godin, R. H., and D. G. Barnett, Global sea ice limits, in *Inventory of Snow Cover and Sea Ice Data*, Glaciological Data Report GD-7, World Data Center A for Glaciology, Boulder, Colorado, 25-36, 1979.

Gordon, A. L., Deep Antarctic convection of Maud Rise, *J. Phys. Oceanogr.*, **8**, 600-612, 1978.

Gordon, A. L., Comments on southern ocean meridional thermohaline flux, *Ocean Modeling*, **11**, 1-4, 1980.

Gordon, A. L., Seasonality of southern ocean sea ice, *J. Geophys. Res.*, **86**, 4193-4197, 1981.

Gordon, A. L., and R. D. Goldberg, Circumpolar characteristics of Antarctic waters, *Antarctic Map Folio Series*, Folio 13, V. Bushnell, ed., American Geographical Society, New York, 1970.

Gordon, A. L., D. G. Martinson, and H. W. Taylor, The wind-driven circulation in the Weddell-Enderby Basin, *Deep Sea Res.*, **28**, 151-163, 1981.

Gordon, A. L., and E. J. Molinelli, *Southern Ocean Atlas: Thermohaline and Chemical Distributions and the Atlas Data Set*, Columbia University Press, New York, 1982.

Gordon, A. L., E. Molinelli, and T. Baker, Large scale relative dynamic topography of the southern ocean, *J. Geophys. Res.*, **83**, 3023-3032, 1978.

Gow, A. J., S. F. Ackley, W. F. Weeks, and J. W. Govoni, Physical and structural characteristics of Antarctic sea ice, *Ann. Glaciol.*, **3**, 113-117, 1982.

Hansen, A. M., The snow cover of sea ice during the Arctic Ice Dynamics Joint Experiment, 1975 to 1976, *Arctic and Alpine Research*, **12**, 215-226, 1980.

Heezen, B., C. M. Thorp, and C. R. Bentley, Morphology of the Earth in the Antarctic and subantarctic, *Antarctic Map Folio Series*, Folio 16, V. Bushnell, ed., American Geographical Society, New York, 1972.

Hibler, W. D., A dynamic thermodynamic sea ice model, *J. Phys. Oceanogr.*, **9**, 815-846, 1979.

Hibler, W. D., and S. F. Ackley, On modeling the Weddell Sea pack ice, *Ann. Glaciol.*, **3**, 125-130, 1982.

Jackson, J. D., *Classical Electrodynamics*, John Wiley & Sons, Inc., New York, 641 pp., 1962.

Jenne, R. L., H. L. Crutcher, H. van Loon, and J. J. Taljaard, A selected climatology of the Southern Hemisphere: Computer methods and data availability. NCAR-TN/STR-92, National Center for Atmospheric Research, Boulder, Colorado, 91 pp., 1974.

Ketchum, R. D., and A. W. Lohanick, Passive microwave imagery at 33 GHz, *Remote Sensing Environ.*, **2**, 211-233, 1980.

Killworth, P. D., On "chimney" formations in the ocean, *J. Phys. Oceanogr.*, **9**, 531-554, 1979.

Knapp, W. W., A satellite study of large stationary polynyas in Antarctic coastal waters, Ph.D. thesis, University of Wisconsin, Madison, 1969.

Kukla, G., and J. Gavin, Summer ice and carbon dioxide, *Science*, **214**, 497-503, 1981.

Lake, R. A., and E. L. Lewis, Salt rejection by sea ice during growth, *J. Geophys. Res.*, **75**, 583-597, 1970.

Lamb, H. H., *Climate: Present, Past, and Future*, Methuen and Co., London, 613 pp., 1972.

Lemke, P., E. W. Trinkl, and K. Hasselmann, Stochastic dynamic analysis of polar sea ice variability, *J. Phys. Oceanogr.*, **10**, 2100-2120, 1980.

Lutjeharms, J. R. E., and D. J. Baker, Intensities and scales of motion in the southern ocean, *South African J. of Sci.*, **75**, 179-182, 1979.

Martinson, D. G., P. D. Killworth, and A. L. Gordon, A convective model for the Weddell polynya, *J. Phys. Oceanogr.*, **11**, 466-488, 1981.

Maykut, G. A., Energy exchange over young sea ice in the central Arctic, *J. Geophys. Res.*, **83**, 3646-3658, 1978.

Maykut, G. A., and N. Untersteiner, Some results from a time-dependent thermodynamic model of sea ice, *J. Geophys. Res.*, **76**, 1550-1575, 1971.

Parkinson, C. L., On the development and cause of the Weddell polynya in a sea ice simulation, *J. Phys. Oceanogr.*, **13**, 501-511, 1983.

Parkinson, C. L., and D. J. Cavalieri, Interannual sea-ice variations and sea-ice/atmosphere interactions in the Southern Ocean, 1973–1975, *Ann. Glaciol.*, **3**, 249-254, 1982.

Parkinson, C. L., and W. M. Washington, A large-scale numerical model of sea ice, *J. Geophys. Res.*, **84**, 311-337, 1979.

Ramseier, R. O., P. Gloersen, and W. J. Campbell, Variation of the microwave emissivity of sea ice in the Beaufort and Bering Seas, in *Proceedings of the URSI Commission II–Specialist Meeting on Microwave Scattering and Emission from the Earth*, E. Schanda, ed., Institute of Applied Physics University, Berne, Switzerland, 87-93, 1974.

Ramseier, R. O., P. Gloersen, W. J. Campbell, and T. C. Chang, Mesoscale description for the principal Bering Sea ice experiment, in *Proceedings of the Final Symposium on the Results of the Joint Soviet-American Expedition, Leningrad, May 12-17, 1974*, K. Ya. Kondratyev, Yu. I. Rabinovich, and W. Nordberg, ed., Gidrometeoizdat, Leningrad, 234-270, 1975.

Rayner, J. N., and D. A. Howarth, Antarctic sea ice: 1972–1975, *Geogra. Rev.*, **69**, 202-223, 1979.

Schwerdtfeger, P., The effect of the Antarctic Peninsula on the temperature regime of the Weddell Sea, *Mon. Weather Rev.*, **103**, 45-51, 1975.

Stiles, W. H., and F. T. Ulaby, The active and passive microwave response to snow parameter 1, Wetness, *J. Geophys. Res.*, **85**, 1037-1044, 1980.

Streten, N. A., Satellite observations of the summer decay of the Antarctic sea-ice, *Arch. Meteorol. Geophys. Bioklimato.*, **Ser. A**, 22, 119-134, 1973.

Sverdrup, H. V., Narrative and oceanography of the Nautilus expedition, *Papers on Phys. Oceanogr. and Meteorol.*, **2**, 1-63, 1933.

Taljaard, J. J., H. van Loon, H. L. Crutcher, and R. L. Jenne, Climate of the upper air: Southern Hemisphere, Vol. 1, Temperatures, dew points, and heights at selected pressure levels, NAVAIR 50-1C-55, Chief Naval Operations, Washington, D.C., 135 pp., 1969.

Tolstikov, Ye. I., ed., *Atlas of the Antarctic*, **1**, Academy of Sciences, Moscow, U.S.S.R., 225 plates, 1966.

Toole, J. M., Sea ice wintertime convection and the temperature minimum layer in the Southern Ocean, *J. Geophys. Res.*, **86**, 8037-8047, 1981.

Tooma, S. G., R. A. Menella, J. P. Hollinger, and R. D. Ketchum, Comparison of sea-ice type identification between airborne dual-frequency passive microwave radiometry and standard laser/infrared techniques, *J. Glaciol.*, **15**, 225-239, 1975.

Troy, B. E., J. P. Hollinger, R. M. Lerner, and M. M. Wisler, Measurement of the microwave properties of sea ice at 90 GHz and lower frequencies, *J. Geophys. Res.*, **86**, 4283-4289, 1981.

Untersteiner, N., On the mass and heat budget of Arctic sea ice, *Arch. Meteorol. Geophys. Bioklimato.*, **12**, 151-182, 1961.

Untersteiner, N., Natural desalination and equilibrium salinity profile of perennial sea ice, *J. Geophys. Res.*, **73**, 1251-1257, 1968.

Vant, M. R., R. B. Gray, R. O. Ramseier, and V. Makios, Dielectric properties of fresh sea ice at 10 and 35 GHz, *J. Appl. Phys.*, **45**, 4712-4717, 1974.

Vant, M. R., R. O. Ramseier, and V. Makios, The complex-dielectric constant of sea ice at frequencies in the range 0.1–40 GHz, *J. Appl. Phys.*, **49**, 1264-1280, 1978.

Walsh, J. E., and C. M. Johnson, An analysis of arctic sea ice fluctuations, 1953–1977, *J. Phys. Oceanogr.*, **9**, 580-591, 1979.

Webster, P. J., Aspects of the climate of the Southern Hemisphere: Preliminary interpretations of the "EOLE" experiment, in *Climate of the Arctic*, G. Weller and S. Bowling, ed., Geophysical Institute, University of Alaska, Fairbanks, 190-203, 1975.

Weller, G., A meridional surface wind speed profile in Mac Robertson Land, Antarctica, *Pure Appl. Geophys.*, **77**, 193-200, 1969.

Weller, G., Spatial and Temporal variations in the south polar surface energy balance, *Mon. Weather Rev.*, **108**, 2006-2014, 1980.

Wilheit, T. T., The Electrically Scanning Microwave Radiometer (ESMR) experiment, in *Nimbus 5 User's Guide*, NASA/Goddard Space Flight Center, 59-105, 1972.

Wilheit, T. T., W. Nordberg, J. C. Blinn, W. J. Campbell, and A. T. Edgerton, Aircraft measurements of microwave emission from Arctic sea ice, *Remote Sensing Environ.*, **2**, 129-139, 1972.

WMO (World Meteorological Organization), *WMO Sea-Ice Nomenclature, Terminology, Codes, and Illustrated Glossary*, WMO/OMM/BMO No. 259, TP 145, Secretariat of the World Meteorological Organization, 1970.

Zillman, J. W., A study of some aspects of the radiation and heat budgets of the Southern Hemisphere oceans, Meteorological Study 26, Bureau of Meteorology, Department of the Interior, Canberra, Australia, 562 pp., 1972.

Zwally, H. J., Microwave emissivity and accumulation rate of polar firn, *J. Glaciol.*, **18**, 195-215, 1977.

Zwally, H. J., J. C. Comiso, and C. L. Parkinson, Satellite-derived ice data sets No. 1: Antarctic monthly average microwave brightness temperatures and sea ice concentrations 1973–1976, NASA TM-83812, Greenbelt, Maryland, 1981.

Zwally, H. J., and P. Gloersen, Passive microwave images of the polar regions and research applications, *Polar Rec.*, **18**, 431-450, 1977.

Zwally, H. J., C. L. Parkinson, F. D. Carsey, P. Gloersen, W. J. Campbell, and R. O. Ramseier, Antarctic sea ice variations 1973–1975, in *Fourth NASA Weather and Climate Review*, E. R. Kreins, ed., National Aeronautics and Space Administration, Washington, D.C., 335-340, 1979.

Zwally, H. J., C. L. Parkinson, and J. C. Comiso, Variability of Antarctic sea ice and CO_2 change, *Science*, **220**, 4601, 1005-1012, 1983.

Zwally, H. J., T. T. Wilheit, P. Gloersen, and J. L. Mueller, Characteristics of Antarctic sea ice as determined by satellite-borne microwave imagers, in *Proceedings of the Symposium on Meteorological Observations from Space: Their Contribution to the First GARP Global Experiment*, Committee on Space Research of the International Council of Scientific Unions, Philadelphia, 94-97, 1976.

APPENDIX A

DATA PROCESSING, COMPILATION, AND STORAGE

A.1 DATA STREAM

The telemetry data from the Nimbus 5 satellite, launched in December 1972, were transmitted to two spaceflight tracking and data network stations located near Fairbanks, Alaska, and Rosman, North Carolina. The data received in Alaska were recorded as the satellite passed and then transmitted over a microwave link to the Meteorological Data Handling System (MDHS) at the Goddard Space Flight Center (GSFC). The data received in North Carolina were relayed directly to GSFC over a wideband data link. At GSFC, the telemetry data were unpacked, decommutated, supplemented with flags and end of files, and stored on magnetic tapes called experimental tapes (ET's). For data processing convenience, the data from the Electrically Scanning Microwave Radiometer (ESMR) from several ET's were combined to form stacked experimental tapes (SET's). The 10-bit telemetry data on the ET's were converted to 32-bit format on the SET's for use on the GSFC computers.

The SET's and ephemeris tapes were then used to generate the Earth-located calibrated brightness temperature (CBT) tapes, which are the primary source of calibrated radiometer data. The CBT tapes contain the time, the calibration parameters, the measured brightness temperatures (T_B), and the corresponding geographical coordinates (Table A-1). Each CBT tape was written at 6250 bits per inch and has approximately 180 files, each of which contains one orbit of data.

In order to provide a synoptic representation of the data in the polar regions, a polar stereographic mapping, described later, is employed. The grid size is 293 by 293, with each map cell representing an area varying from about 32 by 32 kilometers near the poles to about 28 by 28 kilometers near 50 degrees latitude (Figure A-1).

Full coverage of the entire polar area could be obtained from a sequence of six satellite orbits or one-half day of good data if the full set of 78 beam positions were used. However, because of the large disparity in the radiometer field of view from the outer beam position to the middle beam position (70 by 140 kilometers compared to 25 by 25 kilometers), only the middle 52 beam positions are utilized, for a swath-angle coverage of ±30.5 degrees and a minimum resolution of 29 by 42 kilometers. This swath angle corresponds to a spatial coverage of about 1280 kilometers on the Earth's surface. Since the area poleward of the 85-degree latitude is observed by the outer beam positions only, the outer beam positions, which are otherwise discarded, are used to cover the region between 85 degrees and the poles. With this restriction on beam positions and with additional rejection of data because of occasional instrumental problems, about 3 days of data are required to provide adequate spatial coverage of the polar regions. Three-day average maps are therefore generated for all periods that contained valid data from launch until May 1977. From these secondary products, monthly mean T_B maps are created and used with interpolated monthly surface temperature maps to calculate monthly ice concentrations. Yearly and multiyearly average maps are also created. Interpolation and weighting procedures to account for missing data are described in Section A.3.3, "Interpolation Procedures."

A.2 CALIBRATION AND QUALITY-CONTROL PROCEDURES

A.2.1 Latitude and Longitude Determination

Initially, ephemeris data based on several weeks of predictive calculations were used to compute

Table A-1
CBT Data Record Format for ESMR*

Word No.	Quantity	Units	Scale	Description
1	Year	Year		Year associated with data
2	Day	Days		
3	Hour	Hours		
4	Minute	Minutes		
5	Second	Seconds		
6	Program ID			Unique program identification
7	Pitch error	Degrees	x10	Pitch fine error
8	Roll error	Degrees	x10	Roll fine error
9	RMP indicated rate high		x10	
10	Latitude	Degrees	x10	Latitude of subsatellite point
11	Longitude	Degrees	x10	Longitude of subsatellite point
12	Height	Kilometers		Height of spacecraft
13	Hot-load mean		x10	
14	Hot load		x100	
15	Cold-load mean		x10	
16	Cold load		x100	
17	MUX 1			Average antenna temperature
18	MUX 2			Phase-shift temperature
19	MUX 3			Ferrite-switch temperature
20	MUX 4			Ambient-load temperature
21	MUX 5			Hot-load temperature
22	MUX 6			Automatic gain control (AGC)
23-41	Engineering data			
42	Beam position 79			
43-46	MUX 1-MUX 4			
47-124	Latitude	Degrees	x10	Latitudes of the 78 scan positions
125-202	Longitude	Degrees	x10	Longitudes of the 78 scan positions
203-280	Brightness temperature	Degrees (Kelvin)	x10	Brightness temperatures of the 78 scan positions

*Source: Wilheit, 1972.

the latitude and longitude of each scan angle of the radiometer. However, use of these data often caused serious Earth-location errors up to several hundred kilometers. These errors were substantially reduced by utilizing definitive ephemeris data calculated from satellite tracking parameters. The new procedure was implemented in 1975 for newly acquired data, and all prior CBT tapes were revised at that time. Results were checked by comparing Earth locations generated from these data with continental boundaries. The calculated Earth location appears to be accurate to well within 30 kilometers, which is the approximate resolution used for mapping the data.

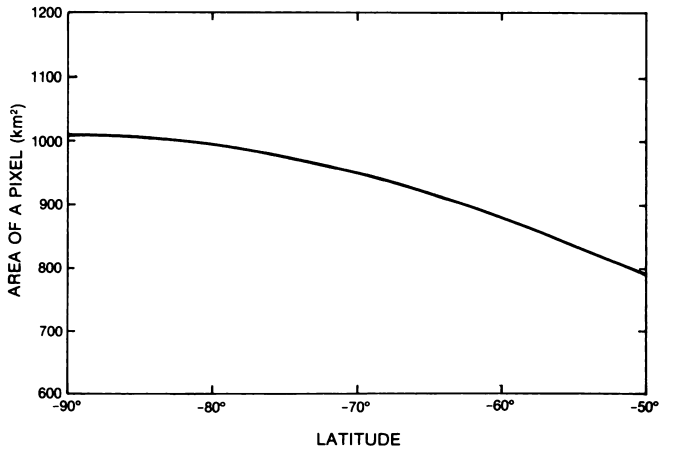

Figure A-1. Area of a map element (pixel) as a function of latitude.

A.2.2 Calibration Algorithm

Calibration of the radiometer was done with the aid of hot and cold reference sources. The cold-load temperature reference (T_C) was provided by a sky horn that measures the 3 K cosmic background. The hot-load temperature was provided by reference to a floating ambient termination in the spacecraft. It takes eight scans of data to produce a complete set of calibration parameters (Table A-2). The calibration temperatures, T_C and T_H, were calculated from the multiplex data (MUX 1 through MUX 6 in Table A-1). The values of four ambient and four cold calibration voltages (V_H and V_C, respectively) were averaged through a set of eight scans. For each beam position, the brightness temperature, T_{IN}, corresponding to voltage, V, was then calculated by:

$$T_{IN} = T_H + \frac{T_C - T_H}{V_C - V_H}(V - V_H). \qquad \text{(A-1)}$$

This algorithm calibrates the microwave radiometer instrument. However, some additional correction to this calibration must be applied to account for the antenna ohmic loss, which is a function of beam position and the temperature of the phase shifters.

Further correction was also required for the effects of side lobes and the different viewing angles. A procedure for providing these corrections by using prelaunch laboratory tests could not be implemented because the antenna properties of the instrument changed substantially after launch. A procedure relying mainly on available ground-truth data, statistical analysis, and modeling had to be implemented for the final calibration. A set of correction parameters, A_0 and A_1, for each beam position were empirically determined using ocean data. These were then used to determine the final calibrated brightness temperature, $T_B(I) = A_0(I) + A_1(I) \times T_{IN}(I)$, where I is the beam position number.

A.2.3 Processing Problems and Data Gaps

Initially, when all available calibrated data were processed, many of the polar stereographic maps were found to be contaminated by abnormal brightness temperatures. Analysis of the problem showed that some orbits or portions of orbits were not properly calibrated because of unforeseen problems with the input data when calibration was made. For example, if there was a parity read error in the middle of input SET's, some calibration parameters would be unpacked improperly, causing the brightness temperature to be unphysical in magnitude.

The initial procedure used for removing the badly calibrated data was crude but effective. A polaroid color image of each map was first produced and checked for abnormal features. These are normally easy to spot because at least eight scans would be affected. The next step was to identify which orbits and portions thereof had problems. The orbit number was determined by using a graphical overlay on the image, and the time interval was then determined by examining a printout of the data for the entire orbit. These time intervals containing bad data were excluded in the final processing of the maps. In a later version of the mapping software, most of these bad data were automatically eliminated by requiring that the values of the calibration parameters fall within certain acceptable limits.

To calibrate the microwave radiometer adequately, both the hot-load and cold-load reference temperatures must be available. Sometimes, the hot-load reference for the Nimbus 5 ESMR was not recoverable because of hardware or processing problems. The ESMR radiometer was in this abnormal mode occasionally during the 1973 through

Table A-2
Framing Format of the ESMR Data in SET Tapes

Word Number	Scan Number	Number of Bits/Word	Description
1-78	1	10	V_{1-78} for beam positions 1-78
79	1		Hot reference
80	1		Average antenna temperature
81-128	2		V_{1-78} for beam positions 1-78
129	2		Cold reference
130	2		Average phase-shifter temperature
131-208	3		V_{1-78} for beam positions 1-78
209	3		Hot reference
210	3		Ferrite-switch temperature
211-288	4		V_{1-78} for beam positions 1-78
289	4		Cold reference
290	4		Ambient-load temperature
291-368	5		V_{1-78} for beam positions 1-78
369	5		Hot reference
370	5		Dicke-load temperature
371-448	6		V_{1-78} for beam positions 1-78
449	6		Cold reference
450	6		AGC count
451-528	7		V_{1-78} for beam positions 1-78
529	7		Hot reference
530	7		Multiplex calibration
531-608	8		V_{1-78} for beam positions 1-78
609	8		Cold reference
610	8		Frame identification number

1976 period, most seriously in March to May and August of 1973. These months have no useable data due to the hot-load abnormality. Although the radiometer operated abnormally for as long as a few days during other times, there were normally enough well-calibrated data left to form monthly averages. The only other months without data are June, July, and August of 1975. For these months, however, the gaps were not due to the abnormality but rather because the data acquisition instruments for Nimbus 5 were turned off when the systems for these instruments were needed for the then newly launched Nimbus 6 satellite. In September 1975, data acquisition for Nimbus 5 ESMR was restored but on an every-other-day basis only.

A.2.4 Anomalous Time-Dependent Shifts in Brightness Temperature

Studies of the temporal variation of brightness temperature in the ice-free areas of the southern ocean revealed some unexpected time-dependent shifts. At 19 GHz, the brightness temperature (T_B) of sea water is expected to have minimal or no seasonal dependence because the emissivity is inversely proportional to the surface physical temperature (Wilheit, 1972). Although T_B is affected by roughness, foam, water vapor, and rainfall, none of these have seasonal characteristics consistent with the observed shifts. Because the observed shifts could not be attributed to any of

these geophysical effects, they were assumed to be caused by calibration or instrumental problems, and a normalization procedure summarized below was therefore applied to the monthly average T_B data (Comiso and Zwally, 1980).

To investigate the time dependence of T_B, the data for each pixel in the monthly maps between 55°S and 65°S were binned; an example of a typical distribution is shown in Figure A-2. The contribution from the ocean appeared as a narrow peak at approximately 135 K with an average width of about ±4 K. The position of the ocean peak varied from month to month, and the value for each month of available ESMR data is shown in Figure A-3. In 1973, a dip of approximately 8 K occurs from January to July. In 1976, a much larger dip than that in 1973 is evident in May and June, followed by a recovery in July with a general decrease for the remainder of the year. During 1974 and 1975, T_B is nearly constant with time.

Further study of the apparently anomalous shift in T_B was made by examining both ocean and highly concentrated sea ice and by using 3-day average maps. Shifts in brightness temperature in both ocean and ice areas occurred at about the same time. Furthermore, although the initial downward shift is about 10 K for the ocean and 8 K for the sea ice, the recovery shift is about 18 K for the ocean and 25 K for the sea ice. The latter shift would correspond to a change in physical temperature of about 27 K on the ice and 40 K in the water if emissivity is assumed to be constant during the time period. Therefore, considering the abrupt nature of the shifts and their magnitude, it is not possible to attribute these anomalies to physical effects in the ocean or atmosphere. Examination of the time variation of T_B of the Antarctic ice sheets also indicated corresponding anomalous time-dependent shifts.

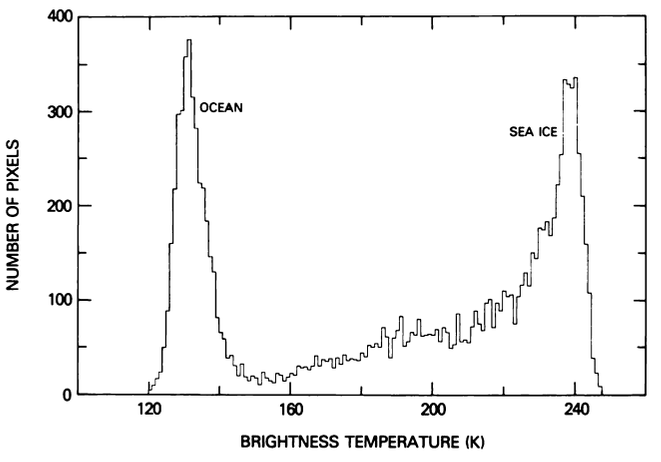

Figure A-2. Typical winter distribution of brightness temperatures in map elements (pixels) between 55°S and 65°S.

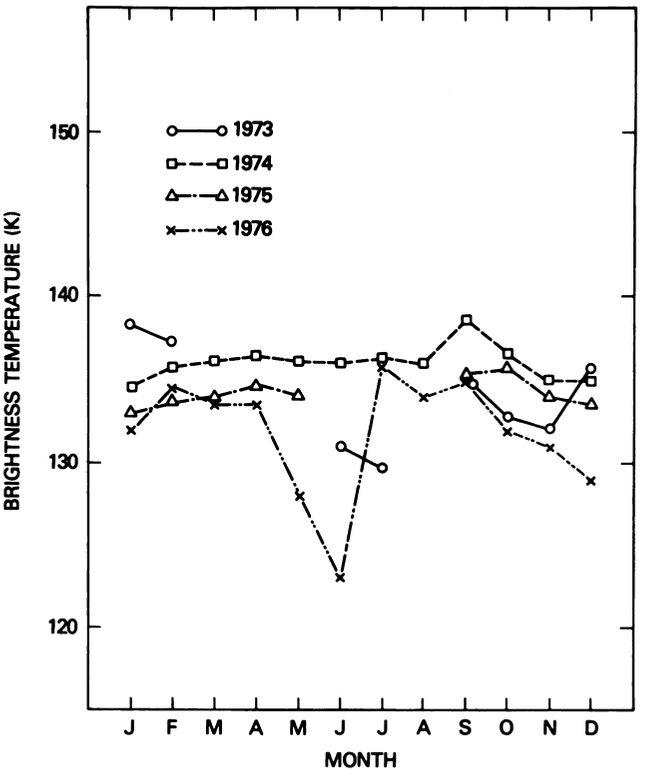

Figure A-3. Mean recorded brightness temperature of the ocean between 55°S and 65°S, plotted for each month, 1973 through 1976, before correction for calibration shifts.

The normalization procedure used to correct anomalous shifts assumed that the ocean T_B, including the atmospheric contribution, was constant at 135 K (Comiso and Zwally, 1980). The correction applied to the period from May to December 1976 was of the form:

$$T_B = a + b\,T_B', \qquad \text{(A-2)}$$

where T_B' is the uncorrected brightness temperature, and T_B is the corrected brightness temperature. Coefficients a and b were determined from the distribution of T_B' in selected ocean and high concentration ice areas. Because the variations were short-term, a separate a and b pair was determined for each 3-day map for May to December 1976. For the earlier data (January 1973 to April 1976), a correction of the form $T_B = a + T_B'$ and

a determination of "a" on a monthly basis was satisfactory. A confirmation of the validity of this procedure is provided by the consistency of the corrected brightness temperatures over the ice sheets, which undergo a seasonal variation but little interannual variation. In this procedure, the absolute calibration of the brightness temperature is unimportant, because the method sets a value of 0-percent ice concentration in known areas of open water and 100-percent ice concentration in sea ice regions where the T_B has its highest values.

A.3 MAPPING AND AVERAGING OF DATA

The brightness temperature data from the CBT tapes in orbital format are mapped into a 293 by 293 uniform grid of cells subdividing a polar stereographic map. The geographic coordinates of the center of the radiometer field of view determine the cell into which the data are placed. Overlapping data in a cell from successive orbits are averaged to give a single brightness temperature assumed to be located at the center of the cell.

A.3.1 Polar Stereographic Map

A polar stereographic map is constructed by projecting points on the Earth's surface onto a plane tangent at a pole. The vertex of the projection is the opposite pole. The concept is illustrated in Figure A-4(a), where a point, B, on the Earth's surface is projected to the polar plane at C.

The coordinates of each element in the projected map are determined as follows. The distance, r, from the pole to the projected point is calculated from:

$$r = d \tan \alpha, \qquad \text{(A-3)}$$

where d is the diameter of the Earth, and α is the angular projection at the opposite pole expressed in terms of the latitude, ϕ, as follows:

$$\alpha = \frac{\gamma}{2} = \frac{90 - \phi}{2}. \qquad \text{(A-4)}$$

Using the axes of Figure A-4(b), with the Greenwich meridian coinciding with the positive ordinate of the map, the x and y components of the data element with latitude ϕ and east longitude λ are given by:

$$x = d \tan \frac{(90 - \phi)}{2} \cos (90 - \lambda), \qquad \text{(A-5)}$$

$$y = d \tan \frac{(90 - \phi)}{2} \sin (90 - \lambda). \qquad \text{(A-6)}$$

As mentioned previously, the standard map is a 293 by 293 grid enclosing the 50°S latitude. For the coordinate system given above and a scaled value of d equal to 401.78, each point on the map can be expressed by a set of integer coordinates, J,I, defined by:

$$J = 147 + x + 0.5, \qquad \text{(A-7)}$$

$$I = 147 - y + 0.5. \qquad \text{(A-8)}$$

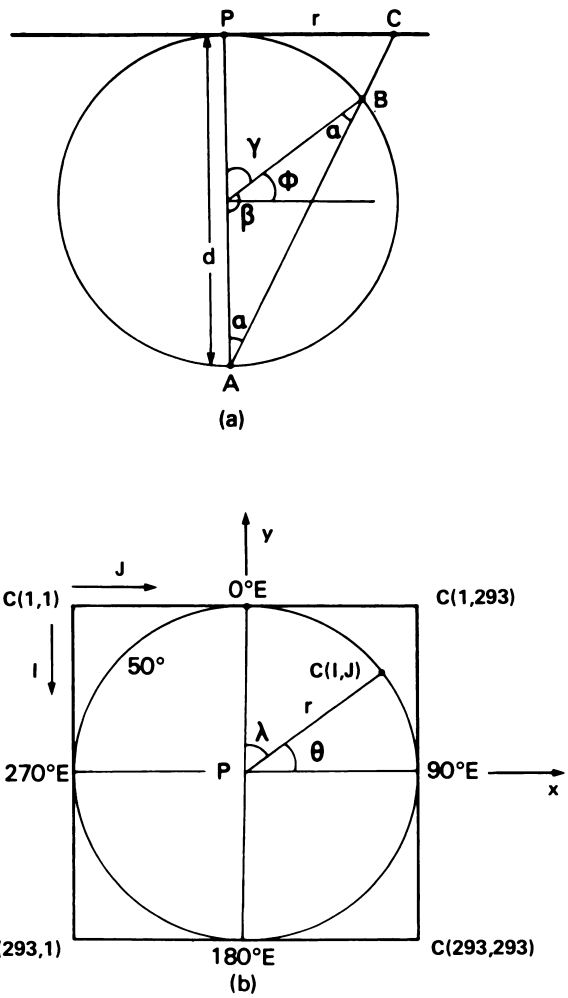

Figure A-4. Schematic diagram for polar stereographic mapping.

The standard tape format is shown in Table A-3. On the computer tapes, each map is separated by end-of-file marks, and data are preceded by a header record containing information about the data and the recording format (see Table A-4). More detailed information about data storage and retrieval is given in Zwally et al. (1981).

A.3.2 Population Distribution

Each data element on the polar stereographic maps represents a quantity (for example, brightness temperature or sea ice concentration) averaged over the number of measurements made in that area within the specified time period. For a 3-day average map, this number of measurements (called population) ranges from 0 to 35, depending on the location of the data element and the availability of good data. During the analysis of the data, this value is used to determine how representative the data-point measurement is as an average over the given time. For most of the polar maps, a record of population normally follows a data record as indicated in Table A-3. An example of the population distribution for a monthly average map is shown in Figure A-5, where the population of each pixel along a line from the South Pole to the edge of the map for longitudes 0°E, 90°E, and 180°E is plotted. The distribution shows a peak in population at about 81 degrees latitude, which is the maximum latitude reached by the satellite. It drops at 85 degrees latitude because only the beam positions corresponding to a ±30.5-degree scan angle were used and rises between 85 degrees and the pole, where the outer beam positions are used. Some variation from this distribution is caused by occasional elimination of bad data as discussed previously.

A.3.3 Interpolation Procedures

Because of processing and calibration problems mentioned earlier, some 3-day average maps had as many as 20 percent of the data cells empty. The 20-percent data loss occurred much more frequently after the Nimbus 6 satellite launch, when data became available only every other day. Fortunately, most of these empty cells are located outside the range of the seasonal sea ice extent. For

Table A-3
Standard Format* for Polar Stereographic Maps

Record Number	Length (bytes)	Format	Number of Words	Description
1	1465	(see below)†	293	Heading (only the first 20 words are meaningful)
2	1465	293 I5	293	Row 1 data (x50)
3	1465	293 I5	293	Observation population of row 1
4	1465	293 I5	293	Row 2 data (x50)
5	1465	293 I5	293	Observation population of row 2
.	.	.	.	.
.	.	.	.	.
.	.	.	.	.
586	1465	293 I5	293	Row 293 data (x50)
587	1465	293 I5	293	Observation population of row 293

*Data format 2 indicates standard format (see Table A-4).
†(9 I5, 2A5, 8 I5, A5, 255 I5, 18 I5).

Table A-4
Header Record for Polar Stereographic Maps

Word	Type	Number of Bytes/Words	Description
1	I5	4	Projection type (1 for polar stereographic)
2	I5	4	Number of columns (293)
3	I5	4	Number of rows (293)
4	I5	4	Scale (2.5×10^6)
5	I5	4	Latitude enclosed (-50.0°)
6	I5	4	Greenwich orientation (270°)
7	I5	4	Radius of the Earth
8	I5	4	J-coordinate of the pole (147)
9	I5	4	I-coordinate of the pole (147)
10-11	A5	4	Data type* (TB, ICE CON, SURF TEMP, or CLIM PRES)
12	I5	4	Start time (day)
13	I5	4	Start time (hour)
14	I5	4	Start time (minutes)
15	I5	4	Stop time (day)
16	I5	4	Stop time (hour)
17	I5	4	Stop time (minutes)
18	I5	4	Year data was collected
19	I5	4	Data format (2 for standard format)
20	A5	4	Data identification
21-293	I5	4	Meaningless

*Variable abbreviations for words 10 and 11 are as follows: TB is brightness temperature, ICE CON is ice concentration, SURF TEMP is mean monthly climatological surface air temperature, and CLIM PRES is mean monthly climatological sea-level pressure.

completeness and proper weighting of data in the monthly average maps, some interpolations are made to fill the empty cells in the 3-day average maps. A combination of time and spatial interpolation is employed. Normally, maps with very few empty cells are filled by linear spatial interpolation. For gaps involving four or more cells, however, time interpolation was found to give a more consistently satisfactory result. To fill in an empty cell by time interpolation, the average is taken of the brightness temperature in the cell for the previous 3-day average map and the one immediately after. In a few extremely bad cases, the procedure is extended to utilize up to three 3-day averages before and after the empty cell. Monthly averages are created from 3-day average maps with appropriate weighting to account for missing 3-day averages.

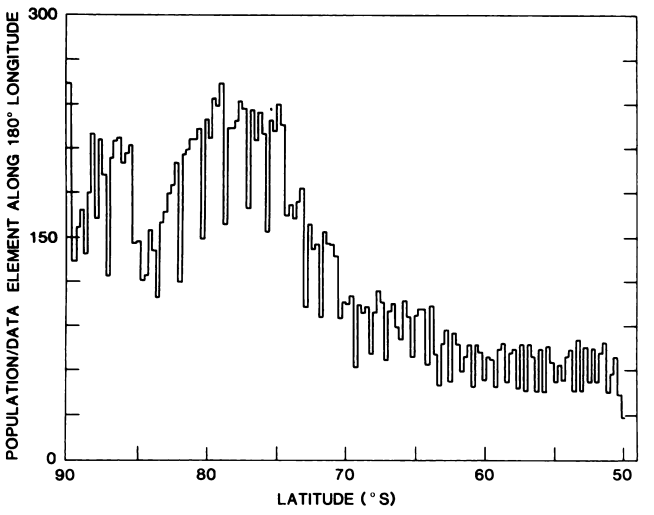

Figure A-5. Typical number of observations (population) in each map element for monthly average maps as a function of latitude.

A.3.4 Time Averaging and Spatial Summations of Ice Areas

The 4-year average monthly maps in Chapter 4 are created by averaging the maps for individual years element by element; i.e.,

$$\bar{C}_{ij} = \frac{1}{4} \sum_{N=3}^{6} C_{ij}^{N}, \qquad \text{(A-9)}$$

where C_{ij}^{N} is the concentration in element ij during year N (N=3 corresponds to 1973, etc. . .), and $\bar{C}_{ij}$ is the 4-year average. The 4-year average extent, for example, is

$$\overline{\text{Extent}} = \sum_{\substack{i,j \\ \bar{C}_{ij} \geq 15}} a_{ij}. \qquad \text{(A-10)}$$

where a_{ij} is the geographic area of element ij, and is calculated as a function of latitude and longitude. The 4-year average actual ice area is

$$\overline{\text{Actual}} = \sum_{\substack{i,j \\ \bar{C}_{ij} \geq 15}} \bar{C}_{ij}\, a_{ij}. \qquad \text{(A-11)}$$

Some error is introduced in equation A-11 by the truncation of concentrations less than 15 percent, but it is small because of the general sharpness of the ice boundary and the weighting by concentration in the summation. It is also less than the error that would be otherwise introduced by the variability of the brightness temperature over ice-free ocean, which would falsely indicate small ice concentrations far from the ice edge. Similar summations are performed for the areal coverage in various concentration categories.

For an individual year, N, the equations for calculating extent and actual ice area are the same as equations A-10 and A-11, but with $\bar{C}_{ij}$ replaced by C_{ij}^{N}. The areas of sea ice cover in the analysis sectors (Figure 2-3 of the main text) are calculated by the same procedure for all a_{ij} located in each sector. If an element, a_{ij}, is located over a sector boundary, the area is assigned proportionately to the respective sectors. The area of the continent (black map elements in Figures 4-2 to 4-7 of the main text) is calculated to be 13.97×10^{6} square kilometers.

In Chapter 4, the difference is noted between the 4-year average extent (equation A-10) and the average of the extent for the 4 individual years, which is

$$\langle \text{Extent} \rangle = \frac{1}{4} \sum_{N=3}^{6} \sum_{\substack{i,j \\ C_{ij}^{N} \geq 15}} a_{ij}. \qquad \text{(A-12)}$$

A similiar difference occurred for actual ice area, for which the average of the actual ice area for 4 years is

$$\langle \text{Actual} \rangle = \frac{1}{4} \sum_{N=3}^{6} \sum_{\substack{i,j \\ C_{ij}^{N} \geq 15}} C_{ij}^{N}\, a_{ij}. \qquad \text{(A-13)}$$

There are two competing effects caused by reversing the order of performing the summations and the time averaging. One effect occurs for the case for which in one or more years, $C_{ij}^{N} < 15$, but $\bar{C}_{ij} \geq 15$; this situation can be caused by large interannual variations in the position of the ice boundary and is the dominant effect causing $\overline{\text{Extent}}$ to be greater than $\langle \text{Extent} \rangle$. An effect in the opposite direction occurs for the case for which in one or more,

but not all, years, $C_{ij}^{N} < 15$, and $\overline{C}_{ij} < 15$; this situation can be caused by small interannual variations in the ice boundary and is the dominant effect causing $\overline{\text{Actual}}$ to be less than $<\text{Actual}>$. Because of these differences, averages of the areas for the individual years (e.g., $<\text{Extent}>$ and $<\text{Actual}>$) have better absolute accuracy than the areas from the 4-year average maps (e.g., $\overline{\text{Extent}}$ and $\overline{\text{Actual}}$).

A.4 REFERENCES

Comiso, J. C., and H. J. Zwally, Corrections for anomalous time dependent shifts in the brightness temperature from Nimbus 5 ESMR, NASA TM-82055, Greenbelt, Maryland, 1980.

Wilheit, T. T., The Electrically Scanning Microwave Radiometer (ESMR) experiment, in *Nimbus 5 User's Guide*, NASA/Goddard Space Flight Center, Greenbelt, Maryland, 59-105, 1972.

Zwally, H. J., J. C. Comiso, and C. L. Parkinson, Satellite-derived ice data sets No. 1: Antarctic monthly average microwave brightness temperatures and sea ice concentrations 1973-1976, NASA TM-83812, Greenbelt, Maryland, 1981.

APPENDIX B

ICE CONCENTRATION BLACK-AND-WHITE IMAGES AND CONTOUR MAPS

In Chapters 4 and 5 of the main text, the ice concentrations derived from the ESMR brightness temperatures and climatological surface air temperatures are shown in color at intervals of 4 percent, which is consistent with the estimated concentration accuracy ranging from 5 to 15 percent (Section 3.6). There are advantages in presenting the data at this percentage interval. Spatial variation in ice concentration at various ice concentration levels can be easily examined, and distinct features in the ice, like polynyas, spring breakup, and ice-edge characteristics are well resolved. The ice concentration data are also stored on magnetic tape, with better than 1-percent precision, as described in Zwally et al. (1981).* This greater precision available on the tapes is small compared to the absolute accuracy of the derived sea ice concentration (Chapter 3), but is useful for studies of relative ice concentrations at finer intervals.

However, a larger concentration interval is adequate for many investigations. If only the principal features of the ice are desired, the more limited but more easily reproducible black-and-white images and contour maps may be satisfactory. Figures B-1 through B-6 show black-and-white images of ice concentration at the following intervals: 0 to 15, 15 to 35, 35 to 50, 50 to 65, 65 to 85, and 85 to 100 percent. These intervals are the same as those used in calculating the area distributions shown in Figures 5-13 through 5-22 of the main text. An even simpler presentation of overall ice conditions is shown in the three-level contour maps (Figures B-7 through B-11).

*H. J. Zwally, J. C. Comiso, and C. L. Parkinson, Satellite-derived ice data sets No. 1: Antarctic monthly average microwave brightness temperatures and sea ice concentrations 1973-1976, NASA TM-83812, Greenbelt, Maryland, 32 pp., 1981.

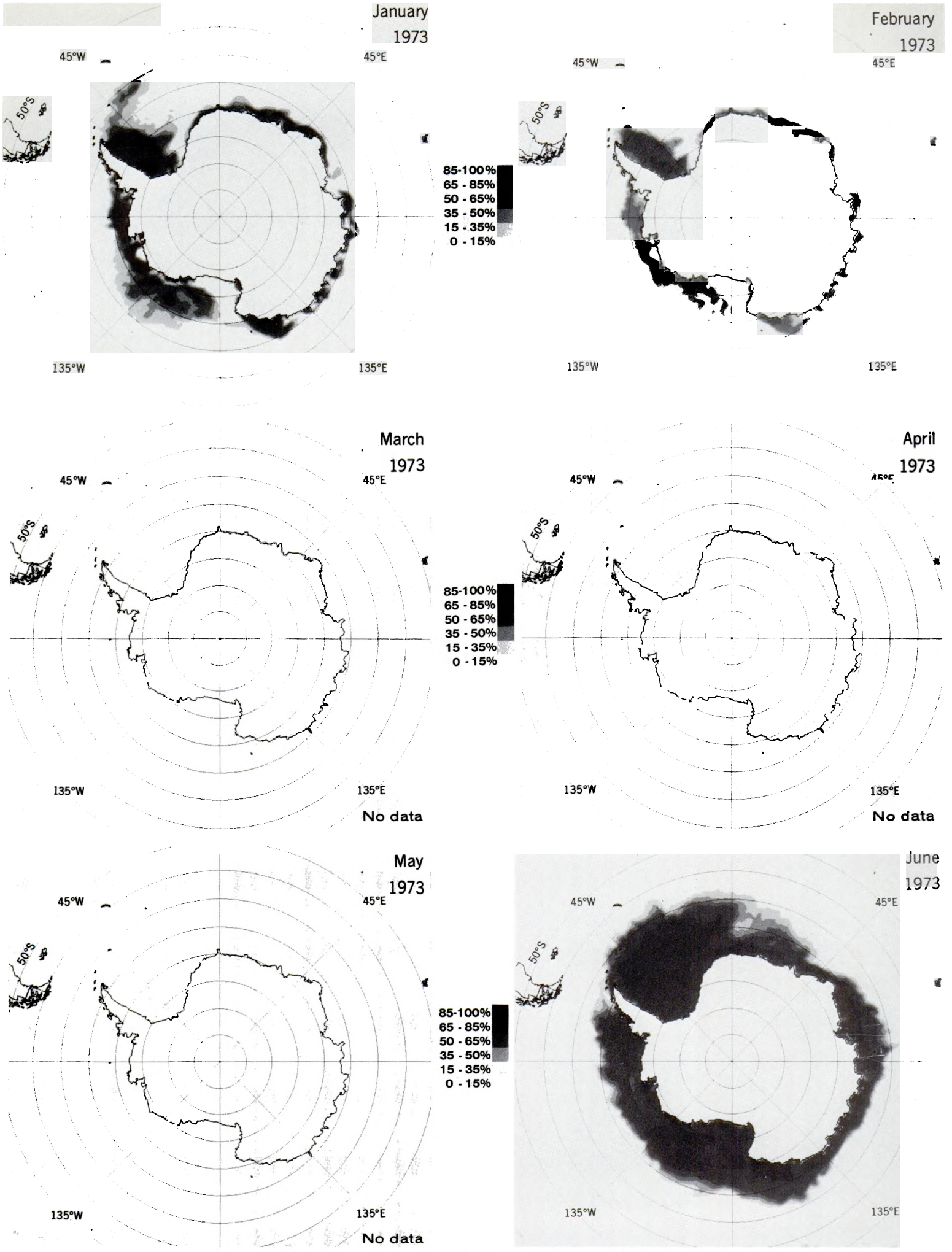

Figure B-1a. Mean monthly ice concentrations for January through June 1973.

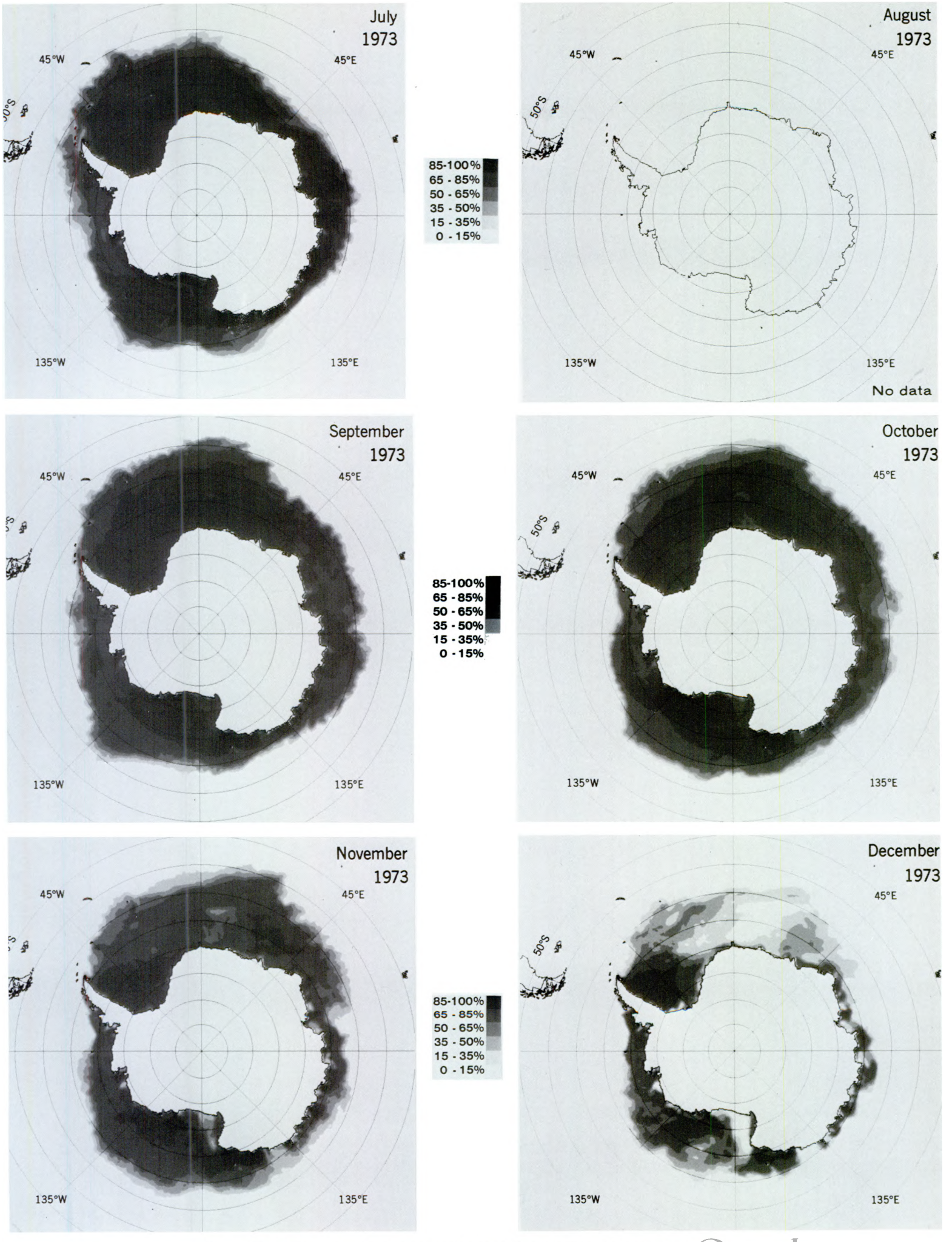

Figure B-1b. Mean monthly ice concentrations for July through December 1973.

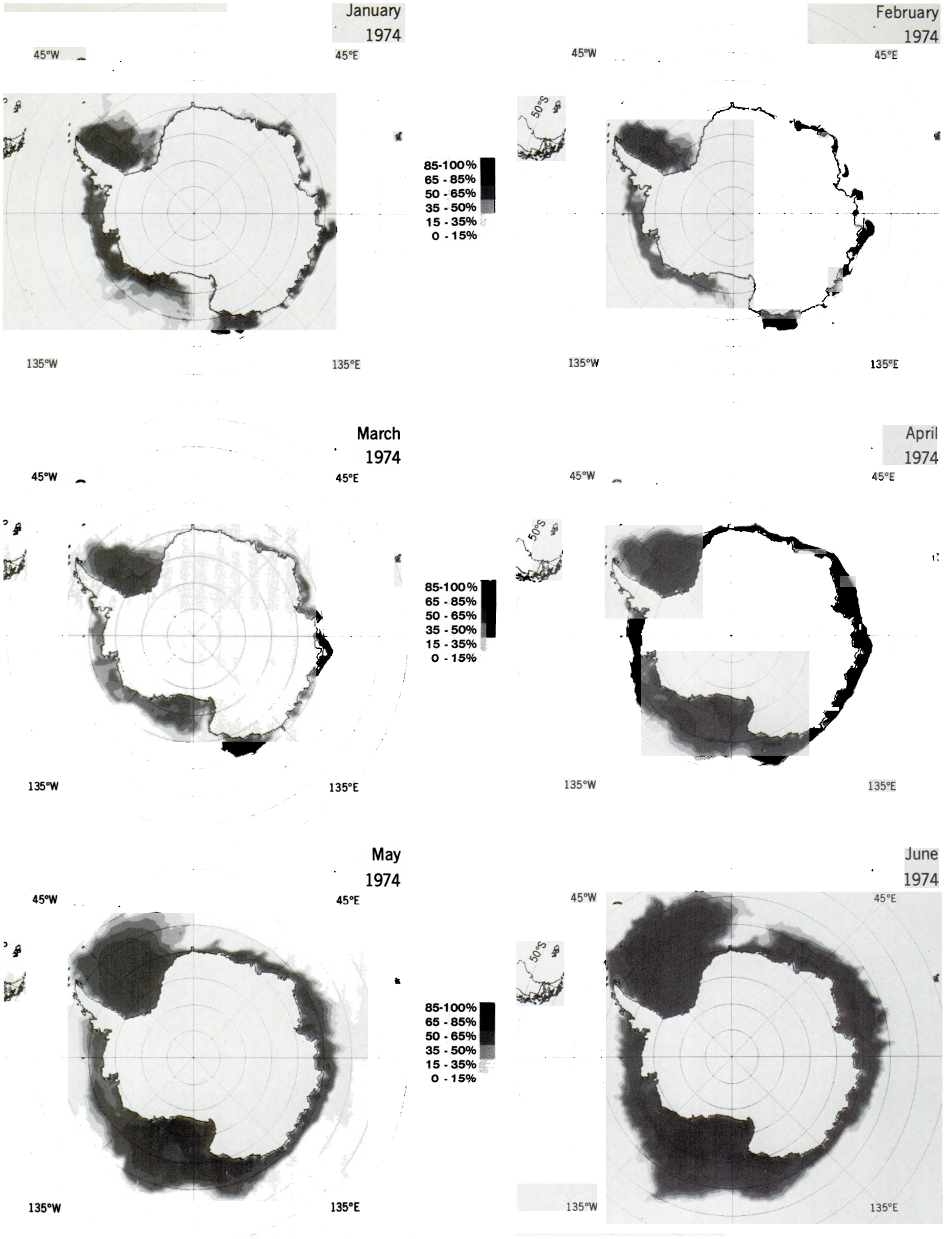

Figure B-2a. Mean monthly ice concentrations for January through June 1974.

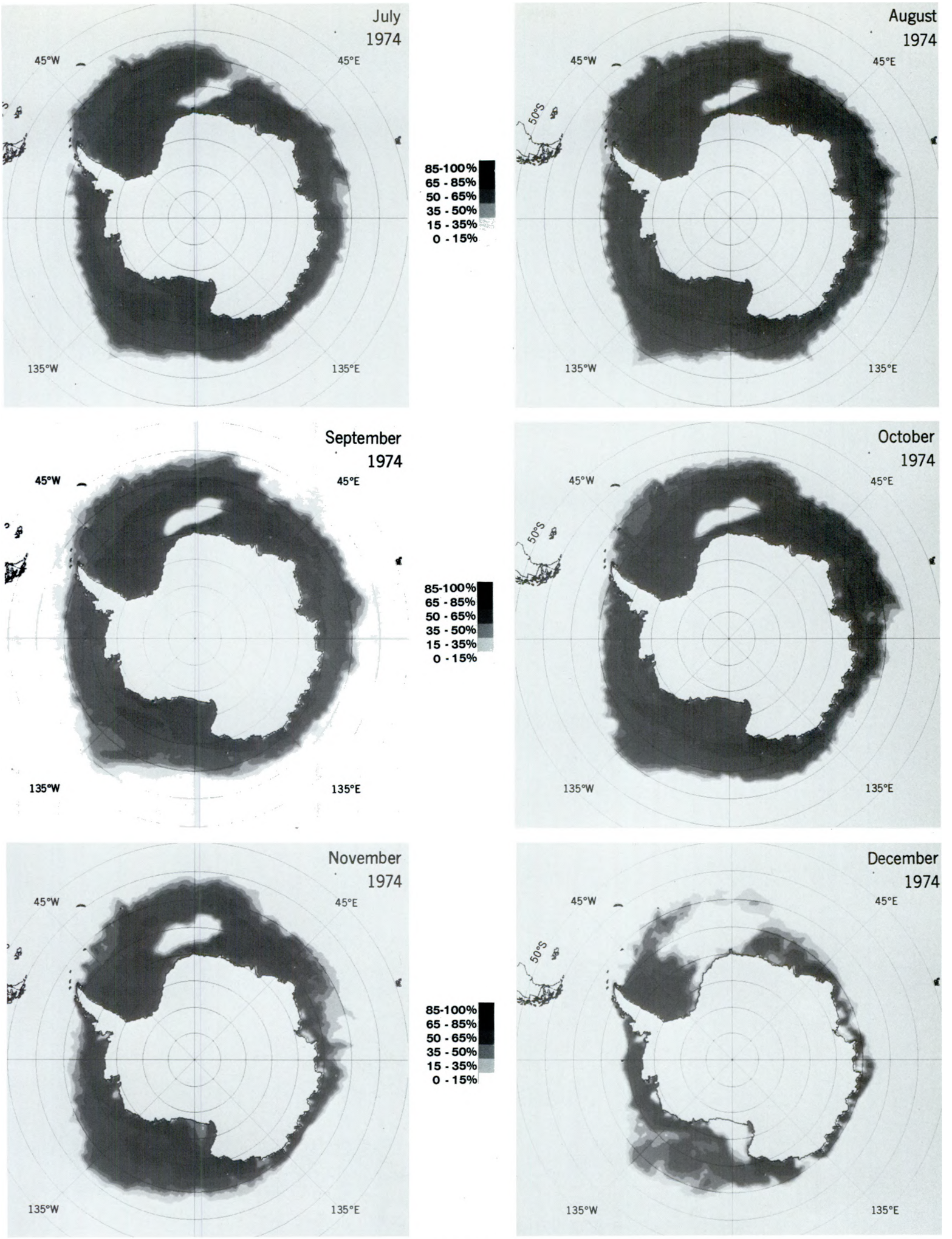

Figure B-2b. Mean monthly ice concentrations for July through December 1974.

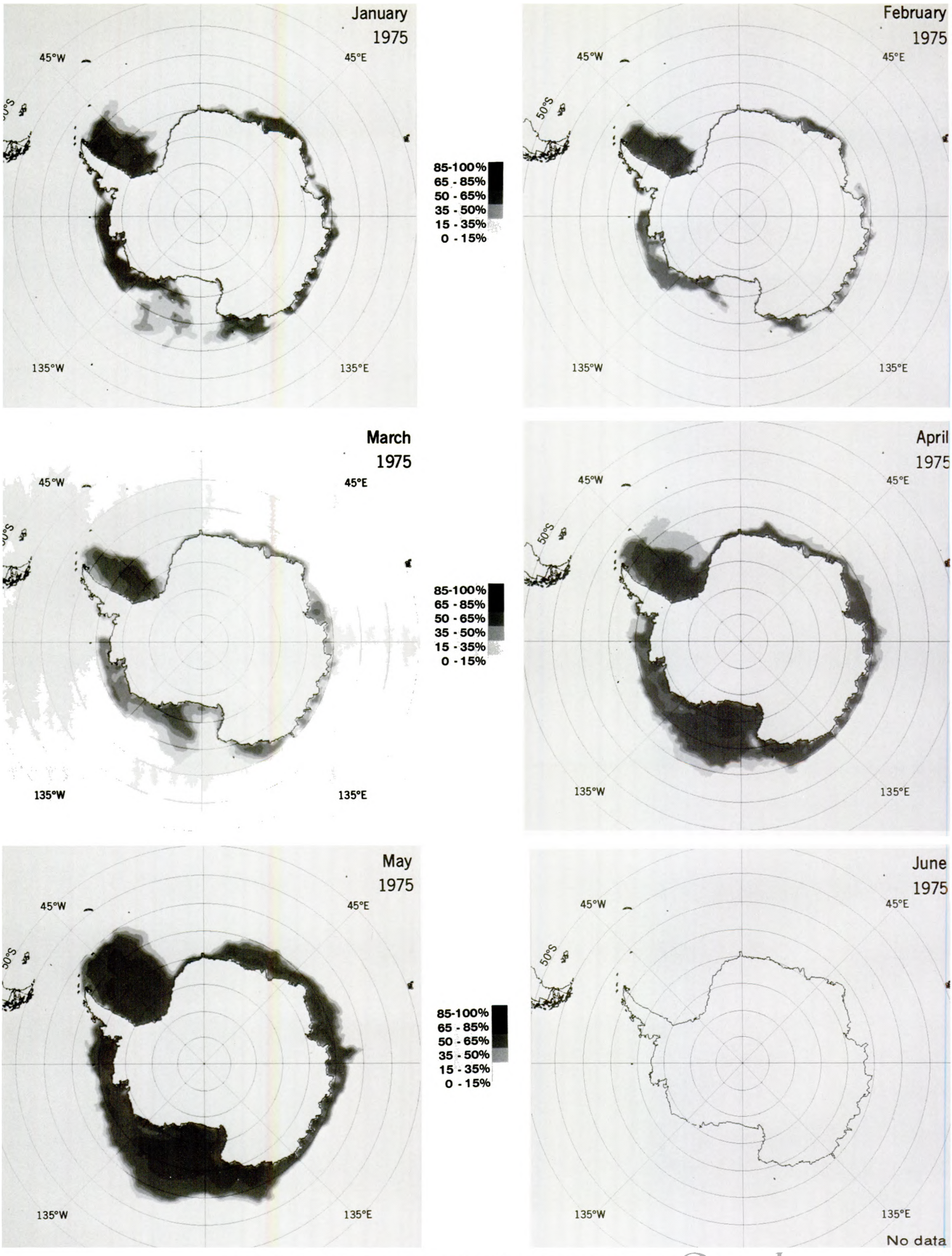

Figure B-3a. Mean monthly ice concentrations for January through June 1975.

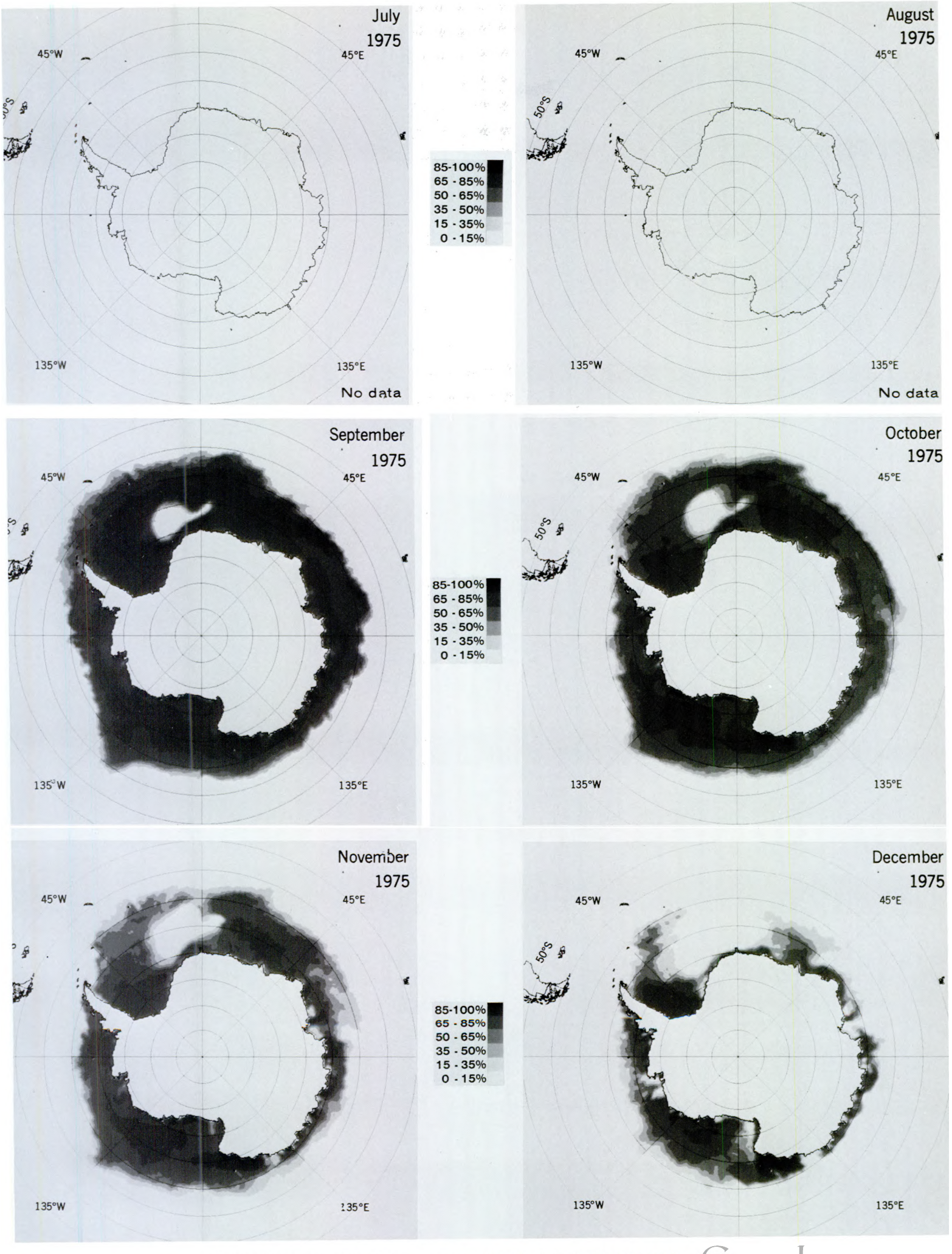

Figure B-3b. Mean monthly ice concentrations for July through December 1975.

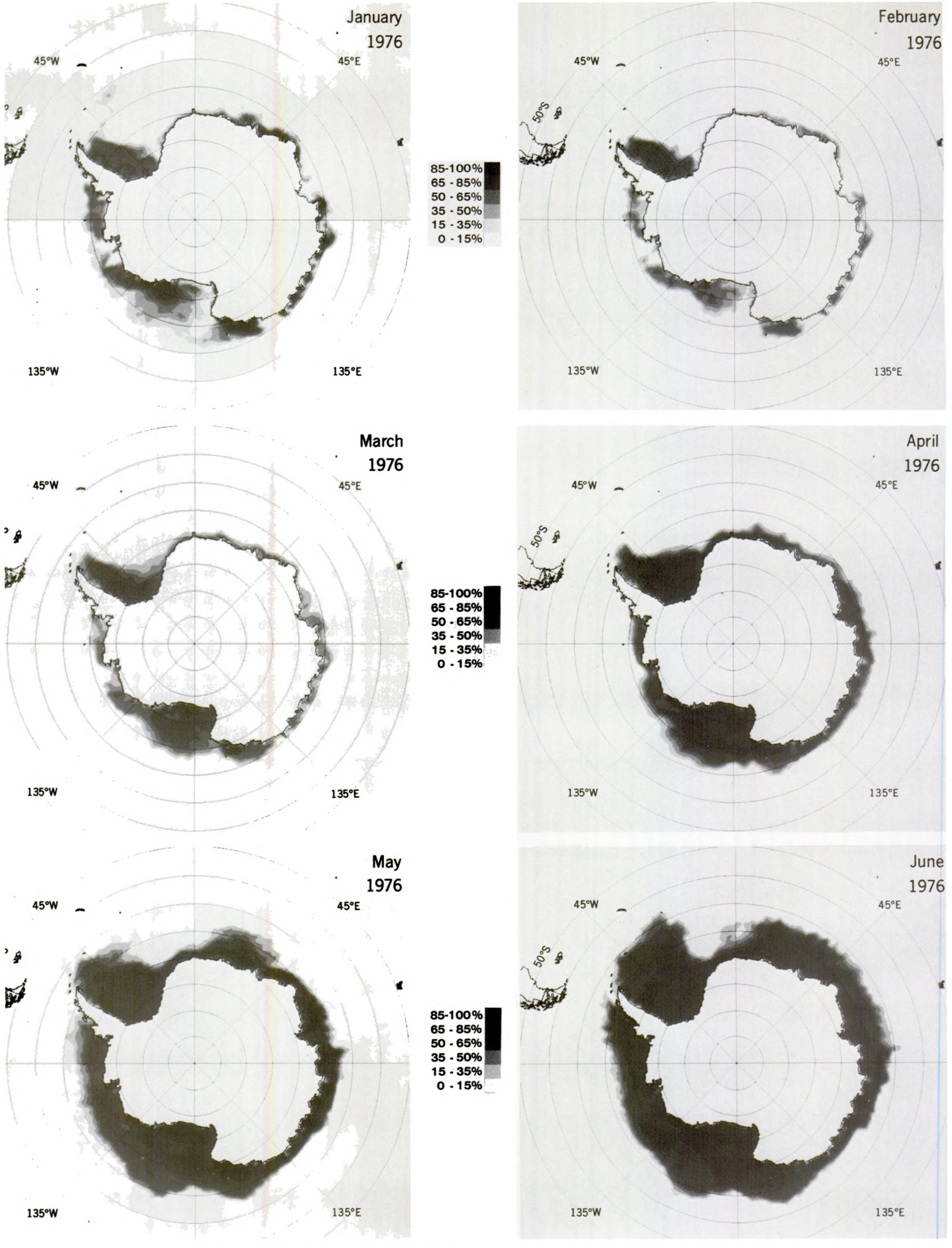

Figure B-4a. Mean monthly ice concentrations for January through June 1976.

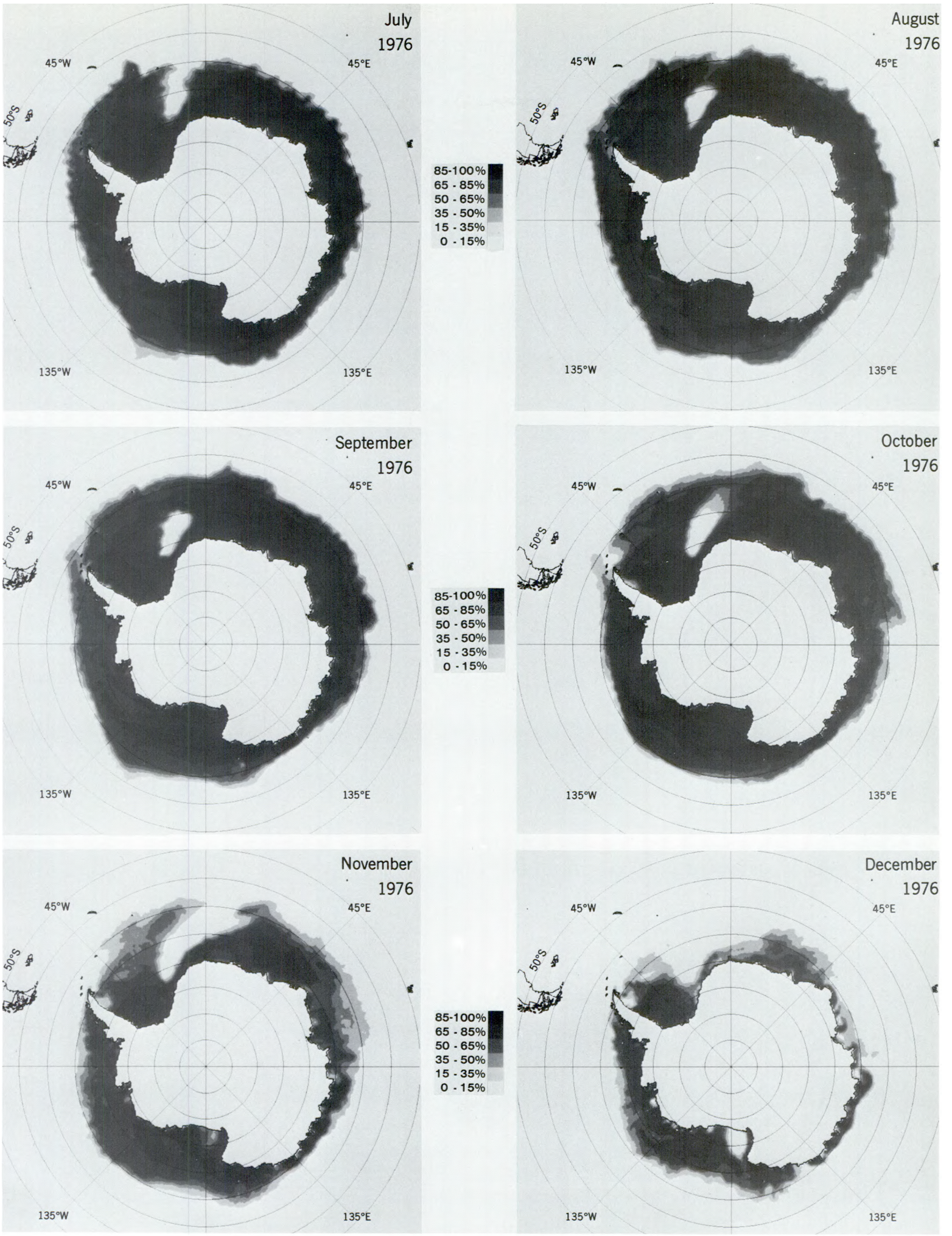

Figure B-4b. Mean monthly ice concentrations for July through December 1976.

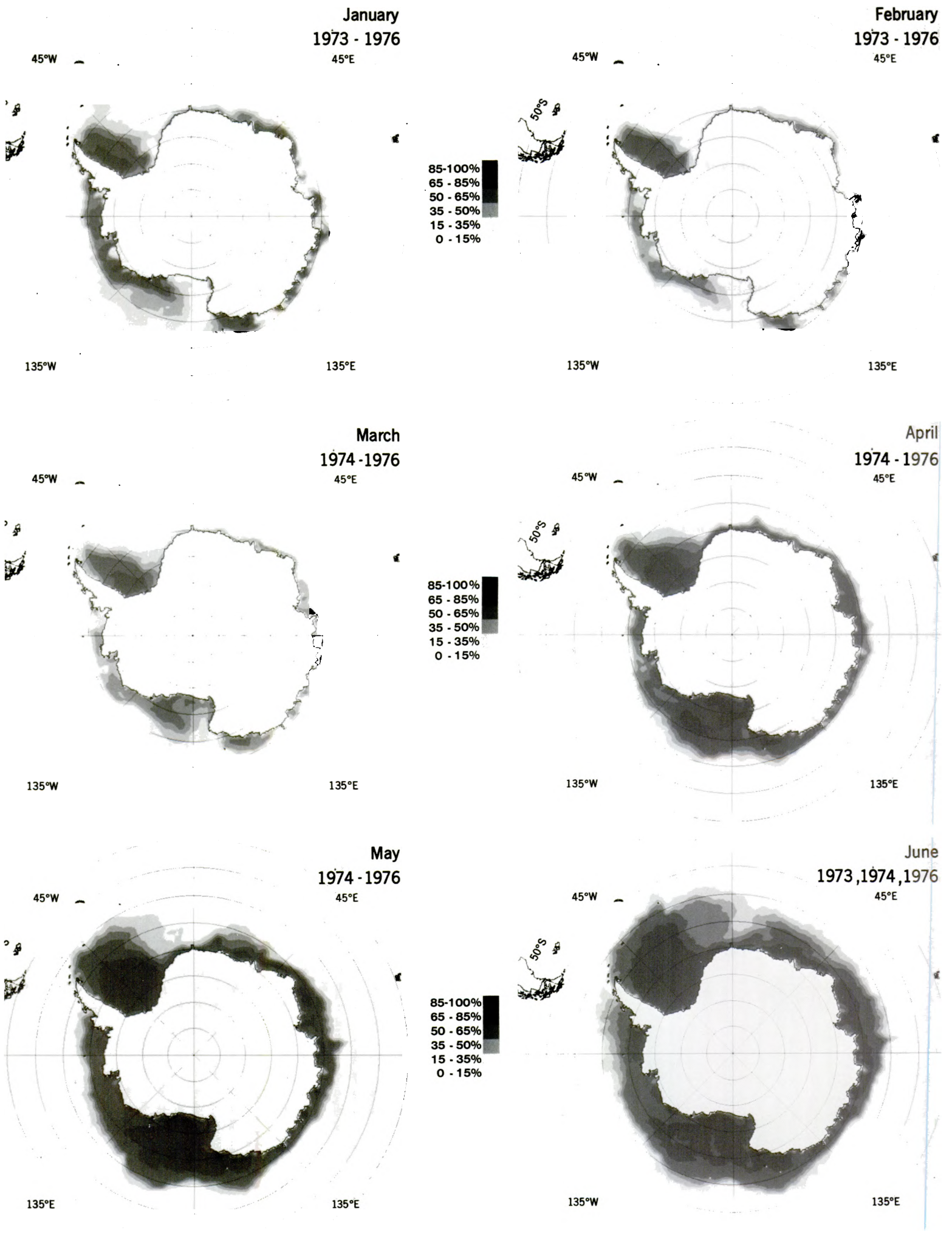

Figure B-5a. Mean monthly ice concentrations for January through June, averaged for the years indicated.

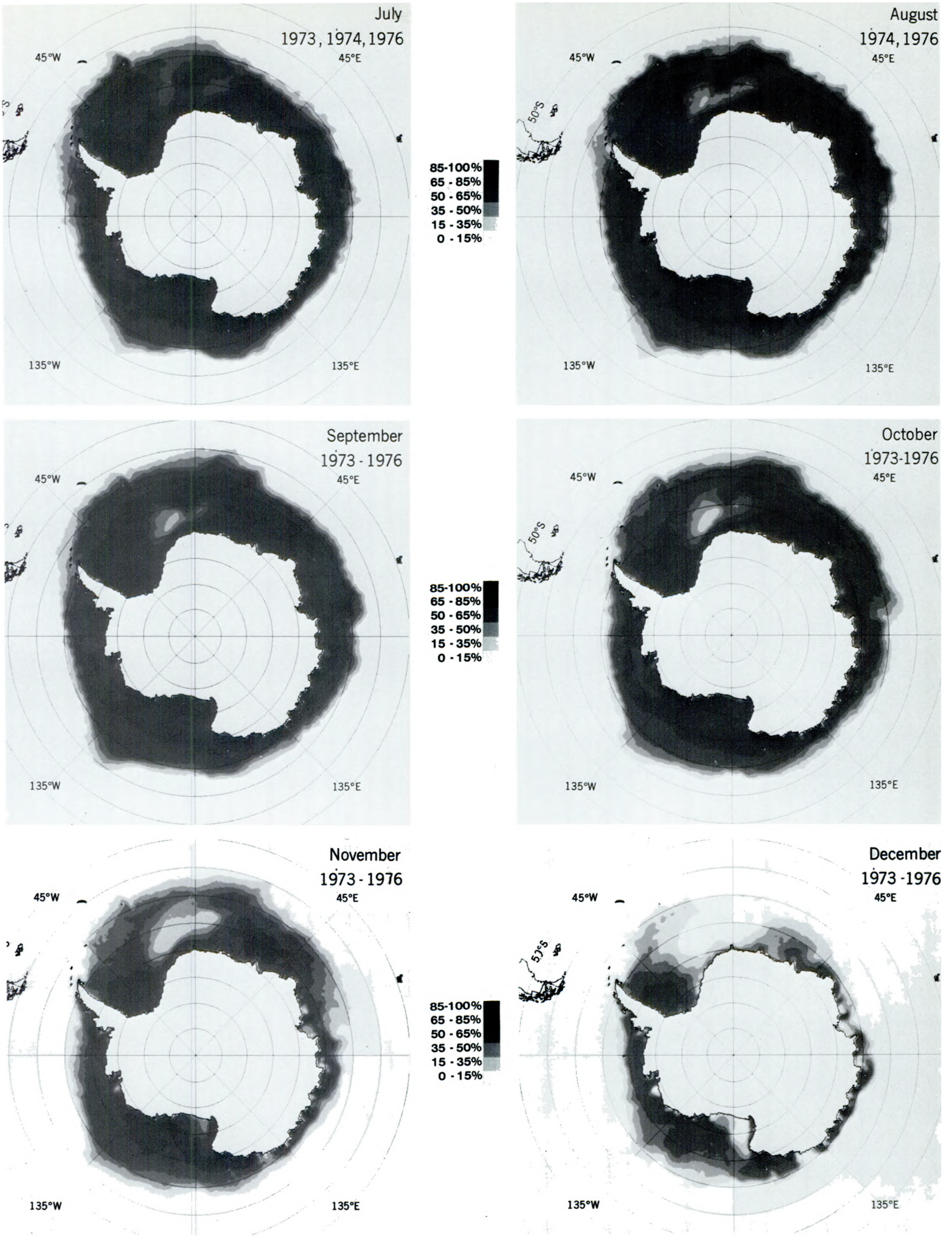

Figure B-5b. Mean monthly ice concentrations for July through December, averaged for the years indicated.

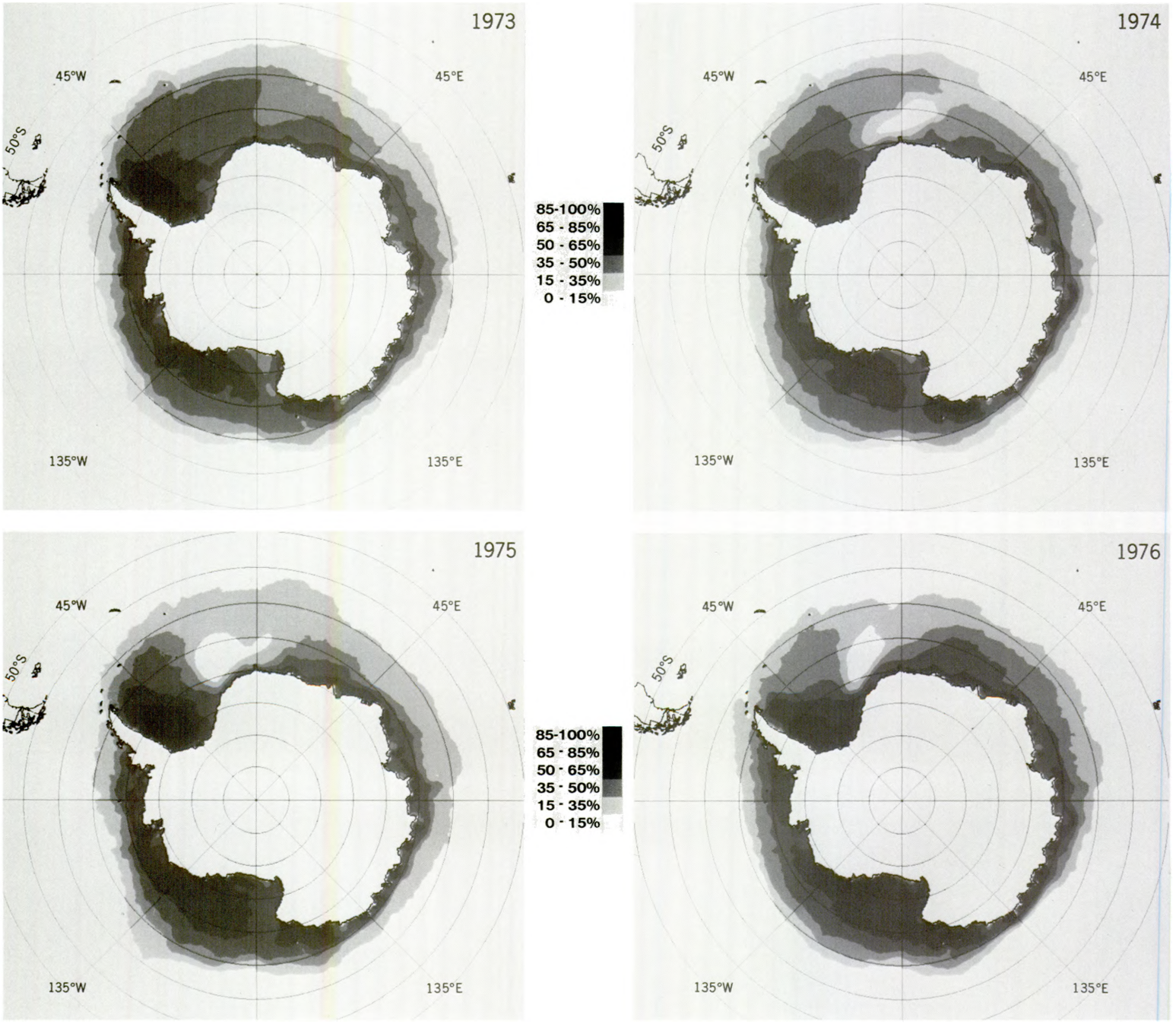

Figure B-6. Mean annual ice concentrations for 1973, 1974, 1975, and 1976.

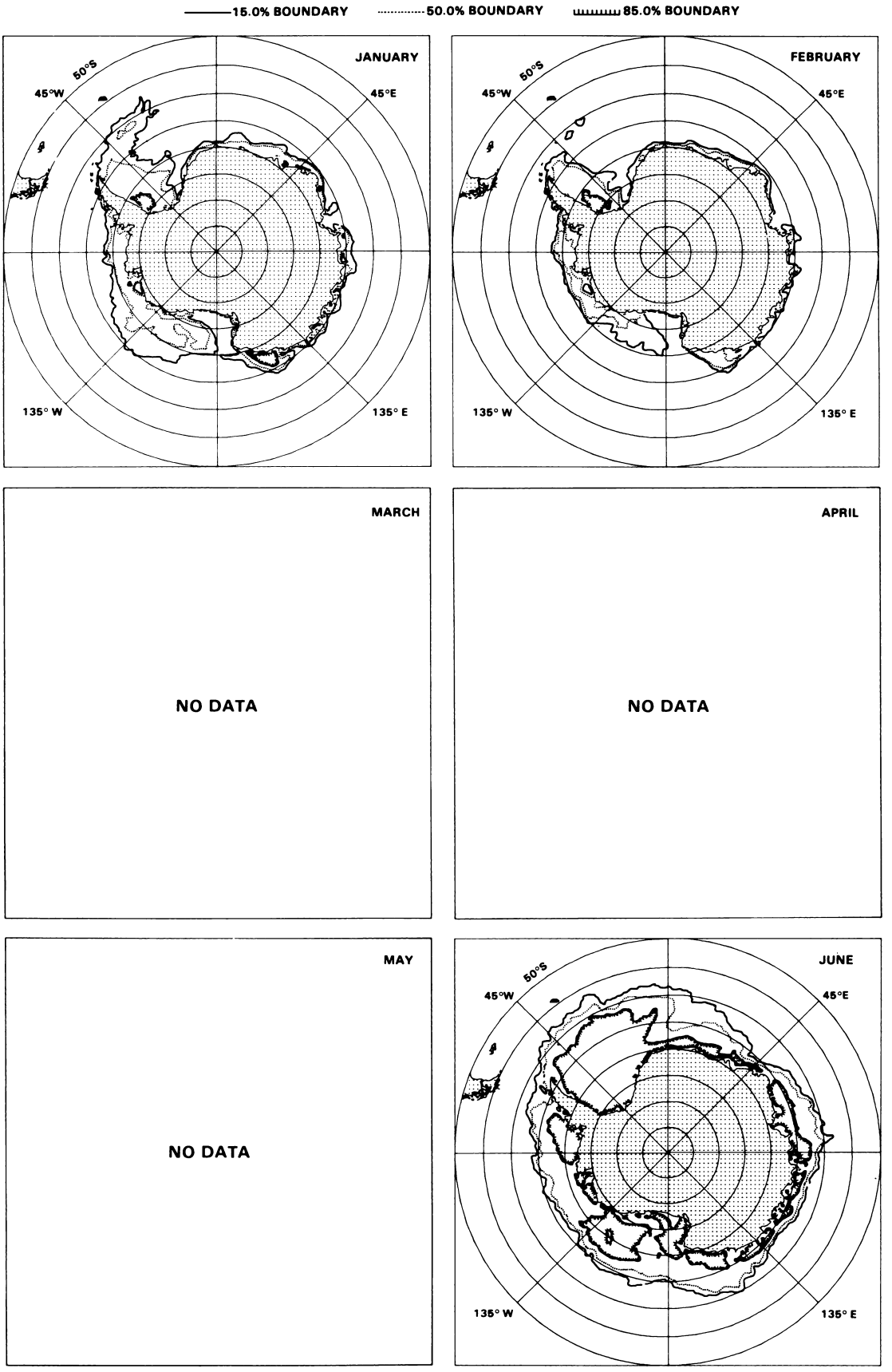

Figure B-7a. Mean monthly ice concentration contours for January through June 1973.

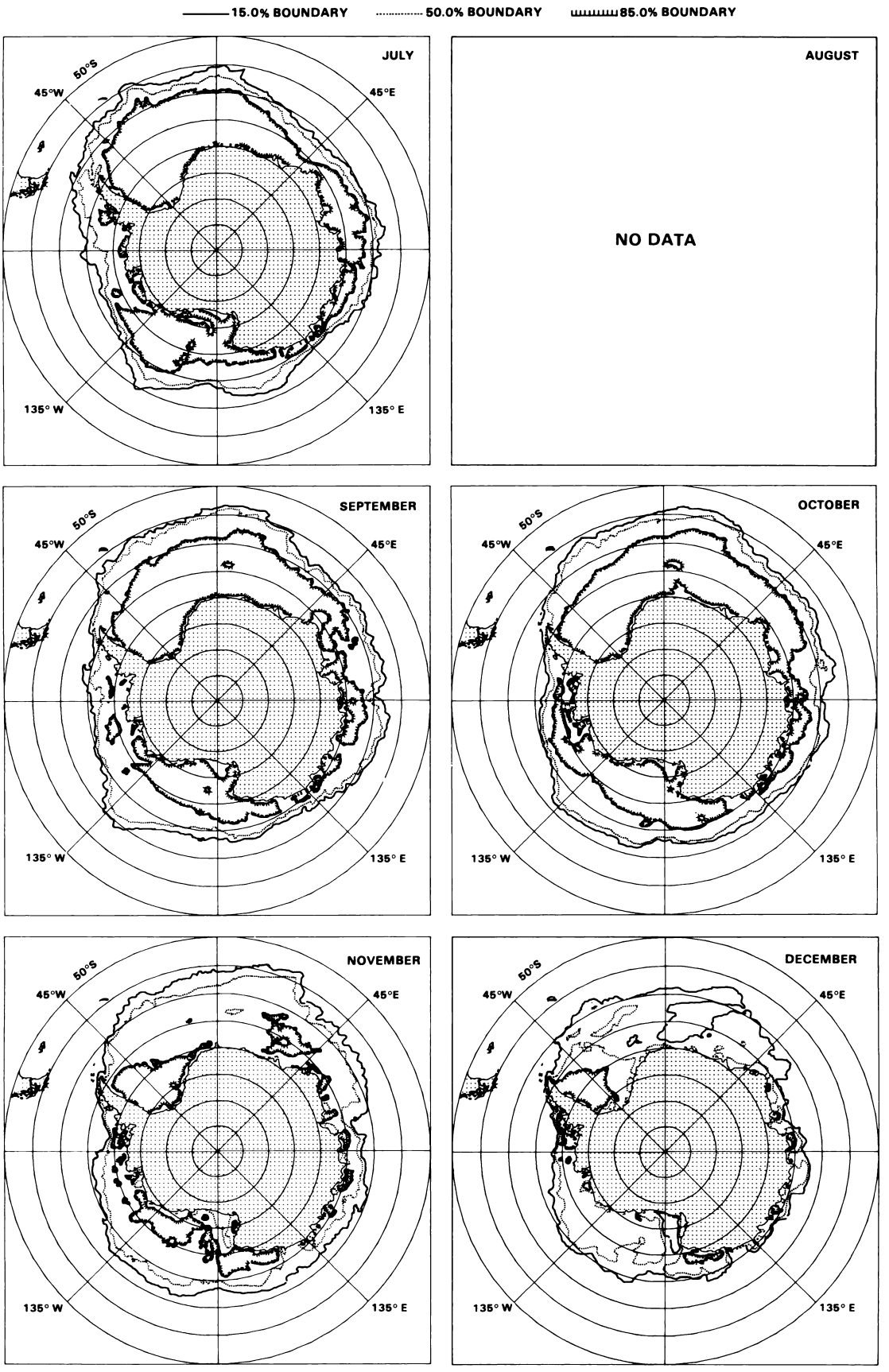

Figure B-7b. Mean monthly ice concentration contours for July through December 1973.

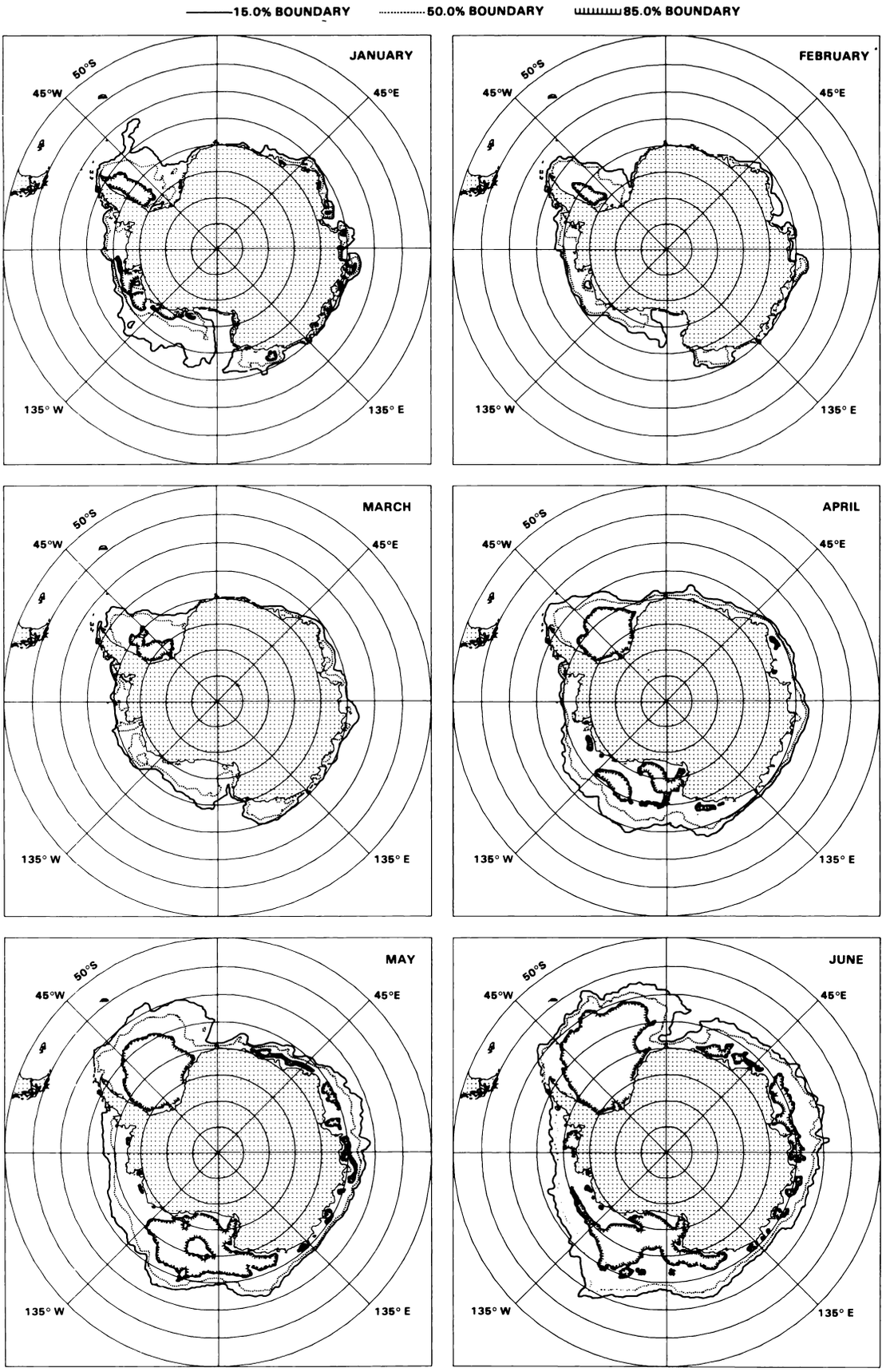

Figure B-8a. Mean monthly ice concentration contours for January through June 1974.

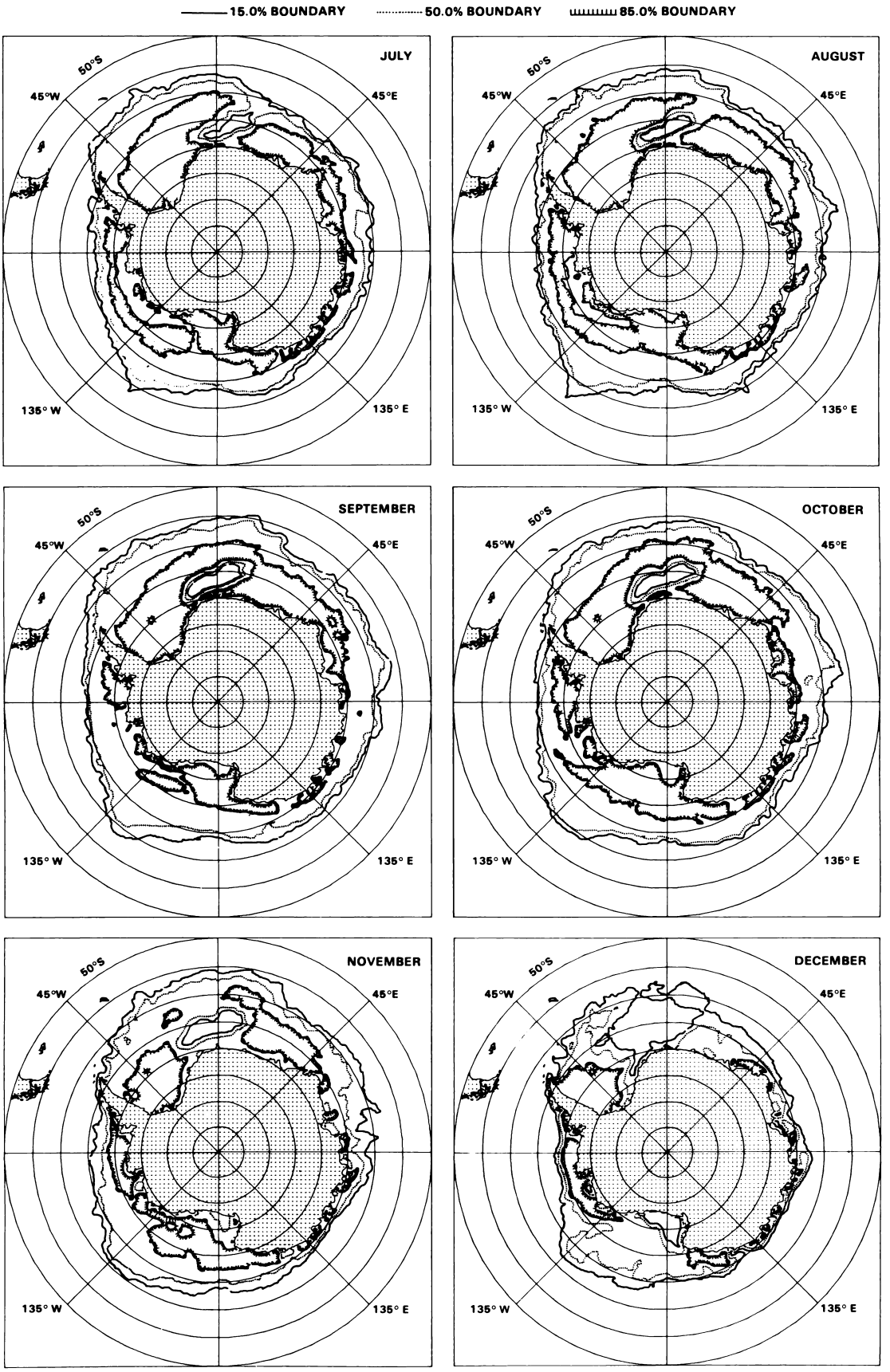

Figure B-8b. Mean monthly ice concentration contours for July through December 1974.

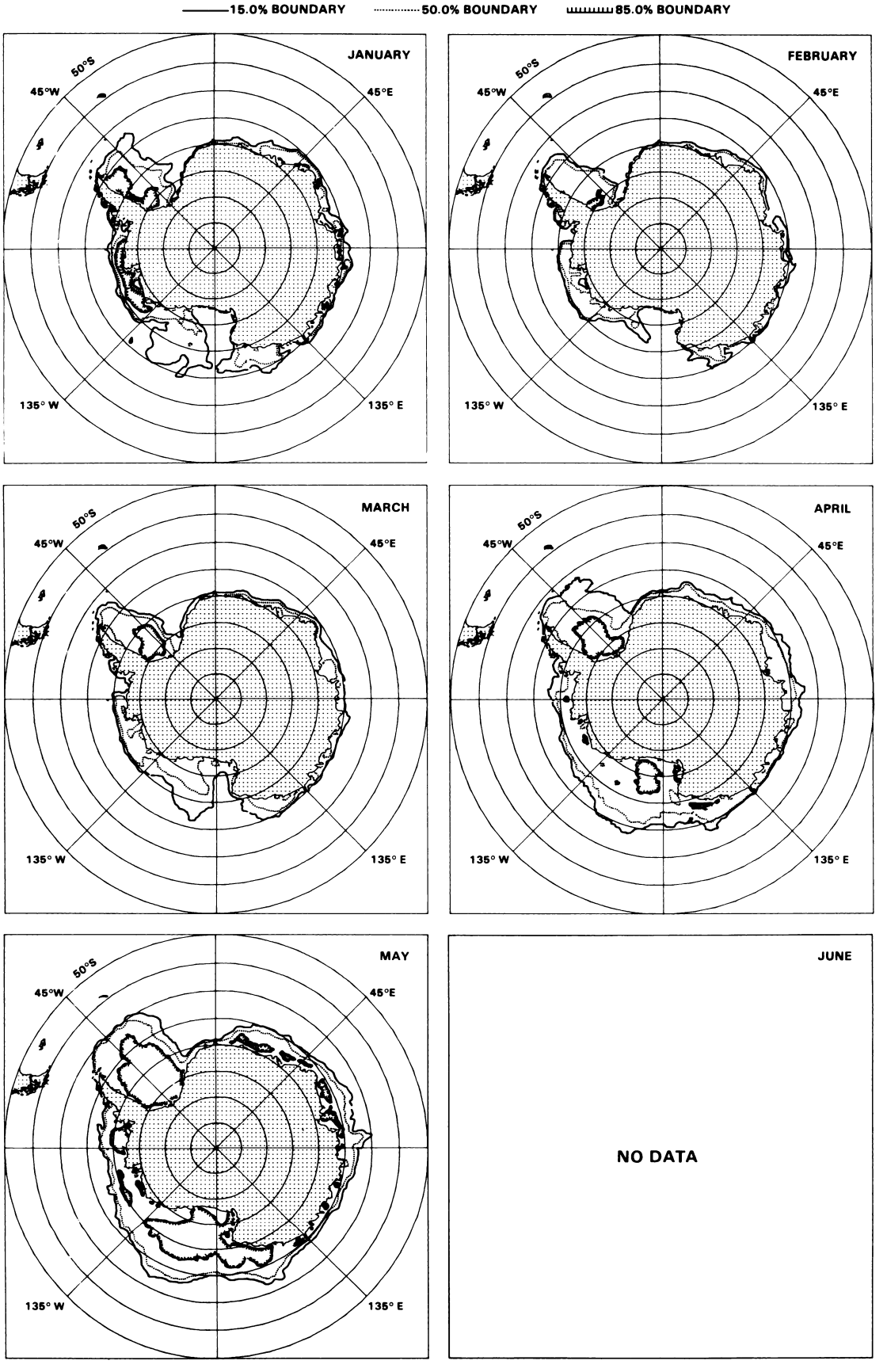

Figure B-9a. Mean monthly ice concentration contours for January through June 1975.

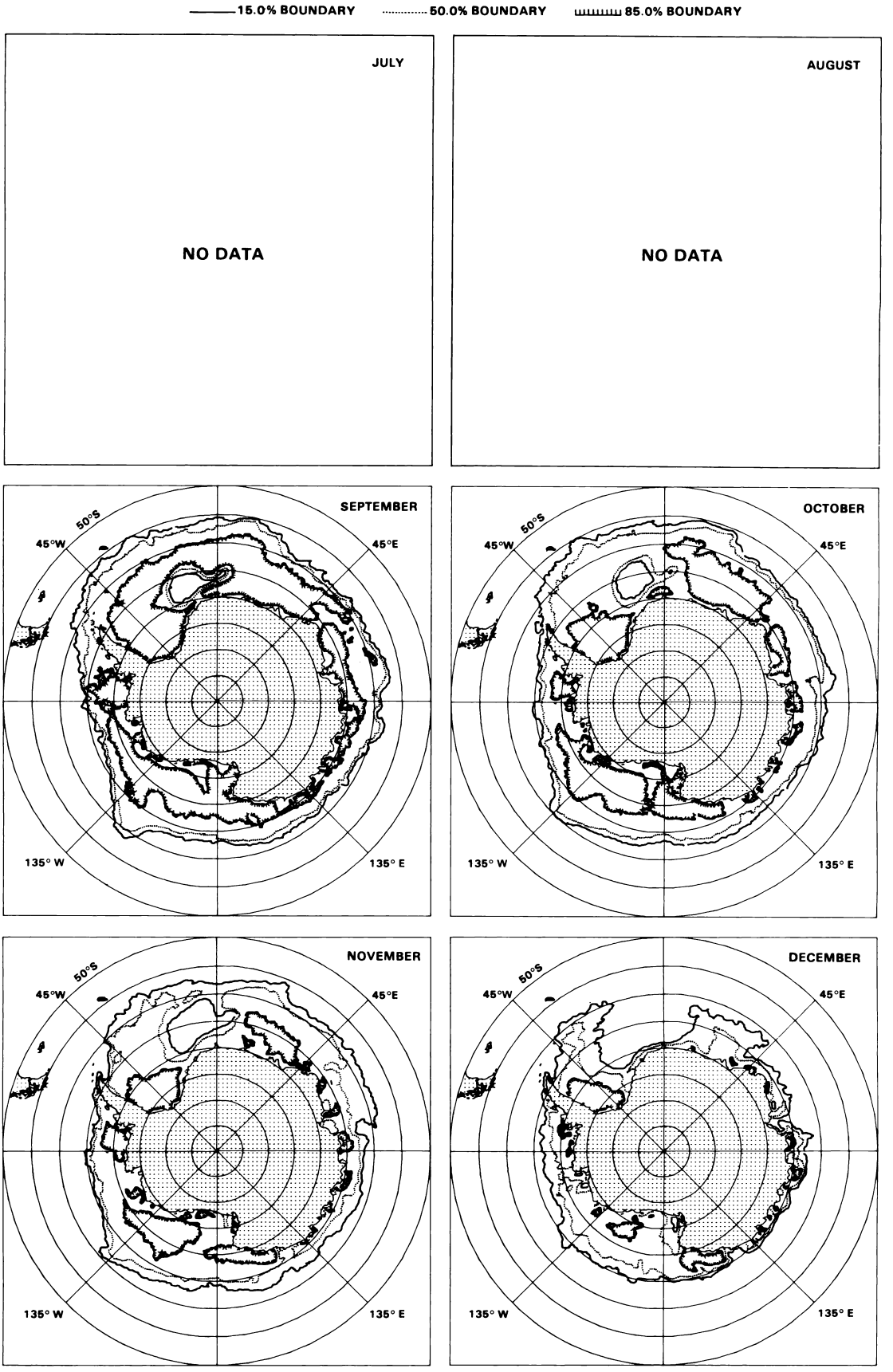

Figure B-9b. Mean monthly ice concentration contours for July through December 1975.

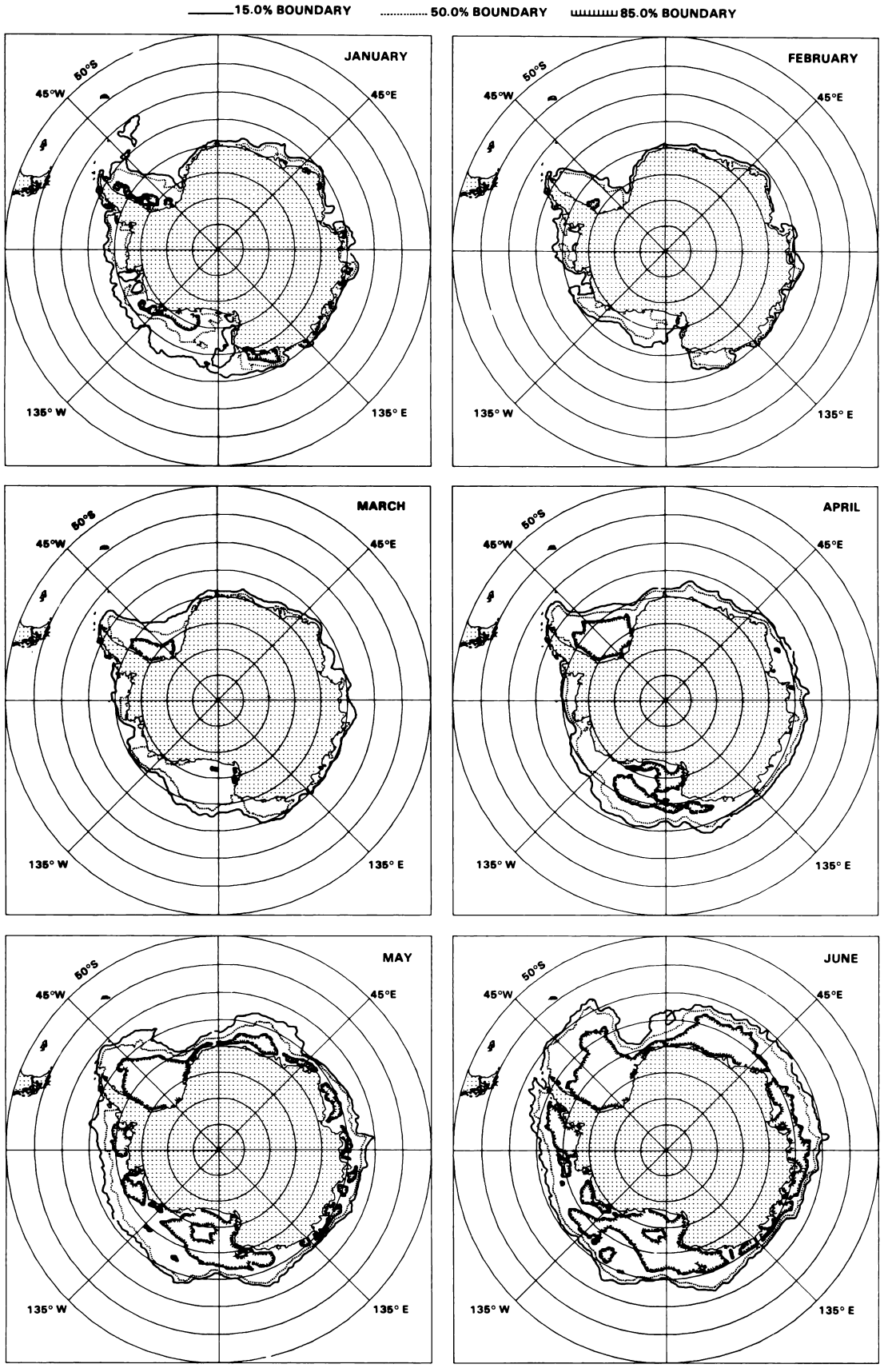

Figure B-10a. Mean monthly ice concentration contours for January through June 1976.

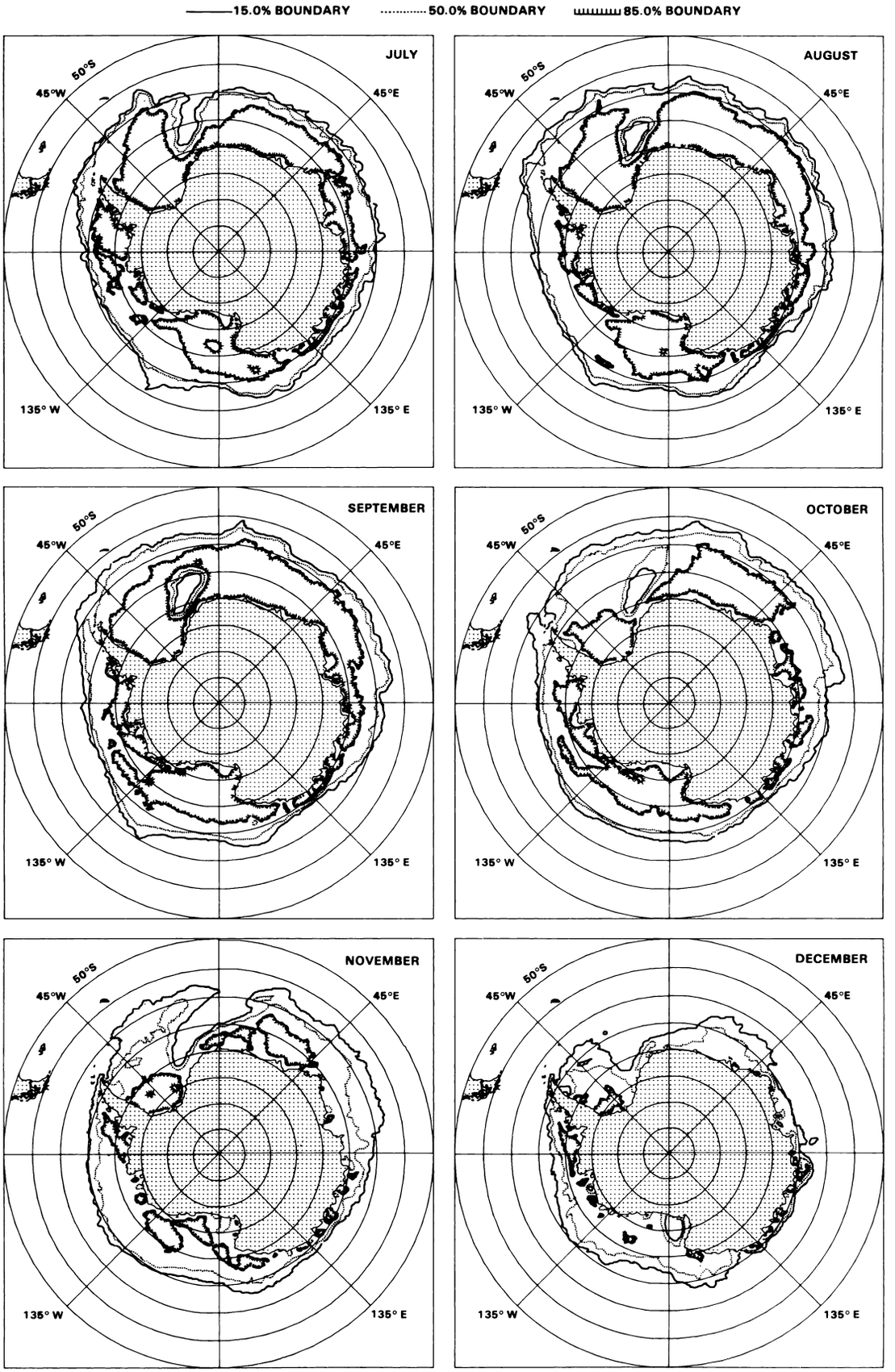

Figure B-10b. Mean monthly ice concentration contours for July through December 1976.

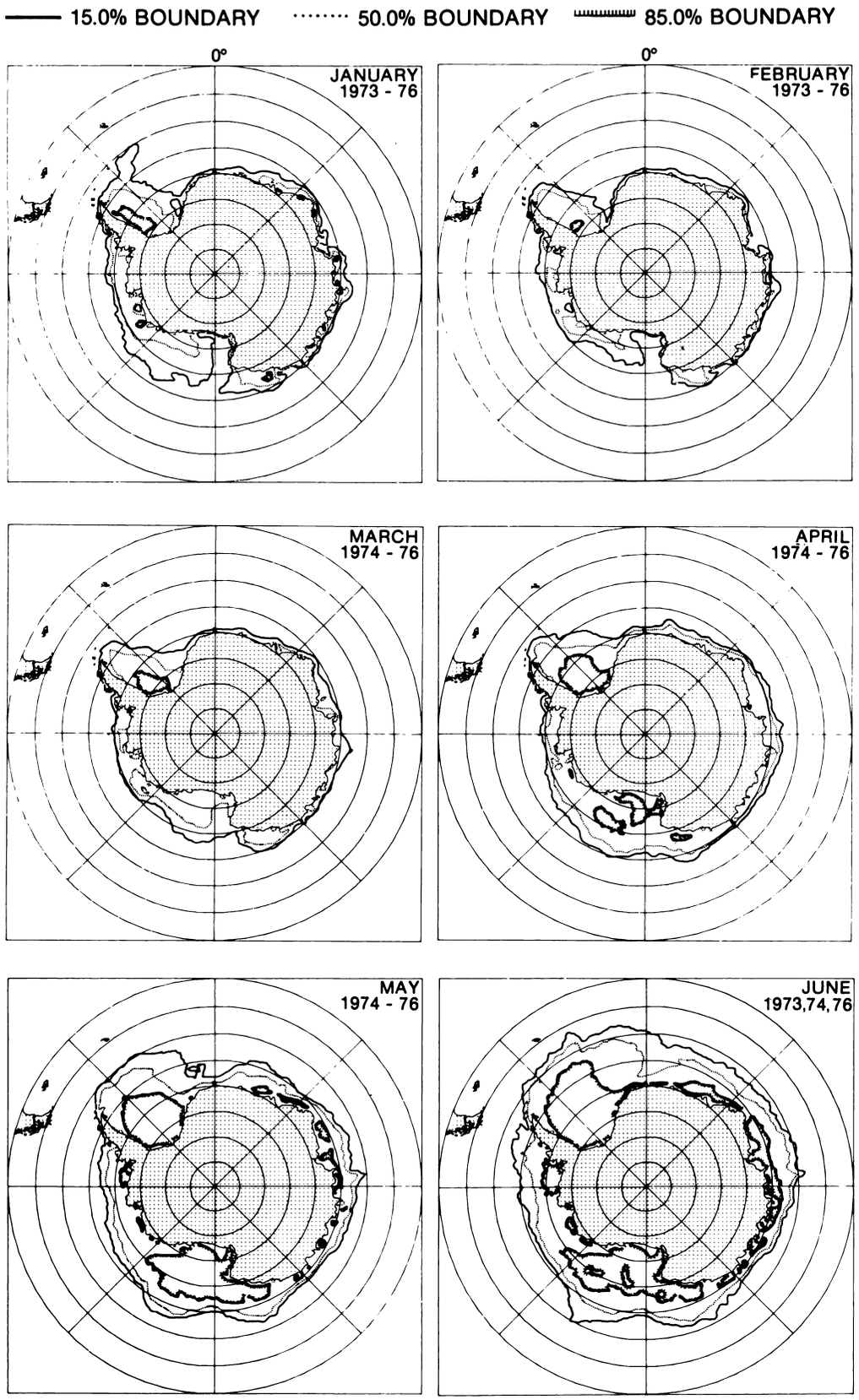

Figure B-11a. Mean monthly ice concentration contours for January through June, averaged for the years indicated.

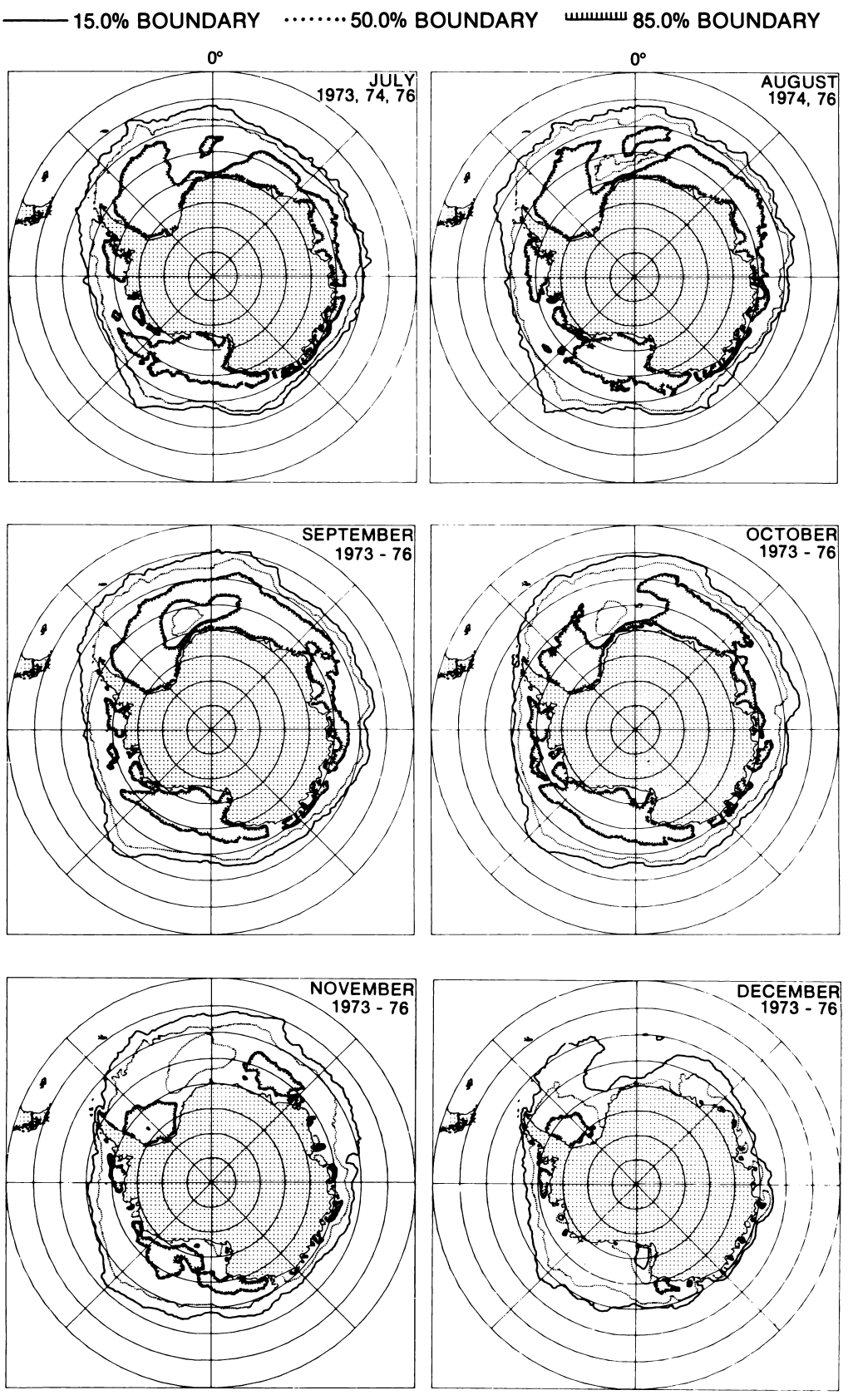

Figure B-11b. Mean monthly ice concentration contours for July through December, averaged for the years indicated.

APPENDIX C

AREAL DISTRIBUTIONS OF ICE CONCENTRATIONS

The most important assumptions for the method used to extract ice concentration from the microwave data, as described in Chapter 3 of the main text, are the approximately constant values of the ocean brightness temperature (135 K) and the sea ice emissivity (0.92) in the Southern Hemisphere (Wilheit, 1972, and Comiso and Zwally, 1980). The climatological surface air temperatures are used to adjust for the spatial variation of the brightness temperature of the ice with physical temperature. However, it is the indirect use of the fact that the ice concentration is zero in ocean areas beyond the edge of the ice pack and 100 percent or less within the ice pack during winter that simplifies extraction of ice concentration. The use of the 0- and 100-percent ice concentration areas as reference points also makes the accuracy of the inferred results almost independent of the existence of an absolute calibration of the instrument.

To show the overall effectiveness of the procedure, area distributions are obtained from the sea ice concentration maps shown in Chapters 4 and 5 of the main text, examples of which are presented in Figures C-1 through C-6. Figures C-1a and C-1b are obtained from the 4-year monthly maps and show the seasonal progression of the distribution in one complete yearly cycle. The area distributions show a huge enhancement at about the 0-percent ice concentration for every month, representing the large ocean area in the maps not covered by ice. In the 20- to 60-percent ice concentration interval, the distribution is remarkably close to constant every month. In the 60- to 100-percent ice concentration region, the large seasonal variation of the ice is clearly evident with minima in February and maxima in September. From June to October, the maximum ice concentration is about 100 percent, which is consistent with the existence of consolidated ice during that period.

Figures C-2 and C-3 show interannual comparisons of the areal distribution of ice concentration during the 4 years for January, April, July, and October. Significant year-to-year variation is clearly evident in the distributions. The January distributions reflect the fact that ice recedes faster in some years than in other years. In April, July, and October, the shape and size of the 60- to 100-percent ice concentration distributions also vary substantially. These variations in areal coverage were quantified and discussed in Chapter 5 of the main text.

A year-to-year comparison of the areal distribution on a sector-by-sector basis and for the southern ocean as a whole is shown in Figures C-4 through C-6 for September. In the Indian Ocean sector, there is a remarkable similarity in the shape of the distributions for all years, with 1976 showing the most enhanced distribution in the 80- to 100-percent interval. The Pacific Ocean sector also shows similar distributions for all years. In the Ross Sea sector, there are two enhancements at about the same points in 1973 and 1974; only one but broader in 1975; and also two but both narrower in 1976. In the Bellingshausen-Amundsen Seas and Weddell Sea sectors, the size and shape of the distributions are also different from year to year.

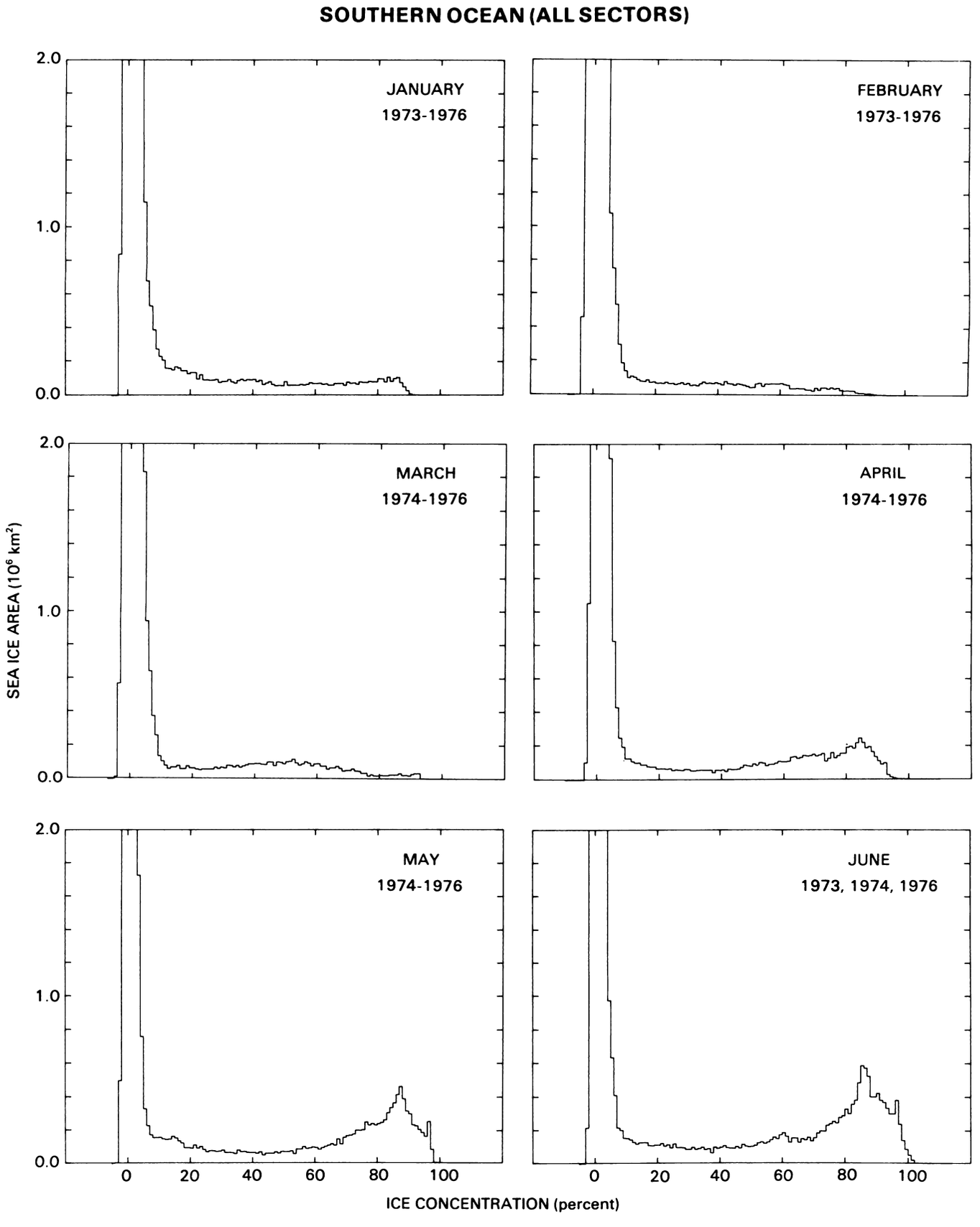

Figure C-1a. Areal distribution of percentage ice concentration in all sectors from January to June (1973-1976).

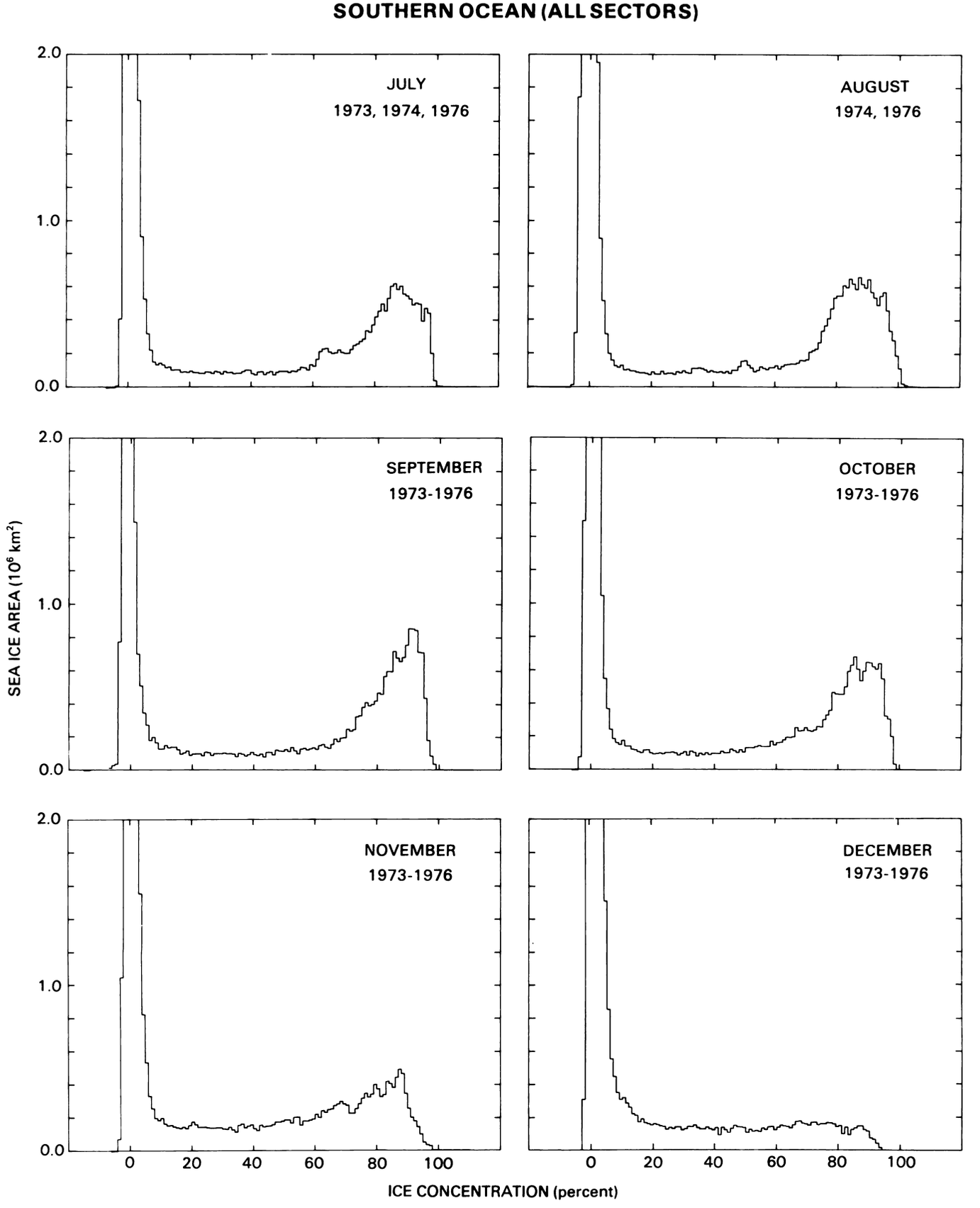

Figure C-1b. Areal distribution of percentage ice concentration in all sectors from July to December (1973-1976).

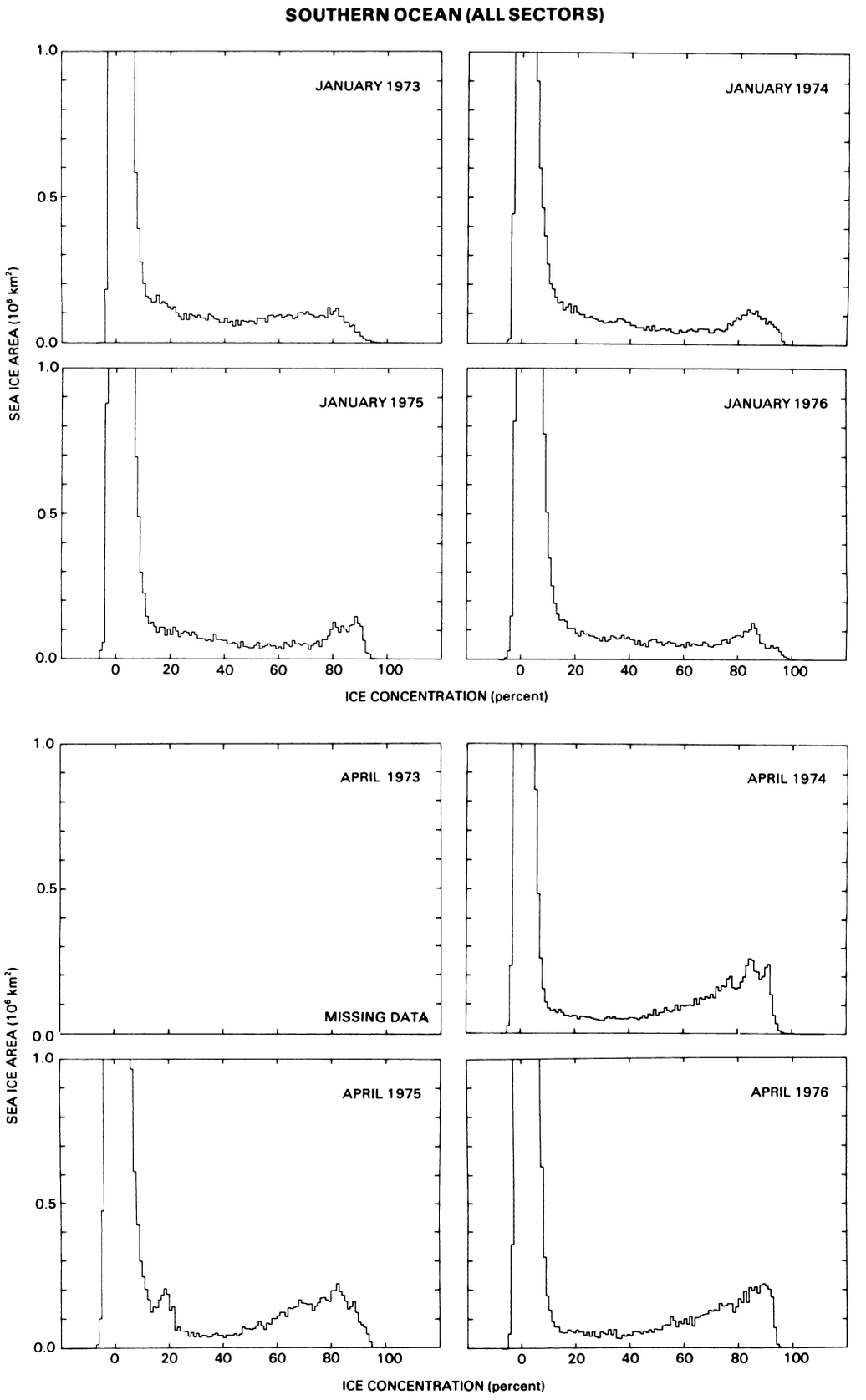

Figure C-2. Year-to-year comparison of areal distribution of percentage ice concentration in all sectors for January and April.

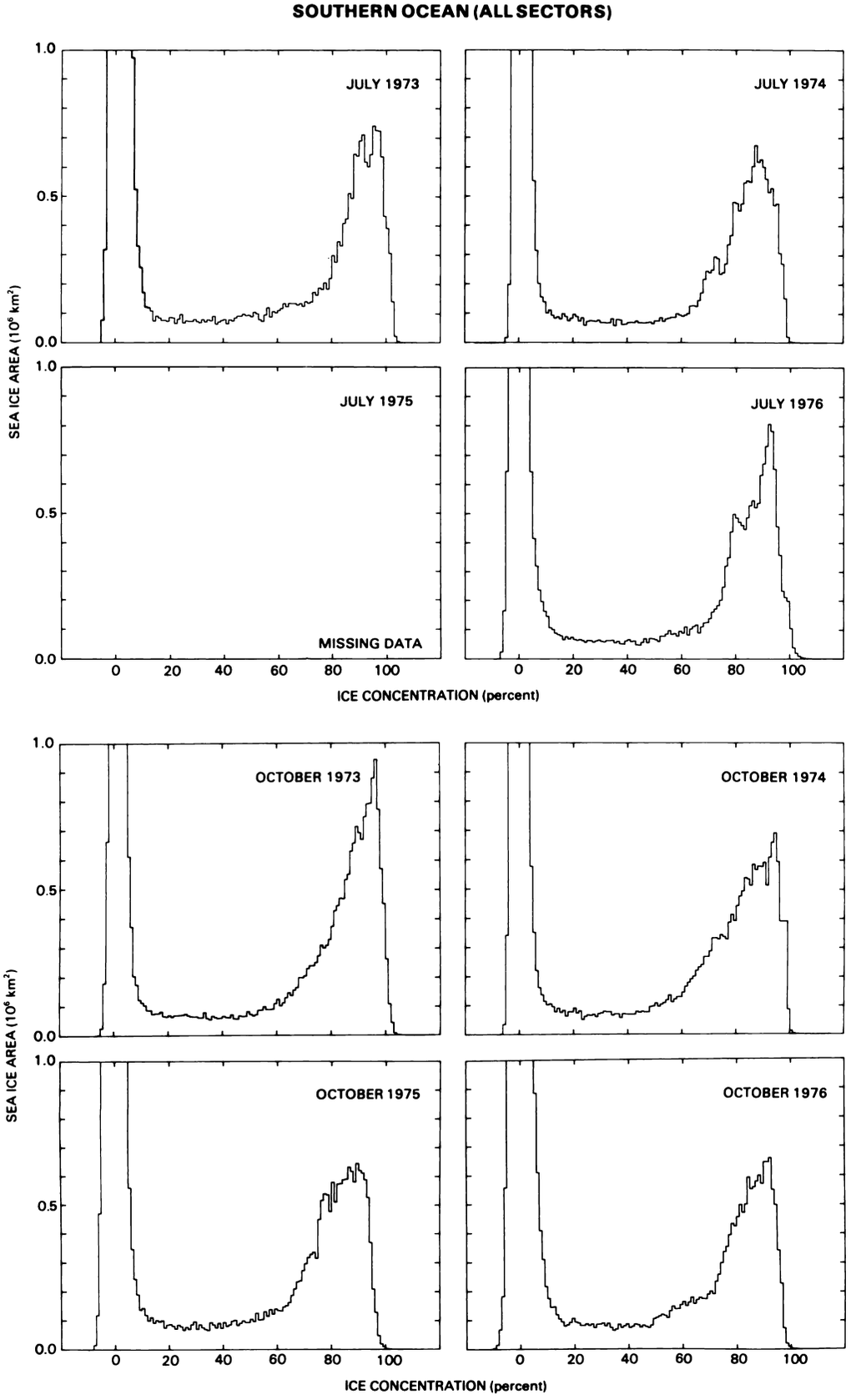

Figure C-3. Year-to-year comparison of areal distribution of percentage ice concentration in all sectors for July and October.

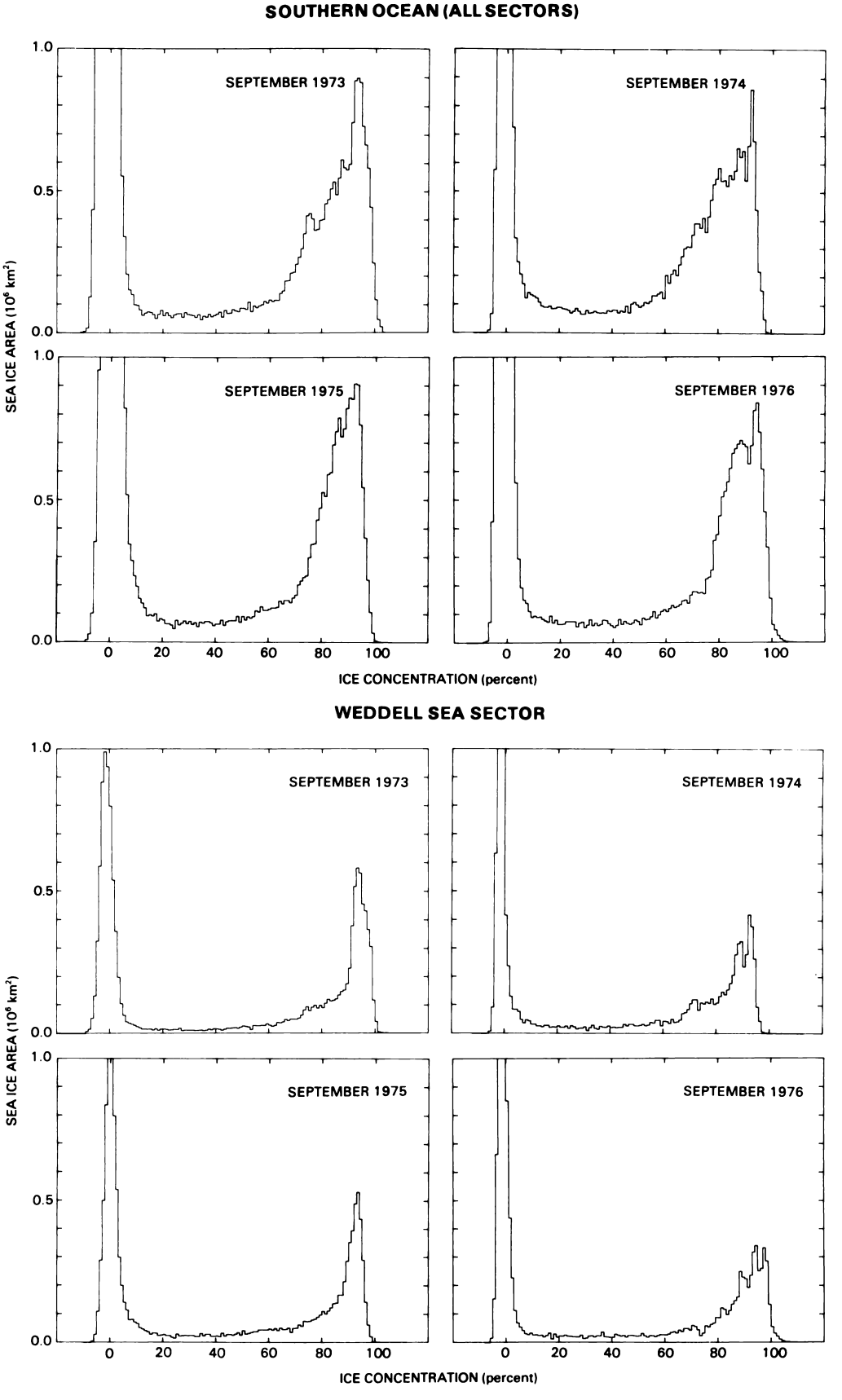

Figure C-4. Year-to-year comparison of areal distribution of percentage ice concentration in all sectors and the Weddell Sea sector for September.

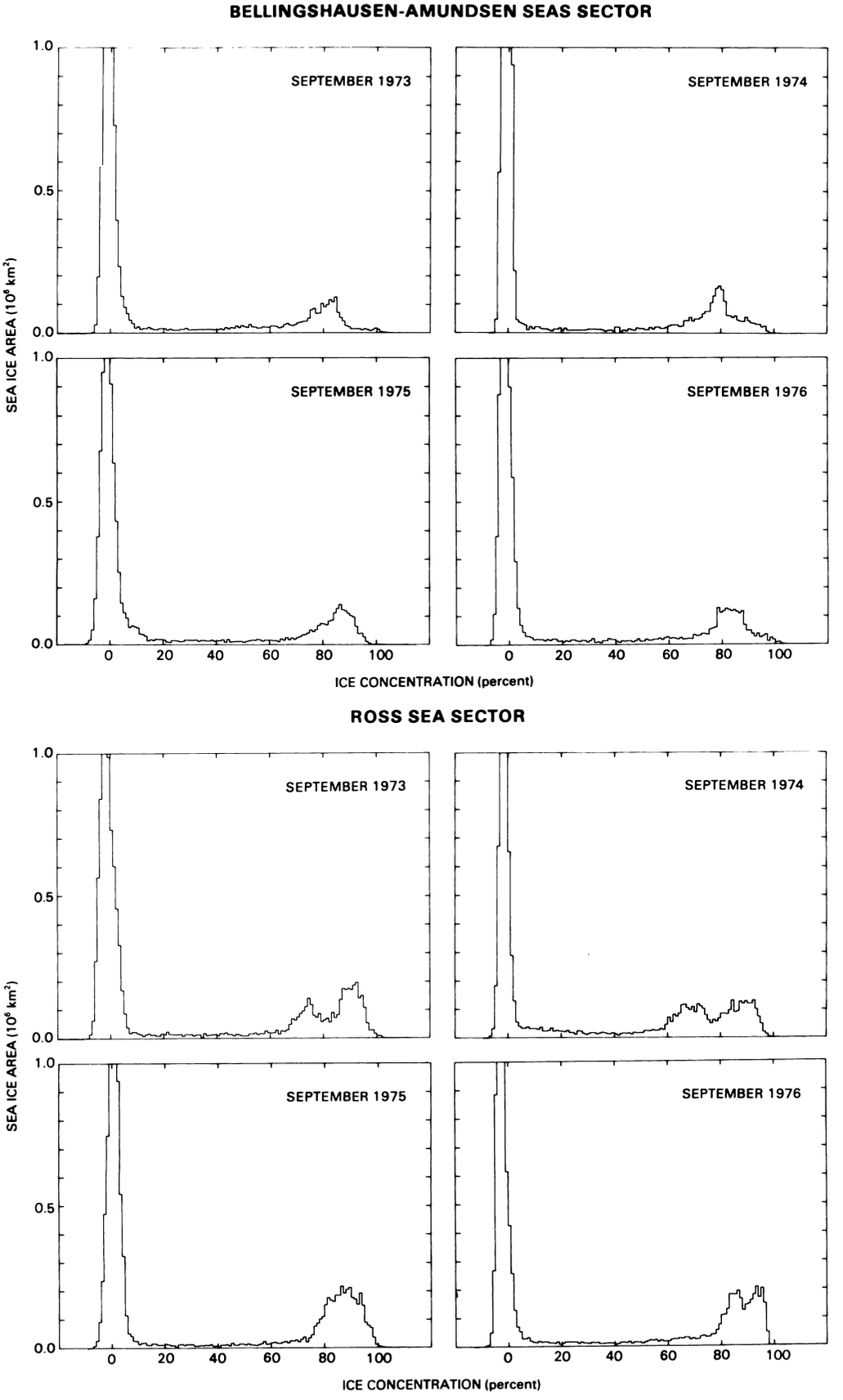

Figure C-5. Year-to-year comparison of areal distribution of percentage ice concentration in the Bellingshausen-Amundsen Seas and the Ross Sea sectors for September.

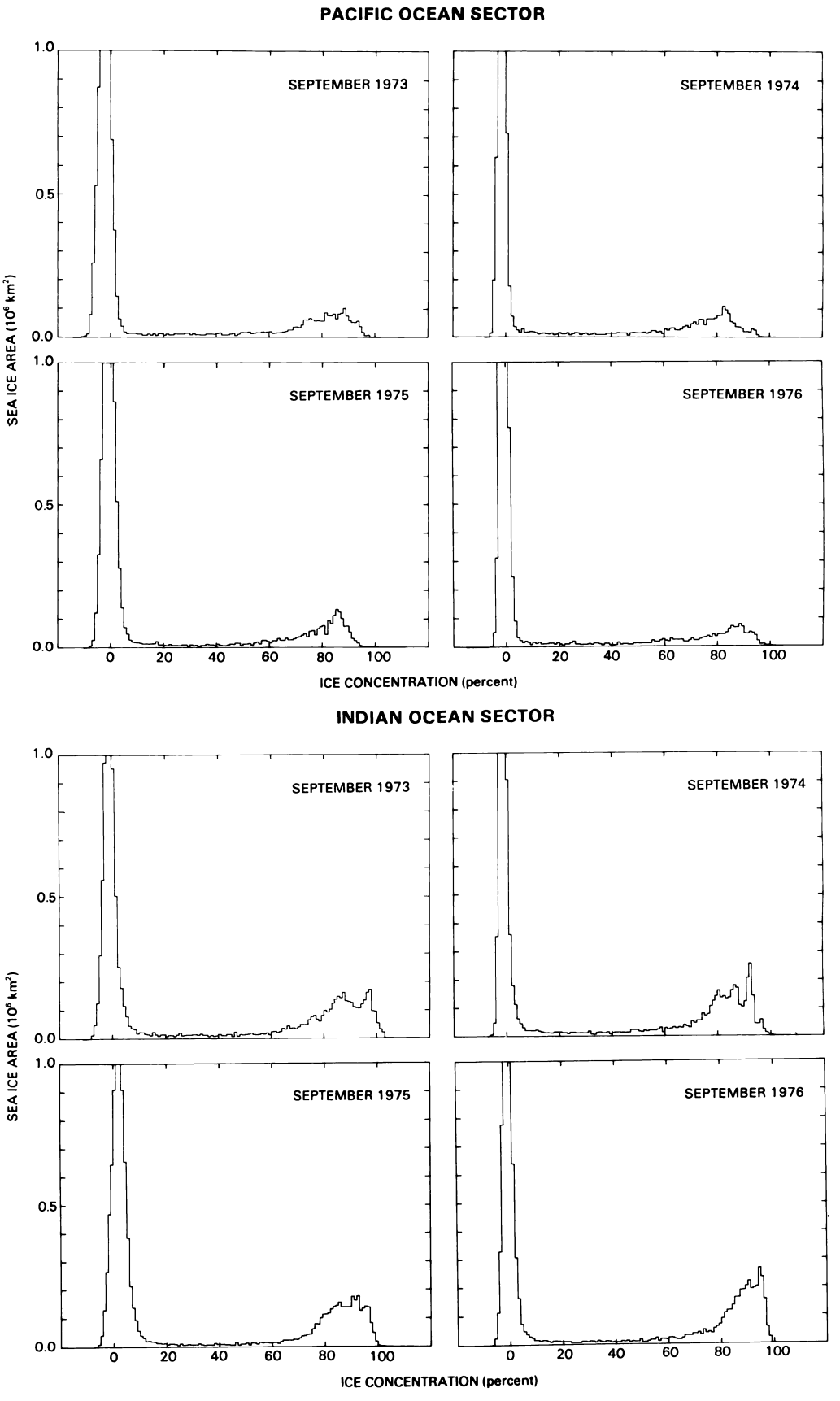

Figure C-6. Year-to-year comparison of areal distribution of percentage ice concentration in the Pacific Ocean and the Indian Ocean sectors for September.

The errors discussed in Chapter 3 of the main text can be better understood by examining some of these distributions. For example, the existence of secondary peaks near 80-percent ice concentration in the Bellingshausen-Amundsen Seas in winter, as in Figure C-5, most likely indicates the presence of desalinated or Arctic-type multiyear ice. In addition, the highest ice concentration level is not consistently the same from year to year or from sector to sector, indicating perhaps the limitation in the use of the simplified time-independent algorithm to extract physical temperature from climatological air temperature data or in the assumption that the ice has constant emissivity. However, the distributions show overall consistency. The ocean distributions are, for example, very consistent, and the variations at the high ice concentration levels are well within the estimated error.

REFERENCES

Comiso, J. C., and H. J. Zwally, Corrections for anomalous time dependent shifts in the brightness temperature from Nimbus 5 ESMR, NASA TM-82055, Greenbelt, Maryland, 18 pp., 1980.

Wilheit, T. T., The Electrically Scanning Microwave Radiometer (ESMR) experiment, in *Nimbus 5 User's Guide*, NASA/Goddard Space Flight Center, Greenbelt, Maryland, 59-105, 1972.

INDEX